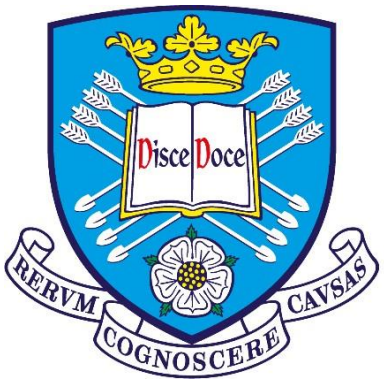

The University Of Sheffield.

Synthesis and Studies on Novel Luminescent Ir(III) Complexes that Interact with Biomolecules

Stephen Opeyemi Aderinto

A Thesis Submitted for the Degree of Doctor of Philosophy of the University of Sheffield

October 2022

Abstract

The syntheses of three novel iridium(III) polypyridyl complexes have been investigated as a potential route to obtain DNA imaging probes and diagnostic agents. The reported metal complexes are: $[Ir(bpy)_2(qtpy)]^{3+}$ **1**, $[Ir(phen)_2(qtpy)]^{3+}$ **2**, $[Ir(dppz)_2(qtpy)]^{3+}$ **3** (where bpy = 2,2'-bipyridine, phen = 1,10-phenanthroline, dppz = dipyrido[3:2- *a*:2',3'-*c*]phenazine and qtpy = 2,2':4,4'':4',4'''-quaterpyridine). This library of isostructural complexes varies in steric and charge properties. Particular attention has been devoted to qtpy, as this was chosen as the bridging ligand. The qtpy ligand can bind to a metal centre through a bidentate diimine site and to two other metal centres through two monodentate imine sites. All the complexes were obtained through a microwave-assisted synthesis as conventional reflux heating proved abortive to afford the complexes. Single X-ray crystallography afforded the crystal structures of 15 precursors used in the synthesis of the eventual title complexes.

Photophysical studies show that the complexes exhibit highly tunable emission, with their triplet state metal-to-ligand (^{3}MLCT) charge-transfer bands extending up to ~500nm. Moreover, luminescence lifetimes measurements show that the three complexes possess long-lived average lifetimes of around ~4–5ns. Luminescent DNA-binding investigations demonstrate the complexes bind to DNA with binding affinities ~ $10^4 M^{-1}$. Contrary to their ruthenium(II)-based analogues, DNA "light-switch" behaviour is not observed upon interaction with duplex DNA; instead, a massive luminescence attenuation occurs. The complexes also produce singlet oxygen to varying extents, up to 71%, as in the case of the dppz complex. The complexes equally binded non-canonical G-quadruplex DNA (human telomeric sequence), with luminescence quenching observed for both Complexes **1** and **2** and luminescence enhancement observed for Complex **3**. Follow up titrations with guanosine-5'-monophosphate (5'-GMP) and adenosine 5'-monophosphate (5'-AMP) showed redox quenching, with consequent luminescence decrease observed in both cases, even though this was more pronounced in the case of 5'-GMP additions. The photocleavage activities of these complexes were investigated using supercoiled plasmid DNA, with Complex **1** (the representative complex selected) cleaving plasmid DNA by producing scissions in the supercoiled structure. The investigated compounds also have a protein target and in fact, are bound to both bovine serum albumin (BSA) and human serum albumin (HSA). The binding interactions were further evidenced by circular dichroism spectroscopic experiments. Molecular docking studies showed that the complexes are true Warfarin site (Sudlow Site I)

binders.

The concluding part of this thesis focuses on the cytotoxicity studies of the complexes. Research attention has been drawn to this area because metal complexes are significantly advantageous as luminescent DNA probes. Cell viability studies of the complexes towards human oral squamous cell carcinoma (H357) demonstrated no or low cytotoxic activity for Complexes **1** and **2**, whereas Complex **3** is particularly selective and potent towards H357 cancer cells.

The work described in this thesis has successfully established novel iridium complexes and reported their duplex and G-quadruplex DNA- and protein-binding interactions and preliminary cellular studies.

Declaration

This thesis is the author's original work, except where specific references are made to other sources. In whole or in part, it has not been submitted to any other degree programme.

Stephen O Aderinto.

October 2022.

Acknowledgements

I thank my supervisor, Professor Jim A Thomas, for affording me the opportunity to undertake my doctoral project under his supervision and especially for his supportive attitude over the past couple of years. My feelings during my time at the University of Sheffield can best be described as “ecstatic”. The research environment you have created is incredibly supportive. Thank you so much for that. I equally greatly thank the University of Sheffield’s Doctoral Academy for having provided the funding to conduct my research. To all the past and present Thomas group members that I met Hawazin, Simon, Fliss, Kirsty, Charlotte, and Shahryar, and several other master’s students, I am expressing my gratitude for all your help. I especially thank Simon for his invaluable guidance at the start of my research. Hawazin’s many kindnesses in buying me some lab chemicals are much appreciated. All the other members of the Thomas group are equally valued for creating a positive, enjoyable atmosphere for me to work in.

The success of this thesis work is partly because of the collaborations developed, and I want to appreciate everyone who has been a part of such. My friend, Abdulmujeeb Onawole, is much appreciated for his assistance on density functional theory (DFT) calculations and molecular docking studies, Raphael Galleh, for his efforts on cytotoxicity assays, and Mohammed Obeis for his additional works on computational studies. Also, Arthur Graf and Alex Auty of the Weinstein Group for their help with laser pulse facilities for singlet oxygen yield and transient absorption spectroscopic measurements.

I will not forget to mention the enormous support received from the department’s technical staff. You are indeed the lifeblood of the department, as research will not progress successfully without you. In this respect, I thank Craig Robertson, Keith Owen, Rob Hanson, Sharon Sprey, and Yusuf Mohammed, especially for their many supports in X-ray crystallography, high-performance liquid chromatography (HPLC), microwave apparatus, and mass spectrometry. You contributed a lot to my research beyond what you could imagine. The administrative assistance of Nick Smith, Denise ED Richards, Elaine Frary, and Louise Brown-Leng is equally greatly valued and appreciated.

The author acknowledges inspiration provided by the Canadian Chemical Crystallography Workshop (CCCW21), which he attended between August 8th – 11th, 2021, which provided some of the methods used in growing the crystals described in this chapter. Equally, the viva team made up of Prof. Julia Weinstein and Dr Martin Gill is appreciated.

Finally, I would like to appreciate my family and friends. Despite being away from home for almost a decade, your encouragement have kept me going. My sincere gratitude goes out to all my friends worldwide for their support.

Contents

1.0 Introduction

1.1 Deoxyribonucleic acid (DNA)

The study of deoxyribonucleic acid (DNA) and its central function in the "central dogma of life or of molecular biology," as first conceptualised by Francis Crick in 1958, is crucial to understanding life at the minutest level. DNA is life's genetic carrier. It stores an organism's genetic information in the form of four distinct building blocks, which determines the characteristics of all living things existing on earth. The retention of such information in eukaryotic cells occurs primarily in the nucleus, with a small amount in the mitochondria, whilst it occurs in prokaryotic cells as a nucleoid structure and plasmids. The recent few years have seen the study of the mechanisms of DNA functions in the cell cycle, including replication and transcription[1–2] (Fig. 1.1). The "central dogma of life or of molecular biology", as earlier mentioned, refers to the process of DNA transcription (into RNA), translation (into amino acid chains), and replication.[3]

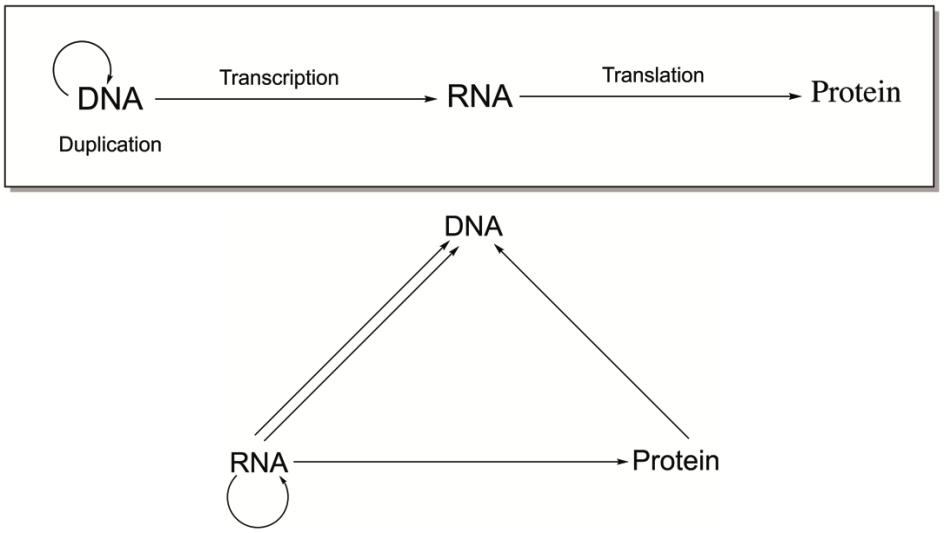

Figure 1.1 – (a): The Central Dogma as postulated by Watson in 1965; **(b):** The situation as proposed by Crick in 1958.[3]

This fantastic piece of work on the structural elucidation of the double-stranded (ds), double-helical structure of DNA by Watson and Crick constituted one of the seminal scientific breakthroughs of the 20th Century, which eventually earned them the much-coveted Nobel Prize in the category of Physiology/Medicine.[4]

1.2 DNA Conformation (The Complementary Structure of DNA) and DNA Major and Minor Grooves

In all cellular life and even in many viruses, DNA is undoubtedly the carrier of genetic information[1]. Although the X-ray crystallographic studies on DNA (both A- and B- forms) have already been put forward by Rosalind Franklin[5–6], it was James Watson and Francis Crick (rather than Franklin) who first formulated the structural description of DNA (referred to as the "Watson-Crick model") in 1953.[7–9] DNA structure consists of a very long chain, the backbone of which is made up of alternate sugar and phosphate groups that are connected by regular 3',5'-phosphate di-ester linkages[10] (Fig. 1.2). There are four nitrogenous bases attached to each sugar in DNA, though they are still further subdivided into two classes.[11] Two of these, adenine (A) and guanine (G) are purines, and the other two, thymine (T) and cytosine (C), are pyrimidines.[12–13] These pairs of sugars, referred to as "complementary strands", are connected together by hydrogen bonds (Figs. 1.3 and 1.4), leading to the formation of GC and AT base pairs. The existence of complementary base pairing is contingent upon the strands running anti-parallel to each other and keeping the backbones at an almost constant width.[14–15] In DNA, apart from hydrogen bonding, other interactions exist - such run parallel to DNA contrastingly to hydrogen bonding that runs perpendicular to DNA.[16] A fifth base, 5-methylcytosine, occurs in smaller amounts in certain organisms, and a 6th base, 5-hydroxy-methylcytosine, is found instead of cytosine in the T even phages. Although the structure of DNA in various cellular organisms can differ, the right-handed, double-helix B-DNA, described by Watson and Crick, is the most prevalent.[15]

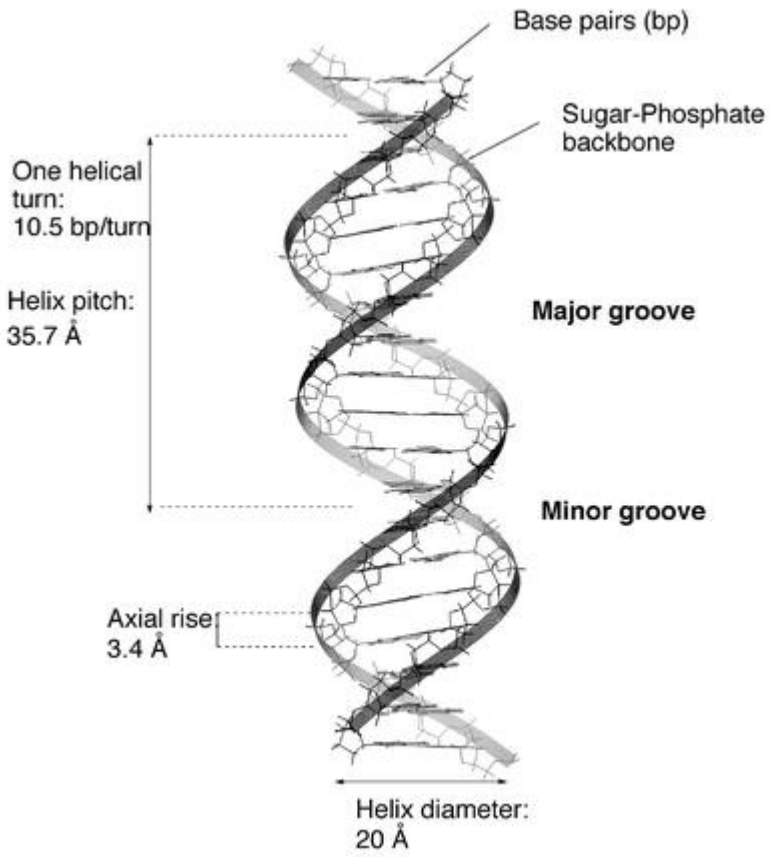

Figure 1.2 – Schematic representation of the structural parameters of the B-DNA double helix.[15]

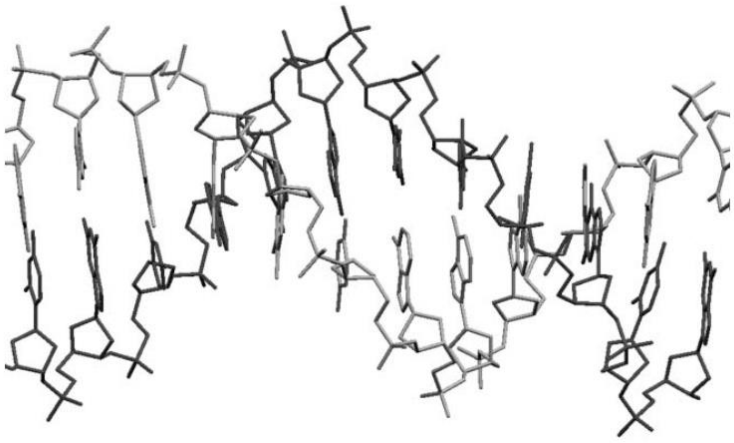

Figure 1.3 – The (Watson–Crick) double-helical structure of B-DNA.[4]

The helical strands of the DNA structure exhibit two grooves diagonally running through them - the major and minor grooves (Fig. 1.4). The grooves exhibit varying sizes with the major groove being the wider groove (12Å) and the minor groove (6Å) being the shorter groove. In these two grooves, the edges of the bases are exposed at the DNA surface, thereby providing sites where protein and/or small molecules can interact or read the DNA code.[15, 17]

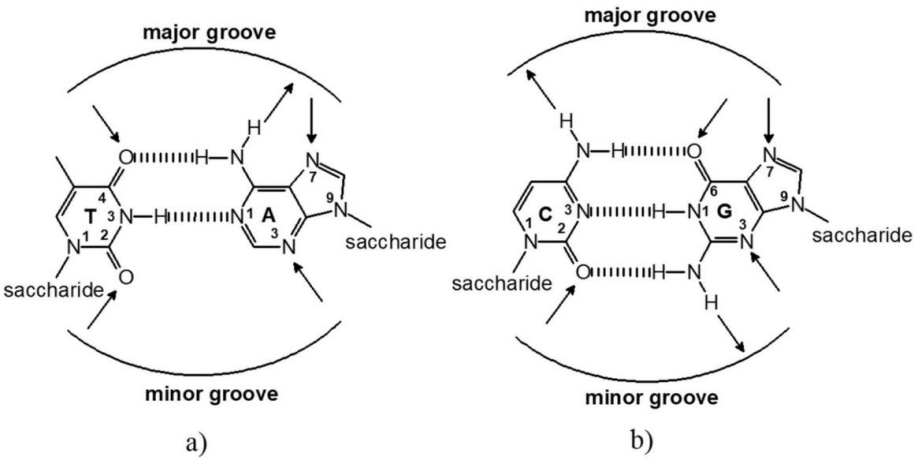

Figure 1.4 – H-bond donor and acceptor sites in DNA major and minor grooves.[18] Original article: see Reference 19.

1.3 Duplex DNA Conformations

Three known, main possible conformations of native DNA duplex have been recognised: A-DNA, B-DNA, and Z-DNA. However, only Z-DNA exists as a left-handed helix whilst the other two, A-DNA and B-DNA, are present as right-handed helices.[20–22] As postulated by Watson and Crick, DNA exists most commonly as the B-DNA. The three DNA conformations are markedly different, and based on diameter, size, helical orientation and shape of the grooves, some notable differences between these DNA forms have been identified as delineated in Table 1.1.

Table 1.1 – Distinguishing structural features of A-DNA, B-DNA, and Z-DNA.

Property	A-DNA	B-DNA	Z-DNA
Helix handedness	Right	Right	Left
Repeating Unit	1 base pair	1 base pair	2 base pair
Diameter	ca. 23 Å	ca. 20 Å	ca. 18 Å
Rotation per base pair	33 º	36 º	30 º
Base pairs per turn	11	10.5	11.6
Helix rise per base pair	2.6 Å	3.4 Å	3.7 Å
Sugar pucker	C3’ endo	C2’ endo	C2’ endo at C C3’ endo at G
Major groove	Narrow and deep	Wide and deep	Narrow and deep

Minor groove	Wide and shallow	Narrow and deep	Narrow and deep

1.4 Non-canonical DNA Conformations

The binding of DNA with non-duplex (i.e., non-canonical) conformations has been demonstrated by many studies as equally feasible. Triplex forming oligos, hairpins and cruciforms, intercalating motif (or i-motif) structures, and G-quadruplex structures are examples of such structures.[23] An overview of the G-quadruplex DNA is given here as the author uses this structure for his DNA-binding investigations in addition to the conventional canonical duplex B-DNA (an in-depth discussion of DNA binding investigations is given in a later chapter of this thesis).

1.4.1 G-quadruplex DNA

G-quadruplexes (G4s) are structures formed from four-stranded guanine-rich nucleic acids. Any single-stranded (ss) DNA sequence comprising four stretches of three or more consecutive guanines that fold through Hoogsteen hydrogen bonding between guanines from each of the runs can lead to a G-quadruplex structure. These interactions can be stabilised further by monovalent cations such as Na^+ and K^+.[24] G4-forming sequences are highly abundant, and can fold into stable structures in human cells, leading to ca. 716, 310 unique G-quadruplexes detected within the human genome.[25] The stability of G-quadruplex could be enhanced by small molecules, which can then disrupt DNA replication and RNA transcription by the stalling of the polymerases.[26–28]

G-quadruplex structures (Fig. 1.5) have been demonstrated to have potential roles in many biological processes as it is involved in the modulation of gene expression, epigenetics, nucleating of DNA replication, and genetic disease.[29–31] The high volume of research into these non-canonical structures, including telomeres and single-stranded telomere sequences located at the end of chromosomes that can fold to form quadruplexes, is a validity of the biological interest in these structures. Telomeres are involved in cell division, with cell division often leading to the shortening of the telomere sequence. Cell immortalisation, a highly prevalent phenomenon in cancer cells, is a consequence of telomere length maintenance. Efficient

methods to facilitate telomere attrition in cancer cells by stabilising G-quadruplex structures is, therefore, a viable area of research.[32–33]

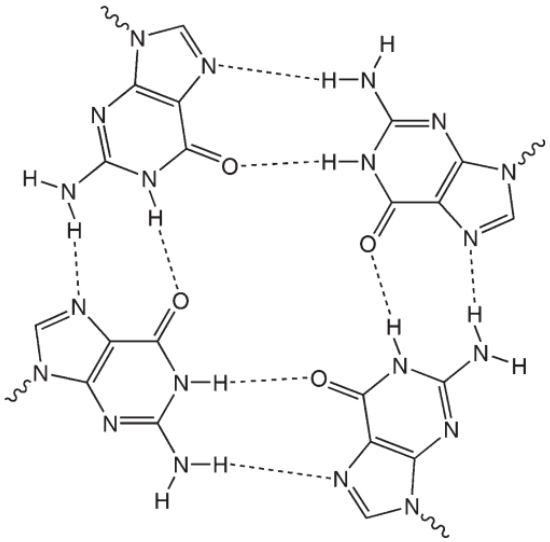

Figure 1.5 – Guanine tetramers - the basis for quadruplex formation.[34–36]

1.5 DNA Binding Mechanisms

DNA recognition dates to the 1960s and has burgeoned over the decades. DNA's double-helical structure provides a variety of sites for a metal complex to bind it through different modes. Covalent bonds can be formed between metals and Lewis's phosphodiester backbones or nitrogen sites on bases. Metal complexes with planar, aromatic ligands are capable of binding via intercalation between adjacent base pairs, or through the insertion of the molecule at mismatched or abasic sites, both of which are dependent on π-π interactions between the ligand and DNA π-stack. The complexes can also bind to the major or minor groove of the double helix depending on size, shape, and ability to form hydrogen bonds. In certain instances, the electrostatic attraction of metal complexes with cationic charges may also strengthen their binding to DNA.

1.5.1 Irreversible (Covalent) Binding

Non-specific covalent binding proceeds via the formation of coordination bonds with either the phosphodiester backbone or the sugar residues of the DNA helix. Irreversible binding can influence transcription processes, which usually is implicated in cell death or gene expression alteration.[37] DNA-irreversible-binding drug molecules can attach to sites either within the same

strand (intrastrand) or crosslink from a base on one strand to a base on the complementary strand.[38] *Cis*-diamminedichloroplatinum (II) (CDDP), or more commonly, cisplatin (Fig. 1.6), which is the most famous anticancer drug on the world healthcare market, is an example of an irreversible binding molecule. It has been proven effective for the treatment of testicular, ovarian, bladder, lung, and stomach cancers. It forms intrastrand bonds with the DNA helix, doing so on the N-7 atom of guanine base or adenine base. The chemotherapeutic effect is not always demonstrated by all irreversibly bound molecules as is with the case of the trans-isomer of cisplatin.[39] The crystal structure of duplex DNA harbouring the cisplatin 1,2-{$Pt(NH_3)_2$}$^{2+}$-d(GpG) cross-link at 1.77 Å resolution has been given by Stephen Lippard and colleagues (Fig. 1.6).[40]

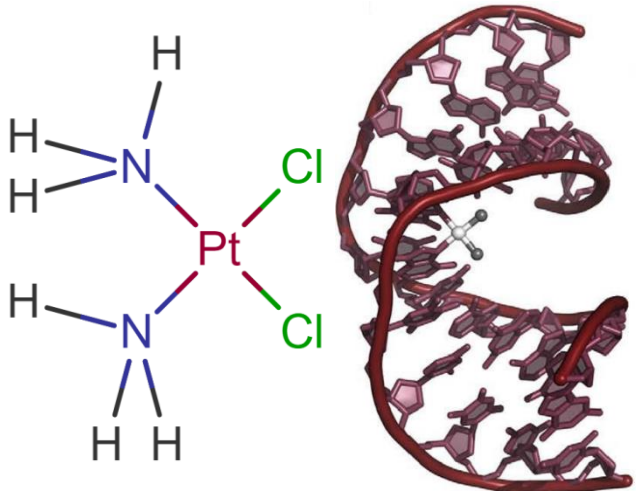

Figure 1.6 – left: the present drugs used in cancer treatment depend heavily, almost exclusively, on platinum(II) complexes, the commonest being the Federal Drug Agency-approved cisplatin, $[PtCl(H_2O)(NH_3)_2]^{+}$[41]; **right:** overall structure of duplex DNA containing a cisplatin cross-link (shown in white/grey).[40]

1.5.2 Reversible Binding

The interaction of many chemical species including water, metal ions and their complexes, proteins, and small molecules with DNA proceeds via reversible binding.[12] These chemical species comprise many anticancer, antibiotic, and antiviral drugs, whose biological effects on nucleic acids proceed by reversible interactions. Reversible binding interactions can occur in three primary modes[18–19, 42] viz.:

1. Electrostatic interaction.
2. Groove binding interaction.
3. Intercalation.

1.5.3 Electrostatic Interaction

Under physiological conditions, the DNA biomolecule is present in the form of a polyanion owing to the negatively charged phosphate groups running along the DNA backbone.[11] This enables cationic molecules to interact with the DNA biopolymer, thus heightening the stability of the DNA conformation. The cations size can span small ions like sodium ion (Na^+) or magnesium ion (Mg^{2+}) to large molecules like polyamines. Typical drugs and/or biomolecules that make use of this type of interaction are spermidine ($H_2N(CH_2)_4NH(CH_2)_3NH$) and spermine ($H_2N(CH_2)_3NH(CH_2)_4NH(CH_2)_3NH_2$), which can undergo protonation to then interact with the negatively-charged DNA phosphate groups readily.[43]

1.5.4 Groove Binding

Major and minor grooves in B-DNA provide suitable binding sites through reversible van der Waals, hydrophobic, and hydrogen bonding interactions. Groove binding, unlike other binding forms, can span multiple base pairs, allowing specific recognition of very long DNA sequences. The hydrogen bonding sites of adenine-thymine (A-T) and guanine-cytosine (G-C) base pairs in the major and minor grooves are delineated in an earlier figure (Fig. 1.4).

While many proteins and oligonucleotide molecules exhibit major groove binding interactions, some proteins and many small molecules will attach to DNA minor groove since this will provide stronger van der Waals contacts. Minor groove binding molecules are usually polyamides incorporating aromatic rings linked by bonds with torsional freedom, so they can twist and assume an isohelical structure with the DNA groove curve. A vast majority of groove binders preferentially bind to AT sequence rather than GC-rich sequence as the groove is narrower in the former sequences, thus enabling van der Waals contact with the groove's walls. A less pronounced binding to GC rich sequences stems from the presence of the N2 amine groups in guanines, which sterically blocks molecules from entering this groove in the GC-rich regions. Noteworthy is the fact that negative electrostatic potentials in AT minor grooves are greater than in GC minor grooves, making cationic molecules to form a stronger bond for AT sequences.[44–46] GC minor groove binding can be increased when the ligands forms hydrogen bonds with the amine group of guanines. Groove binders are usually positively charged, as the charge density of the DNA helix is decreased, thus releasing condensed counter ions. These effects are best illustrated by the interaction of netropsin and distamycin with DNA.[47]

Fig. 1.7 gives the hypothetical model of groove binding.

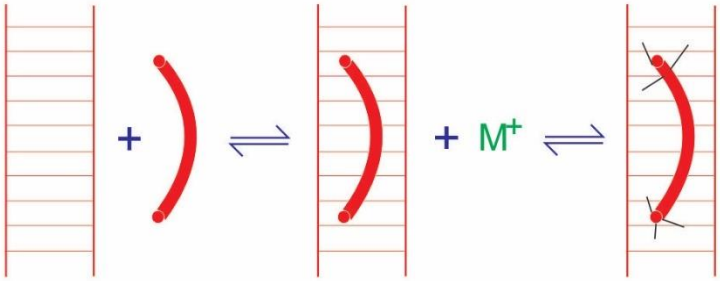

Figure 1.7 – Groove binding hypothetical model.

1.5.5 Intercalation

Intercalation is one of the most common ways that small aromatic molecules recognise DNA. L.S. Lerman in 1960s gave the first proposition of intercalation by demonstrating the great affinity of acridine and proflavine to DNA.[48] Intercalation involves a planar aromatic molecule inserting itself into the open gap (herein referred to as hydrophobic pocket) between the stacked base pairs, leading to the formation of face–face π–π/ π…π interactions with the upper and lower bases. Achieving effective intercalation requires that the accommodating DNA bases be separated by ca. 0.34nm, which corresponds to the van der Waals (vdW) thickness of a phenyl ring.[18] Electrostatic interaction contribute significantly to the binding energy of synthetic intercalators just as is the case with synthetic minor-groove binders. As such, synthetic intercalators are often cationic. Intercalators can insert either from the major or minor groove between the base pairs. Unwinding of DNA contour length occurs when the inter-base-pair separation opens up. The DNA backbone is not flexible enough to permit insertion of drugs into every gap between the bases; rather once one gap is filled, the adjacent ones must remain empty, allowing one drug to be inserted per two gaps at the maximum. This is termed the "neighbour-group exclusion principle." Intercalators are typically employed as DNA stains (most notably ethidium, usually in the form of ethidium bromide) and as well as anticancer agents. Doxorubicin (trade name "Adriamycin" or "Rubex") (Figs. 1.8 and 1.9) is an early example of a drug that acts by intercalation. As a result of the invention of this drug in the 1960s, numerous variants of it have been developed over the years including ethidium bromide, which is now a major nucleic acid stain used in gel electrophoresis (Fig. 1.9).[4] However, many of these drugs suffer severe limitations in terms of lack of specificity and undesirable side effects, making their eventual commercialisation grossly impaired.[49–50]

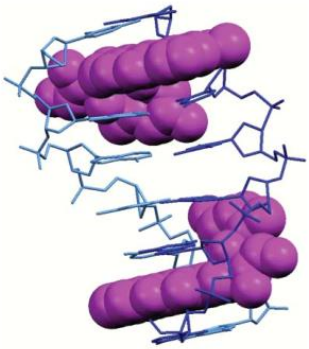

Figure 1.8 – Structure of a DNA oligonucleotide with two doxorubicin drugs intercalated between the base pairs, with insertion from the minor groove side (PDB ref. 1D12).[51]

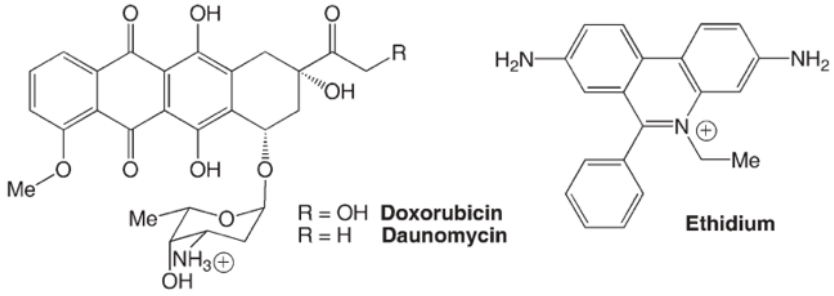

Figure 1.9 – Examples of organic intercalators.

J. B. Chaires have demonstrated intercalation to proceed enthalpically.[47] Its hypothetical model given in Fig. 1.10.

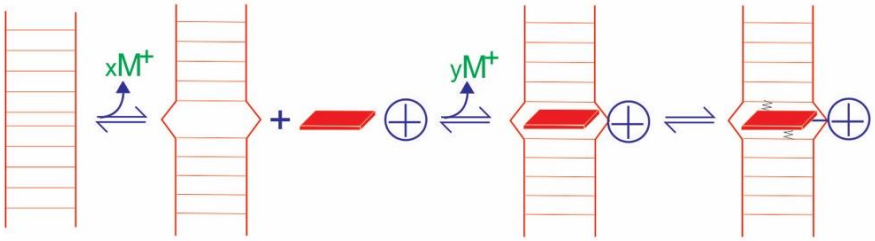

Figure 1.10 – Intercalation hypothetical model.

1.5.5.1 Metallo-intercalators

Metallo-intercalators are metal complexes that houses at least one intercalating ligand. They orient parallel to the base pairs and protrude away from the metal center, and then easily π-stack in the DNA duplex. Then, upon binding, the ligands serve as a stable anchor for the metal complex with respect to the double helix and direct the orientation of the ancillary ligands with

respect to the DNA duplex. Two well-known examples of intercalating ligands are phi (9,10-phenanthrenequinone diimine) and dppz (dipyrido[3,2-*a*:2',3'-*c*]phenazine) (Fig. 1.11).[52] Lerman's first demonstration of ligand intercalation by photophysical studies[48], were advanced by the extensive NMR studies by Barton and co-workers.[53–56] High-resolution crystal structures furnished more detailed structural studies of the intercalative binding mode (Fig.1.12).[57] Metallo-intercalators penetrate the double helix through the major groove, with the intercalating ligand acting as a new base pair. No bases are ejected from the duplex. Furthermore, intercalation results in a doubling of the rise and a widening of the major groove at the binding site. It is noteworthy that intercalative interaction only minimally distorts the DNA structure. Intercalation typically occurs via the major groove even though it is not always so in all situations.[58–59] For instance, NMR studies have shown that metal complexes bearing dpq (dipyrido[2,2-*d*:2',3'-*f*]quinoxaline), a close analogue of dppz with one terminal aromatic ring removed, preferentially binds through the minor groove.[60–62]

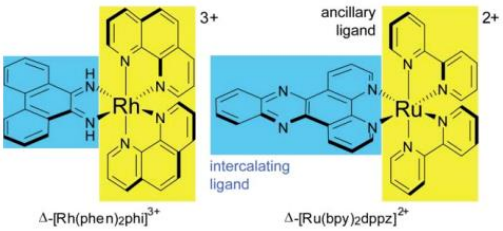

Figure 1.11 – Structures of two common metallo-intercalators: (a) Δ-$[Rh(phen)_2(phi)]^{3+}$ and Δ-$[Ru(bpy)_2(dppz)]^{2+}$. The intercalating ligands are highlighted in blue, the ancillary ligands in yellow.

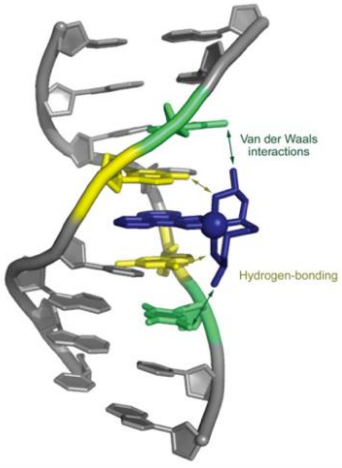

Figure 1.12 – Crystal structure of the metallo-intercalator Δ-α-$[Rh\{(R,R)\text{-}Me_2trien\}(phi)]^{3+}$ bound to its target sequence, 5'-TGCA-3'.

1.5.5.2 Simple Metallo-intercalators

Simple metallo-intercalators (i.e., metallo-intercalators containing only one intercalating unit/ligand) show restricted sequence preference and their π-surfaces tend to interact with just two pairs by their nature. With octahedral metallo-intercalators, additional coligands located in a groove make it possible to introduce groups that make specific contacts with bases above and below the intercalation site, thus allowing extended sequence to be recognised. An example of an intercalating metal complex is the X-ray crystallography-characterised rhodium phi complex developed by Barton and co-workers which was demonstrated as capable of binding to DNA.[57] This is a sterling example of the metallo-intercalator-DNA structures whose crystallographic data is currently available.[59] In the structure, there is an aromatic ligand inserted between the GC and CG base-pairs and the metal and co-ligand sit in the major groove of DNA (Fig. 1.13). The amines of the trien co-ligand form hydrogen-bonds to the guanine O, with further water-mediated H-bonds to the guanine N7 also proposed.

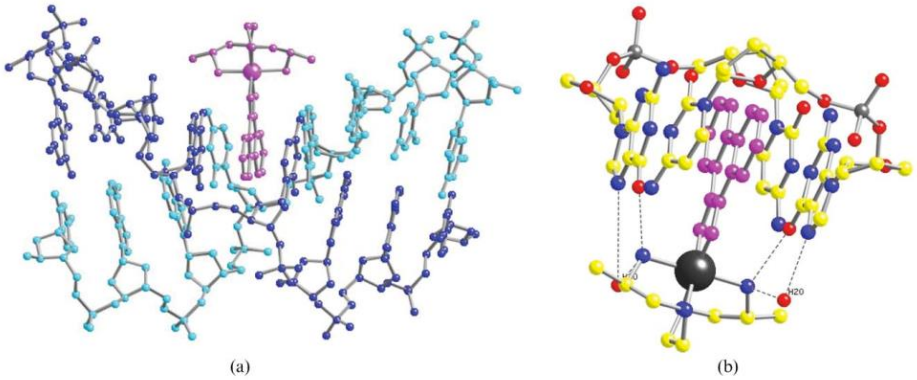

Figure 1.13 – (a) Binding of $[Rh(phi)(Me_2trien)]^{3+}$ (pink) to DNA by intercalation. (b) Close-up illustrating the π-stacking and H-bonding. (PDB ref. 454D).[57]

1.5.5.3 Bis-intercalators and Threading Intercalators

There have also been various reports of bis-intercalators and threading intercalators. Bis-intercalators refer to molecules with two intercalators linked together, and an example of these is given in Figs. 1.14. For some complexes to bind to DNA through intercalation, the point at which the intercalating units are linked must be the same as the point through which they would also typically insert into DNA.[4] This phenomenon is referred to as "threading". An example of threading intercalators is the complex such as $[\Delta,\Delta\text{-}\mu\text{-(bidppz)-(phen)}_4Ru_2]^{4+}$reported by Lincoln and Norden containing two linked $[Ru(phen)_2(dppz)]^{2+}$ motifs (Fig. 1.14).[63] To intercalate, part of this molecule must "thread" through the DNA. For this to happen, an initial

groove-bound non-luminescent state rearranging slowly to form an intercalated emissive state in which one of the bulky $Ru(phen)_2$ moieties has been threaded through the DNA base stack.

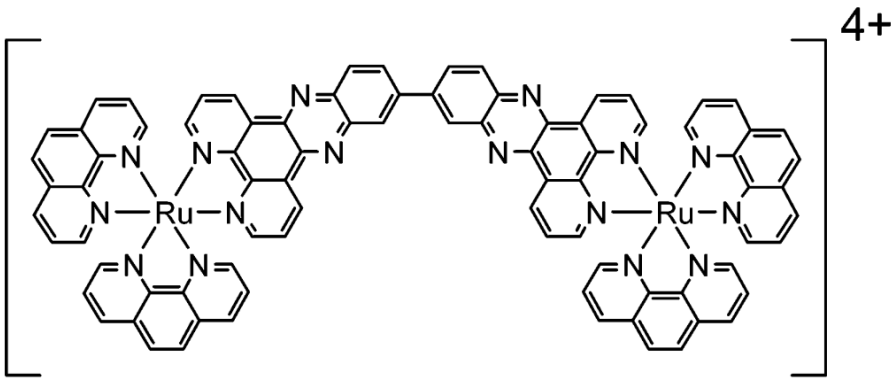

Figure 1.14 – The threading bis-intercalator $[\Delta,\Delta\text{-}\mu\text{-(bidppz)-(phen)}_4Ru_2]^{4+}$ or $[\mu\text{-(11,11'-bidppz)(phen)}_4Ru_2]^{4+}$.

1.5.5.4 Metallo-insertors

It was also L. S. Lerman that first proposed a third non-covalent binding mode referred to as "insertion"[48] According to him, a molecule may bind "a DNA helix with separation and displacement of a base-pair", herein referred to as metallo-insertion. As with metallo-intercalators analogues, metallo-insertors incorporate a planar aromatic ligand that extends into the base-stack upon DNA-binding. Metallo-insertors, however, eject the bases of a single base-pair with their planar ligand acting as a π-stacking replacement in the DNA base stack in contrast to metallo-intercalators that lead to DNA unwinding by an insertion of their planar ligand between two base pairs in their unperturbed positions. Barton and co-workers in their research into mismatch-specific DNA-binding agents reported a family of rhodium complexes that bind DNA via the metallo-insertion modality.[64]

The beauty of the existence of multiple DNA binding modalities (summarised in Fig. 1.15) is that a substrate can bind to DNA by more than one mode, thus strengthening the degree of binding. Through the combination of two or more binding modes, metal complexes can interact with DNA to give rise to several desirable advantages such as increased stability of the complex-DNA adduct and target specificity with respect to DNA structure and sequence, which can lead to a novel mechanism for their biological action.

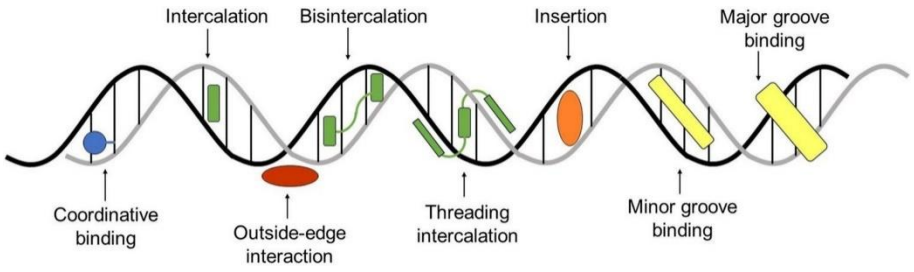

Figure 1.15 – A schematic summary of various DNA binding modes of metal complexes.[18]

1.6 Transition Metal Complexes as DNA Binding Agents

Transition metal complexes usually absorb strongly in the visible spectral region and are quite more photostable than most organic fluorophores and lanthanide metal complexes. Predominantly and for a long time, the development of luminescent d^6 transition metal complexes had been limited to ruthenium (Ru) complexes, but in the last few years, the employment of Ru has been accompanied by the use of other transition metals such as iridium (Ir), osmium (Os), platinum (Pt), and rhenium (Re), which are increasingly being used in cellular imaging. Moreover, luminescent complexes of copper (Cu), gold (Au), silver (Ag), nickel (Ni), and zinc (Zn) have been synthesised for the investigation of their DNA-binding properties.[65–68]

1.7 Early Works on the Interaction of DNA with Metal Complexes

The earliest sets of research into the interactions between metals and DNA have mostly focused on the binding strength and location of metal-aquo ions.[69] DNA melting temperature measurements in the presence of each of the first-row transition metal ions were conducted to gain insights into assess which and which metal ions could stabilise or destabilise the DNA duplex.[70] Early 1950s saw the rise in the research area of the interaction of inert metal complexes with DNA due most notably to F. P. Dwyer's works on the biological activities of metal polypyridyl complexes.[71–72] In the mid-1970s, S. J. Lippard and co-workers synthesised a foremost non-covalent DNA-binding complex.[73] Their work on metal-binding to thiolated bases showed that $[Pt(terpy)Cl]^+$ (terpy = 2,2':6',2"-terpyridine), a planar complex, could induce a spectral shift for 4-thiouridine when tRNA is present. D. S. Sigman's lab gave the

report of $[Cu(phen)_2]^+$ in the late 1970s and early 1980s uncovering the dense chemistry of groove-binding metal complexes.[74] $[Cu(phen)_2]^+$ complex was serendipitously discovered for DNA degradation in the course of studies into the inhibition of E. coli DNA polymerase by 1,10-phenanthroline. That DNA cleavage reaction was found out to be oxygen dependent.[75]

1.8 Tris(phenanthroline) Complexes

The earliest work on the DNA-binding of octahedral metal centers focused on tris(phenanthroline) complexes of ruthenium, chromium, zinc, nickel, and cobalt.[76–82] Extensive photophysical and NMR experiments suggested that these complexes bind to DNA *via* two distinct modes: (a) hydrophobic interactions in the minor groove and (b) partial intercalation of a phenanthroline ligand into the helix in the major groove. Perhaps more important than the discovery of these dual binding modes, however, was the revelation these complexes provided regarding the importance of chirality in DNA-binding.[83] In the case of $[Ru(phen)_3]^{2+}$, for example, the Δ-enantiomer is preferred in the semi-intercalative binding mode, while the complementary Λ-enantiomer is favoured in the minor groove binding mode. In subsequent years, it was discovered that metal centers bearing more sterically demanding phenanthroline ligand derivatives, such as diphenylphenanthroline (DIP), display even more dramatic chiral discrimination. Luminescence and hypochromism assays have revealed enantioselective binding on the part of $[Ru(DIP)_3]^{2+}$; the D-enantiomer binds enantiospecifically to right-handed B-DNA and the L-enantiomer binds only to left-handed Z-DNA.[84] This enantiospecificity has been exploited to map left-handed Z-DNA sites in supercoiled plasmids using $[L\text{-}Co(phen)_3]^{3+}$.[60] Indeed, this trend in enantiomeric selectivity for octahedral tris(chelate) complexes, matching the symmetry of the complex to that of the DNA helix, has repeatedly and consistently been observed for non-covalent DNA-binding complexes developed in the years since these initial discoveries.[52, 85–86]

These earliest tris(phenanthroline) complexes do not represent exhaustive examples of complexes that bind DNA via the minor or major grooves. The extensively studied $[Cu(phen)_2]^+$, for instance, has been shown to bind DNA via the minor groove. Indeed, these groove-binding complexes not only bind DNA but also cleave the macromolecule in the presence of hydrogen peroxide. Hydrogen peroxide generates a superoxide intermediate, which rapidly oxidises the redox-active $[Cu(phen)_2]^+$ to the cupric complex, $[Cu(NC)_2]^+$.[87, 74] Groove-

binding metal complexes have multiplied since these early studies and are now extensively researched. Turro and co-workers, for instance, developed an artificial photonuclease by linking the metallo-groove-binder $[Ru(bpy)_3]^{2+}$ to an electron-acceptor chain containing two viologen units.[88] The chemistry of metallo-groove-binders have become a mainstay in supramolecular self-assembly. Following the initial work of Lehn[89] on the interaction and cleavage of DNA with a cuprous double-helicate, Hannon and co-workers designed a triple-helicate capable of recognising three-way junctions in DNA. This recognition architecture has been characterised by single crystal X-ray.[90–92]

1.9 The Molecular "Light Switch" Effect of Metallo-intercalators

The photophysical and photochemical properties of metallo-intercalators can be exploited to create interesting DNA interaction properties. Perhaps the most vital feature metallo-intercalators possess is their ability to explore the structure of DNA even without having to bind to DNA irreversibly. So long as an intercalating complex is coordinately saturated and substitutionally inert, there cannot be direct coordination with DNA. Ligands such as dipyrido[3,2-a:2',3'-c]phenazine, or dppz, which possess a great aromatic surface area for intercalation to augment the binding affinity have been explored. This informed the synthesis of $[Ru(bpy)_2(dppz)]^{2+}$ (Fig. 1.16), including the exploration of its DNA-binding properties, leading to a seminal breakthrough work in this field. The complex's DNA-binding ability was escalated (K_b ca. $10^6 M^{-1}$), resulting in a photophysical effect termed the "light switch effect", which was conceptualised by Barton's group.[93–94]

A molecular light switch does not conform to "solvatochromic luminescence" (defined as the ability of the emission colour of a chemical substance to vary with solvent polarity). This is because a transition from zero luminescence to strong luminescence is observed upon undergoing an environmental change. The complex is "switched off" (with little to no luminescence) in one environment while it is switched on in another, thus allowing for a comparison with the switching on of a light (Fig. 1.17). This phenomenon proves highly useful as it can be used to monitor micro-environmental changes. In an aqueous solution, the archetypical molecular light switch complex, $[Ru(bpy)_2(dppz)]^{2+}$, exhibits no photoluminescence because the excited state of the phenazine nitrogen atoms is quenched

through the hydrogen bonding of water molecules.[95] There is a resurgence of this quenched luminescence upon DNA interaction as the dppz moiety becomes shielded from water by the bipyridine ligand.

Sauvage, *et al*. reported the characterisation of metal-to-ligand-charge-transfer (MLCT) luminescence of $[Ru(phen)_2(dppz)]^{2+}$ (Figs. 1.16 and 1.17) and $[Ru(bpy)_2(dppz)]^{2+}$ whereby they assumed that the light-induced charge transfer (CT) proceeded from the central ruthenium atom to a π^* orbital located on the dppz ligand.[96] This MLCT excited state then rapidly decays through intersystem crossing (ISC) to a ^{3}MLCT excited state located on the phenazine nitrogen atoms.

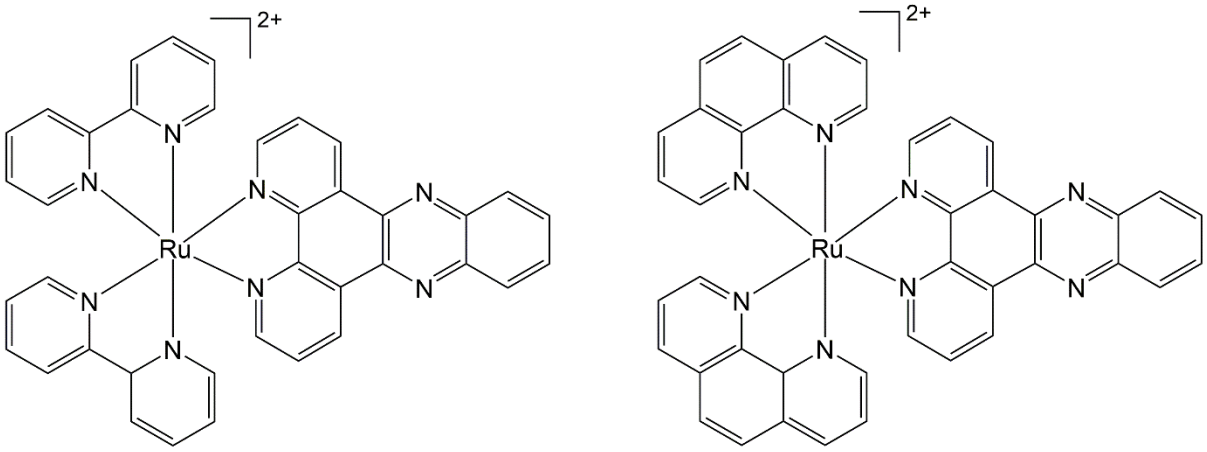

Figure 1.16 – Molecular light switch complexes, $[Ru(bpy)_2dppz]^{2+}$ (left) and $[Ru(phen)_2dppz]^{2+}$ (right).

The molecular light switch properties of $[Ru(phen)_2(dppz)]^{2+}$ have also been tailored towards the recognition of quadruplex and intercalated motif (or i-motif) DNA.[97] Instances of other molecular light switches have also been well documented including the case of complex $[Ru(bpy)_2(tpphz)]^{2+}$ (where tetrapyrido[3,2-a:2,3'-c:3",2"-h:2",3"-j]phenazine) reported by Tysoe, *et al.* which possessed, in most respects, similar properties to $[Ru(bpy)_2(dppz)]^{2+}$.[98]

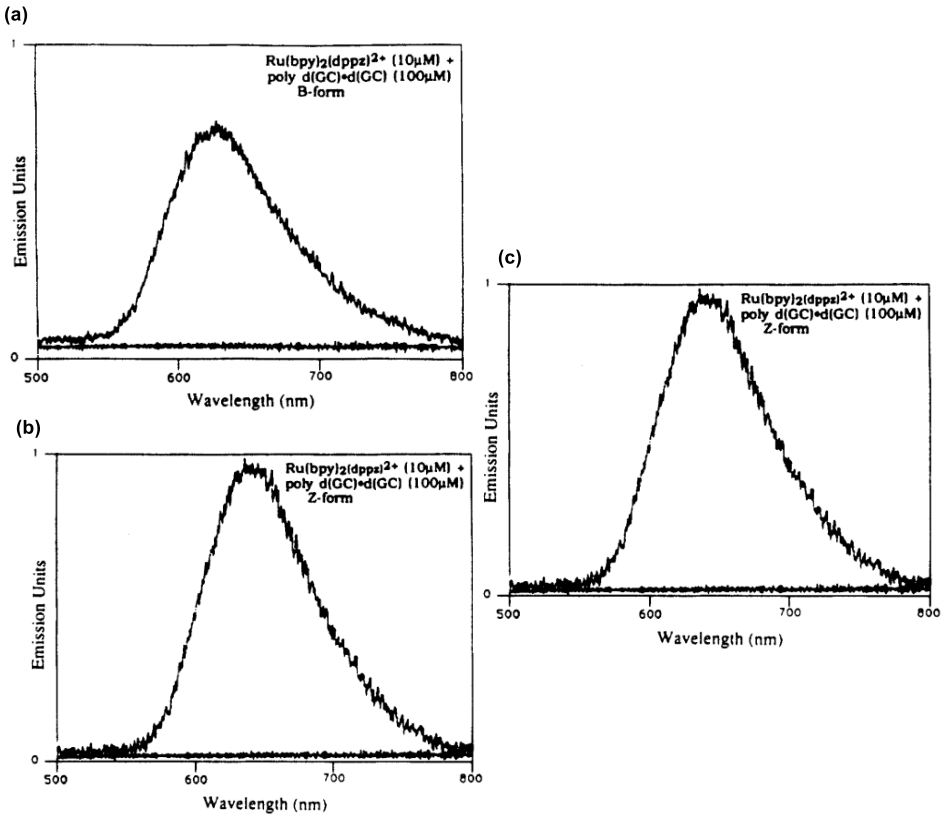

Figure 1.17 – Steady-state emission spectra of $[Ru(bpy)_2dppz]^{2+}$ (10μM) in the absence and presence of B-form (top left), Z-form (top right), and A-form (right) double-helical DNA.[101]

1.10 Cisplatin and its Derivatives as Anticancer Agents

In a previous subsection on irreversible (covalent) DNA binding mechanism, cisplatin (Fig. 1.6) was cited as a phenomenal example of an irreversible DNA-binding drug. The author considers it helpful to discuss cisplatin and its other anticancer derivatives further. The phenomenal though serendipitous discovery of Barnet Rosenberg's cisplatin dateable to 1965 gave a breakthrough in metal-based chemotherapy.[99–101] Cisplatin was approved by the FDA as treatment for testicular and advanced ovarian and bladder cancer. Ever since then, research into the mode of action of cisplatin and second generation of platinum-based drugs (oxaliplatin and carboplatin) have paved the way for many subsequent investigations (Fig. 1.18).[102] Cisplatin and its analogues are effective anticancer agents in cancer chemotherapy but suffer some obvious serious drawbacks in form of side effects such as undesirable systemic toxicity, lack of selectivity for healthy and unhealthy cells, and intrinsic chemotherapeutic platinum resistance via overexpression of nucleotide excision repair.[103] The limitation accrued from this has prompted the development of new alternative anticancer agents with superior reactivity

and lesser side effects coupled with an alternative mode of drug action. Significant efforts have been made towards the development of numerous non-platinum-based complexes of iron (Fe), ruthenium (Ru), titanium (Ti), amongst others (Figs. 1.18–1.19).[104–105] KP1019 (imidazolium trans-[tetra-chlorobis(1H–indazole)-ruthenate(III)]) **1** and NAMI-A (imidazolium trans-DMSO-imidazole-tetrachlororuthenate) **2** are examples of alternative anticancer drugs being clinically trialled (Fig. 1.20).[106–107] A sodium variant of KP1019, NKP-1339 **3** has also enter Phase II clinical trials for bladder cancer treatment[108], while the anti-proliferative agent, titanocene dichloride **4** (Fig. 1.20)[106, 109] has been trialled in both Phase I and Phase II clinical trials.

The mechanism of cisplatin's action is worth understanding. Cisplatin goes through thermal ligand exchange in an aqueous form, producing $[Pt(NH_3)_2(OH_2)Cl]^+$, which is a mono-aqua complex. This then proceeds by another ligand exchange to form cis-$[Pt(NH_3)_2(OH_2)_2]^{2+}$, which is a bis-aqua active species. The species, which harbours labile $PtOH_2$ bonds, preferentially binds to the N7 on guanine bases, forming 1,2-GpG intrastrand crosslinks, which give rise to a kinking of the DNA double helix. The platinum-guanine irreversible binding implicates both DNA transcription and replication, which constitute cisplatin's mode of action against tumorous cells (Fig. 1.6).[18]

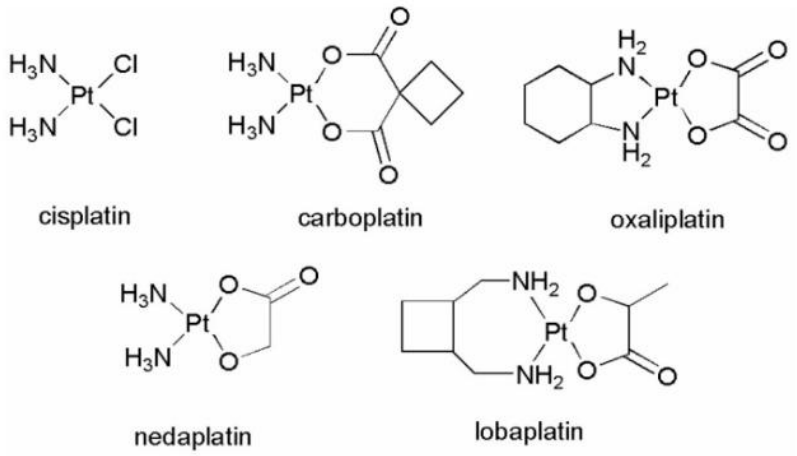

Figure 1.18 – Structures of different platinum complexes.[104]

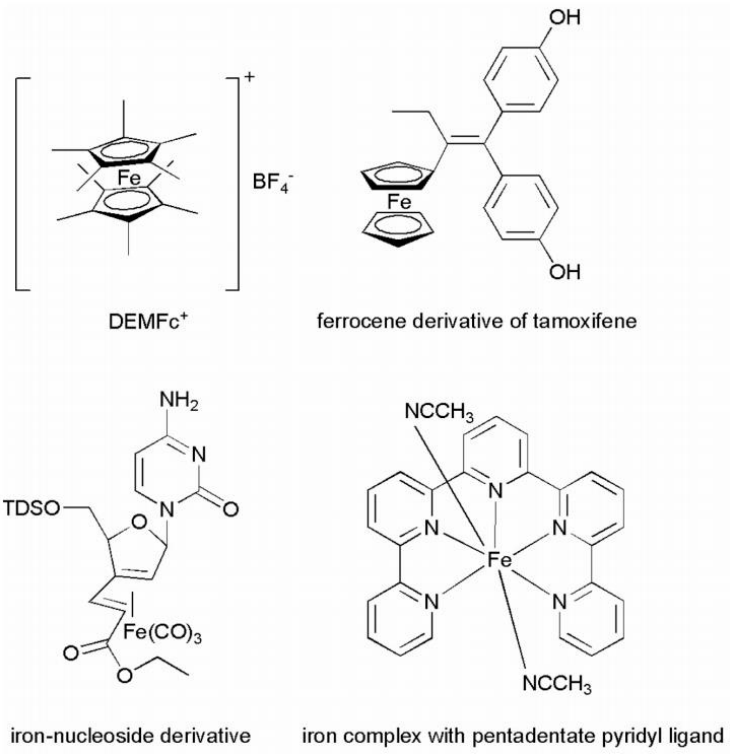

Figure 1.19 – Structures of several iron complexes.[104]

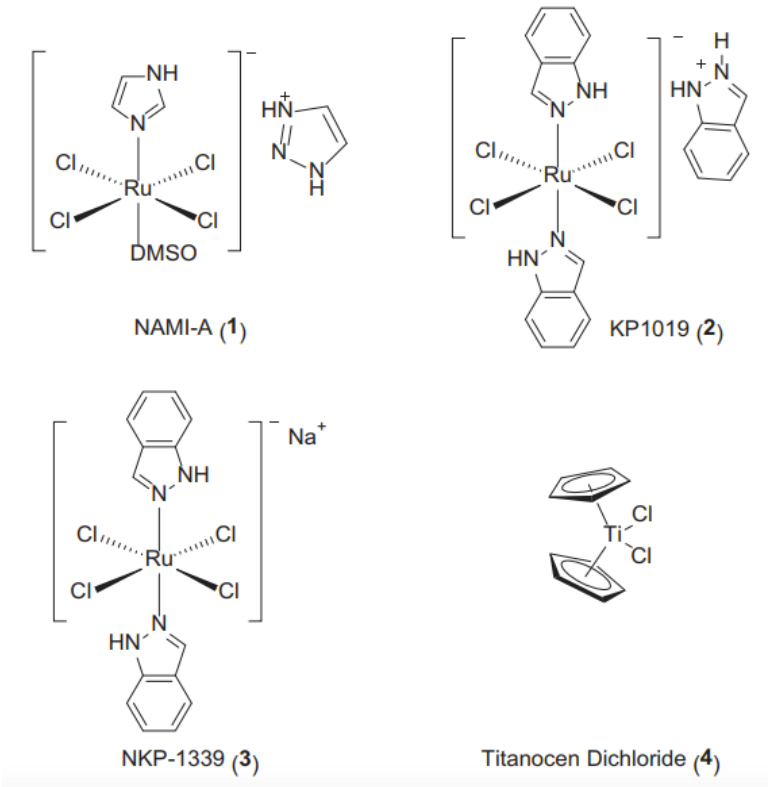

Figure 1.20 – Structure of NAMI-A (1), KP1010 (2), NKP-1339 (3) and titanocene dichloride (MKT4) (4).[106–108]

1.11 G-quadruplex DNA Binders

As earlier explained, transition metal complexes can also bind with non-canonical DNA structures such as G-quadruplex DNA. Metal complexes, as detailed in the review article from the lab of Georgiades and co-workers, have been tailored towards the recognition of G-quadruplex DNA conformation.[110] The Thomas group in 2006 reported that although $[(Ru(bpy)_2)_2(tpphz)]^{4+}$ and $[(Ru(phen)_2)_2(tpphz)]^{4+}$ exhibit duplex DNA with high affinities ($K_b > 10^6\ M^{-1}$) and a x50 increase in luminescence, both complexes also bind to the anti-parallel conformation of the quadruplex folded human telomere sequence (HTS). The interaction with HTS is around an order of magnitude greater than that with duplex. The binding event is accompanied by > 150 times luminescence enhancement relative to the duplex signal besides the fact that the maxima is also blue-shifted by >30nm.[111] Further work down the line from the same lab demonstrated that the quadruplex light switch effect was accruable to the structure of the bound quadruplex and that high binding affinities and an upsurge in emission is only observed on binding to quadruplex structures with diagonal loops or pseudo loops over the G-tetrad face at the end of the quadruplex structure.[112]

Yao and colleagues investigated the interaction of $[Ru(bpy)_2(dppz)]^{2+}$ with HTS and the intercalated double duplex $C–C^+$ i-motif structure. They observed that despite the compound showing minimal emission enhancement and weak binding to the i-motif, its binding interaction with HTS is associated with a more pronounced affinity ($>10^5\ M^{-1}$), which is characteristic of a proper molecular light switch effect. In addition, CD data revealed that the complex could induce quadruplex folding, even in the absence of the usually required alkali metal ion templates.[113]

Qu and co-workers envisaged the potential of helicates as quadruplex binding substrates. In their preliminary work, they reported that while the ΔΔ-diastereomers of Fe(II) and Ni(II)-based helicates such as that shown in Fig. 1.21 have a large binding preference for quadruplex folded HTS over duplex DNA, the ΔΔ-diastereomers only bind to duplex DNA.[114] They later found that the ΔΔ-helicate also shows binding discrimination between quadruplex structures as in the folding of the *c-kit* and *c-my* sequences into quadruplexes, which is disrupted by the helicate.[115] It was also found that binding to HTS is dependent on the structure of the diagonal loop, aligning with what the Thomas group later reported.[116]

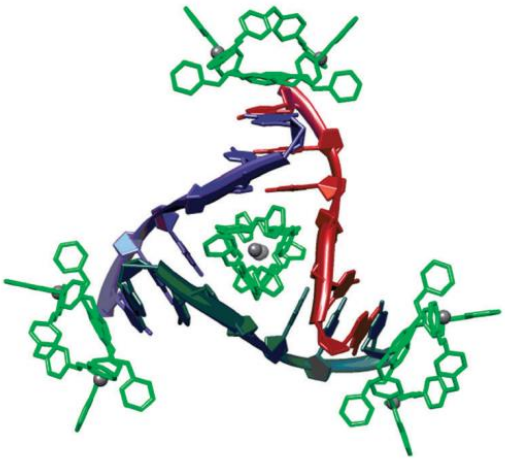

Figure 1.21 – X-ray crystal structure of Fe(II) helicates (green) bound to a three-way DNA junction (NDB: DD007.[117]

In 2019, the Thomas group improved upon a previously reported luminescent dinuclear complex that functions as a DNA probe in live cells based on $Ru^{II}(TAP)_2$ fragments (TAP = 1,4,5,8-tetraazaphenanthrene). Single crystal X-ray analysis, amongst other techniques, duly confirmed the structure of this compound (Fig. 1.22). The complex binds with duplex and quadruplex DNA with high affinity as its photoexcited state becomes quenched by DNA. Displaying a similar behaviour with its parent complex, $[\{Ru^{II}(phen)_2\}_2(tpphz)]^{4+}$, this compound is taken up by live cells displaying preferential localisation within the nucleus and displaying low dark cytotoxicity. However, in sharp contrast to $[\{Ru^{II}(phen)_2\}_2(tpphz)]^{4+}$, $[\{Ru^{II}(TAP)_2\}_2(tpphz)]^{4+}$ under light irradiation becomes highly phototoxic toward human melanoma cell lines demonstrating its potential as a therapeutic lead for the treatment of this malignant cancer.[118]

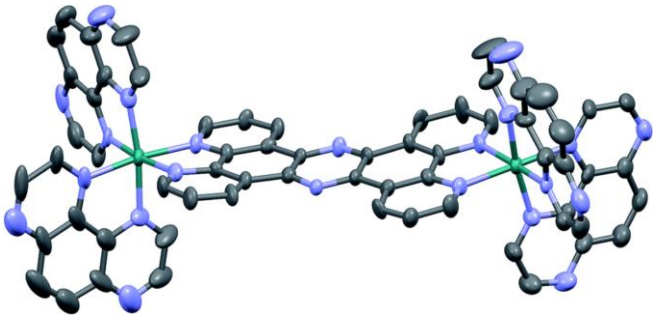

Fig. 1.22 – Thermal ellipsoid plot showing the Δ,Δ cation of the chloride salt of $[\{Ru^{II}(phen)_2\}_2(tpphz)]^{4+}$.[118]

1.12 Early Works on Iridium Complexes

Iridium is a third-row transition metal, a relative of cobalt (Co) and rhodium (Rh), and a routinely researched element of the platinum group of "precious metals". Iridium is a relatively rare element discovered by the British chemist Smithson Tennant in 1803 as an impurity in platinum, and it is both inert and corrosion resistant. Tennant named iridium after the Greek goddess "iris", the personification of the rainbow, due to the bright and diverse colors of the iridium salts, resulting from different oxidation states. The global demand for iridium as of 2007 was 3700kg, with half being tailored towards electrical and electrochemical applications and 20% for catalysis.[119–120] The wide range of oxidation states of iridium in combination with its numerous possible coordination geometries and coordination numbers lead to the increasing attention of iridium complexes not limited to the field of catalysis but now progressively also in the field of therapeutic development.[121]

Back in the 1970s, the development of iridium anticancer compounds was devoted solely to d^8 square-planar 1,5-cyclooctadiene iridium(I) complexes, mononuclear [Ir(acac)(cod)] and dinuclear $[IrCl(cod)]_2$ (Fig. 1.23) owing to the closeness of their chemistry to those of platinum(II) complexes.[120, 122]

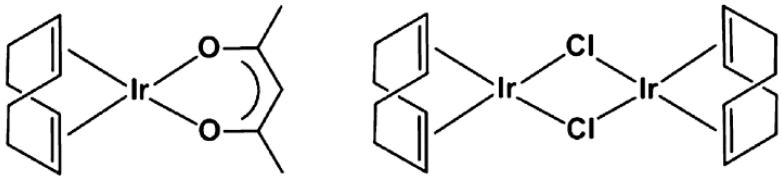

Figure 1.23 – Early Ir(I) anticancer compounds of [Ir(acac)(cod)] and $[IrCl(cod)]_2$.[120]

Since iridium(III) complexes were perceived to be relatively less reactive because of their chemical stability and slow solvent exchange rates, they did not receive as much attention until recently. The variable oxidation states of iridium metal make way for the possibility of other organoiridium complexes. Iridium(III) complexes, for instance, are stable as a combined result of their d^6 electron configuration, octahedral geometry, and low spin state. Interestingly, some studies have focussed on the activation of iridium(III) complexes by adopting suitable ligands upon irradiation. A typical example is $[(\sigma^5\text{-}C_p^*)Ir(phen)Cl]$ (C_p^* = tetramethyl(phenyl)cyclopentadiene).[123] The presence of one or more chloride ions coordinated to iridium(III) metal center seems essential in achieving the photoactivation of the complexes.

Importantly, many of the complexes above were also shown to be capable of acting as DNA-cleaving agents upon irradiation; this finding is promising for the use of phototherapy for selective and efficient cancer treatment.

It was not until of late that the photophysical studies of the iridium(III) bis-diimine complexes, $[Ir(N\hat{}N)_2Cl_2]Cl$, began to be researched even though they have been known for a long time. Iridium(III) complexes anchoring two bidentate cyclometallating (C^N) ligands such as the deprotonated form of 2-phenylpyridine (Hppy) are a class of iridium(III) whose original report was given by Watts. Research on iridium(III) complexes has since then burgeoned, and many photophysical and photochemical studies have gradually replaced ruthenium(II) polypyridyl complexes with cyclometallated iridium(III) complexes including $[Ir(C\hat{}N)_2X_2]^+$ and $[Ir(C\hat{}N)_2(L\hat{}L)]^{n+}$ (where C^N = cyclometallating ligand; n = 1 when L^L = neutral bidentate ligand; n = 0 when L–L = monoanionic bidentate ligand). This owes its reason to the wider colour tunability, synthetic versatility, sturdy photochemical stabilities, less thermally accessible ^{3}MC state, and great electrochemical reversibility of cyclometallated iridium(III) complexes. The revival of interest in iridium(III) systems as triplet emitters and dopants in the development of phosphorescent organic light emitting devices (PHOLEDs), pioneered by Thompson and Forrest and later elaborated by others, is primarily responsible for the continuation of their extensive studies.[124]

In comparison with well-developed Ir-based catalysts, Ir-based pharmaceuticals are still in their infancy. So far, there are three main applications for organoiridium compounds in biology: luminescent biological labels and probes, protein inhibitors, and anticancer agents.[120]

1.13 Iridium(III) Polypyridyl Complexes as Anticancer Agents

Among transition-metal complexes, those constructed from iridium(III) have attracted much traction as therapeutically active.[125] Iridium(III) complexes are largely inert, biocompatible, stable, non-toxic, possess large Stokes shifts, display long-lived red phosphorescence, have outstanding colour-tuning capability, good photobleaching resistance, and can interact with specific cellular targets.[126–127] Moreover, Iridium(III) complexes can exhibit strong two-photon

luminescence and have been applied successfully in biosensing and bioimaging.[127–128] Another striking peculiarity of iridium(III) complexes is their chemical versatility stemming from their molecular structure. The versatile octahedral coordination geometry of iridium(III) complexes offers many great possibilities, allowing the ready modulation of their photophysical properties by tunability of the ligands in their coordination sphere. As such, homoleptic and heteroleptic iridium(III) complexes built from ligands such as phenylpyridines, dipyridines, or phenanthrolines have been widely tailored towards applications in different areas as photosensitisers and/or bio-imaging.[129–141]

The first use of cyclometalated iridium(III) probes to stain the cytoplasm in living cells were reported by Li and co-workers in 2008.[142] Complexes **1** $[Ir(dfpy)_2(bpy)]^+PF_6^-$ and **2** $[Ir(dfpy)_2(quqo)]^+PF_6^-$ **Ir2** [dfpy = 2-(2,4-difluorophenyl)pyridine, quqo = 2-(2-quinolinyl)quinoxaline] present the same fluorinated phenylpyridine moiety and different diimine ligands (Fig. 1.24). The positive charge and the fluorination of the cyclometalated ligands, influencing the lipophilicity and aqueous solubility of the complexes, were argued to be the main factor for the internalisation of these probes within the cells. Confocal images of live HeLa cells incubated with **1** and **2** in DMSO-PBS (1:49 v/v), at a concentration of 20µM and for an incubation time of 10min, show intense intracellular luminescence with high signal-to-noise ratio between the cytoplasm (I_c) and the background (I_b), with a ratio of I_c/I_b over 50 (Figs. 1.25–1.26).

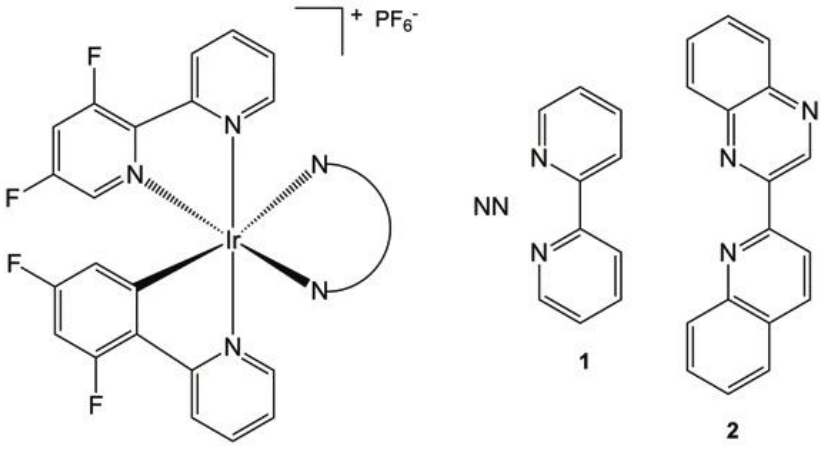

Figure 1.24 – Examples of iridium complexes with cytoplasmic localisation.

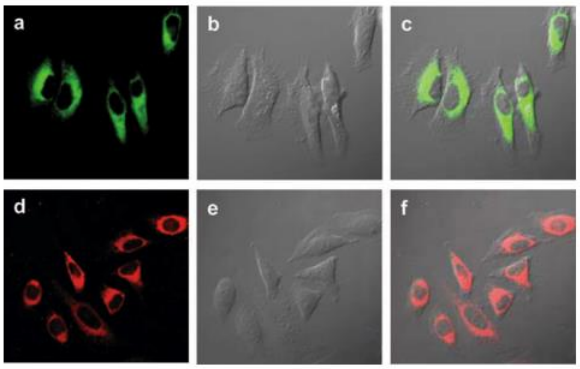

Figure 1.25 – Confocal luminescence (a and d) and brightfield images (b and e) of living HeLa cells incubated with 20 mM **1** (top) or **2** (bottom) in DMSO/PBS (pH 7, 1:49, v/v) for 10 min at 25 ^{o}C. Overlays of luminescence and brightfield images are shown in (c) and (f) for 1 or 2, respectively (λ_{ex} = 405 nm).

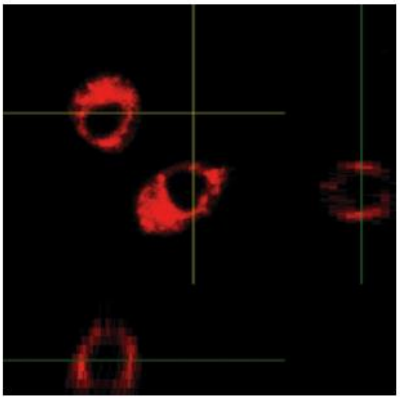

Figure 1.26 – The overlap Z-scan confocal image of the living HeLa cells incubated with 20μM **2** in DMSO/PBS (pH 7, 1:49, v/v) for 10min at 25^{o}C (λ_{ex} = 405nm).

Prieto-Castañeda, *et al*. directed the synthesis of three new heteroleptic dipyrrinato-iridium(III) complexes (i.e., **Ir(dipy)-1**, **Ir(dipy)-2** and **Ir(dipy)-3**) using a rather synthetically direct and inexpensive protocol (Fig. 1.27). Their phosphorescence emission at ambient temperature and in aerated solutions, and their singlet oxygen generation ability were well characterised. The iridium complexes were applied to human melanoma cancer cell line SK-Mel-103 *in vitro* for their photocytotoxic effect. **Ir(dipy)-2** and **Ir(dipy)-3** under visible-light irradiation (λ > 475 nm) give high yield of reactive oxygen species (ROS) leading to apoptotic cell death at low concentration. The two structurally similar complexes also demonstrate two-photon absorption (TPA) under 900nm irradiation. Studies of colocalisation in organelles of **Ir(dipy)-2** and **Ir(dipy)-3** and cell apoptosis/necrosis were equally assayed by flow cytometry.[143]

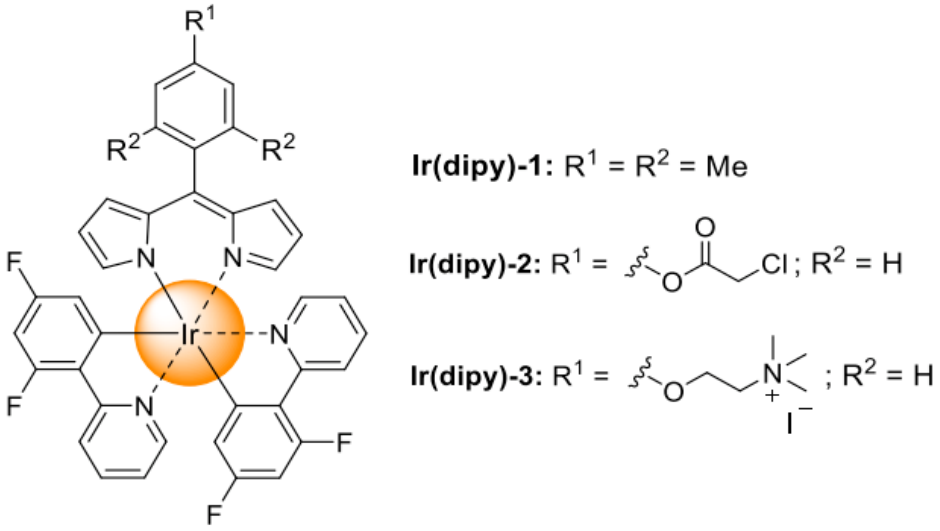

Figure 1.27 – Novel PSs based on dipyrrinate-iridium(III) complexes.[143]

Jing-Hui Zhu, *et al.* in 2021 successfully reported three new molecular hybrids incorporating a cyclometallated iridium(III) core and a polyhedral oligomeric silsesquioxane (POSS) unit $[Ir(pqe)_2(N^X)](PF_6)_n$ (N^X = mbpy-POSS, *n* = 1 (**1**); pic-POSS, *n* = 0 (**2**); picpy-POSS, *n* = 1 (**3**)). Their POSS-free analogues (N^X = dmbpy, n = 1 (**1a**); pic, *n* = 0 (**2a**); picpy, *n* = 1 (**3a**)) (Fig. 1.28) were equally described (pqe = phenylquinoline-4-carboxylate, and the structures of mbpy, pic, picpy, and POSS are given in Fig. 1.28). These luminescent iridium(III) cyclometalated complexes functioned as effective imaging reagents and photosensitisers that showed tuneable organelle-targeting properties, low dark cytotoxicity, and significant photocytotoxicity in hypoxic environments. The bipyridine complexes **1** and **1a** displayed orange-red emission while the picolinate complexes **2**, **2a**, **3**, and **3a** all demonstrated deep-red emission, accruing from a triplet metal-to ligand charge-transfer (^{3}MLCT) excited state. Complexes **1** and **1a** gave the highest photoinduced reactive oxygen species (ROS) generation capabilities while complexes **3** and **3a** exhibited the lowest ROS generation efficiencies.[144]

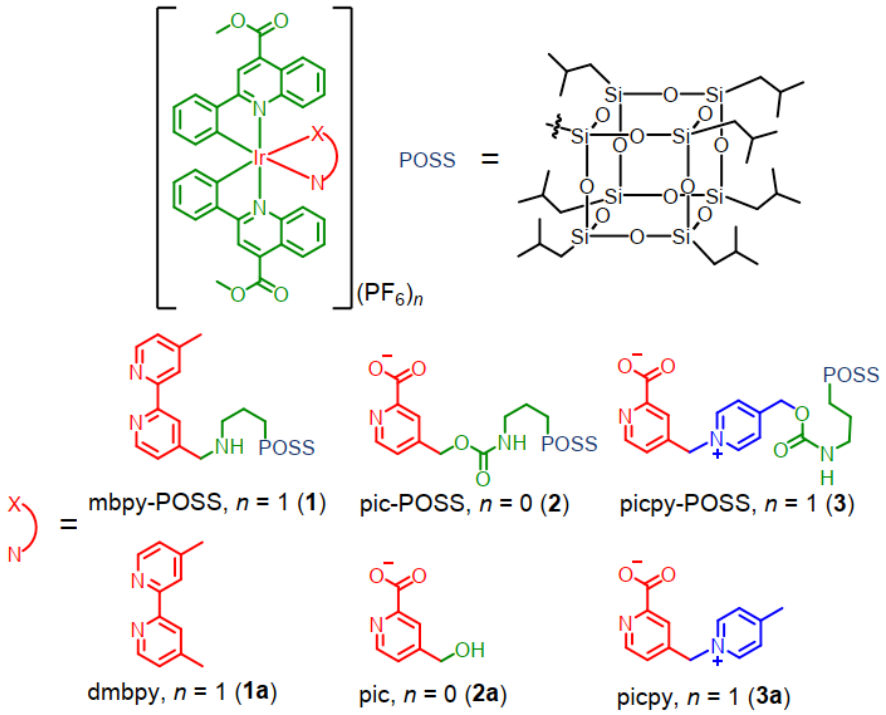

Figure 1.28 – Molecular structures of complexes **1–3** and **1a–3a**.[144]

The organelle-targeting selectivity of these complexes are markedly different despite their structural similarity. The POSS complexes **1**, **2**, and **3,** for instance, localise preferentially in the mitochondria, lipid droplets, and lysosomes, respectively, with Pearson's colocalisation coefficients (PCCs) of 0.87, 0.99, and 0.77, respectively (Fig. 1.29). By contrast, the POSS-free complexes **1a** and **2a** target the endoplasmic reticulum (ER) with PCCs of 0.90 and 0.93, respectively while complex **3a** stains the lysosomes with a PPCC of 0.83 (Fig. 1.29). The ready tunability of iridium(III) complexes as demonstrated by these results by the differences in their organelle-targeting selectivities paves the way to the design of future organelle-selective bioimaging reagents and photosensitisers.

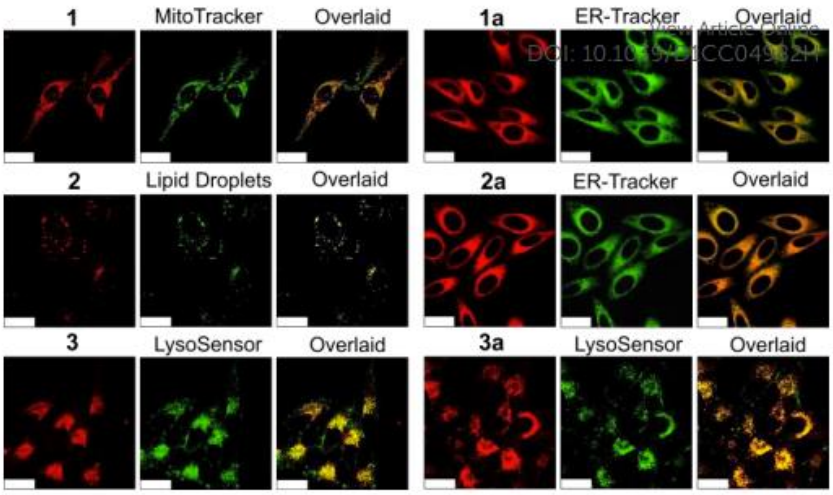

Figure 1.29 – Laser scanning confocal microscopy (LSCM) images of live HepG2 cells incubated with complexes **1–3** (10μM) or **1a–3a** (5μM) for 3h (for all complexes, λ_{ex} = 405nm, λ_{em} = 600–750nm) and then with organelle tracker (MitoTracker Green, 500nM, 15min; BODIPY 493/503, 10μM, 15min; LysoSensor Green, 500nM, 15min; or ER-Tracker Green 1μM, 30min. All trackers were excited at λ_{ex} = 488nm and collected at λ_{em} = 500–550nm) at 37°C. Scale bar = 25μm.[144]

All the complexes were evaluated for their cytotoxicity towards human liver, breast, and glioblastoma cancer cells (HepG2, MCF-7, and U87MG) under normoxia condition employing the MTT assays. The POSS-free complexes **1a–3a** demonstrate lower dark IC_{50} values, indicating higher cytotoxicity. Upon irradiation at 450nm and 10mWcm^{-2} for ca. 5mins, all complexes showed substantial attenuation of their IC_{50} values, making them potentially potent anticancer drugs (Table 1.2).[144]

Table 1.2 – Cytotoxicity (IC_{50}, μM) of complexes **1–3** and **1a–3a** towards various cancer cell lines. The cells were first incubated in the dark for 24h, incubated in the dark or upon irradiation at 450nm (10mWcm^{-2}) for 5min and subsequently incubated in the dark for 24h.[144]

	HepG2			MCF-7			U87 MG		
Complex	Dark	Light	PI[a]	Dark	Light	PI[a]	Dark	Light	PI[a]
1	25.9 ± 1.9	2.0 ± 0.1	12.9	22.2 ± 2.7	0.8 ± 0.2	27.8	31.6 ± 1.9	2.7 ± 0.3	11.7
1a	4.8 ± 0.3	0.1 ± 0.01	48.0	2.0 ± 0.1	0.3 ± 0.04	6.7	3.1 ± 0.9	0.2 ± 0.01	15.5
2	>100	8.3 ± 1.1	>12.0	>100	8.0 ± 0.9	>12.5	>100	16.7 ± 1.6	>6.0
2a	8.6 ± 0.7	1.9 ± 0.2	4.5	15.3 ± 1.1	4.6 ± 0.7	3.3	10.8 ± 1.4	3.6 ± 0.3	3.0
3	25.5 ± 3.9	4.7 ± 0.2	5.4	28.8 ± 1.5	3.2 ± 1.5	9.0	35.6 ± 4.8	6.2 ± 0.23	5.7
3a	19.5 ± 2.3	2.9 ± 0.1	6.7	8.0 ± 0.1	3.4 ± 0.2	2.4	16.1 ± 2.6	3.0 ± 0.2	5.4

[a] Photocytotoxicity index (PI) = IC_{50} (dark)/IC_{50} (light).

Following a modification of the methods established by Watts, *et al.* and Keene, *et al.*, Dr Sasha Stimpson in her PhD work within the Thomas group reported the synthesis of a series of iridium(III) polypyridyl and cyclometallated complexes prepared as their hexafluorophosphate salts, using a multi-step synthetic procedure which adopted the triflato intermediate pathway (Fig. 1.30).[145] The photophysical studies show that the complexes display intense π-π*/π…π* transitions around 200–400nm and ^{3}MLCT emission transitions around 500nm). The DNA-binding investigations and cellular uptake of the complexes were successfully accomplished. The chloride salts of M^{2+}/M^{3+} complexes $[Ir(bpy)_2(dppz)][PF_6]_3$ and $[Ir(phen)_2(C\text{^}N\ dppz)][PF_6]_2$ were demonstrated to stain the lysosomes while the chloride salt of M^{3+}complex $[Ir(phen)_2(dppz)][PF_6]_3$ was internalised in the mitochondria (Fig. 1.31). The dark cytotoxicity study of $[Ir(phen)_2(dppz)][PF_6]_3$ was also performed. Experimental results showed that a 48-hour MTT assay of $[Ir(phen)_2(dppz)][PF_6]_3$ on MCF-7 cell line gave the IC_{50} of $[Ir(phen)_2(dppz)][PF_6]_3$ as 177 μM (implying that the complex impinged no prominent activity on the cell line) as compared to that of cisplatin which was calculated to be 10 μM. However, under light irradiation, the complex progressively became phototoxic.

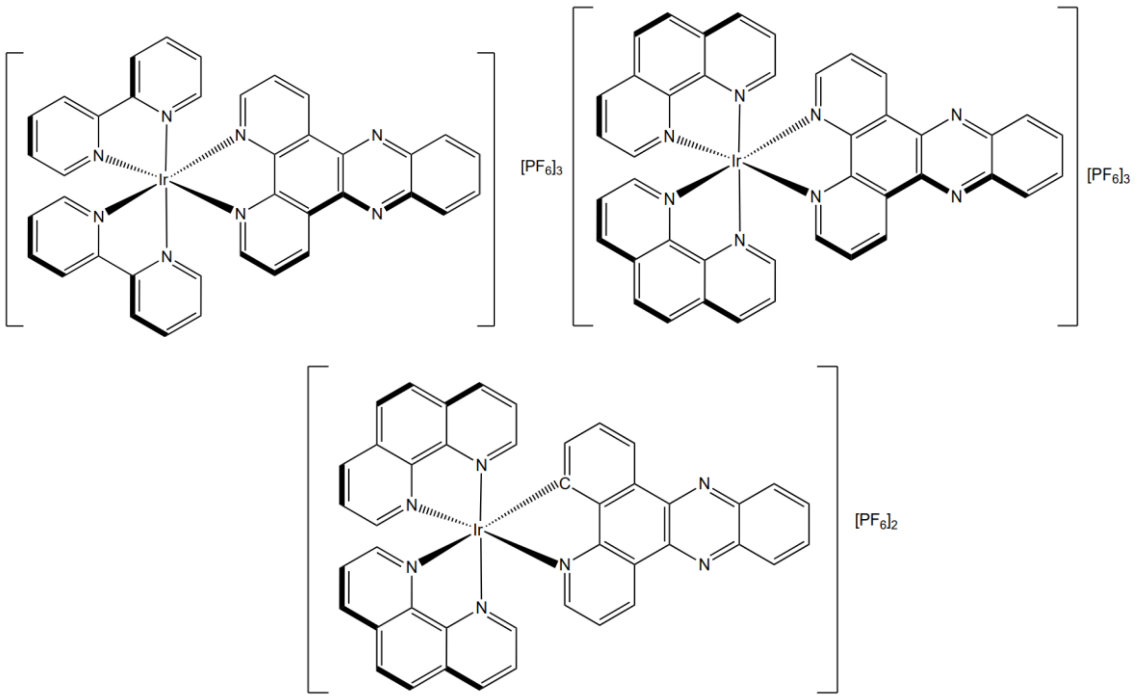

Figure 1.30 – Isostructural iridium(III) polypyridyl and cyclometallated complexes $[Ir(bpy)_2(dppz)][PF_6]_3$ (right up), $[Ir(phen)_2(dppz)][PF_6]_3$ (right left), and $[Ir(phen)_2(C\text{^}N\ dppz)][PF_6]_3$ (down).[145]

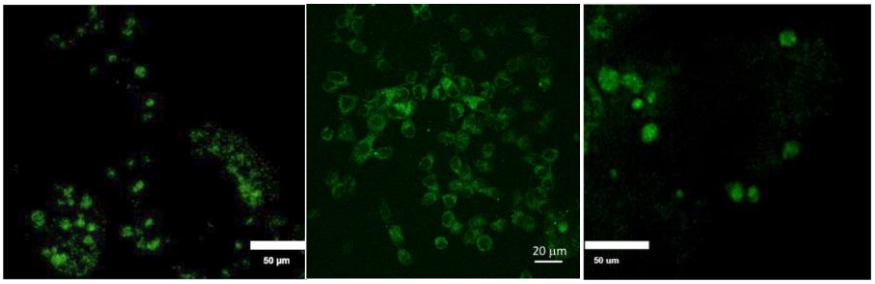

Figure 1.31 – Wide field microscopy luminescence emission of MCF-7 cells incubated with isostructural iridium(III) polypyridyl and cyclometallated complexes **1** (200 µM, 24 hours), **2** (400 µM, 24 hours), and **3** (200 µM, 24 hours).[145]

1.14 Why are Metal Complexes Luminescent: A Background

It is important to note that metal complexes emit light (or luminesce or are luminescent) as a result of a variety of processes. An explanation of the Jablonski diagram, the decay process, and excited state processes to bring home this point is worth giving in this subsection.

1.14.1 Jablonski Diagram, Decay Process, and Excited States

A Jablonski diagram gives a breakdown of production and decay processes of excited states in the form of various energy states. The Jablonski diagram describes most of the relaxation mechanisms for excited state molecules. The ground state (S_0) and lowest singlet and triplet states (S_1) and (T_1) are comprise multiple vibrational states as a result of vibronic motions of atoms that make up a molecule. When energy larger than the highest occupied molecular orbital (HOMO) minus lowest unoccupied molecular orbital (LUMO) energy difference is introduced into a molecule, either a higher vibronic state within S_1 states or higher singlet excited states S_2 and S_3 are formed. The higher vibronic states of S_1 relax to the lowest vibronic state of S_1 within a time scale of a few picoseconds. The higher energy singlet states S_2 and S_3 relax to the S_1 state via nonradiative internal conversion (IC) processes. Triplet states usually ensue from an intersystem crossing (ISC) process from $S_1 \rightarrow T_1$. Consequently, radiative transitions occur as an electronic transition from the lowest excited states, S_1 or T_1, to the ground state, S_0. The radiative transition from S_1 to S_0 is a spin-allowed transition and has the time scale of several nanoseconds. Conversely, the T_1 to S_0 transition is delayed and its timescale is much longer, ranging from microseconds to milliseconds, the process being a spin-forbidden one. An emission spectrum is, therefore, more or less looks the mirror image of a molecule's absorption

spectrum. Fig. 1.32 gives a detailed description of the Jablonski diagram and associated radiative and non-radiative processes:[146]

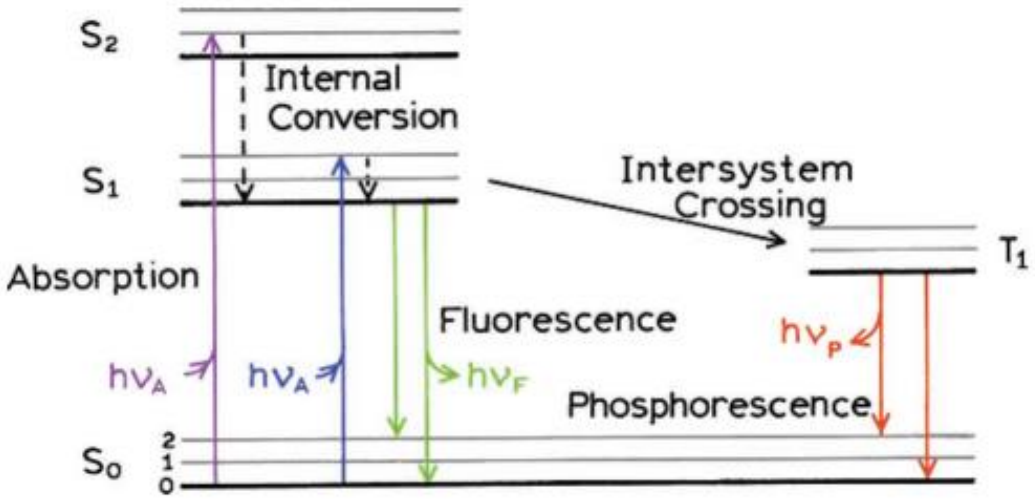

Figure 1.32 – A simplified Jablonski diagram (without energy and distance axes) illustrating the electronic and vibrational energy levels (rotational levels not shown) and the radiative and non-radiative transitions among them. Radiative transitions from excited singlet states are referred to as fluorescence whereas optically forbidden transitions from excited triplet states are called phosphorescence. Phosphorescence is characterised by a longer excited state lifetime compared to fluorescence.[147]

1.14.2 Absorption

The first transition in any Jablonski diagram is usually the absorption of a photon of a specific energy by the molecule of interest (Fig. 1.32). Absorption is a process involving the excitation of an electron from one level (i.e., a lower energy level) to another level (i.e., a higher energy level). In absorption, an electron receives the energy of a photon. In proportion to the amount of energy transferred, the electron transitions to a different eigenstate. In order for light to be absorbed, it must have wavelengths that correspond to the energy difference between two eigenstates of the molecule. Absorption is an extremely fast transition, in the order of 10^{-15} seconds. As most electrons at reasonable temperatures occupy a low-lying state, this transition will usually occur from the lowest electronic state (i.e., ground state).[146]

1.14.2 Luminescence: Fluorescence and Phosphorescence

Luminescence occurs when an electronic state excites a substance to emit light. Luminescence can be further divided into two categories based on the nature of the excited state: fluorescence

and phosphorescence. Fluorescence occurs when an electron in the first excited state returns to the ground state, this being accompanied by the release of emission of a photon as it is spin allowed. The fluorescence lifetime (τ) is typically 10ns. Fluorescence is typically observed by aromatic organic molecules. Phosphorescence is the emission of light from triplet excited states. Electrons in the excited state have the same spin orientation as electrons in the ground state. There is a prohibition on transitions to the ground state and a delay in emission rates (10^3–$10^0 s^{-1}$), making phosphorescence lifetimes to be typically in the order of milliseconds to seconds even though longer lifetimes are possible. Phosphorescence to be a slower decay process than fluorescence. Due to many deactivation/decay and quenching processes, phosphorescence in fluid solutions at room temperature is rarely observed. Fluorescence and phosphorescence usually do not have any clear-cut difference. Transition metal complexes built from different ligand architectures may exhibit mixed singlet-triplet states with intermediate lifetimes of 400ns to several microseconds.[147] A summary of the timescales for various transition processes is given in Table 1.3 and a classification of luminescence for organic molecules is given in Fig. 1.33.

Table 1.3 – Timescales for various processes.

Transition	Time Scale	Radiative Process?
Absorption	10^{-15} s	yes
Internal Conversion	10^{-14} - 10^{-11} s	no
Vibrational Relaxation	10^{-14} - 10^{-11} s	no
Fluorescence	10^{-9} - 10^{-7} s	yes
Intersystem Crossing	10^{-8} - 10^{-3} s	no
Phosphorescence	10^{-4} - 10^{-1} s	yes

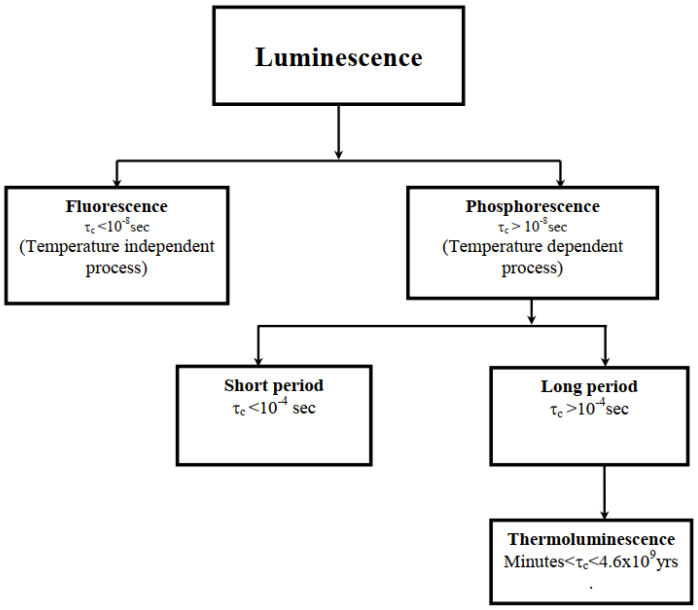

Figure 1.33 – Classification of luminescence for organic molecules based on duration of emission.[146]

The iridium(III) transition metal complexes investigated in this thesis, as with many other transition metal complexes, exhibit phosphorescent emission properties. They possess mixed singlet-triplet states, which give rise to intermediate lifetimes of hundreds of nanoseconds to several microseconds.

1.15 Project Aims

Iridium(III) complexes are gaining increasing research attention in the development of anticancer therapeutics due to their kinetic inertness, sturdy photostability, interesting photophysical, photochemical and electrochemical properties. Even though $[Ru(bpy)_2(qtpy)]^{2+}$ and its phen and dppz analogues have been successfully studied as potent DNA-binding complexes[148], no report of their iridium(III) equivalents has been given. The thesis aims to synthesise and characterise iridium(III) polypyridyl complexes **1**–**3** based on the well-researched Ru(II) counterparts that can reversibly bind to DNA under cell-free conditions.[148] The author intends to see if their structural similarities (the same moieties of auxiliary and bridging ligands) but charge differences (+3 iridium compounds versus +2 ruthenium compounds) will impact any DNA-binding similarities and/or differences in terms of binding constants and binding modes between the two sets of metal complexes. Since the photoluminescent properties of these complexes are interestingly more readily tunable than

those of their ruthenium(II) counterparts, it is worthwhile exploring their duplex and G-quadruplex DNA-binding and protein-binding studies using a range of biophysical techniques. With this successfully done, preliminary work on selected cancer cell lines to investigate their cellular uptakes and cytotoxic activities were also conducted.

Thus, this thesis has added to the library of phosphorescent polypyridyl iridium(III)-based complexes for use as duplex and G-quadruplex DNA probes. In the subsequent chapter, a detailed investigation is given into the development of this novel family of isostructural iridium(III) polypyridyl DNA probes depicted in Fig. 1.34.

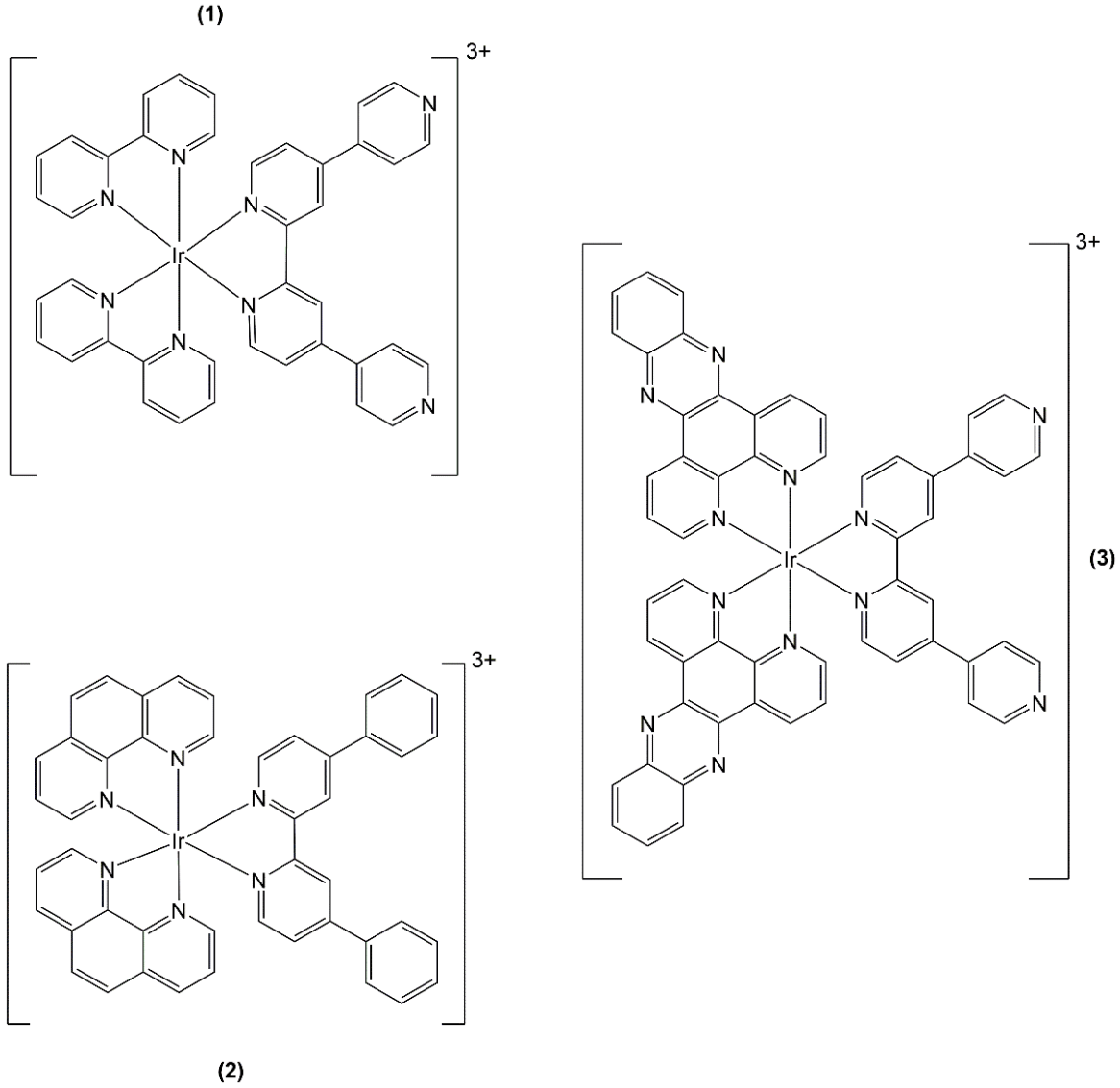

Figure 1.34 – Reported iridium(III) polypyridyl complexes.

1.16 References

1. D. Voet, J.G. Voet, Biochemistry, John Wiley and Sons: New York, 1995.

2. J. McMurry, Organic Chemistry, 3rd edition ed., Brooks/Cole, 1992.

3. D. Thieffry, S. Sarkar, Forty years under the central dogma, *Trends Biochem. Sci.*, 1998, 23(8), 312–316.

4. M. J. Hannon, Supramolecular DNA recognition, *Chem. Soc. Rev.*, 2007, 36, 280–295.

5. A. Klug, Rosalind Franklin and the Discovery of the Structure of DNA, *Nature*, 1968, 219, 808–810.

6. P. Dai, C. T. Williams, A. M. Witucki, D. W. Rudge, Rosalind Franklin and the Discovery of the Structure of DNA, *Science & Education*, 2021, 30, 659–692.

7. J. D. Watson, F. H. C. Crick, Molecular Structure of Nucleic Acids: A Structure for Deoxyribose Nucleic Acid, *Nature*, 1953, 171, 737–738.

8. M. H. F. Wilkins, A. R. Stokes, H. R. Wilson, Molecular Structure of Nucleic Acids: Molecular Structure of Deoxypentose Nucleic Acids, *Nature*, 1953, 171, 738–740.

9. J. D. Watson, F. H. C. Crick, Genetical Implications of the Structure of Deoxyribonucleic Acid, *Nature*, 1953, 171, 964–967.

10. W. I. P. Mainwaring, J. H. Parish, J. D. Pickering, N. H. Mann, Nucleic acid biochemistry and molecular biology, Blackwell Scientific Publications, Oxford and London, 1982, 557.

11. L. Stryer, *Biochemistry*, Third Edition, W.H. Freeman, New York, 1988, 1136.

12. G. M. Blackburn, M. J. Gait, D. Loakes, D. M. Williams, *Nucleic Acids in Chemistry and Biology*, 3rd ed., Royal Society of Chemistry (RSC), Cambridge, 2006.

13. F. H. C. Crick and J. D. Watson, The complementary structure of deoxyribonucleic acid, *Proc. R. Soc. Lond. A*, 1954, 223, 80–96.

14. B. Alberts, A. Johnson, J. Lewis, M. Raff, K. Roberts, and P. Walter, *Molecular biology of the cell*, 4th Edition, New York, Garland Science, 2002.

15. P. Belmont, J.-F. Constant, M. Demeunynck, Nucleic acid conformation diversity: from structure to function and regulation, *Chem. Soc. Rev.*, 2001, 30, 70.

16. R. E. Franklin, R. G. Gosling, Evidence for 2-Chain Helix in Crystalline Structure of Sodium Deoxyribonucleate, *Nature*, 1953, 172, 156–157.

17. B. Albert, A. Johnson, J. Lewis, D. Morgan, M. Raff, K. Roberts, P. Walter; with Problems by J. Wilson and T. Hunt, *Molecular biology of the cell*, 6th Edition, New York (N.Y.), Garland Science, Taylor and Francis Group, 2015.

18. L. Andrezálová, Z. Országhová, Covalent and noncovalent interactions of coordination compounds with DNA: An overview, 2021, 225, 111624.

19. M. E. Vázquez, A. M. Caamaño, J. L. Mascareñas, From transcription factors to designed sequence-specific DNA-binding peptides, *Chem. Soc. Rev.*, 2003, 32, 338–349.

20. R. E. Dickerson, H. R. Drew, B. N. Conner, R. M. Wing, A. V. Fratini, M. L. Kopka, The Anatomy of A-, B-, and Z-DNA, *Science*, 1982, 216, 475–485.

21. A. G. W. Leslie, S. Arnott, R. Chandrasekaran, R. L. Ratliff, Polymorphism of DNA double helices, *J. Mol. Biol.*, 1980, 143, 49–72.

22. A. Rich, A. Nordheim, A.H.-J. Wang, The chemistry and biology of left-handed Z-DANN, *Annu. Rev. Biochem.*, 1984, 53, 791–846.

23. T. Biver, Stabilisation of non-canonical structures of nucleic acids by metal ions and small molecules, *Coord. Chem. Rev.*, 2013, 257, 2765–2783 and all references therein.

24. M. L. Bochman, K. Paeschke, and V. A. Zakian, DNA secondary structures: stability and function of G-quadruplex structures. *Nat. Rev. Genet.*, 2012, 13, 770–780.

25. V. S. Chambers, G. Marsico, J. M. Boutell, M. D. Antonio, G. P. Smith, and S. Balasubramanian, High-throughput sequencing of DNA G-quadruplex structures in the human genome, *Nat. Biotechnol.*, 2015, 33, 877–881.

26. A. Piazza, J. B. Boule, J. Lopes, K. Mingo, E. Largy, M. P. Teulade-Fichou, and A. Nicolas, Genetic instability triggered by G-quadruplex interacting Phen-DC compounds in Saccharomyces cerevisiae, *Nucleic Acids Res.*, 2010, 38, 4337–4348.

27. P. Castillo Bosch, S. Segura-Bayona, W. Koole, J. T. van Heteren, J. M. Dewar, M. Tijsterman, and P. Knipscheer, FANCJ promotes DNA synthesis through G-quadruplex structures, *EMBO J.*, 2014, 33, 2521–2533.

28. S. K. Bharti, J. A. Sommers, F. George, J. Kuper, F. Hamon, K. Shin-ya, M. P. Teulade-Fichou, C. Kisker, and R. M. Jr Brosh, Specialization among iron-sulfur cluster helicases to resolve G-quadruplex DNA structures that threaten genomic stability, *J. Biol. Chem.*, 2013, 288, 28217–28229.

29. G. Biffi, D. Tannahill, J. McCafferty and S. Balasubramanian, Quantitative visualization of DNA G-quadruplex structures in human cells, *Nat. Chem.*, 2013, 5, 182–186.

30. R. H¨ansel-Hertsch, M. Di Antonio, and S. Balasubramanian, DNA G-quadruplexes in the human genome: detection, functions and therapeutic potential, *Nat. Rev. Mol. Cell Biol.*, 2017, 18, 279–284.

31. S. Neidle, Quadruplex nucleic acids as targets for anticancer therapeutics, *Nat. Rev. Chem.*, 2017, 1, 0041.

32. T. de Lange, *How Telomeres Solve the End-Protection Problem*, Science, 2009, 326, 948–952.

33. S. E. Artandi and R. A. DePinho, Telomeres and telomerase in cancer, *Carcinogenesis*, 2010, 31, 9–18.

34. J. M. Berg, J. L. Tymoczko, and L. Stryer, Biochemistry, Freeman, New York, 5th edn, 2002.

35. C. Branden and J. Tooze, *Introduction to Protein Structure*, Garland, New York, 2nd edn, 1999.

36. S. Neidle, Nucleic Acid Structure and Function, Nucleic Acid Structure and Function, OUP, Oxford, 2002.

37. M. B. Kastan, J. Bartek, Cell-cycle checkpoints and cancer, *Nature*, 2004, 432, 316–323.

38. R. M. Roat-Malone, Hoboken, New Jersey: J. Wiley & Sons, Bioinorganic Chemistry: A short Course, 2002.

39. P. M. Takahara, A. C. Rosenzweig, C. A. Frederick, S. J. Lippard, Crystal structure of double-stranded DNA containing the major adduct of the anticancer drug cisplatin, *Nature*, 1995, 377, 649.

40. R. C. Todd, S. J. Lippard, Structure of duplex DNA containing the cisplatin 1,2-$\{Pt(NH_3)_2\}^{2+}$-d(GpG) cross-link at 1.77 Å resolution, *J. Inorg. Biochem.*, 2010, 104(9), 902–908.

41. https://www.drugbank.ca/drugs/DB00515.

42. D. S. Johnson, D. L. Boger, Chapter 3, *In Comprehensive Supramolecular Chemistry*, M. Lehn, Y. Murakami, Ed., Pergamon Press, Oxford, 1996.

43. T. Thomas, U. Gunnia, T. Thomas, Polyamine-induced B-DNA to Z-DNA conformational transition of a plasmid DNA with (dG-dC)n insert, *J. Bio. Chem.*, 1991, 266, 6137–6141.

44. R. M. Wartell, J. E. Larson, R. D. Wells, Netropsin, A Specific Probe for A-T Regions of Duplex Deoxyribonucleic Acid, *J. Bio. Chem.*, 1974, 249, 6719–6731.

45. D. S. Goodsell, M. L. Kopka, R. E. Dickerson, Refinement of Netropsin Bound to DNA: Bias and Feedback in Electron Density Map Interpretation, *Biochemistry*, 1995, 34, 4983–4993.

46. A. Pullman, B. Pullman, Molecular electrostatic potential of the nucleic acids, *Q. Rev. Biophys.*, 1981, 14, 289–380.

47. J. B. Chaires, A thermodynamic signature for drug-DNA binding mode, *Archives of Biochemistry and Biophysics*, 2006, 453, 26–31.

48. L. S. Lerman, Structural considerations in the interaction of DNA and acridines, *J. Mol. Biol.*, 1961, 3, 18.

49. D. R. Boer, A. Canals, M. Coll, DNA-binding drugs caught in action: the latest 3D pictures of drug-DNA complexes, *Dalton Trans.*, 2009, 31, 399–414.

50. R. Martínez, L. Chacón-García, The Search of DNA-Intercalators as Antitumoral Drugs: What it Worked and What did not Work, *Curr. Med. Chem.*, 2005, 12(2), 127–151(25).

51. C. A. Frederick, L. D. Williams, G. Ughetto, G. A. van der Marel, J. H. van Boom, A. Rich and A. H. Wang, Structural Comparison of Anticancer Drug-DNA Complexes: Adriamycin and Daunomycin, *Biochemistry*, 1990, 29, 2538–2549.

52. K. E. Erkilla, D. T. Odom and J. K. Barton, Recognition and Reaction of Metallointercalators with DNA, *Chem. Rev.*, 1999, 99, 2777–2796.

53. S. J. Franklin and J. K. Barton, Differential DNA Recognition by the Enantiomers of 1-Rh(MGP)2phi: A Combination of Shape Selection and Direct Readout, *Biochem.*, 1998, 37, 16093–16105.

54. B. P. Hudson and J. K. Barton, Solution Structure of a Metallointercalator Bound Site Specifically to DNA, *J. Am. Chem. Soc.*, 1998, 120, 6877–6888.

55. C. M. Dupureur and J. K. Barton, Use of Selective Deuteration and 1H NMR in Demonstrating Major Groove Binding of .DELTA.-[Ru(phen)$_2$dppz]$^{2+}$ to d(GTCGAC)$_2$, *J. Am. Chem. Soc.*, 1994, 116, 10286–10287.

56. J. G. Collins, T. P. Shields and J. K. Barton, ^{1}H-NMR of Rh(NH$_3$)$_4$phi^{3+} Bound to d(TGGCCA)$_2$: Classical Intercalation by a Nonclassical Octahedral Metallointercalator, *J. Am. Chem. Soc.*, 1994, 116, 9840–9846.

57. C. L. Kielkopf, K. E. Erkkila, B. P. Hudson, J. K. Barton and D. C. Rees, Structure of a photoactive rhodium complex intercalated into DNA, *Nat. Struct. Biol.*, 2000, 7, 117–121.

58. V. C. Pierre, J. T. Kaiser and J. K. Barton, Insights into finding a mismatch through the structure of a mispaired DNA bound by a rhodium intercalator, *Proc. Natl. Acad. Sci. U. S. A.*, 2007, 104, 429–434.

59. A. H. J. Wang, J. Nathans, G. van der Marel, J. H. van Boom and A. Rich, Molecular structure of a double helical DNA fragment intercalator complex between deoxy CpG and a terpyridine platinum compound, *Nature*, 1978, 276, 471–474.

60. I. Greguric, J. R. Aldrichwright and J. G. Collins, A ^{1}H NMR Study of the Binding of Δ-[Ru(phen)$_2$DPQ]$^{2+}$ to the Hexanucleotide d(GTCGAC)$_2$. Evidence for Intercalation from the Minor Groove, *J. Am. Chem. Soc.*, 1997, 119, 3621–3622.

61. J. V. Fry and J. G. Collins, NMR Study of the Sequence-Specific Binding of the Δ-Tris(ethylenediamine)cobalt(III) Cation with d(TCGGGATCCCGA)$_2$, *Inorg. Chem.*, 1997, 36, 2919–2921.

62. J. G. Collins, A. D. Sleeman, J. R. Aldrich-Wright, I. Greguric and T. W. Hambley, A ^{1}H NMR Study of the DNA Binding of Ruthenium(II) Polypyridyl Complexes, *Inorg. Chem.*, 1998, 37, 3133.

63. F. Westerlund, L. M. Wilhelmsson, B. Norden and P. Lincoln, A 1H NMR Study of the DNA Binding of Ruthenium(II) Polypyridyl Complexes, *J. Phys. Chem. B*, 2005, 109, 21140–21144 and refs therein.

64. Brian M. Zeglis, Valerie C. Pierre and Jacqueline K. Barton, Metallo-intercalators and metallo-insertors, *Chem. Commun.*, 2007, 4565–4579.

65. E. Wong and C. M. Giandomenico, Current status of platinum-based antitumor drugs, *Chem. Rev.*, 1999, 99, 2451–2466.

66. T. C. Johnstone, K. Suntharalingam, S. J. Lippard, Third row transition metals for the treatment of cancer, *Phil. Trans. R. Soc.*, 2015, A373(2037), 20140185.

67. U. Ndagi, N. Mhlongo, M. E. Soliman, Metal complexes in cancer therapy – an update from drug design perspective, *Drug Des. Devel. Ther.*, 2017, 11, 599–616.

68. R. W.-Y. Sun, D.-L. Ma, E. L.-M. Wong and C.-M. Che, Some uses of transition metal complexes as anti-cancer and anti-HIV agents, *Dalton Trans.*, 2007, 4884–4892.

69. R. M. Izatt, J. J. Christensen and J. W. Rytting, Sites and Thermodynamic Quantities Associated with Proton and Metal Ion Interaction with Ribonucleic Acid, Deoxyribonucleic Acid, and their Constituent Bases, Nucleosides, and Nucleotides, *Chem. Rev.*, 1971, 71, 439–481.

70. G. A. Eichhorn and Y. A. Shin, Interaction of Metal Ions with Polynucleotides and Related Compounds. XII. The Relative Effect of Various Metal Ions on DNA Helicity, *J. Am. Chem. Soc.*, 1968, 90, 7323–7328.

71. W. W. Brandt, F. P. Dwyer and E. C. Gyarfas, Chelate Complexes of 1,10-Phenanthroline and Related Compounds, *Chem. Rev.*, 1954, 54, 959–1017.

72. F. P. Dwyer, E. C. Gyarfas, W. P. Rogers and J. H. Koch, Biological Activity of Complex Ions, *Nature*, 1952, 170, 190–191.

73. K. W. Jennette, S. J. Lippard, G. A. Vasiliades and S. J. Lippard, Metallointercalation Reagents. 2-Hydroxyethanethiolato(2,2',2"-terpyridine)-platinum(II) Monocation Binds Strongly to DNA By Intercalation, *Proc. Natl. Acad. Sci. U. S. A.*, 1974, 71, 3839–3843.

74. D. S. Sigman, R. Landgraf, D. M. Perrin and L. Pearson, Nucleic Acid Chemistry of the Cuprous Complexes of 1,10-Phenanthroline and Derivatives, *Met. Ions Biol. Syst.*, 1996, 33, 485–513.

75. D. S. Sigman, D. R. Graham, V. D'Aurora and A. M. Stern, Oxygen-Dependent Cleavage Of DNA By the 1,10-Phenanthroline, Cuprous Complex. Inhibition of Escherichia Coli DNA Polymerase I, *J. Biol. Chem.*, 1979, 254(24), 12269–12272.

76. J. K. Barton, J. J. Dannenberg and A. L. Raphael, Enantiomeric selectivity in binding tris(phenanthroline)zinc(II) to DNA, *J. Am. Chem. Soc.*, 1982, 104, 4967–4969.

77. J. K. Barton, A. T. Danishefsky and J. M. Goldberg, Tris(phenanthroline)ruthenium(II): Stereoselectivity in Binding to DNA, *J. Am. Chem. Soc.*, 1984, 106, 2172–2176.

78. C. V. Kumar, J. K. Barton and N. J. Turro, Photophysics of Ruthenium Complexes Bound to Double Helical DNA, *J. Am. Chem. Soc.*, 1985, 107, 5518–5523.

79. J. K. Barton, J. M. Goldberg, C. V. Kumar and N. J. Turro, Binding Modes and Base Specificity of Tris(phenanthroline)ruthenium(II) Enantiomers with Nucleic Acids: Tuning the Stereoselectivity, *J. Am. Chem. Soc.*, 1986, 108, 2081–2088.

80. J. K. Barton and A. L. Raphael, Site-specific cleavage of left-handed DNA in pBR322 by lambda-tris(diphenylphenanthroline)cobalt(III), *Proc. Natl. Acad. Sci. U. S. A.*, 1985, 82(19), 6460–6464.

81. J. P. Rehmann and J. K. Barton, ^{1}H NMR Studies of Tris(phenanthroline) Metal Complexes Bound to Oligonucleotides: Characterization of Binding Modes, *Biochem.*, 1990, 29, 1701–1709.

82. J. P. Rehmann and J. K. Barton, ^{1}H NMR Studies of Tris(phenanthroline) Metal Complexes Bound to Oligonucleotides: Structural Characterizations via Selective Paramagnetic Relaxation, *Biochem.*, 1990, 29, 1710–1717.

83. J. K. Barton, Metals and DNA: Molecular Left-Handed Complements, *Science*, 1986, 233, 727–734.

84. J. K. Barton, L. A. Basile, A. T. Danishefsky and A. Alexandrescu, Chiral probes for the handedness of DNA helices: enantiomers of tris(4,7-diphenylphenanthroline)ruthenium(II), *Proc. Natl. Acad. Sci. U. S. A.*, 1984, 81, 1961–1965.

85. S. Satyanaraana, J. C. Dabrowiak and J. B. Chaires, Tris(phenanthroline)ruthenium(II) enantiomer interactions with DNA: Mode and specificity of binding, *Biochem.*, 1992, 32, 2573–2584.

86. M. Eriksson, M. Leijon, C. Hiort, B. Norden and A. Graslund, Binding of Δ- and Λ-$[Ru(phen)_3]^{2+}$ to $[d(CGCGATCGCG)]_2$ Studied by NMR, *Biochem.*, 1994, 33, 5031–5040.

87. C.-H. B. Chen, L. Milne, R. Landgraf, D. M. Perrin, and D. S. Sigman, Artificial Nucleases, *ChemBioChem*, 2001, 2, 735–740.

88. P. K.-L. Fu, A. M. Bradley, D. van Loyen, H. Durr, S. H. Bossmann and C. Turro, DNA Photocleavage by a Supramolecular Ru(II)−Viologen Complex, *Inorg. Chem.*, 2002, 41, 3808–3810.

89. B. Schoentjes and J.-M. Lehn, Interaction of Double-Helical Polynuclear Copper(I) complexes with double-stranded DNA, *Helv. Chim. Acta*, 1995, 78, 1–12.

90. L. J. Childs, J. Malina, B. E. Rolfsnes, M. Pascu, M. J. Prieto, M. J. Broome, P. M. Rodger, E. Sletten, V. Moreno, A. Rodger and M. J. Hannon, A DNA-Binding Copper(I) Metallosupramolecular Cylinder that Acts as an Artificial Nuclease, *Chem. – Eur. J.*, 2006, 12, 4919–4927.

91. M. J. Hannon and L. J. Childs, Helices and Helicates: Beautiful Supramolecular Motifs with Emerging Applications, *Supramol. Chem.*, 2004,16:1, 7–22.

92. C. Uerpmann, J. Malina, M. Pascu, G. J. Clarkson, V. Moreno, A. Rodger, A. Grandas and M. J. Hannon, Design and DNA Binding of an Extended Triple-Stranded Metallo-supramolecular Cylinder, *Chem. – Eur. J.*, 2005, 11, 1750–1756.

93. A. E. Friedman, J.-C. Chambron, J.-P. Sauvage, N. J. Turro, J. K. Barton, Molecular "Light Switch" for DNA: $Ru(bpy)_2(dppz)^{2+}$, *J. Am. Chem. Soc.*, 1990, 112, 4960–4962.

94. A. M. Pyle, J. P. Rehmann, R. Meshoyrer, C. V. Kumar, N. J. Turro, J. K. Barton, Mixed-Ligand Complexes of Ruthenium(II): Factors Governing Binding to DNA, *J. Am. Chem. Soc.*, 1989, 111, 3051–3058.

95. C. Turro, S. H. Bossman, Y. Jenkins, J. K. Barton, N. J. Turro, Proton Transfer Quenching of the MLCT Excited State of $Ru(phen)_2dppz^{2+}$ in Homogeneous Solution and Bound to DNA, *J. Am. Chem. Soc.*, 1995, 117, 9026–9032.

96. Y. Jenkins, A.E. Friedman, N.J. Turro, J.K. Barton, Characterization of Dipyridophenazine Complexes of Ruthenium(II): The Light Switch Effect as a Function of Nucleic Acid Sequence and Conformation, *Biochem.*, 1992, 31, 10809–10816.

97. S. Shi, J. Zhao, X. Geng, T. Yao, H. Huang, T. Liu, L. Zheng, Z. Li, D. Yang, L. Ji, Molecular "light switch" for G-quadruplexes and i-motif of human telomeric DNA: $[Ru(phen)_2(dppz)]^{2+}$, *Dalton Trans.*, 2010, 39, 2490–2493.

98. S.A. Tysoe, R. Kopelman, D. Schelzig, Flipping the Molecular Light Switch Off: Formation of DNA-Bound Heterobimetallic Complexes Using $Ru(bpy)_2tpphz^{2+}$ and Transition Metal Ions, *Inorg. Chem.*, 1999, 38, 5196–5197.

99. B. Rosengberg, L. V. Camp, T. Trigas, Inhibition of Cell Division in Escherichia coli by Electrolysis Products from a Platinum Electrode, *Nature*, 1965, 205, 698–699.

100. B. Rosengberg, L. V. Camp, J. E. Trosko, V. H. Mansour, Platinum Compounds: a New Class of Potent Antitumour Agents, *Nature*,1969, 222, 385–386.

101. T. C. Johnstone, G. Y. Park, S. J. Lippard, Understanding and Improving Platinum Anticancer Drugs – Phenanthriplatin, *Anticancer Res.*, 2014, 34, 471–476.

102. M. Redrado, V. Fernández-Moreira, M. C. Gimeno, Theranostics Through the Synergistic Cooperation of Heterometallic Complexes, *ChemMedChem*, 2021, 16, 932–941.

103. R. Oun, Y. E. Moussa, N. J. Wheate, The side effects of platinum-based chemotherapy drugs: a review for chemists, *Dalton Trans.*, 2018, 47, 6645–6653.

104. Ingo Ott and Ronald Gust, Non-Platinum Metal Complexes as Anti-cancer Drugs, *Arch. Pharm. Chem. Life Sci.*, 2007, 340, 117–126.

105. Y. Ellahioui, S. Prashar, S. Gomez-Ruiz, Anticancer Applications and Recent Investigations of Metallodrugs Based on Gallium, Tn, and Titanium, *Inorganics*, 2017, 5(1), 4.

106. C. V. Christodoulou, A. G. Eliopoulos, L. S. Young, L. Hodgkins, D. R. Ferry, and D. J. Kerr, Antiproliferative activity and mechanism of action of titanocene dichloride, *Br. J. Cancer*, 1998, 77(12), 2088–2097.

107. M. Redrado, V. Fernández-Moreira, M. C. Gimeno, Theranostics Through the Synergistic Cooperation of Heterometallic Complexes, *ChemMedChem*, 2021, 16(6), 932–941.

108. R. Trondl, P. Heffeter, C. R. Kowol, M. A. Jakupec, W. Berger, and B. K. Keppler, NKP-1339, the first ruthenium-based anticancer drug on the edge to clinical application, *Chem. Sci.*, 2014, 5, 2925–2932.

109. N. Kroger, U. R. Kleeberg, K. Mross, L. Edler, D. K. Hossfeld, Phase II Clinical Trial of Titanocene Dichloride in Patients with Metastatic Breast Cancer, *Onkologie*, 2000, 23, 60–62.

110. S. Georgiades, N. Abd Karim, K. Suntharalingam and R. Vilar, Interaction of Metal Complexes with G-Quadruplex DNA, *Angew. Chem. Int. Ed.*, 2010, 49, 4020–4034.

111. C. Rajput, R. Rutkaite, L. Swanson, I. Haq and J. A. Thomas, Dinuclear Monointercalating RuII Complexes That Display High Affinity Binding to Duplex and Quadruplex DNA, *Chem. – Eur. J.*, 2006, 12, 4611–4619.

112. T. Wilson, M. P. Williamson, and J. A. Thomas, Differentiating quadruplexes: binding preferences of a luminescent dinuclear ruthenium(II) complex with four-stranded DNA structures, *Org. Biomol. Chem.*, 2010, 8, 2617–2621.

113. S. Shi, X. Geng, J. Zhao, T. Yao, C. Wang, D. Yang, L. Zheng, and L. Ji, Interaction of $[Ru(bpy)_2(dppz)]^{2+}$ with human telomeric DNA: Preferential binding to G-quadruplexes over i-motif, *Biochimie*, 2010, 92, 370–377.

114. H. Yu, X. Wang, M. Fu, J. Ren and X. Qu, Chiral metallo-supramolecular complexes selectively recognize human telomeric G-quadruplex DNA, *Nucleic Acids Res.*, 2008, 36, 5695–5703.

115. C. Zhao, J. Geng, L. Feng, J. Ren and X. Qu, Chiral Metallo–Supramolecular Complexes Selectively Induce Human Telomeric G-Quadruplex Formation under Salt-Deficient Conditions, *Chem. – Eur. J.*, 2011, 17, 8209–8215.

116. A. Ghosh, P. Das, M. R. Gill, P. Kar, M. G. Walker, J. A. Thomas and A. Das, Photoactive Ru^{II}–Polypyridyl Complexes that Display Sequence Selectivity and High-Affinity Binding to Duplex DNA through Groove Binding, *Chem. – Eur. J.*, 2011, 17, 2089–2098.

117. A. Oleksi, A. G. Blanco, R. Boer, I. Uson, J. Aymamı, A. Rodger, M. J. Hannon, and M. Coll, Molecular Recognition of a Three-Way DNA Junction by a Metallosupramolecular Helicate, *Angew. Chem., Int. Ed.*, 2006, 45, 1227–1253.

118. S. A. Archer, A. Raza, F. Droge, C. Robertson, A. J. Auty, D. Chekulaev, J. A. Weinstein, T. Keane, A. J. H. M. Meijer, J. W. Haycock, S. MacNeil, and J. A. Thomas, A dinuclear ruthenium(II) phototherapeutic that targets duplex and quadruplex DNA, *Chem. Sci.*, 2019, 10, 3502–3513.

119. D. Jollie, *Platinum*, Johnson Matthey: Hertfordshire, UK, 2008, 42–43.

120. Z. Liu and P. J. Sadler, Organoiridium Complexes: Anticancer Agents and Catalysts, *Acc. Chem. Res.*, 2014, 47(4), 1174–1185.

121. R. H. Crabtree, In Iridium Catalysis; G. P. Andersson, Ed.; Springer Berlin Heidelberg: Berlin, Heidelberg, 2011, 1–10.

122. S. Medici, M. Peana, V. Marina Nurchi, J. I. Lachowicz, G. Crisponi, M. A. Zoroddu, Noble metals in medicine: Latest advances, *Coord. Chem. Rev.*, 2015, 284, 329–350.

123. Z. Liu, I. Romero-Canelón, B. Qamar, J. M. Hearn, A. Habtemariam, N. P. E. Barry, A. M. Pizarro, G J. Clarkson, P. J. Sadler, The Potent Oxidant Anticancer Activity of Organoiridium Catalysts, *Angew. Chem.*, 2014, 126, 4022 –4027.

124. V. W.-W. Yam, and K. M.-C. Wong, Luminescent metal complexes of d^6, d^8 and d^{10} transition metal centres, *Chem. Commun.*, 2011, 47, 11579–11592.

125. K. K.-W. Lo and K. Y. Zhang, Iridium(III) complexes as therapeutic and bioimaging reagents for cellular applications, *RSC Adv.*, 2012, 2, 12069–12083.

126. J. Zhao, W. Wu, J. Sun, and S. Guo, Triplet photosensitizers: from molecular design to applications, *Chem. Soc. Rev.*, 2013, 42, 5323–5351.

127. L. K. McKenzie, H. E. Bryant, J. A. Weinstein, Transition metal complexes as photosensitisers in one- and two-photon photodynamic therapy, *Coord. Chem. Rev.*, 2019, 379, 2–29.

128. L. Wu, J. Liu, P. Li, B. Tang, T. D. James, Two-photon small-molecule fluorescence-based agents for sensing, imaging, and therapy within biological systems, *Chem. Soc. Rev.*, 2021, 50, 702–734.

129. T. Huang, Q. Yu, W. Huang, Q. Zhao, Phosphorescent iridium(III) complexes: a versatile tool for biosensing and photodynamic therapy, *Dalton Trans.*, 2018, 47, 7628–7663.

130. E. Baranoff and P. Kumar, Iridium complexes as photoactive center for light harvesting and solar cell applications. In: Zysman-Colman E, editor. Iridium(III) in optoelectronic and photonics applications. first ed., vol. 1. John Wiley & Sons Ltd; 2017, 655–681.

131. Q.-B. Mei, L. Liu, J.-C. Yang, S.-H. Ye, B.-H. Tong, The novel synthesis of triscyclometalated iridium(III) complexes for saturated red organic light-emitting diodes with low efficiency roll-off, *Dyes Pigments*, 2021, 191, 109360.

132. H. Zhang, H. Wang, K. Tanner, A. Schlachtr, Z. Chen, P. D. Harvey, S. Chen, W.-Y. Wong, New phosphorescent iridium(III) dipyrrinato complexes: synthesis, emission properties and their deep red to near-infrared OLEDs, *Dalton Trans.*, 2021, 50, 10629–10639.

133. L. Zhang, Y. Li, W. Che, D. Zhu, G. Li, Z. Xir, N. Song, S. Liu, B. Z. Tang, X. Liu X, Z. Su, M. R. Bryce, AIE multinuclear Ir(III) complexes for biocompatible organic

nanoparticles with highly enhanced photodynamic performance, *Adv. Sci.*, 2019, 6, 1802050.

134. L. Zhang, Y. Geng, L. Li, X. Tong, S. Liu, X. Liu, Z. Su, Z. Xie, D. Zhu, M. R. Bryce, Rational design of iridium–porphyrin conjugates for novel synergistic photodynamic and photothermal therapy anticancer agents, *Chem. Sci.*, 2021, 12, 5918–5925.

135. J. Li and T. Chen, Transition metal complexes as photosensitizers for integrated cancer theranostic applications, *Coord. Chem. Rev.*, 2020, 418, 213355.

136. E. Palao, R. Sola-Llano, A. Tabero, H. Manzano, A. R. Agarrabeitia, A. Villanueva, I. Lopez-Arbeloa, V. Martínez-Martínez, M. J. Ortiz, Acetylacetonate BODIPY Biscyclometalated iridium(III) complexes: effective strategy towards smarter fluorescent photosensitizer agents, *Chem. Eur J.*, 2017, 23, 10139–10147.

137. Y. Deng, S. Pan, J. Zheng, Y. Hong, J. Liu, H. Chang, Y. Miao, Y. Sun, Y. Li, Electrostatic self-assembled Iridium(III) nano-photosensitizer for selectively disintegrated and mitochondria targeted photodynamic therapy, *Dyes Pigments*, 2020, 175, 108105.

138. S. A. Sharma, P. Sudhindra, R. Nilmadhab, P. Priyankar, Advances in novel iridium (III) based complexes for anticancer applications: a review, *Inorg. Chim. Acta.*, 2020, 513, 119925.

139. K. Qiu, Y. Chen, T. W. Rees, L. Ji, H. Chao, Organelle-targeting metal complexes: from molecular design to bio-applications, *Coord. Chem. Rev.*, 2019, 378, 66–86.

140. P.-Y. Ho, C.-L. Ho, W.-Y., Wong, Recent advances of iridium(III) metallophosphors for health-related applications, *Coord. Chem. Rev.*, 2020, 413(15), 213267.

141. R. Guan, L. Xie, L. Ji, H. Chao, Phosphorescent iridium(III) complexes for anticancer applications, *Eur. J. Inorg. Chem.*, 2020, 3978–3986.

142. M. Yu, Q. Zhao, L. Shi, F. Li, Z. Zhou, H. Yang, T. Yi and C. Huang, Cationic iridium(III) complexes for phosphorescence staining in the cytoplasm of living cells, *Chem. Commun.*, 2008, 2115–2117.

143. A. Prieto-Castañeda, A. Lérida-Viso, E. Avellanal Zaballa, R. Sola-Llano, J. Bañuelos, A. R. Agarrabeitia, R. Martínez-Máñez, and M. J. Ortiz, Phosphorogenic Dipyrrinato-Iridium(III) Complexes as Photosensitizers for Photodynamic Therapy, *Dyes and Pigments*, 2022, 197, 109886.

144. J.-H. Zhu, G.-X. Xu, J. Shum, Lawrence C.-C. Lee, and K. K.-W. Lo, Tuning the Organelle Specificity and Cytotoxicity of Iridium(III) Photosensitisers for Enhanced Phototheranostic Applications, *Chem. Commun.*, 2021, 57, 12008–12011.

145. Biophysical studies on a novel family of iridium polypyridyl complexes, S.M. Stimpson, PhD Thesis, University of Sheffield, 2018.

146. K.V.R. Murthy and H.S. Virk, Luminescence Phenomena: An Introduction, *Defect and Diffusion Forum*, 2013, 347, 1–34.

147. Principles of Fluorescence Spectroscopy, 3rd Edition, Introduction to Fluorescence, Joseph R. Lakowicz, Springer, Boston, M. A., 2006, 1–26.

148. H. Ahmad, A. Wragg, W. Cullen, C. Wombwell, A. J. H. M. Meijer, and J. A. Thomas, From Intercalation to Groove Binding: Switching the DNA-Binding Mode of Isostructural Transition-Metal Complexes, *Chem. Eur. J.*, 2014, 20, 3089–3096.

2.0 Synthesis and Characterisation

This chapter reports on the synthesis and characterisation of a family of three new, photostable, iridium(III) polypyridyl complexes $[Ir(bpy)_2(qtpy)]^{3+}$ **1**, $[Ir(phen)_2(qtpy)]^{3+}$ **2**, and $[Ir(dppz)_2(qtpy)]^{3+}$ **3**, all bearing +3 charge in their core (Fig. 2.1). The structures reported herein are the iridium(III) variants of the well-studied ruthenium(II) parent complexes, $[Ru(bpy)_2(qtpy)]^{2+}$, $[Ru(phen)_2(qtpy)]^{2+}$, and $[Ru(dppz)_2(qtpy)]^{2+}$. The complexes all utilise qtpy as the bridging ligand and bpy, phen, and dppz as the ancillary ligands whist gradually increasing the bulkiness and intercalative ability of the auxiliary ligands from bpy to phen to dppz.

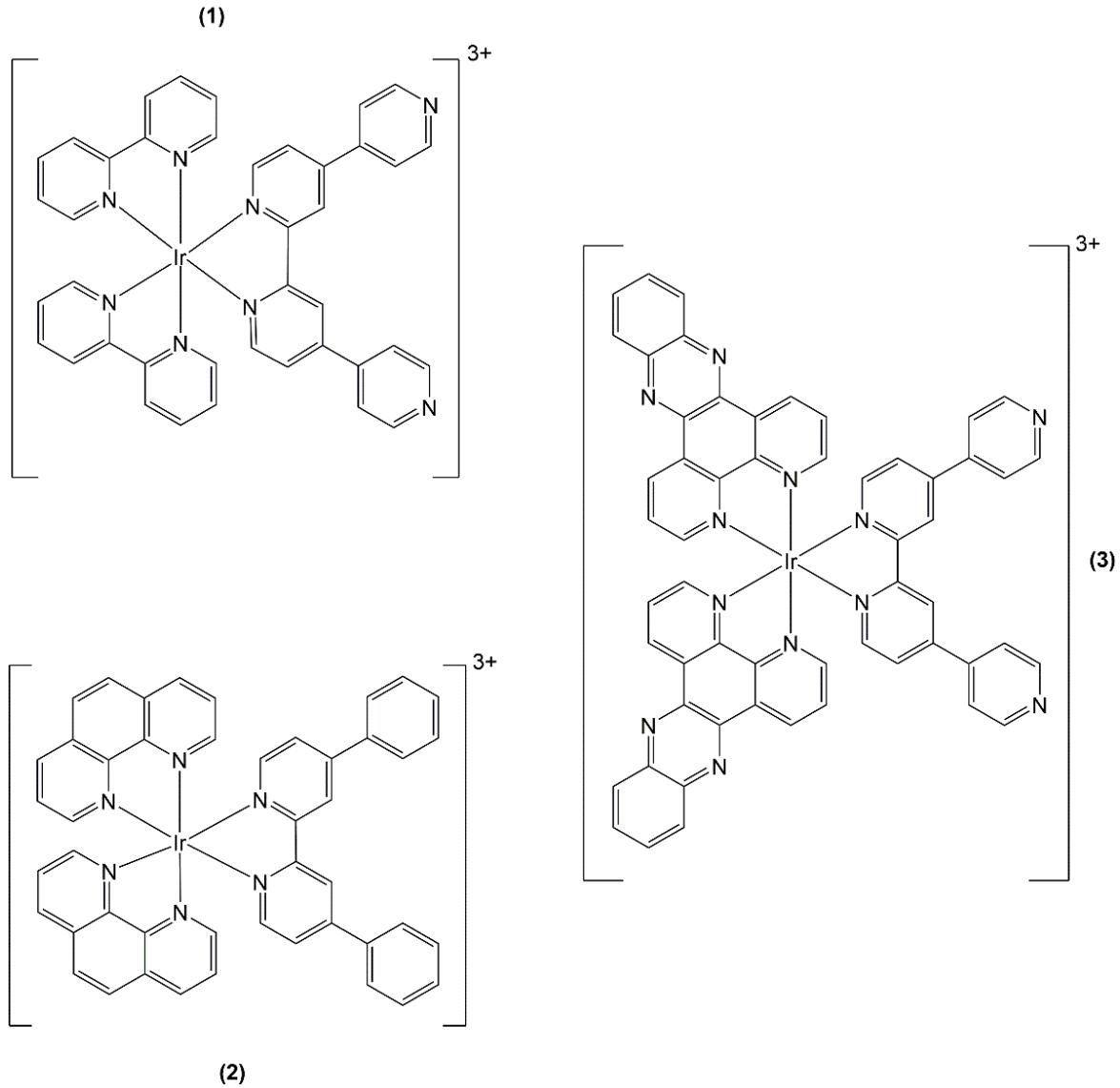

Figure 2.1 – Reported iridium(III) polypyridyl complexes.

2.1 Preparation of the Intercalative Bridging Ligand, 2,2':4,4'':4',4'''-quaterpyridine (qtpy)

Qtpy is an important bridging ligand used in synthetic inorganic chemistry in the development of many transition metal complexes (TMCs), including those employed as DNA-binding probes.[1–2] Previously, bridging ligands that provide low inter-metal communication (due to the absence of conjugation between two ligands subunits connected by saturated carbon chains as experienced in bridging ligands that contain isolated bipyridine, bpy subunits) have been obtained by the direct fusion of two bpy moieties. To date, qtpy represents one of the few instances of a ligand formed from two fused bpy units whose coordination chemistry has been widely explored.[3–4]

In fact, the first report of qtpy dates to 1938 when Burstall and colleagues obtained the ligand as a by-product of the reaction between 4,4'-bipyridine (4,4'-bpy) and iodine.[5] However, since the 1990s, studies in the use of the ligand as a building block for oligonuclear supramolecular assemblies of photoactive and redox-active chromophoric sites have multiplied.[6] Qtpy's suitability for such a role arises from its possession of a bidentate diamine site that can coordinate through chelation to a metal centre and two monodentate imine sites, which can both coordinate to other metal centres (Fig. 2.2).

In a number of studies, the Thomas group has employed qtpy as a bridging ligand to synthesize novel luminescent TMCs towards therapeutic, diagnostic, theranostic and bioimaging ends. This work has involved chiefly $Ru^{(II)}$ and other d^6-metal ions.[7–13]

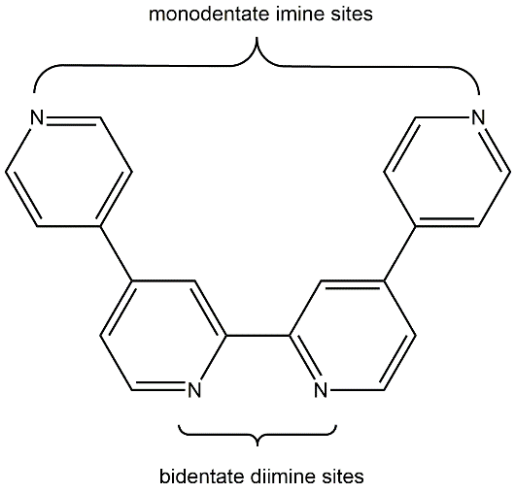

Figure 2.2 – Qtpy structure showing monodentate and bidentate coordination sites.

The qtpy described herein was synthesised according to the published method given by Baker and colleagues.[14] The ligand was isolated as a dull white or creamy-white solid. Essentially, its synthetic procedure involves the dimerisation of 4,4'-bpy using palladium on charcoal (Pd/C) as a catalyst (Fig. 2.3). Several crude qtpy crops were generated by repeated recycling of the unreacted 4,4'-bpy during the synthetic process. Slow recrystallization of crude qtpy in refluxing EtOH yielded X-ray quality white or creamy-white pure crystals of the compound, which were subjected to X-ray crystallographic analysis. Despite its structural simplicity and synthetic significance, there is no report of the single-crystal structure of pure crystalline qtpy.

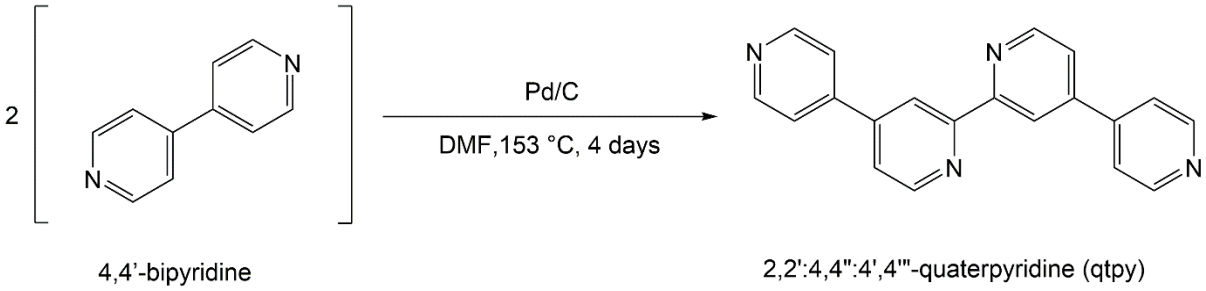

Figure 2.3 – Synthetic pathway to qtpy.

Qtpy has also been shown to be a DNA-intercalating ligand in recent work from the Thomas group.[15]

2.2 Preparation of the Intercalative Ligand, Dipyrido[3,2-a:2',3'-c]phenazine (dppz)

Dipyrido[3,2-a:2',3'-c]phenazine (dppz) ligand was obtained as a product of the Schiff base condensation of 1,10-phenanthroline-5,6-dione (dpq) with *o*-phenylenediamine (Fig. 2.4).[16] Though the reaction was allowed to proceed for ca. 30 minutes, deep brown crystals of heterocyclic dppz were obtained upon reacting the starting materials together even at a reaction time of ca. 5 minutes. The ligand was afforded in ca. 70 % yield.

Theoretically the intercalative ligand, dppz, can be divided into two subparts: the bpy portion and the phenazine portion (Fig. 2.5). The "light switch" properties of dppz have been attributed to the two metal-to-ligand charge transfer (MLCT) states on the dppz ligand. The "bright state" is associated with the MLCT located on the bpy section of the dppz ligand whilst the "dark and non-luminescent" state is assigned to the MLCT state located on the phenazine (phz) section of the ligand. The "light switch" effect depends on subtle changes in enthalpy and entropy on moving between protic and non-protic environments for the dark state and bright state.[17]

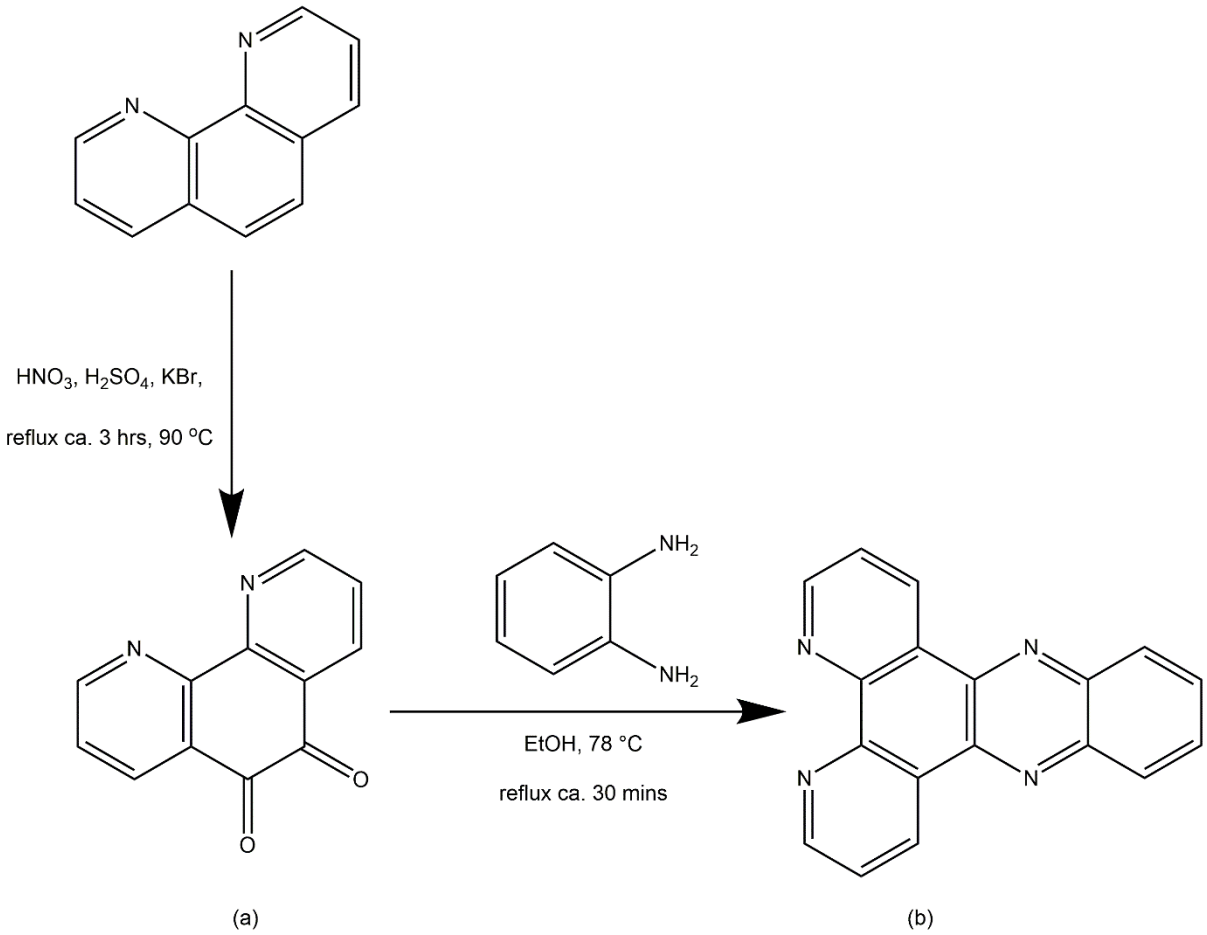

Figure 2.4 – Synthetic route to dpq (a) and dppz (b) ligands.

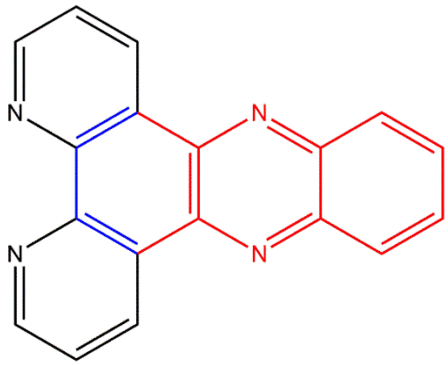

Figure 2.5 – Dppz ligand showing both the bpy and phenazine units (bpy unit in black and phenazine unit in red).

2.3 Synthesis of Iridium(III) Polypyridyl Complexes

The three iridium(III) complexes given in this report were prepared as their triflate salts, following the same general experimental procedure. A multi-step synthetic pathway has to be

employed due to the kinetic inertness of the iridium core, which makes ancillary ligands difficult to coordinate to it. The first reaction step involves the coordination of iridium(III) trichloride hydrate to either bidentate bpy, phen, or dppz unit followed by precipitation with NH_4PF_6 to afford $[Ir(bpy)_2Cl_2]PF_6$ or $[Ir(phen)_2Cl_2]PF_6$ or $[Ir(dppz)_2Cl_2]PF_6$ in quantitative yields of 60 %, 97.20 %, and 81.15 %, respectively (Fig. 2.6). This reaction procedure is totally different from the one used for the synthesis of the ruthenium analogues. While the synthesis of Ru(II) complexes employed a one-pot synthetic route, the synthesis of Ir(III) complexes makes use of the triflato-intermediate pathway; the triflato group being derived from trifluoromethanesulfonic acid (or triflic acid, CF_3SO_3H, i.e., TFMS). In this route the PF_6^- counter ion group in $[Ir(bpy)_2Cl_2]PF_6$ or $[Ir(phen)_2Cl_2]PF_6$ or $[Ir(dppz)_2Cl_2]PF_6$, was first replaced by water-soluble chloride moiety to afford $[Ir(bpy)_2Cl_2]Cl$ or $[Ir(phen)_2Cl_2]Cl$ or $[Ir(dppz)_2Cl_2]Cl$ in yields of ca. 89 %, 91 %, and 93 %, respectively (Fig. 2.6). The chloride moiety in $[Ir(bpy)_2Cl_2]Cl$ or $[Ir(phen)_2Cl_2]Cl$ or $[Ir(dppz)_2Cl_2]Cl$ was consequently converted to the triflato counter ion groups upon the addition of triflic acid to first give $[Ir(bpy)_2Cl_2]CF_3SO_3$ or $[Ir(phen)_2Cl_2]CF_3SO_3$ or $[Ir(dppz)_2Cl_2]CF_3SO_3$ in yields of 60 %, 63 %, and 91 %, respectively, and then $[Ir(bpy)_2(CF_3SO_3)_2]CF_3SO_3$ or $[Ir(phen)_2(CF_3SO_3)_2]CF_3SO_3$ or $[Ir(dppz)_2(CF_3SO_3)_2]CF_3SO_3$ in yields of 83 %, 99 %, and 65 %, respectively when excess triflic acid was added (Fig. 2.7).

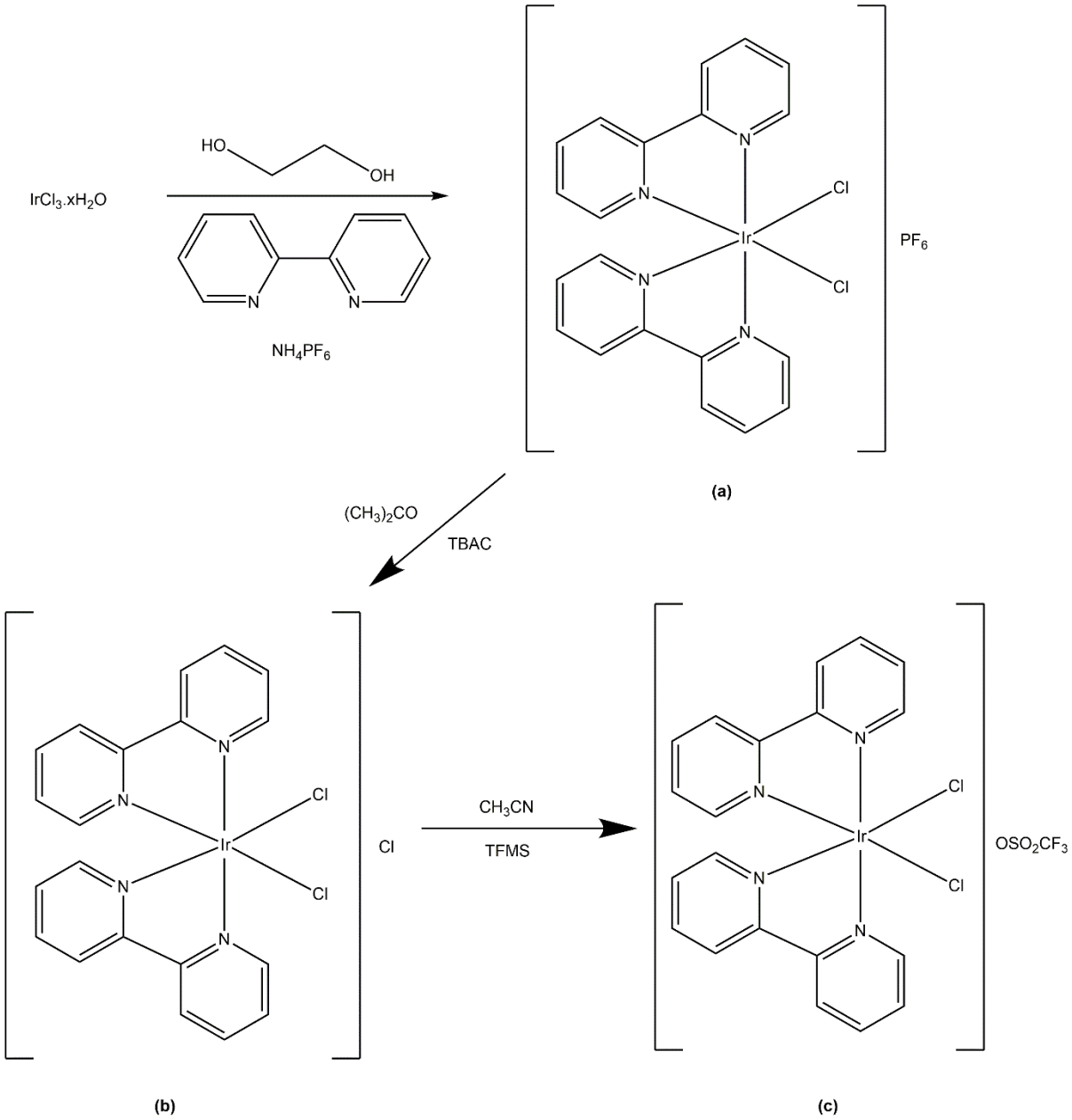

Figure 2.6 – Synthetic route to intermediate compounds $[Ir(bpy)_2Cl_2]PF_6$ **(a)**, $[Ir(bpy)_2Cl_2]Cl$ **(b)**, and $[Ir(bpy)_2Cl_2]CF_3SO_3$ **(c)**.

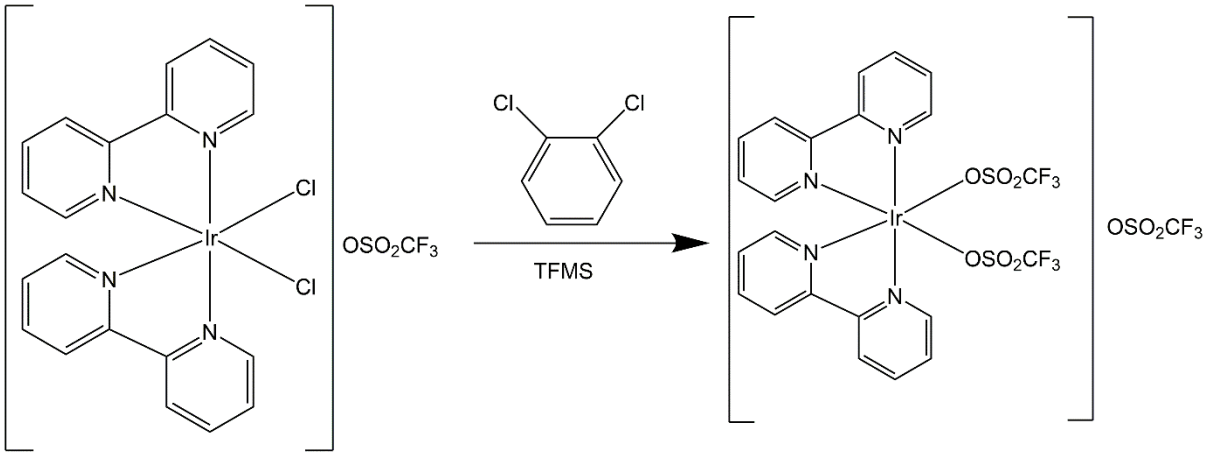

(c) **(d)**

Figure 2.7 – Synthetic route to intermediate compound $[Ir(bpy)_2(CF_3SO_3)_2]CF_3SO_3$ **(d)**.

The triflato complexes now allow the easy coordination of the bridging ligand, qtpy, directly onto the iridium centre. As established by Scott and Taube, triflato complexes are appealing in this role as they possess high thermal stability and are poorly coordinated ligands.[18] The triflato group is one of the strongest electron-withdrawing groups known, and its anion, $CF_3SO_3^-$, has been widely used as an excellent leaving group in nucleophilic substitution reactions in organic chemistry.[19] The lability of such complexes has provided facile route to a range of synthetically difficult iridium(III) complexes. Once prepared, the triflato complexes have desirable properties such as great lability of the acid leaving group, excellent solubility in a range of polar solvents, relatively low reactivity with atmospheric moisture, and simple high-yielding preparative routes from readily available reagents.[20] Due to the excellent leaving capabilities of the triflate anions, the bridging ligand can be added to the iridium centre with the correct geometry needed for DNA binding. Despite containing labile triflato groups, the iridium metal centre is still kinetically inert, implying that the coordination of the bridging qtpy ligand requires long reaction times and brutal reaction conditions. This poses a great difficulty in the synthesis of the complexes. As conventional heating under reflux would not afford the complexes, attention was directed to microwave-assisted synthesis, which successfully led to the derivation of the reported complexes.

The routes that lead to the formation of the intermediate complexes of the phen and dppz analogues of the bpy complexes are essentially the same. So, for simplicity, descriptions of these intermediate steps (and eventual compounds) are excluded from this section, but details

are included in the Experimental chapter.

2.4 Microwave-assisted Synthesis of the Complexes

Microwave radiation is a popular tool to heat reaction mixtures providing an accelerated and direct heating method, and the literature is replete with the use of microwave technology.[21–26] Microwave heating or irradiation can dramatically lower reaction times from several hours to just minutes. Moreover, it frequently increases product yields and enhances product purity.[27] Early reports of microwave-assisted synthesis date back to 1986[28–29], and since then, microwave technology has evolved rapidly over the years. To ensure accurate measurements, modern-day scientific microwave systems are typically designed to incorporate a temperature control based on either an infrared sensor or a fibre-optic probe. As a safety precaution, microwave reactions are typically performed in a small, sealed cavity in the apparatus to hold materials in case the reaction vessel fails. Large-scale reactions can also be conducted by conveniently scaling up small-scale reactions. Microwaves are insufficiently energetic to directly break any chemical bonds, which is interesting from a synthetic viewpoint.[30] Microwave irradiation utilises polar solvents for very effective internal temperature control[31–32] affording fast temperature equilibration besides expedited reaction times/kinetics.[33–34]

The inert coordination sphere of iridium(III) makes the formation $[Ir(N—N)_2(qtpy)](CF_3SO_3)_3$ (where N–N = bpy, phen and dppz) very challenging. The coordination of six nitrogen donors to an iridium centre has been shown by previous research works to be difficult to access. Needless to say, conventional reactions of qtpy bridging ligand with $[Ir(N–N)_2Cl_2]^+$ (where N–N = bpy, phen, and dppz ligands auxiliary ligands) required very harsh reaction conditions and led to meagre product yields and issues with product purity. The synthetic procedure that led to the formation of the complexes used a trifluoromethanesulfonato (or triflate) intermediate. The reaction intermediates, $[Ir(bpy)_2(CF_3SO_3)_2]CF_3SO_3$, $[Ir(phen)_2(CF_3SO_3)_2]CF_3SO_3$, and $[Ir(dppz)_2(CF_3SO_3)_2]CF_3SO_3$ were synthesised through the reaction scheme depicted in Fig. 2.7 as previously discussed. Since the synthesis of complexes $[Ir(bpy)_2(qtpy)](CF_3SO_3)_3$, $[Ir(phen)_2(qtpy)](CF_3SO_3)_3$, and $[Ir(dppz)_2(qtpy)](CF_3SO_3)_3$ could not be achieved via traditional reflux technique even after 10days, the microwave technique described in the preceding paragraphs was employed. Microwave heating utilises polar solvents for efficient internal temperature control[35] allowing for fast temperature equilibration and, in many

instances, enhanced reaction kinetics.[35] Ethylene glycol is a popular solvent for microwave irradiation, which has been reported to provide an increased "heating" factor quotient (tan δ) of 1.350. "Heating" factor quotient is quantified by the ratio of the dielectric loss factor (ε″) (which designates heating efficiency) to the dielectric constant (ε′) (which depicts the polarisation of molecules and describes the possibility of microwave excitation) (Equation 2.1). These values, for instance, range from 1.350 for polar solvents like ethylene glycol to 0.020 for nonpolar solvents such as hexane.[36] Ethylene glycol was first tried as the reaction solvent, but despite its general suitability for microwave irradiation, it proved inappropriate for isolating iridium(III) complexes reported herein. An alternative option was to substitute ethylene glycol for ethanol (ethanol has a tan δ value of 0.941, which is sufficiently high to drive a successful microwave reaction); this alternative was attempted, and fortunately, the desired complexes were obtained.

$$\tan \delta = \frac{\varepsilon''}{\varepsilon'}$$

Equation 2.1

First, Ir-bpy qtpy complex, being the structurally simplest complex of the three complexes, was synthesised (Figs. 2.1 and 2.8; full experimental procedures are given in the Experimental Section). After that, the more structurally complex Ir-phen qtpy and Ir-dppz qtpy analogues were tried and successfully obtained following the same protocol. Their syntheses all followed the triflato route, which offers much milder reaction conditions for generating these complexes.

Equimolar quantities of either $[Ir(bpy)_2(CF_3SO_3)_2]CF_3SO_3$, $[Ir(phen)_2(CF_3SO_3)_2]CF_3SO_3$, or $[Ir(dppz)_2(CF_3SO_3)_2]CF_3SO_3$ and crystalline qtpy were refluxed in EtOH for two days using conventional reflux and then transferred onto a microwave apparatus. Initially, the reaction was first carried out for ca. 3hours, then for ca. 6hours, and finally for ca. 9hours, with continuous analysis of the reaction products over these reaction time windows. It was discovered the reaction only reached completion yielding the desired complexes, i.e., $[Ir(bpy)_2(qtpy)](CF_3SO_3)_3$, $[Ir(phen)_2(qtpy)](CF_3SO_3)_3$, and $[Ir(dppz)_2(qtpy)](CF_3SO_3)_3$ after 9 to 12hours of reflux time, which became the standard for repeated experiments. All the three complexes were obtained in low yields as their triflate salts, and their characterisations were proceeded using ^{1}H NMR spectroscopy and MS.

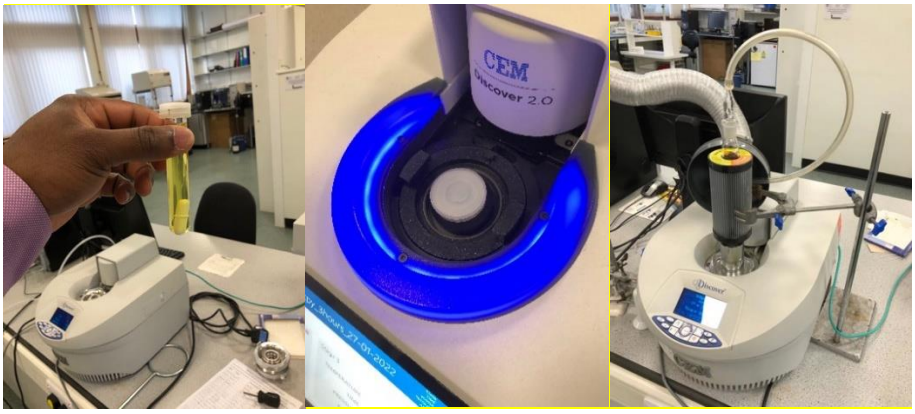

Figure 2.8 – Microwave setup showing a 10mL microwave vial with a magnetic stir bar inside. **Content:** $[Ir(N–N)_2(CF_3SO_3)_2]CF_3SO_3$, qtpy, and EtOH, where N–N = chelating diamine ligand bpy, phen, or dppz **(left)**. The sealed reaction starting materials were pre-stirred for ca. 1-2minutes and then heated at 78^{o}C at a heating rate of 28^{o}Cmin^{-1} for ca. 9hours for bpy and phen compounds and ca. 12hours for dppz compound at atmospheric pressure **(middle)**. A scaled-up version of the setup displaying a 50mL RBF equipped with a reflux condenser for the preparation of $[Ir(bpy)_2(qtpy)](CF_3SO_3)_3$, $[Ir(phen)_2(qtpy)](CF_3SO_3)_3$, and $[Ir(dppz)_2(qtpy)](CF_3SO_3)_3$ by microwave irradiation **(right)**.

2.5 High-Performance Liquid Chromatography (HPLC)

Initial attempt to purify the complexes solely by column chromatography failed. With both silica and alumina as the stationary phase in a column, the complexes adhered too firmly to be removed by a solvent system, including saturated potassium nitrate solution, methanol and weak sulphuric acid. Purification of the complexes by size exclusion chromatography using SP Sephadex C-25 cation exchanger (eluent: 0.5M NaCl solution) also proved abortive. Therefore, HPLC was critical in obtaining analytical pure samples of the synthesised complexes. Not only were the syntheses of the complexes reported in this project challenging, but their purification is also equally difficult. Hence the need for the employment of HPLC towards their final purification.

Chromatography is a separation method that involves distributing sample mixtures between two phases in a chromatographic bed, either in columns or in planes. One phase is the stationary phase whilst the other phase is the mobile phase. The mobile phase passes through the chromatographic bed. There are two types of stationary phases: small-particle, porous solids or thin films of liquid coated on solid supports or columns, whilst the mobile phase, on the other hand, is either a gas or liquid. If a gas is used, the process is known as gas chromatography, but

if a liquid is used, the process is referred to as liquid chromatography.[37]

High-Performance Liquid Chromatography (HPLC) is a powerful separation method capable of resolving mixtures with many similar analytes, invented by Martin and Synge. This chromatographic method provides both qualitative and quantitative information in a direct manner. There is a different elution time for each compound in the mixture (which is the time when a signal emerges on the HPLC instrumentation screen) under a given set of conditions. There is a direct relationship between the area and height of each signal and the concentration of each substance. HPLC is very efficient as it yields excellent separations within a short period. In HPLC, the stationary phase requires very “small particles”, which is why a “high pressure” is needed to force the mobile phase through the column. Because of this pressure factor, HPLC is sometimes referred to as “high-pressure liquid chromatography”.[37]

2.5.1 HPLC Instrumentation

Fig. 2.9 depicts a typical HPLC instrument which possesses the following elements/components: solvent reservoir, transfer line fit, high-pressure pump, sample injection device, column, UV-Vis detector, waste, and data acquisition (usually together with data evaluation). Although the column is the most important part, it is usually the smallest component of an HPLC system. Solvent mixtures are typically used, so a mixer and controller are needed in an HPLC instrumentation. In most cases, data acquisition is usually done by a computer, which is used to control of the entire system.

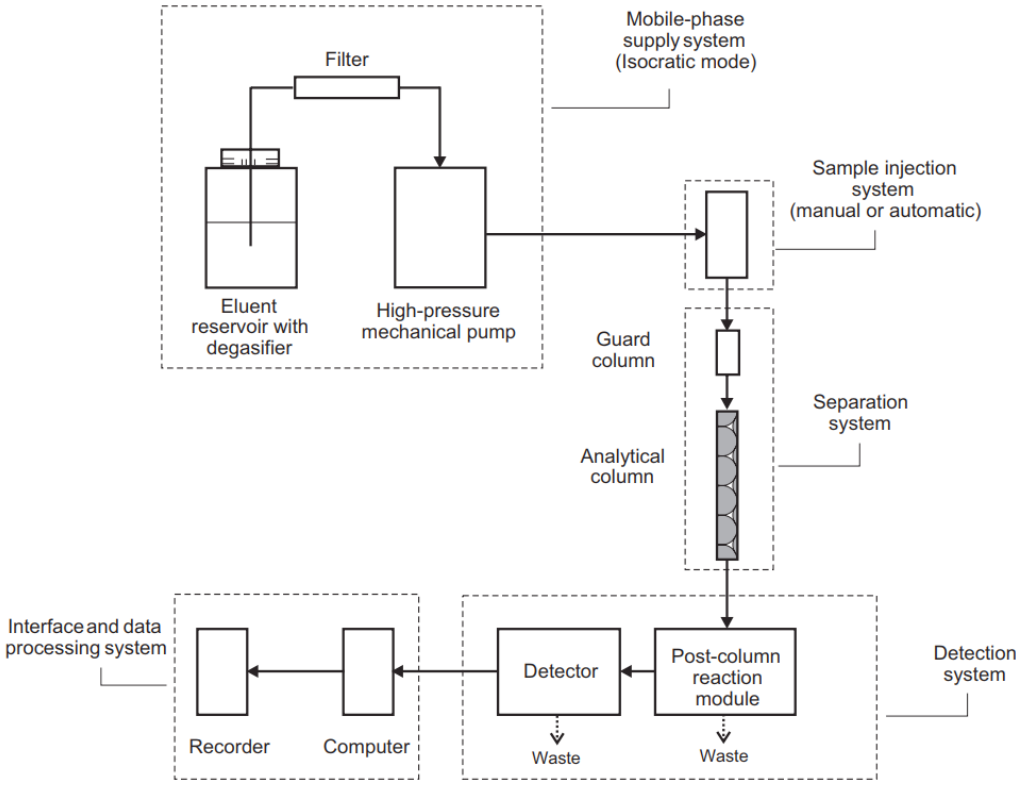

Figure 2.9 – Schematic diagram of a typical HPLC set-up with a simple isocratic mobile phase system. A chromatographic system basically consists of five modules: mobile-phase supply system; sample injection system; separation system; detection system; and interface and data processing system.[38]

In reversed-phase HPLC the following conditions apply:

a. The stationary phase is very nonpolar.

b. The mobile phase is quite polar (water to tetrahydrofuran).

c. Solvents with more polarity, such as water, elute more slowly than those with less polarity, such as acetonitrile.

2.5.2 HPLC Conditions Employed for the Purification of Reported Complexes

For full experimental protocol employed for HPLC, readers are kindly referred to the Experimental section of this thesis. Using RP-HPLC, the compounds were injected into the column after being dissolved in HPLC-grade MeCN (and sometimes MeOH or H_2O) using 15% acetonitrile in water, which was increased over 20 minutes to 60% organic phase with a flow rate of 17 ml/min.[1] The major peak, which began to elute at 8.08, 8.16, and 12.35 minutes for $[Ir(bpy)_2(qtpy)]^{3+}$, $[Ir(phen)_2(qtpy)]^{3+}$, and $[Ir(dppz)_2(qtpy)]^{3+}$, respectively, as detected by UV-Vis spectroscopy was collected. Purification of the crude complexes via RP-HPLC required a high level of meticulousness during the analytical process. It seems impurities of various oxidation states coexisted with the desired, pure iridium(III) complexes as the colours (ranging from red to purple) and (eventual chemical analysis) of the undesired HPLC fractions showed.

2.6 Luminescence Excited State Lifetime Studies

All luminescence lifetimes (Table 2.1) were measured using a mini-tau filter-based fluorescence lifetime spectrometer ("Mini-τ Edinburgh Instruments" in this instance with the following settings applied for the experiment: intensity control: 8; pulse period: 2µs; time range: either 200ns or 2µs; emission filter: 475–525nm; fitting range: 80-1023channel), which uses a time-correlated single photon counting method. In this experiment, samples were excited at a particular wavelength using a laser with defined pulse width and recording single excitation/emission events one photon at a time, producing a time-dependent intensity profile of the emitted light. The delay between the excitation event and the detected emission is measured over numerous single-photon cycles producing a cumulative time profile of the exponential decay curve for each complex.

When fitting a dual exponential, there is one consistently short lifetime component, τ_1, and a longer lifetime component, τ_2, with the percentage contribution always larger from the second lifetime. The quality of the biexponential can be monitored by the τ_2 value. The biexponential

[1] The triflate analogues of the compounds were dissolved in MeCN whilst the chloride salts were dissolved in either MeOH or H_2O before injection into the HPLC column.

(dual exponential) nature of the complexes could accrue from two close lying electronic states (i.e., MLCT and π-π*)/all complexes exhibit two lifetimes, (τ_1) shorter and (τ_2) longer. The lifetimes of $[Ir(bpy)_2(qtpy)](CF_3SO_3)_3$, $[Ir(phen)_2(qtpy)](CF_3SO_3)_3$, and $[Ir(dppz)_2(qtpy)](CF_3SO_3)_3$ were measured in aerated MeCN at an absorbance of 0.1 at their ^{1}MLCT/^{1}LLCT bands and at an excitation wavelength of ca. 300 nm, 365 nm, and 384 nm, respectively. The number of photons collected ranged from 0 to 10000.

Table 2.1 – Excited state lifetime values of $[Ir(bpy)_2(qtpy)](CF_3SO_3)_3$, $[Ir(phen)_2(qtpy)](CF_3SO_3)_3$, and $[Ir(dppz)_2(qtpy)](CF_3SO_3)_3$ recorded in air-equilibrated HPLC-grade MeCN.

Complex	Wavelength (nm)	τ_1 (ns) (%)	τ_2 (ns) (%)
$[Ir(bpy)_2(qtpy)](CF_3SO_3)_3$	300	0.56 (73.42)	9.22 (26.58)
$[Ir(phen)_2(qtpy)](CF_3SO_3)_3$	365	0.82 (53.07)	8.43 (34.10)
$[Ir(dppz)_2(qtpy)](CF_3SO_3)_3$	384	0.61 (65.90)	7.40 (46.93)

All complexes were found to have their excited state lifetimes in the nanosecond range (7.40–9.22ns) in aerated MeCN solutions. These results are within the same range as with the excited state lifetimes of iridium(III) complexes in previous reports.[39] Table 2.2 above shows that the emissions have both a longer-lived and very short-lived component. The longer of these two lifetimes can be assigned to the MLCT onto the qtpy bridging ligand. The short-lived lifetime is assigned as a π-π* of the N–N polypyridyl auxiliary ligand onto the qtpy bridging ligand. The short lifetimes of the emissions could be because they have been recorded under aerated conditions. Their large Stokes shifts suggest these emissions are from a triplet state; therefore, they will most likely be quenched by singlet oxygen. Experiments in de-aerated solutions are currently underway but have not been completed in time for this thesis The creation of singlet oxygen quenches the luminescence of the complexes so a high quantum yield for this process would explain the short wavelengths and suggest they would be longer in oxygen free conditions. The following section casts light on this issue.

2.7 Singlet Oxygen ($^1O_2$) Yield Measurements

Singlet oxygen measurements were obtained using Tektronis oscilloscope instrument. Singlet oxygen was detected directly in an organic solution by measurement of singlet oxygen

luminescence (λ_{max} ~1275nm) following photoexcitation of the compound at 25°C in air-saturated dichloromethane (DCM) or acetonitrile (MeCN). The method employed herein is a direct method as opposed to another method based on the oxidation of 1,3-diphenylisobenzofuran, DPBF (yellow) to 1,2-dibenzoylbenzene (colourless) by a photosensitized compound of interest and subsequent UV-Vis spectroscopic monitoring of singlet oxygen yield.[40] Amongst other commonly used photosensitizer standards, 1-phenalenone is a leading singlet oxygen generator whose efficacy in generating singlet oxygen equals one in MeCN.[41] All singlet oxygen measurements in this investigation are done using 1-phenalenone as the standard.

The yield of the formation of $^1O_2$, i.e., Φ ($^1O_2$), was determined by measuring its phosphorescence intensity using an optically matched solution of perinapthenone as a reference sensitizer.[42] Experimental measurements were done after preparing solutions of both the test compound and reference compound at a maximum absorbance of 0.1–0.2 at the MLCT absorption wavelength of 355nm, which corresponds to the MLCT wavelength of 1-phenalenone (Fig. 2.10).

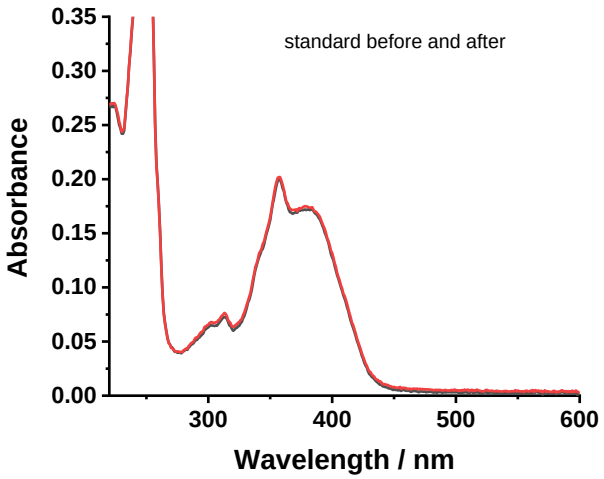

Figure 2.10 – UV-Vis spectrum of 1-phenalenone in MeCN.

The absorption of a single photon has the capacity to generate one molecule of singlet oxygen, so in an ideal situation, the Φ_Δ is expressed as an integer with a value between zero and one. A Φ_Δ of 1 would correspond to a system where every single photon observed by the metal complex correlates to the generation of a singlet oxygen molecule. $[Ir(bpy)_2(qtpy)]^{3+}$ possesses long-lived luminescent triplet-state lifetimes, which promotes and enables efficient energy

transfer with the triplet ground state of molecular oxygen.[43] This interaction with the ground state oxygen, results in simultaneous luminescence quenching and formation of triplet oxygen.

A summary of the experimental data is given in Figs. 2.11–2.15.

2.7.1 $[Ir(bpy)_2(qtpy)]^{3+}$

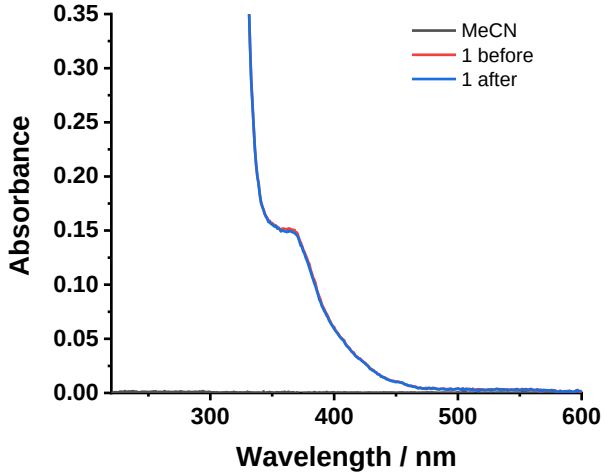

Figure 2.11 – UV-Vis spectral check of $[Ir(bpy)_2(qtpy)]^{3+}$ in MeCN before and after laser photoirradiation. No photodegradation occurred.

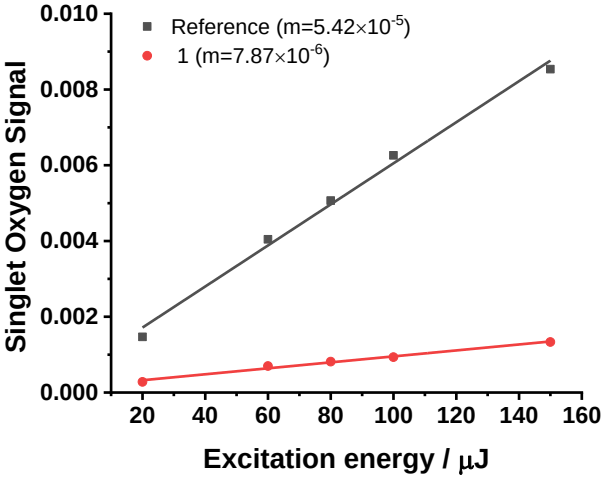

Figure 2.12 – Singlet oxygen data plot of amplitude versus power for $[Ir(bpy)_2(qtpy)^{2+}$ (red trace) and for 1-phenalenone (black trace). Measurement was done at an absorbance of ca. 0.2 at 355nm.

2.7.2 $[Ir(phen)_2(qtpy)]^{3+}$

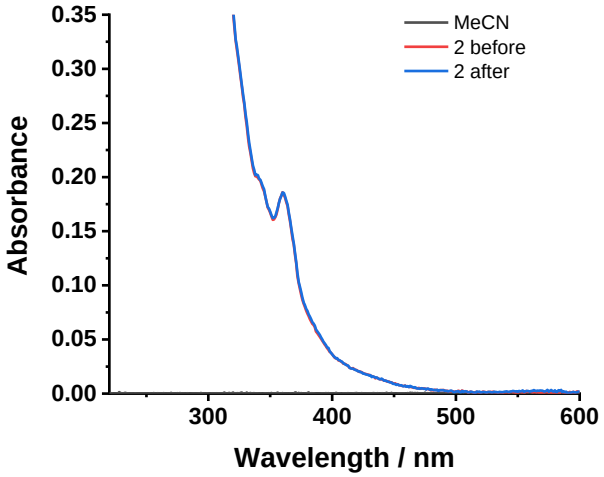

Figure 2.13 – UV-Vis spectral check of $[Ir(phen)_2(qtpy)]^{3+}$ in MeCN before and after laser photoirradiation. No photodegradation occurred.

The singlet oxygen data plot of amplitude versus power for $[Ir(phen)_2(qtpy)^{2+}$ and $[Ir(phen)_2(qtpy)^{2+}$ against the reference standard 1-phenalenone could not be given as the value of the singlet oxygen yield is very low.

2.7.3 $[Ir(dppz)_2(qtpy)]^{3+}$

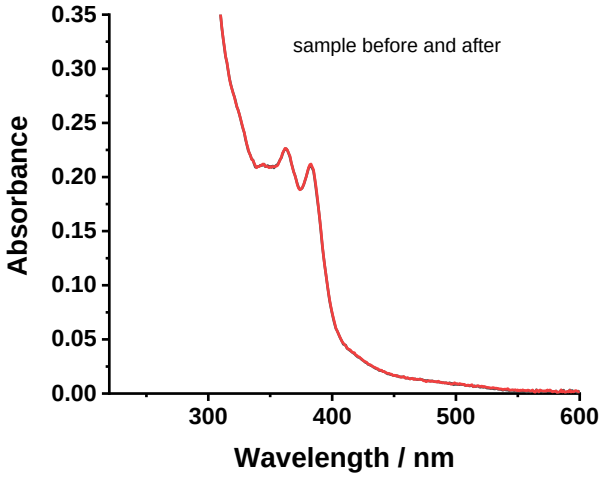

Figure 2.14 – UV-Vis spectral check of $[Ir(dppz)_2(qtpy)]^{3+}$ in MeCN before and after laser photoirradiation. No photodegradation occurred.

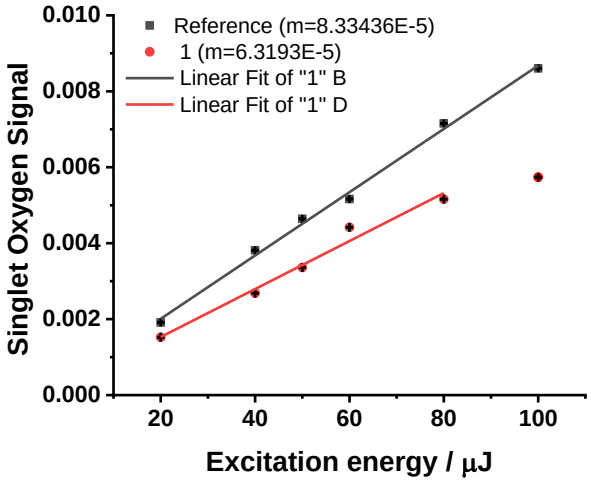

Figure 2.15 – Singlet oxygen data plot of amplitude versus power for $[Ir(dppz)_2(qtpy)^{2+}$ and $[Ir(dppz)_2(qtpy)^{2+}$ against the reference standard 1-phenalenone. Measurement was done at an absorbance of ca. 0.2 at 355nm.

The experimental results above give singlet oxygen yields of ~13%, ~4% and ~71% for $[Ir(bpy)_2(qtpy)]^{3+}$, $[Ir(phen)_2(qtpy)]^{3+}$, and $[Ir(dppz)_2(qtpy)]^{3+}$, respectively. The value obtained for $[Ir(dppz)_2(qtpy)]^{3+}$ is particularly high and is comparable to those of reported PDT leads. Indeed, the generation of singlet oxygen is a major requirement for classical photodynamic therapy (PDT); therefore, it can be implied that $[Ir(dppz)_2(qtpy)]^{3+}$ shows promise as a potential photosensitizer for PDT.

2.8 Photophysical Characterisations

2.8.1 Steady-state UV-Vis Spectroscopic Studies

The UV-Vis absorption spectra of all the desired complexes were measured in MeOH, EtOH, H_2O, and/or MeCN. Every compound shows a characteristic absorption band in the UV region corresponding to N–N-centred (or π–π) transitions. Comparative spectrum of the free qtpy ligand with those of the three complexes prepared confirm the incorporation of qtpy in the three complexes. The transitions at 249/250nm, 224/225nm, and 284nm in $[Ir(bpy)_2(qtpy)]^{3+}$, $[Ir(phen)_2(qtpy)]^{3+}$, and $[Ir(dppz)_2(qtpy)]^{3+}$, respectively correspond to the coordinated qtpy ligand.

Apart from the anticipated high-energy intraligand N–N-centred (or π–π) transitions, at lower energies the complexes possess weak MLCT transitions with a weak tail extending up to 500nm. The absorption between 250–300nm corresponds to an energy typical for a Ir / L ^{1}MLCT and/or ^{1}LLCT transition, which is substantially most intense for the dppz complex. The weak absorptions with tails (300–500nm) that extend into the visible region (up to 800nm) are assignable to ^{3}MLCT transition.[44] The energy of the MLCT does not significantly change in MeCN compared to other solvent environments, although changes in relative intensities within the band suggest that it is composed of at least two intense, overlapping transitions.

UV-Vis spectra simulated through TD-DFT calculations provide a basis for experimental data analysis and comparison, and it was shown that there is a qualitative agreement with the experimental absorption spectra for the three title complexes investigated, with the dppz complex having the longest ^{3}MLCT wavelength. These are given in relevant sections of the Appendix.

All measurements were carried out using RP HPLC-purified samples of the compounds, and all data used for all plots have been baseline corrected.

2.8.1.1 Absorption Spectrum of Qtpy

Unbound qtpy prominently absorbs at 202nm and 241nm, with a shoulder that arises at ca. 280nm and gradually descends afterwards to 337nm. No absorption occurs beyond this wavelength (Fig. 2.16).

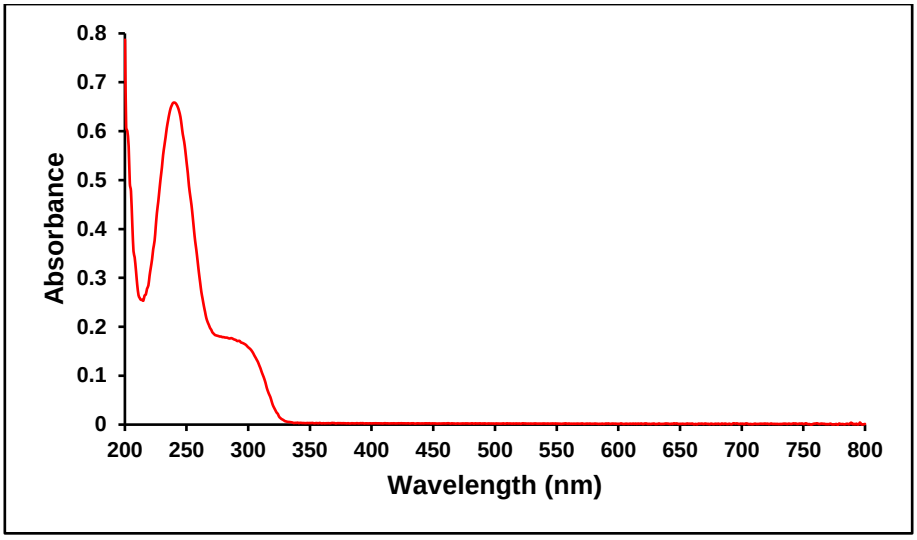

Figure 2.16 – UV-Vis spectrum of 11.90µM qtpy recorded in EtOH. ε_{202} = 53697. ε_{241} = 83361.

2.8.1.2 Complex $[Ir(bpy)_2(qtpy)]^{3+}$

The UV-Vis spectra of $[Ir(bpy)_2(qtpy)]^{3+}$ are depicted in Figs. 2.17–2.18 whilst a summary of the data obtained from the investigation is given in Tables 2.3 and 2.4.

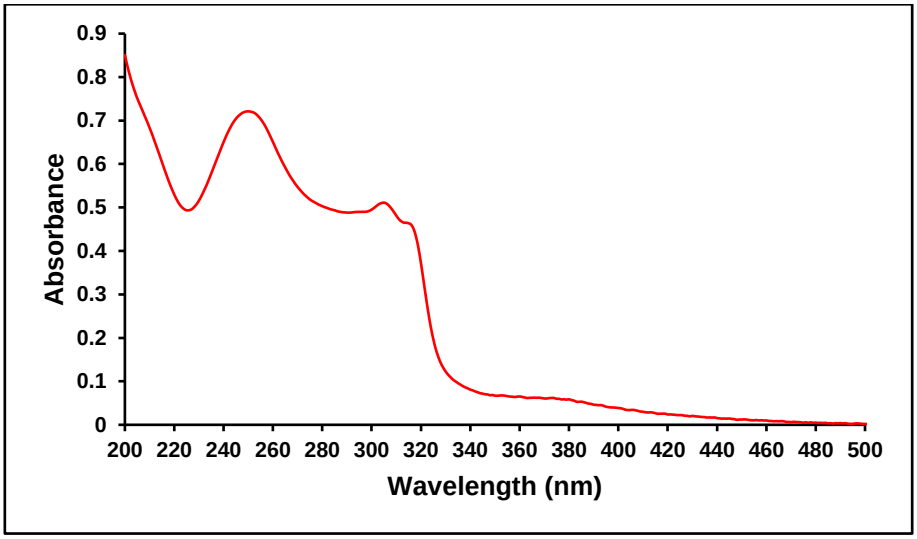

Figure 2.17 – UV-Vis spectrum of 29.60µM $[Ir(bpy)_2(qtpy)]Cl_3$ in H_2O.

The most prominent peaks are summarised in Table 2.3 below.

Table 2.3 – UV-Visible data for 29.60µM of $[Ir(bpy)_2(qtpy)]Cl_3$ recorded in milli-Q H_2O.

Compound	λ_{max} (nm)	ε (M^{-1} cm^{-1})	Assignment
$[Ir(bpy)_2(qtpy)]Cl_3$	200	41710	π-π*
	250	35363	π-π*
	305	25054	^{3}MLCT
	380	2879	^{3}MLCT

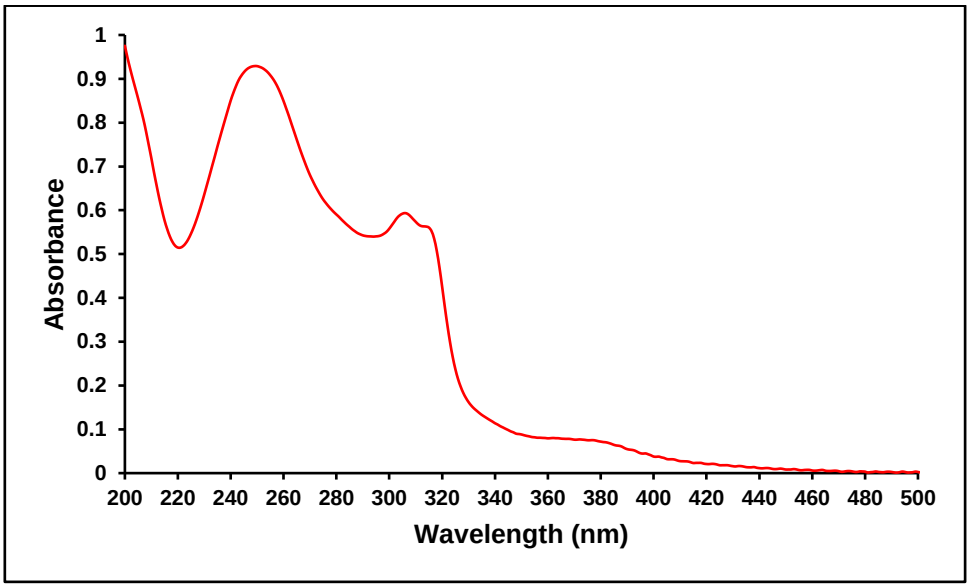

Figure 2.18 – UV-Visible spectrum of 37.82µM of $[Ir(bpy)_2(qtpy)](CF_3SO_3)_3$ in MeCN.

The most prominent peaks are summarised in Table 2.4 below.

Table 2.4 – UV-Visible data for 37.82µM of $[Ir(bpy)_2(qtpy)](CF_3SO_3)_3$ recorded in MeCN.

Compound	λ_{max} (nm)	ε (M^{-1} cm^{-1})	Assignment
$[Ir(bpy)_2(qtpy)](CF_3SO_3)_3$	200	25790	π-π*
	249	24566	^{1}MLCT
	306	15694	^{3}MLCT
	380	1902	^{3}MLCT

2.8.1.3 Complex $[Ir(phen)_2(qtpy)]^{3+}$

The UV-Vis spectra of $[Ir(phen)_2(qtpy)]^{3+}$ are depicted in Figs. 2.19–2.20 whilst a summary of the data obtained from the investigation is given in Tables 2.5 and 2.6.

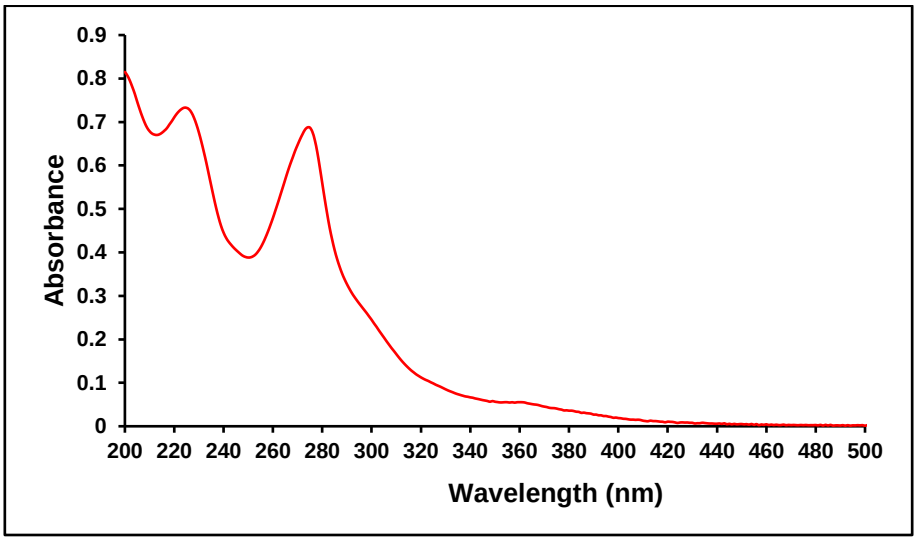

Figure 2.19 – Steady-state UV-Vis spectrum of 22.68µM $[Ir(phen)_2(qtpy)](CF_3SO_3)_3$ in MeCN.

The most prominent peaks are summarised in Table 2.5 below.

Table 2.5 – UV-Visible data for 22.68µM $[Ir(phen)_2(qtpy)](CF_3SO_3)_3$ recorded in acetonitrile.

Compound	λ_{max} (nm)	ε (M^{-1} cm^{-1})	Assignment
$[Ir(phen)_2(qtpy)](CF_3SO_3)_3$	201	35714	π-π*
	224	32187	π-π*
	274	30423	^{1}MLCT
	360	2646	^{3}MLCT

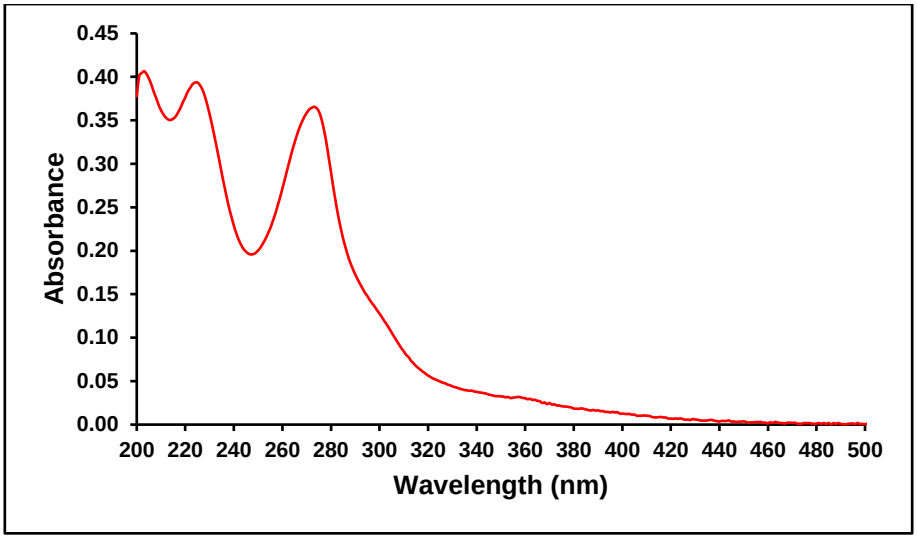

Figure 2.20 – Steady-state UV-Vis spectrum of 8.37µM $[Ir(phen)_2(qtpy)]Cl_3$ in tris buffer.

The most prominent peaks are summarised in Table 2.6 below.

Table 2.6 – UV-Visible data for 8.37µM of $[Ir(phen)_2(qtpy)]Cl_3$ recorded in 5mM tris, 25mM NaCl buffer, pH 7.4.

Compound	λ_{max} (nm)	ε (M^{-1} cm^{-1})	Assignment
$[Ir(phen)_2(qtpy)]Cl_3$	203	48985	π-π*
	225	46595	π-π*
	273	44206	^{1}MLCT
	357	3806	^{3}MLCT

2.8.1.4 Complex $[Ir(dppz)_2(qtpy)]^{3+}$

The UV-Vis spectrum of $[Ir(dppz)_2(qtpy)]^{3+}$ is depicted in Fig. 2.21 whilst a summary of the data obtained from the investigation is given in Table 2.7.

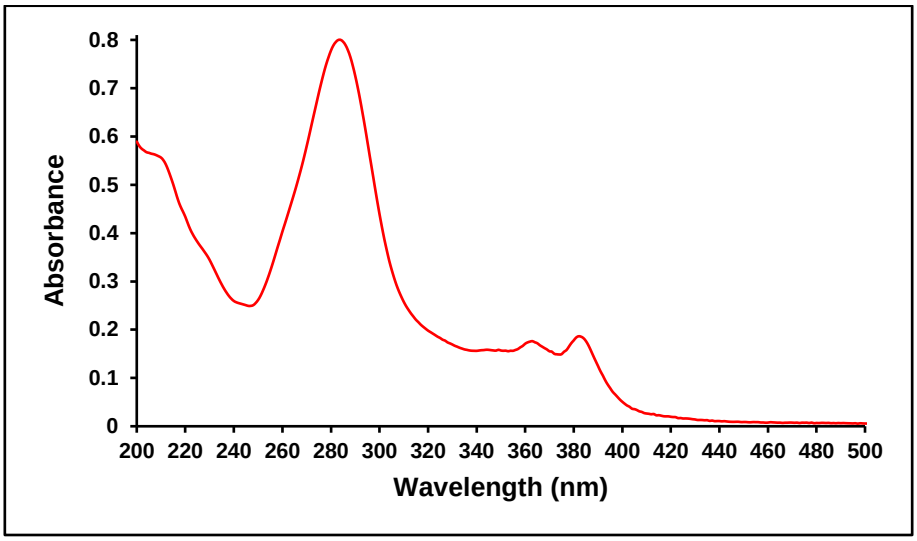

Figure 2.21 – Steady-state UV-Vis spectrum of 8.23µM $[Ir(dppz)_2(qtpy)]^{3+}$ in MeCN at ambient temperature.

The most prominent peaks are summarised in Table 2.7 below.

Table 2.7 – UV-Visible data for 8.23µM of $[Ir(dppz)_2(qtpy)](CF_3SO_3)_3$ recorded in MeCN.

Compound	λ_{max} (nm)	ε (M^{-1} cm^{-1})	Assignment
$[Ir(dppz)_2(qtpy)](CF_3SO_3)_3$	210	67972	π-π*
	284	97205	^{1}MLCT
	363	21385	^{3}MLCT
	382	22600	^{3}MLCT

2.8.2 Steady-state Photoluminescence (PL) Studies

Steady-state luminescence of all complexes were recorded in a quartz cuvette at room temperature by exciting them at a wavelength characteristic to that of their MLCT band concluded from previous UV-Visible assignments. The use of an emission slit width of 10nm

gave a more pronounced emission signal than 5nm, especially if any of the complexes investigated was available only in low concentrations.

The three complexes investigated each display a unique emission signature lending validity to the assumption that the emission properties of iridium complexes are highly tunable.

2.8.2.1 Complex $[Ir(bpy)_2(qtpy)]^{3+}$

The luminescence spectra of $[Ir(bpy)_2(qtpy)]^{3+}$ are depicted in Figs. 2.22 and 2.23.

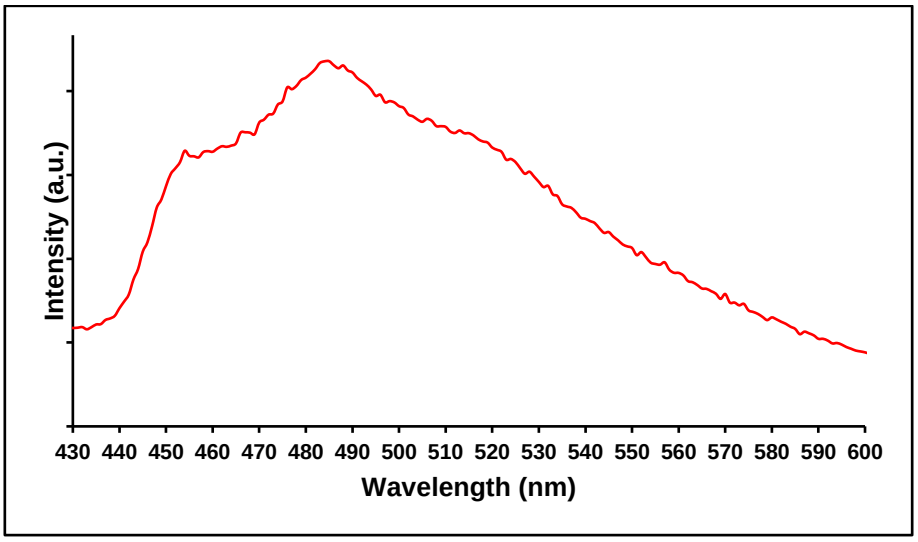

Figure 2.22 – Emission spectrum of $[Ir(bpy)_2(qtpy)]Cl_3$ in 5mM tris, 25mM NaCl buffer. Excitation at 310nm.

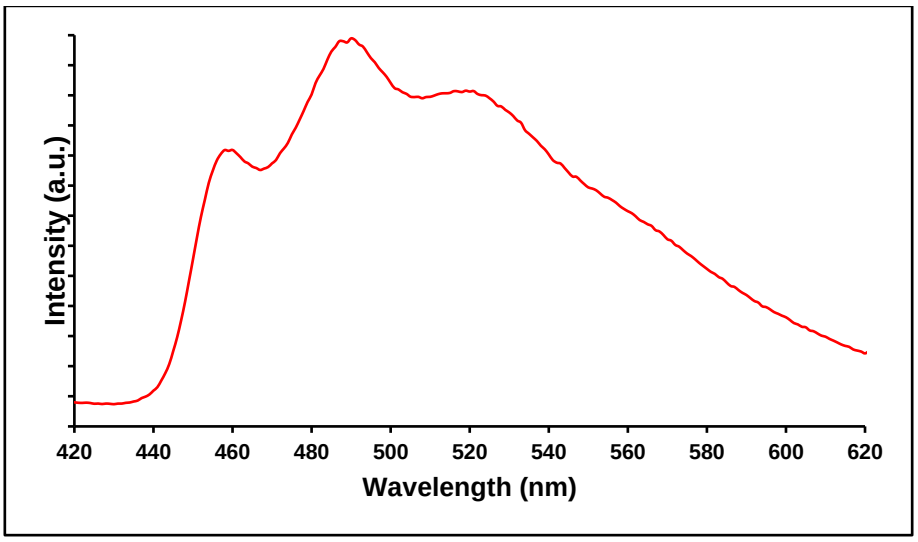

Figure 2.23 – Luminescence spectrum of 6.29µM of $[Ir(bpy)_2(qtpy)](CF_3SO_3)_3$ in MeCN. Excitation at

316nm. Excitation slit width = 5nm. Emission slit width = 5nm.

Emission maxima are situated at 484nm and 489nm in tris buffer and MeCN, respectively.

2.8.2.2 Complex $[Ir(phen)_2(qtpy)]^{3+}$

The luminescence spectra of $[Ir(phen)_2(qtpy)]^{3+}$ are depicted in Figs. 2.24 and 2.25.

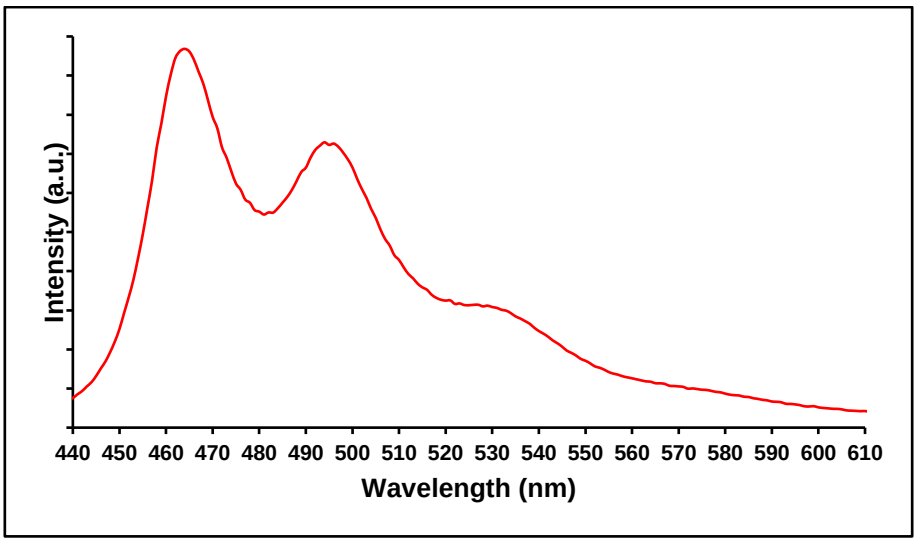

Figure 2.24 – Steady-state luminescence spectrum of 8.37µM $[Ir(phen)_2(qtpy)]Cl_3$ in tris buffer.

Emission maxima are situated at 464nm and 494nm in tris buffer.

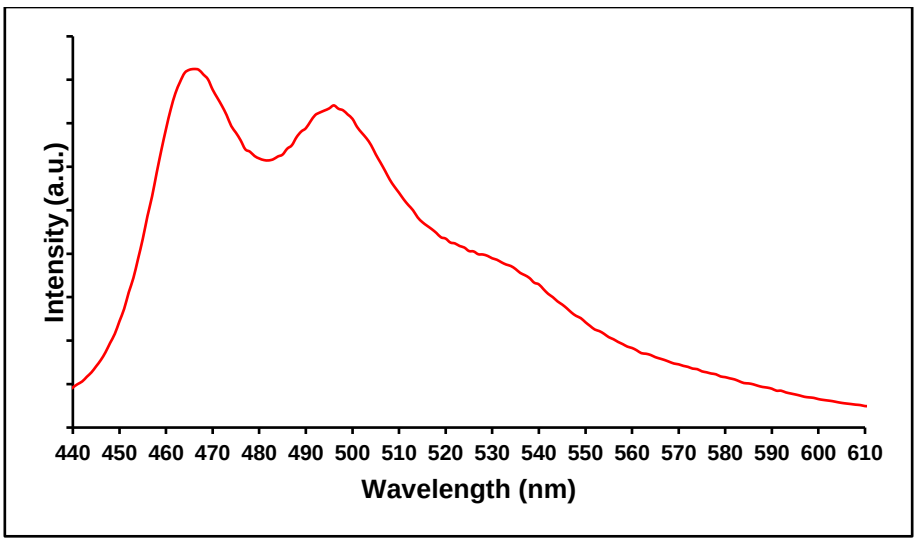

Figure 2.25 – Steady-state luminescence spectrum of 22.68µM $[Ir(phen)_2(qtpy)](CF_3SO_3)_3$ in MeCN.

Emission maxima are situated at 466nm and 496nm in MeCN. Emission in MeCN is slightly red shifted compared to the one in tris buffer.

2.8.2.3 Complex $[Ir(dppz)_2(qtpy)]^{3+}$

The luminescence spectrum of $[Ir(dppz)_2(qtpy)]^{3+}$ is depicted in Fig. 2.26.

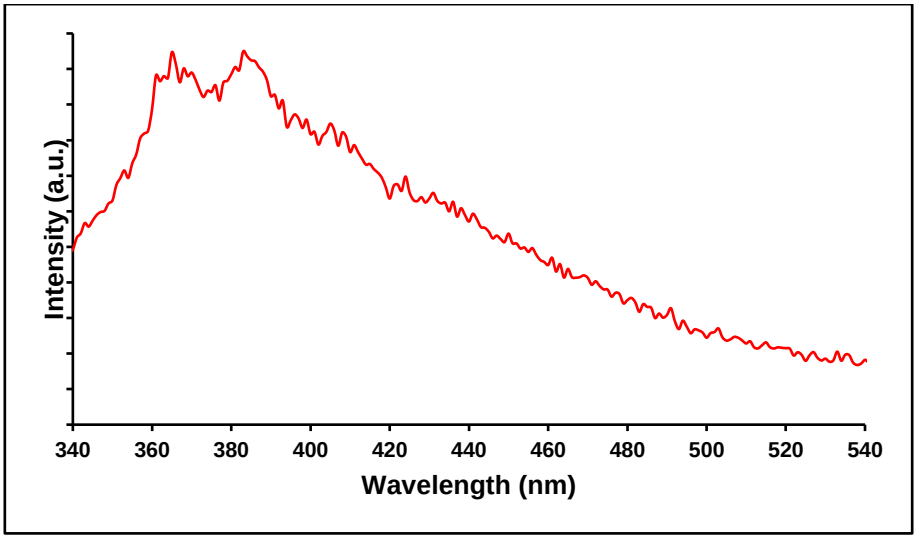

Figure 2.26 – Emission spectrum of 4.45µM $[Ir(dppz)_2(qtpy)]Cl_3$ in 5mM tris, 50mM NaCl buffer, pH 7.4. Excitation wavelength = 284nm. Dual emission located at 365nm and 383nm.

Emission maxima are situated at 365nm and 383nm in tris buffer.

The complex is weakly emissive in organic solvents like MeCN with no defined maxima.

2.9 Computational Studies

The use of computational methods has multiplied over the past several decades to corroborate spectroscopy results, allowing advancements in the study of photophysical and photochemical properties of metal complexes. Amongst these methods, density functional theory (DFT) and time-dependent DFT (TD-DFT) have been widely used to study many molecular systems as they provide a detailed description of the excited state energy in comparison with the ground state, as well as furnish information on the excited-state electronic and geometrical features. Experimental data including absorption spectra and vibrational frequencies could be employed to validate computational data, which can strategically guide the interpretation of subtle

spectroscopic properties. DFT, for instance, has been used to characterise forbidden states (e.g., d-d ligand field (LF) states) that are spectroscopically silent or tricky to detect due to their involvement in ultrafast relaxation processes or photochemical reactions.[45]

The photophysical properties of complexes synthesised in this work were investigated, and these complexes have been modelled using quantum chemistry methods to get a deeper understanding of their excited state properties. The density functional theory (DFT) calculations were carried by, Mr Onawole Abdulmujeeb, now based at the University of Queensland, Australia as of this writing.

2.9.1 DFT Analyses

The optimised geometries showed that all the complexes form quasi-octahedral complexes with iridium as the central metal ion (Fig. 2.27), which is expected of six-coordinated iridium(III) compounds.[46] This octahedral geometry of the complex is maintained at the centre irrespective of the size of the polypyridyl ligands attached to it. Complex **1** shows a more compact structure compared to Complexes **2** and **3**. This is because there is less steric hindrance among the polypridyl ligands which have less number of rings in Complex **2** compared to the others. The selected bond lengths (Table 2.8) of iridium to the six N atoms bonded to it show an average bond length of 2.088, 2.092, and 2.089 Å, respectively, for Complexes **1**, **2** and **3**.

The electrostatic potential (esp) map depicts complexes' charge distribution. A deep blue colour denotes a highly positively charged region whilst a deep red colour signifies a highly negatively charged region (Fig. 2.28). A lighter shade of blue or red implies the level of positive or negative charge as the case may be. Complex **1** has the largest region of deep blue, which originates from the iridium(III), followed by Complex **2**, and then **3**. This implies that Complex **1** has the most localised positive charge and this is expected since the ligands attached to Ir(III) has less aromatic rings compared to the other two complexes.

The Highest Occupied Molecular Orbitals (HOMO) and Lowest Unoccupied Molecular Orbitals (LUMO) make up the frontier molecular orbitals. The orbital distribution for both the HOMO and LUMO maps is found in the polypyridyl rings (Figs. 2.29 and 2.30). However, in

the latter, the 5d-orbital on the iridium(III) metal centre contributes to the LUMO map besides the polypyridyl rings, which indicates metal to ligand charge transfer.

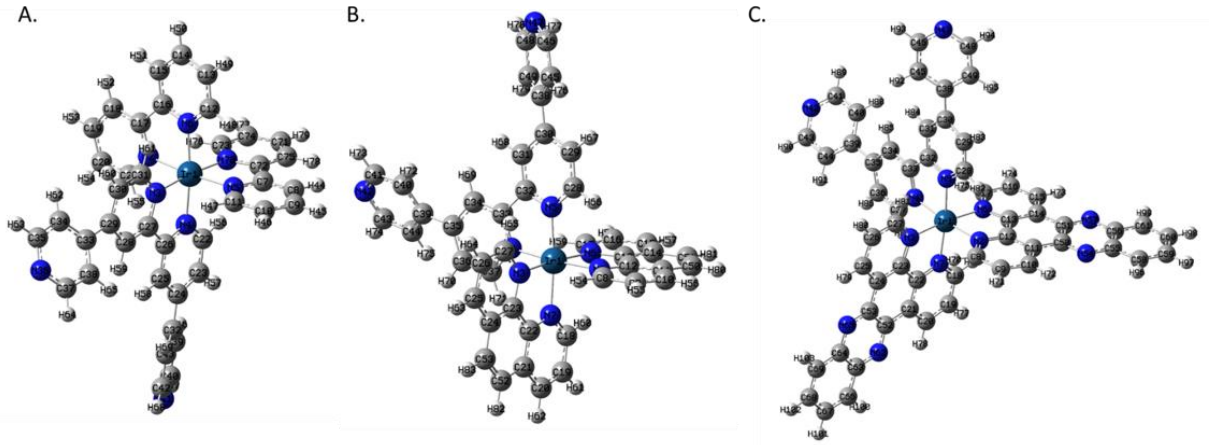

Figure 2.27 – The optimised geometries of Complexes **1** (a) **2** (b) and **3** (c).

Table 2.8 – Selected bond lengths of the studied title complexes.

Complex 1		**Complex 2**	**Complex 3**
Bond		Length (Å)	
Ir–N_2	2.089	2.102	2.095
Ir–N_3	2.079	2.089	2.088
Ir–N_4	2.083	2.081	2.083
Ir–N_5	2.089	2.080	2.081
Ir–N_6	2.092	2.097	2.094
Ir–N_7	2.094	2.101	2.095

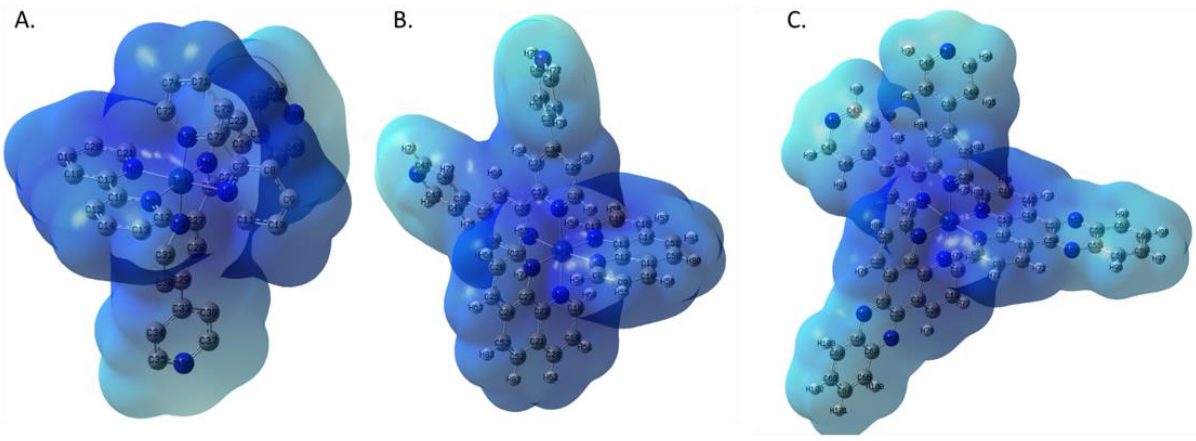

Figure 2.28 – The electrostatic potential map of Complexes (a) **1** (b) **2** and (c) **3**.

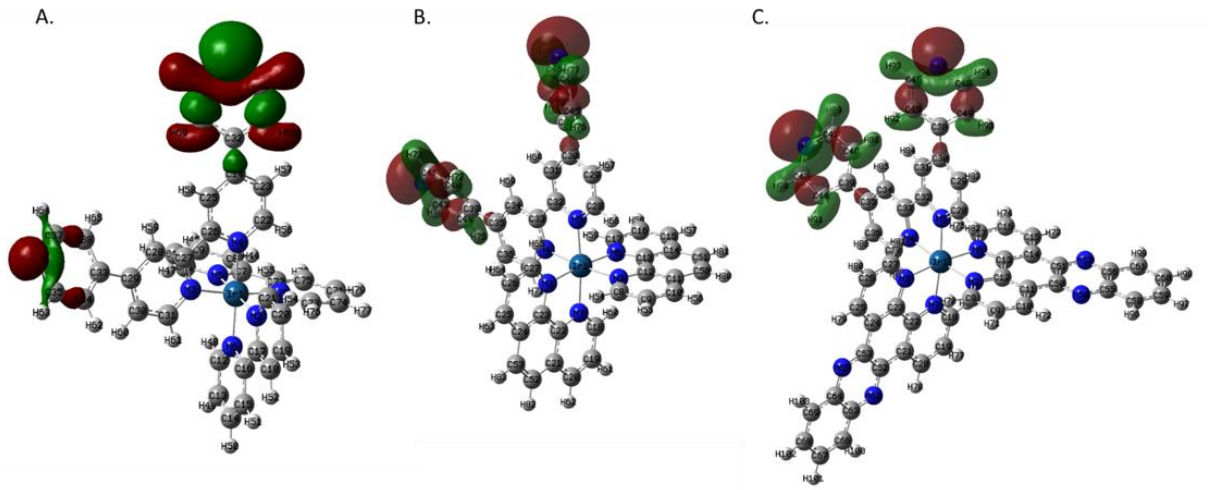

Figure 2.29 – The HOMO maps of Complexes (a) **1** (b) **2** and (c) **3**.

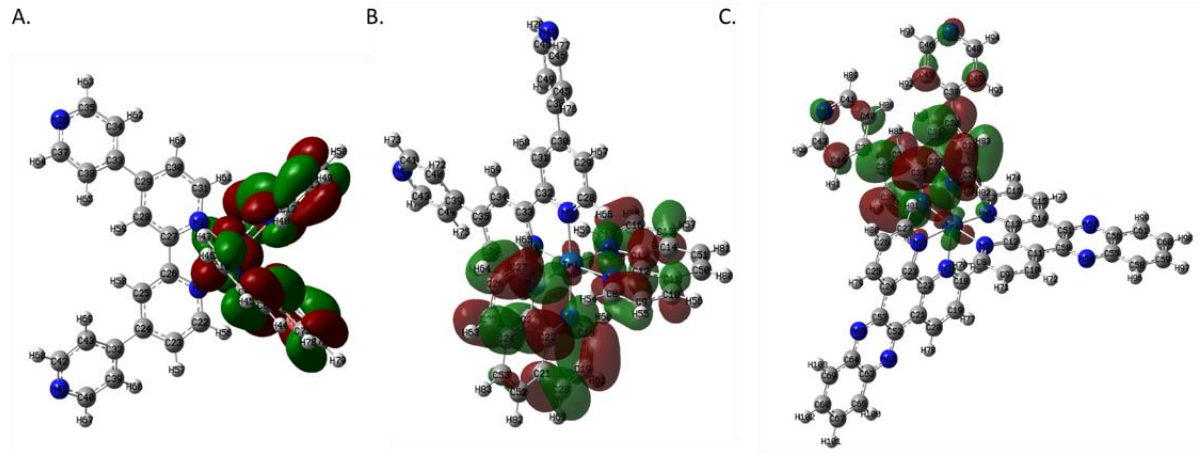

Figure 2.30 – The LUMO maps of Complexes (a) **1** (b) **2** and (c) **3**.

2.9.2 UV-Visible Spectra Analyses

The calculated TD-DFT UV-Visible spectra of the studied complexes in MeCN show that the maximum peaks occur between 250 to 350nm (Fig. 2.31). Complex **3** has the highest peak, which occurs around 352nm. However, Complexes **1** and **2** seem to have the maximum peaks at around 275nm. The most prominent peak observed in Complex **3** is due to the higher number of conjugated systems present compared to Complexes **1** and **2**.

These data compare well with the UV-Vis experimental results. The UV-Vis wavelengths obtained herein are in the same region as the π-π* wavelengths of the complexes, which occur between 200–305nm. In other words, both experimental and computational data are in good

agreement.

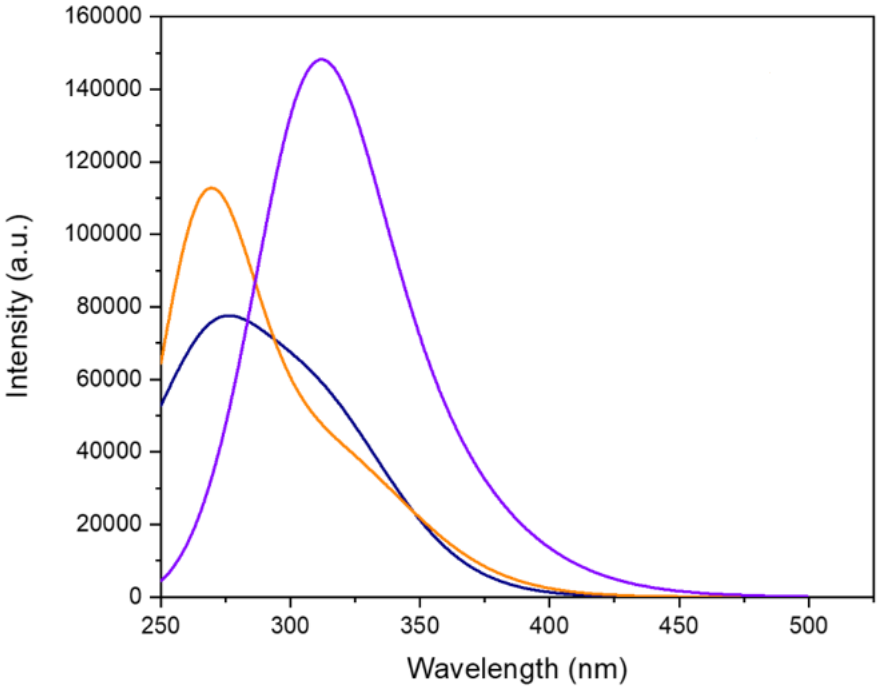

Figure 2.31 – Calculated/simulated TD-DFT UV-Visible spectra of the studied complexes in MeCN. Blue trace – Complex **1**; orange trace – Complex **2**; and purple trace – Complex **3**.

Additional DFT studies of some precursors and ligands are given in relevant sections of the Appendix.

2.10 Chapter Summary

This chapter gives a successful report of three synthetically challenging novel, photostable Ir-qtpy complexes (Fig. 2.1) afforded by microwave-assisted synthesis, purified by RP HPLC, and characterised by absorption and luminescence spectroscopies. Characterisation using UV-Visible studies shows the presence of π-π*, ^{1}MLCT/^{1}LLCT, and ^{3}MLCT bands for all three complexes. All the complexes show strong π-π* transitions around 200–250nm, ^{1}MLCT/^{1}LLCT around 250–300nm, and ^{3}MLCT transitions around 300–500nm and go up to 800nm. Luminescence experiments carried out for all three complexes showed that the three complexes display multiple emission maxima with interesting signatures; the bpy complex $[Ir(bpy)_2(qtpy)]^{3+}$ shows the longest emission up to 620nm of the three complexes. Despite the fact that the three complexes are isostructural, their emissions are differently tuned, a

characteristic property of iridium(III) complexes. Meanwhile, the phen complex, $[Ir(phen)_2(qtpy)]^{3+}$, exhibits the most highly-tuned emission of the three complexes, giving two distinct maxima at 464nm and 494nm in tris buffer. Contrary to what would be expected of a planar dppz ligand complex, the dppz complex $[Ir(dppz)_2(qtpy)]^{3+}$ shows the highest energy and shortest wavelength, this being perhaps a result of the incorporation of two dppz ligands in its moiety. All three complexes were found to possess bi-exponential lifetimes in MeCN and produce singlet oxygen yields of up to 71% as in the case for the dppz complex.

DFT studies showed that the highest occupied molecular orbital (HOMO) is on the iridium metal, and the lowest unoccupied molecular orbital (LUMO) is centred on the N-substituted ligand. Furthermore, it was gathered from DFT results that complex $[Ir(bpy)_2(qtpy)]^{3+}$ has the most compact structure and the most positive charge of the three complexes. This suggests why it gives the highest binding affinity of the investigated three complexes (Chapter 4 of this thesis). TD-DFT UV-Visible spectra of the studied complexes in MeCN showed that $[Ir(dppz)_2(qtpy)]^{3+}$ has the longest absorption wavelength, which is in correlation with experimental studies.

2.11 References

1. R. J. Morgan, S. Chatterjee, A. D. Baker, and T. C. Strekas, Effects of Ligand Planarity and Peripheral Charge on Intercalative Binding of Ru(2,2'-bipyridine)$_2$L^{2+} to Calf Thymus DNA, *Inorg. Chem.*, 1991, 30, 2687–2692.

2. A. M. Pyle, J. P. Rehman, R. Meshoyrer, C. V. Kumar, N. J. Turro and J. K. Barton, 1989, Mixed-Ligand Complexes of Ruthenium(II): Factors Governing Binding to DNA, *J. Am. Chem. Soc.*, 111, 3051–3058.

3. A. J. Downard, G. E. Honey, L. F. Phillips P. J. and Steel, Synthesis and Properties of a Tris(2,2'-bipyridine)ruthenium(II) Dimer Directly Coupled at the C4 Carbon, 1991, *Inorg. Chem. 30(10)*, 2259–2260.

4. J. B. Cooper, D. B. MacQueen, J. D. Petersen D. W. and Wertz, 1990, Role of the LUMO in Determining Redox Stability for 2,3-Dipyridylpyrazine- and 2,3-Dipyridylquinoxaline-Bridged Ruthenium(II) Bimetallic Complexes, *Inorg. Chem.*, 29(19), 3701–3705.

5. F. H. Burstall, Researches on the PolyPyridyls, *J. Chem. Soc. (Resumed)*, 1938, 1662–1672.

6. A. Gorczyński, J. M. Harrowfield, V. Patroniak; A. R. Stefankiewicz, Quaterpyridines as Scaffolds for Functional Metallosupramolecular Materials, *Chem. Rev.*, 2016, 116 (23), 14620–14674.

7. P. de Wolf, P. Waywell, M. Hanson, S. L. Heath, A. J. H. M. Meijer, S. J. Teat, J. A. Thomas, Self-Assembled, Kinetically Locked, Ru^{II}-Based Metallomacrocycles: Physical, Structural, and Modeling Studies, *Chem. - A Eur. J.*, 2006, 12, 2188–2195.

8. D. Ghosh, H. Ahmad and J. A. Thomas, Kinetically locked luminescent metallomacrocycles as duplex DNA binding substrates, *Chem. Commun.*, 2009, 2947–2949.

9. H. Ahmad, A. J. H. M. Meijer, J. A. Thomas, Tuning the Excited State of Photoactive Building Blocks for Metal-Templated Self-Assembly, *Chem. Asian J.*, 2011, 6 (9), 2339–2351.

10. H. Ahmad, B. W. Hazel, A. J. H. M. Meijer, J. A. Thomas, K. A. Wilkinson, A Self-Assembled Luminescent Host That Selectively Senses ATP in Water, *Chem. - A Eur. J.*, 2013, 19 (16), 5081–5087.

11. H. Ahmad, D. Ghosh, J. A. Thomas, Using ancillary ligands to tune the DNA binding properties of self-assembled luminescent metallomacrocycles, *Chem. Commun.*, 2014, 50, 3859–3861.

12. H. Ahmad, A. Wragg, W. Cullen, C. Wombwell, A. J. H. M. Meijer, J. A. Thomas, From Intercalation to Groove Binding: Switching the DNA-Binding Mode of Isostructural Transition-Metal Complexes, *Chem. - A Eur. J.*, 2014, 20 (11), 3089–3096.

13. M. G. Walker, P. J. Jarman, M. R. Gill, X. Tian, H. Ahmad, P. A. N. Reddy, L. McKenzie, J. A. Weinstein, , A. J. H. M. Meijer, G. Battaglia, C. G. W. Smythe, J. A. Thomas, *Chem. - A Eur.*, J. 2016, 22 (17), 5996–6000.

14. R. J. Morgan and Baker A. D., 2,2':4,4":4',4"'-Quaterpyridyl: A Building Block for the Preparation of Novel Redox Reagents. 1. Preparation and Quaternization, *J. Org. Chem.*, 1990, 5(7), 1986-1993.

15. H. Ahmad, A. Wragg, W Cullen, C. Wombwell, A. J. H. M. Meijer, and J. A. Thomas, From Intercalation to Groove Binding: Switching the DNA-Binding Mode of Isostructural Transition-Metal Complexes, *Chem. Eur. J.*, 2014, 20, 3089–3096.

16. J. E. Dickeson, L. A. Summers, Derivatives of 1,10-Phenanthroline-5,6-quinone, *Austr. J. Chem.*, 1970, 23, 1023–1027.

17. M. K. Brennaman, T. J. Meyer, & J. M. Papanikolas, $Ru(bpy)_2dppz]^{2+}$ light-switch mechanism in protic solvents as studied through temperature-dependent lifetime measurements, *J. Phys. Chem. A*, 2004, 108(45), 9938–9944.

18. K. E. Reinert, DNA stiffening and elongation caused by the binding of ethidium bromide, *Biochim. Biophys.*, 1973, 319, 135–139.

19. D. Suh and J. B. Chaires, Criteria for the mode of binding of DNA binding agents, *Bioorg. Med. Chem.*, 1995, 3, 723–728.

20. S. Stimpson, D. R. Jenkinson, A. Sadler, M. Latham, D. A. Wragg, A. J. H. M. Meijer and J. A. Thomas, Tuning the Excited State of Water-Soluble Ir^{III}-Based DNA Intercalators that are Isostructural with $[Ru^{II}(NN)_2(dppz)]$ Light-Switch Complexes, *Angew. Chemie Int. Ed.*, 2015, 127, 3043–3046.

21. S. Caddick, Microwave assisted organic reactions, *Tetrahedron*, 1995, 38, 10403–10432.

22. J. Berlan, Microwaves in chemistry: Another way of heating reaction mixtures, *J. Radiat. Phys. Chem.*, 1995, 45(4), 581–589.

23. C. R. Strauss, Invited Review. A Combinatorial Approach to the Development of Environmentally Benign Organic Chemical Preparations, *Aust. J. Chem.*, 1999, 52, 83–96.

24. P. Lindström, J. Tierney, B. Wathey, J. Westman, Microwave assisted organic synthesis – a review, *Tetrahedron*, 2001, 57, 9225–9283.

25. L. Perreux, and A. Loupy, A Tentative Rationalization of microwave effects in organic synthesis according to the reaction medium, and mechanistic considerations, *Tetrahedron*, 2001, 57, 9199–9223.

26. A. Loupy, Microwaves in Organic Synthesis, Wiley-VCH, Wenheim, Hayes, B. L. Microwave synthesis: Chemistry at the Speed of Light, CEM Publishing, Matthews, 2002.

27. N. Kuhnert, T. N. Danks, Highly diastereoselective synthesis of 1,3-oxazolidines under thermodynamic control using focused microwave irradiation under solvent-free conditions, *Green Chem.*, 2001, 3, 68–70.

28. R. Gedye, F. Smith, K. Westaway, A. Humera, L. Baldisera, L. Laberge, J. Roussell, The use of microwave ovens for rapid organic synthesis, *Tetrahedron Lett.*, 1986, 27, 279–282.

29. R. Gigure, T. L. Bray, S. M. Duncan, G. Majetich, Application of commercial microwave ovens to organic synthesis, *Tetrahedron Lett.*, 1986, 27, 4945–4948.

30. N. E. Leadbeater, H. M. Torenius, H. Tye, Microwave-Promoted Organic Synthesis Using Ionic Liquids: A Mini Review, *Comb. Chem. High Throughput Screen.*, 2004, 7(18), 511–528.

31. C. O. Kappe, Controlled Microwave Heating in Modern Organic Synthesis, *Angew. Chem., Int. Ed.*, 2004, 43, 6250–6284.

32. A. de la Hoz, Á. Díaz-Ortiz, A. Moreno, Microwaves in organic synthesis. Thermal and non-thermal microwave effects, *Chem. Soc. Rev.*, 2005, 34, 164–178.

33. A. de la Hoz, Á. Díaz-Ortiz, A. Moreno, Microwaves in organic synthesis. Thermal and non-thermal microwave effects, *Chem. Soc. Rev.*, 2005, 34, 164–178.

34. C. O. Kappe, Controlled Microwave Heating in Modern Organic Synthesis, *Angew. Chem. Int. Ed.*, 2004, 43, 6250–6284.

35. T. M. Monos, A. C. Sun, R. C. McAtee, J. J. Devery, III, and C. R. J. Stephenson, Microwave-Assisted Synthesis of Heteroleptic Ir(III)$^{+}$ Polypyridyl Complexes, *J. Org. Chem.*, 2016, 81, 16, 6988–6994.

36. B. L. Hayes, Microwave Synthesis: Chemistry at the Speed of Light; CEM Publishing: Matthews, NC, 2002.

37. V. R. Meyer, Practical High-Performance Liquid Chromatography, Fifth Edition, John Wiley & Sons Ltd, The Atrium, Southern Gate, Chichester, West Sussex, PO19 8SQ, United Kingdom.

38. S. P. Verma, E. Santoyo, High-Performance Liquid and Ion Chromatography: Separation and Quantification Analytical Techniques for Rare Earth Elements, *Geostand. Geoanal. Res.*, 2007, 31(3), 161–184.

39. X. Jiang, J. Peng, J. Wang, X. Guo, D. Zhao, and Y. Ma, Iridium-Based High-Sensitivity Oxygen Sensors and Photosensitizers with Ultralong Triplet Lifetimes, *ACS Appl. Mater. Interfaces*, 2016, 8, 6, 3591–3600.

40. I. Echevarría, E. Zafon, S. Barrabes, M. A. Martínez, S. Ramos-Gomez, N. Ortega, B. R. Manzano, F. A. Jalon, R. Quesada, G. Espino, A. Massaguer, Rational design of mitochondria targeted thiabendazole-based Ir(III) biscyclometalated complexes for a multimodal photodynamic therapy of cancer, *J. Inorg. Biochem.*, 2022, 231, 111790.

41. J. Arnbjerg, M. J. Paterson, C. B. Nielsen, M. Jørgensen, O. Christiansen, and P. R. Ogilby, One- and Two-Photon Photosensitized Singlet Oxygen Production: Characterization of Aromatic Ketones as Sensitizer Standards, *J. Phys. Chem.* A, 2007, 111, 5756–5767.

42. N. M. Shavaleev, H. Adams, J. Best, R. Edge, S. Navaratnam and J. A. Weinstein, Deep-red luminescence and efficient singlet oxygen generation by cyclometalated platinum(II) complexes with 8-hydroxyquinolines and quinoline-8-thiol, *Inorg. Chem.*, 2006, 45, 9410–9415.

43. P. I. Djurovich, D. Murphy, M. E. Thompson, B. Hernandez, R. Gao, P. L. Hunt and M. Selke, Cyclometalated iridium and platinum complexes as singlet oxygen photosensitizers: Quantum yields, quenching rates and correlation with electronic structures, *Dalt. Trans.*, 2007, 3763–3770.

44. E. Zafon, I. Echevarría, S. Barrabés, B. R. Manzano, F. A. Jalón, A. M. Rodríguez, A. Massaguer, and G. Espino, Photodynamic Therapy with Mitochondria-targeted Biscyclometallated Ir(III) Complexes. Multi-action Mechanism and Strong influence of the Cyclometallating Ligand, *Dalton Trans.*, 2021, 51, 111–128.

45. C. Garino and L. Salassa, The photochemistry of transition metal complexes using density functional theory, *Phil Trans R Soc A*, 371: 20120134.

46. M. X. Song, G. Q. Xi, H. Y. Chi, K. C. He, L. U. Peng, Z. K. Qin, Y. L. Zhang, L. U. Shi-Quan, H. J. Zhang, A Theoretical Study: Green Phosphorescent Iridium(III) Complexes with Low-Efficiency Roll-Off, *Appl. Organomet. Chem.*, 2020, 34 (5), 1–9.

3.0 X-ray Crystallography and Crystal Engineering

3.1 Introduction

Whilst the characterisation of most structures of simple organic and inorganic compounds is usually carried out by various spectroscopic measurements including NMR, IR, and MS, detailed structural characterisation of coordination compounds is achieved by X-ray diffraction methods, which can not only provide information on geometrical structures, but also full bond parameters.

Without doubt, single crystal X-ray diffraction (i.e., XRD) is one of the most powerful tools for detailed structural analysis of coordination compounds. Single crystal XRD studies provide a valuable probe to directly visualize molecules. Although some problems such as disorder and twining can exist in measurements and analyses, XRD still represents the most important analytical method for coordination chemists, and it continues to undergo further development.[1]

Since iridium exhibits various oxidation states ranging from 0 to +9, the single crystal analysis of each of the precursors is worth investigating to rule out the possibility of undesired intermediate complexes along the synthetic route. A brief description of the crystal growth techniques employed for each of the obtained crystals is given in the Experimental chapter of this thesis.

Crystal engineering as defined by Desiraju in his words is the "understanding of intermolecular interactions in the context of crystal packing and the utilisation of such understanding in the design of new solids with desired physical and chemical properties".[2] Herein, Hirshfeld surfaces analysis (HSA) is used to map the intermolecular interactions in the crystals obtained. A summary of the 15 crystal structures studied in this work is given in Table 3.1.

Table 3.1 – Relevant information for the crystal systems studied in this work.

Crystals	Chemical Formula	Crystal System	Space Group	Z	Final R Index
Qtpy	$C_{20}H_{14}N_4$	triclinic	P-1	1	0.0473
$[Ir(bpy)_2Cl_2]PF_6$, crystallised as $[Ir(bpy)_2Cl_2]PF_6CH_3NO_2$	$C_{21}H_{19}Cl_2F_6IrN_5O_2P$	monoclinic	$P2_1/n$	4	0.0430
$[Ir(phen)_2Cl_2]PF_6$	$C_{24}H_{16}Cl_2F_6IrN_4P$	monoclinic	C2/c	4	0.0340
$[Ir(dppz)_2Cl_2]PF_6$	$C_{36}H_{20}Cl_2F_6IrN_8P$	triclinic	P-1	4	0.0427
$[Ir(bpy)_2Cl_2]Cl$, crystallised as $[Ir(bpy)_2Cl_2]Cl\ 2H_2O$	$C_{20}H_{20}Cl_3IrN_4O_2$	triclinic	P-1	2	0.0940
$[Ir(phen)_2Cl_2]Cl$, crystallised as $[Ir(phen)_2Cl_2]Cl\ H_2O\ MeCN$	$C_{25}H_{19.5}Cl_3IrN_{4.5}O$	orthorhombic	Pbcn	8	0.0470
$[Ir(bpy)_2Cl_2]CF_3SO_3$	$C_{21}H_{16}Cl_2F_3IrN_4O_3S$	monoclinic	$P2_1/c$	8	0.0934
$[Ir(phen)_2Cl_2]CF_3SO_3$	$C_{25}H_{16}C_{l2}F_3IrN_4O_3S$	monoclinic	C2/c	4	0.0380
$[Ir(dppz)_2Cl_2]CF_3SO_3$, crystallised as $[Ir(dppz)_2Cl_2]CF_3SO_3CH_3NO_2$	$C_{38}H_{23}Cl_2F_4IrN_9O_5S$	monoclinic	C2/c	4	0.0593
$[Ir(bpy)_2(CF_3SO_3)_2]CF_3SO_3$	$C_{23}H_{16}F_9IrN_4O_9S_3$	triclinic	P-1	2	0.0459
$[Ir(phen)_2(CF_3SO_3)_2]CF_3SO_3$	$C_{27}H_{16}F_9IrN_4O_9S_3$	triclinic	P-1	4	0.0483
$[Ir(dppz)_2(CF_3SO_3)_2]CF_3SO_3$	$C_{39}H_{20}F_9IrN_8O_9S_3$	monoclinic	$P2_1/n$	4	0.1177
$[Ir(dppz)_2Cl_2](CF_3SO_3)_2$ (an adventitious discovery)	$C_{37}H_{20}Cl_2F_3IrN_8O_3S$	monoclinic	C2/c	4	0.0478
$[Ir(phen)_2Cl(CH_3CN)](CF_3SO_3)_2CH_3NO_2$ (an adventitious discovery)	$C_{29}H_{22}ClF_6IrN_6O_8S_2$	triclinic	P-1	2	0.0597
$[Ir(bpy)_2Cl_2]CH_3OH$ (an adventitious discovery)	$C_{21}H_{19}Cl_2IrN_4O$	monoclinic	$P2_1/c$	4	0.0236

Where Z = No. of formula unit per unit cell and R Index = Refractive Index.

The full description of each of these crystals is given in relevant sections of this chapter. All crystals were solved by Dr Craig C. Robertson at the University of Sheffield's Department of Chemistry Crystallographic Service.

3.2 Hirshfeld Surfaces Analysis

Hirshfeld Surfaces Analysis (HSA) and fingerprint maps for all reported compounds were generated on CrystalExplorer 17.5 programme using their respective CIF files. HSA is an established technique to understand the various intermolecular interactions present in a crystal structure and quantify such weak interactions. In mapping such interactions, internal consistency is highly crucial when comparing structures. As such, all reported Hirshfeld surfaces reported herein have their bond lengths to hydrogen (or deuterium) atoms set to typical neutron values (C–H = 1.083Å, N–H = 1.009Å, and O–H = 0.983Å). The attraction of the Hirshfeld surface is that it is unique for a given crystal structure and set of spherical atomic electron densities and can help structural chemists gain additional insight into the intermolecular interactions present in molecular.[3–5] The d_{norm} values are mapped onto the Hirshfeld surface by using a red-blue-white colour scheme: where red colour signifies shorter contacts, white colour represents contacts around the van der Waals separation, and blue symbolises longer.[6] The 2D-fingerprint plot presents the decomposition of Hirshfeld surfaces into the contribution of different intermolecular interactions present in a crystal structure. 2D fingerprint plots of Hirshfeld surfaces are usually given as plots of d_i against d_e.[6]

3.3 Structural Complementary and Supramolecular Features of Qtpy

The full crystal structure (Fig. 3.1) shows that the ligand comprises 20 carbon atoms, 14 hydrogen atoms, and 4 nitrogen atoms with no co-crystallised solvent molecules. Only half of the molecule occupies the asymmetric unit, the other half being related to the first by inversion symmetry. The crystal is triclinic within the P-1 space group as shown in the crystal lattice. The unit cell packing of the structure and an ORTEP diagram with atom labelling scheme are equally depicted in Fig. 3.1. Important crystallographic information for qtpy is summarised in Table 3.1.

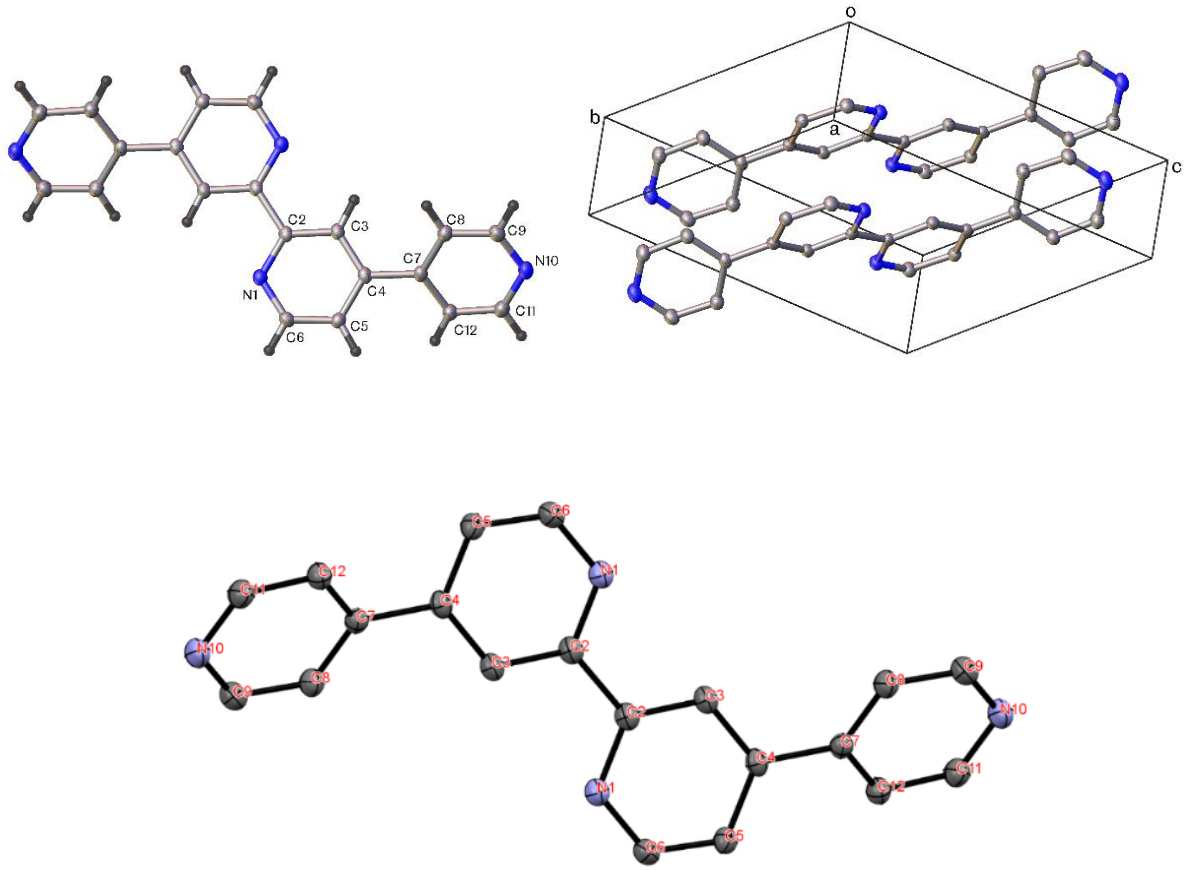

Figure 3.1 – **top left:** crystal structure of qtpy; **top right:** Unit cell packing structural representation of qtpy indicating 50% probability; and **bottom:** ORTEP plot of qtpy showing thermal ellipsoids drawn at 50% probability.

The qtpy structure displayed here has been refined anisotropically with a Final R index [I>=2σ (I)] value of 0.0473. N–C bond lengths range from 1.333(2) (N10–C11) to 1.343(2) Å (N1–C2) and display an average bond length of 1.336 Å is recorded. The bond angles between any C, N, and C atoms in close distance range from 116.5(2) (C9–N10–C11) to 123.9(2) (N1–C6–C5) and is averagely measured to be 121.3 °. As can be seen from $C_{4,4'\text{-bpy}}$–N–$C_{4,4'\text{-bpy}}$ and/or N–$C_{4,4'\text{-bpy}}$–$C_{4,4'\text{-bpy}}$ bond angle parameters, the 4,4'-bpy ligands are highly rigid, displaying values lower than the linear bond angle of 180 °. This deviation from planarity might be attributed to the existence of crystal packing forces within the molecule. In the crystal packing, the 4,4'-bpy units are seen to be facing each whilst the other two 4,4'-bpy units are seen to be pointed away from each other (Fig. 3.1). The most important torsion (or dihedral) angle in the molecule is perhaps that existing along two 4,4'-bpy aromatic rings of the crystal, i.e., N1–C2–N1–C2, which is measured to be -180 °. A summary of important crystallographic parameters for qtpy is given in Table 3.2.

Table 3.2 – Crystal data and structure refinement for the qtpy ligand.

Parameters	Qtpy
Empirical formula	$C_{20}H_{14}N_4$
Formula weight	310.35
Crystal system	Triclinic
Space group	P-1
Crystal size/mm^3	0.4 x 0.35 x 0.15
a/Å	3.7794(9)
b/Å	9.132(2)
c/Å	11.115(3)
α/°	106.477(2)
β/°	96.768(2)
γ/°	92.720(2)
Volume/Å^3	363.98(15)
Z	1
ρ_{calc}g/cm^3	1.416
F(000)	162.0
μ/mm^{-1}	0.087
Final R indexes [I>= 2σ (I)]	R_1 = 0.0473, wR_2 = 0.1112

All other crystallographic data obtained for qtpy can be found in the Appendix Section.

3.4 HSA for Qtpy

The d_{norm} values are mapped onto the Hirshfeld surface by using a red-blue-white colour scheme, where red colour signifies shorter contacts, white colour represents contacts around the van der Waals separation, and blue colour symbolises longer contacts.[6] The 2D fingerprint plot presents the decomposition of Hirshfeld surfaces into the contribution of different intermolecular interactions present in a crystal structure. 2D fingerprint plots of Hirshfeld surfaces are usually given as plots of d_i against d_e.[6]

Hirshfeld surfaces of qtpy ligand are given in Figs. 3.2–3.4. To visualise the calculated molecular structure the surfaces were set to be transparent.[7] The intermolecular interactions

listed in Table 3.3 are summarised effectively in the spots with the large circular depressions (deep red) visible on the d_{norm} surfaces indicative of hydrogen bonding contacts and other weak contacts. The major contact points of the intermolecular interactions in the ligand involve H•••H as shown by the clearly visible light red spots on the d_{norm}.[8–9] Shape index is used to identify complementary hollows (red) and bumps (blue) where two molecular surfaces touch one another. On the Hirshfeld surface mapped with shape index function, C–H•••pi interactions appear as hollow orange areas (pi•••H) and bulging blue areas (H•••pi). Curvedness is a function of the root-mean-square curvature of the surface, and maps of curvedness typically show large regions of green (relatively flat) separated by dark blue edges (large positive curvature). The π-π stacking interactions are further evidenced by the appearance of flat surfaces towards the bottom of the compound as clearly visible on the curvedness surface.

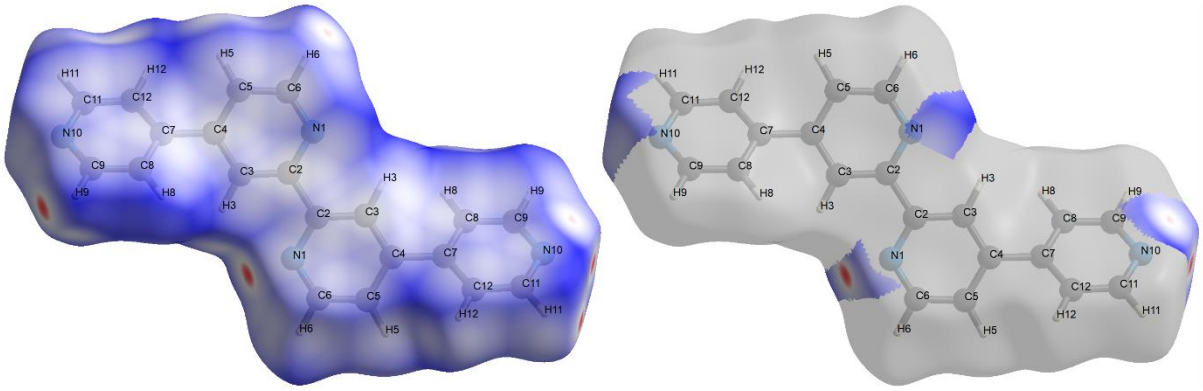

Figure 3.2 – Hirshfeld surfaces of qtpy ligand mapped with d_{norm} for all the interactions (**left**) and N•••H/H•••N interactions (**right**).

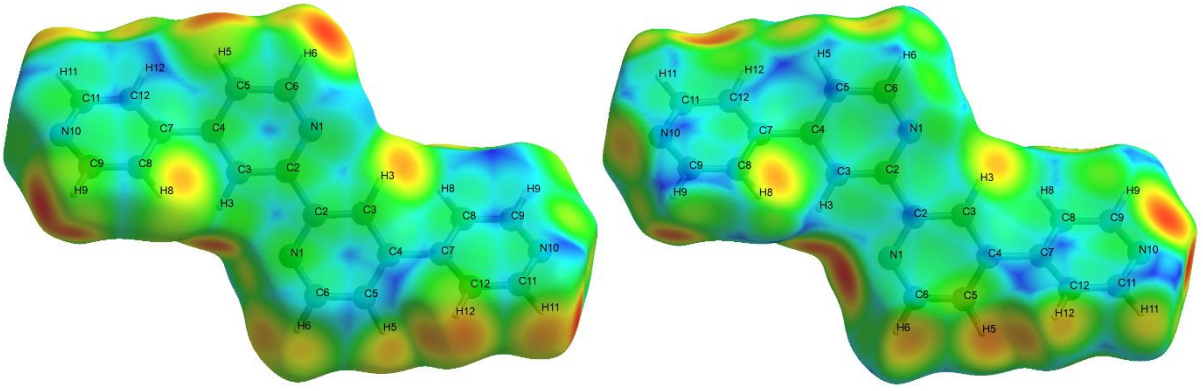

Figure 3.3 – Hirshfeld surfaces of qtpy ligand mapped with d_i (**left**) and d_e (**right**) for all the interactions.

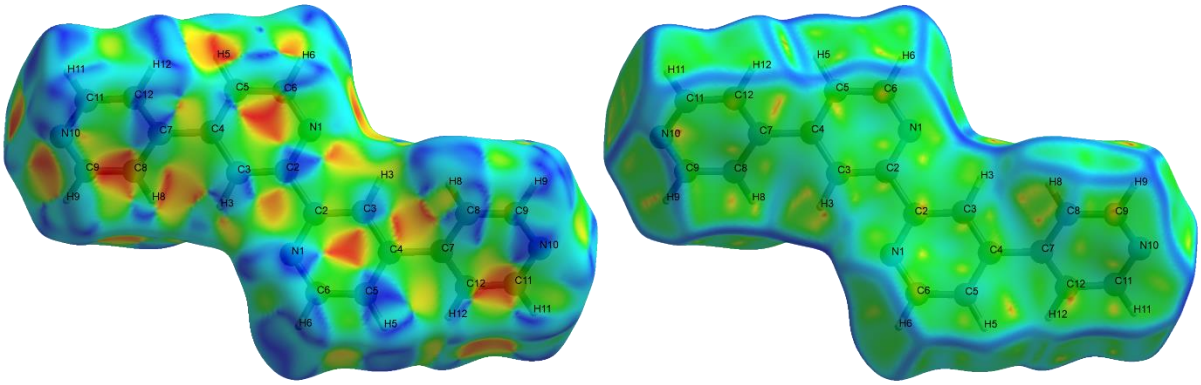

Figure 3.4 – Hirshfeld surfaces of qtpy ligand mapped with shape index (**left**) and curvedness (**right**) for all the interactions.

The 2D fingerprint plots of HSA for the ligand for all the interactions is shown in Fig. 3.5. A decomposition of the fingerprint plot to elucidate H•••H interactions is also displayed in Fig. 10. In the plot, complementary regions are visible whereby one molecule acts as donor ($d_e > d_i$) and the other as an acceptor ($d_e < d_i$) It was observed that the highest contributions/proportion extents of H•••H interactions covered 48.5% in the full Hirshfeld surface of the ligand (Fig. 3.5). This is followed by C•••C interactions, which accounts for 15.5% in the full Hirshfeld surface of the ligand (Fig. 3.5). C•••C contacts associated with π-π stacking interactions are quite pronounced and are seen in the $d_i \approx d_e = 2.2$Å region (Fig. 3.5). Despite the high percentage contribution of these interactions, their roles in the stabilisation of structure are minimal in magnitude as these interactions are between the same species/atoms.[10] Noteworthy is the contribution of H•••N/H•••N interactions, which make up 10.6% and 7.6% of the total surface (Fig. 3.5). These interactions are represented by two sharp upper and lower spikes of equal length. The spike at the top left corresponds to the points on the surface around the N–H donor whilst the one at the bottom right corresponds to the surface around the π acceptor. These spikes are indicative of strong hydrogen-bond interactions and are the most important interactions in the structure of qtpy ligand. The middle spike is for the weak H•••H interactions (accounting for almost half of the surface area as noted earlier). The stability of the structure of this ligand can be attributed to the existence of these N•••H/H•••N intermolecular bonds.[11–12] C–H/H–C close contacts, attributed to C–H•••pi interactions, make up 6.7% and 4.2% of the total surface (Fig. 3.6). The contributions of other intermolecular contacts are summarised in Table 3.3.

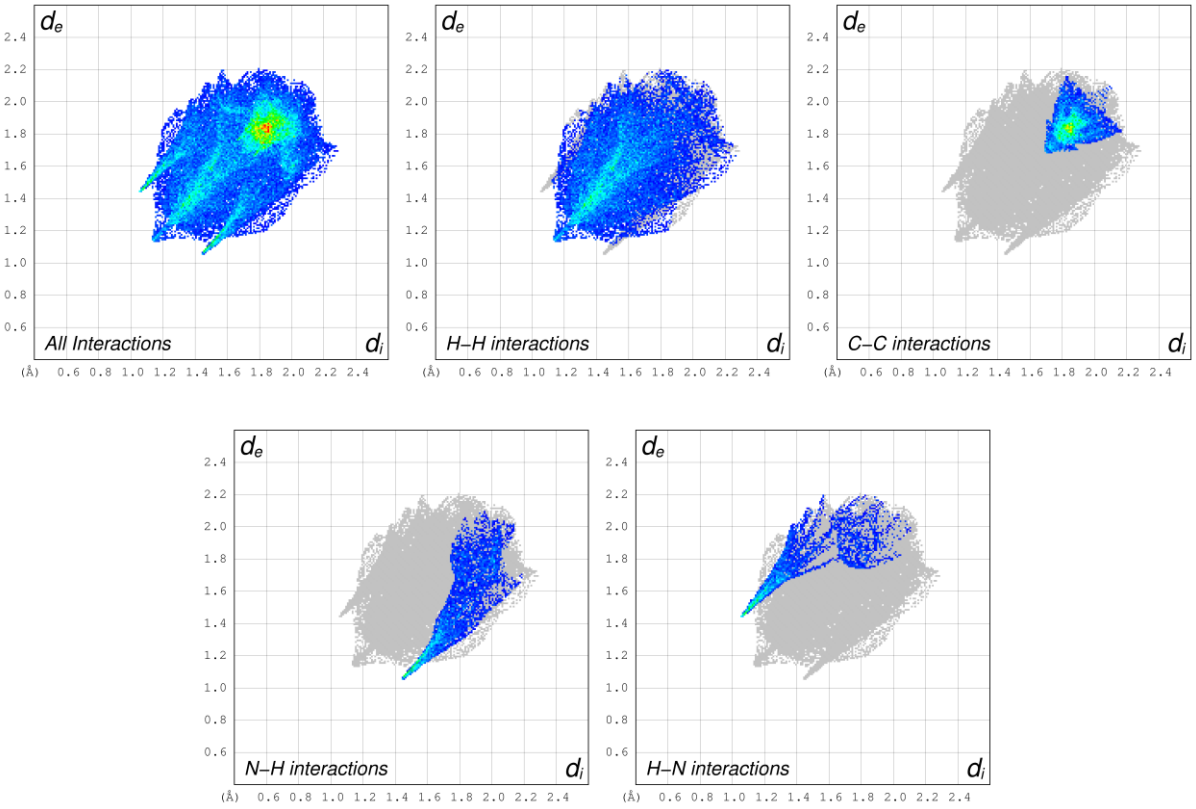

Figure 3.5 – 2D fingerprint plots of qtpy ligand for all the interactions (**top left**), H•••H interactions (**top middle**), C•••C interactions (**top right**) and N•••H/H•••N interactions (**bottom**).

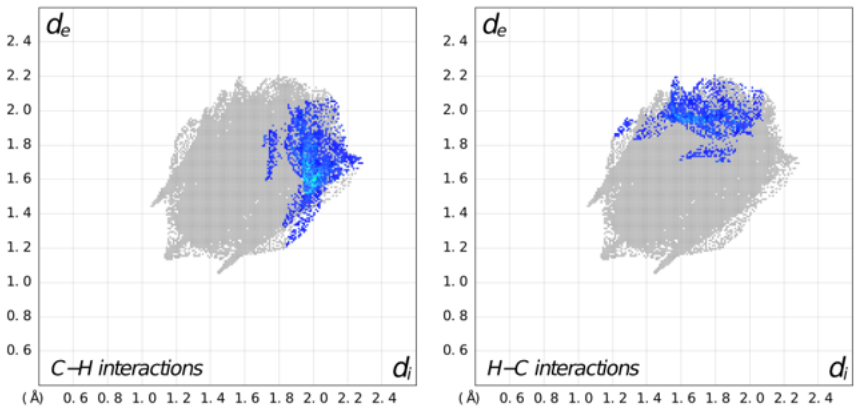

Figure 3.6 – 2D fingerprint plots of qtpy ligand for C•••H/H•••C interactions.

Table 3.3 – Summary of the percentages of intermolecular contacts contributed to the HSA surface of qtpy ligand.

Inside Atom	**Outside Atom**			**Total Contributions**
	N	C	H	**25.5**

C	3.2	15.5	6.7	**60.4**
H	7.6	4.2	48.5	**14.2**
N	0.4	3.1	10.6	
Total Contributions	**11.2**	**22.8**	**65.9**	

3.5 Bpy Family of Compounds

Only $[Ir(bpy)_2Cl_2]Cl$ and $[Ir(bpy)_2(CF_3SO_3)_2]CF_3SO_3$ are chosen to discuss the crystal structures of the bpy family of compounds. A summary of the crystallographic information for the related structures, $[Ir(bpy)_2Cl_2]PF_6$ and $[Ir(bpy)_2Cl_2]CF_3SO_3$, which were also determined during this project are given in the Appendix.

3.5.1 $[Ir(bpy)_2Cl_2]Cl$

The structure of the expected compound co-crystalised with two molecules of water per molecule of the complex, i.e., the compound crystallises as $[Ir(bpy)_2Cl_2]Cl.2H_2O$. The crystal structure, unit cell packing diagram and ORTEP plot of the compound are depicted in Fig. 3.7. $[Ir(bpy)_2Cl_2]Cl.2H_2O$ is isostructural with similar complexes formed with Rh or Co metal centres (CSD identifiers KIKPEZ and QQQEQG01, respectively). A crystal structural determination of $[Rh(bpy)_2Cl_2]Cl.2H_2O$ has been reported previously and confirmed the presence and stereochemistry of the expected cis-$[Rh(bpy)_2Cl_2]^+$ cation[13] although no structures of the aqua complexes have been reported. $[Co(bpy)_2Cl_2]Cl.2H_2O$ was described by Jaeger and co-workers[14–15]

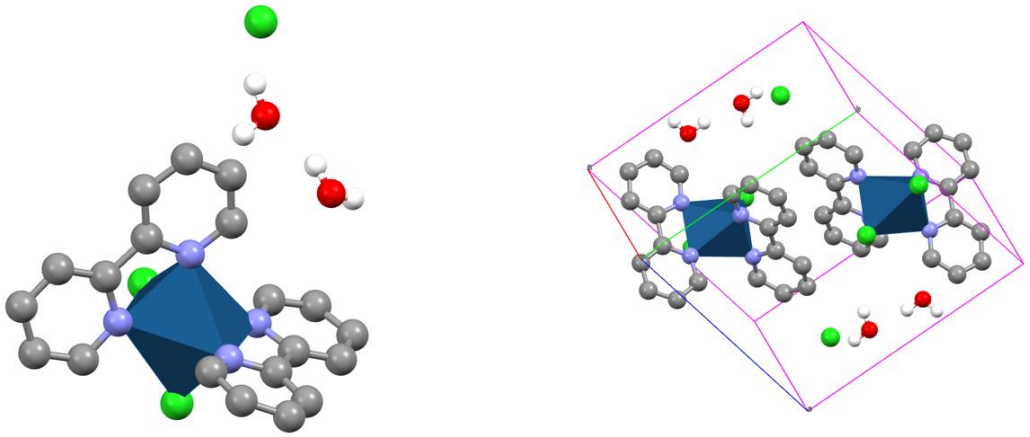

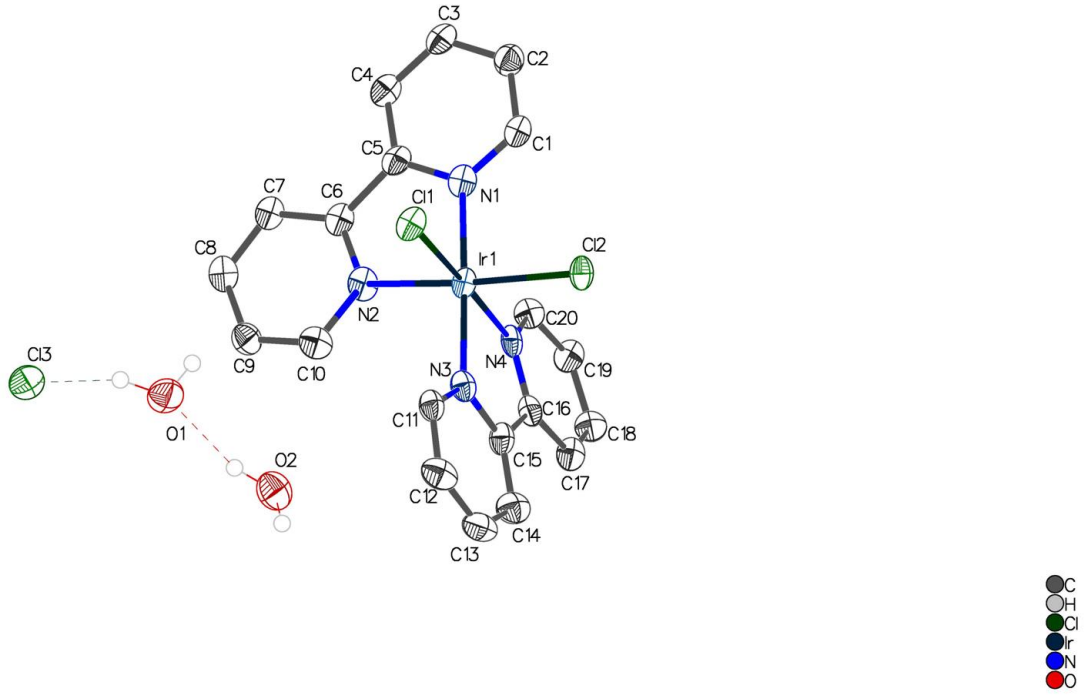

Figure 3.7 – top left: crystal structure of triclinic $[Ir(bpy)_2Cl_2]Cl$. Atom labelling – blue: Ir; grey: C; purple: N; green: Cl; red: O. Space group = P-1. Final R indexes [I>=2σ (I)] value = 0.0470; **top right:** Crystal packing of $[Ir(bpy)_2Cl_2]Cl$ with Cl counterions arrayed both in the channels and along the diagonals. Z = 2. Unit cell parameters: α/° = 90.264(4); β/° = 94.047(4); γ/° = 100.007(4); **bottom:** ORTEP diagram and atom labelling scheme for $[Ir(bpy)_2Cl_2]Cl$ drawn at 50% thermal ellipsoids.

The solid-state structure of $[Ir(bpy)_2Cl_2]Cl$ is held together by hydrogen bonding interactions as illustrated in Fig. 3.8.

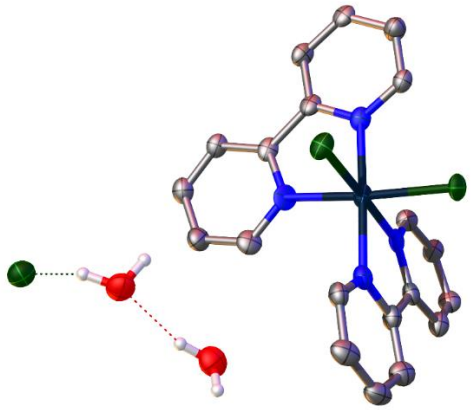

Figure 3.8 – Crystal structure of $[Ir(bpy)_2Cl_2]Cl$ showing O–H···Cl and O–H···O intermolecular interactions. Atom labelling – black: Ir; grey: C; blue: N; green: Cl; red: O.

Table 3.4 summarises the hydrogen bond parameters existent in $[Ir(bpy)_2Cl_2]Cl$.

Table 3.4 – Hydrogen Bonds for $[Ir(bpy)_2Cl_2]Cl$.

D	H	A	d(D-H)/Å	d(H-A)/Å	d(D-A)/Å	D-H-A/°
O1	H1A	Cl3	0.87	2.56	3.132(17)	124.3
O2	H2A	O1[1]	0.87	1.97	2.83(2)	166.5
O2	H2B	O1	0.87	1.99	2.84(2)	163.1

3.5.2 $[Ir(bpy)_2(CF_3SO_3)_2]CF_3SO_3$

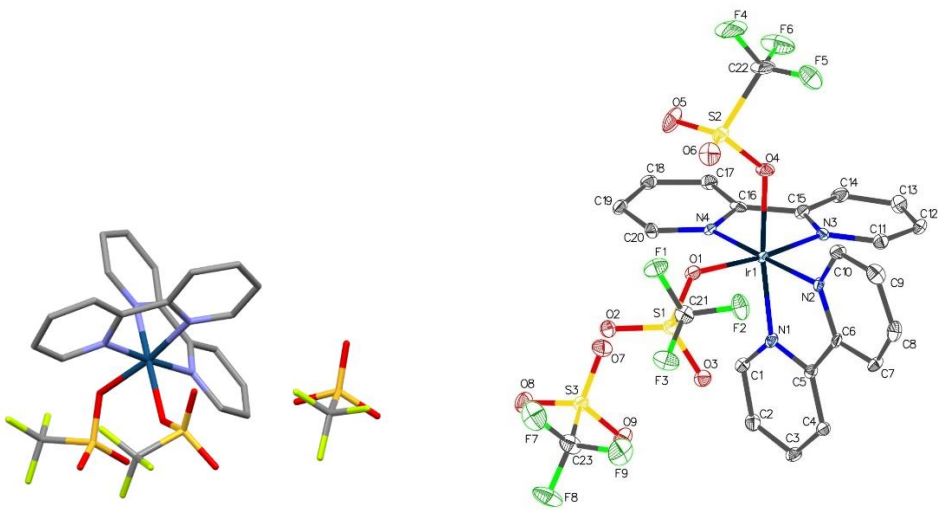

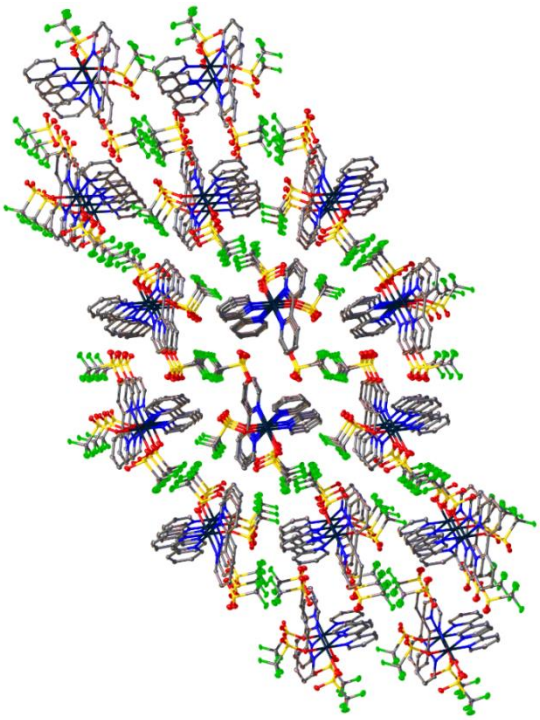

Figure 3.9 – top left: crystal structure of triclinic $[Ir(bpy)_2(CF_3SO_3)_2]CF_3SO_3$. Atom labelling – deep blue: Ir; grey: C; purple: N; light green: F; S: yellow; red: O; **top right:** ORTEP diagram and atom labelling scheme for $[Ir(bpy)_2(CF_3SO_3)_2]CF_3SO_3$ showing 50% thermal probability; **bottom:** Crystal packing of $[Ir(bpy)_2(CF_3SO_3)_2]CF_3SO_3$ along AB plane.

$[Ir(bpy)_2(CF_3SO_3)_2]CF_3SO_3$ crystallised as the expected structure. The full crystal structure shows that the title compound comprises one iridium(III) atom, two bpy ligands, two Cl ligands, and one CF_3SO_3 counterion. The crystal structure of the compound is depicted in Fig. 3.9. The asymmetric unit (structure not included due to space constraint) consists of the full compound. The crystals are seen to give a triclinic crystal system with a P-1 space group as shown in the crystal lattice. The structure displayed here has been refined anisotropically by full-matrix least-squares on F^2 with Final R index [I>=2σ (I)] value of 0.0390. The coordination geometry around the iridium metal centre deviates from what is considered as the perfect Werner's octahedral geometry[16–17] with some twisting of the two bpy non-rigid ligands (α/° = 104.574(3); β/° = 92.555(3); γ/° = 97.512(3)). The compound has an average bond length of 2.108Å for Ir–O and 2.025Å for Ir–N. The O4–Ir1–O1 bond angle was measured to be 90.32(16)° whilst the bond angles between any N, O, and Ir atoms in close distance range from 85.91(17)° (N3–Ir1–O4) to 176.63(18)° (N2–Ir1–O4). There is a significant deviation of the (N_{bpy}–Ir1–N_{bpy}) bond angles from 90°. The average S–O bond length is calculated as 1.444Å and the average F–C bond length is 1.341Å whilst the average O–S–O bond angle is measured

to be 115.16° and the average F–C–S bond angle is measured to be 110.26°. The average S–O–Ir bond angle is measured to be 131.50°. The full packing diagram and ORTEP plot of the complex are shown in Fig. 3.9.

All crystal data, including other bond lengths and angles, HSA and fingerprint diagrams obtained for $[Ir(bpy)_2(CF_3SO_3)_2]CF_3SO_3$, can be found in the Appendix Section.

3.6 Phen Family of Compounds

Only $[Ir(phen)_2Cl_2]Cl$ and $[Ir(phen)_2(CF_3SO_3)_2]CF_3SO_3$ are discussed as representative crystal structures of the phen family of compounds herein. A summary of the crystallographic information of the related $[Ir(phen)_2Cl_2]PF_6$ and $[Ir(phen)_2Cl_2]CF_3SO_3$ structures are given in the Appendix.

3.6.1 $[Ir(phen)_2Cl_2]Cl$

X-ray quality crystals of $[Ir(phen)_2Cl_2]Cl.H_2O.MeCN$ were grown through slow evaporation of Et_2O into a solution of the complex in MeCN. The determined structure of the target complex was as expected and includes one molecule of H_2O and one molecule of MeCN per two complexes. The crystal structure, packing diagram, and ORTEP plot of the complex are shown in Fig. 3.10. The crystals give an orthorhombic crystal system with a Pbcn space group as shown in the crystal lattice, and the asymmetric unit is for half of the complex. The structure was refined anisotropically with a Final R index [I>=2σ (I)] value of 0.0470. The iridium(III) ion in the compound is six-coordinate and is flanked by four N atoms from two phen ligands and two Cl atoms from two chloride ligands in its coordination sphere. The coordination geometry around the iridium metal centre is a perfect Werner's octahedral geometry[16–17] (α/° = 90; β/° = 90; γ/° = 90).

The unit cell parameters observed in this phen compound makes its geometry to be closer to the ideal octahedral geometry than those observed in its dppz counterpart (see later for details), which is more distorted from the ideal octahedral geometry. Anticipated variations in the Ir-N and Ir-Cl bond lengths occur due to their equivalence in the structure, but an average bond length of 2.0455Å is recorded for Ir-N and 2.3498Å for Ir-C. The C11-Ir1-Cl1 bond angle was

measured to be 90.38(6)° whilst the bond angles between any N, Cl, and Ir atoms in close distance range from 88.58(13) (N1–Ir1–$Cl1^1$)/88.58(14) ($N1^1$–Ir1–Cl1) to 175.13(14) ($N1^1$–Ir1–$Cl1^1$)/175.13(14) (N1–Ir1–Cl1). There is a minimal deviation of the (N_{phen}–Ir1–N_{phen}) bond angles from 90°. The average P–F bond length is calculated 1.58Å as whilst the average F–P–F bond angle is measured to be 112.5°.

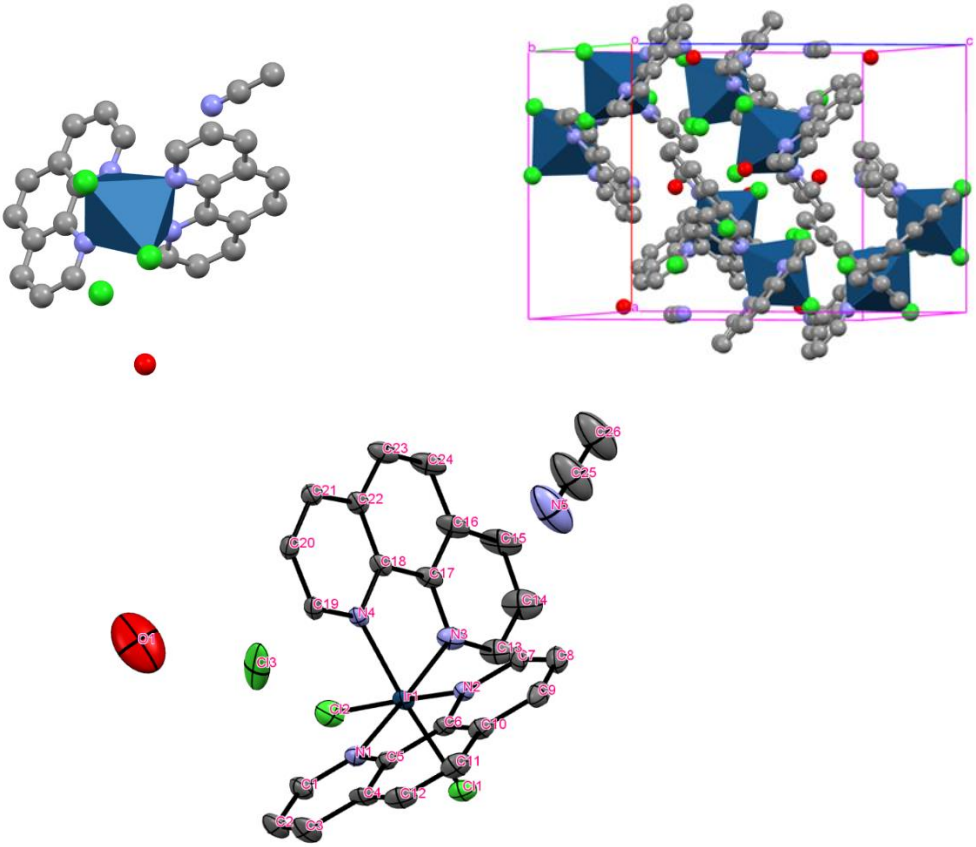

Figure 3.10 – top left: Crystal structure of orthorhombic **[**$Ir(phen)_2Cl_2]Cl.H_2O.MeCN$ (**NB:** $[Ir(phen)_2Cl_2]Cl$ is a solvate; a solvate is a crystal that contains solvents of crystallisation); **top right:** Unit cell packing diagram of $[Ir(phen)_2Cl_2]Cl.H_2O.MeCN$ with H_2O and MeCN molecules in between the channels; **bottom:** ORTEP diagram and atom labelling scheme for **[**$Ir(phen)_2Cl_2]Cl.H_2O.MeCN$ drawn at 50% thermal ellipsoids. Atom labelling – blue: Ir; grey: C; purple: N; green: Cl: red: O.

In the packing diagram, the phen ligands of the complex are seen to point towards each other with the Cl counterions sequentially layered in-between the phen ligands in the unit cell. The component ions in the compound's crystal unit are linked mainly by the O–H···Cl and Cl H···O hydrogen bond, as depicted in Fig. 3.11.

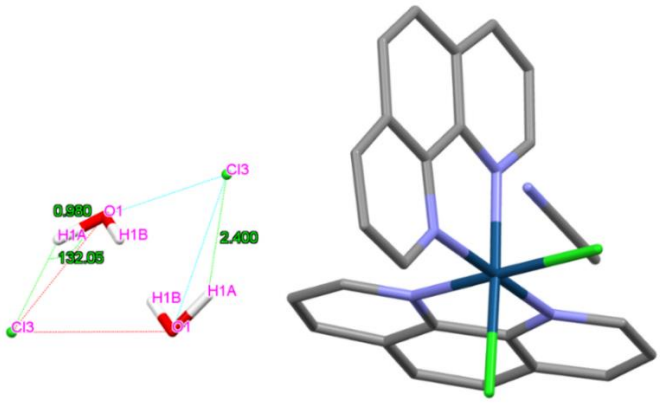

Figure 3.11 – Crystal structure of orthorhombic $[Ir(phen)_2Cl_2]Cl.H_2O.MeCN$ exemplifying O–H···Cl hydrogen bond interaction in the compound.

Table 3.5 summarises the hydrogen bond parameters existent in $[Ir(phen)_2Cl_2]Cl.H_2O.MeCN$.

Table 3.5 – Hydrogen Bonds for $[Ir(phen)_2Cl_2]Cl.H_2O.MeCN$.

D	H	A	d(D-H)/Å	d(H-A)/Å	d(D-A)/Å	D-H-A/°
O1	H1A	Cl3	0.98	2.40	3.142(11)	132.1
C14	H14	$O1^1$	0.95	2.39	3.176(11)	139.9

All crystal data obtained for **[**$Ir(phen)_2Cl_2]Cl.H_2O.MeCN$ can be found in the Appendix Section.

HSA could not be obtained for this compound since it has fractional occupancies, meaning it is disordered. All other crystal summary and/or data obtained for **[**$Ir(phen)_2Cl_2]Cl.H_2O.MeCN$ can be found in the Appendix Section.

3.6.2 $[Ir(phen)_2(CF_3SO_3)_2]CF_3SO_3$

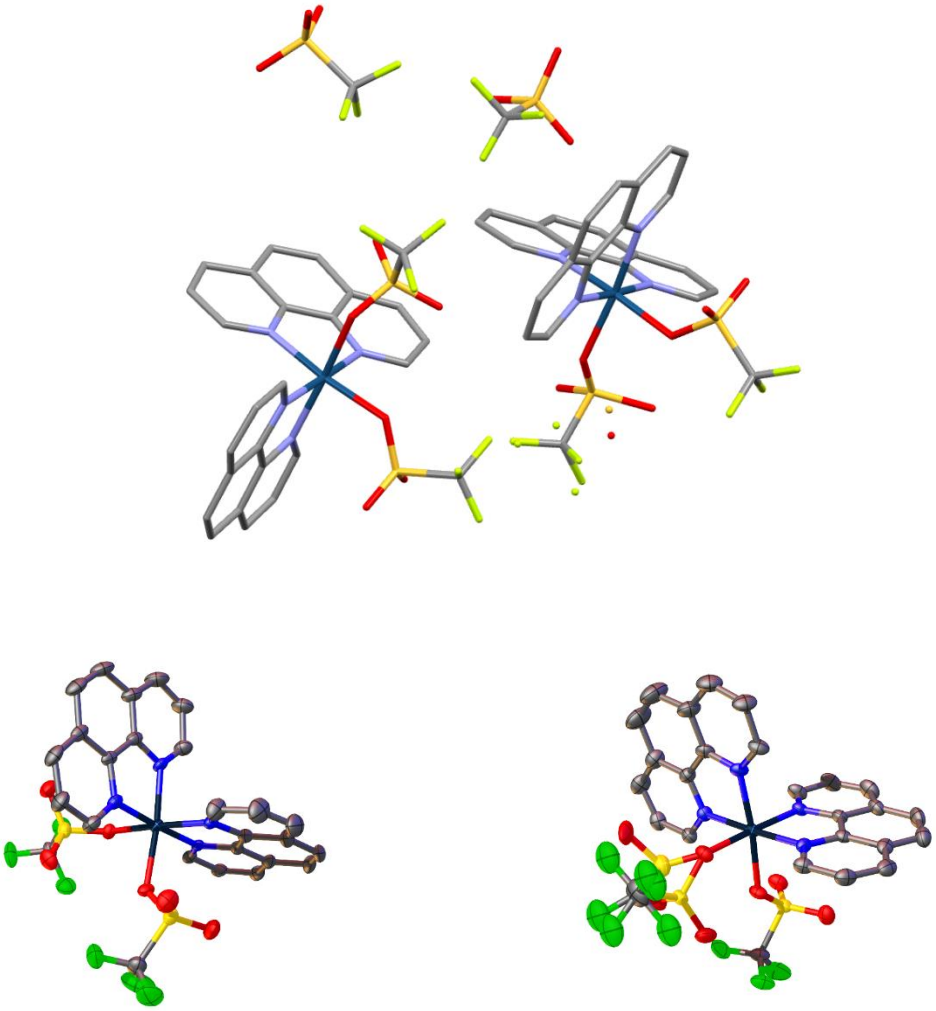

Figure 3.12 – top: Crystal structure of triclinic $[Ir(phen)_2(CF_3SO_3)_2]CF_3SO_3$. Hydrogen atoms are omitted for clarity. Colour scheme – blue: Ir; grey: C; purple: N; light green: F; yellow: S; red: O; **bottom left:** Δ-$[Ir(phen)_2(CF_3SO_3)_2]CF_3SO_3$; **bottom right:** Λ-$[Ir(phen)_2(CF_3SO_3)_2]CF_3SO_3$.

X-ray quality crystals of compound $[Ir(phen)_2(CF_3SO_3)_2]CF_3SO_3$ (crystallised as expected) were grown through slow vapour diffusion of THF into a solution of the complex in CH_3NO_2. The coordination sphere of the compound shows that its crystal structure is six-coordinate comprising one iridium(III) atom, two phen ligands, two triflate ligands, and one triflate counteranion (Fig. 3.12). Since the compound's Z value equals 4, it has four molecules in the unit cell. The crystals give a triclinic crystal system with a P-1 space group as shown in the crystal lattice. The structure was refined anisotropically with a Final R index [I>=2σ (I)] value

of 0.0483. The coordination geometry around the iridium metal centre is almost octahedral with a small twisting of the two phen non-rigid ligands (α/° = 103.907(4); β/° = 95.410(4); γ/° = 90.424(4)). The asymmetric unit of this crystal structure is somewhat complicated, having two molecules of the complex in it, which look like one pseudo delta structure and one pseudo lambda structure. The Λ-complex looks to have some disorder at one of the triflate coordination sites. The crystal lattice structures and ORTEP plots of each of these putative conformations are given in Figs. 3.12 and 3.14.

Anticipated variations in the Ir–N and Ir–O bond lengths occur due to their equivalence in the structure, but an average bond length of 2.033Å is recorded for Ir–N and 2.090Å for Ir–O, with Ir–N being longer of the two. This is well expected as the combined electronegativity value of Ir and N (5.24Å) is lesser than that of Ir and O (5.64Å). The bond angle (O–Ir–O) from the two triflate ligands directly coordinated to the Ir(III) metal centre 86.53(16)° (O4A–Ir1A–O1A) and 88.84(17)° (O4B–Ir1B–O1B) and is averagely measured to be 87.69°. The bond angles between any N, O, and Ir atoms in close distance varied from 86.19(19)° (N2B–Ir1B–O4B) to 174.27(18)° (N2A–Ir1A–O4A). The bond angles between any C, N, and Ir atoms in close distance range from 111.5(4)° (C5A–N1A–Ir1A) to 128.7(4)° (C1A–N1A–Ir1A). There is a significant deviation of the (N_{phen}–Ir1–N_{phen}) bond angles from 90°, which is considered the ideal octahedral geometry. To conserve space, all bond lengths and angles are provided in the Appendix.

The packing diagram of the complex is shown in Fig. 3.13. In this diagram, the phen ligands of the compound are seen to point towards each other though not so much in proximity with triflate counterions arrayed both in the channels in the unit cell.

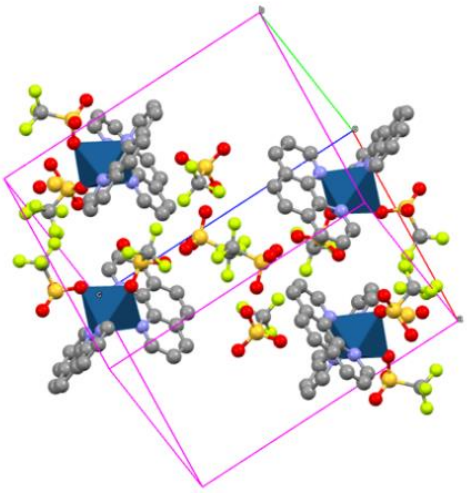

Figure 3.13 – Packing diagram of $[Ir(phen)_2(CF_3SO_3)_2]CF_3SO_3$.

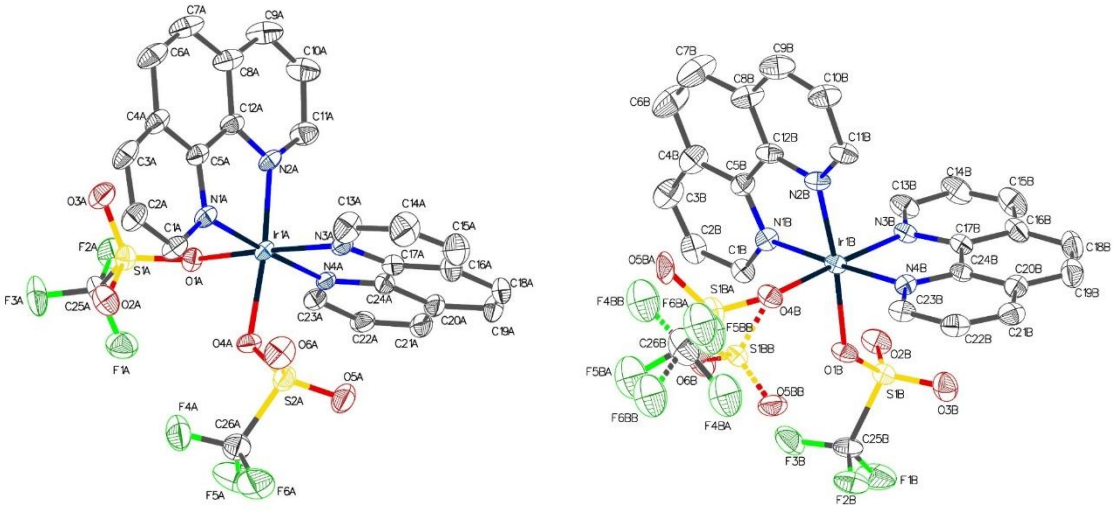

Figure 3.14 – left: ORTEP diagram and atom labelling scheme for Δ-$[Ir(phen)_2(CF_3SO_3)_2]CF_3SO_3$ showing 50% thermal ellipsoids. Hydrogen atoms and atom labelling are omitted for clarity; **right:** ORTEP diagram and atom labelling scheme for Λ-$[Ir(phen)_2(CF_3SO_3)_2]CF_3SO_3$ showing 50% thermal ellipsoids. Hydrogen atoms and atom labelling are omitted for clarity.

HSA could not be obtained for the compound since it has fractional occupancies, being disordered along the triflate counterion. All other crystal summaries and/or data obtained for the $[Ir(phen)_2(CF_3SO_3)_2]CF_3SO_3$ can be found in the Appendix Section.

3.7 Dppz Family of Compounds

Only the crystal structures of $[Ir(dppz)_2Cl_2]PF_6$, and $[Ir(dppz)_2(CF_3SO_3)_2]CF_3SO_3$ are discussed herein as representative examples. Complex $[Ir(dppz)_2Cl_2]CF_3SO_3$ is given in the Appendix, and complex $[Ir(dppz)_2Cl_2]Cl$ could not be obtained.

3.7.1 $[Ir(dppz)_2Cl_2]PF_6$

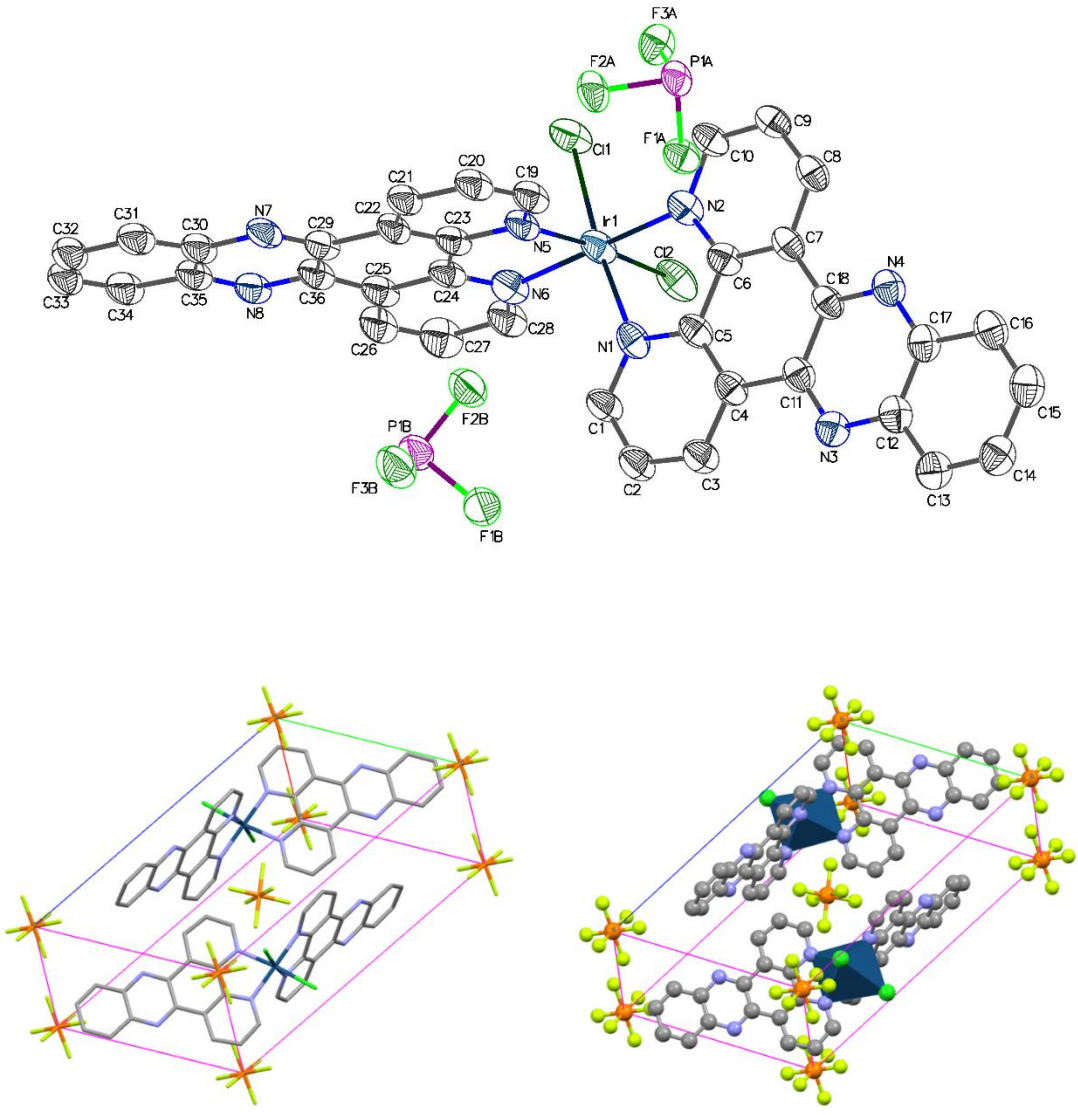

Figure 3.15 – top: ORTEP structure of triclinic $[Ir(dppz)_2Cl_2]PF_6$ drawn at 50% thermal probability ellipsoid with atom labels. Hydrogen atoms are omitted for clarity and crystal packing of $[Ir(dppz)_2Cl_2]PF_6$ with PF_6 counterions arrayed both in the channels and along the diagonals showing capped sticks (**bottom left**) and polyhedral (**bottom right**) representations. Atom labelling – blue: Ir; grey: C; purple: N; deep green: Cl; light green: F; orange: P.

$[Ir(dppz)_2Cl_2]PF_6$ was obtained as yellow crystals by vapour diffusion of THF into a solution of the compound in CH_3NO_2. The asymmetric unit consists of one iridium(III) atom, two dppz ligands, two Cl ligands, and 2 x 0.5 PF_6 counterions, with the counterions sitting in the channels and along the diagonals of the unit cell. In one of the figures, a single complete PF_6 is shown for clarity. There was also evidence of some solvents included in the structure. It looks like there is a channel where disordered THF sits, but as this could not be modelled satisfactorily, the missing electron density was accounted for by a solvent mask. Since the compound's Z value equals 2, it has two molecules in the unit cell.

The crystals are seen to give a triclinic crystal system with a P-1 space group. The structure displayed was refined anisotropically by full-matrix least-squares on F^2 with a Final R index [I>=2σ (I)] value of 0.0427. The iridium(III) ion in the compound is six-coordinate and is flanked by four N atoms from two dppz ligands and two Cl atoms from two Cl ligands in its coordination sphere. The coordination geometry around the iridium metal centre deviates from what is considered the perfect Werner's octahedral geometry[16–17] with some twisting of the two dppz non-rigid ligands (α/° = 102.166(3); β/° = 94.123(2); γ/° = 114.224(3)). Anticipated variations in the Ir–N and Ir–Cl bond lengths occur due to their inequivalence in the structure, but an average bond length of 2.04800Å is recorded for Ir-N and 2.35485Å for Ir-Cl. The Cl1–Ir1–Cl2 bond angle was measured to be 93.32° whilst the bond angles between any N, Cl, and Ir atoms in close distance range from 87.31(12) (N6–Ir1–Cl1) to 128.8(3) (C19–N5–Ir1). There is a significant deviation of the (N_{dppz}–Ir1–N_{dppz}) bond angles from 90°. The average P–F bond length is calculated as 1.60Å whilst the average F–P–F bond angle is measured to be 109.97°.

All other crystal summaries and/or data obtained for the $[Ir(dppz)_2Cl_2]PF_6$ can be found in the Appendix Section.

3.7.2 $[Ir(dppz)_2(CF_3SO_3)_2]CF_3SO_3$

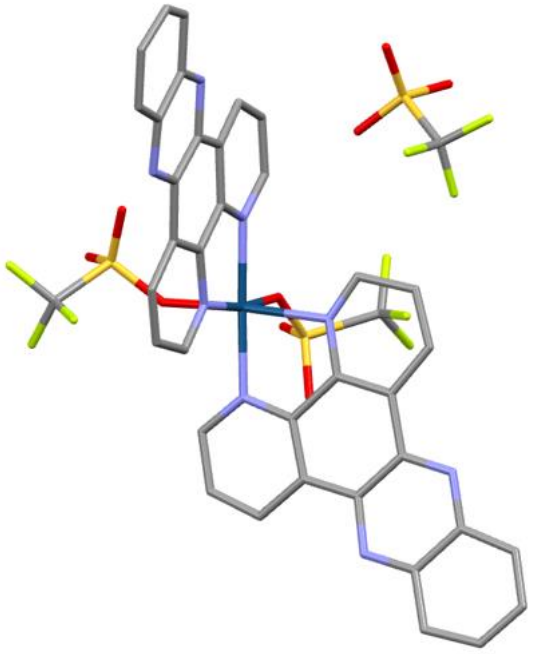

Figure 3.16 – Crystal structure of monoclinic $[Ir(dppz)_2(CF_3SO_3)_2]CF_3SO_3$. Hydrogen atoms are omitted for clarity. Colour scheme – blue: Ir; grey: C; purple: N; light green: F; yellow: S; red: O.

X-ray quality crystals of the expected $[Ir(dppz)_2(CF_3SO_3)_2]CF_3SO_3$ were grown through slow vapour diffusion of THF into a solution of the complex in CH_3NO_2. The coordination sphere of the compound shows that its crystal structure is six-coordinate comprising one Ir(III) atom, two dppz ligands, two triflate ligands, and one triflate counteranion (Fig. 3.16). Since the compound's Z value equals 4, it has four molecules of itself in the unit cell. The crystals are seen to give a monoclinic crystal system with a $P2_1/n$ space group as shown in the crystal lattice. The asymmetric unit is for the full complex. The structure displayed here has been refined anisotropically with an *acceptable* Final R index [I>=2σ (I)] value of 0.1177. Although this is too high to be of publication quality, an analysis of selected bond lengths and angles is provided herein. The coordination geometry around the iridium metal centre is close to octahedral with small twisting of the two dppz non-rigid ligands (α/° = 90; β/° = 117.137(6); γ/° = 90).

Expected variations in the Ir–N and Ir–O bond lengths occur due to their equivalence in the structure, but an average bond length of 2.063Å is recorded for Ir–N and 2.056Å for Ir–O, Ir–

N being longer of the two. This is expected as the combined electronegativity value of Ir and N (5.24) is lesser than that of Ir and O (5.64). The bond angle of the triflate ligand directly coordinated to the iridium(III) metal centre (O1–Ir1–O4) is measured to be 87.0(7)° whilst the bond angles between any N, O, and Ir atoms in close distance varies from 89.7(8)° (N1–Ir1–O1) to 175.2(10)° (O1–Ir1–N6). The bond angles between any C, N, and Ir atoms in close distance range from 110.9(19)° (C6–N2–Ir1) to 129(2)° (C10–N2–Ir1/C1–N1–Ir1) and is averagely measured to be 118.46°. There is a significant deviation of the (N_{dppz}–Ir1–N_{dppz}) bond angles from 90° due to chelation.

The S–C bond lengths between the SO_2 and CF_3 groups of the two triflate ligands directly coordinated to the iridium(III) metal centre are 1.80(4)Å (S1–C37) and 1.82(4)Å (S2–C37) whilst that of the triflate counterion is 1.78(4)Å (S3–C39). Meanwhile, the average F–C bond lengths of the CF_3 groups of the two triflate ligands directly coordinated to the iridium(III) metal centre are 1.31Å (F1–C37, F2–C37, and F3–C37) and 1.32Å (F4–C38, F5–C38, and F6–C38) whilst that of the triflate counterion is 1.32Å (F7–C39, F8–C39, and F9–C39). These average bond lengths tally with the ideal bond length of CF_3 which is usually within the range 1.30–1.35Å.[16] The average S–O bond lengths of the SO_2 groups of the two triflate ligands directly coordinated to the iridium(III) metal centre are 1.45Å (S1–O1, S1–O2, and S1–O3) and 1.44Å (S2–O4, S2–O5, and S2–O6) whilst that of the triflate counterion is 1.44Å (S3–O7, S3–O8, and S3–O8). The average bond length of F–C in CF_3 being shorter than that of S–O in SO_2 is expected due to that the combined electronegativity values of C and F (6.53) is greater than that of S and O (6.02), thereby leading to a smaller bond (and of course a more stable bond) in CF_3 than in SO_2.[18]

The average F–C–S bond angles of the two triflate ligands directly coordinated to the iridium(III) metal centre are 112.67° (F1–C37–S1, F2–C37–S1, and F3–C37–S1) and 111.33° (F4–C38–S2, F5–C38–S2, and F6–C38–S2) whilst that of the triflate counterion is 109.33° (F7–C39–S3, F8–C39–S3, and F9–C39–S3). The average O–S–C bond angles of the two triflate ligands directly coordinated to the iridium(III) metal centre are 104.33° (O1–S1–C37, O2–S1–C37, and O3–S1–C37) and 103.73° (O4–S2–C38, O5–S2–C38, and O6–S2–C38) whilst that of the triflate counterion is 103.9° (O7–S3–C39, O8–S3–C39, and O9–S3–C39). The average O–S–O bond angles of the two triflate ligands directly coordinated to the iridium(III) metal centre are 114.03° (O2–S1–O1, O3–S1–O1, and O3–S1–O2) and 114.57°

(O4–S2–O5, O6–S2–O4, and O6–S2–O5) whilst that of the triflate counterion is 114.43° (O7–S3–O9, O8–S3–O7, and O8–S3–O9). The average F–C–F bond angles of the two triflate ligands directly coordinated to the iridium(III) metal centre are 106° (F2–C37–F1, F2–C37–F3, and F3–C37–F1) and 107.67° (F5–C38–F4, F6–C38–F4, and F6–C38–F5) whilst that of the triflate counterion is 106° (F7–C39–F8, F7–C39–F9, and F8–C39–F9). This deviates slightly (lower than the value) from the ideal F–C–F bond angle which is typically within the range 109.5°–112.0 °.

The ORTEP structure of the complex is shown in Fig. 3.17. In these diagrams, the dppz ligands of the compound are seen to point towards each other though not so much in close proximity with triflate counterions arrayed both in the channels in the unit cell. Within the packed structure, channels are structured by a large array of π-π stacking between the two dppz rings on the iridium cation, which define the large channels through the unit cell. The large planar aromatic rings and their observed potential for π-π stacking interactions indicates they should intercalate into the base pairs of double-helical DNA. In the compound, there is an existence of two N···O bonds between the O groups of the two triflate ligands coordinated to the iridium(III) metal centre and N groups of the two dppz rings coordinated to the iridium(III) metal centre. These interactions are non-identical in lengths, and they have been measured to be 2.808Å (N5–H···O5) and 2.823Å (N2–H···O2). There is also the presence of various short contacts within the compound's crystal packing. For instance, there are short contacts between C22 of one of the dppz rings and O3 of one of the triflate groups coordinated to the iridium(III) metal centre (length: 3.09(3)Å), C26 of one of the dppz rings and O8 of the one of the triflate groups coordinated to the iridium(III) metal centre (length: 3.16(5)Å), and O9 of one of the triflate groups coordinated to the iridium(III) metal centre and O3 of another adjacent triflate ligand coordinated to the iridium(III) metal centre (length: 2.97(3)Å).

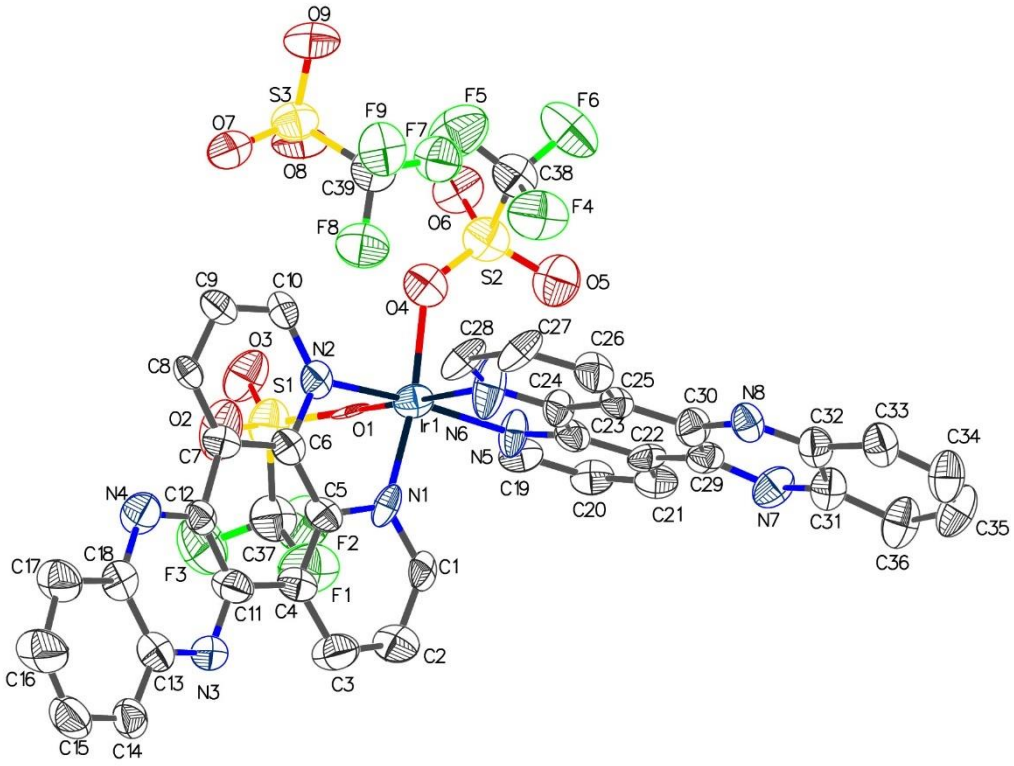

Figure 3.17 – ORTEP diagram and atom labelling scheme for $[Ir(dppz)_2(CF_3SO_3)_2]CF_3SO_3$ showing 50% thermal ellipsoids. Hydrogen atoms and atom labelling are omitted for clarity.

All other crystal summaries and/or data obtained for the $[Ir(dppz)_2(CF_3SO_3)_2]CF_3SO_3$ can be found in the Appendix Section.

Three adventitious crystals are discovered in this work. Their crystal structure summaries are given in an appropriate section of the Appendix.

3.8 Chapter Summary

This chapter briefly reports on the single-crystal X-ray structural description and Hirshfeld Surface Analysis (HSA) of qtpy bridging ligand and selected precursors employed for the synthesis of the final complexes tailored towards DNA- and protein-binding studies given in subsequent chapters. The qtpy structure described represents the first instance of the report of its crystal structure even though the compound is a much-used ligand in the research field of coordination chemistry. All crystal structures discussed in this investigation are the first reported for the complexes described. All given crystals, except for $[Ir(phen)_2Cl_2]Cl$, exhibit a

quasi-octahedral geometry. All the crystals except for $[Ir(phen)_2Cl_2]Cl$ display either monoclinic system (nature's choice crystal system) (herein $a \neq b \neq c$, $\alpha = \gamma = 90^o$; $\beta \neq 90^o$) or triclinic system (herein $a \neq b \neq c$, $\alpha = \beta = \gamma = 90^o$); $[Ir(phen)_2Cl_2]Cl$ crystallises in the orthorhombic crystal system (herein $a \neq b \neq c$, $\alpha \neq \beta \neq \gamma = 90^o$). The most prevalent space group displayed by the crystals is the P-1 space group, the others being C2/c, $P2_1/c$, $P2_1/n$, and Pbcn. Some of crystals exhibit different space groups with varying lattice parameters even though they are isostructural. Important crystallographic parameters such as crystal structure, crystal system, space groups, unit cell parameters and selected bond distances and angles, packing structure, and ORTEP diagram are given for each of the crystals. Even though some of the crystals suffer some distortion, especially in their triflate coordinative ligands or counterions, the crystallographic information obtained for them sufficiently confirm their structural identities. HSA, a particularly helpful tool for gaining insight into the solid-state surface information of a crystal, was used to obtain important intermolecular contacts present on the surface of the reported crystals. Fingerprint plots proved useful in mapping the percentage contributions of such interactions, especially if the interactions stabilise the surfaces of the crystal structures as in the case of qtpy ligand, which was employed as the bridging ligand for the construction of the iridium(III)-based anticancer agents explored in this thesis.

3.9 References

1. D. Oyama, Role of X-Ray Crystallography in Structural Studies of Pyridyl-Ruthenium Complexes (Chapter 9), A. Chandrasekaran (Ed.), *Current Trends in X-Ray Crystallography*, InTech, Rijeka, 2011, 219–238.

2. G. R. Desiraju, G. W. Parshall, Crystal Engineering: The Design of Organic Solids, Materials science monographs, 1989, 54, XIV-312 p. [326 p.], Elsevier, Amsterdam.

3. M. A. Spackman and J. J. McKinnon, Fingerprinting intermolecular interactions in molecular crystals, *CrystEngComm*, 2002, 4(66), 378–392.

4. M. A. Spackman and D. Jayatilaka, Hirshfeld surface analysis, *CrystEngComm*, 2009, 11, 19–32.

5. P. R. Spackman, M. J. Turner, J. J. McKinnon, S. K. Wolff, D. J. Grimwood, D. Jayatilaka, M. A. & Spackman, *J. Appl. Cryst.*, 2021, 54, 3, 1006–1011.

6. M. Montazerozohori, S. Farokhiyani, A. Masoudiasl, J.M. White, Crystal structures, Hirshfeld surface analyses and thermal behavior of two new rare tetrahedral terminal zinc azide and thiocyanate Schiff base complexes, *RSC Adv.*, 2016, 6, 23866–23878.

7. M. Jayendran, M. Sithambaresan, P. M. S. Begum M. R. P. Kurup, *Polyhedron*, 2019, 158, 386–397.

8. Q. Hu, Y. H. Yue, L. Q. Chai, L. J. Tang, *J. Mol. Struct.*, 2019, 1197, 508–518.

9. Y. Q. Pan, Y. Zhang, M. Yu, Y. Zhang, L. Wang, *Appl. Organomet. Chem.*, 2020, 34(3), e5441.

10. C. F. Matta, J. Hernandez-Trujillo, T. -H. Tang, and R. F. W. Bader, *Chem.-Eur. J.*, 2003, 9, 1940–1951.

11. D. A. Safin, M. G. Babashkina, M. P. Mitoraj, P. Kubisiak, K. Robeyns, M. Bolte, Y. Garcia, *Inorg. Chem. Front.*, 2016, 3, 1419–1431.

12. S. Konar, S. K. Datta, M. Dolai, A. Das, S. Pathak, S. Chatterjee, K. Das, *J. Mol. Struct.*, 2019, 1178, 682–691.

13. P. Lahuerta, J. Latorre, R. Martinez-Manez, S. Garcia-Granda, F. Gomez-Beltran, Structure of bis(2,2'-bipyridine)dichlororhodium(III) chloride dihydrate, *Acta Crystallogr. Sect. C Cryst. Struct. Commun.*, 1991, 47, 519–522.

14. F. M. Jaeger, J. A. van Dijk, Die verschiedenen Typen von Komplexsalzen des α-α'-Dipyridyls mit Kupfer, Zink, Cadmium, Eisen, Nickel, Kobalt und Rhodium, *Z. Anorg. Allg. Chem.*, 1936, 227, 273–327.

15. F. M. Jaeger and J. A. van Dijk, Complex salts of bipyridyl with bivalent and trivalent cobalt, *Proc. K. Ned. Akad. Wet.*, 1936, 39, 164–175.

16. K. Bowman-James, Alfred Werner revisited: the coordination chemistry of anions, *Acc. Chem. Res.*, 2005, 38(8), 671–678.

17. E. C. Constable and C. E. Housecroft, Coordination chemistry: the scientific legacy of Alfred Werner, *Chem. Soc. Rev.*, 2013, 42, 1429–1439.

18. D. O'Hagan, Understanding organofluorine chemistry. An introduction to the C–F bond, *Chem. Soc. Rev.*, 2018, 37 (2), 308–319.

4.0 Duplex and G-quadruplex DNA-Binding Studies

4.1 Introduction: Duplex DNA-Binding Studies

DNA is the prime target of many metal-based anticancer drugs,[1] and various techniques have been used to investigate the possible interaction between metal complexes and the DNA biomolecule.[2] In the first section of this chapter, the interaction between $[Ir(bpy)_2(qtpy)]^{3+}$, $[Ir(phen)_2(qtpy)]^{3+}$ or $[Ir(dppz)_2(qtpy)]^{3+}$ with duplex DNA has been investigated by spectroscopic titration.[3]

4.2 DNA-binding Investigation by Electronic Absorption Spectroscopy

Absorption spectroscopy is usually the first technique to see if a metal complex interacts with the DNA biomolecule. As transition metal complexes usually possess colours visible to the eyes, their DNA binding interactions can easily be followed by monitoring the changes in their ^{3}MLCT or π- π^* bands, as these are often perturbed upon interaction with DNA. A typical DNA binding mode is intercalation, which can be potentially identified using absorption spectroscopy.[4] If DNA binding proceeds through intercalation, both hypochromism and bathochromism is frequently observed. The extent of an intercalative binding modality depends on the strength of the interaction between a metal complex and DNA.[5] The chemistry behind this is simple: in the intercalative mode of DNA binding, the π^* orbitals of the intercalated ligand overlap with the π orbitals of the DNA base pairs resulting in a decrease of the transition energy and hence bathochromism. As the coupling π orbital has partially filled electrons, such interaction results in a decrease of the transition probabilities leading to a decrease in absorption or what is known as hypochromism.[6] Thus, upon addition of DNA, changes in the absorption (decrease/increase in absorbance) and wavelength (as either red or blue shift) of the complex at a fixed concentration provide evidence of compound-DNA interactions.[7]

Because the complexes investigated absorb in the same wavelength region as CT-DNA and their MLCT wavelengths are weak, this thesis excludes DNA-binding experiments using absorption spectroscopy.

4.3 DNA-binding Investigations by Luminescence Spectroscopy

Luminescence spectroscopy is usually the second common method used to investigate the binding interaction between a transition metal complex and DNA. Steady-state luminescence measurements can be used to probe the variations in emission intensities for metal complexes in the presence of increasing DNA concentrations.[6] The intensity of a complex's ^{3}MLCT emission band can be a signature of its DNA-binding affinity.[8] The titration of DNA into a known concentration of binding substrate solution impinges a shift in a particular band being monitored; this shift is proportional to the fraction of the complex bound to DNA. The fraction of complex bound (χ) can be evaluated spectroscopically by monitoring this specific change as given in the equation below:

$$\chi = \frac{I_{obs} - I_f}{I_b - I_f}$$

(Equation 4.1)

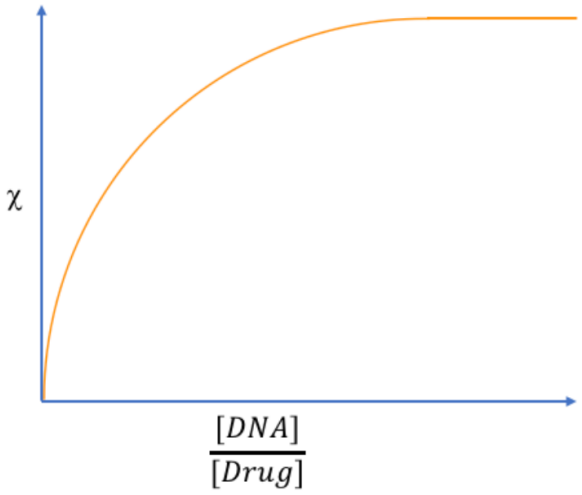

Figure 4.1 – Binding curve exemplifying saturation binding.

Where I_f is the emission of the free complex, I_b is the emission of the fully bound complex and I_{obs} is the emission at a given point. To give an accurate determination of the binding constant, it is crucial that saturation binding has occurred. Based on this, a binding curve can be produced from a plot of χ against the mixing ratio, R/([DNA]/[Drug]) (Figure 4.1).[9]

$$C_b = \chi . C_i$$

(Equation 4.2)

The concentration of bound complex (C_b) can then be calculated having known both the initial concentration of complex (C_i) and the fraction bound (χ):

C_f is the concentration of free complex[10]:

$$C_i = C_f + C_b$$

(Equation 4.3)

A rearrangement to make C_f the subject gives the equation below:

$$C_f = C_i - C_b$$

(Equation 4.4)

The binding ratio can then be calculated, as the concentrations of bound and free drug at any given time can be found:

$$r = \frac{C_b}{[DNA]}$$

(Equation 4.5)

Primary data like these can be used to construct a Scatchard plot, which is a plot of the degree of binding saturation against the free ligand concentration, i.e., r/C_f vs. r. In the Scatchard plot, the slope measures the intrinsic equilibrium binding constant, K_i and the intercept gives the number of ligand binding sites, n:[11–12]

$$\frac{r}{C_f} = K_i(n - r)$$

(Equation 4.6)

The Scatchard equation is a conventional way of analysing equilibrium ligand binding data. The equation is based on the following assumptions: (i) all ligands are identical, (ii) the activity (both chemical and biological) will not suffer any change except by binding, and (iii) all sites of each set are both discrete and equivalent.[13]

Getting a Scatchard plot for a DNA-binding event is a bit more complicated. Small molecules interacting with DNA can be divided into two classes: (i) those characterised by "specific" binding, and (ii) those characterised by "nonspecific" binding. The classical Scatchard model holds for species exhibiting specific binding, expressing an overwhelming affinity for one, or a very few particular base sequences on certain DNA molecules. In other words, a simple Scatchard plot would only be valid if a ligand binds to one repeating unit of the lattice. However, when a ligand binds over an extended lattice site, complications occur. Thus, an inaccurate Scatchard analysis of the system might be experienced. Since DNA, for instance, is an isotropic lattice, having no discrete binding sites, most sites involved in ligand binding overlap. Therefore, at any degree of binding saturation, the number of free binding sites is not just dependent on the number of ligands already bound but also on the distribution of these bound ligands on the lattice. The occurrence of this type of binding means a curvature would arise instead of a linear Scatchard plot. Consequently, binding data are not linear as a result of the overlap of potential binding sites. Such data can only be quantitated by a nonlinear least squares fitting procedure to the McGhee and von Hippel (MVH) simple neighbour exclusion model (Equation 4.7) for non-cooperative binding.[14–15]

$$\frac{r}{C_f} = K(1 - nr).\left[\frac{(1 - nr)}{1 - (n - 1)r}\right]^{n-1}$$

(Equation 4.7)

The derivation of this equation assumes an infinite lattice. However, real macromolecules are finite and end effects will accrue. To reduce any associated error with this effect, only experimental data between 30–90% bound drug is typically fitted.[16]

4.3.1 $[Ir(N–N)_2(qtpy)]^{3+}$ Luminescence Spectroscopic Titrations with CT-DNA

Luminescent titrations were used to parameterise the binding property of $[Ir(N–N)_2(qtpy)]^{3+}$ (where N–N = bpy, phen or dppz) with DNA. The iridium complexes in this study contain the moiety qtpy, so, it was of great interest to investigate their luminescent behaviours upon binding to DNA. In this context, the interactions of the three complexes with double-stranded

duplex CT-DNA and G-quadruplex (HTS quadruplex (d[$AG_3(T_2AG_3)_3$])) were investigated using emission titrations.

4.3.1.1 $[Ir(bpy)_2(qtpy)]^{3+}$ Luminescence Titration Studies

The compound functions as an "on-off" probe for DNA detection. It is emissive in aqueous solution, but the emission became gradually quenched upon the increasing addition of CT-DNA. $[Ir(bpy)_2(qtpy)]^{3+}$ was excited at 310nm and the variation in its structured band at ~ 487nm on incremental additions of DNA was recorded (Fig. 4.2).

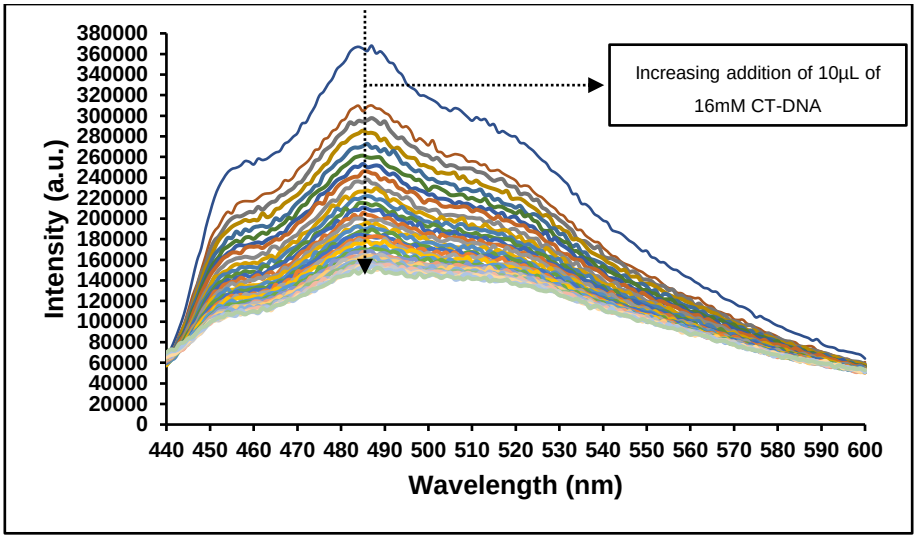

Figure 4.2 – Luminescent titration of 16mM CT-DNA into a solution of 100µM of $[Ir(bpy)_2(qtpy)]^{3+}$ in 5mM tris buffer, 25mM NaCl, pH 7.4, at 27°C. Excitation wavelength: 310nm; emission region: 440–600nm. Excitation slit width: 5nm. Emission slit width: 5nm. Stokes shift = 177nm.

Data Fitting

The data in Fig. 4.2 were fitted to the plots in Figs. 4.3 and 4.4.

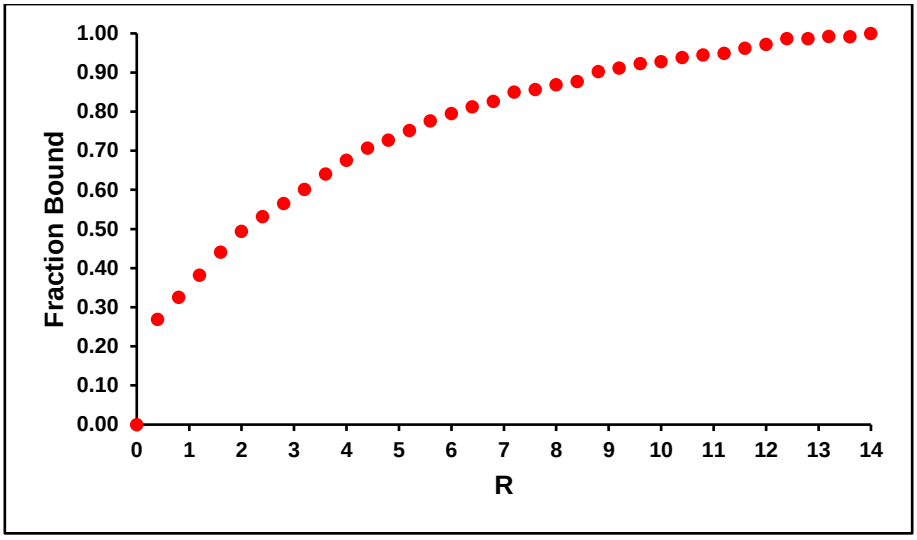

Figure 4.3 – Binding curve obtained from luminescent titrations of CT-DNA into $[Ir(bpy)_2(qtpy)]^{3+}$, where R = [DNA]/[complex].

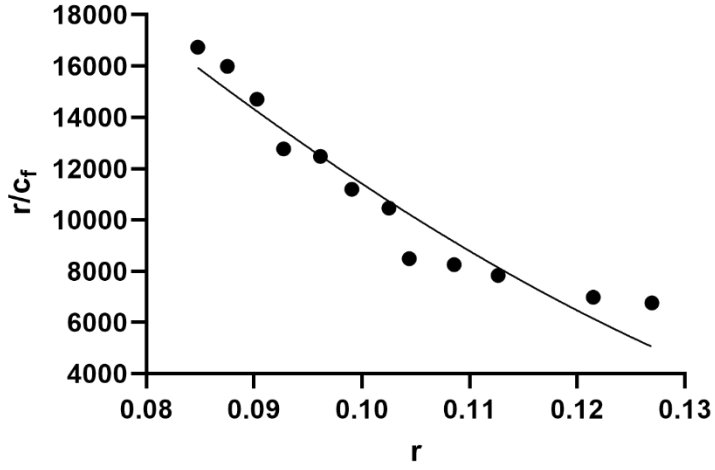

Figure 4.4 – Non-linear Scatchard plots for the luminescent titrations of 16mM CT-DNA into a solution of 100µM of $[Ir(bpy)_2(qtpy)]^{3+}$ in 5mM tris buffer, 25mM NaCl, pH 7.4, at 27°C. Experimental data between 30–90% bound drug are fitted. $R^2 = 0.9247$.

No significant DNA-induced wavelength increase or decrease was observed during the binding event. The non-linear Scatchard plot fitted to the commonly employed McGhee von Hippel (MVH) for non-cooperative binding produces the binding parameters summarised in Table 4.1.

Table 4.1 – CT-DNA binding parameters for $[Ir(bpy)_2(qtpy)]^{3+}$ including emission λ_{max} values, and from a MVH fit of binding data, K_b and n.

Complex	λ_{max} (nm) (aqueous)	λ_{max} (nm) (CT-DNA)	Binding affinity, K_b $[M^{-1}]$	Site size, n, (base pairs)
$[Ir(bpy)_2(qtpy)]^{3+}$	487	487	4.77×10^4	5

DNA-induced emission spectral variations of $[Ir(bpy)_2(qtpy)]^{3+}$ show sharp decrease in the intensity of the complex. The decrease in intensity of the high energy luminescence of $[Ir(bpy)_2(qtpy)]^{3+}$ upon DNA addition perhaps indicates redox quenching by DNA nucleobase sites, especially as the complex possesses a low singlet oxygen quantum yield of ~ 13% as measured with the help of Dr Alexander Auty.[17] DNA strands are often cleaved due to oxidative damage caused by nucleotide base reactions within nucleic acids. As a result of these reactions, metallo-intercalators lose much of their luminescent properties, experiencing luminescence quenching.[18–19]

4.3.1.2 $[Ir(phen)_2(qtpy)]^{3+}$ Luminescence Titration Studies

The compound equally functions as an "on-off" probe for DNA detection. It is emissive in aqueous solution, but the emission became gradually quenched upon the increasing addition of CT-DNA (Fig. 4.5). $[Ir(phen)_2(qtpy)]^{3+}$ was excited at 316nm giving a dual emission, one at 464nm and the other at 494nm. The variations in its structured band at both wavelengths upon incremental additions of DNA were recorded.

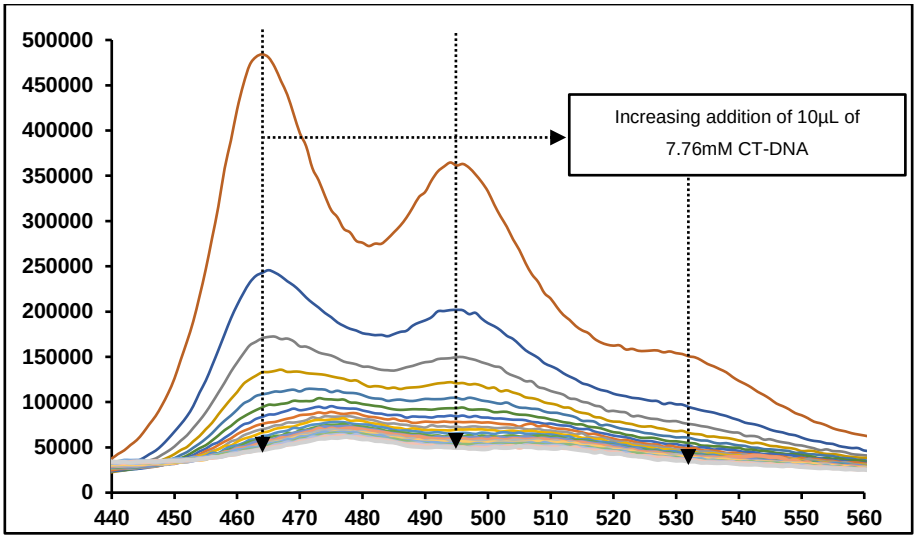

Figure 4.5 – Luminescent titration of 7.76mM CT-DNA into a solution of 8.37µM of $[Ir(phen)_2(qtpy)]^{3+}$ in 5mM tris buffer, 25mM NaCl, pH 7.4 at 27°C. Excitation wavelength: 316nm; emission region: 440–560nm. Excitation slit width: 5nm. Emission slit width: 5nm. Dual emission located at 464nm and 494nm. Stokes shift = 148nm.

Data Fitting

Two sets of graphs and binding fits are given since the complex shows a dual emission signature (Figs. 4.6–4.9).

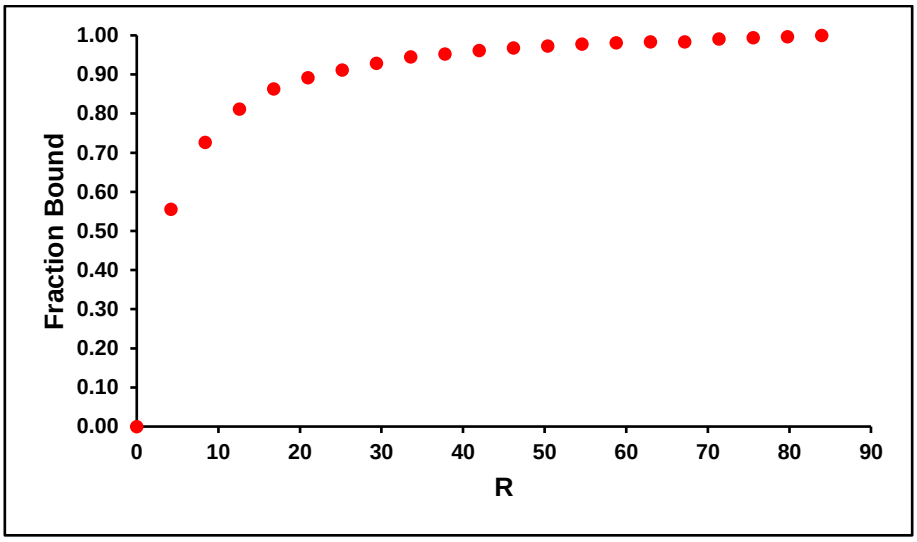

Figure 4.6 – Binding curve obtained from luminescent titrations of CT-DNA into $[Ir(phen)_2(qtpy)]^{3+}$, where R = [DNA]/[complex]. Wavelength monitored = 464nm.

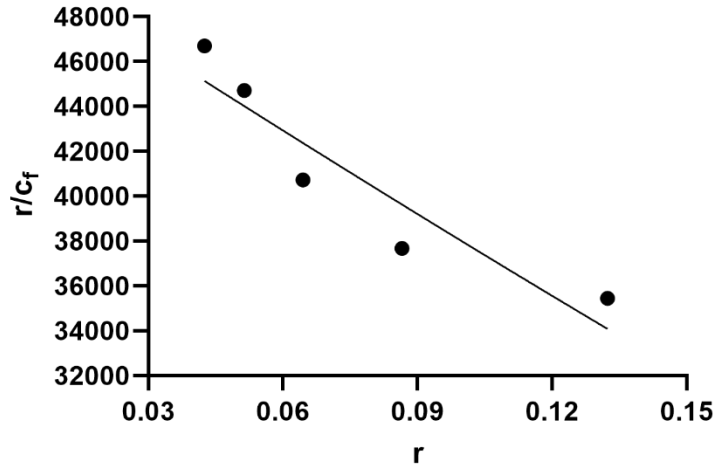

Figure 4.7 – Non-linear Scatchard plots for the luminescent titrations of 7.76mM CT-DNA into a solution of 8.40µM of $[Ir(phen)_2(qtpy)]^{3+}$ in 5mM tris buffer, 25mM NaCl, pH 7.4 at 27°C. Wavelength monitored = 464nm. Experimental data between 30–90% bound drug are fitted. $R^2 = 0.8719$.

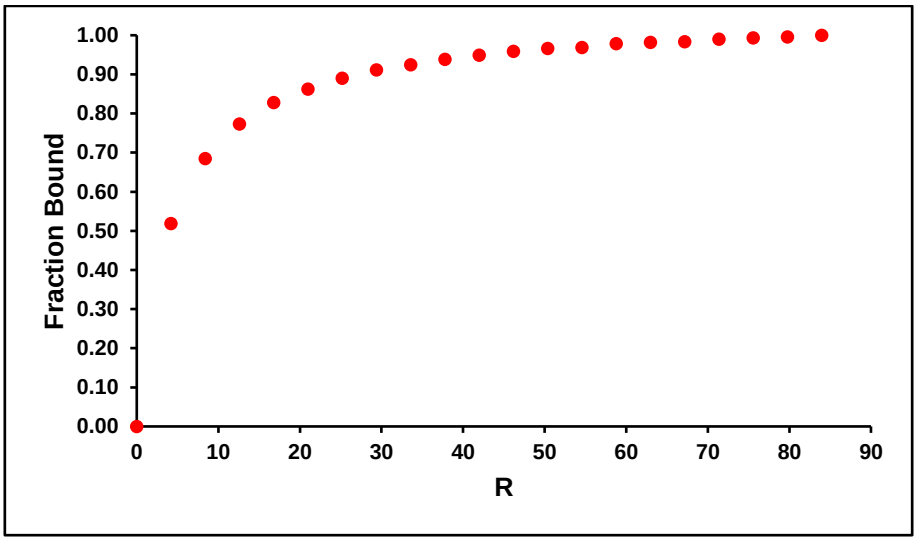

Figure 4.8 – Binding curve obtained from luminescent titrations of CT-DNA into $[Ir(phen)_2(qtpy)]^{3+}$, where R = [DNA]/[complex]. Wavelength monitored = 494nm.

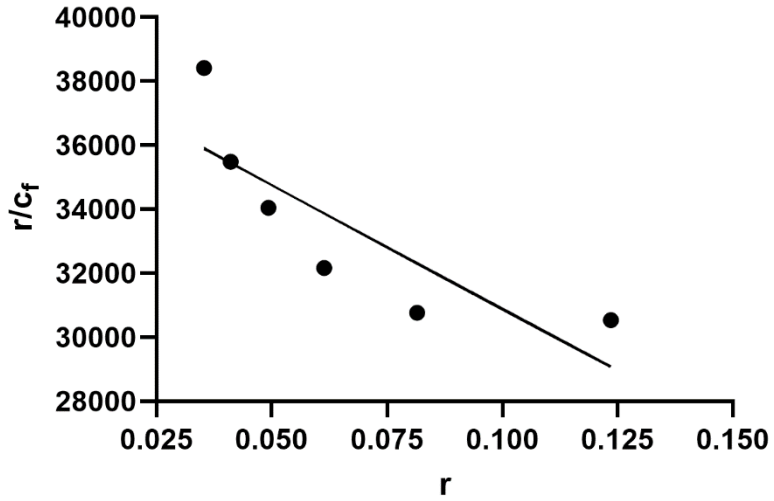

Figure 4.9 – Non-linear Scatchard plots for the luminescent titrations of 7.76mM CT-DNA into a solution of 8.40µM of $[Ir(phen)_2(qtpy)]^{3+}$ in 5mM tris buffer, 25mM NaCl, pH 7.4, at 27°C. Wavelength monitored = 494nm. Experimental data between 30–90% bound drug are fitted. $R^2 = 0.6946$.

No significant DNA-induced increase or decrease in wavelength was observed during the binding event. The non-linear Scatchard plot fitted to the commonly employed McGhee von Hippel (MVH) for non-cooperative binding produces the binding parameters summarised in Table 4.2.

Table 4.2 – CT-DNA binding parameters for $[Ir(phen)_2(qtpy)]^{3+}$ including emission λ_{max} values, and from a MVH fit of binding data, K_b and n.

Complex	**λ_{max} (nm) (aqueous)**	**λ_{max} (nm) (CT-DNA)**	**Binding affinity, K_b [M^{-1}]**	**Site size, n, (base pairs)**
$[Ir(phen)_2(qtpy)]^{3+}$	464	464	5.06×10^4	2
$[Ir(phen)_2(qtpy)]^{3+}$	494	494	3.87×10^4	2

4.3.1.3 $[Ir(dppz)_2(qtpy)]^{3+}$ Luminescence Titration Studies

The behaviour of this compound $[Ir(dppz)_2(qtpy)]^{3+}$ is similar to those of the two ones previously discussed. Emission quenching upon CT-DNA addition was experienced.

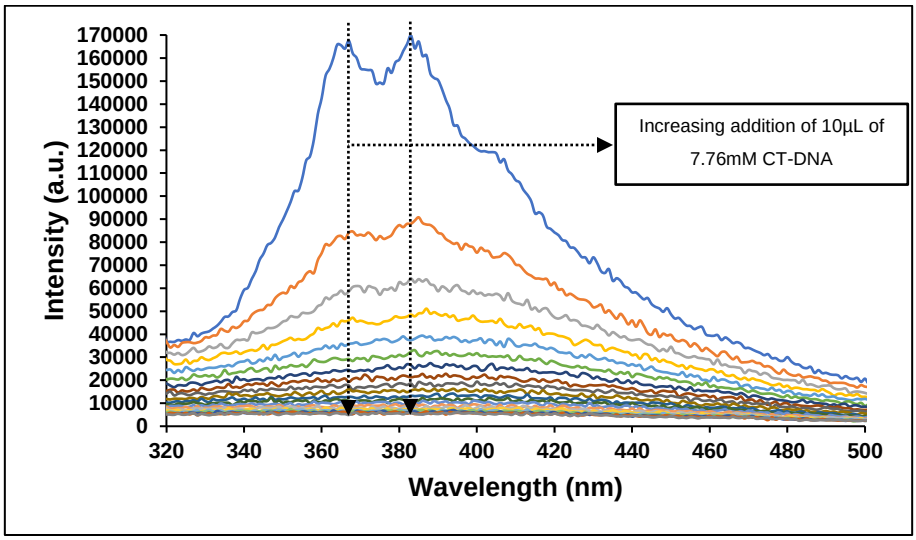

Figure 4.10 – Luminescent titration of 7.76mM CT-DNA into a solution of 22.27µM of $[Ir(dppz)_2(qtpy)]^{3+}$ in 5mM tris, 25mM NaCl buffer, pH 7.4 at 27°C. Excitation wavelength: 282nm; emission region: 320–500nm. Excitation slit width: 5nm. Emission slit width: 5nm. Dual emission located at ca. 367nm and 383nm. Stokes shift = 85–101nm.

Data Fitting

Two sets of graphs and binding fits are given since the complex shows a dual emission signature (Figs. 4.11–4.14).

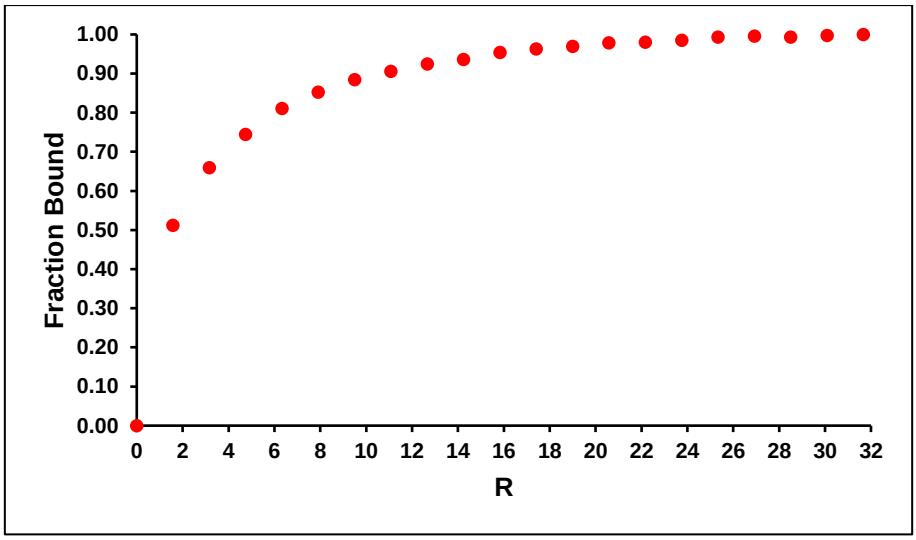

Figure 4.11– Binding curve obtained from luminescent titrations of CT-DNA into $[Ir(dppz)_2(qtpy)]^{3+}$, where R = [DNA]/[complex]. Wavelength monitored = 367nm.

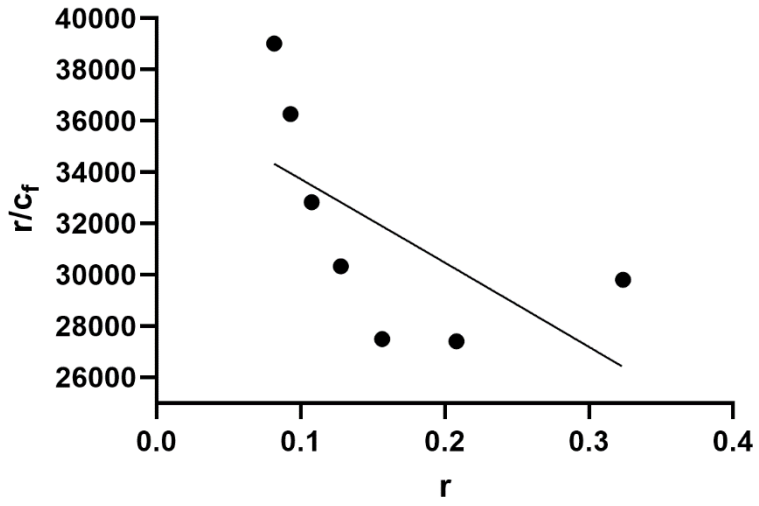

Figure 4.12 – Non-linear Scatchard plots for the luminescent titrations of 7.76mM CT-DNA into a solution of 22.27µM of $[Ir(dppz)_2(qtpy)]^{3+}$ in 5mM tris buffer, 25mM NaCl, pH 7.4 at 27°C. Wavelength monitored = 367nm. Experimental data between 30–90% bound drug is fitted. $R^2 = 0.3793$.

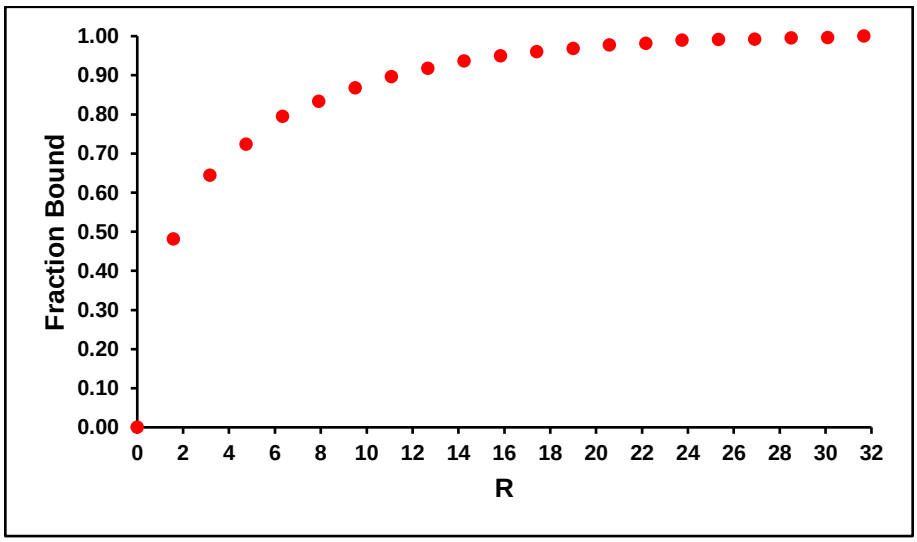

Figure 4.13 – Binding curve obtained from luminescent titrations of CT-DNA into $[Ir(dppz)_2(qtpy)]^{3+}$, where R = [DNA]/[complex]. Wavelength monitored = 383nm.

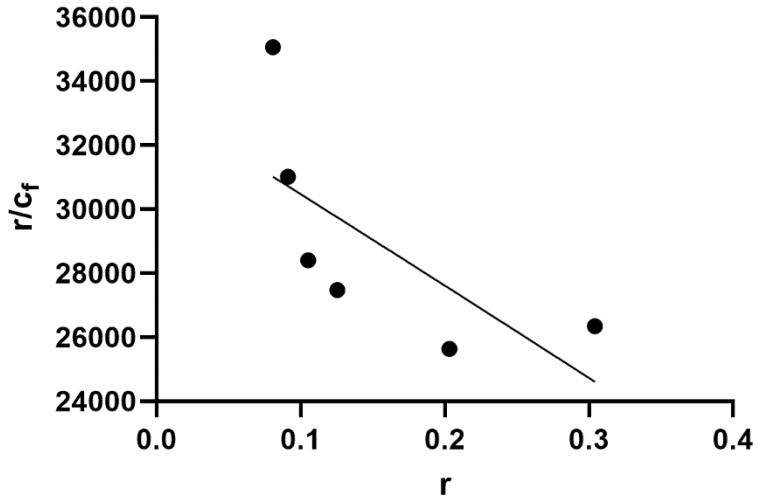

Figure 4.14 – Non-linear Scatchard plots for the luminescent titrations of 7.76mM CT-DNA into a solution of 22.27μM of $[Ir(dppz)_2(qtpy)]^{3+}$ in 5mM tris buffer, 25mM NaCl, pH 7.4 at 27°C. Wavelength monitored = 383nm. Experimental data between 30–90% bound drug is fitted. $R^2 = 0.4852$.

No significant DNA-induced wavelength increase or decrease was observed during the binding event. The non-linear Scatchard plot fitted to the commonly employed McGhee von Hippel (MVH) for non-cooperative binding produces the binding parameters summarised in Table 4.3.

Table 4.3 – CT-DNA binding parameters for $[Ir(dppz)_2(qtpy)]^{3+}$ including emission λ_{max} values, and from a MVH fit of binding data, K_b and n.

Complex	λ_{max} (nm) (aqueous)	λ_{max} (nm) (CT-DNA)	Binding affinity, K_b $[M^{-1}]$	Site size, n, (base pairs)
$[Ir(dppz)_2(qtpy)]^{3+}$	367	367	3.70×10^4	1
$[Ir(dppz)_2(qtpy)]^{3+}$	383	383	2.63×10^4	1

4.4 Three-dimensional (3D) Luminescence Spectroscopic Investigations of the Binding of $[Ir(bpy)_2(qtpy)]^{3+}$, $[Ir(phen)_2(qtpy)]^{3+}$ and $[Ir(dppz)_2(qtpy)]^{3+}$ with CT-DNA

A three-dimensional view of the interactions of the complexes with CT-DNA explain the binding processes clearly. The 3D luminescence spectra (i.e., excitation wavelength versus emission wavelength versus luminescence intensity) of $Ir(bpy)_2(qtpy)]^{3+}$, $[Ir(phen)_2(qtpy)]^{3+}$ and $[Ir(dppz)_2(qtpy)]^{3+}$ binding with CT-DNA were investigated to corroborate the binding of CT-DNA with the three complexes investigated. Figs. 4.15–4.20 illustrate the luminescent peaks of the complexes at three different excitation wavelengths before and after DNA additions.

4.4.1 $[Ir(bpy)_2(qtpy)]^{3+}$

Excitation of $[Ir(bpy)_2(qtpy)]^{3+}$ at 324nm resulted in the strongest emission, followed by excitation at 316nm resulted while excitation at 320nm produced the weakest emission (Fig. 4.15). Even though the magnitudes of these emission intensities vary slightly, incremental addition of CT-DNA led to quenching of the complex's emission intensities across the board. CT-DNA was continuously added, until the magnitudes of the emission intensities for the three excitation wavelengths became almost the same upon saturation binding. A look at the excitation at 316nm indicates that the luminescent intensity of $[Ir(bpy)_2(qtpy)]^{3+}$ substantially declined from slightly more than 300,000a.u. to slightly less than 60,000a.u., thus not only confirming that CT-DNA is associated with the complex but also indicating ca. 5-fold quenching during the process (Fig. 4.16).

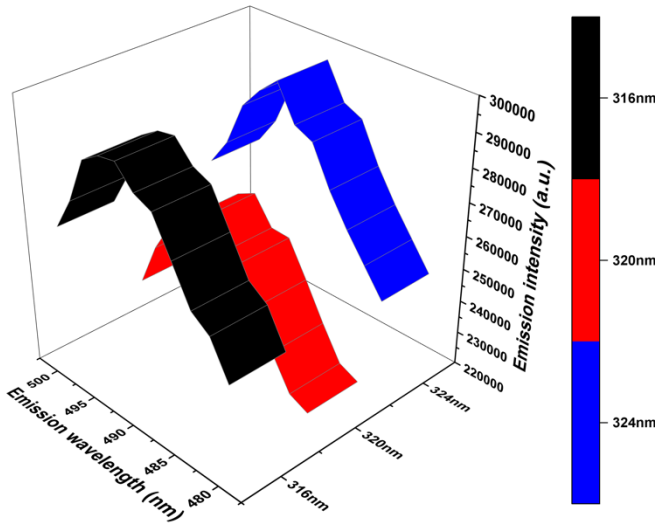

Figure 4.15 – 3D luminescence spectra of 1µL of 0.923mM of $[Ir(bpy)_2(qtpy)]^{3+}$ in 2200µL of 5mM tris, 25mM NaCl buffer (pH 7.4) (before saturation). Emission region: 400–800nm. Excitation slit width: 5nm. Emission slit width: 5nm.

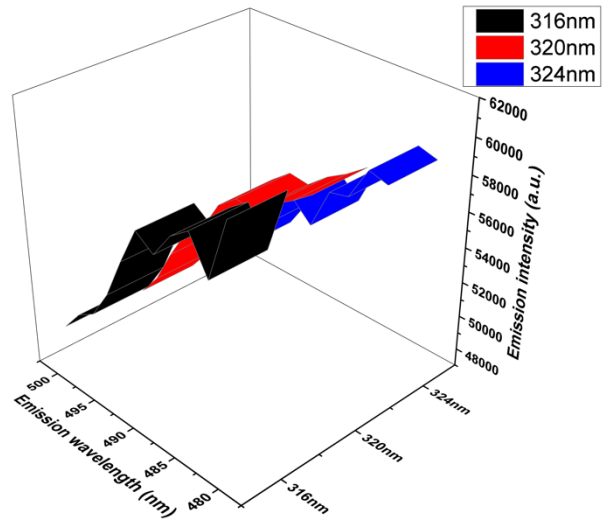

Figure 4.16 – 3D luminescence spectroscopic investigation of the binding of 600µL of 7.76mM CT-DNA with 1µL of 0.923mM of $[Ir(bpy)_2(qtpy)]^{3+}$ in 2200µL of 5mM tris, 25mM NaCl buffer (pH 7.4) (after saturation). Emission region: 400–800nm. Excitation slit width: 5nm. Emission slit width: 5nm.

4.4.2 $[Ir(phen)_2(qtpy)]^{3+}$

The same experiment for $[Ir(bpy)_2(qtpy)]^{3+}$ was undertaken for $[Ir(phen)_2(qtpy)]^{3+}$. There was a decrease in the emissions across the board for excitations at 316nm, 320nm, and 324nm with the excitation at 316nm giving the strongest emission (Fig. 4.17). Emission decreased from ca.

140,000a.u. to ca. 60,000 indicates CT-DNA association with the complex > 2-fold quenching during the binding event (Fig. 4.18).

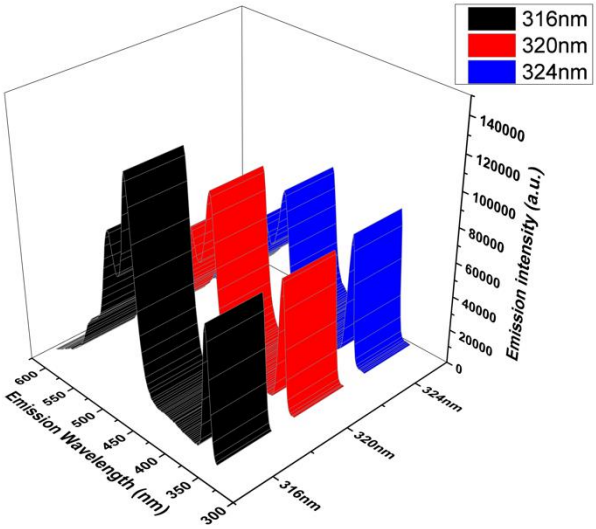

Figure 4.17 – 3D luminescence spectra of 2µL of 2.31mM of $[Ir(phen)_2(qtpy)]^{3+}$ in 2200µL of 5mM tris, 25mM NaCl buffer (pH 7.4) (before saturation). Emission region: 340–800nm. Excitation slit width: 5nm. Emission slit width: 5nm.

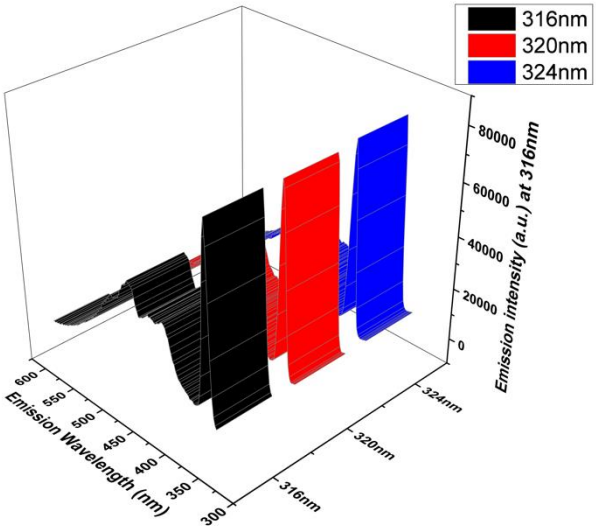

Figure 4.18 – 3D luminescence spectroscopic investigation of the binding of 80µL of 7.76mM CT-DNA with 2µL of 2.31mM of $[Ir(phen)_2(qtpy)]^{3+}$ in 2200µL of 5mM tris, 25mM NaCl buffer (pH 7.4) (after saturation). Emission region: 340–800nm. Excitation slit width: 5nm. Emission slit width: 5nm.

4.4.3 $[Ir(dppz)_2(qtpy)]^{3+}$

Similar experiments done for $[Ir(bpy)_2(qtpy)]^{3+}$ and $[Ir(phen)_2(qtpy)]^{3+}$ were undertaken for $[Ir(dppz)_2(qtpy)]^{3+}$. There was a decrease in the emissions across the board for excitations at 282nm and 286nm with the excitation at 282nm giving the strongest emission. Emission decrease from ca. 100,000a.u. to ca. 4,000 indicates CT-DNA association with the complex > 25-fold quenching during the binding event (Figs. 4.19 and 4.20).

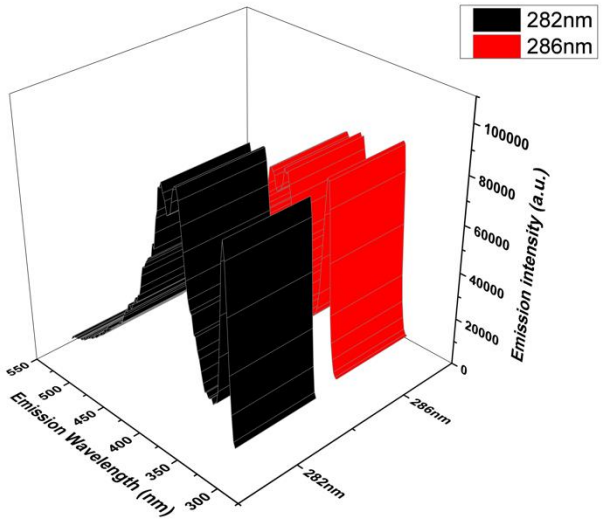

Figure 4.19 – 3D luminescence spectra of 50µL of 0.49mM of $[Ir(dppz)_2(qtpy)]^{3+}$ in 2200µL of 5mM tris, 50mM NaCl buffer (pH 7.4) (before saturation). Emission region: 300–800nm. Excitation slit width: 5nm. Emission slit width: 5nm.

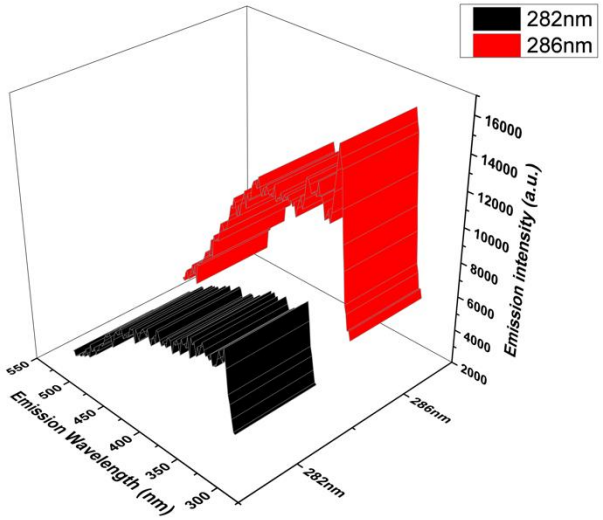

Figure 4.20 – 3D luminescence spectra of 50µL of 0.49mM of $[Ir(dppz)_2(qtpy)]^{3+}$ in 2200µL of 5mM tris, 25mM NaCl buffer (pH 7.4) (after saturation). Emission region: 300–800nm. Excitation slit width: 5nm. Emission slit width: 5nm.

4.5 Influence of Salt Concentration on the DNA Binding of $Ir(bpy)_2(qtpy)]^{3+}$, $[Ir(phen)_2(qtpy)]^{3+}$ and $[Ir(dppz)_2(qtpy)]^{3+}$

An efficient approach to discern the type of binding between DNA and small molecule drugs is the study of ionic stability. Salts cations such as sodium cation (Na^+) or magnesium cation (Mg^{2+}) may make DNA phosphate backbone negative charges become neutral. Na^+, for instance, covers the DNA surface affecting the ionic strength in the case that the compound is bound to DNA through an electrostatic interaction mode, hence, producing a reduction in the interaction strength of the complex with DNA.

Thus, the impact of aqueous NaCl on the phosphorescence emissions of $[Ir(bpy)_2(qtpy)]^{3+}$, $[Ir(phen)_2(qtpy)]^{3+}$, and/or $[Ir(dppz)_2(qtpy)]^{3+}$ + CT-DNA were examined. The outcomes indicated that the phosphorescence intensity values, i.e., normalised P_0/P values of [NaCl] suffer no significant perturbations despite increasing the NaCl concentration (Figs. 4.21–4.23).

4.5.1 $[Ir(bpy)_2(qtpy)]^{3+}$

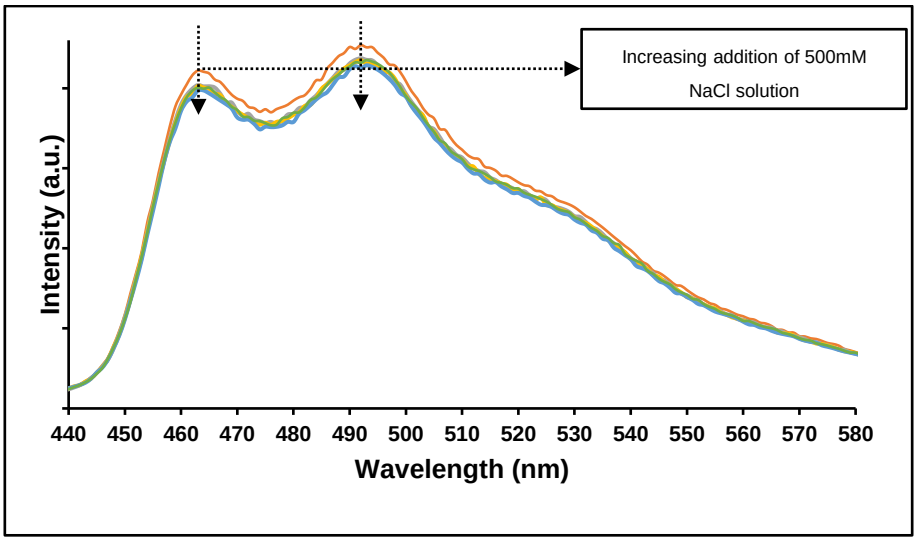

Figure 4.21 – Reverse-salt titration of NaCl solution to CT-DNA-bound $[Ir(bpy)_2(qtpy)]^{3+}$. [NaCl] = 500mM; [CT-DNA] = 50µL of 16mM; $[Ir(bpy)_2(qtpy)]^{3+}$] = 50µM. Excitation wavelength: 310nm. Emission region: 440–580nm. Excitation slit width: 5nm. Emission slit width: 5nm.

4.5.2 $[Ir(phen)_2(qtpy)]^{3+}$

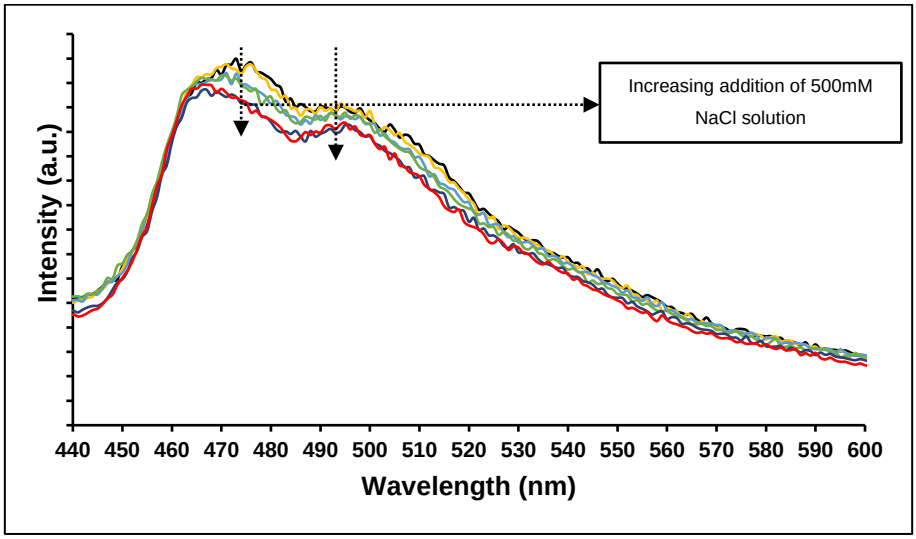

Figure 4.22 – Reverse-salt titration of NaCl solution to CT-DNA-bound $[Ir(phen)_2(qtpy)]^{3+}$. [NaCl] = 500mM; [CT-DNA] = 50µL of 7.76mM; $[Ir(phen)_2(qtpy)]^{3+}$] = 5.25µM. Excitation wavelength: 316nm. Emission region: 440–600nm. Excitation slit width: 5nm. Emission slit width: 5nm.

4.5.3 $[Ir(dppz)_2(qtpy)]^{3+}$

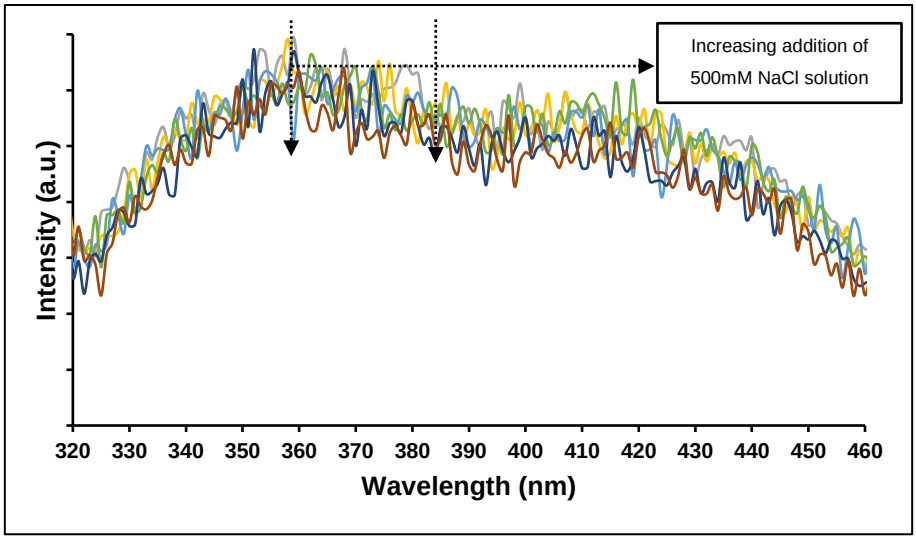

Figure 4.23 – Reverse-salt titration of NaCl solution to CT-DNA-bound $[Ir(dppz)_2(qtpy)]^{3+}$. [NaCl] = 500mM; [CT-DNA] = 50µL of 7.76mM; $[Ir(dppz)_2(qtpy)]^{3+}$] = 5.25µM. Excitation wavelength: 282nm. Emission region: 320–460nm. Excitation slit width: 5nm. Emission slit width: 5nm.

It may, therefore, be concluded that the interaction of the three complexes with CT-DNA does not proceed primarily through an electrostatic mode, as salt-induced emission decrease of the investigated compounds are very minimal. As such, electrostatic interaction does not contribute significantly to the overall binding strength of the complexes with DNA.

4.6 Ferrocyanide Quenching Studies of the Interactions of $[Ir(N–N)_2(qtpy)]^{3+}$ (where N–N = bpy, phen, or dppz) with CT-DNA

The inspiration for this section came from previous studies, "Scott J. Burya, Daniel A. Lutterman and Claudia Turro, Absence of quenching by $[Fe(CN)_6]^{4-}$ is not proof of DNA intercalation, Chem. Commun., 2011, 47, 1848–1850"[20], in which emission quenching of a DNA probe by ferrocyanide indicates whether or not the probe is deeply or loosely bound to DNA, which can provide some evidence of a probe's binding modality to DNA even though not definitively. Based on this premise, any possible correlation between the quenching behaviour by $[Fe(CN)_6]^{4-}$ of CT-DNA-bound $[Ir(bpy)_2(qtpy)]^{3+}$, $[Ir(phen)_2(qtpy)]^{3+}$, and/or $[Ir(dppz)_2(qtpy)]^{3+}$ and their DNA-binding modes was investigated.

Ferrocyanide, $[Fe(CN)_6]^{4-}$ (Fig. 24) remains free in the aqueous environment in the presence of polyanionic DNA owing to Coulombic repulsion between the two species. Ferrocyanide can easily quench the emission of probes that are electrostatically bound to the DNA backbone. However, its quenching efficiency is reduced significantly when the luminescent compound is intercalated between the DNA bases, as they are protected from quenchers in solution. Therefore, a comparison of the emission quenching by $[Fe(CN)_6]^{4-}$ for the three reported complexes bound to DNA is expected to provide further insight into their binding mode. Ferrocyanide is often employed in biological applications owing to its good solubility in water and ease of detection by absorption spectroscopy.[21]

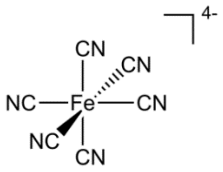

Figure 4.24 – Ferrocyanide anion.

4.6.1 Protocol Employed

All quenching experiments were performed in 5mM tris buffer with differing ionic strengths (i.e., [NaCl] = 5, 25, and 50mM, respectively) in the absence and presence of CT-DNA so that practical conclusions could be drawn. Increasing aliquots of the quencher, i.e., $[Fe(CN)_6]^{4-}$, were added to the three complexes in the three buffers, which is then followed by electronic absorption and spectroscopic emission measurements.

4.6.2 UV-Vis Spectroscopic Pre-association Checks

Before any quenching experiments were launched, UV-Vis absorbance was monitored for the quenching experiments to see if ferrocyanide has any influence on the ^{3}MLCT transition of the complexes. To investigate this, $[Ir(bpy)_2(qtpy)]^{3+}$ was selected of the three complexes and since all the complexes exhibit similar UV-Vis spectroscopic behaviours, the pre-association checks for $[Ir(phen)_2(qtpy)]^{3+}$ and $[Ir(dppz)_2(qtpy)]^{3+}$ were not conducted. The plots (Figs. 4.25–4.30) below show that the ^{3}MLCT absorption bands of $[Ir(bpy)_2(qtpy)]^{3+}$ in the three buffers of differing ionic strengths were not greatly perturbed by the anionic quencher, and no unique bands appeared that represented ground state associated species of $[Fe(CN)_6]^{4-}$. In other words, ferrocyanide absorption spectra are distinct from those of the complex even after several additions of the quencher, implying that solution pre-association is insignificant.

4.6.2.1 Without CT-DNA

The absorbance of the ^{3}MLCT transition of $[Ir(bpy)_2(qtpy)]^{3+}$ remained independent of quencher concentration.

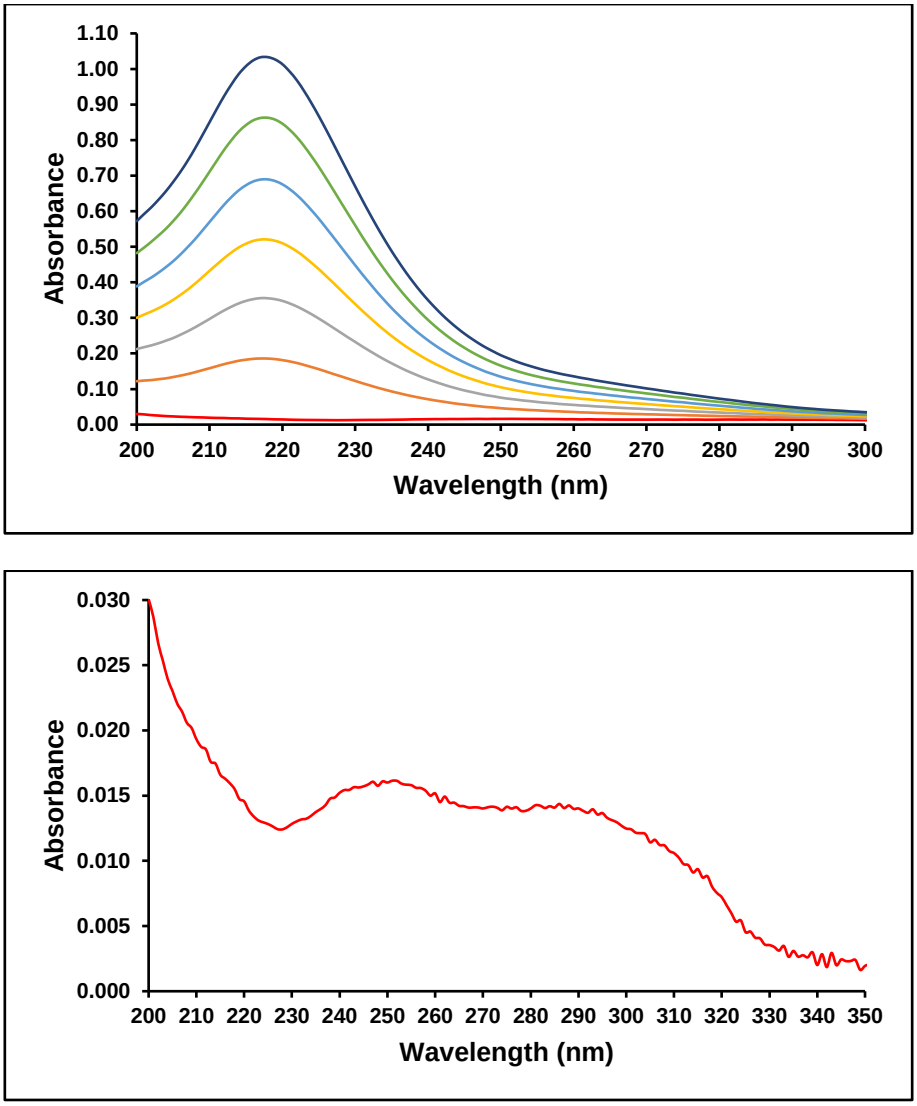

Figure 4.25 – Electronic absorption spectrum of 0.8391µM $[Ir(bpy)_2(qtpy)]^{3+}$ in absence of CT-DNA at different $[Fe(CN)_6]^{4-}$ concentrations (0–6mM) in 5mM tris, 5mM NaCl buffer (top) and the expanded view of the electronic absorption spectrum of $[Ir(bpy)_2(qtpy)]^{3+}$ complex without $[Fe(CN)_6]^{4-}$, i.e., the first trace of the upper figure (bottom).

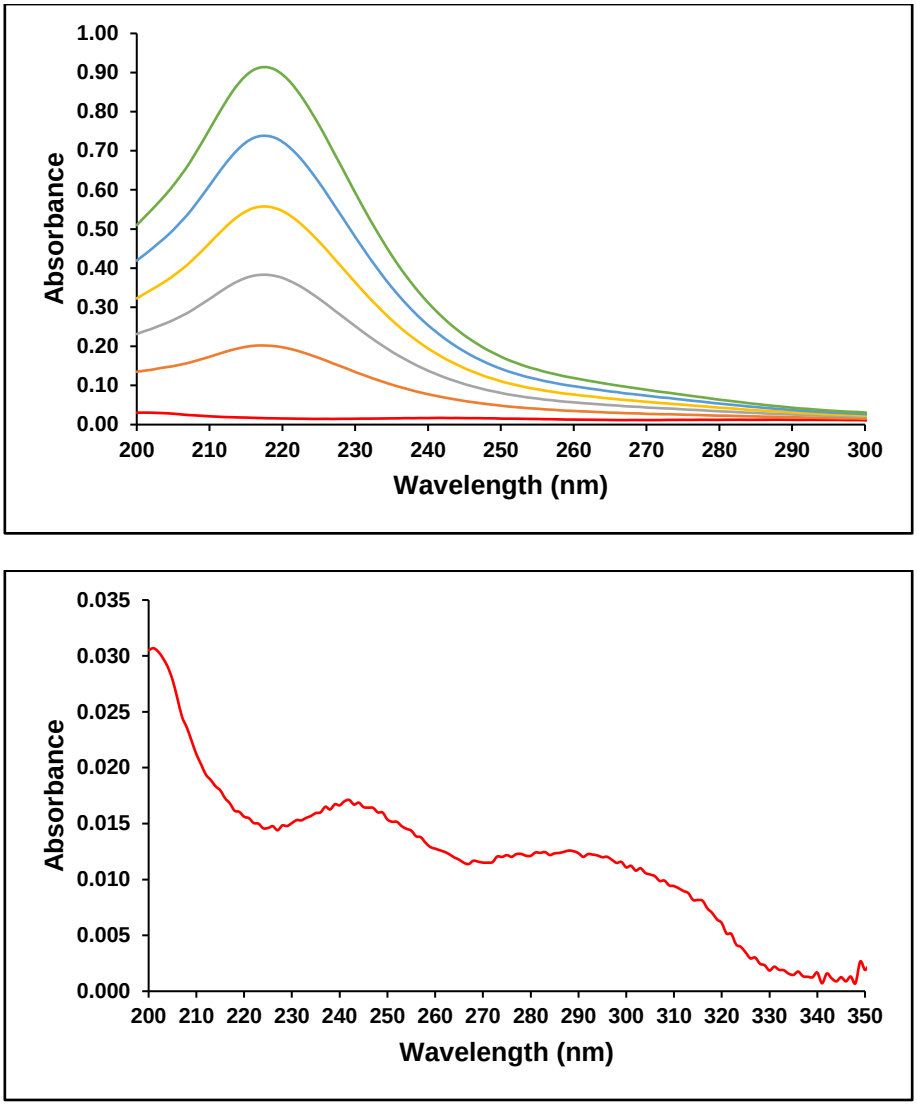

Figure 4.26 – Electronic absorption spectrum of 0.8391µM $[Ir(bpy)_2(qtpy)]^{3+}$ in absence of CT-DNA at different $[Fe(CN)_6]^{4-}$ concentrations (0–6mM) in 5mM tris, 25mM NaCl buffer (top) and the expanded view of the electronic absorption spectrum of $[Ir(bpy)_2(qtpy)]^{3+}$ complex without $[Fe(CN)_6]^{4-}$, i.e., the first trace of the upper figure (bottom).

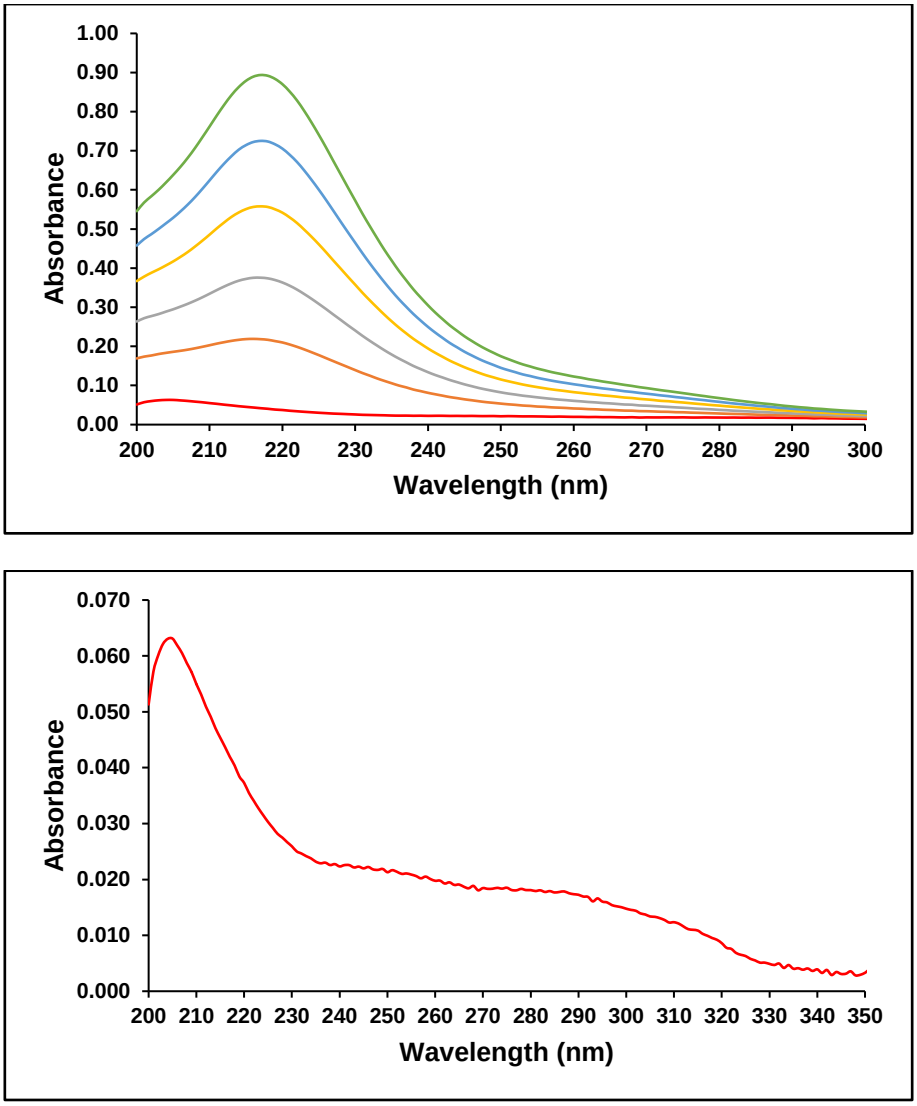

Figure 4.27 – Electronic absorption spectrum of 0.8391µM $[Ir(bpy)_2(qtpy)]^{3+}$ in absence of CT-DNA at different $[Fe(CN)_6]^{4-}$ concentrations (0–6mM) in 5mM tris, 50mM NaCl buffer (top) and the expanded view of the electronic absorption spectrum of $[Ir(bpy)_2(qtpy)]^{3+}$ complex without $[Fe(CN)_6]^{4-}$, i.e., the first trace of the upper figure (bottom).

4.6.2.2 With CT-DNA

DNA absorbance band appears at ca. 260nm and the absorbance of the ^{3}MLCT transition of the complex remained independent of quencher concentration. The same behaviours are observed in the presence of CT-DNA in the three buffers of differing ionic strengths, and repetitive spectra are omitted for space conservation.

4.6.3 Steady-state Luminescence Investigations of Quenching of $[Ir(N–N)_2(qtpy)]^{3+}$ (N–N = bpy, phen, or dppz) by $[Fe(CN)_6]^{4-}$

To further evaluate the Ferrocyanide quenching of $[Ir(bpy)_2(qtpy)]^{3+}$, $[Ir(phen)_2(qtpy)]^{3+}$ and/or $[Ir(dppz)_2(qtpy)]^{3+}$ in the absence or presence of DNA, luminescence emission quenching experiments were performed. A highly negatively charged quencher is expected to be repelled by the negatively charged phosphate backbone of the DNA, and therefore, a more deeply DNA-bound cationic complex should be more protected from quenching than a shallowly bound complex.

All calculations herein follow the simple Stern-Volmer kinetics represented by the equation below:

$$\frac{P_0}{P} = 1 + K_{sv}[Q]_0$$

(Equation 4.8)

where P_o and P are the emission intensities of a luminophore in the non-existence and existence of a quencher, respectively. The Stern-Volmer constant, K_{sv}, can be evaluated by plotting P_o/P vs. quencher concentration, $[Q]_0$, where the quencher is in excess. The intercept of this plot is unity, and the slope provides an indication of the quenching efficiency.

4.6.3.1 $[Ir(bpy)_2(qtpy)]^{3+}$

4.6.3.1.1 Without CT-DNA

5mM tris, 5mM NaCl Buffer Solution, pH 7.4

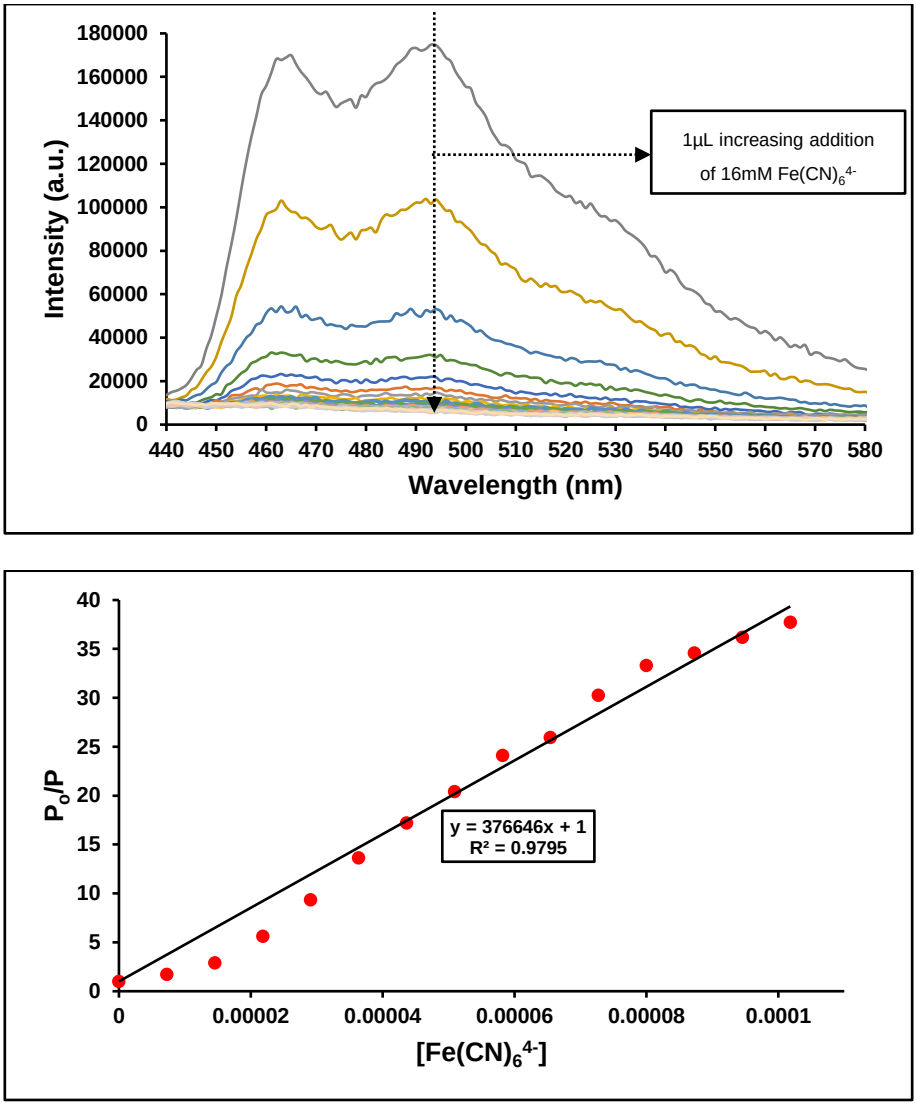

Figure 4.28 – Emission intensity of 0.8391µM $[Ir(bpy)_2(qtpy)]^{3+}$ complex upon successive addition of 16mM $Fe(CN)_6^{4-}$ in 5mM tris, 5mM NaCl buffer solution, pH 7.4 (top) and the Stern-Volmer plot of the emission intensity of the complex versus concentration of $Fe(CN)_6^{4-}$ to determine the quenching constant (bottom).

5mM tris, 25mM NaCl Buffer Solution, pH 7.4

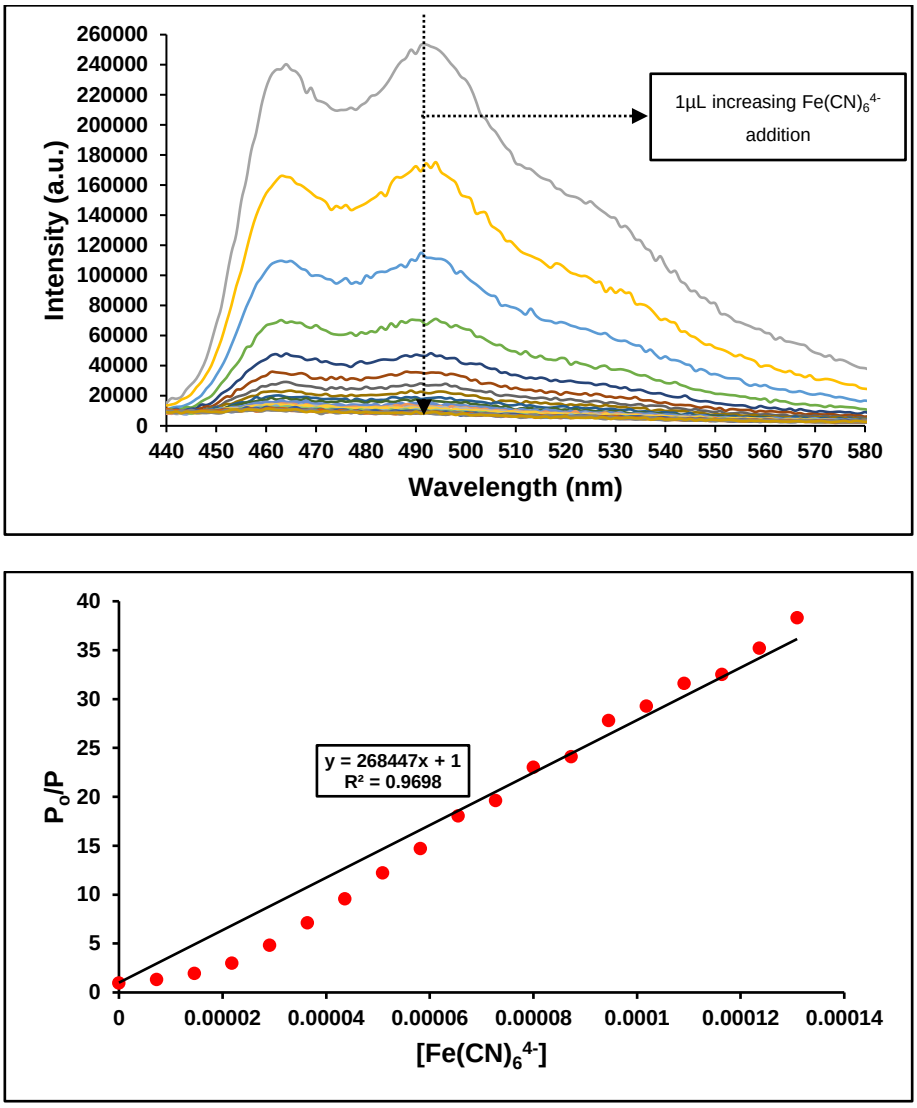

Figure 4.29 – Emission intensity of 0.8391µM $[Ir(bpy)_2(qtpy)]^{3+}$ upon successive addition of 16mM $Fe(CN)_6^{4-}$ in 5mM tris, 25mM NaCl buffer solution, pH 7.4 (top) and the Stern-Volmer plot of the emission intensity of the complex versus concentration of $Fe(CN)_6^{4-}$ to determine the quenching constant (bottom).

5mM tris, 50mM NaCl Buffer Solution, pH 7.4

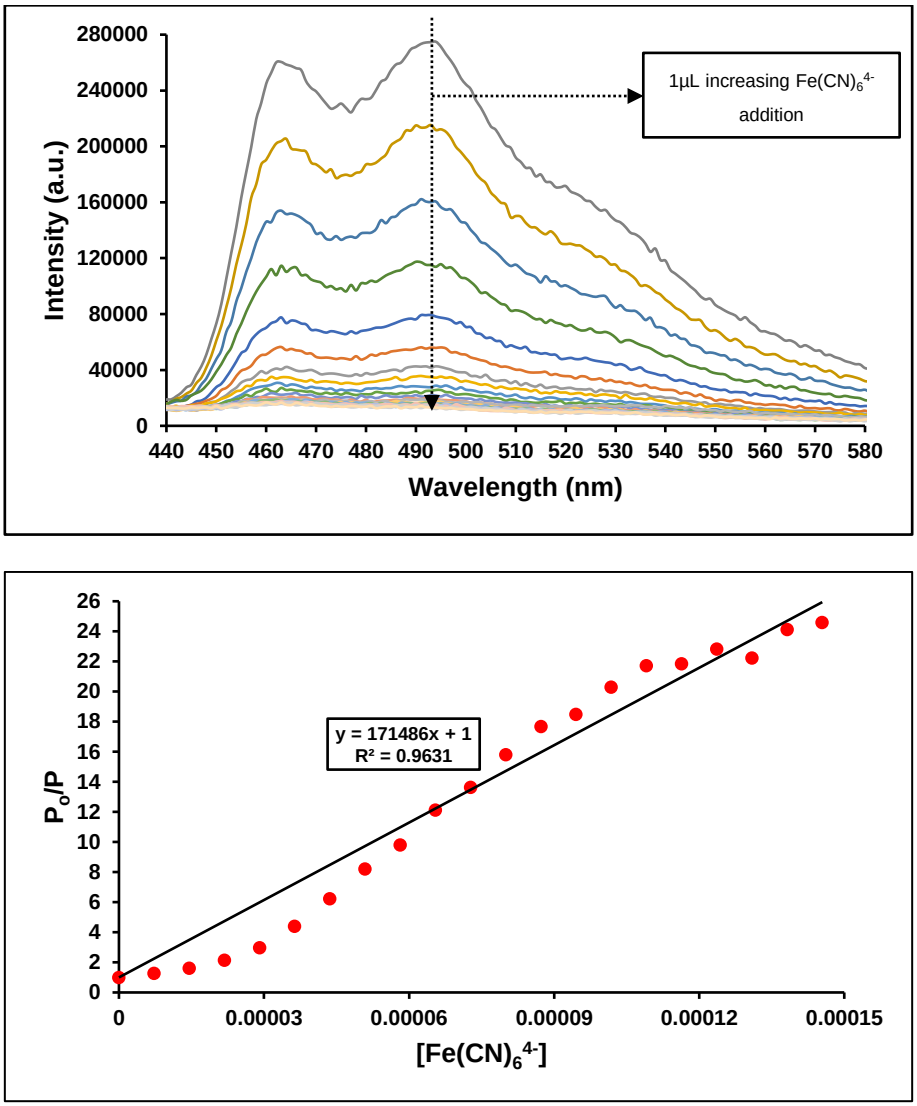

Figure 4.30 – Emission intensity of 0.8391µM $[Ir(bpy)_2(qtpy)]^{3+}$ upon successive addition of 16mM $Fe(CN)_6^{4-}$ in 5mM tris, 50mM NaCl buffer solution, pH 7.4 (top) and the Stern-Volmer plot of the emission intensity of the complex versus concentration of $Fe(CN)_6^{4-}$ to determine the quenching constant (bottom).

4.6.3.1.2 With CT-DNA (1-fold)

5mM tris, 5mM NaCl Buffer Solution, pH 7.4

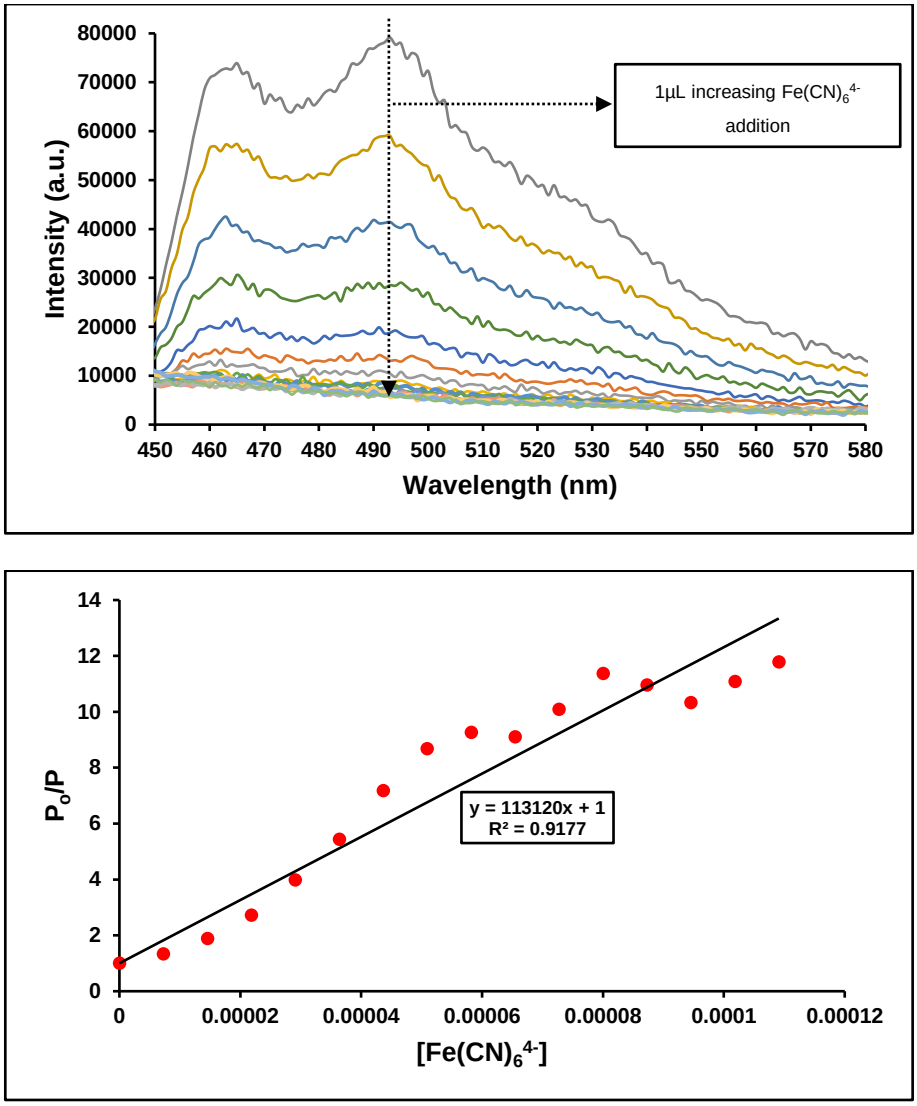

Figure 4.31 – Emission intensity of 0.4195µM $[Ir(bpy)_2(qtpy)]^{3+}$ and CT-DNA (72.73µM) upon successive addition of 16mM $Fe(CN)_6^{4-}$ in 5mM tris, 5mM NaCl buffer solution, pH 7.4 (top) and the Stern-Volmer plot of the emission intensity of the complex versus concentration of $Fe(CN)_6^{4-}$ to determine the quenching constant (bottom).

5mM tris, 25mM NaCl Buffer Solution, pH 7.4

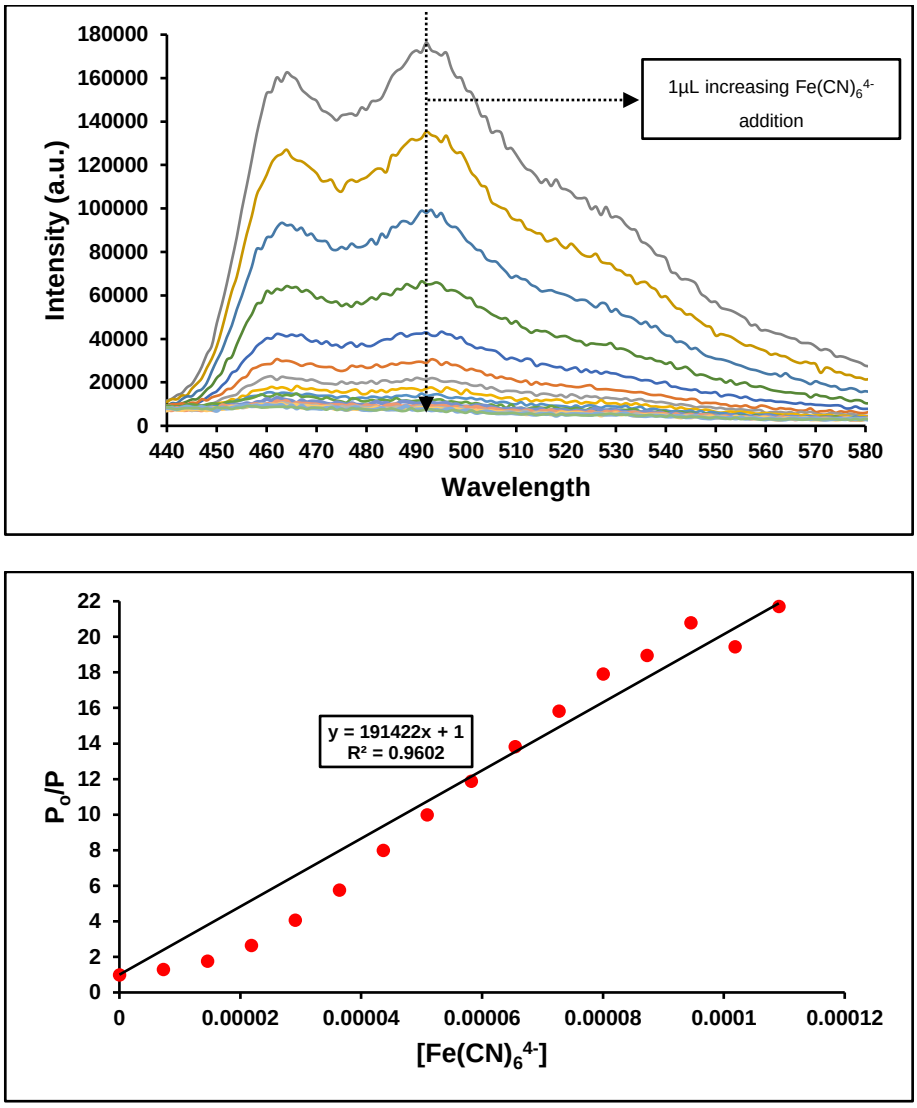

Figure 4.32 – Emission intensity of 0.4195µM $[Ir(bpy)_2(qtpy)]^{3+}$ and CT-DNA (72.73µM) upon successive addition of 16mM $Fe(CN)_6^{4-}$ in 5mM tris, 25mM NaCl buffer solution, pH 7.4 (top) and the Stern-Volmer plot of the emission intensity of the complex versus concentration of $Fe(CN)_6^{4-}$ to determine the quenching constant (bottom).

5mM tris, 50mM NaCl Buffer Solution, pH 7.4

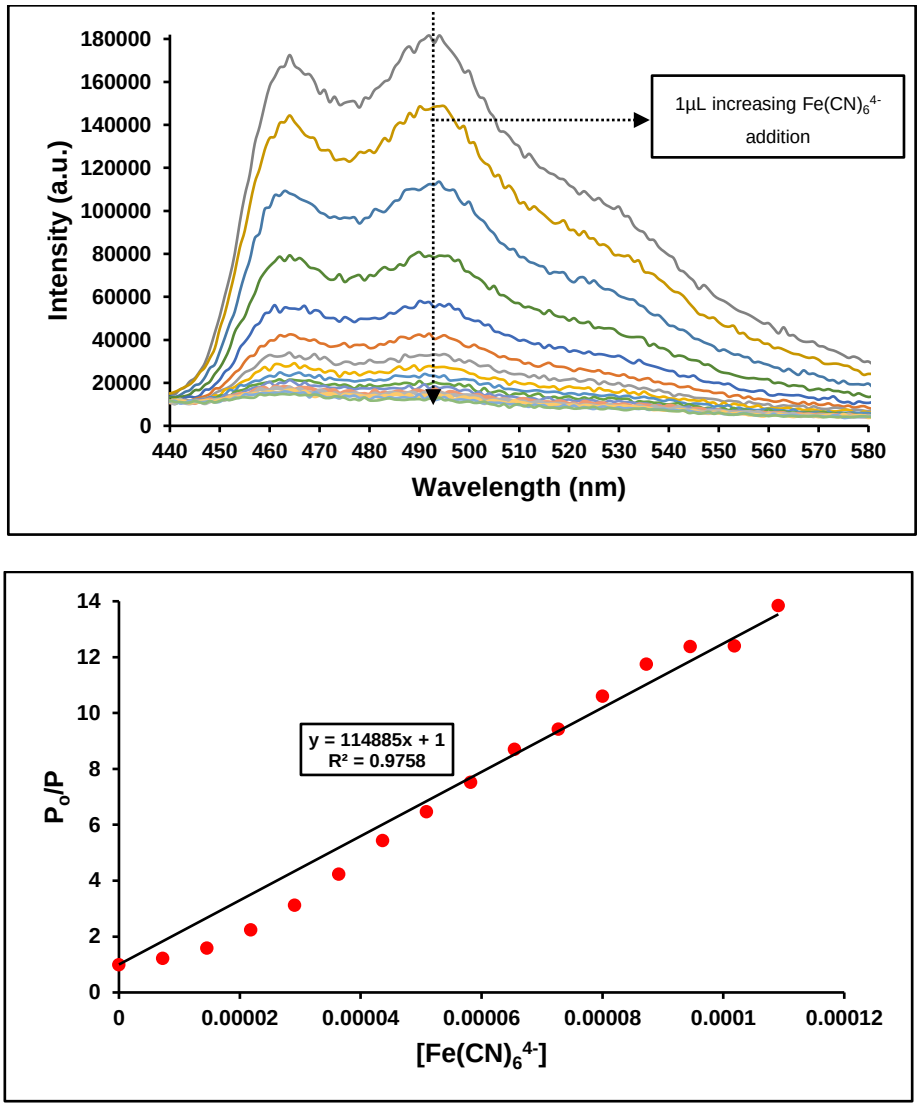

Figure 4.33 – Emission intensity of 0.4195µM $[Ir(bpy)_2(qtpy)]^{3+}$ and 72.73µM CT-DNA upon successive addition of 16mM $Fe(CN)_6^{4-}$ in 5mM tris, 50mM NaCl buffer solution, pH 7.4 (top) and the Stern-Volmer plot of the emission intensity of the complex versus concentration of $Fe(CN)_6^{4-}$ to determine the quenching constant (bottom).

4.6.3.1.3 With CT-DNA (3-fold excess)

5mM tris, 5mM NaCl Buffer Solution, pH 7.4

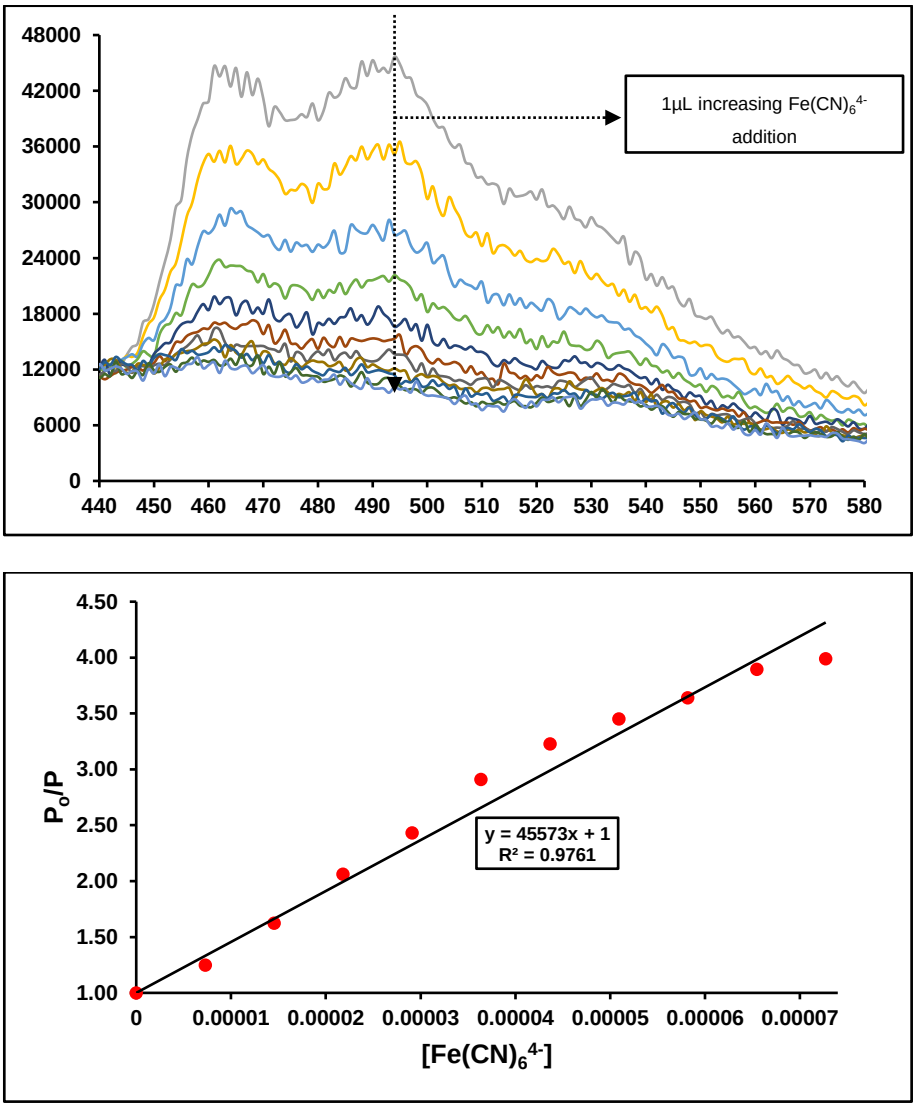

Figure 4.34 – Emission intensity of 0.4195µM $[Ir(bpy)_2(qtpy)]^{3+}$ and 3-fold excess CT-DNA (2.182×10^{-4}M) upon successive addition of 16mM $Fe(CN)_6^{4-}$ in 5mM tris, 5mM NaCl buffer solution, pH 7.4 (top) and the Stern-Volmer plot of the emission intensity of the complex versus concentration of $Fe(CN)_6^{4-}$ to determine the quenching constant (bottom).

5mM tris, 25mM NaCl Buffer Solution, pH 7.4

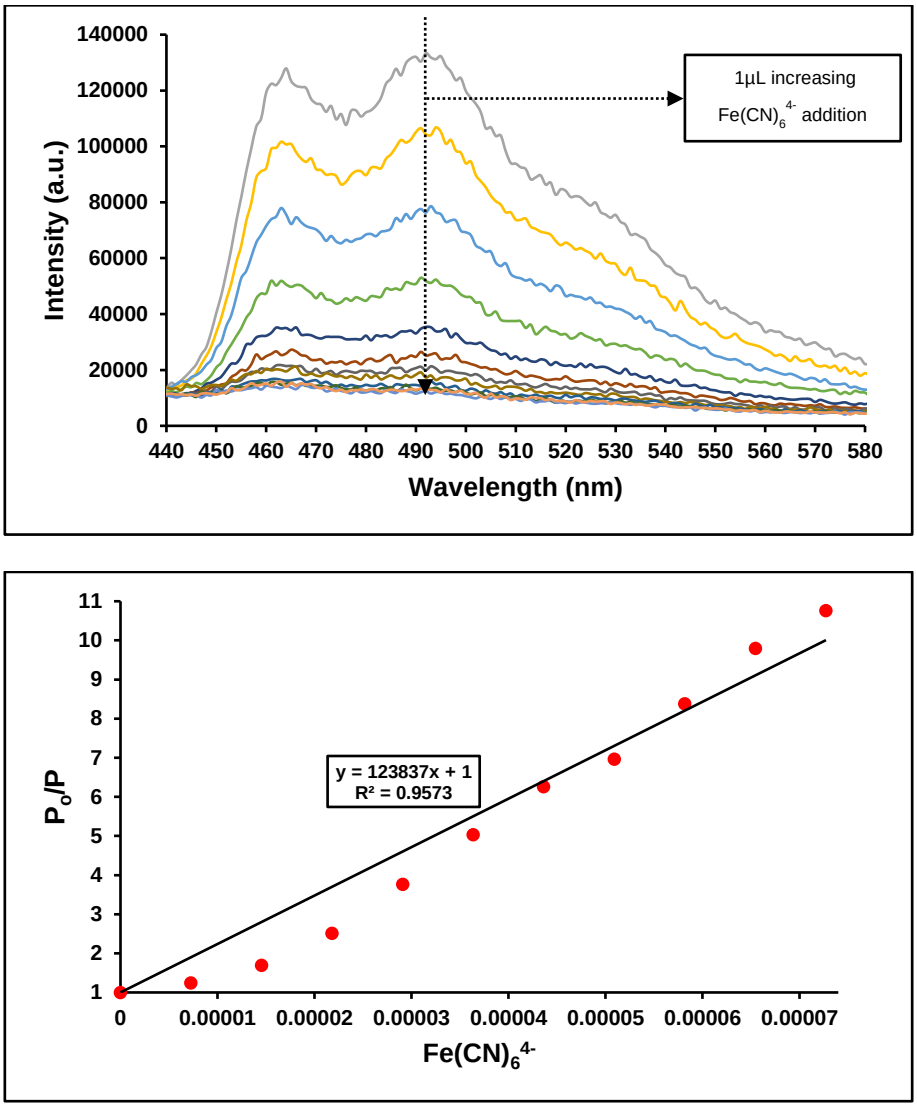

Figure 4.35 – Emission intensity of 0.4195µM $[Ir(bpy)_2(qtpy)]^{3+}$ and 3-fold excess CT-DNA (2.182×10^{-4}M) upon successive addition of 16mM $Fe(CN)_6^{4-}$ in 5mM tris, 25mM NaCl buffer solution, pH 7.4 (top) and the Stern-Volmer plot of the emission intensity of the complex versus concentration of $Fe(CN)_6^{4-}$ to determine the quenching constant (bottom).

5mM tris, 50mM NaCl Buffer Solution, pH 7.4

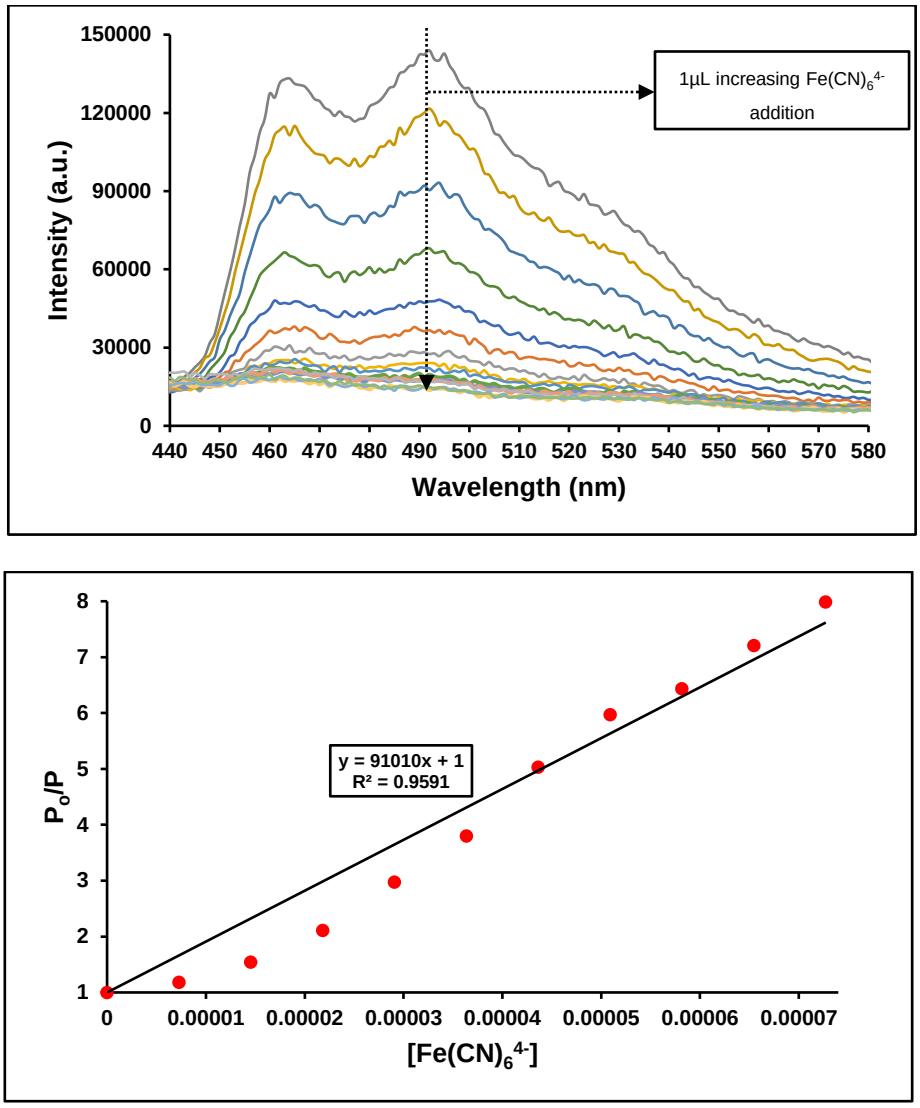

Figure 4.36 – Emission intensity of 0.4195µM $[Ir(bpy)_2(qtpy)]^{3+}$ and 3-fold excess CT-DNA (2.182×10^{-4}M) upon successive addition of 16mM $Fe(CN)_6^{4-}$ in 5mM tris, 50mM NaCl buffer solution, pH 7.4 (top) and the Stern-Volmer plot of the emission intensity of the complex versus concentration of $Fe(CN)_6^{4-}$ to determine the quenching constant (bottom).

Table 4.4 – Ferrocyanide Quenching Data for the Interaction of $[Ir(bpy)_2(qtpy)]^{3+}$ without and with DNA.

Buffer	Without CT-DNA	With CT-DNA (1-fold)	With CT-DNA (3-fold excess)
5mM tris, 5mM NaCl buffer	$3.77 \times 10^5 M^{-1}$	$1.13 \times 10^5 M^{-1}$	$4.56 \times 10^4 M^{-1}$

5mM tris, 25mM NaCl buffer	2.68 x 10^5M^{-1}	1.91 x 10^5M^{-1}	1.24 x 10^5M^{-1}
5mM tris, 50mM NaCl buffer	1.71 x 10^5M^{-1}	1.15 x 10^5M^{-1}	9.10 x 10^4M^{-1}

In the absence of the DNA, $[Ir(bpy)_2(qtpy)]^{3+}$ was efficiently quenched by $[Fe(CN)_6]^{4-}$, with increased quenching behaviour experienced in the presence of DNA. The emission quenching diagrams and the Stern-Volmer plots for the free complex in the three buffers employed and those of the complex in the presence of (one-fold and three-fold excess) CT-DNA are shown in Figs. 4.28–4.36. A summary of the values of Stern-Volmer quenching constant (K_{sv}) in each scenario are tabulated in Table 4.4.

The quenching of the complex by Ferrocyanide proceeded most rapidly in solution of the least ionic strength, i.e., 5mM tris, 5mM NaCl buffer, whether in the absence or presence of CT-DNA. The quenching constants were higher for the complex in the three buffers of varying ionic strengths when no CT-DNA as added. Upon the addition of CT-DNA, the quenching constants were decreased slightly and when 3-fold excess CT-DNA was added, the quenching constants became diminished by a factor of 10, meaning the complex still retains its strong binding constant even after the addition of 3-fold excess CT-DNA. All these results show that Ferrocyanide has a strong effect on the quenching of the luminescence of $[Ir(bpy)_2(qtpy)]^{3+}$ whether in the absence or presence of CT-DNA, but effect is stronger in the second instance and strongest in the third instance. The interpretation of the emission quenching data, i.e., quenching diagrams, S-V plots, and quenching constants, all taken together suggest that the complex "might be loosely bound" to CT-DNA. Further insights into the probable binding mode of the complex with DNA by molecular dynamic (MD) simulation is currently underway. MD simulations can lend insights into the binding of the reported complexes in this thesis with DNA, enabling the understanding of such binding over a particular chosen time with the application of an experimental force field.[22]

Stern-Volmer equation seems to be more obeyed in the presence of CT-DNA than in the absence of CT-DNA as evidently shown by the better linearity of plots in the presence of CT-DNA than in the absence of CT-DNA.

4.6.3.2 $[Ir(phen)_2(qtpy)]^{3+}$

Analogous experiments as for those of $[Ir(bpy)_2(qtpy)]^{3+}$ were undertaken for $[Ir(phen)_2(qtpy)]^{3+}$. The emission quenching diagrams and the Stern-Volmer plots for the free complex in the three buffers employed and those of the complex in the presence of (one-fold and three-fold excess) CT-DNA are shown in Figs. 4.37–4.63.

4.6.3.2.1 Without CT-DNA

5mM tris, 5mM NaCl buffer solution, pH 7.4

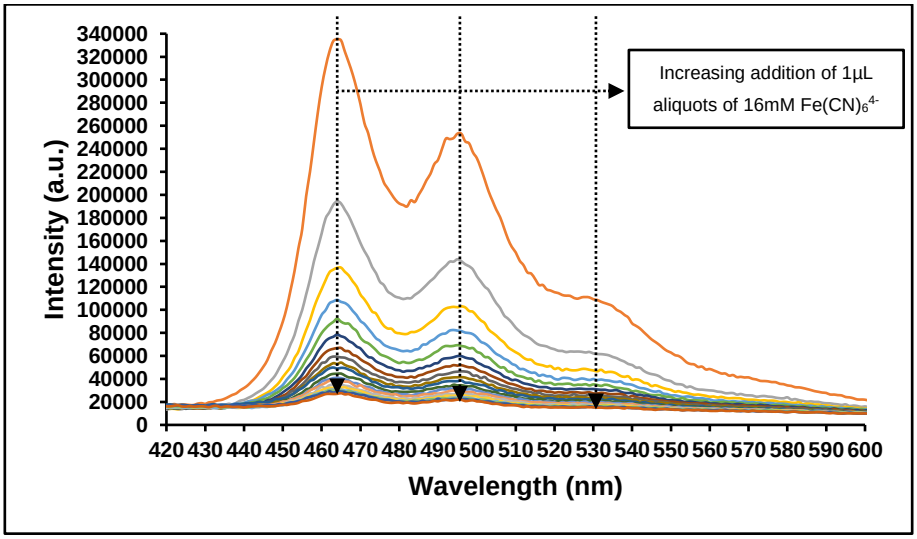

Figure 4.37 – Emission intensity decrease of 6.30µM complex upon successive additions of 0–1.31 x 10^{-4}M $Fe(CN)_6^{4-}$ in 5mM tris, 5mM NaCl buffer solution, pH 7.4.

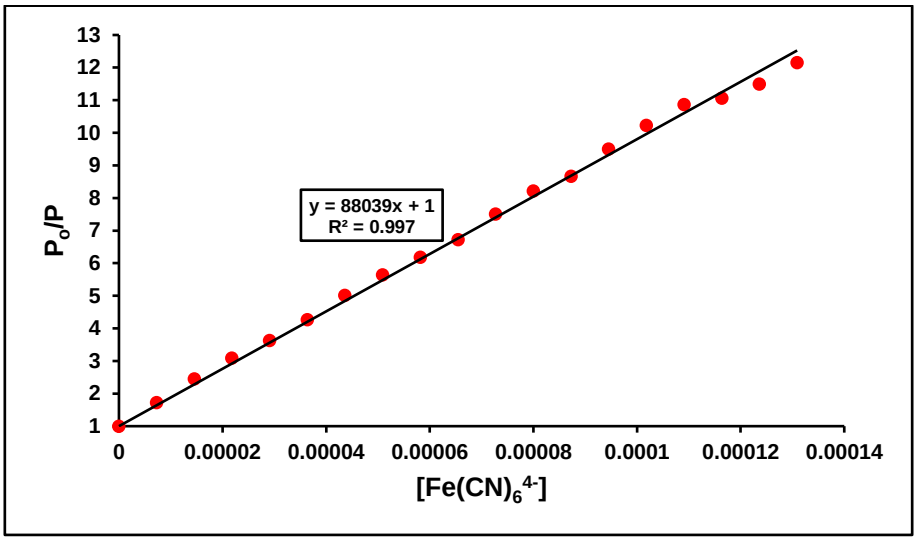

Figure 4.38 – Stern-Volmer plot of the emission intensity of the complex versus concentration of $Fe(CN)_6^{4-}$ to determine the quenching constant. Wavelength monitored = 464nm. P_0 = phosphorescence intensity of the complex before the addition of $Fe(CN)_6^{4-}$ and P = phosphorescence intensity of the complex upon sequential addition of $Fe(CN)_6^{4-}$.

$K_{sv} = 8.80 \times 10^4 M^{-1}$.

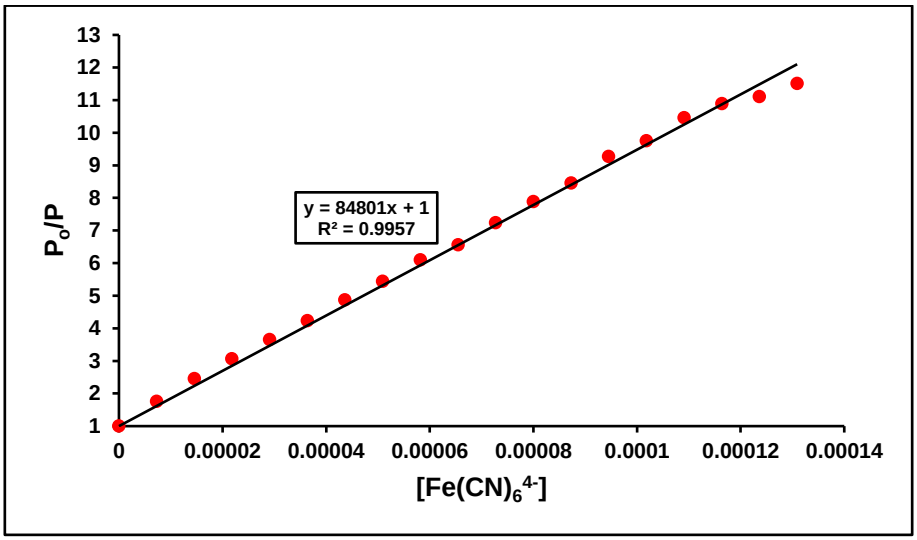

Figure 4.39 – Stern-Volmer plot of the emission intensity of the complex versus concentration of $Fe(CN)_6^{4-}$ to determine the quenching constant. Wavelength monitored = 494nm. P_0 = phosphorescence intensity of the complex before the addition of $Fe(CN)_6^{4-}$ and P = phosphorescence intensity of the complex upon sequential addition of $Fe(CN)_6^{4-}$.

$K_{sv} = 8.48 \times 10^4 M^{-1}$.

5mM tris, 25mM NaCl buffer solution, pH 7.4

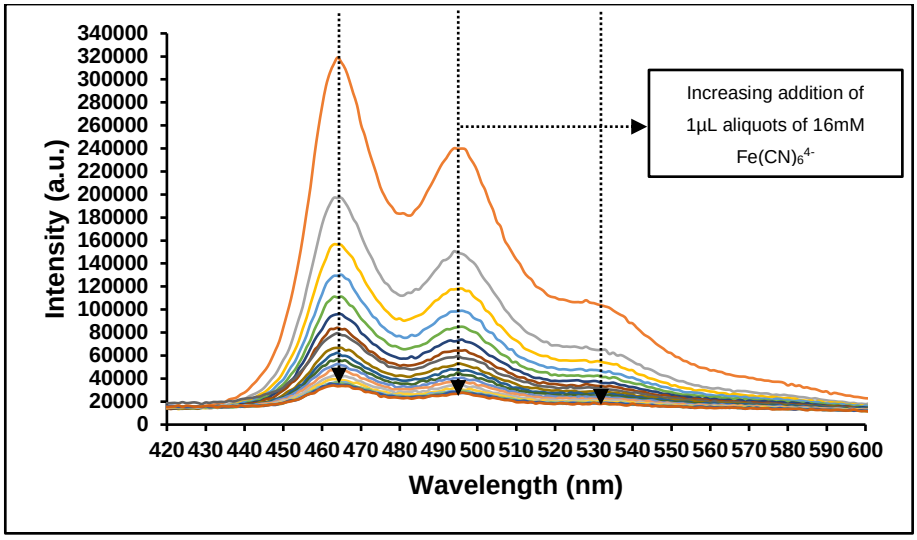

Figure 4.40 – Emission intensity decrease of 6.30µM complex upon successive additions of 0–1.31 x 10^{-4}M $Fe(CN)_6^{4-}$ in 5mM tris, 25mM NaCl buffer solution, pH 7.4.

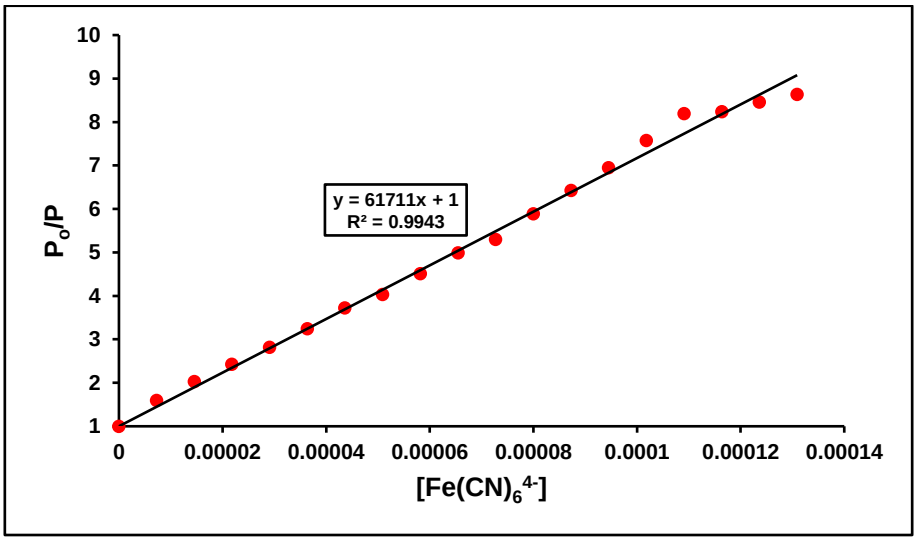

Figure 4.41 – Stern-Volmer plot of the emission intensity of the complex versus concentration of $Fe(CN)_6^{4-}$ to determine the quenching constant. Wavelength monitored = 464nm. P_0 = phosphorescence intensity of the complex before the addition of $Fe(CN)_6^{4-}$ and P = phosphorescence intensity of the complex upon sequential addition of $Fe(CN)_6^{4-}$.

$K_{sv} = 6.17 \times 10^4 M^{-1}$.

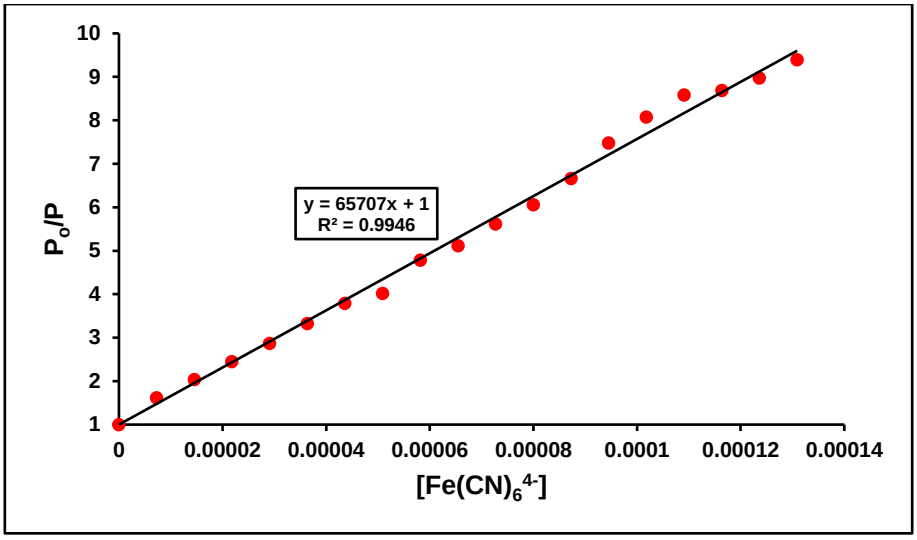

Figure 4.42 – Stern-Volmer plot of the emission intensity of the complex versus concentration of $Fe(CN)_6^{4-}$ to determine the quenching constant. Wavelength monitored = 494nm. P_0 = phosphorescence intensity of the complex before the addition of $Fe(CN)_6^{4-}$ and P = phosphorescence intensity of the complex upon sequential addition of $Fe(CN)_6^{4-}$.

$K_{sv} = 6.57 \times 10^4 M^{-1}$.

5mM tris, 50mM NaCl buffer solution, pH 7.4

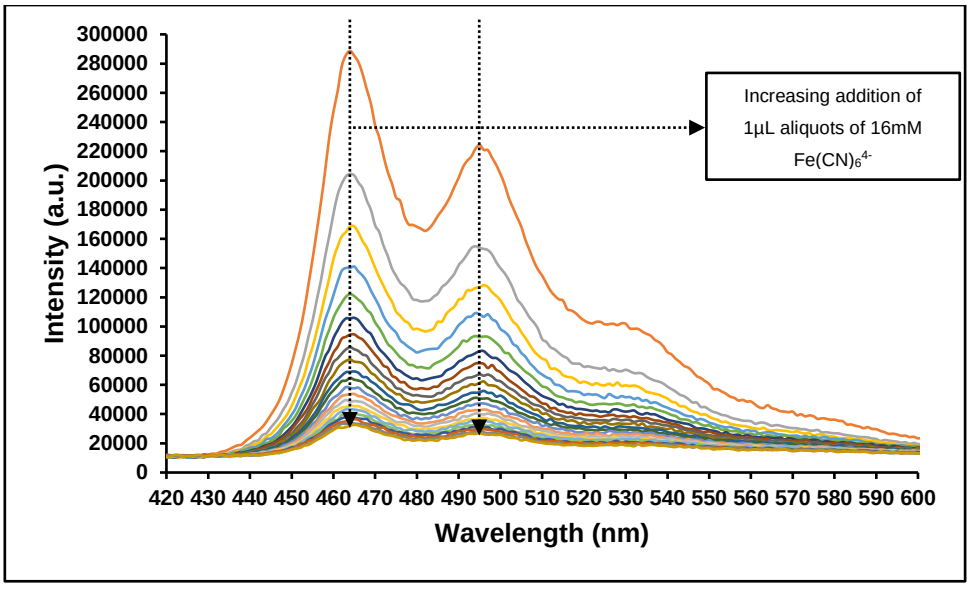

Figure 4.43 – Emission intensity decrease of 6.30µM complex upon successive additions of 0–1.45 x 10^{-4}M $Fe(CN)_6^{4-}$ in 5mM tris, 50mM NaCl buffer solution, pH 7.4.

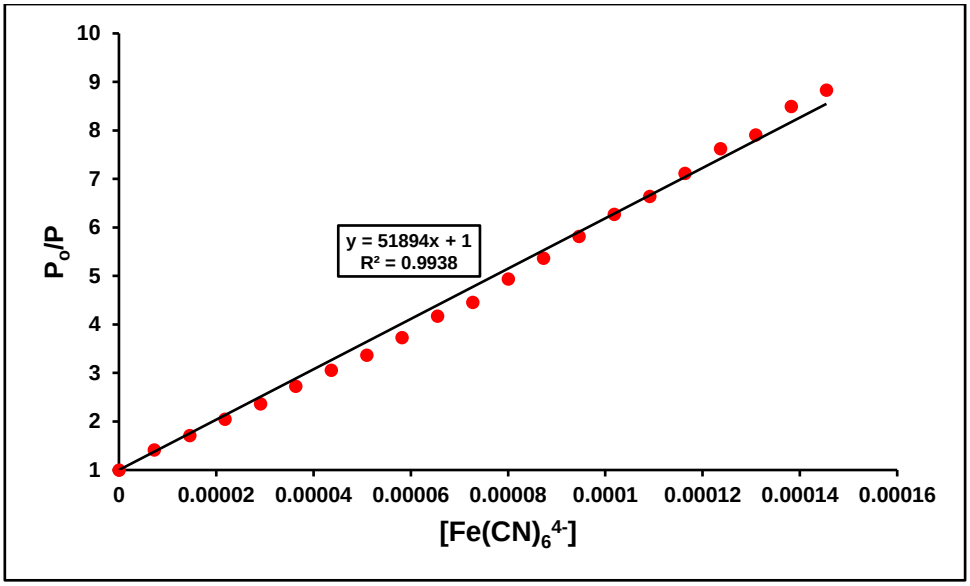

Figure 4.44 – Stern-Volmer plot of the emission intensity of the complex versus concentration of $Fe(CN)_6^{4-}$ to determine the quenching constant. Wavelength monitored = 464nm. P_0 = phosphorescence intensity of the complex before the addition of $Fe(CN)_6^{4-}$ and P = phosphorescence intensity of the complex upon sequential addition of $Fe(CN)_6^{4-}$.

$K_{sv} = 5.19 \times 10^4 M^{-1}$.

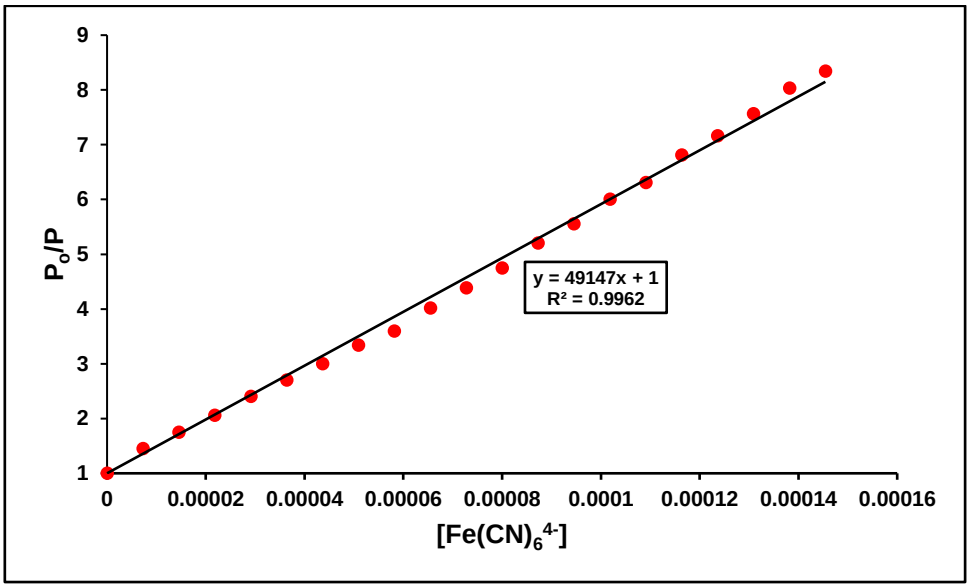

Figure 4.45 – Stern-Volmer plot of the emission intensity of the complex versus concentration of $Fe(CN)_6^{4-}$ to determine the quenching constant. Wavelength monitored = 494nm. P_0 = phosphorescence intensity of the complex before the addition of $Fe(CN)_6^{4-}$ and P = phosphorescence intensity of the complex upon sequential addition of $Fe(CN)_6^{4-}$.

$K_{sv} = 4.91 \times 10^{4} M^{-1}$.

4.6.3.2.2 With CT-DNA (One-fold)

5mM tris, 5mM NaCl buffer Solution, pH 7.4

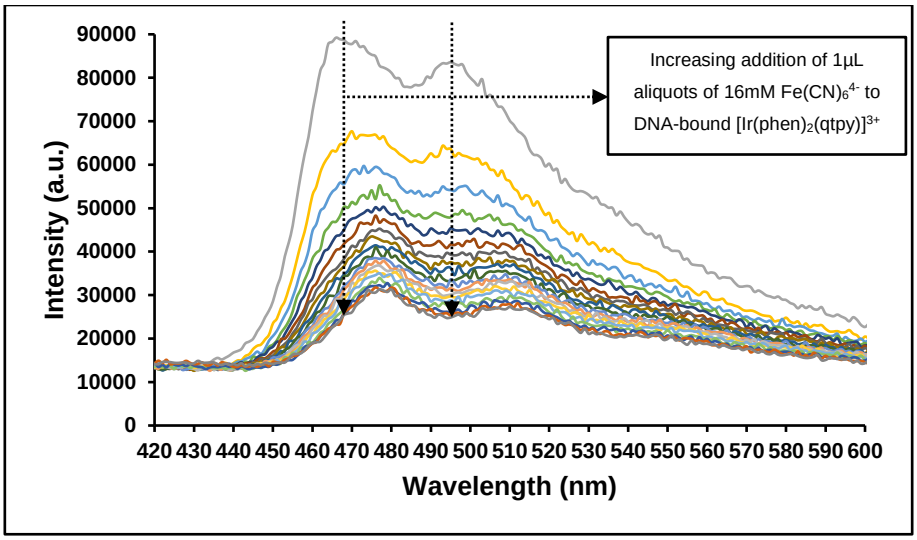

Figure 4.46 – Emission intensity decrease of DNA-bound complex upon successive additions of 0–1.31 x 10^{-4}M $Fe(CN)_6^{4-}$ in 5mM tris, 5mM NaCl buffer solution, pH 7.4. $[[Ir(phen)_2(qtpy)]^{3+}]$ = 6.30µM. [CT-DNA] = 35.27µM.

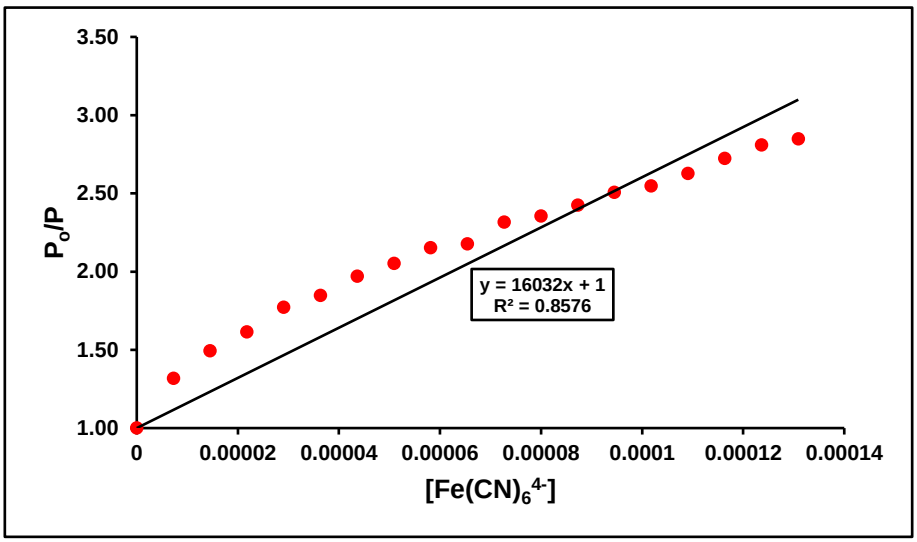

Figure 4.47 – Stern-Volmer plot of the emission intensity of the complex versus concentration of $Fe(CN)_6^{4-}$ to determine the quenching constant. Wavelength monitored = 464nm. P_0 = phosphorescence intensity of the complex before the addition of $Fe(CN)_6^{4-}$ and P = phosphorescence intensity of the complex upon sequential addition of $Fe(CN)_6^{4-}$.

K_{sv} = 1.60 x $10^4 M^{-1}$.

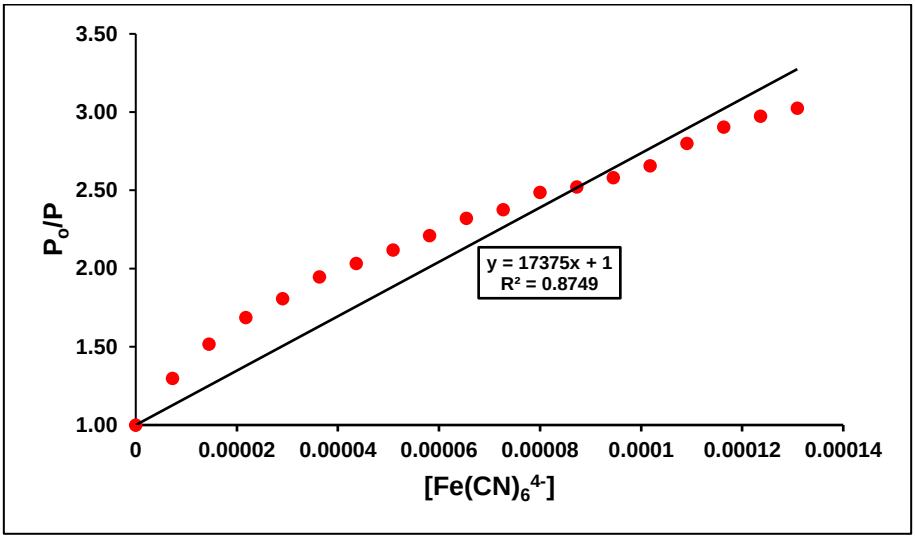

Figure 4.48 – Stern-Volmer plot of the emission intensity of the complex versus concentration of $Fe(CN)_6^{4-}$ to determine the quenching constant. Wavelength monitored = 494nm. P_0 = phosphorescence intensity of the complex before the addition of $Fe(CN)_6^{4-}$ and P = phosphorescence intensity of the complex upon sequential addition of $Fe(CN)_6^{4-}$.

K_{sv} = 1.74 x $10^4 M^{-1}$.

5mM tris, 25mM NaCl Buffer Solution, pH 7.4

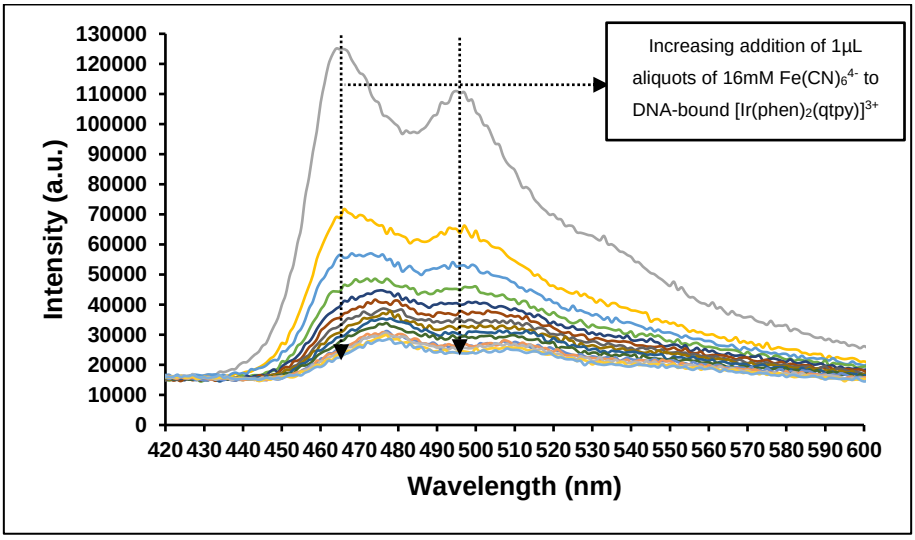

Figure 4.49 – Emission intensity decrease of DNA-bound complex upon successive additions of 0–1.02 x 10^{-4}M $Fe(CN)_6^{4-}$ in 5mM tris, 25mM NaCl buffer solution, pH 7.4. $[[Ir(phen)_2(qtpy)]^{3+}]$ = 6.30µM. [CT-DNA] = 35.27µM. An associated red shift in the emission maxima at 464nm and 494nm was noticed.

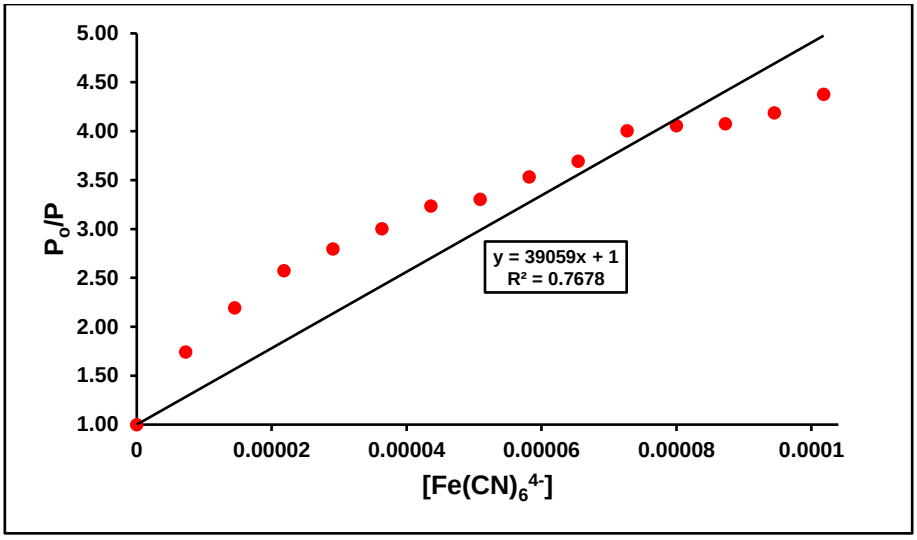

Figure 4.50 – Stern-Volmer plot of the emission intensity of the complex versus concentration of $Fe(CN)_6^{4-}$ to determine the quenching constant. Wavelength monitored = 464nm. P_0 = phosphorescence intensity of the complex before the addition of $Fe(CN)_6^{4-}$ and P = phosphorescence intensity of the complex upon sequential addition of $Fe(CN)_6^{4-}$.

$K_{sv} = 3.91 \times 10^4 M^{-1}$.

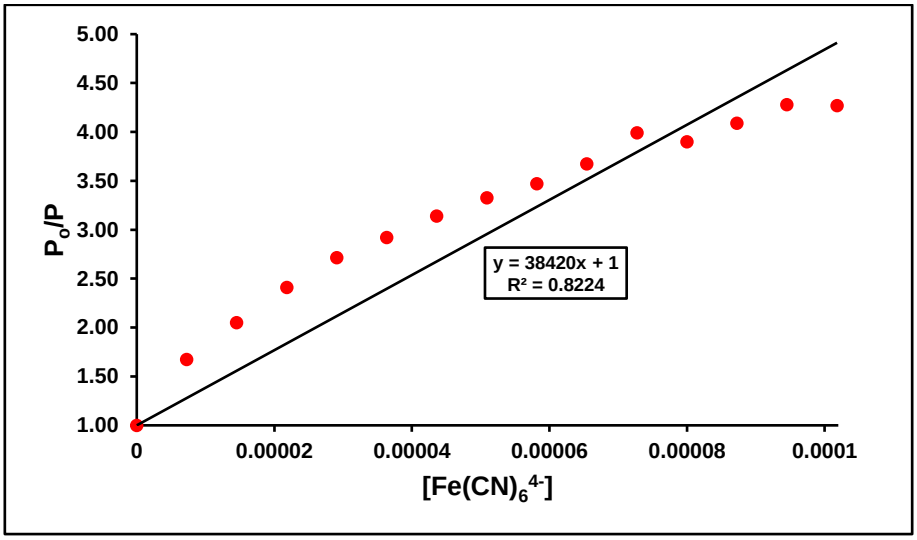

Figure 4.51 – Stern-Volmer plot of the emission intensity of the complex versus concentration of $Fe(CN)_6^{4-}$ to determine the quenching constant. Wavelength monitored = 494nm. P_0 = phosphorescence intensity of the complex before the addition of $Fe(CN)_6^{4-}$ and P = phosphorescence intensity of the complex upon sequential addition of $Fe(CN)_6^{4-}$.

$K_{sv} = 3.84 \times 10^4 M^{-1}$.

5mM tris, 50mM NaCl Buffer Solution, pH 7.4

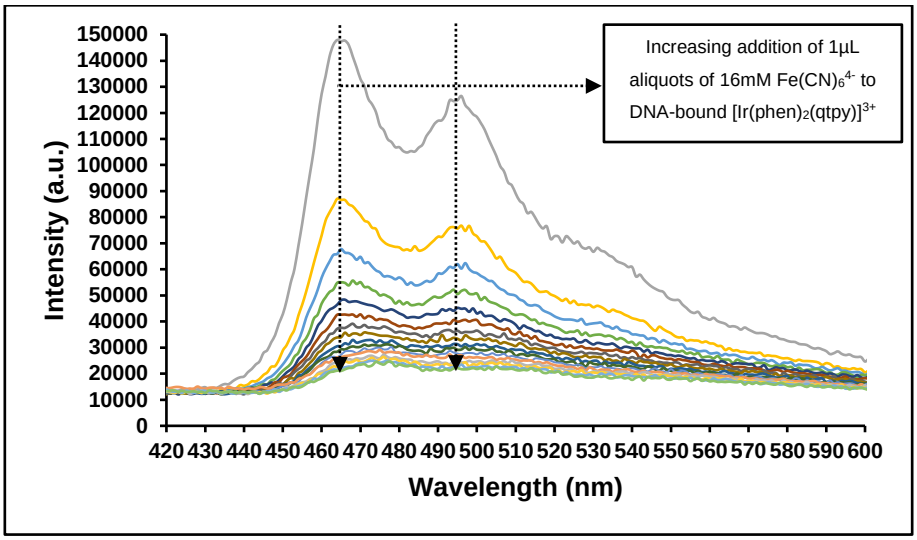

Figure 4.52 – Emission intensity decrease of DNA-bound complex upon successive additions of 0–1.1 x 10^{-4}M $Fe(CN)_6^{4-}$ in 50mM tris, 5mM NaCl buffer solution, pH 7.4. $[[Ir(phen)_2(qtpy)]^{3+}]$ = 6.30µM. [CT-DNA] = 35.27µM. An associated red shift in the emission maxima at 464nm and 494nm was noticed.

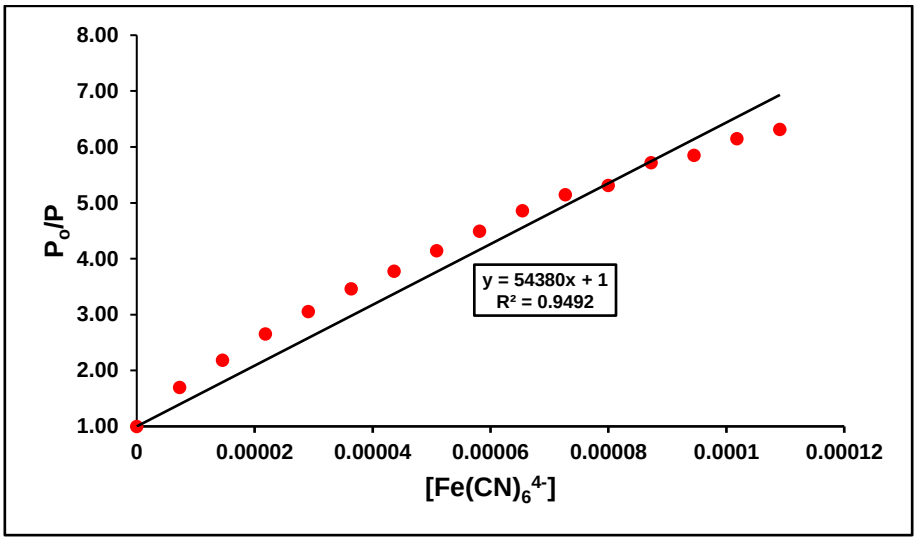

Figure 4.53 – Stern-Volmer plot of the emission intensity of the complex versus concentration of $Fe(CN)_6^{4-}$ to determine the quenching constant. Wavelength monitored = 464nm. P_0 = phosphorescence intensity of the complex before the addition of $Fe(CN)_6^{4-}$ and P = phosphorescence intensity of the complex upon sequential addition of $Fe(CN)_6^{4-}$.

K_{sv} = 5.44 x 10^4M^{-1}.

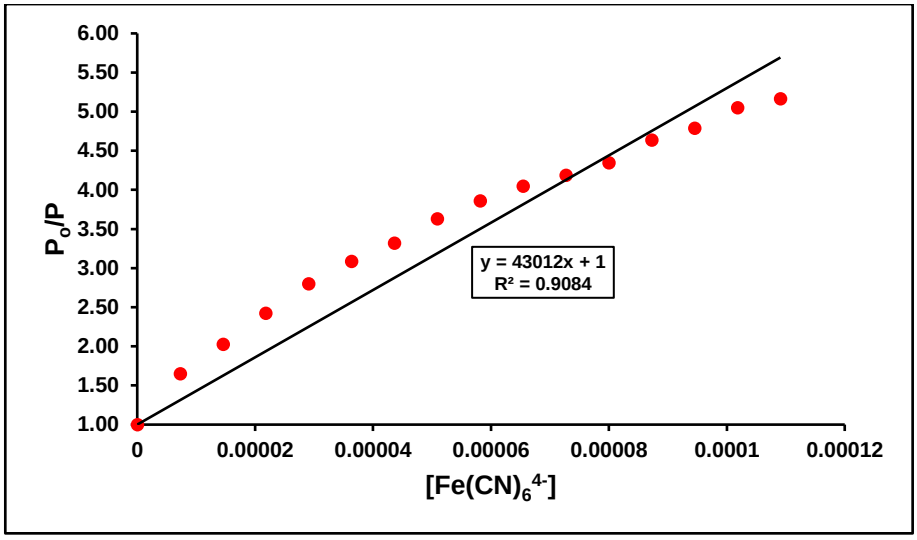

Figure 4.54 – Stern-Volmer plot of the emission intensity of the complex versus concentration of $Fe(CN)_6^{4-}$ to determine the quenching constant. Wavelength monitored = 464nm. P_0 = phosphorescence intensity of the complex before the addition of $Fe(CN)_6^{4-}$ and P = phosphorescence intensity of the complex upon sequential addition of $Fe(CN)_6^{4-}$.

$K_{sv} = 4.30 \times 10^4 M^{-1}$.

4.6.3.2.3 With CT-DNA (Three-fold excess)

5mM tris, 5mM NaCl Buffer Solution

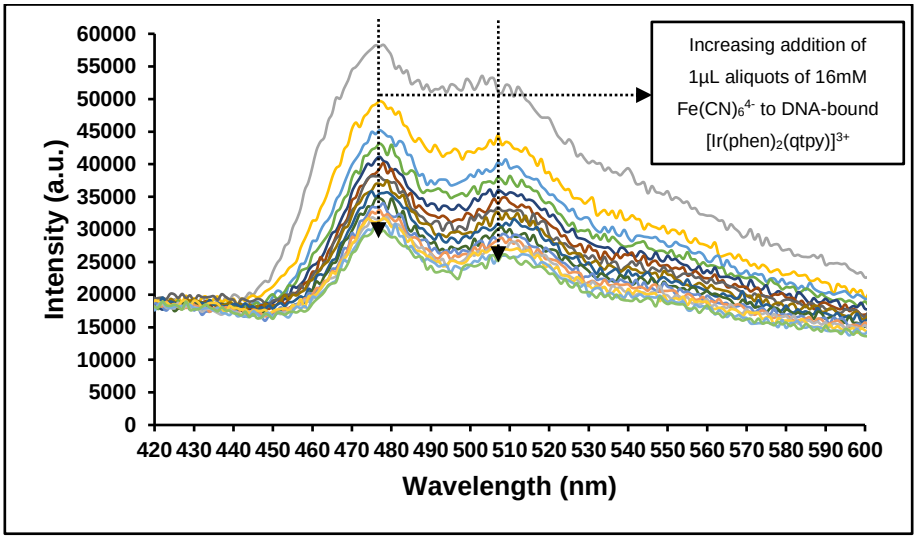

Figure 4.55 – Emission intensity decrease of DNA-bound complex upon successive additions of 0–1.1 x 10^{-4}M $Fe(CN)_6^{4-}$ in 5mM tris, 5mM NaCl buffer solution, pH 7.4. $[[Ir(phen)_2(qtpy)]^{3+}]$ = 6.30µM. [CT-DNA] = 105.81µM. An associated red shift in the emission maxima at 464nm and 494nm was noticed.

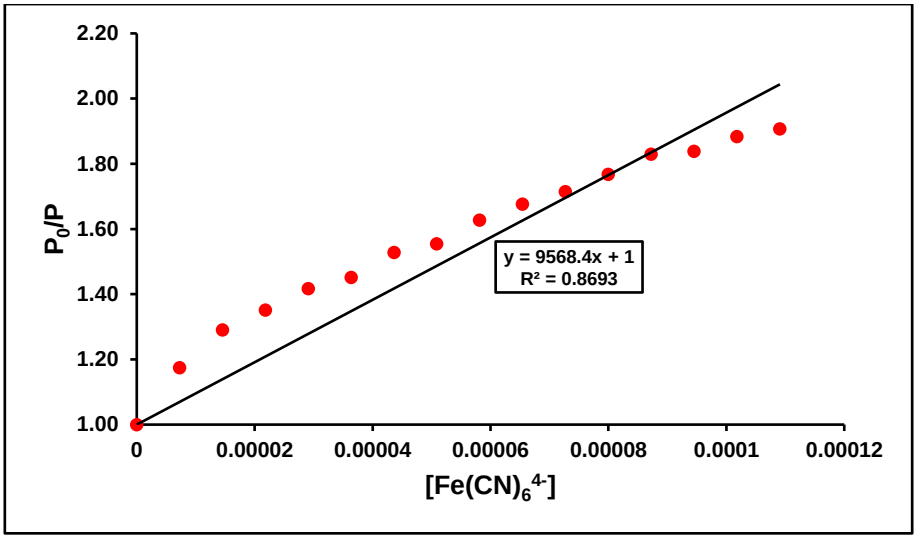

Figure 4.56 – Stern-Volmer plot of the emission intensity of the complex versus concentration of $Fe(CN)_6^{4-}$ to determine the quenching constant. Wavelength monitored = 464nm. P_0 = phosphorescence intensity of the complex before the addition of $Fe(CN)_6^{4-}$ and P = phosphorescence intensity of the complex upon sequential addition of $Fe(CN)_6^{4-}$.

$K_{sv} = 9.57 \times 10^3 M^{-1}$.

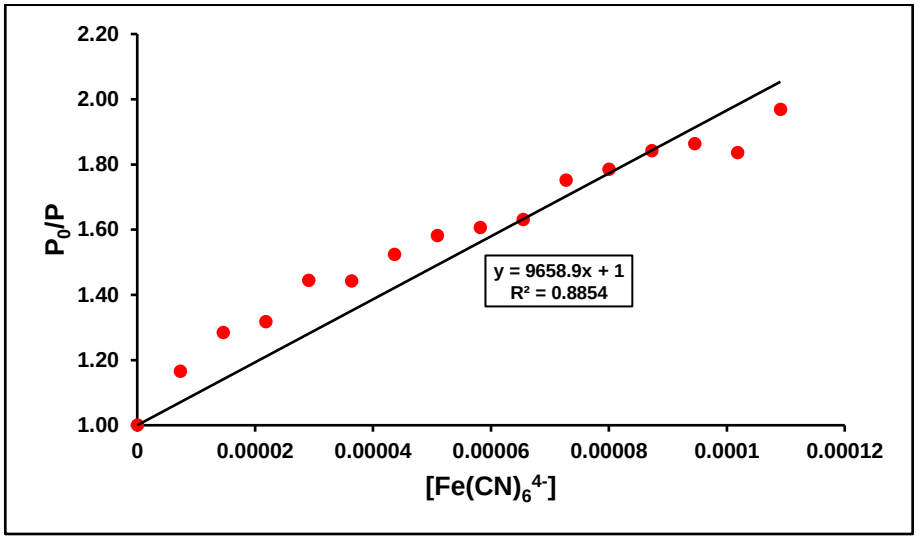

Figure 4.57 – Stern-Volmer plot of the emission intensity of the complex versus concentration of $Fe(CN)_6^{4-}$ to determine the quenching constant. Wavelength monitored = 494nm. P_0 = phosphorescence intensity of the complex before the addition of $Fe(CN)_6^{4-}$ and P = phosphorescence intensity of the complex upon sequential addition of $Fe(CN)_6^{4-}$.

$K_{sv} = 9.66 \times 10^3 M^{-1}$.

5mM tris, 25mM NaCl Buffer Solution

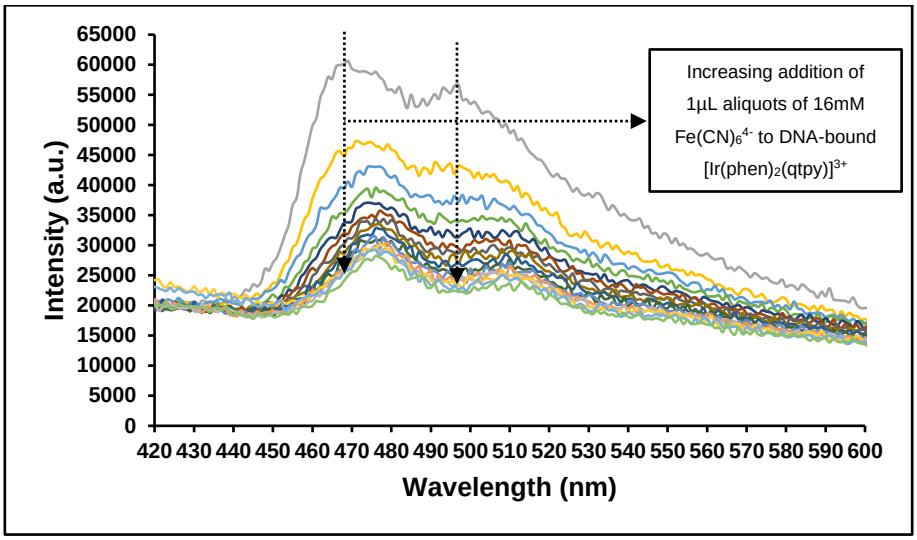

Figure 4.58 – Emission intensity decrease of DNA-bound complex upon successive additions of 0–1.1 x 10^{-4}M $Fe(CN)_6^{4-}$ in 5mM tris, 25mM NaCl buffer solution, pH 7.4. $[[Ir(phen)_2(qtpy)]^{3+}]$ = 6.30µM. [CT-DNA] = 105.81µM. An associated red shift in the emission maxima at 464nm and 494nm was noticed.

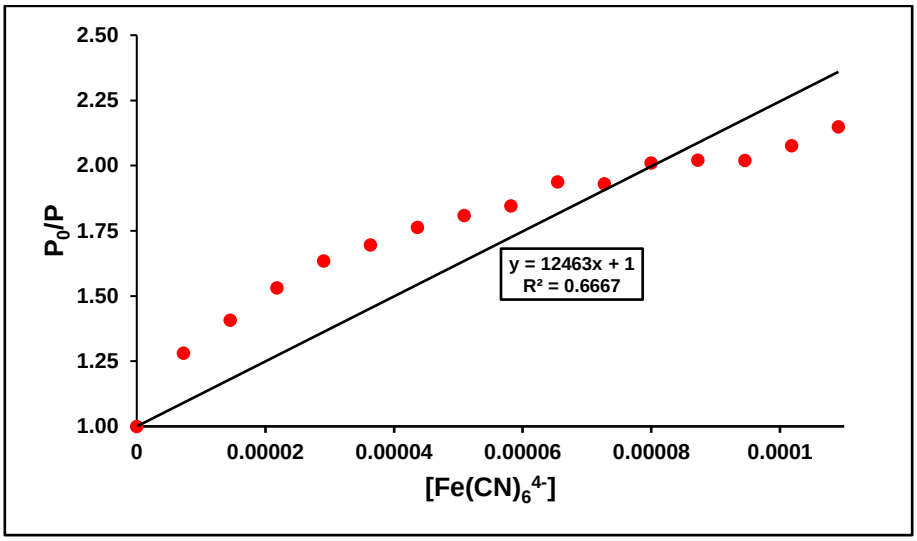

Figure 4.59 – Stern-Volmer plot of the emission intensity of the complex versus concentration of $Fe(CN)_6^{4-}$ to determine the quenching constant. Wavelength monitored = 464nm. P_0 = phosphorescence intensity of the complex before the addition of $Fe(CN)_6^{4-}$ and P = phosphorescence intensity of the complex upon sequential addition of $Fe(CN)_6^{4-}$.

$K_{sv} = 1.25 \times 10^4 M^{-1}$.

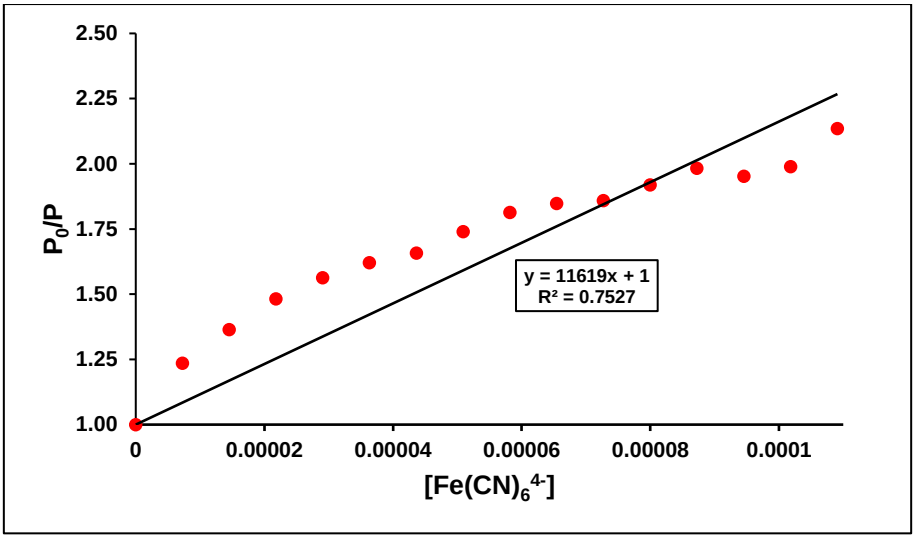

Figure 4.60 – Stern-Volmer plot of the emission intensity of the complex versus concentration of $Fe(CN)_6^{4-}$ to determine the quenching constant. Wavelength monitored = 494nm. P_0 = phosphorescence intensity of the complex before the addition of $Fe(CN)_6^{4-}$ and P = phosphorescence intensity of the complex upon sequential addition of $Fe(CN)_6^{4-}$.

$K_{sv} = 1.16 \times 10^4 M^{-1}$.

5mM tris, 50mM NaCl Buffer Solution

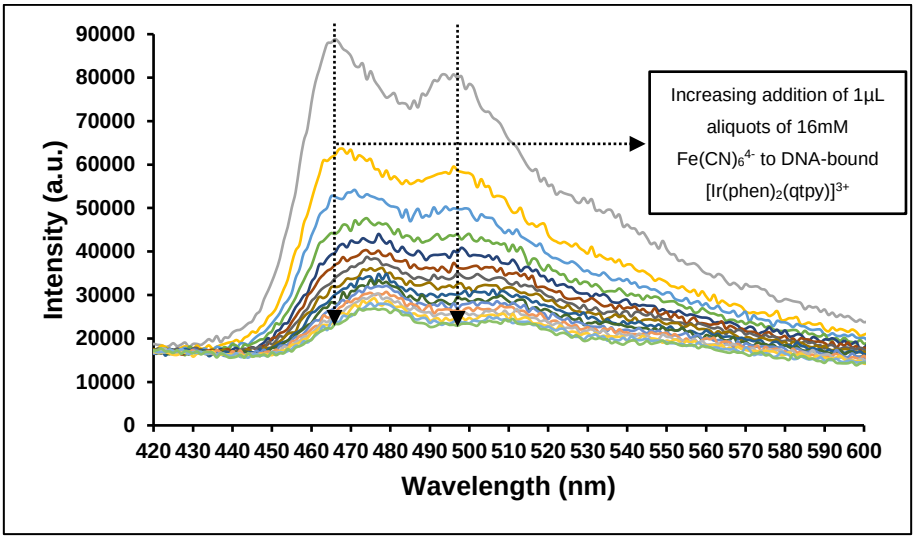

Figure 4.61 – Emission intensity decrease of DNA-bound complex upon successive additions of 0–1.1 x 10^{-4}M $Fe(CN)_6^{4-}$ in 5mM tris, 50mM NaCl buffer solution, pH 7.4. $[[Ir(phen)_2(qtpy)]^{3+}]$ = 6.30µM. [CT-DNA] = 105.81µM. An associated red shift in the emission maxima at 464nm and 494nm was noticed.

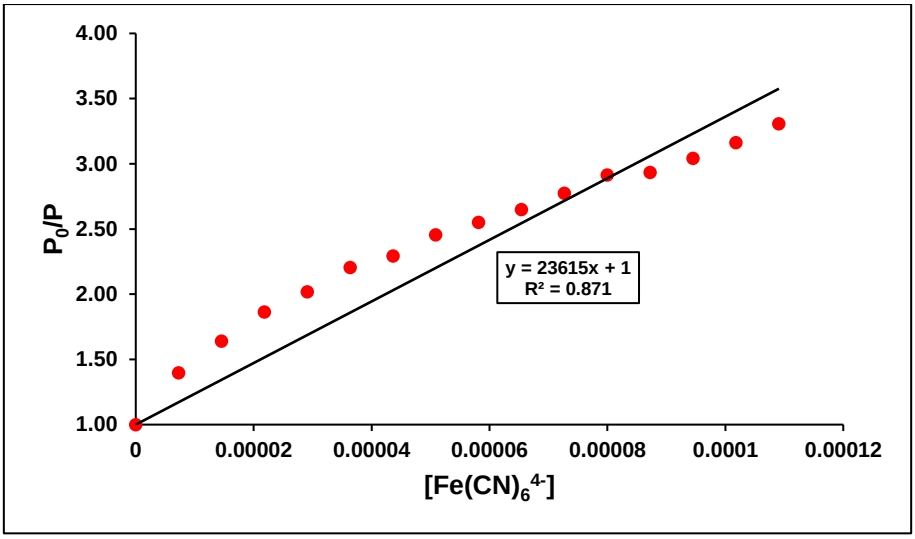

Figure 4.62 – Stern-Volmer plot of the emission intensity of the complex versus concentration of $Fe(CN)_6^{4-}$ to determine the quenching constant. Wavelength monitored = 464nm. P_0 = phosphorescence intensity of the complex before the addition of $Fe(CN)_6^{4-}$ and P = phosphorescence intensity of the complex upon sequential addition of $Fe(CN)_6^{4-}$.

$K_{sv} = 2.36 \times 10^4 M^{-1}$.

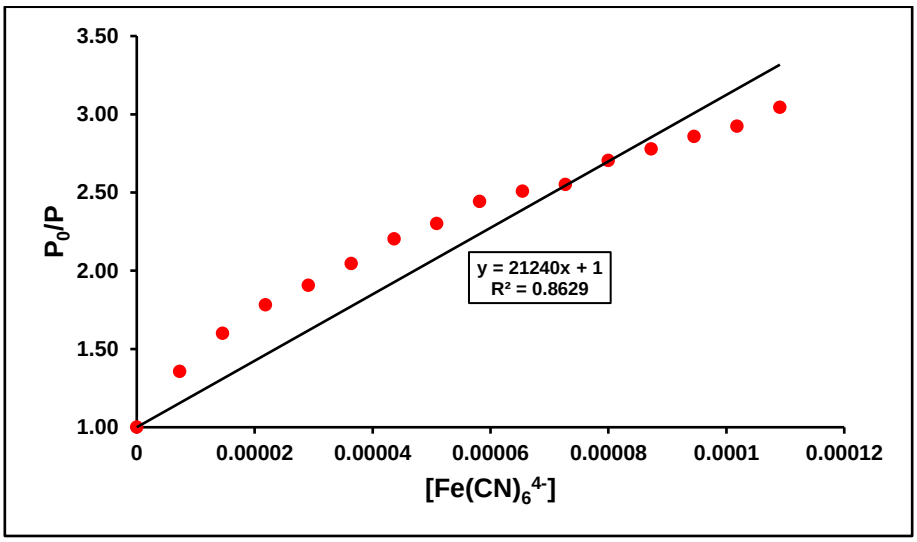

Figure 4.63 – Stern-Volmer plot of the emission intensity of the complex versus concentration of $Fe(CN)_6^{4-}$ to determine the quenching constant. Wavelength monitored = 494nm. P_0 = phosphorescence intensity of the complex before the addition of $Fe(CN)_6^{4-}$ and P = phosphorescence intensity of the complex upon sequential addition of $Fe(CN)_6^{4-}$.

$K_{sv} = 2.12 \times 10^4 M^{-1}$.

Tables 4.5 and Table 4.6 summarises the results of the Stern-Volmer quenching constants (K_{sv}) obtained from the ferrocyanide quenching of $[Ir(phen)_2(qtpy)]^{3+}$ in either 5mM tris, 5mM NaCl buffer, 5mM tris, 25mM NaCl buffer, or 5mM tris, 50mM NaCl buffer in the absence of CT-DNA and in the presence of 1-fold CT-DNA and 3-fold excess CT-DNA for the emission at 464nm and 484nm, respectively. In all the three buffer solutions employed, the value of the quenching constant is highest in the absence of CT-DNA and decreases accordingly as more CT-DNA was added up to a 3-fold addition. In other words, quenching of $[Ir(phen)_2(qtpy)]^{3+}$ by Ferrocyanide is highest in the absence of CT-DNA and lowest upon the addition of 3-fold CT-DNA. Further insight into the results show that quenching of $[Ir(phen)_2(qtpy)]^{3+}$ happened most rapidly in 5mM tris, 5mM NaCl buffer solution.

Table 4.5 – Ferrocyanide Quenching Data for the Interaction of $[Ir(phen)_2(qtpy)]^{3+}$ without and with DNA. Emission wavelength monitored = 464nm.

Buffer	**Without CT-DNA**	**With CT-DNA (1-fold)**	**With CT-DNA (3-fold excess)**
5mM tris, 5mM NaCl buffer	$8.80 \times 10^4 M^{-1}$	$1.60 \times 10^4 M^{-1}$	$9.57 \times 10^3 M^{-1}$
5mM tris, 25mM NaCl buffer	$6.17 \times 10^4 M^{-1}$	$3.91 \times 10^4 M^{-1}$	$1.25 \times 10^4 M^{-1}$
5mM tris, 50mM NaCl buffer	$5.19 \times 10^4 M^{-1}$	$5.44 \times 10^4 M^{-1}$	$2.36 \times 10^4 M^{-1}$

Table 4.6 – Ferrocyanide Quenching Data for the Interaction of $[Ir(phen)_2(qtpy)]^{3+}$ without and with DNA. Emission wavelength monitored = 494nm.

Buffer	**Without CT-DNA**	**With CT-DNA (1-fold)**	**With CT-DNA (3-fold excess)**
5mM tris, 5mM NaCl buffer	$8.48 \times 10^4 M^{-1}$	$1.74 \times 10^4 M^{-1}$	$9.66 \times 10^3 M^{-1}$

5mM tris, 25mM NaCl buffer	6.57 x $10^4 M^{-1}$	3.84 x $10^4 M^{-1}$	1.16 x $10^4 M^{-1}$
5mM tris, 50mM NaCl buffer	4.91 x $10^4 M^{-1}$	4.30 x $10^4 M^{-1}$	2.12 x $10^4 M^{-1}$

4.6.3.3 $[Ir(dppz)_2(qtpy)]^{3+}$

Analogous experiments as for those of $[Ir(bpy)_2(qtpy)]^{3+}$ and $[Ir(phen)_2(qtpy)]^{3+}$ were undertaken for $[Ir(dppz)_2(qtpy)]^{3+}$. The emission quenching diagrams and Stern-Volmer plots for the free complex in the three buffers employed and those of the complex in the presence of (one-fold and three-fold excess) CT-DNA are shown in Figs. 4.64–4.81.

4.6.3.3.1 Without CT-DNA

5mM tris, 5mM NaCl Buffer Solution

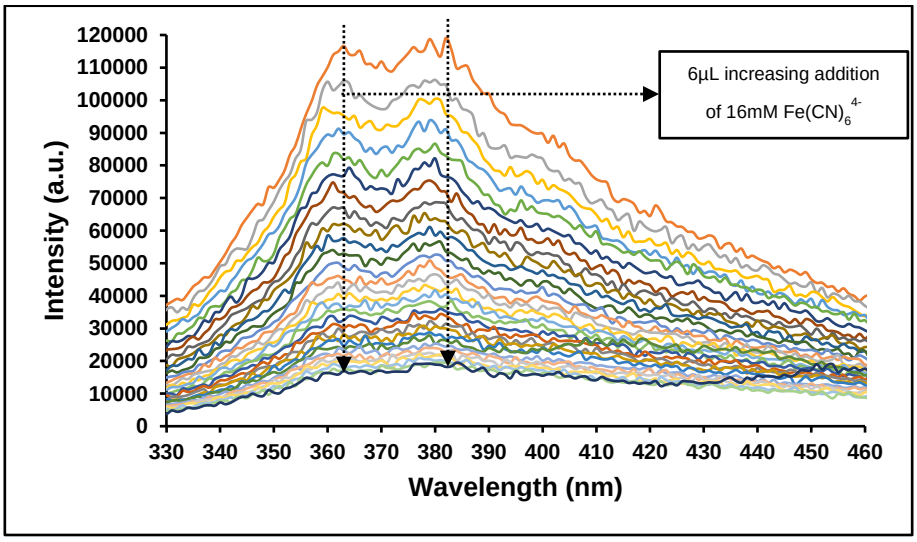

Figure 4.64 – Emission intensity of 27.91µM $[Ir(dppz)_2(qtpy)]^{3+}$ complex upon successive addition of 16mM $Fe(CN)_6^{4-}$ in 5mM tris, 5mM NaCl buffer solution, pH 7.4.

Quenching Fits

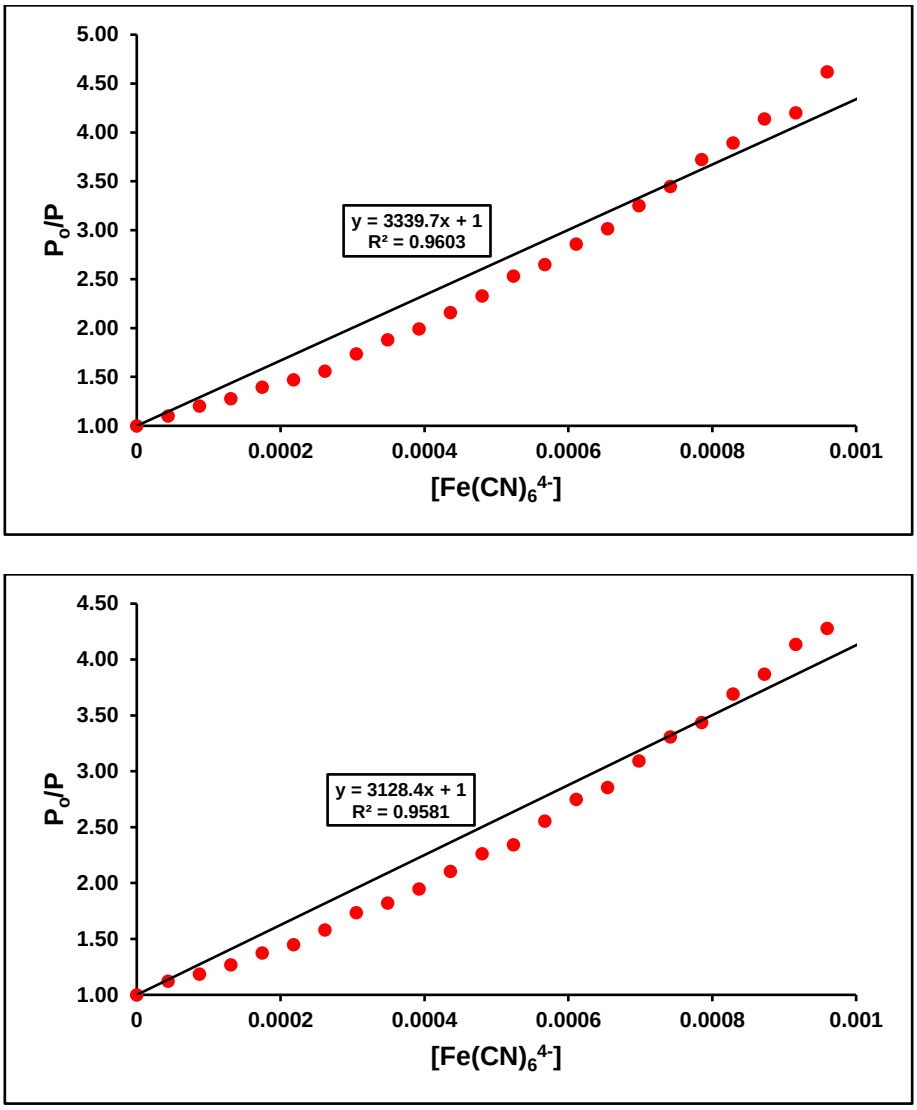

Figure 4.65 – Stern-Volmer plot of the emission intensity of the complex versus concentration of $Fe(CN)_6^{4-}$ to determine the quenching constant (top – emission intensity monitored at 363nm and bottom – emission intensity monitored at 382nm).

$K_{sv} = 3.34 \times 10^3 M^{-1}$ at 363nm and $K_{sv} = 3.13 \times 10^3 M^{-1}$ at 382nm.

5mM tris, 25mM NaCl Buffer Solution

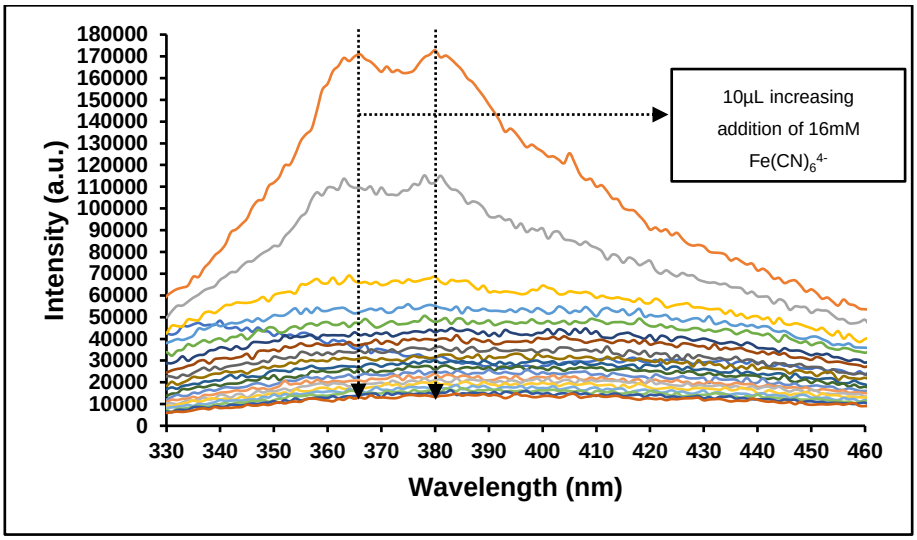

Figure 4.66 – Emission intensity of 27.91µM $[Ir(dppz)_2(qtpy)]^{3+}$ complex upon successive addition of 16mM $Fe(CN)_6^{4-}$ in 5mM tris, 25mM NaCl buffer solution, pH 7.4.

Quenching Fits

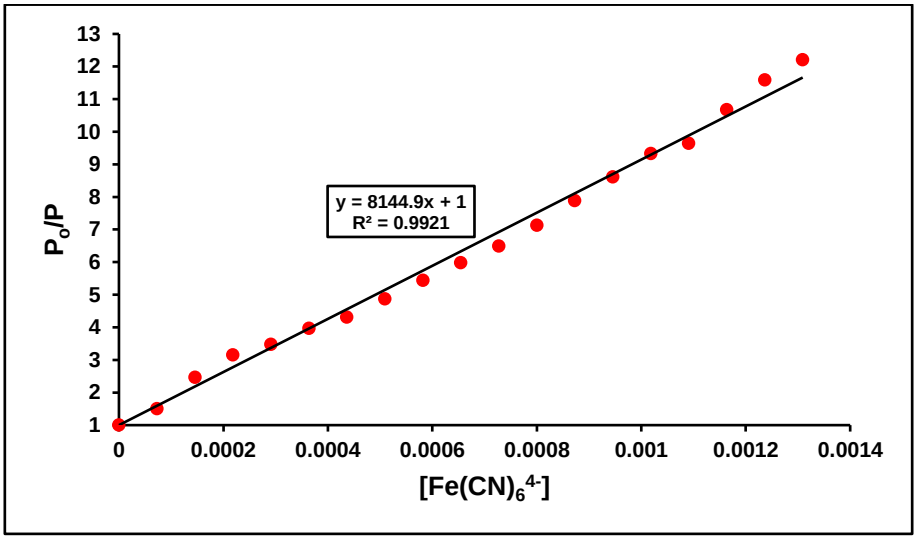

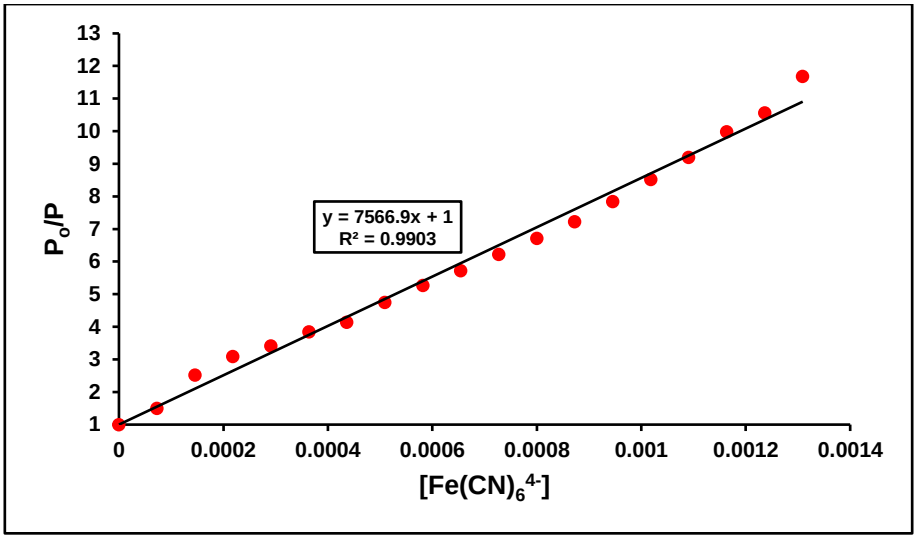

Figure 4.67 – Stern-Volmer plot of the emission intensity of the complex versus concentration of $Fe(CN)_6^{4-}$ to determine the quenching constant (top – emission intensity monitored at 363nm and bottom – emission intensity monitored at 380nm).

K_{sv} = 8.14 x $10^3 M^{-1}$ at 363nm and K_{sv} = 7.57 x $10^3 M^{-1}$ at 380nm.

5mM tris, 50mM NaCl Buffer Solution

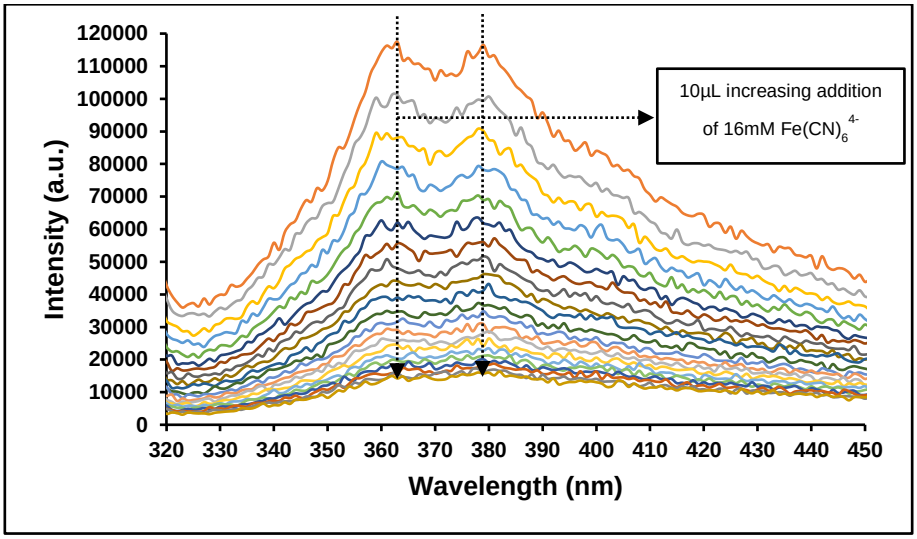

Figure 4.68 – Emission intensity of 27.91µM $[Ir(dppz)_2(qtpy)]^{3+}$ complex upon successive addition of 16mM $Fe(CN)_6^{4-}$ in 5mM tris, 50mM NaCl buffer solution, pH 7.4.

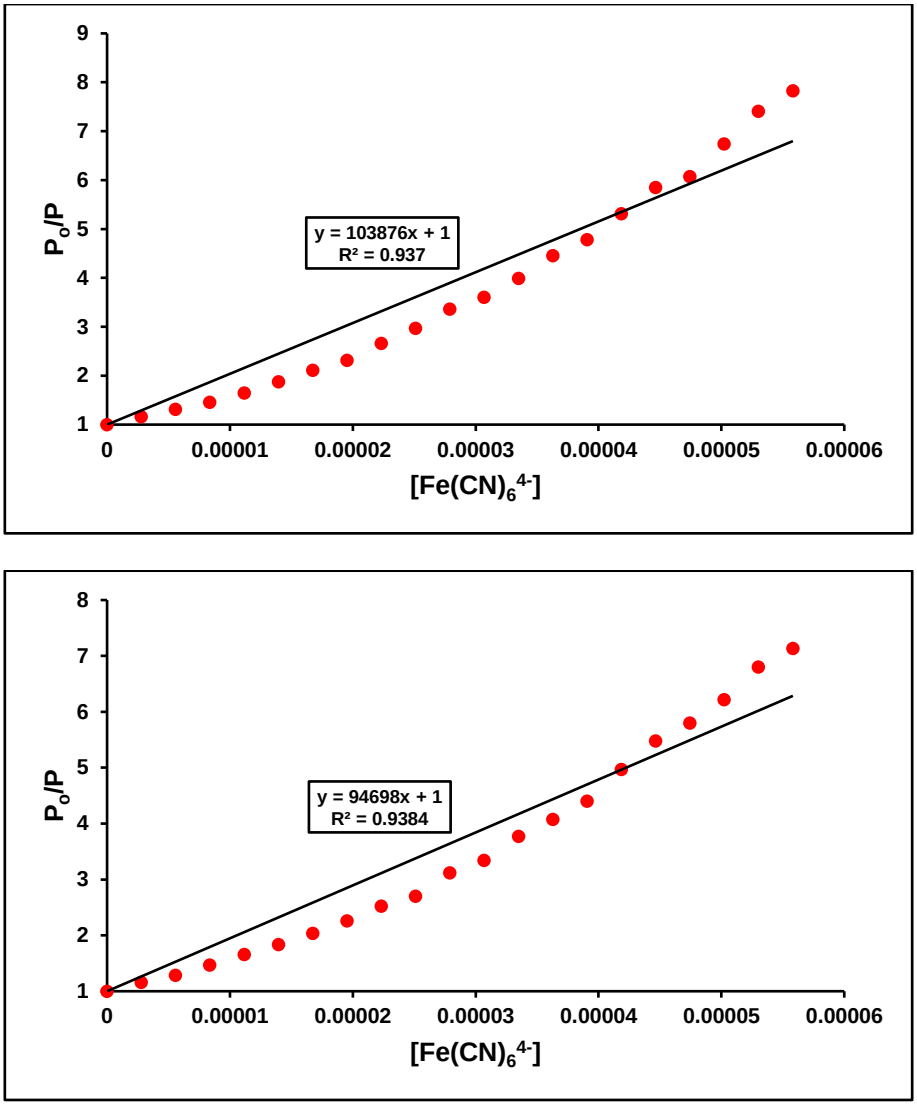

Figure 4.69 – Stern-Volmer plot of the emission intensity of the complex versus concentration of $Fe(CN)_6^{4-}$ to determine the quenching constant (top – emission intensity monitored at 363nm and bottom – emission intensity monitored at 380nm).

K_{sv} = 1.05 x $10^5 M^{-1}$ at 363nm and K_{sv} = 9.47 x $10^4 M^{-1}$ at 380nm.

4.6.3.3.2 With CT-DNA (1-fold)

5mM tris, 5mM NaCl Buffer Solution

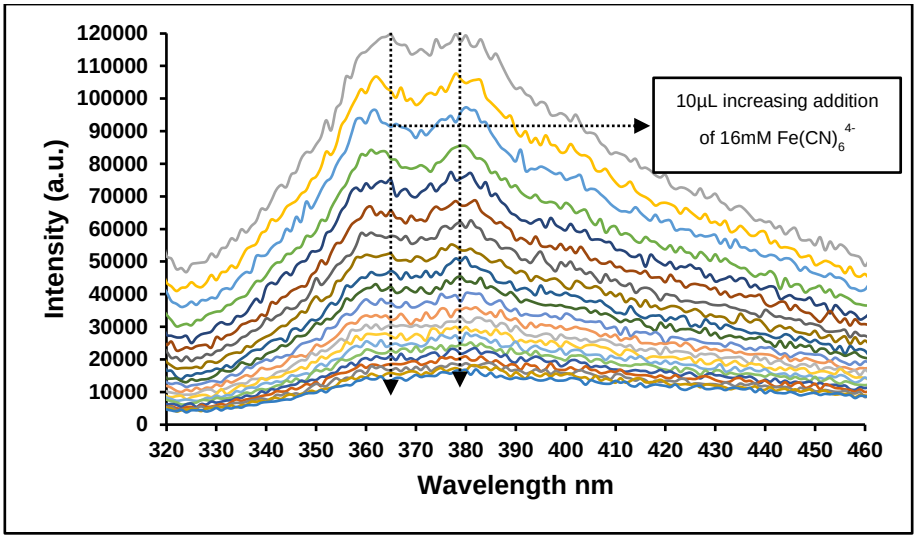

Figure 4.70 – Emission intensity of 27.91µM $[Ir(dppz)_2(qtpy)]^{3+}$ complex upon successive addition of 16mM $Fe(CN)_6^{4-}$ in 5mM tris, 5mM NaCl buffer solution, pH 7.4. [CT-DNA] = 1.06 x 10^{-5}M.

Quenching Fits

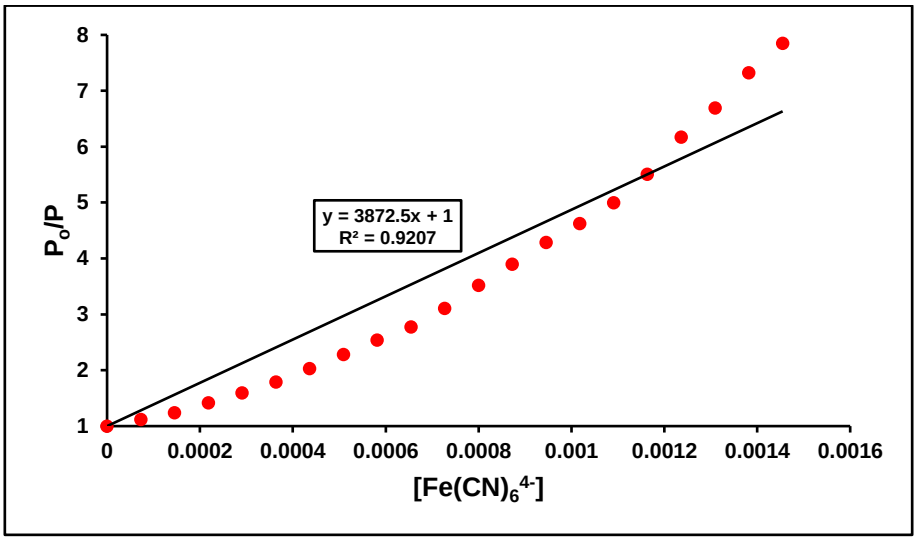

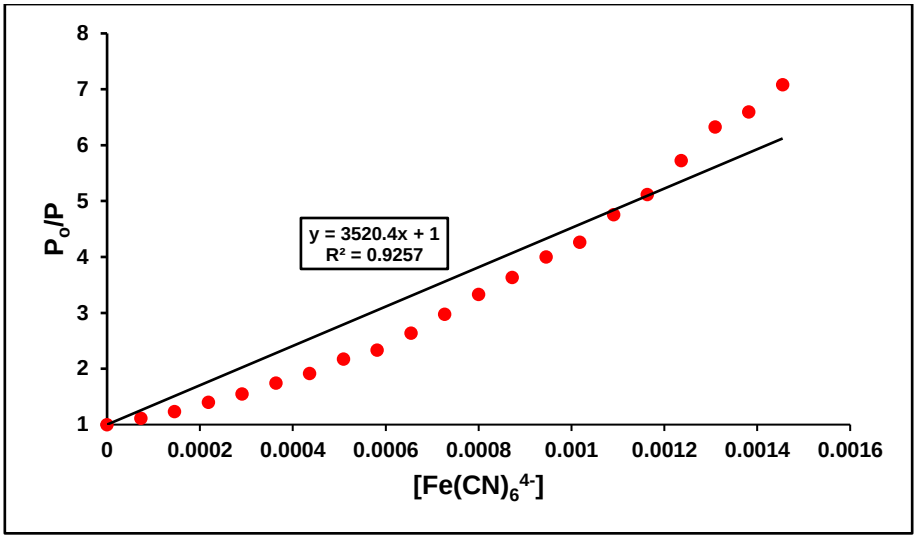

Figure 4.71 – Stern-Volmer plot of the emission intensity of the complex versus concentration of $Fe(CN)_6^{4-}$ to determine the quenching constant (top – emission intensity monitored at 363nm and bottom – emission intensity monitored at 380nm).

K_{sv} = 3.67 x $10^3 M^{-1}$ at 363nm and K_{sv} = 3.52 x $10^3 M^{-1}$ at 380nm.

5mM tris, 25mM NaCl Buffer Solution

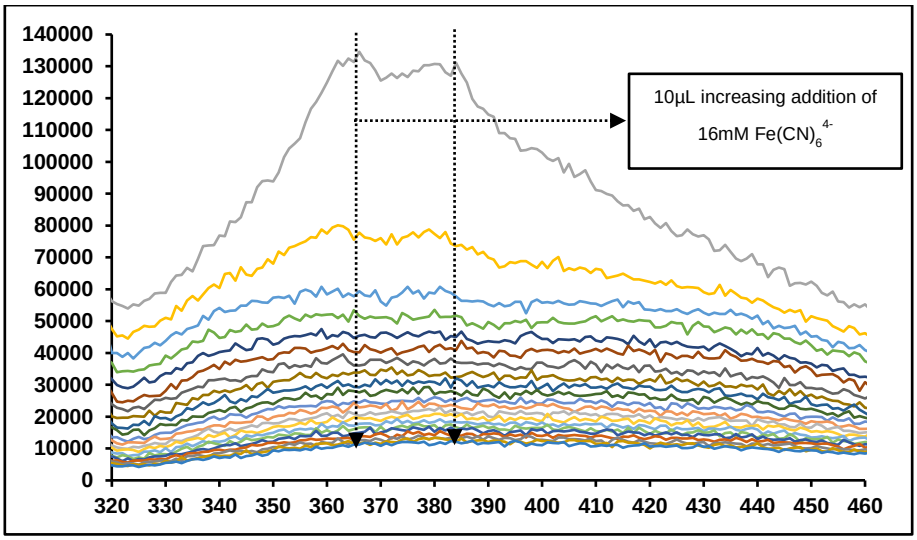

Figure 4.72 – Emission intensity of 27.91µM $[Ir(dppz)_2(qtpy)]^{3+}$ complex upon successive addition of 16mM $Fe(CN)_6^{4-}$ in 5mM tris, 25mM NaCl buffer solution, pH 7.4. [CT-DNA] = 1.06 x 10^{-5}M.

Quenching Fits

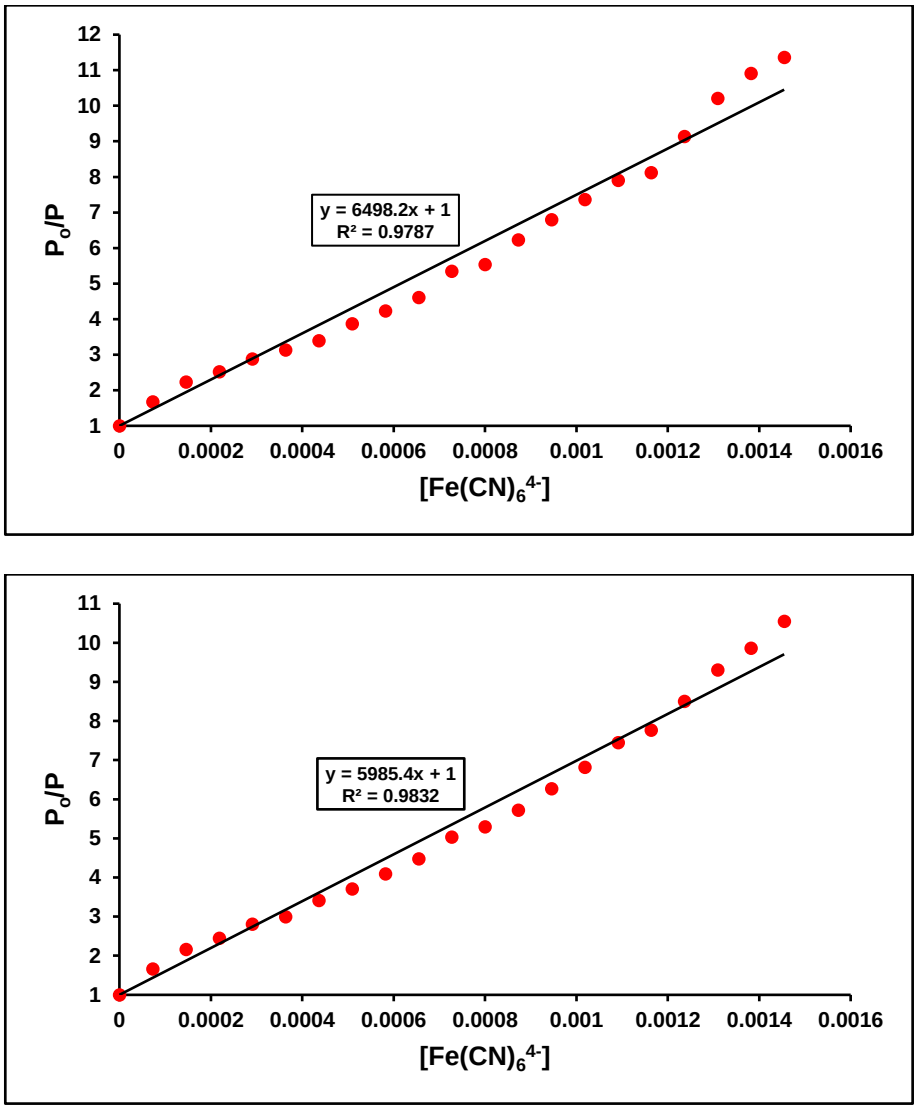

Figure 4.73 – Stern-Volmer plot of the emission intensity of the complex versus concentration of $Fe(CN)_6^{4-}$ to determine the quenching constant (top – emission intensity monitored at 363nm and bottom – emission intensity monitored at 380nm).

$K_{sv} = 6.50 \times 10^3 M^{-1}$ at 363nm and $K_{sv} = 5.99 \times 10^3 M^{-1}$ at 380nm.

5mM tris, 50mM NaCl Buffer Solution

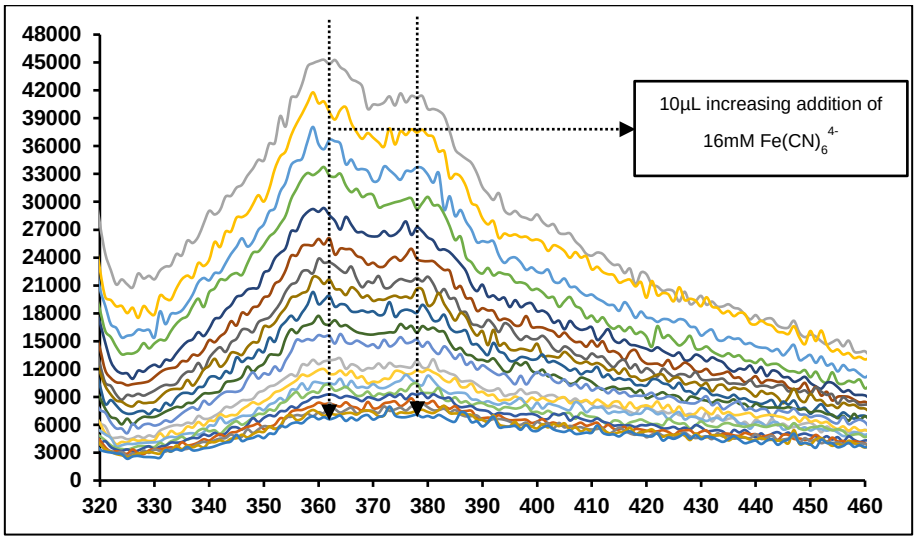

Figure 4.74 – Emission intensity of 27.91µM $[Ir(dppz)_2(qtpy)]^{3+}$ complex upon successive addition of 16mM $Fe(CN)_6^{4-}$ in 5mM tris, 50mM NaCl buffer solution, pH 7.4. [CT-DNA] = 1.06 x 10^{-5}M.

Quenching Fits

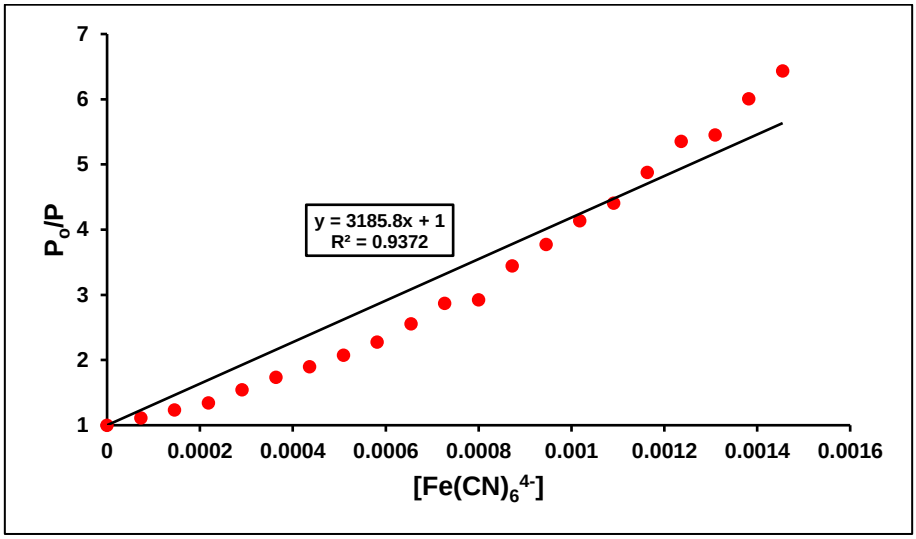

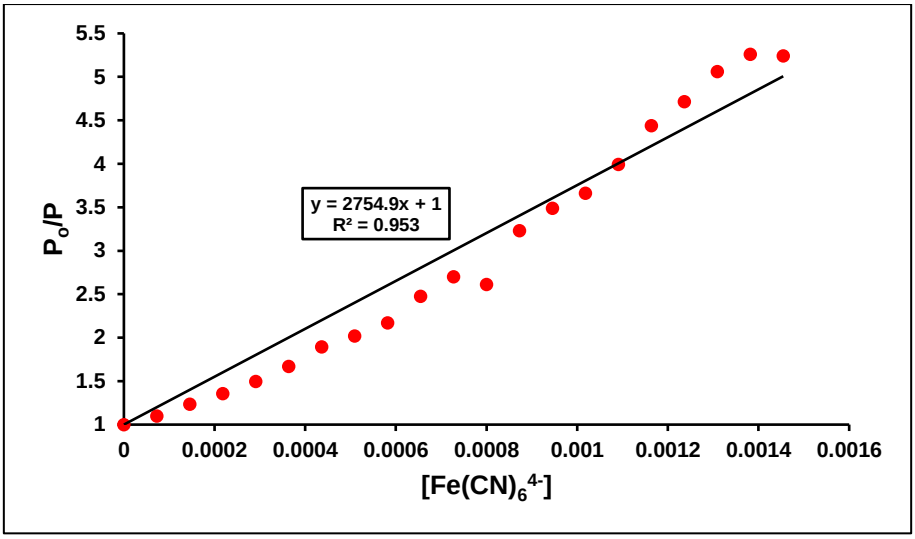

Figure 4.75 – Stern-Volmer plot of the emission intensity of the complex versus concentration of $Fe(CN)_6^{4-}$ to determine the quenching constant (top – emission intensity monitored at 363nm and bottom – emission intensity monitored at 380nm).

K_{sv} = 3.19 x $10^3 M^{-1}$ at 363nm and K_{sv} = 2.75 x $10^3 M^{-1}$ at 380nm.

4.6.3.3.3 With CT-DNA (3-fold excess)

5mM tris, 5mM NaCl Buffer Solution

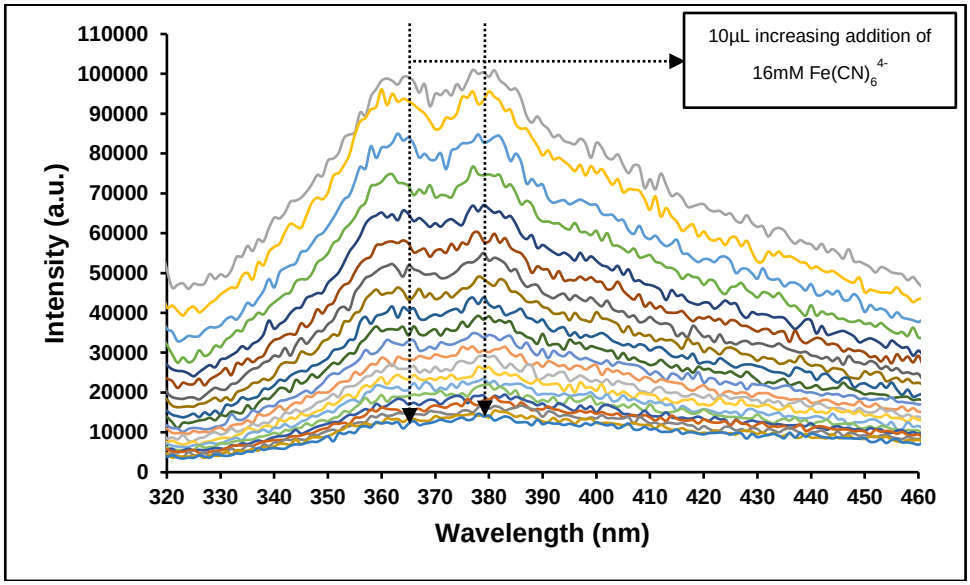

Figure 4.76 – Emission intensity of 27.91µM $[Ir(dppz)_2(qtpy)]^{3+}$ complex upon successive additions of 16mM $Fe(CN)_6^{4-}$ in 5mM tris, 5mM NaCl buffer solution, pH 7.4. [CT-DNA] = 3.17 x 10^{-5}M.

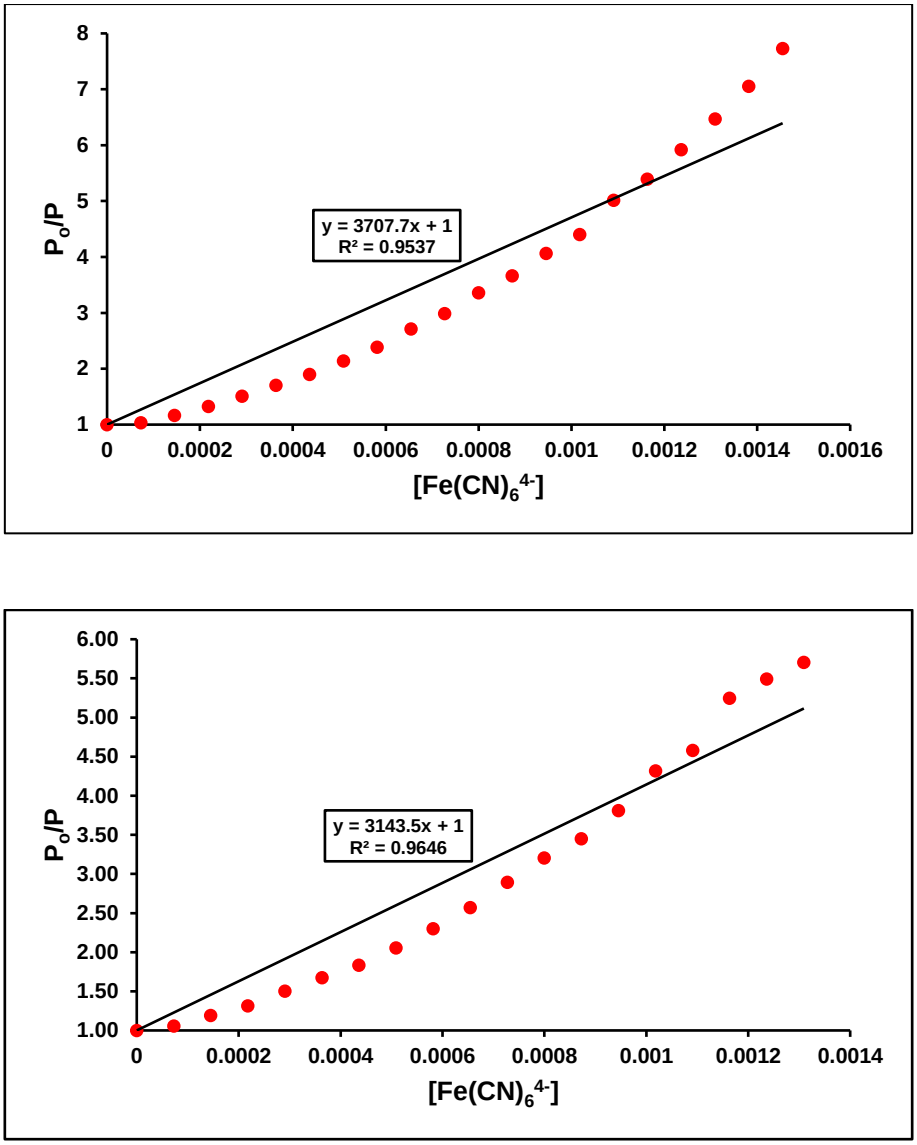

Figure 4.77 – Stern-Volmer plot of the emission intensity of the complex versus concentration of $Fe(CN)_6^{4-}$ to determine the quenching constant (top – emission intensity monitored at 363nm and bottom – emission intensity monitored at 380nm).

$K_{sv} = 3.71 \times 10^3 M^{-1}$ at 363nm and $K_{sv} = 3.14 \times 10^3 M^{-1}$ at 380nm.

5mM tris, 25mM NaCl Buffer Solution

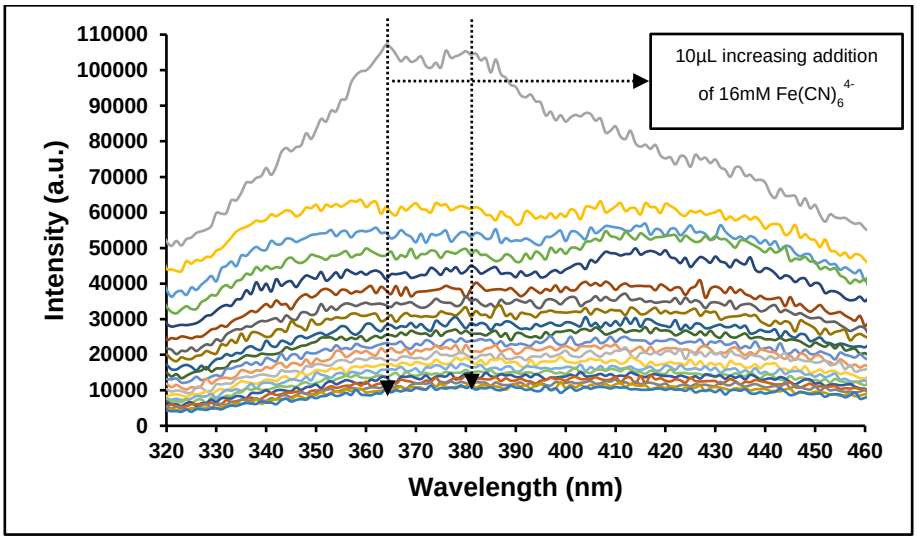

Figure 4.78 – Emission intensity of 27.91µM $[Ir(dppz)_2(qtpy)]^{3+}$ complex upon successive additions of 16mM $Fe(CN)_6^{4-}$ in 5mM tris, 25mM NaCl buffer solution, pH 7.4. [CT-DNA] = 3.17 x 10^{-5}M.

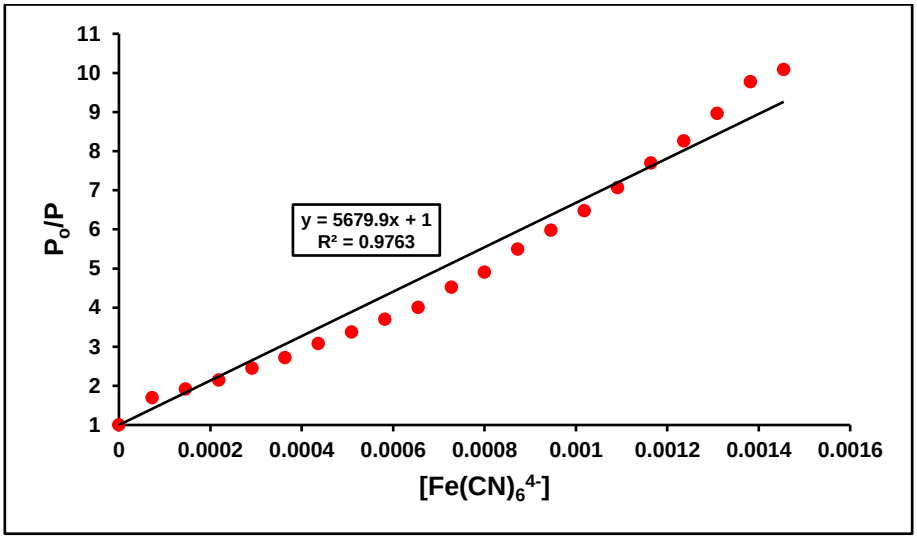

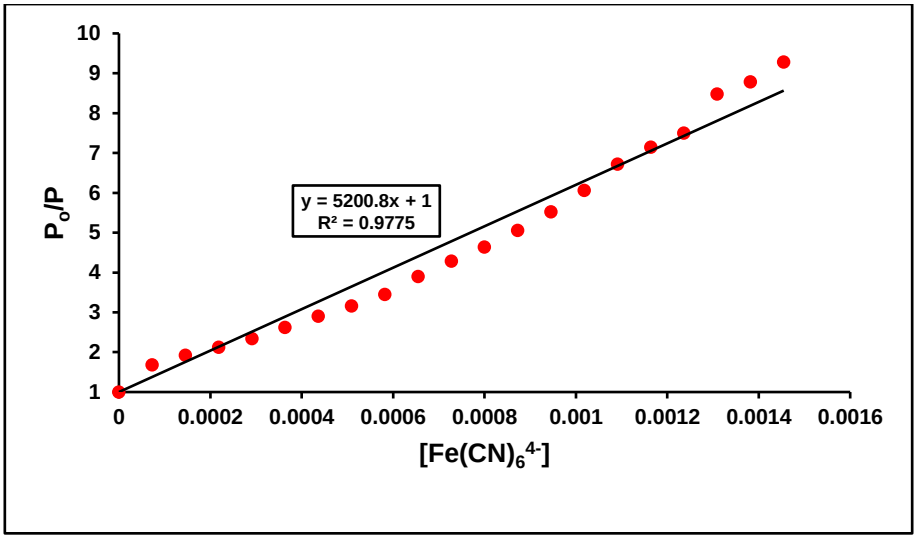

Figure 4.79 – Stern-Volmer plot of the emission intensity of the complex versus concentration of $Fe(CN)_6^{4-}$ to determine the quenching constant (top – emission intensity monitored at 363nm and bottom – emission intensity monitored at 380nm).

K_{sv} = 5.68 x $10^3 M^{-1}$ at 363nm and K_{sv} = 5.20 x $10^3 M^{-1}$ at 380nm.

5mM tris, 50mM NaCl Buffer Solution

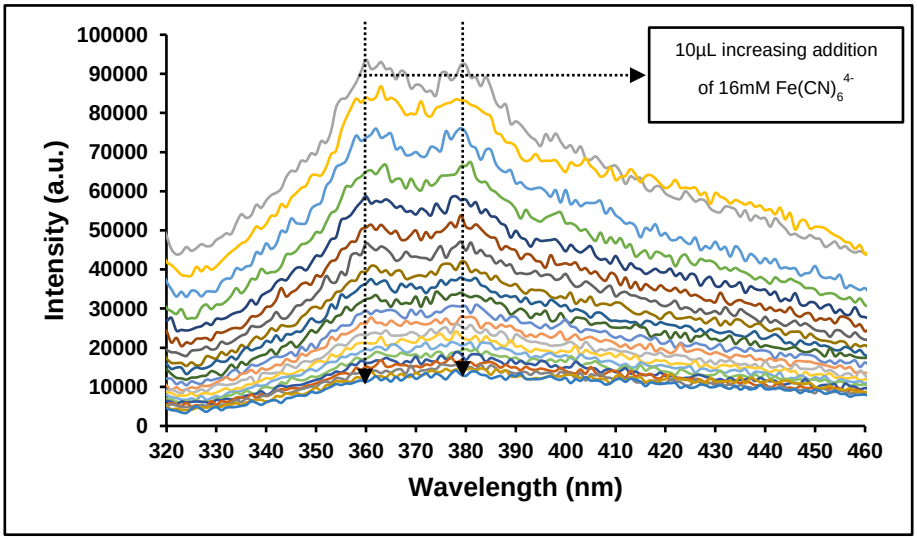

Figure 4.80 – Emission intensity of 27.91µM $[Ir(dppz)_2(qtpy)]^{3+}$ complex upon successive additions of 16mM $Fe(CN)_6^{4-}$ in 5mM tris, 50mM NaCl buffer solution, pH 7.4. [CT-DNA] = 3.17 x 10^{-5}M.

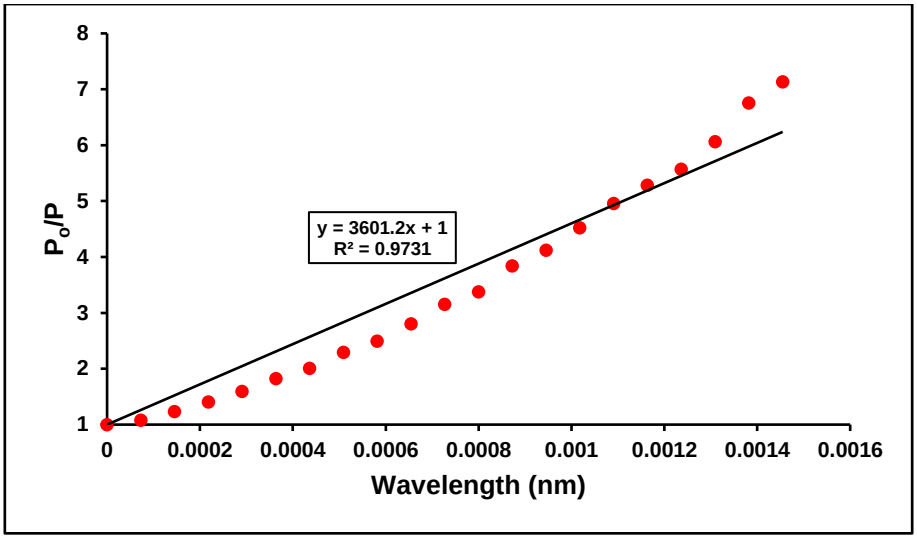

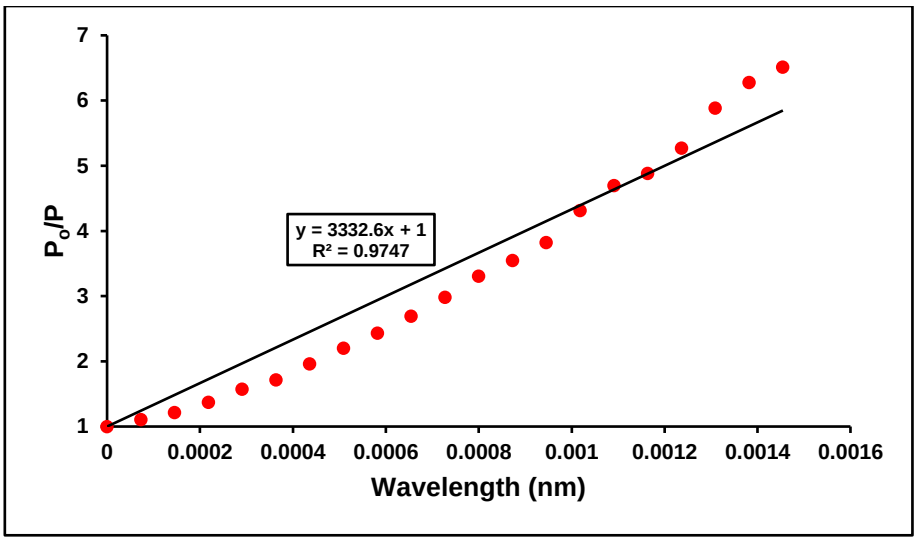

Figure 4.81 – Stern-Volmer plot of the emission intensity of the complex versus concentration of $Fe(CN)_6^{4-}$ to determine the quenching constant (top – emission intensity monitored at 363nm and bottom – emission intensity monitored at 380nm).

K_{sv} = 3.60 x $10^3 M^{-1}$ at 363nm and K_{sv} = 3.32 x $10^3 M^{-1}$ at 380nm.

A summary of the results of the Stern-Volmer quenching constants (K_{sv}) obtained from the ferrocyanide quenching of $[Ir(dppz)_2(qtpy)]^{3+}$ in either 5mM tris, 5mM NaCl buffer, 5mM tris, 25mM NaCl buffer, or 5mM tris, 50mM NaCl buffer in the absence of CT-DNA, and in the presence of 1-fold CT-DNA and 3-fold excess CT-DNA is given in Tables 4.7 and Table 4.8 for the emission at 363nm and 380nm, respectively. In 5mM tris, 5mM NaCl buffer, the values of the quenching constants obtained are pretty constant whether CT-DNA is present or not and

there is no pronounced difference whether 1-fold or 3-fold excess CT-DNA was used. In 5mM tris, 25mM NaCl buffer, the value of the quenching constant is highest in the absence of CT-DNA and decreases accordingly as more CT-DNA was added. In 5mM tris, 50mM NaCl buffer, the same quenching observation as for 5mM tris, 25mM NaCl buffer applies - quenching is highest in the absence of CT-DNA and lowest when 3-fold CT-DNA was added. Further insight into the results show that quenching of $[Ir(dppz)_2(qtpy)]^{3+}$ proceeded most rapidly in 5mM tris, 25mM NaCl buffer solution.

Table 4.7 – Ferrocyanide Quenching Data for the Interaction of $[Ir(dppz)_2(qtpy)]^{3+}$ without and with DNA. Emission wavelength monitored = 363nm.

Buffer	Without CT-DNA	With CT-DNA (1-fold)	With CT-DNA (3-fold excess)
5mM tris, 5mM NaCl buffer	$3.34 \times 10^3 M^{-1}$	$3.67 \times 10^3 M^{-1}$	$3.14 \times 10^3 M^{-1}$
5mM tris, 25mM NaCl buffer	$8.14 \times 10^3 M^{-1}$	$6.50 \times 10^3 M^{-1}$	$5.68 \times 10^3 M^{-1}$
5mM tris, 50mM NaCl buffer	$1.05 \times 10^5 M^{-1}$	$3.19 \times 10^3 M^{-1}$	$3.60 \times 10^3 M^{-1}$

Table 4.8 – Ferrocyanide Quenching Data for the Interaction of $[Ir(dppz)_2(qtpy)]^{3+}$ without and with DNA. Emission wavelength monitored = 380nm.

Buffer	Without CT-DNA	With CT-DNA (1-fold)	With CT-DNA (3-fold excess)
5mM tris, 5mM NaCl buffer	$3.13 \times 10^3 M^{-1}$	$3.52 \times 10^3 M^{-1}$	$3.71 \times 10^3 M^{-1}$
5mM tris, 25mM NaCl buffer	$8.14 \times 10^3 M^{-1}$	$5.99 \times 10^3 M^{-1}$	$5.20 \times 10^3 M^{-1}$

5mM tris, 50mM NaCl buffer	$9.47 \times 10^4 M^{-1}$	$2.75 \times 10^3 M^{-1}$	$3.32 \times 10^3 M^{-1}$

4.6.4 Quenching of $[Ir(N–N)_2(qtpy)]^{3+}$'s Emission by 5'-Guanosine Monophosphate (where N–N = bpy, phen, or dppz)

Previous studies using photo-redox active metal complexes have demonstrated that G-rich sequences, particularly runs of neighbouring G-sites, are susceptible to redox[23–24] even when distal to the metal complex binding site.[25–28]

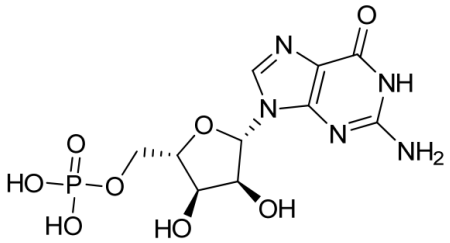

Figure 4.82 – Structure of the nucleotide 5'-GMP.

The quenching of the excited state of iridium complexes by photoredox processes can be monitored by the addition of 5'-guanine monophosphate (5'-GMP) (Fig. 4.82) using the previously stated Stern-Volmer relationship. Therefore, the emission profiles of aqueous solutions of reported iridium(III) complexes upon successive additions of 5'-GMP were monitored. As the luminescence of each of the complexes decreases upon the addition of 5'-GMP, it is assumed that the high-energy ^{3}MLCT excited state of all the complex is capable of photo-oxidising guanine/guanosine. As $[Ir(N–N)_2(qtpy)]^{3+}$ strongly luminesce in water, without possessing light-switch behaviour, it is possible that a photo-induced proton-coupled electron transfer can occur with 5'-GMP. In the following subsection, the redox photo-oxidising properties of $[Ir(N–N)_2(qtpy)]^{3+}$ is presented.

The classical Stern-Volmer equation followed for the evaluation of the quenching constant in the photooxidation of the investigated complexes is given in the figure below (Fig. 4.83):

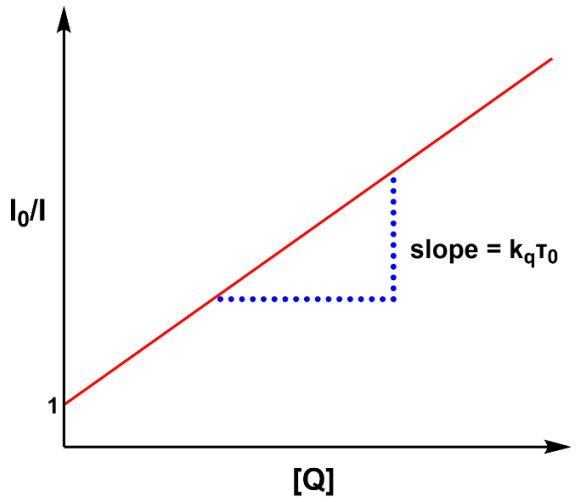

Figure 4.83 – Classical Stern-Volmer equation.

4.6.4.1 Quenching of $[Ir(bpy)_2(qtpy)]^{3+}$'s Emission by 5'-GMP

The emission of $[Ir(bpy)_2(qtpy)]^{3+}$ was quenched upon addition of increasing concentrations of 5'-GMP in air-saturated solutions at room temperature (Fig. 4.84).

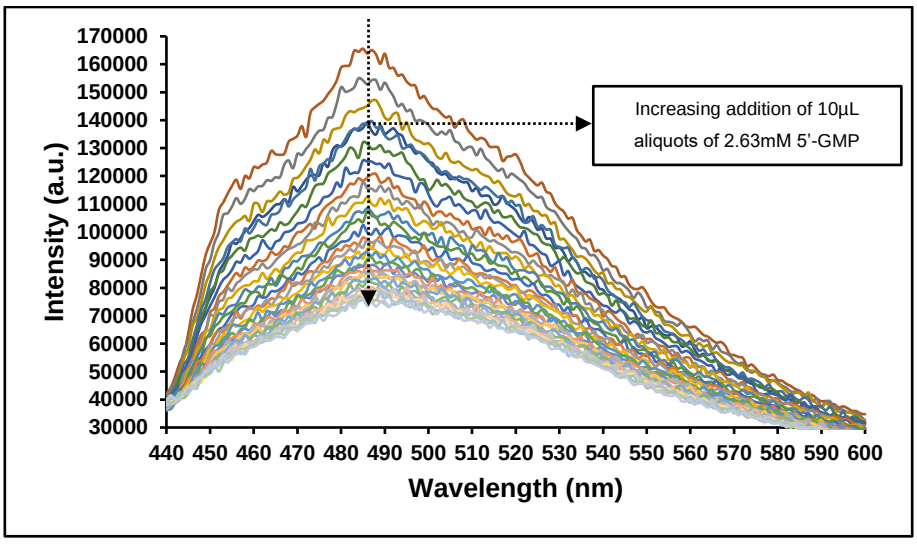

Figure 4.84 – Subsequent decrease in the emission intensity of 100µM $[Ir(bpy)_2(qtpy)]^{3+}$ upon successive addition of 2.63mM 5'-GMP. Excitation wavelength: 310nm. Emission region: 440–600nm. Excitation slit width: 5nm. Emission slit width: 5nm.

Data Fitting

Using Stern-Volmer kinetics, the quenching rate constant was calculated to be 1.24 x $10^{10}dm^3$ $mol^{-1}s^{-1}$ (Fig. 4.85), which is more or less of the same magnitude as that of $[Ir(bpy)_2(dppz)]^{3+}$

(1.25 x10^{10}dm^{3}mol^{-1}s^{-1}) previously reported. This indicates that the complex is a powerful photooxidiser.

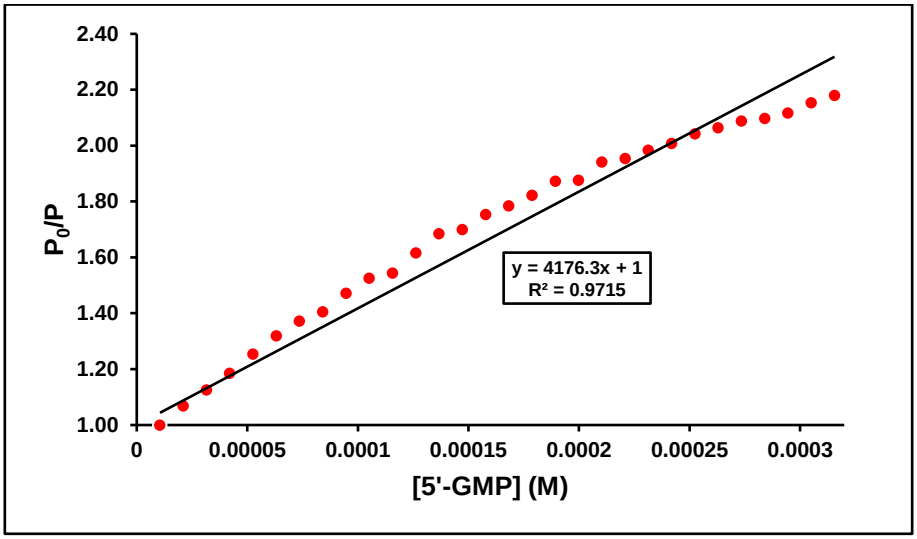

Figure 4.85 – A Stern-Volmer plot of the integrated intensity of $[Ir(bpy)_2(qtpy)]^{3+}$ versus concentration of 5'-GMP to determine the quenching rate. P_0 = phosphorescence intensity of the complex before the addition of 5'-GMP and P = phosphorescence intensity of the complex upon sequential addition of 5'-GMP. τ_0 = 305.52ns.

4.6.4.2 Binding Interaction of $[Ir(bpy)_2(qtpy)]^{3+}$ with 5'-GMP

Binding constants were calculated by fitting the experimental data to a binding isotherm using 14Allmaster, a macro-based Excel fitting programme written by Prof. Christopher A Hunter of the University of Cambridge. K_b was estimated to be 7.54 x 10^3 M^{-1}.

4.6.4.3 Quenching of $[Ir(bpy)_2(qtpy)]^{3+}$'s Emission by 5'-AMP

Adenosine monophosphate (AMP), also known as 5'-adenylic acid (Fig. 4.86), is the second most readily oxidized nucleotide, therefore, the interaction of AMP with $[Ir(N–N)_2(qtpy)]^{3+}$ (where N–N = bpy, phen, or dppz) was also investigated to see whether the introduction of AMP leads to quenching of the emission of the metal complexes.

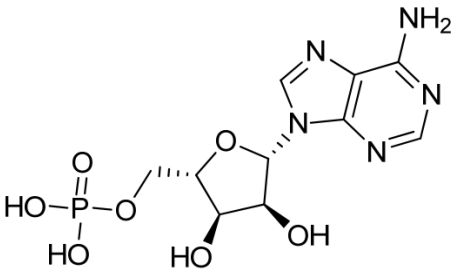

Figure 4.86 – Structure of the nucleotide 5'-AMP.[28]

Therefore, using the same procedure used to probe the emission quenching and binding of 5'-GMP, were investigated, the quenching and binding interactions of 5'-AMP with $[Ir(bpy)_2(qtpy)]^{3+}$ were studied (Fig. 4.87).

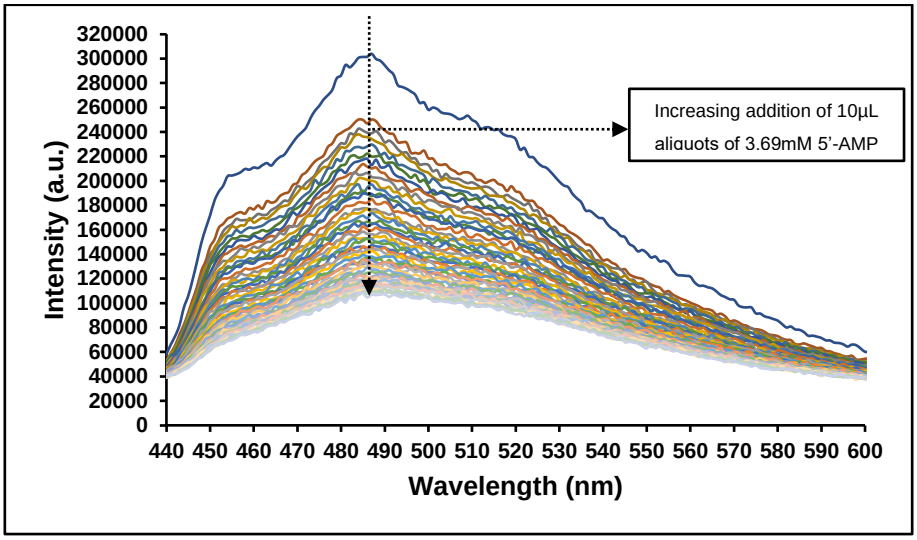

Figure 4.87 – Decrease in the emission intensity of 100µM $[Ir(bpy)_2(qtpy)]^{3+}$ upon successive addition of 3.69mM 5'-AMP. Excitation wavelength: 310nm. Emission region: 440–600nm. Excitation slit width: 5nm. Emission slit width: 5nm. P_0 = phosphorescence intensity of the complex before the addition of 5'-AMP and P = phosphorescence intensity of the complex upon sequential addition of 5'-AMP.

Data Fitting

Using Stern-Volmer kinetics, the quenching rate constant was calculated to be 7.64 x 10^9 dm^3 mol^{-1} s^{-1} (Fig. 4.88). This suggests that the complex is a potent photo-oxidising agent.

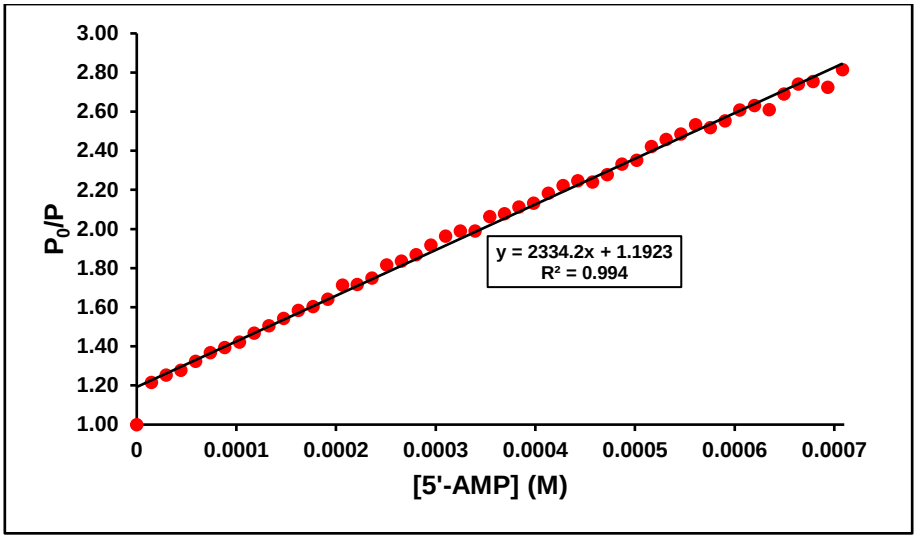

Figure 4.88 – A Stern-Volmer plot of the integrated intensity of $[Ir(bpy)_2(qtpy)]^{3+}$ versus concentration of 5'-AMP to determine the quenching rate. τ_0 = 305.52ns.

Moreover, K_q for $[Ir(bpy)_2(qtpy)]^{3+}$ by 5'-AMP is lesser than K_q for $[Ir(bpy)_2(qtpy)]^{3+}$ by 5'-GMP.

4.6.4.5 Quenching of $[Ir(phen)_2(qtpy)]^{3+}$'s Emission by 5'-GMP

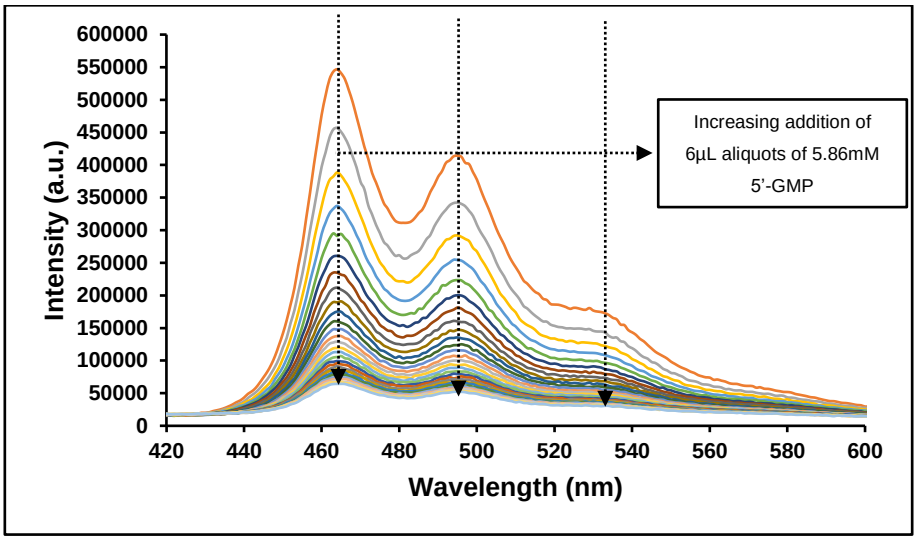

Figure 4.89 – Emission intensity of 10.45µM $[Ir(phen)_2(qtpy)]^{3+}$ upon successive addition of 5.86mM 5'-GMP. Excitation wavelength: 316nm. Emission region: 420–600nm. Excitation slit width: 5nm. Emission slit width: 5nm.

Data Fitting

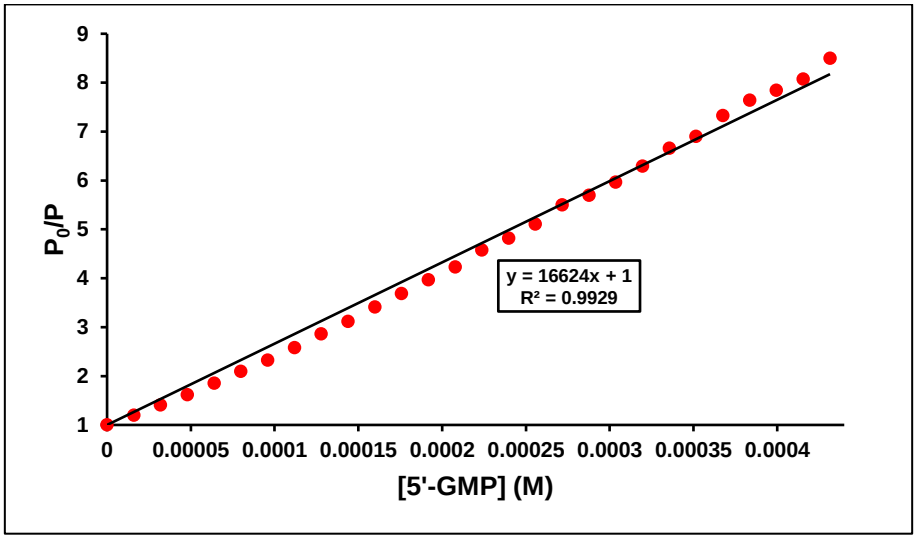

Figure 4.90 – A Stern-Volmer plot of the integrated intensity of $[Ir(phen)_2(qtpy)]^{3+}$ versus concentration of 5'-GMP to determine the quenching rate. Wavelength monitored = 464nm. P_0 = phosphorescence intensity of the complex before the addition of 5'-GMP and P = phosphorescence intensity of the complex upon sequential addition of 5'-GMP. τ_0 = 305.52ns.

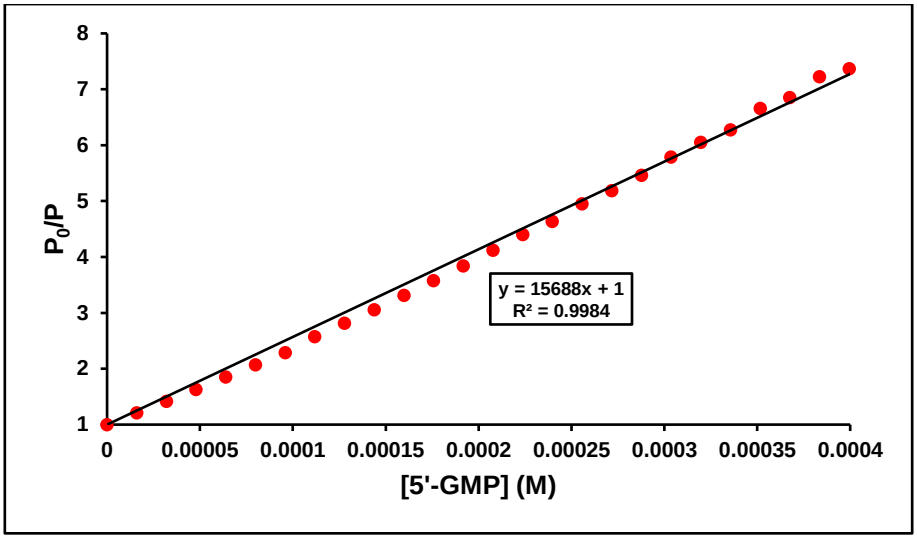

Figure 4.91 – A Stern-Volmer plot of the integrated intensity of $[Ir(phen)_2(qtpy)]^{3+}$ versus concentration of 5'-GMP to determine the quenching rate. Wavelength monitored = 494nm. P_0 = phosphorescence intensity of the complex before the addition of 5'-GMP and P = phosphorescence intensity of the complex upon sequential addition of 5'-GMP. τ_0 = 305.52ns.

Using Stern-Volmer kinetics, the quenching rate constant was calculated to be 5.44 x 10^{10} dm^3 mol^{-1} s^{-1} if we choose to monitor the emission at 464nm (Fig. 4.90) or 5.13 x 10^{10} dm^3 mol^{-1} s^{-1} if we choose to monitor the emission at 494nm (Fig. 4.91). The magnitude of the K_q for $[Ir(phen)_2(qtpy)]^{3+}$ is greater than that of $[Ir(phen)_2(dppz)]^{3+}$ (2.78 x$10^{10}$$dm^3$$mol^{-1}$$s^{-1}$) previously reported. This suggests that the complex is a potent photo-oxidising agent.

4.6.4.6 Quenching of $[Ir(phen)_2(qtpy)]^{3+}$'s Emission by 5'-AMP

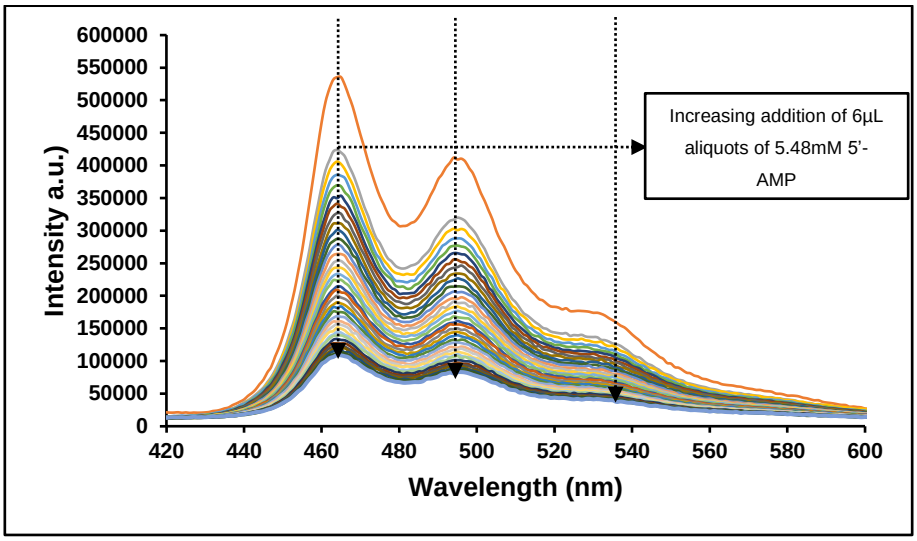

Figure 4.92 – Emission intensity of 10.45µM $[Ir(phen)_2(qtpy)]^{3+}$ upon successive addition of 5.48mM 5'-AMP. Excitation wavelength: 316nm. Emission region: 420–600nm. Excitation slit width: 5nm. Emission slit width: 5nm.

Data Fitting

The data in the figure above were fitted to the Stern-Volmer plots below (Figs. 4.93 and 4.94):

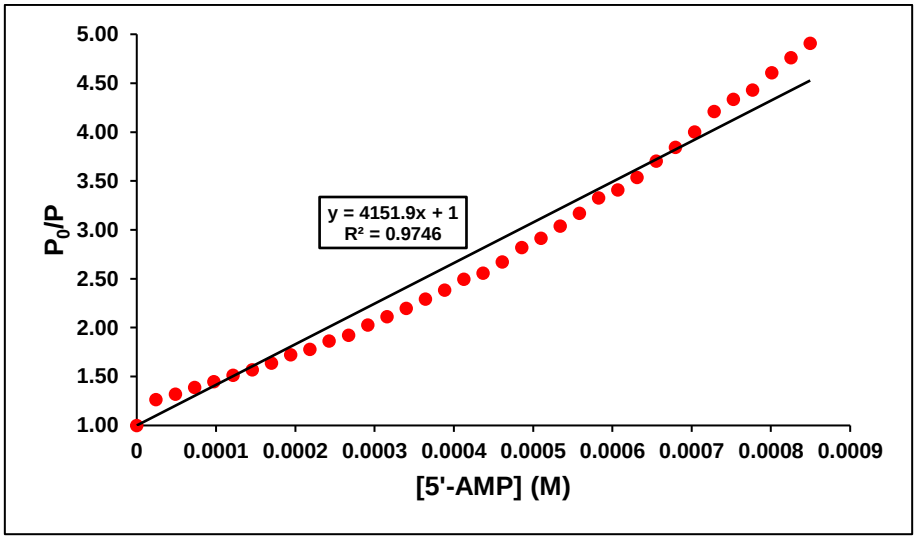

Figure 4.93 – A Stern-Volmer plot of the integrated intensity of $[Ir(phen)_2(qtpy)]^{3+}$ versus concentration of 5'-GMP to determine the quenching rate. Wavelength monitored = 464nm. P_0 = phosphorescence intensity of the complex before the addition of 5'-AMP and P = phosphorescence intensity of the complex upon sequential addition of 5'-AMP. τ_0 = 305.52ns.

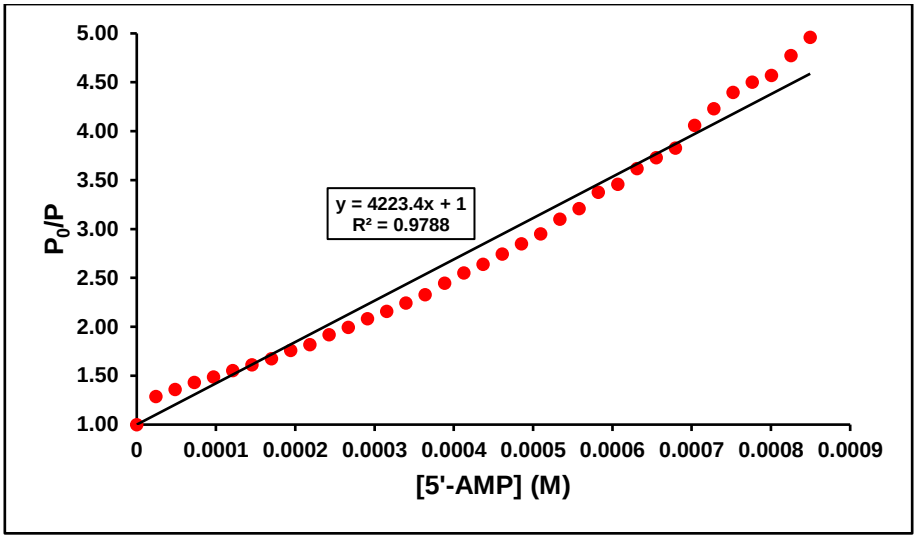

Figure 4.94 – A Stern-Volmer plot of the integrated intensity of $[Ir(phen)_2(qtpy)]^{3+}$ versus concentration of 5'-GMP to determine the quenching rate. Wavelength monitored = 494nm. P_0 = phosphorescence intensity of the complex before the addition of 5'-AMP and P = phosphorescence intensity of the complex upon sequential addition of 5'-AMP. τ_0 = 305.52ns.

Using Stern-Volmer kinetics, the quenching rate constant was calculated to be 1.36 x 10^{10} dm^3 mol^{-1} s^{-1} if we choose to monitor the emission at 464nm (Fig. 4.93) or 1.38 x 10^{10} dm^3 mol^{-1} s^{-1} if we choose to monitor the emission at 494nm (Fig. 4.94).

Generally, K_q for $[Ir(phen)_2(qtpy)]^{3+}$'s quenching by 5'-AMP is ca. 5 times lesser than K_q for $[Ir(phen)_2(qtpy)]^{3+}$'s quenching by 5'-GMP.

4.6.4.7 Quenching of $[Ir(dppz)_2(qtpy)]^{3+}$'s Emission by 5'-GMP

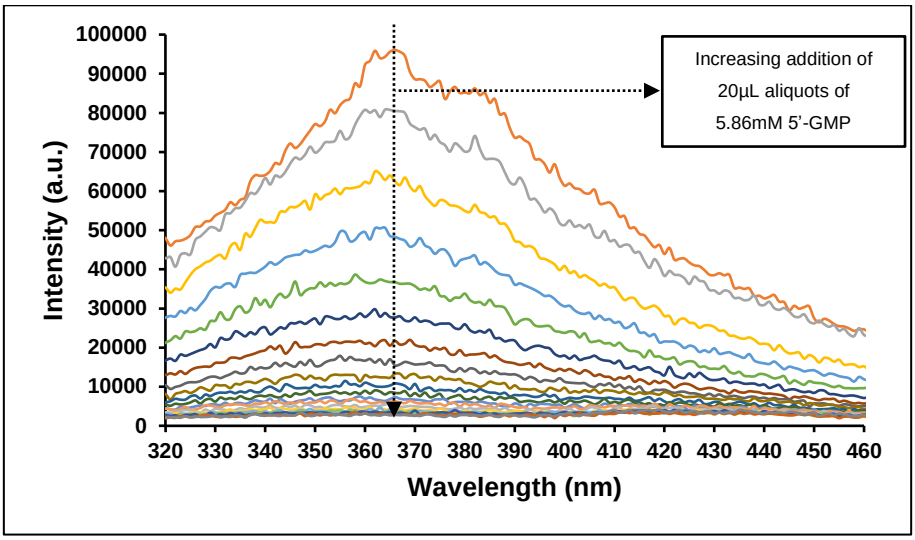

Figure 4.95 – Emission intensity of 13.36µM $[Ir(dppz)_2(qtpy)]^{3+}$ upon successive additions of 5.86mM 5'-GMP. Excitation wavelength: 282nm. Emission region: 320–460nm. Excitation slit width: 5nm. Emission slit width: 5nm.

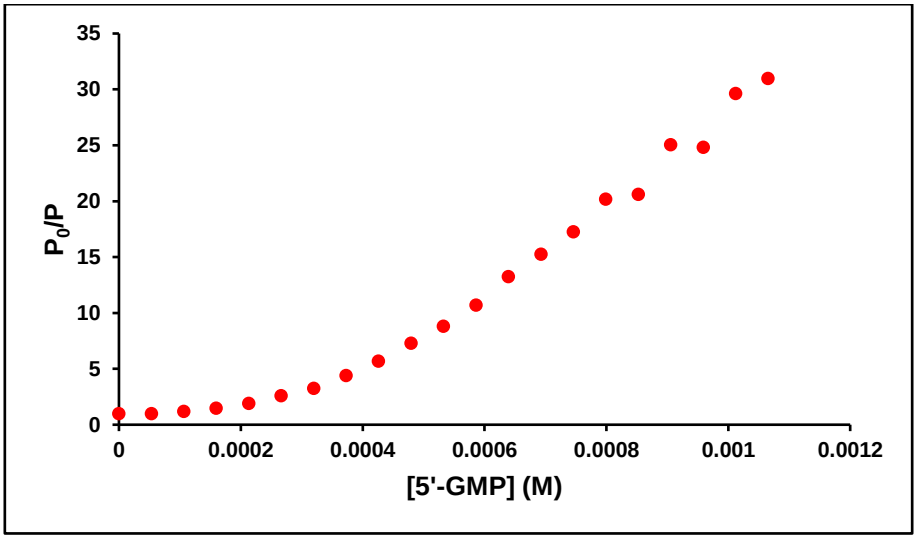

Figure 4.96 – A Stern-Volmer plot of the integrated intensity of $[Ir(dppz)_2(qtpy)]^{3+}$ versus concentration of 5'-GMP to determine the quenching rate. Wavelength monitored = 365nm. P_0 = phosphorescence intensity of the complex before the addition of 5'-GMP and P = phosphorescence intensity of the complex upon sequential addition of 5'-GMP. τ_0 = 305.52ns.

The above quenching is not linear, and so, static quenching may be occurring.

4.6.4.8 Quenching of $[Ir(dppz)_2(qtpy)]^{3+}$'s Emission by 5'-AMP

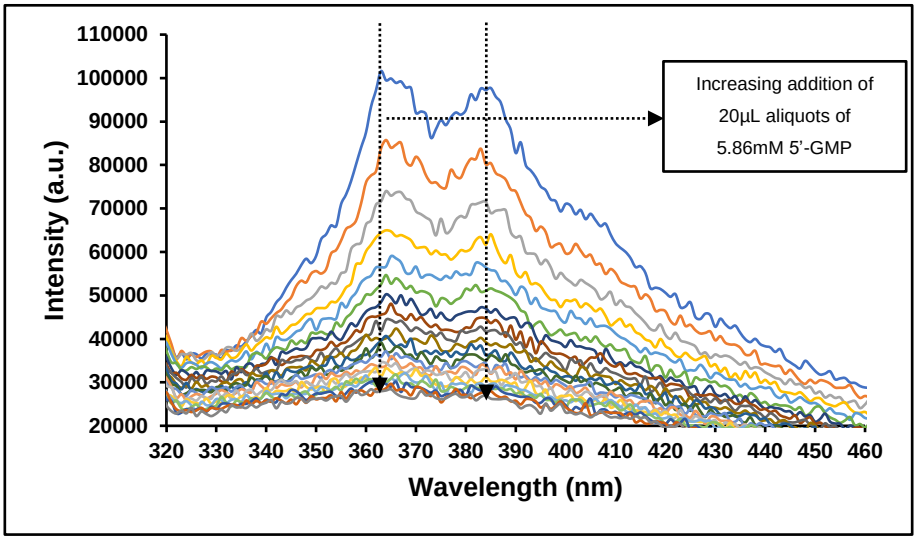

Figure 4.97 – Emission intensity of 13.36µM $[Ir(dppz)_2(qtpy)]^{3+}$ upon successive additions of 5.48mM 5'-AMP. Excitation wavelength: 282nm. Emission region: 320–460nm. Excitation slit width: 5nm. Emission slit width: 5nm.

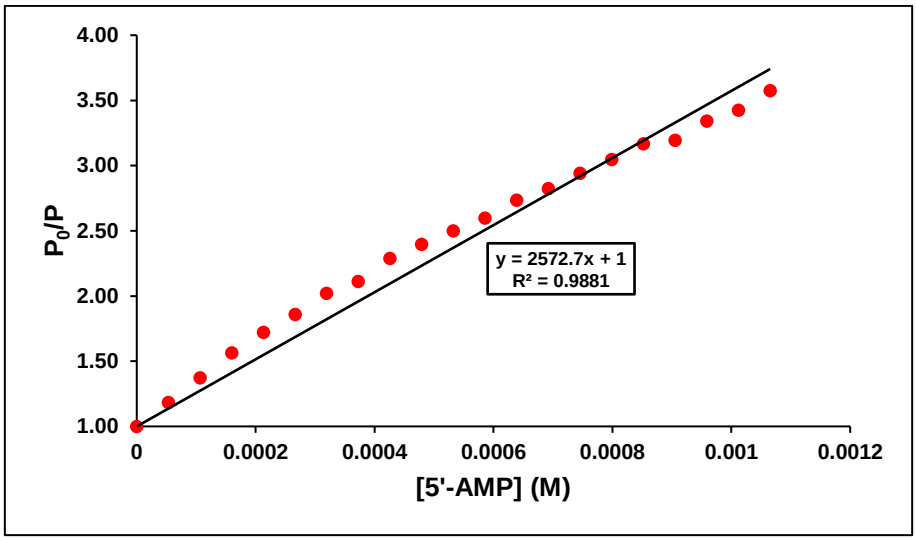

Figure 4.98 – A Stern-Volmer plot of the integrated intensity of $[Ir(dppz)_2(qtpy)]^{3+}$ versus concentration of 5'-AMP to determine the quenching rate. Wavelength monitored = 365nm. P_0 = phosphorescence intensity of the complex before the addition of 5'-AMP and P = phosphorescence intensity of the complex upon sequential addition of 5'-AMP. τ_0 = 305.52ns.

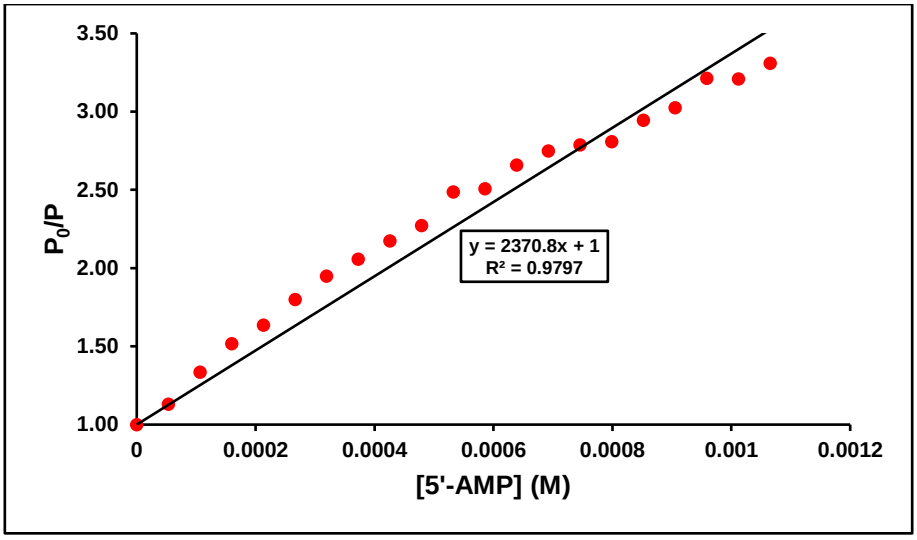

Figure 4.99 – A Stern-Volmer plot of the intensity of $[Ir(dppz)_2(qtpy)]^{3+}$ versus concentration of 5'-AMP to determine the quenching rate. Wavelength monitored = 383nm. P_0 = phosphorescence intensity of the complex before the addition of 5'-AMP and P = phosphorescence intensity of the complex upon sequential addition of 5'-AMP. τ_0 = 305.52ns.

Using Stern-Volmer kinetics, the quenching rate constant was calculated to be 8.42 x $10^9 dm^3$ mol^{-1} s^{-1} if we choose to monitor the emission at 365nm (Fig. 4.98) or 7.76 x $10^9 dm^3$ mol^{-1} s^{-1} if we choose to monitor the emission at 383nm (Fig. 4.99).

The three investigated complexes were sufficiently quenched by 5'-GMP in an order of magnitude higher compared to their Ru(II) analogues. $[Ru(TAP)_2(dppz)]^{2+}$, for instance, possesses a 5'-GMP quenching rate of K_q = 1.7 x $10^9 dm^3 mol^{-1} s^{-1}$.[29]

4.6.6 Agarose Gel Electrophoresis

Electrophoresis is defined by the migration of charged particles upon the induction of an electric field (Fig. 4.100). Metal-ion-induced DNA endonucleolytic reactions have been of considerable interest for some time.[30–32]

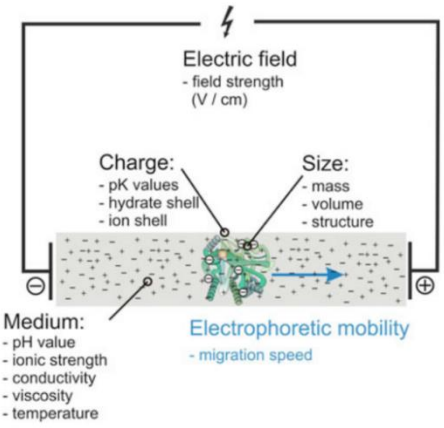

Electrophoresis setup, Figure 4.100 – The dependence of the electrophoretic mobility of an ionised compound (here a protein molecule) on its own properties and the properties of the separation medium.[33]

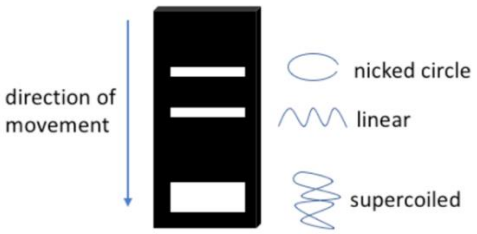

Figure 4.101 – Schematic showing the different types of plasmid DNA produced after photocleavage and how they separate using gel electrophoresis.

Agarose gel electrophoresis is perhaps the most commonly used method for the size-and shape-based separation of DNA molecules, such as plasmid DNA. The electrophoretic mobility of the DNA fragments using this technique is considerably affected by both their size and shape. Superhelically packed circular plasmid DNA has a very compact structure, and this smaller hydrodynamic size increases the electrophoretic mobility compared to linear DNA. Cutting one of the strands ensues in the unravelling of DNA to adopt a much more relaxed circular form analogously to an elastic band. With increased scission, the plasmid DNA adopts a linear conformation. As this structure is not globular, it can travel faster than the single-strand break form through the agarose gel (Fig. 4.101). The photonuclease activity of complex $[Ir(bpy)_2(qtpy)]^{3+}$ was studied using supercoiled pBR322 in 5mMtris, 25mM NaCl buffer under both unilluminated and illuminated conditions with a bit of modification in the experimental conditions in all experiments conducted (365nm, 125mV, 10minutes exposure) (Figs. 4.102–4.104).[34]

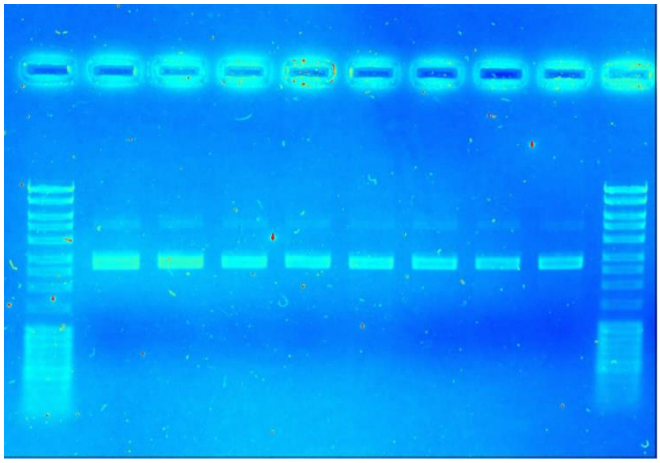

Figure 4.102 – Photocleavage of supercoiled pBR322 DNA by $[Ir(bpy)_2(qtpy)]^{3+}$, **1**, (no illumination, i.e., in the dark) in 5mM Tris, 25mM NaCl buffer. (Right to left) Lane 1: 1X Mass Ruler DNA Ladder; Lane 2: DNA control; Lane 3: DNA + complex (1X of the complex, 10µM); lane 4: DNA + complex (2X of the complex, 20µM); lane 5: DNA + complex (3X of the complex, 30µM); Lanes 6 to 9 are simply a repetition of Lanes 2–5; Lane 10: 1X Mass Ruler DNA Ladder. Gel ran at 100mV for 25 minutes.

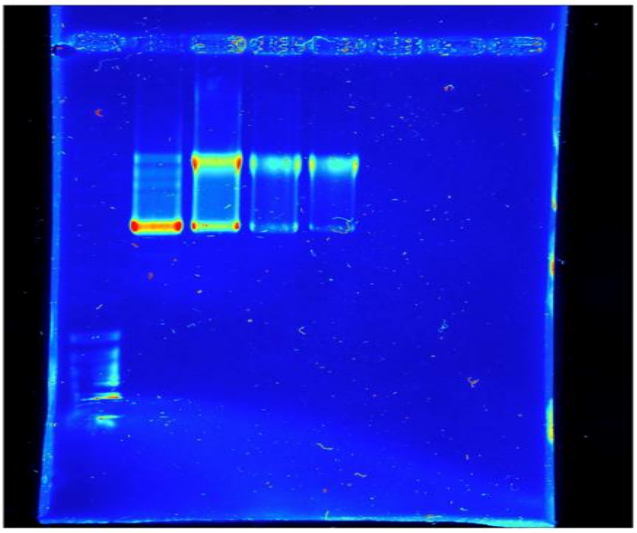

Figure 4.103 – Photocleavage of supercoiled pBR322 DNA by $[Ir(bpy)_2(qtpy)]^{3+}$, **1**, (with illumination) in 5mM Tris, 25mM NaCl buffer. (Right to left) Lane 1: 50bp 1X Mass Ruler DNA Ladder; Lane 2: DNA control; Lane 3: DNA + complex (1X of the complex, 10µM); lane 4: DNA + complex (2X of the complex, 20µM); lane 5: DNA + complex (3X of the complex, 30µM); Lane 6: DNA Gel Loading Dye; Lane 7: DNA Gel Loading Dye; Lane 8: DNA Gel Loading Dye. Gel ran at 100mV for 25 minutes.

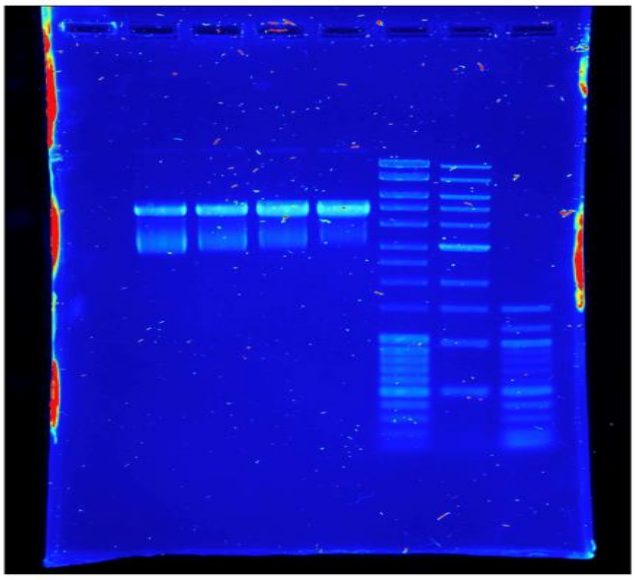

Figure 4.104 – Photocleavage of supercoiled pBR322 DNA by $[Ir(bpy)_2(qtpy)]^{3+}$, **1**, (with illumination) in 5mM Tris, 25mM NaCl buffer. (Right to left) Lane 1: DNA Gel Loading Dye; Lane 2: DNA control; Lane 3: DNA + complex (1X of the complex, 10µM); lane 4: DNA + complex (2X of the complex, 20µM); lane 5: DNA + complex (3X of the complex, 30µM); Lane 6: MassRuler DNA Ladder; Lane 7: MassRuler DNA Ladder; Lane 8: MassRuler DNA Ladder. Gel ran at 100mV for 25 minutes.

$[Ir(bpy)_2(qtpy)]^{3+}$ exhibits an interesting electrophoretic impact on the supercoiled form(I) of DNA in agarose gel. In the dark, there was no cleavage whatsoever observed. The photoirradiation of complex $[Ir(bpy)_2(qtpy)]^{3+}$ in the presence of the plasmid DNA pBR322 led to the cleavage of the supercoiled form (I) of DNA to the nicked form (II) of DNA in a concentration-dependent manner, and 30µM of the complex proved sufficient for the progression of supercoiled DNA cleavage.[35]

Due to constraints imposed by the COVID-19 pandemic, the gel electrophoretic studies of $[Ir(phen)_2(qtpy)]^{3+}$ and $[Ir(dppz)_2(qtpy)]^{3+}$ could not be progressed.

4.6.8 Molecular Docking Analysis

The binding of Complexes **1**, **2**, and **3** to duplex DNA was studied via molecular docking. This computational method is renowned for predicting the binding energy and pose of molecules with biological targets[36–37] The binding poses demonstrates that Complexes **1**, **2**, and **3** are intercalators as they incorporate ancillary ligands which are made of polypyridyl rings that

form π-π stacking interactions (Figs. 4.105–4.107) between adjacent DNA base pairs. The DNA-ligand complex formed is stabilised by these interactions with Complex **1** having the largest number of π-π stacking interactions compared to Complexes **2** and **3**. Complex **3** shows only one π-π stacking interaction with the other interactions being a π-anion and hydrogen bond interaction. The binding poses of the complexes indicate that they will be intercalators that will bring strong perturbation in the duplex DNA as they only interact with the guanine and cytosine base pairs. Both Complexes **2** and **3** have a negative binding energy (Table 4.9) where a negative binding energy implies good binding with the DNA target. Moreover, Complex **1** has a larger binding energy of -7.39 kcal/mol, which correlates with it having the highest number of π-π stacking interactions. However, Complex **3** gave a positive value of 1.16 kcal/mol, which is evident in the few interactions it has with the duplex DNA target. Complex **3** only interacts with GUA13, unlike the other two complexes, which interact with CYT12, GUA13, GUA5 and CYT4 base pairs. The physicochemical properties (Table 4.9) depict that both Complexes **1** and **2** violate the Lipinski's rule of five[38] for the drug-likeness of a molecule by exceeding the recommended molecular weight of 500 and also logP value of 5. However, other properties, such as the total polar surface area (TPSA), fall within the recommended range of being less than 100 Å^2.[39–40]

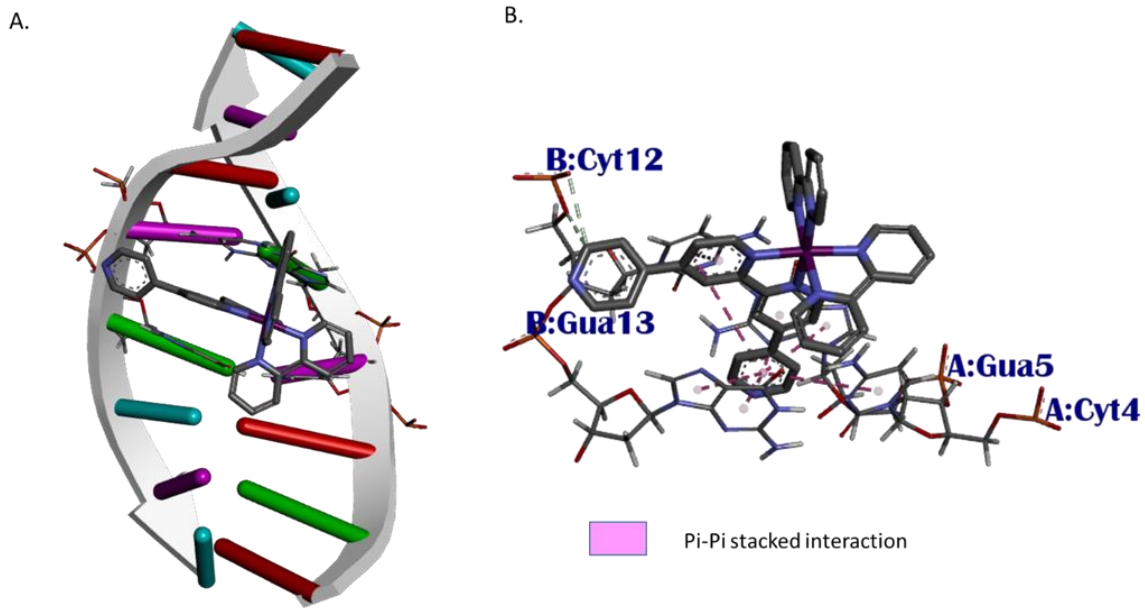

Figure 4.105 – The **(a)** binding mode and **(b)** molecular interaction of Complex **1** in duplex DNA.

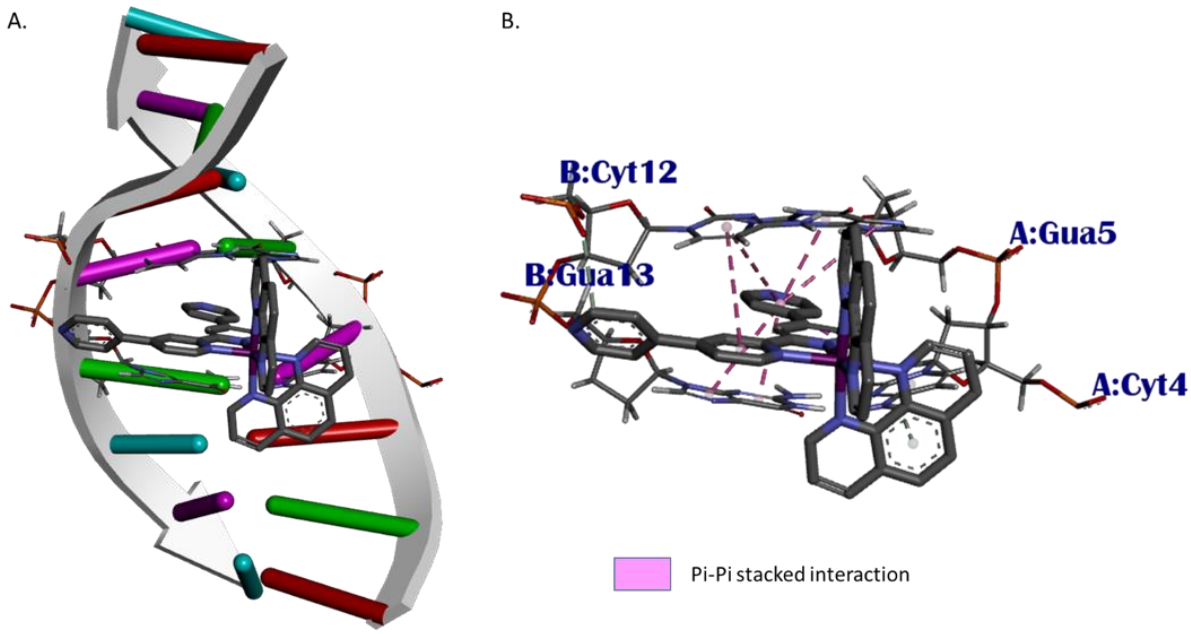

Figure 4.106 – The **(a)** binding mode and **(b)** molecular interaction of Complex **2** in duplex DNA.

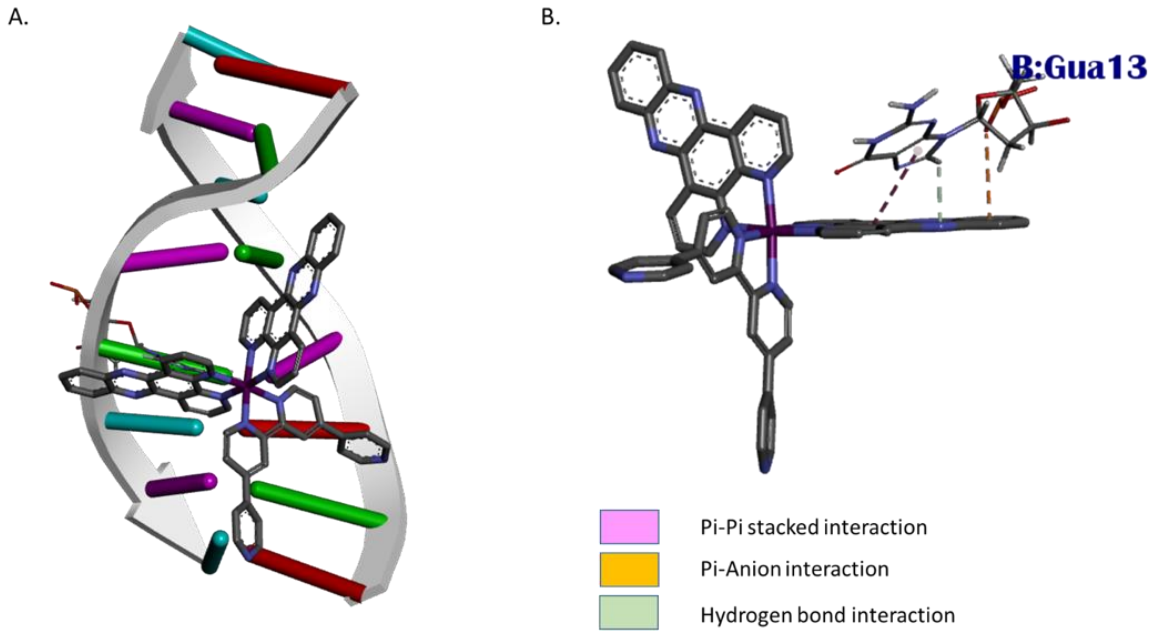

Figure 4.107 – The **(a)** binding mode and **(b)** molecular interaction of Complex **3** in duplex DNA.

Table 4.9 – The physicochemical properties of the promising complexes.

Parameter	Complex 1	Complex 2
Formula	$C_{40}H_{30}IrN_8$	$C_{44}H_{30}IrN_8$

Binding Energy (kcal/mol)	-7.14	-7.39
TPSA	55.39	55.39
Number of atoms	49	53
MW	814.95	863
HBA	8	8
HBD	0	0
Rotational bonds	2	2

4.6.9 Duplex DNA-Binding Studies Summary

The duplex DNA-binding properties of iridium (III) polypyridyl complexes $[Ir(bpy)_2(qtpy)]^{2+}$ (**1**), $[Ir(phen)_2(qtpy)]^{3+}$ (**2**) and $[Ir(dppz)_2(qtpy)]^{2+}$ (**3**) form the focus of research investigation in this chapter. All of these complexes incorporate a qtpy moiety.

The three complexes bind with DNA in cell-free conditions. DNA-engendered luminescent quenching is a well-studied phenomenon, with work showing that complexes containing organic-based intercalators are strongly oxidising and capable of directly oxidising guanine-abundant sites. This quenching is mainly due to electron transfer from photo-oxidised guanine sites, however, it can also involve adenine sites, depending on the redox potentials.[41–43] 3D DNA-binding experiments further corroborated the result of the luminescence binding investigations. As well as spectrophotometric experiments, there is scope to use cyclic voltammetry to determine binding interactions with DNA. The electrochemical behaviour of the iridium complexes in the absence and presence of DNA can be measured. If there is a dramatic shift in both the cathodic and anodic peak potential, it can be deduced that the complexes have the ability to bind into DNA. The net shift in the potential can be used to estimate the equilibrium constants for the binding of the complexes to DNA.[44] To create a complete thermodynamic profile of the interaction of these metal complexes with DNA could be investigated using isothermal titration calorimetry. This technique directly measures the heat either released or absorbed in a biomolecular binding event, enabling accurate determinations of binding constants, enthalpy (ΔH), and entropy (ΔS).

Additional investigations into the decrease in the luminescence of the complexes upon titration of DNA were undertaken. Titration experiments with 5-GMP (and 5'-AMP) confirm that quenching displaying Stern-Volmer kinetics occurs as a result of redox chemistry between the metal complex and guanine sites. $[Ir(dppz)_2(qtpy)]^{2+}$ gave the highest value of the quenching constant (K_q) for 5-GMP oxidation and lowest value of 5'-AMP oxidation. A future experiment could be using Complexes **1–3** to introduce a photo-excited hole into the DNA helix at a specific site, using a linker, to evaluate oxidative damage to the strand from a distance. Barton *et al.* document this well, demonstrating that by using piperidine, the oxidative damage site can be changed into a cleavage site, ejecting the damaged guanine base. This approach can be used to monitor the extent of oxidative damage as a result of "hole migration" along the DNA π-stack.[45]

Gel electrophoresis for $[Ir(bpy)_2(qtpy)]^{2+}$ was successfully launched. The possible photocleavage mechanisms of plasmid DNA for the indicated that singlet oxygen radicals promote the cleavage of DNA. To confirm this, gel electrophoresis under an argon atmosphere to monitor any photocleavage mechanisms in an oxygen-free environment should be carried in the future. Therefore, work on this issue could determine how much of each effect contributes to DNA damage. Given the well-established tunable nature of the excited states of Ir(III)-based polypyridyl complexes, the potential of these systems and their derivatives for a range of applications, including as sensitisers for photodynamic therapy, is apparent and should be part of the author's future investigations.

Molecular docking revealed that the three complexes bind to DNA via intercalation, and $[Ir(bpy)_2(qtpy)]^{3+}$ has the highest number of π-π stacking interactions with DNA and, therefore, the largest binding energy.

4.7 Introduction: G-quadruplex DNA-Binding Studies

G-quadruplexes (G4s) are four-stranded structures formed by guanine-rich nucleic acids. Any single-stranded (ss) DNA sequence containing four stretches of three or more consecutive guanines can fold into a G-quadruplex through Hoogsteen hydrogen bonding between guanines from each run. These interactions are additionally stabilised by monovalent cations such as Na^+

and K^+.[46] G4-forming sequences are highly abundant and fold into stable structures in human cells, with as many as 716, 310 unique G-quadruplexes identified within the human genome.[47] This staggering number of structures is not formed simultaneously, but any that persist can interfere with DNA metabolism. Small molecules that enhance G-quadruplex stability can disrupt DNA replication and RNA transcription by stalling the respective polymerases.[48–50]

Chapter One of this thesis has demonstrated the biological significance of the G-quadruplex DNA conformation, especially its relevance in the modulation of gene expression, epigenetics, nucleating of DNA replication and genetic disease. To demonstrate the potential of the reported iridium(III) complexes as sequence-selective probes, their G-quadruplex DNA binding ability are dealt with in this chapter. The G-quadruplex sequence studied in this section of the thesis is AGGGTTAGGGTTAGGGTTAGGG (22mer) or simply human telomere sequence (HTS) quadruplex (d[$AG_3(T_2AG_3)_3$]). All binding investigations of the three reported complexes with G-quadruplex DNA were undertaken analogously to their duplex DNA-binding studies using luminescence spectroscopy.

Experimental binding plots are given in Figs. 4.108–4.110. Experimental data were fitted to a standard binding isotherm to calculate binding constants. A summary of the binding parameters is given in Tables 4.10–4.12 below.

4.8 G4 HTS Binding Studies

4.8.1 $[Ir(bpy)_2(qtpy)]^{3+}$

The G4 HTS binding property of this compound follows the same luminescence quenching pattern as with its duplex DNA binding behaviour though the binding event proceeded much rapidly in this instance.

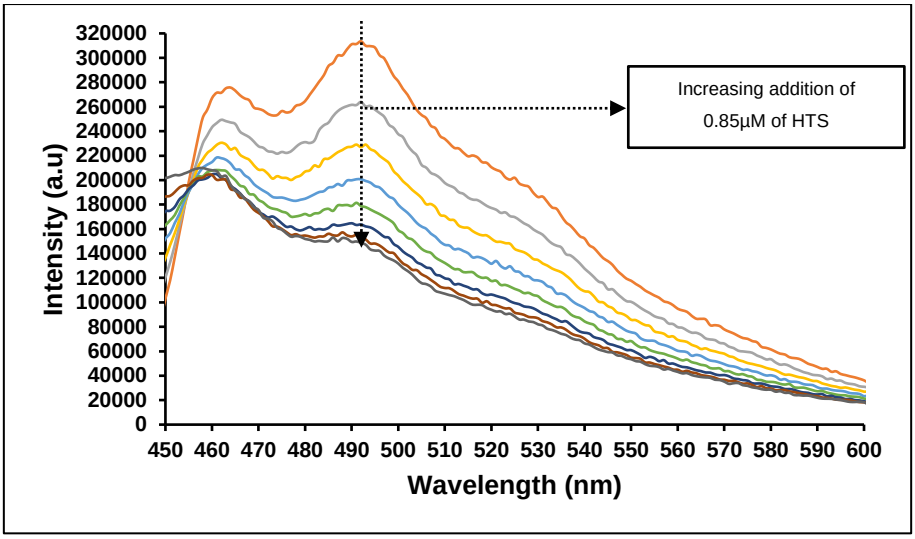

Figure 4.108 – Luminescent titration of 0.85µM HTS (G4 oligonucleotide sequence) into a solution of 0.84µM of $[Ir(bpy)_2(qtpy)]^{3+}$ in PBS buffer, pH 7.41 at 27°C. Excitation wavelength: 316nm; emission region: 450–600nm. Excitation slit width: 5nm. Emission slit width: 5nm.

Table 4.10 – G4 HTS binding parameters for $[Ir(bpy)_2(qtpy)]^{3+}$.

Complex	λ_{max} (nm) (aqueous)	λ_{max} (nm) (CT-DNA)	Binding affinity, K_b $[M^{-1}]$	% Bound
$[Ir(bpy)_2(qtpy)]^{3+}$	491	491	2.19×10^{13}	1

4.8.2 $[Ir(phen)_2(qtpy)]^{3+}$

Like what was obtained in the case of $[Ir(bpy)_2(qtpy)]^{3+}$, the G4 HTS binding property of $[Ir(phen)_2(qtpy)]^{3+}$ follow the same luminescence quenching pattern as with its binding to duplex DNA conformation though the binding event progressed quickly in this instance.

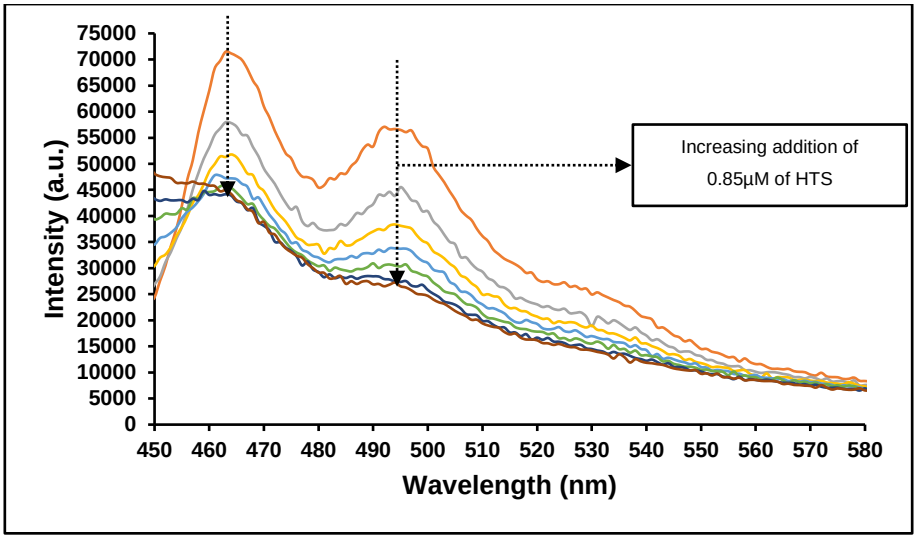

Figure 4.109 – Luminescent titration of 0.85µM HTS (G4 oligonucleotide sequence) into a solution of 12.45µM of $[Ir(phen)_2(qtpy)]^{3+}$ in PBS buffer, pH 7.41 at 27°C. Excitation wavelength: 316nm; emission region: 450–580nm. Excitation slit width: 5nm. Emission slit width: 5nm.

Table 4.11 – G4 HTS binding parameters for $[Ir(phen)_2(qtpy)]^{3+}$.

Complex	λ_{max} (nm) (aqueous)	λ_{max} (nm) (CT-DNA)	Binding affinity, K_b $[M^{-1}]$	% Bound
$[Ir(phen)_2(qtpy)]^{3+}$	464	464	8.74×10^4	18
$[Ir(dppz)_2(qtpy)]^{3+}$	494	494	9.33×10^4	19

4.8.3 $[Ir(dppz)_2(qtpy)]^{3+}$

Instead of luminescence quenching pattern observed in the cases of $[Ir(bpy)_2(qtpy)]^{3+}$ and $[Ir(phen)_2(qtpy)]^{3+}$, this compound exhibited luminescence enhancement in its binding to G4 HTS in sharp contrast to what was observed in its binding investigation to duplex DNA conformation.

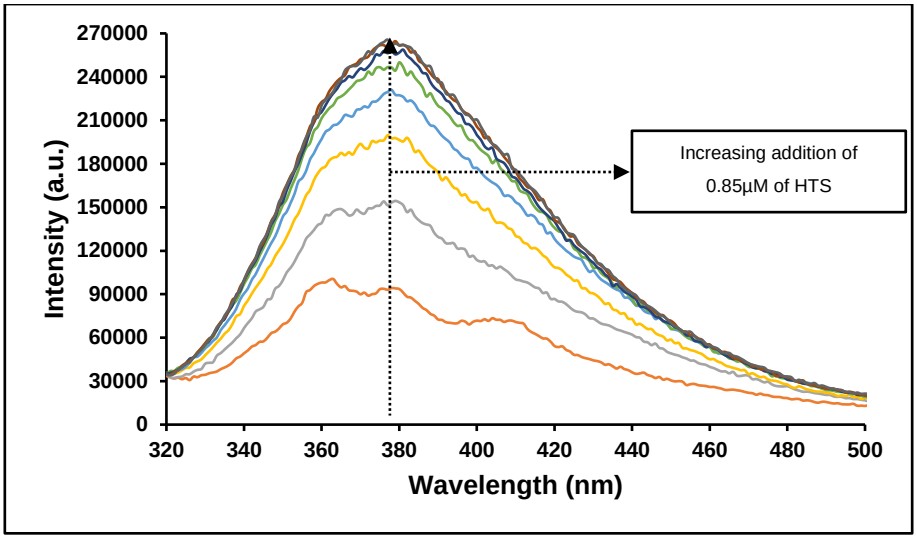

Figure 4.110 – Luminescent titration of 0.85µM HTS (G4 oligonucleotide sequence) into a solution of 55.82µM of $[Ir(dppz)_2(qtpy)]^{3+}$ in PBS buffer, pH 7.41 at 27°C. Excitation wavelength: 282nm; emission region: 320–500nm. Excitation slit width: 5nm. Emission slit width: 5nm.

Table 4.12 – G4 HTS binding parameters for $[Ir(dppz)_2(qtpy)]^{3+}$.

Complex	λ_{max} (nm) (aqueous)	λ_{max} (nm) (CT-DNA)	Binding affinity, K_b $[M^{-1}]$	% Bound
$[Ir(dppz)_2(qtpy)]^{3+}$	378	378	9.51×10^{12}	11

Except for the phen iridium(III) complex, the G-quadruplex DNA binding affinities of the bpy and dppz iridium(III) complexes are >2 times order of magnitude higher than their duplex-DNA binding affinities. The interpretation of this is that the complexes are better binders of G4 conformation than the duplex conformation and may be more effective as DNA metallodrugs that target specific sequences. Further insight into this will constitute part of the author's future research investigations.

Previous works have demonstrated stronger binding of oligonuclear transition metal complexes to G-quadruplex than duplex.[51–52] Whilst the estimated binding constants obtained in such studies are in the order of 10^6–$10^7 M^{-1}$, the binding constants obtained for G-quadruplex binding in this work seems unbelievably high, and are, therefore, inconclusive. Future attention will be turned to isothermal calorimetry (ITC) to obtain a more exact picture of the binding constants.[53]

4.9 Circular Dichroism Investigations of the Binding of $[Ir(N–N)_2(qtpy)]^{3+}$ (where N–N = bpy, phen, or dppz) with HTS Quadruplex

As G-quadruplex DNA is chiral, it is logical to undertake its metal complex-binding property using circular dichroism (CD). CD experimental technique as described in the preceding chapter is then used to probe the binding of the three iridium(III) complexes with Q-quadruplex DNA. G-quadruplex DNA gives characteristic CD signals in the 240–310nm range depending on the specific conformation of the G-quadruplex. The G-quadruplex studied herein is the antiparallel conformation, which shows specific CD bands at 245nm (positive), 260nm (negative), and 295nm (positive).[54]

4.9.1 $[Ir(bpy)_2(qtpy)]^{3+}$

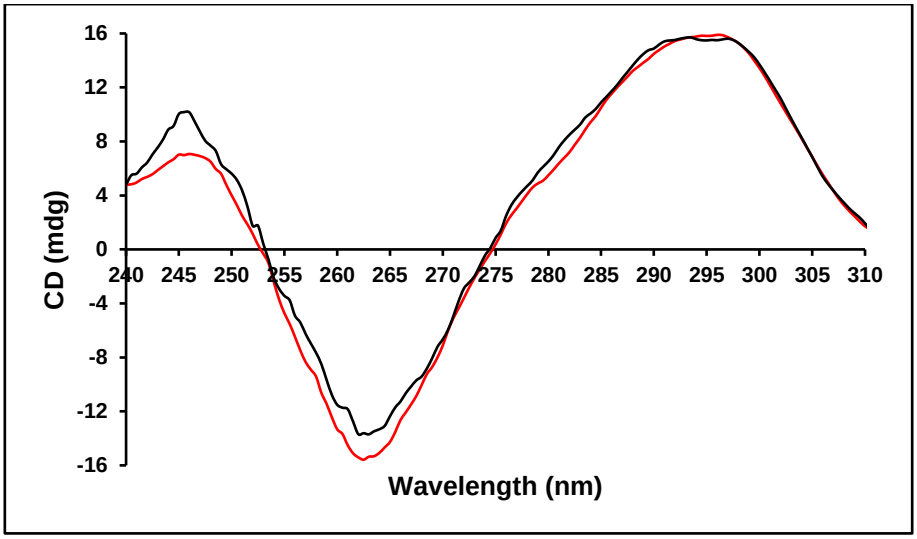

Figure 4.111 – The CD spectral variation of 5.65µM HTS (G4 oligonucleotide sequence) (red trace) in the presence of a solution of 31.50µM of $[Ir(bpy)_2(qtpy)]^{3+}$ in PBS buffer, pH 7.41 at 25°C (black trace).

4.9.2 $[Ir(phen)_2(qtpy)]^{3+}$

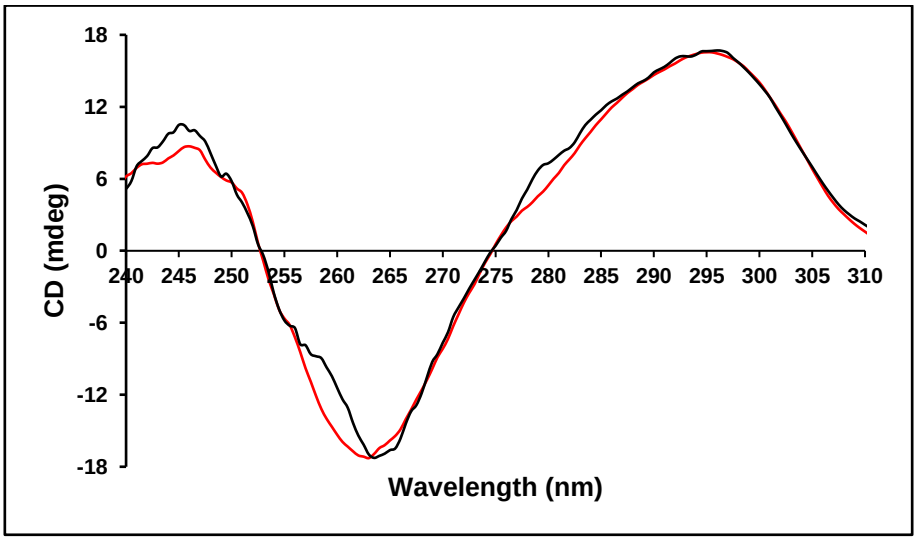

Figure 4.112 – The CD spectral variation of 5.65µM HTS (G4 oligonucleotide sequence) (red trace) in the presence of a solution of 37.36µM of $[Ir(phen)_2(qtpy)]^{3+}$ in PBS buffer, pH 7.41 at 25°C (black trace).

4.9.3 $[Ir(dppz)_2(qtpy)]^{3+}$

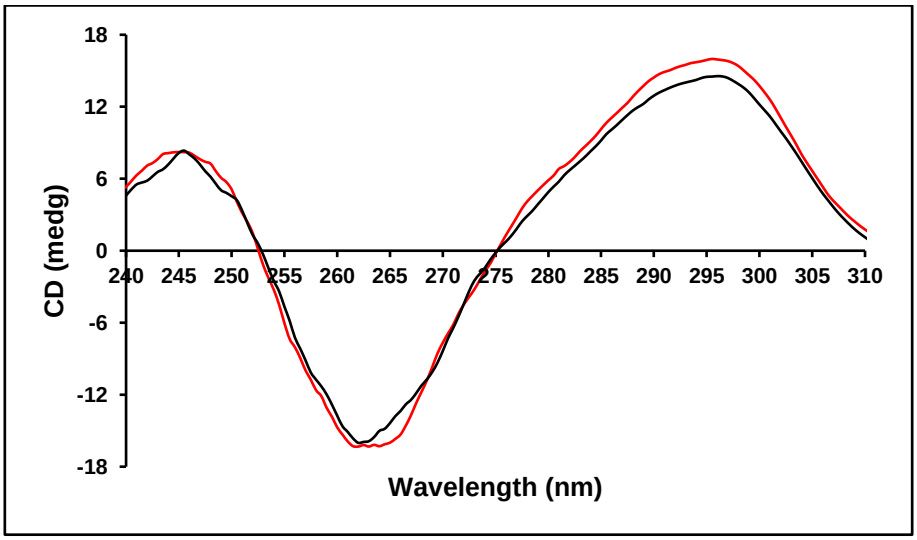

Figure 4.113 – The CD spectral variation of 5.65µM HTS (G4 oligonucleotide sequence) (red trace) in the presence of a solution of 22.33µM of $[Ir(dppz)_2(qtpy)]^{3+}$ in PBS buffer, pH 7.41 at 25°C (black trace).

The CD data are presented in Figs. 4.111–4.113 above. Results revealed that the complexes induce G-quadruplex folding in the presence of stabilising monovalent metal ions Na^+ and K^+

in the form of phosphate buffered saline (PBS). This is accruable to the ellipticity changes observed in the bands at 245nm, 260nm, and/or 295nm after the test compounds were added.

4.10 G-quadruplex DNA-Binding Studies Summary

This chapter has dealt with the investigation of the G-quadruplex DNA binding of the three iridium(III) complexes synthesised in this work. Strikingly, all the complexes display strong affinity to the G4 DNA conformation. The bpy compound give the highest binding affinity of the three complexes. The binding affinity of the dppz compound is also in a good order of magnitude. This is particularly interesting as dppz-based metallodrugs have been demonstrated to intercalate between two adjacent DNA base pairs. The G4 HTS binding interactions of the complexes were further corroborated by the perturbation of their CD signals, indicating the potency of the complexes to unfold G-quadruplex conformation, which is especially useful in the disruption of cellular activities such as DNA replication of infected cells.

4.11 Chapter Summary

This chapter has successfully investigated the binding of $[Ir(N–N)_2(qtpy)]^{3+}$ and $[Ru(N–N)_2(qtpy)]^{2+}$ (where N–N = bpy, phen, or dppz) with duplex DNA and G-quadruplex DNA (G4 human telomeric sequence) using a spectrum of techniques including UV-Vis absorption spectroscopy, steady-state luminescence spectroscopy, 3D luminescence spectroscopy, reverse-salt titration experiments, ferrocyanide quenching experiments, and gel electrophoretic analyses.

4.12 References

1. M. Pal, U. Nandi and D. Mukherjee, Detailed account on activation mechanisms of ruthenium coordination complexes and their role as antineoplastic agents, *Eur. J. Med. Chem.*, 2018, 150, 419–445.

2. A. Kellett, Z. Molphy, C. Slator, V. McKee and N. P. Farrell, Molecular methods for assessment of non-covalent metallodrug–DNA interactions, *Chem. Soc. Rev.*, 2019, 48, 971–988.

3. G. F. Grawe, K. M. Oliveira, C. M. Leite, T. D. de Oliveira, J. Honorato, A. G. Ferreira, E. Castellano, M. R. Cominetti, R. S. Correa and A. A. Batista, Ruthenium(II)-diphosphine complexes containing acylthiourea ligands are effective against lung and breast cancers, *Dalton Trans.*, 2022.

4. A. Hofmann, A. Simon, T. Grkovic, M. Jones, Methods of Molecular Analysis in the Life Sciences, Cambridge University Press, 2014.

5. T. Topală, A. Bodoki, L. Oprean and R. Oprean, Experimental techniques employed in the study of metal complexes-DNA-interactions, *Farmacia*, 2014, 62, 1049–1061.

6. N. Sohrabi, Binding and UV/Vis spectral investigation of interaction of Ni(II) piroxicam complex with calf thymus deoxyribonucleic acid (Ct-DNA): A thermodynamic approach, *J. Pharm. Sci. Res.*, 2015, 7, 533–537.

7. P. A. Channar, N. Arshad, S. I. Farooqi, F. A. Larik, A. Saeed, T. Hökelek, S. A. Shehzadi, N. Abbas, U. Flörke, Synthesis, Crystal Structure, Hirshfeld Surface Analysis, DFT, and DNA-Binding Studies of (E)-2-(3-Hydroxy-4 Methoxybenzylidene)Hydrazinecarbothioamide, *Appl. Biochem. Biotechnol.*, 2019, 189 , 175–192.

8. A. E. Friedman, J. K. Barton, J. C. Chambron, J. P. Sauvage, N. J. Turro and J. K. Barton, Molecular "Light Switch" for DNA: $Ru(bpy)_2(dppz)^{2+}$, *J. Am. Chem. Soc.*, 1990, 112, 4960–4962.

9. S. R. Byrn and G. D. Dolch, Analysis of Binding of Daunorubicin and Doxorubicin to DNA Using Computerized Curve-Fitting Procedures, *J. Pharm. Sci. Res.*, 1978, 67, 688–693.

10. S. Satyanarayana, J. C. Dabrowiak and J. B. Chaires, Neither Δ-nor Λ-Tris(phenanthroline)ruthenium(II) Binds to DNA by Classical Intercalation, *Biochem.*, 1992, 31, 9319–9324.

11. G. Scatchard, the Attractions of Proteins for Small Molecules and Ions, THE ATTRACTIONS OF PROTEINS FOR SMALL MOLECULES AND IONS, *Ann. N. Y. Acad. Sci.*, 1949, 51, 660–672.

12. X. Qu and J. B. Chaires, Analysis of Drug-DNA Binding Data, Analysis of drug-DNA binding data, *Methods Enzymol.*, 2000, 321, 353–369.

13. H. G. Weder, J. Schildknecht, R. A. Lutz and P. Kesselring, Determination of binding parameters from Scatchard plots. Theoretical and practical considerations., *Eur. J. Biochem.*, 1974, 42, 475–481.

14. J. D. McGhee and P. H. von Hippel, Theoretical Aspects of DNA-protein Interactions: Co-operative and Non-cooperative Binding of Large Ligands to a One-dimensional Homogeneous Lattice, *J. Mol. Biol.*, 1974, 86, 469–489.

15. P. H. von Hippel and J. D. McGhee, DNA-Protein Interactions, *Annu. Rev. Biochem.*, 1972, 41, 231–300.

16. A. Valazquez-Campoy, Ligand binding to one-dimensional lattice-like macromolecules: Analysis of the McGhee-von Hippel theory implemented in isothermal titration calorimetry, *Anal. Biochem.*, 2006, 348, 94–104.

17. L. F. Agnez-Lima, J. T. A. Melo, A. E. Silva, A. H. S. Oliveira, A. R. S. Timoteo, K. M. Lima-Bessa, G. R. Martinez, M. H. G. Medeiros, P. Di Mascio, R. S. Galhardo, C. F. M. Menck, DNA damage by singlet oxygen and cellular protective mechanisms, *Mutat. Res. - Rev. Mutat. Res.*, 2012, 751, 15–28.

18. M. B. Fleisher, K. C. Waterman, N. J. Turro and J. K. Barton, Light Induced Cleavage of DNA by Metal Complexes, *Inorg. Chem.*, 1986, 25, 3551–3552.

19. H. K. Saeed, P. J. Jarman, S. Archer, S. Sreedharan, I. Q. Saeed, L. K. Mckenzie, J. A. Weinstein, N. J. Buurma, C. G. W. Smythe and J. A. Thomas, Homo- and Heteroleptic Phototoxic Dinuclear Metallo-Intercalators Based on Ru^{II}(dppn) Intercalating Moieties: Synthesis, Optical, and Biological Studies, *Angew. Chemie - Int. Ed.*, 2017, 56, 12628–12633.

20. S. J. Burya, D. A. Lutterman and C. Turro, Absence of quenching by $[Fe(CN)_6]^{4-}$ is not proof of DNA intercalation, *Chem. Commun.*, 2011, 47, 1848–1850.

21. L. Z. Zhang, G.-Q. Tang, The binding properties of photosensitizer methylene blue to herring sperm DNA: a spectroscopic study, *J. Photochem. Photobiol. B.*, 2004, 74, 119–125.

22. S. A. Hollingsworth, and Ron O. Dror, Molecular Dynamics Simulation for All, *Neuron*, 2018, 99, 1129–1143.

23. J. P. Hall, F. E. Poynton, P. M. Keane, S. P. Gurung, J. A. Brazier, D. J. Cardin, G. Winter, T. Gunnlaugsson, I. V. Sazanovich, M. Towrie, C. J. Cardin, J. M. Kelly and S. J. Quinn, Monitoring one-electron photo-oxidation of guanine in DNA crystals using ultrafast infrared spectroscopy, *Nat. Chem.*, 2015, 7, 961–967.

24. I. Saito, T. Nakamura, K. Nakatani, Y. Yoshioka, K. Yamaguchi and H. Sugiyama, Mapping of the Hot Spots for DNA Damage by One-Electron Oxidation: Efficacy of GG Doublets and GGG Triplets as a Trap in Long-Range Hole Migration, *J. Am. Chem. Soc.*, 1998, 120, 12686–12687.

25. D. B. Hall, R. E. Holmlin and J. K. Barton, Oxidative DNA damage through long-range electron transfer, *Nature*, 1996, 382, 731–735.

26. C. Z. Wan, T. Fiebig, S. O. Kelley, C. R. Treadway, J. K. Barton and A. H. Zewail, *Proc. Natl. Acad. Sci. U. S. A.*, 1999, 96, 6014–6019.

27. G. B. Schuster, Long-Range Charge Transfer in DNA: Transient Structural Distortions Control the Distance Dependence, *Acc. Chem. Res.*, 2000, 33, 253–260.

28. G. D. Reid, D. J. Whittaker, M. A. Day, D. A. Turton, V. Kayser, J. M. Kelly and G. S. Beddard, Femtosecond Electron-Transfer Reactions in Mono- and Polynucleotides and in DNA, *J. Am. Chem. Soc.*, 2002, 124, 5518–5527.

29. I. Ortmans, B. Elias, J. M. Kelly, C. Moucheron and A. Kirsch DeMesmaeker, $[Ru(TAP)_2(dppz)]^{2+}$: a DNA intercalating complex, which luminesces strongly in water and undergoes photo-induced proton-coupled electron transfer with guanosine-5'-monophosphate., *Dalton Trans.*, 2004, 2, 668–676.

30. http://www.ymdb.ca/compounds/YMDB00097.

31. F. Gao, H. Chao, F. Zhou, Y.-X. Yuan, B. Peng and L.-N. Ji, DNA interactions of a functionalised ruthenium(II) mixed-polypyridyl complex $[Ru(bpy)_2(ppd]^{2+}$, *J. Biol. Inorg. Chem.*, 2006, 100, 1487–1494.

32. M. Mariappan, R. Alagarsamy, A. P. Panneerselvam, A. Veerappan, S. Rajendran and J. Arunachalam, Synthesis, solvatochromism, photochemistry, DNA binding, photocleavage, cytotoxicity and molecular docking studies of a ruthenium(II) complex bearing photoactive subunit, *J. Photochem. Photobiol. A Chem.*, 2018, 356, 617–626.

33. Electrophoresis Reiner Westermeier SERVA Electrophoresis GmbH, Heidelberg, Germany.

34. K. R. Wyland, E. E. Hoffman and A. Jain, DNA interaction studies and photoinduced ligand exchange kinetics of a sterically strained ruthenium(II) complex, *Inorg. Chim. Acta*, 2017, 454, 62–66.

35. M. G. Walker, P. J. Jarman, M. R. Gill, X. Tian, H. Ahmad, P. A. N. Reddy, L. McKenzie, J. A. Weinstein, A. J. H. M. Meijer, G. Battaglia, C. G. W. Smythe and J. A. Thomas, A Self-Assembled Metallomacrocycle Singlet Oxygen Sensitizer for Photodynamic Therapy, *Chem. - A Eur. J.*, 2016, 22, 5996–6000.

36. A. Margetić, S. Nikolić, S. Grgurić-Šipka, M. T. Vujčić, Interaction of organoruthenium(II)-polypyridyl complexes with DNA and BSA, *Biometals*, 2022, 35, 813–829.

37. C. Platella, U. Raucci, N. Rega, S. D'Atri, L. Levati, G. N. Roviello, M. P. Fuggetta, D. Musumeci, D. Montesarchio, Shedding Light on the Interaction of Polydatin and Resveratrol with G-Quadruplex and Duplex DNA: A Biophysical, Computational and Biological Approach, *Int. J. Biol. Macromol.*, 2020, 151, 1163–1172.

38. S. Elleuchi, I. O. De Luzuriaga, A. Sanchez-Gonzalez, X. Lopez, K. Jarraya, M. J. Calhorda, A. Gil, Computational Studies on the Binding Preferences of Molybdenum(II) Phenanthroline Complexes with Duplex DNA. The Important Role of the Ancillary Ligands, *Inorg. Chem.*, 2020, 59, 17, 12711–12721.

39. C. A. Lipinski, F. Lombardo, B. W. Dominy, P. J. Feeney, Experimental and Computational Approaches to Estimate Solubility and Permeability in Drug Discovery and Development Settings, *Adv. Drug Deliv. Rev.*, 2001, 46 (1–3), 3–26.

40. H. van de Waterbeemd, B. Testa, Drug Bioavailability: Estimation of Solubility, Permeability, Absorption and Bioavailability, Wiley-VCH Verlag GmbH and Co. KGaA, 2009, 40.

41. A. T. Onawole, K. O. Sulaiman, T. U. Kolapo, F. O. Akinde, R. O. Adegoke, COVID-19: CADD to the Rescue, *Virus Res.*, 2020, 285 (1980222), 1–12.

42. D. A. McGovern, A. Selmi, J. E. O'Brien, J. M. Kelly and C. Long, Reduction of dipyrido-[3,2-a:2′,3′-c]-phenazine (dppz) by photolysis in ethanol solution, *Chem. Commun.*, 2005, 1402–1404.

43. T. Phillips, I. Haq, A. J. H. M. Meijer, H. Adams, I. Soutar, L. Swanson, M. J. Sykes and J. A. Thomas, DNA binding of an organic dppz-based intercalator, *Biochem.*, 2004, 43, 13657–13665.

44. T. Phillips, C. Rajput, L. Twyman, I. Haq and J. A. Thomas, Water soluble organic dppz analogues - Tuning DNA binding affinities, luminescence, and photo-redox properties, *Chem. Commun.*, 2005, 44, 4327–4329.

45. X. Lu, K. Zhu, M. Zhang, H. Liu and J. Kang, Voltammetric studies of the interaction of transition-metal complexes with DNA, *J. Biochem. Biophys. Methods*, 2002, 52, 189–200.

46. D. B. Hall, R. E. Holmlin and J. K. Barton, Nature, 1996, 382, 731–735; M.-H. Chung, H. Kiyosawa, E. Ohtsuka, S. Nishimura, and H. Kasai, DNA strand cleavage at 8-Hydoxyguanine residues by hot piperidine treatment, *Biochem. Biophys. Res. Commun.*, 1992, 188, 1–7.

47. M. L. Bochman, K. Paeschke, V. A. and Zakian, DNA secondary structures: stability and function of G-quadruplex structures, *Nat. Rev. Genet.*, 2012, 13, 770–780.

48. V. S. Chambers, G. Marsico, J. M. Boutell, M. Di Antonio, G. P. Smith, and S. Balasubramanian, High-throughput sequencing of DNA G-quadruplex structures in the human genome, *Nat. Biotechnol.*, 2015, 33, 877–881.

49. A. Piazza, J. B. Boule, J. Lopes, K. Mingo, E. Largy, M. P. Teulade-Fichou, and A. Nicolas, Genetic instability triggered by G-quadruplex interacting Phen-DC compounds in Saccharomyces cerevisiae, *Nucleic Acids Res.*, 2010, 38, 4337–4348.

50. P. Castillo Bosch, S. Segura-Bayona, W. Koole, J. T. van Heteren, J. M. Dewar, M. Tijsterman, and P. Knipscheer, FANCJ promotes DNA synthesis through G-quadruplex structures, *EMBO J.*, 2014, 33, 2521–2533.

51. C. Rajput, R. Rutkaite, L. Swanson, I. Haq, and J. A. Thomas, Dinuclear Monointercalating RuII Complexes That Display High Affinity Binding to Duplex and Quadruplex DNA, Chem. Eur. J. 2006, 12, 4611 – 4619.

52. T. Wilson, P. J. Costa, V. Felix, M. P. Williamson, and J. A. Thomas, Structural Studies on Dinuclear Ruthenium(II) Complexes That Bind Diastereoselectively to an Antiparallel Folded Human Telomere Sequence, *J. Med. Chem.*, 2013, 56, 8674-8683.

53. Michael R. Duff, Jr. 1 , Jordan Grubbs1 , Elizabeth E. Howell, Isothermal Titration Calorimetry for Measuring Macromolecule-Ligand Affinity, J. Vis. Exp. (55), e2796, 2011.

54. T. Wilson, M. P. Williamson, and J. A Thomas, Differentiating quadruplexes: binding preferences of a luminescent dinuclear ruthenium(II) complex with four-stranded DNA structures, *Org. Biomol. Chem.*, 2010, 8, 2617–2621.

5.0 Serum Albumins Binding Investigations

5.1 Introduction

There are many proteins in the body, but serum albumin (SA), is the most abundant in the blood plasma of most higher species. It accounts for about 60% of the plasma's total protein content and its concentration is up to 40mgmL^{-1} or 0.6mM. As SA reversibly binds to a wide variety of substances such as fatty acids, hormones, and medicinal drugs it plays a vital role in the transport and deposition of these substances. Two common types of serum albumins have been extensively studied: bovine serum albumin (BSA) and human serum albumin (HSA). The three-dimensional structures of these proteins appear to be roughly similar among many living organisms. X-ray crystallographic structural elucidation of the albumins from bovine serum and human serum show they are composed of a single polypeptide chain with 583 and 585 amino acids, respectively, and as such have similar sequences and conformations with BSA being ~ 76% homologous with HSA. The original structure of BSA (PDB 4F5S structure) was crystallised at pH 7.5 and resolved at 2.30Å. However, researchers have simulated the crystallisation of the biomolecule under different pH conditions – from acidic to neutral to alkaline pH environments[1] (Fig. 5.1) and it is seen that conformation changes occur under different pH conditions and ionic strength.

The study of ligand binding to albumins has spanned >80years. Over the years, attention has shifted to the interaction between SA and exogenous molecules, especially drugs, many of which are hydrophobic with low solubility in aqueous media. The elucidation of the binding properties of such drugs with SA are essential, as they provide a pathway to the pharmacokinetic and pharmacodynamic mechanisms of these substances in various tissues. SA is mostly helical and is arranged into three similar structures that form a heart-shaped molecule. Site I and site II, which are located in the hydrophobic cavities of Subdomains IIA and IIIA, are the principal discrete binding sites with distinct specificities. Other highly specific binding sites include Subdomain IB, which binds polycyclic aromatic hydrocarbon epoxides and there are up to six other sites that bind fatty acids.

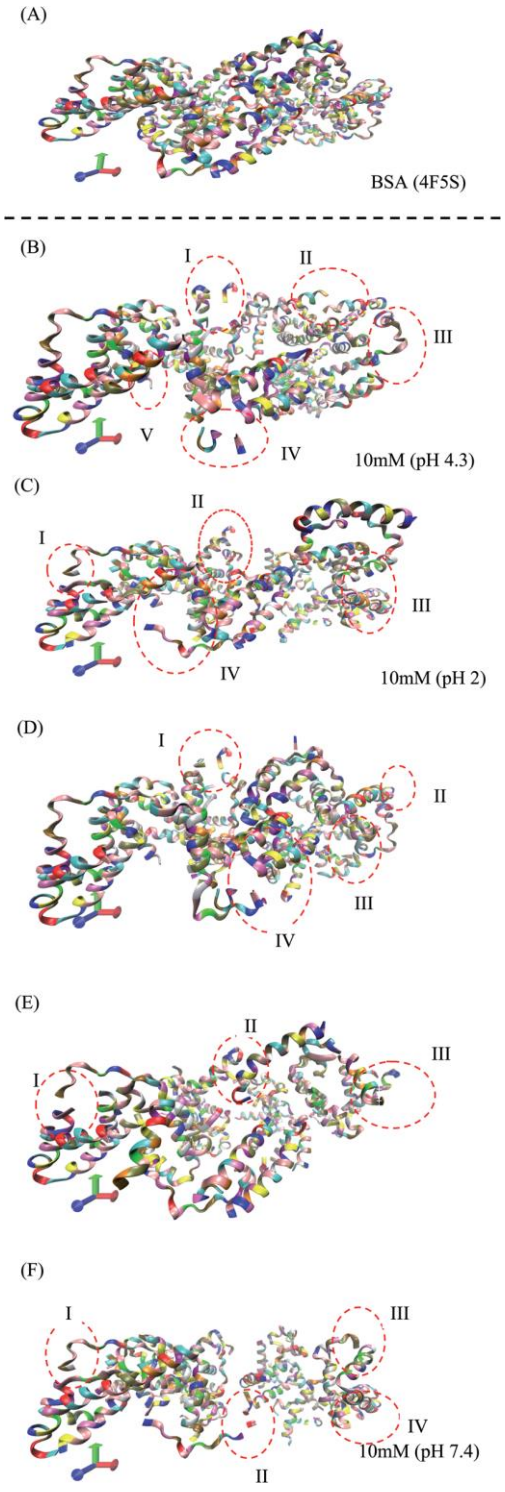

Figure 5.1 – (A): 3D structure of the original BSA structure (4F5S); **(B–F)**: simulated BSA protein (PDB 4F5S) at pH 4.3, 2.0, 3.5, 7.4, and 9.0, respectively, and 10mM ionic concentration.[1] The different colors represent the different amino acid residues in the simulated protein structure: ALA (blue), GLY (white), ILE (green), LEU (pink), MET (yellow), PHE (purple), PRO (ochre), TRP (silver), TYR (green), and VAL (tan).

Several techniques have been used to investigate the interaction of drugs with SA, including luminescence spectroscopy, UV-Vis spectroscopy, equilibrium dialysis, circular dichroism spectroscopy, and electrochemistry. In particular, luminescence spectroscopy has been useful in studying the nature of binding sites, as well as their specificity and affinity for specific ligands, using luminescence probes as site markers. Site markers are small molecules that bind to specific sites in SA and include warfarin, phenylbutazone, dansyl-l-asparagine, dansylamide and iodipamide for site I, and ibuprofen, flufenamic acid and diazepam for site II.[2] Direct titration and displacement experiments with such site markers are used in these studies.

Inherent luminescence in proteins is attributed to tryptophan (Trp), tyrosine (Try) and phenylalanine (Phe) residues. Among these, the intrinsic luminescence of SA is largely due to tryptophan, as the quantum yield of phenylalanine is much lower, and the luminescence of tyrosine is almost totally quenched if it is ionised or comes near an amino group or tryptophan residues. Static quenching proceeds through fluorophore-quencher complex formation in the ground state. In dynamic (or collisional) quenching, however, the fluorophore and the quencher closely associate during the short-lived existence of the excited state. Static and dynamic quenching are distinguishable by the effect of temperature on their quenching behaviour.[3]

Research on potential anticancer drugs has traditionally focused on DNA-binding studies since DNA is considered to be the prime target for platinum-based chemotherapy. However, recent studies have suggested that alternative target for novel metallodrugs may be enzymes or proteins.[4–6] In this context, studies on the binding of metal complexes with proteins are becoming increasingly important as they provide insight into the pharmacokinetics of metallodrugs. Furthermore, biophysical studies of the interactions between SA and metallodrugs can yield valuable information about structural factors that govern SA-drug binding. For example, these studies can furnish information on; (i) the dynamics of quenching of SA upon interaction with a drug, revealing whether a drug interacts with the ground state of the protein (static process) or with the excited state of the protein (dynamic process), (ii) the binding strength and stability of SA-drug complexes, (iii) the number of binding sites of SA-drug complex formation, (iv) the nature of the binding forces (electrostatic, hydrophobic, hydrogen bonding and van der Waals interactions) involved in the SA-drug complex, and (v) conformational and microenvironmental changes within the SA.

5.2 Drug Interactions with Sudlow Sites I and II

In their pioneering studies between 1975 and 1976, Sudlow, *et al.* reported the use of a fluorescent probe displacement method to furnish two specific drug binding sites on HSA, namely, site I (or the warfarin binding site) and site II (or the benzodiazepine binding site).[7–8] These studies promoted topology analysis and mapping of the drug binding sites within HSA. Using albumin fragments derived from pepsin and trypsin digestions, Bos, *et al.* proposed that sites I and II are located in domains II and III, respectively.[9–10] Current crystallographic studies have proved that the majority of drugs bind to these two main binding sites.[11–14] Certainly, these findings do not exclude the presence of other special binding sites on HSA.[15– 20]

Site I is a large hydrophobic cavity that can potentially hold several drugs at the same time.[21–22] In subdomain IIA, Site I consists of six helices and a loop-helix feature (residues 148–154). Trp214, Leu219, Phe223, Leu238, His242, Leu260, Ile264, Ser287, Ile290, and Ala291 form the pocket's interior, which is predominantly hydrophobic. Two clusters of polar residues are found in the pocket, one at the bottom (Tyr150, His242, Arg257), the other at the entrance (Lys195, Lys199, Arg218, Arg222) (Fig. 5.2). Three distinct compartments extend from the central zone of the large binding cavity.[23]

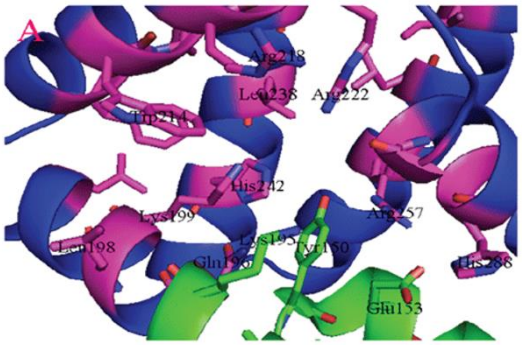

Figure 5.2 – HSA structure showing different binding sites.

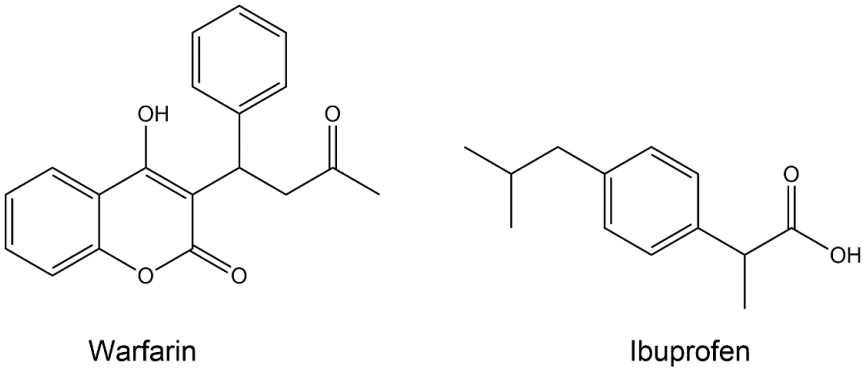

Warfarin Ibuprofen

Figure 5.3 – Structural formulas of Warfarin and Ibuprofen, two commonly-employed Site I and Site II markers for SA.

A key theme of this thesis is the use of optical spectroscopic methods to investigate the modalities by which potential drugs interact with both DNA and serum albumins. This section explores the interaction of one of the new iridium(III) complexes, $[Ir(bpy)_2(qtpy)]^{3+}$, and three previously reported ruthenium(II) complexes $[Ru(N–N)_2(qtpy)]^{2+}$ (where N–N = bpy, phen, or dppz)[24] with BSA. The binding of $[Ir(phen)_2(qtpy)]^{3+}$ and $[Ir(dppz)_2(qtpy)]^{3+}$ to BSA could not be accomplished due to time restriction.

5.3 Protocol Employed for the Binding Investigations of BSA and HSA with Iridium(III) and Ruthenium(II) Complexes

All protein-binding studies were carried out in 5mM tris, 25mM NaCl buffer (pH = 7.4) at ambient temperature unless otherwise mentioned.[25] The purity of the iridium(III) and ruthenium(II) complexes investigated is >95% as indicated by HPLC and NMR.

5.4 Fourier Transform Infrared (FTIR) Spectroscopy

Proteins are irregular biopolymers composed essentially of 20 amino acids with four levels of spatial organisation. Most commonly-employed absorption bands as structural probes in protein FT-IR spectroscopy are the amide I vibrations (1690–1600cm^{-1}) and amide II stretching vibrations (1600–1500cm^{-1})[26] with amide I assignable to both C=O stretching vibration and ring stretching vibrations and amide II assignable to C–N stretching vibrations.[27]

BSA and HSA purchased from commercial sources were characterised by FTIR spectroscopy before subjecting to any binding studies as proteins are easily denatured with the passage of time. The FTIR spectra of pure BSA and HSA obtained in their solid forms are shown in Figs. 5.4 and 5.5. It was found that amide I bond at ca. 1646cm^{-1} and amide II band at1534cm^{-1} show the characteristics of pure BSA whilst amide I bond at ca. 1648cm^{-1} and amide II band at 1534cm^{-1} show the characteristics of pure HSA.[28] These results confirm the intactness of BSA and HSA used for the binding investigations reported in this section.

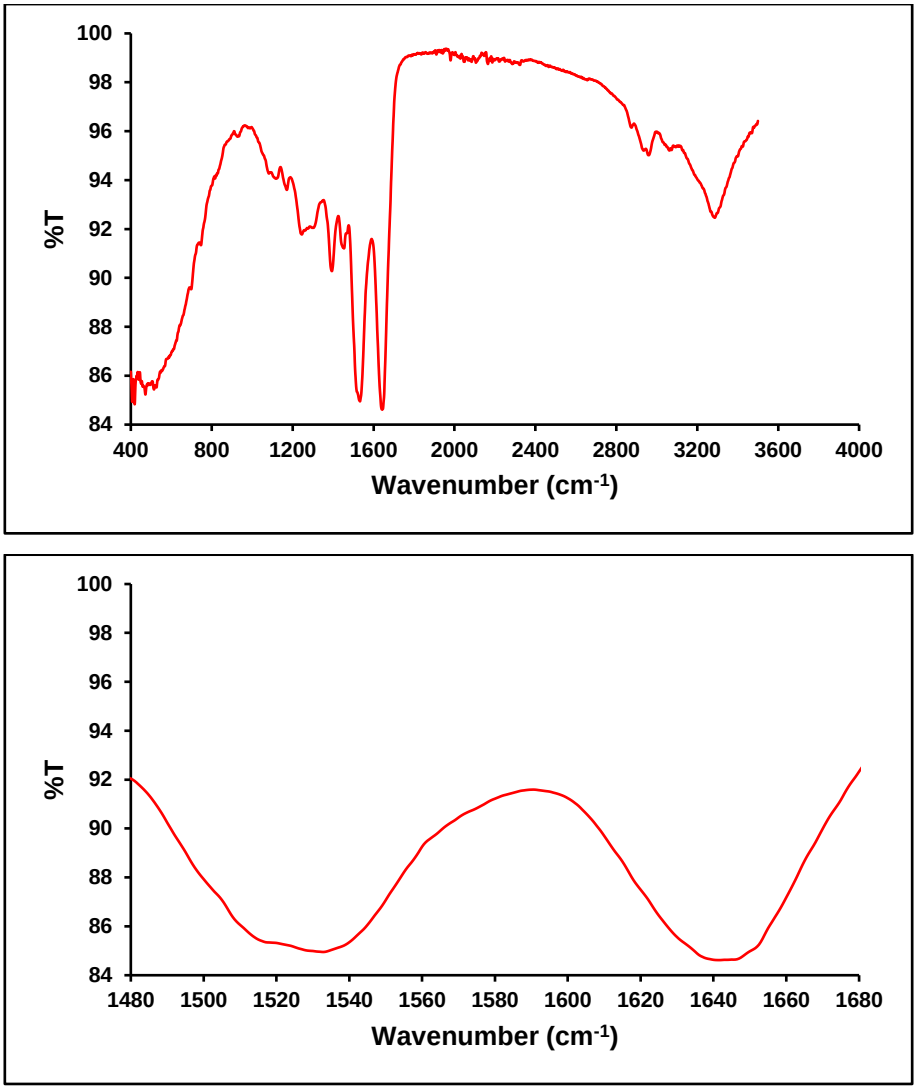

Figure 5.4 – FTIR spectrum of BSA (top). Amide I and II peaks attributable to the alpha-helix structure at ca. 1646cm^{-1} and 1534cm^{-1} (bottom).[29]

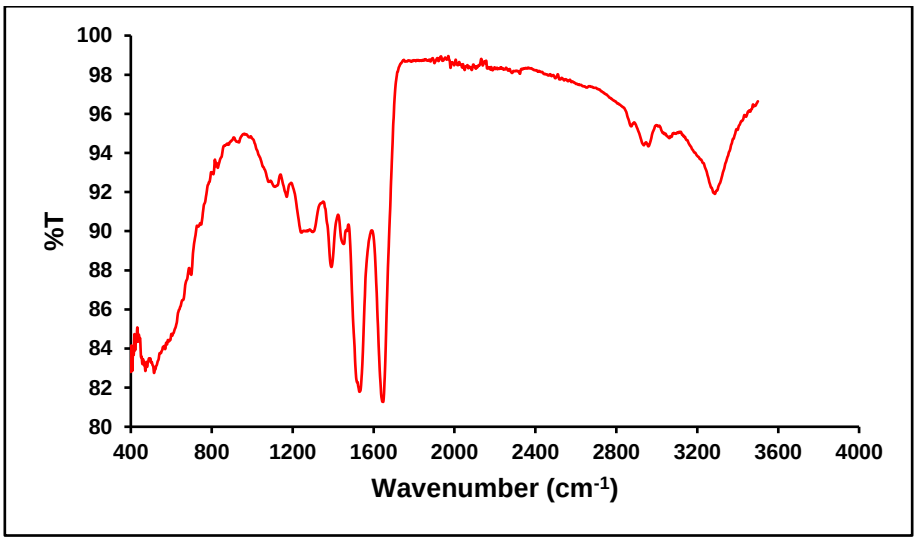

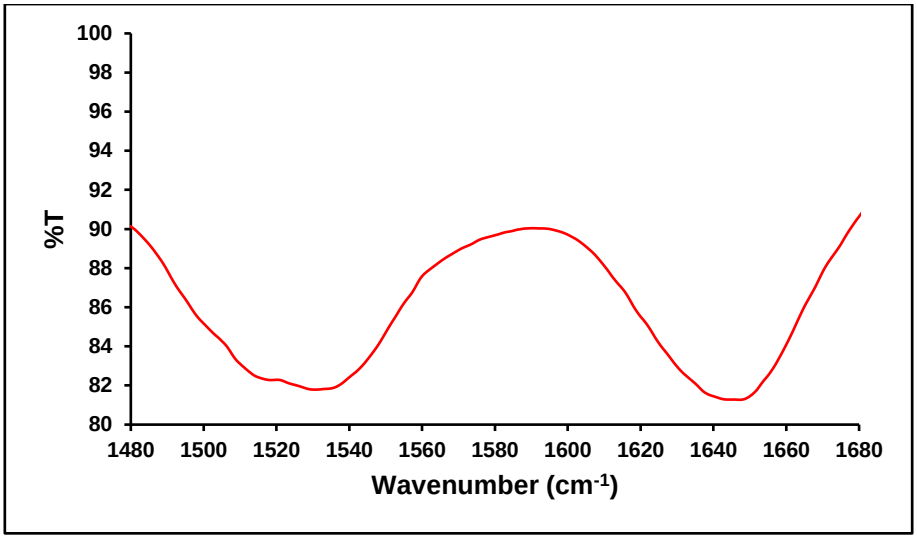

Figure 5.5 – FTIR spectrum of HSA (top). Amide I and II peaks attributable to the alpha-helix structure at ca. 1648cm^{-1} and 1534cm^{-1} (bottom).[29]

5.5 BSA Binding and Quenching Studies

The UV-Vis spectrum of BSA was first measured in tris buffer. The most intense absorption was observed at 278nm, which was also chosen as the excitation wavelength for subsequent luminescence titration studies (Fig. 5.6).

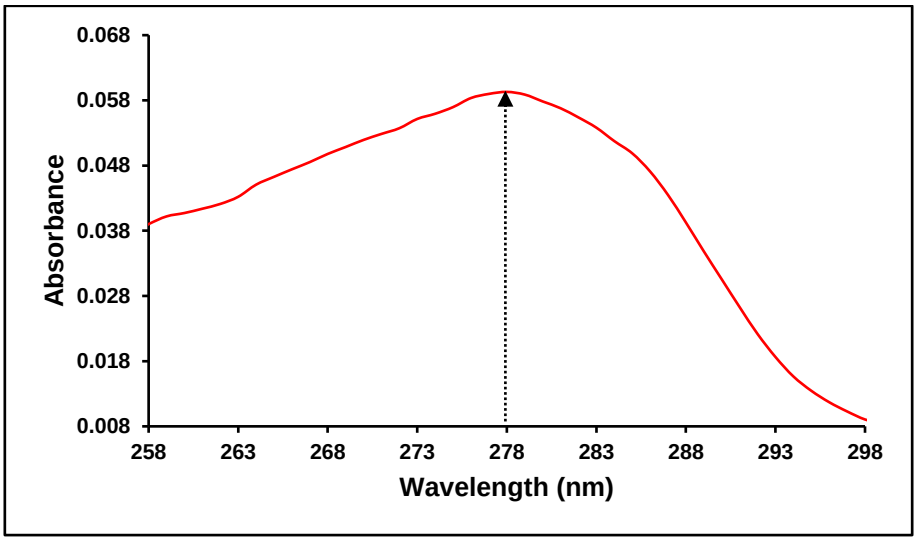

Figure 5.6 – UV-Vis spectrum of 1.52µM BSA in 5mM tris, 25mM NaCl buffer, pH 7.4.

Since the complexes show absorption in the wavelength region where BSA and HSA equally absorb, UV-Vis spectroscopy could not be used to monitor the binding of the complexes with serum proteins and attention was simply switched to luminescence spectroscopy.

5.6 Luminescence Spectroscopic Studies

In these experiments, the concentration of BSA was fixed whilst that of the complexes was gradually increased. Since luminescence is a powerful and sensitive detection technique, a small aliquot of BSA sample solution - as little as 0.5µL of 1.35 x 10^{-4}M - was micropipetted into 2200µL of tris buffer (resulting into BSA concentration of 3.07 x 10^{-8}M) for the experiment. Increasing amounts (i.e., 3µL of 9.23 x 10^{-4}M) of the iridium(III) or ruthenium(II) complexes was then successively added into the BSA or HSA solution until binding saturation was reached. The maximum emission spectrum of BSA at ca. 350nm was monitored, which has been associated with the tryptophan residues contained within the biomolecule.[30] The quenching process is described by the classical Stern-Volmer equation.

$$\frac{F_0}{F} = 1 + K_{sv}[Q] = 1 + K_q\tau_0[Q]$$

(Equation 5.1)

where F_0 and F are the steady-state luminescence intensities of protein BSA in the absence and presence of iridium(III) complex $[Ir(bpy)_2(qtpy)]^{3+}$, respectively, [Q] is the concentration of the ruthenium(II) complexes, τ_0 is the average lifetime of protein in the absence of metal complex $[Ir(N–N)_2(qtpy)]^{3+}$ and/or $[Ru(N–N)_2(qtpy)]^{2+}$, K_{sv} is Stern-Volmer quenching constant, and K_q is quenching rate constant.

$$K_q = \frac{K_{SV}}{\tau_0}$$

(Equation 5.2)

5.6.1 BSA Binding with $[Ir(bpy)_2(qtpy)]^{3+}$

Figs. 5.7 and 5.8 below show the UV-Vis and luminescence profiles of $[Ir(bpy)_2(qtpy)]^{3+}$ as reported in a previous section of the thesis. Quick scans of these were done before proceeding with the titration experiments.

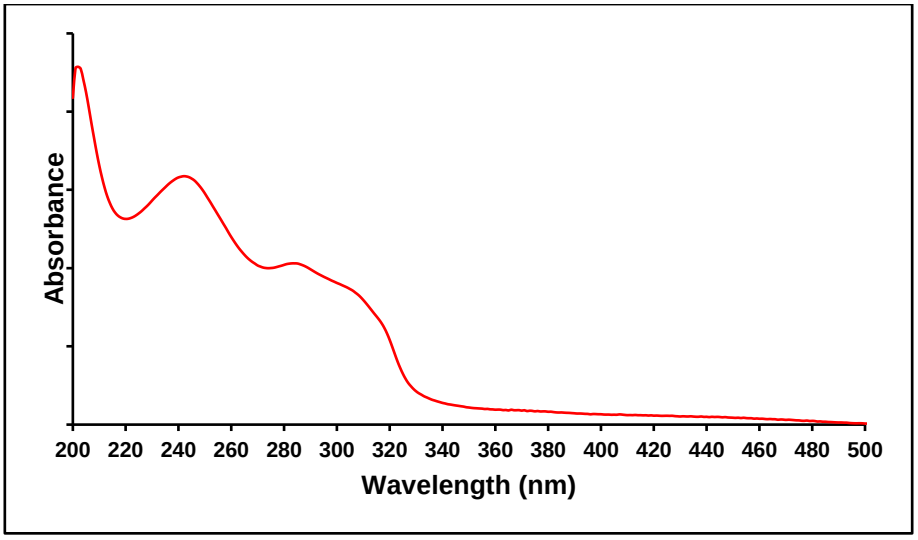

Figure 5.7 – Absorption spectrum of 29.60µM $[Ir(bpy)_2(qtpy)]Cl_3$ recorded in H_2O at ambient temperature.

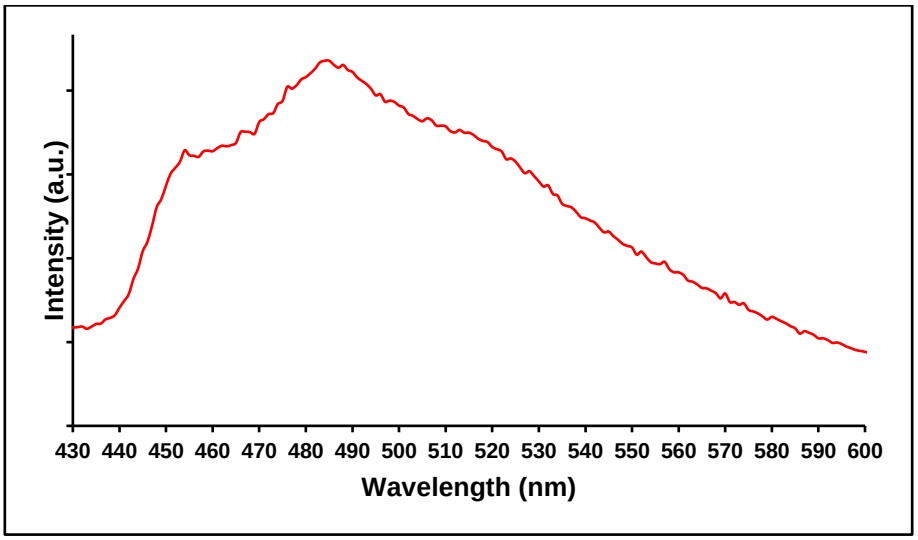

Figure 5.8 – Luminescence spectrum of $[Ir(bpy)_2(qtpy)]Cl_3$ in 5mM tris, 25mM NaCl buffer at ambient temperature. Excitation wavelength = 310nm. Excitation slit width = 5nm. Emission slit width = 5nm.

The luminescence spectra of BSA upon increasing addition of the complex is given in Fig. 5.9. The decrease in the protein's intrinsic luminescence is indicative of a definite binding interaction occurring between the serum albumin and the complex.

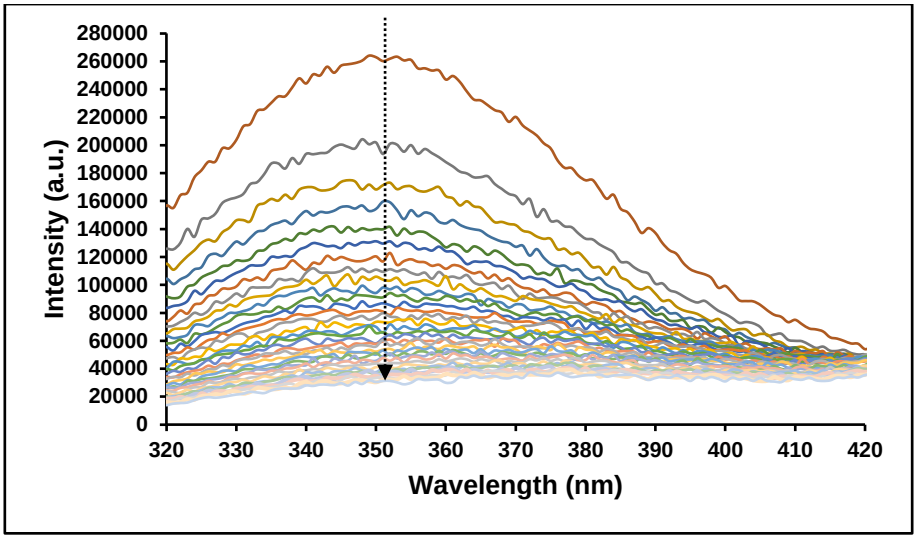

Figure 5.9 – Luminescent titration of 0–41.54µM $[Ir(bpy)_2(qtpy)]^{3+}$ into a solution of 3.07 x 10^{-8}M BSA in 5mM tris buffer, 25mM NaCl, pH 7.4 at ambient temperature. Excitation wavelength: 278nm; emission region: 320–420nm. Excitation slit width = 5nm. Emission slit width = 5nm.

5.6.1.1 Binding and Quenching Fits

Fig. 5.9 above was then fitted to the binding plots given in Fig. 5.10.

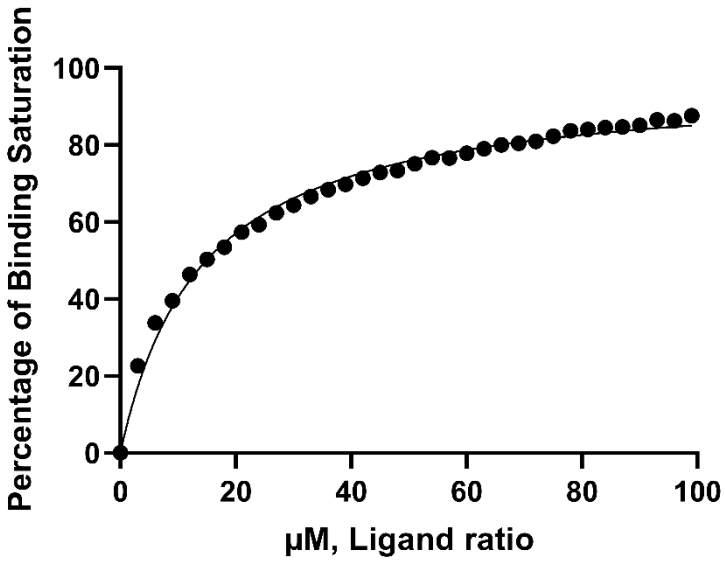

Figure 5.10 – Binding plot of BSA with $[Ir(bpy)_2(qtpy)]^{3+}$ derived from luminescent titration.

The Stern-Volmer plot for quenching of BSA by the complex is shown in Fig. 5.11. The values of K_{sv} and K_q were obtained from the slope of plot between (F_0/F) versus [Q]. The fit gives a linear plot, indicating that the quenching obeys Stern-Volmer equation although the quenching

mechanism may be either static or dynamic. The K_{sv} and K_q values obtained from the Stern-Volmer plot for the iridium(III) complex $[Ir(bpy)_2(qtpy)]^{3+}$ are 1.52 x $10^5 M^{-1}$ and 1.27 x $10^{13} M^{-1}$, respectively. K_{sv} was simply obtained as the value of the slope. τ_0 of BSA protein in tris buffer was measured to be 11.9225ns, and a simple mathematical manipulation was done to arrive at the value of K_q. The decay kinetics is biexponential, and the value of the longer component of the lifetime was used to derive τ_0.

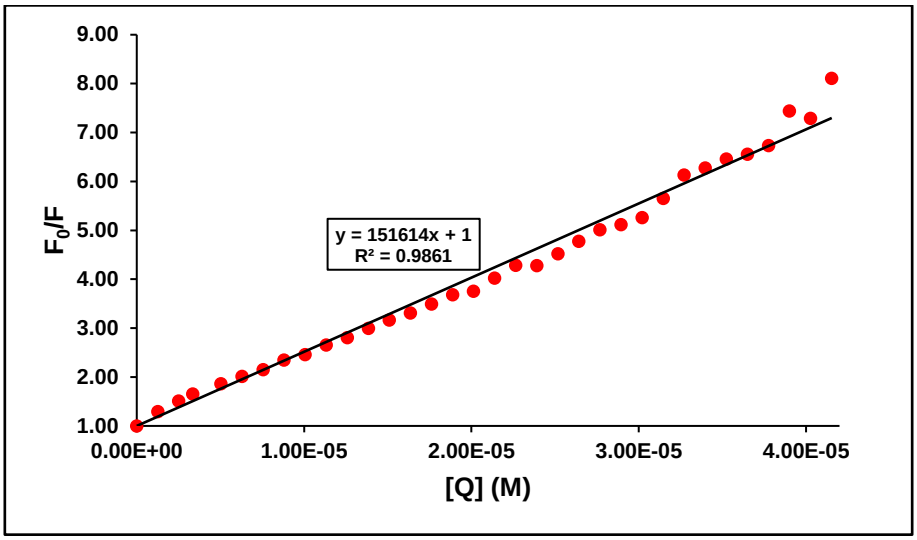

Figure 5.11 – Stern–Volmer plot for the quenching of 3.07 x 10^{-8}M BSA by 0–41.54μM $[Ir(bpy)_2(qtpy)]^{3+}$.

Dynamic and static quenching are distinguishable based on the dependence of K_{sv} and K_q values on the temperature. Dynamic quenching depends upon diffusion, since higher temperatures result in higher diffusion coefficient; the dynamic quenching constant will increase with increase in temperature. In contrast, an increase in temperature is likely to decrease the stability of ground state complexes, and thus, static quenching constants are expected to decrease with increasing temperature.[31]

When molecules bind independently to a set of equivalent sites on a macromolecule, the binding constant (K_b) and the binding number (N) can be determined using the equation below:[32]

$$\frac{\mathrm{Log}\,[(F_0 - F)]}{F} = \mathrm{Log}K_b + N\mathrm{Log}[Q]$$

(Equation 5.3)

Herein, F_0 and F are the luminescence intensities of BSA in the non-existence and existence of the complex, respectively, [Q] is the concentration of the metal complex, K_b stands for the binding constant, and N is the binding number. A double logarithmic plot furnishing both K_b and N is given in Fig. 5.12.

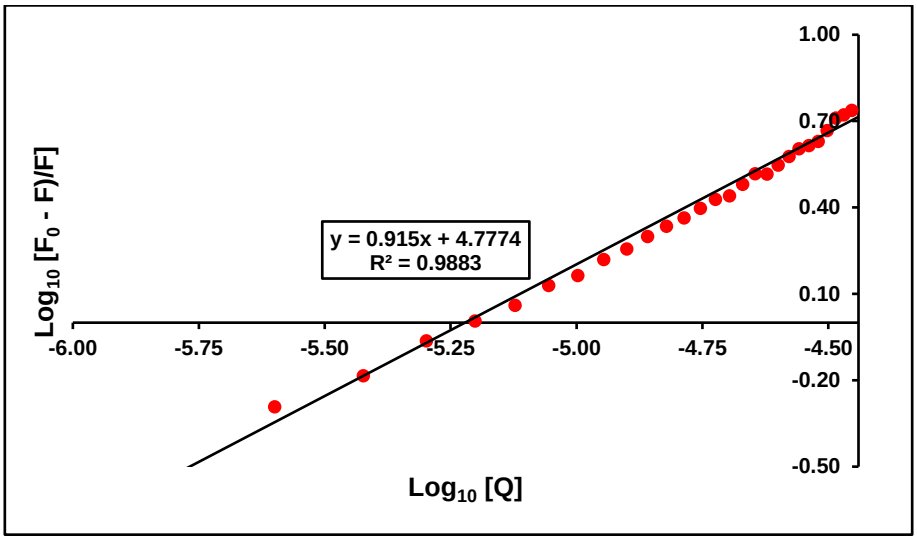

Figure 5.12 – Double–logarithmic plot for the interaction of 3.07 x 10^{-8}M BSA with 0–41.54µM $[Ir(bpy)_2(qtpy)]^{3+}$.

Using Equation 3.3 earlier stated, K_b and n values were obtained from the antilog of the intercept and slope of the plots of $Log_{10}[(F_0–F)/F]$ versus $Log_{10}[Q]$ at physiological pH 7.4, respectively, with K_b = 5.94 x 10^4M^{-1} and n = 1. The estimated values of the binding constant (K_b) and binding number (n) indicate a strong binding of the complex with BSA. The value of N being ca. 1 demonstrates that a single type of binding occurs between iridium(III) complex $[Ir(bpy)_2(qtpy)]^{3+}$ and BSA.

5.6.2 Subdomain IIA (Sudlow Site I) Competition – Displacement of Warfarin from BSA-Warfarin Adduct by $[Ir(bpy)_2(qtpy)]^{3+}$

Warfarin displacement experiments were undertaken. In these experiments, warfarin was mixed with BSA and left for 5 minutes to equilibrate and then monitored using luminescence spectroscopy. The warfarin luminescence when bound to BSA is seen at ~375 nm. With

Warfarin strongly bound to BSA, $[Ir(bpy)_2(qtpy)]^{3+}$ was then increasingly added to compete with the drug and thus displace Warfarin from the BSA-Warfarin adduct. This allows for the direct monitoring of Warfarin being removed from Sudlow site I. Therefore, results show that $[Ir(bpy)_2(qtpy)]^{3+}$ positively competed with Warfarin for BSA's site I, giving a decrease in BSA-bound Warfarin emission with increasing metal complex concentration (Fig. 5.13). The same observation has been made in a previous study.[33]

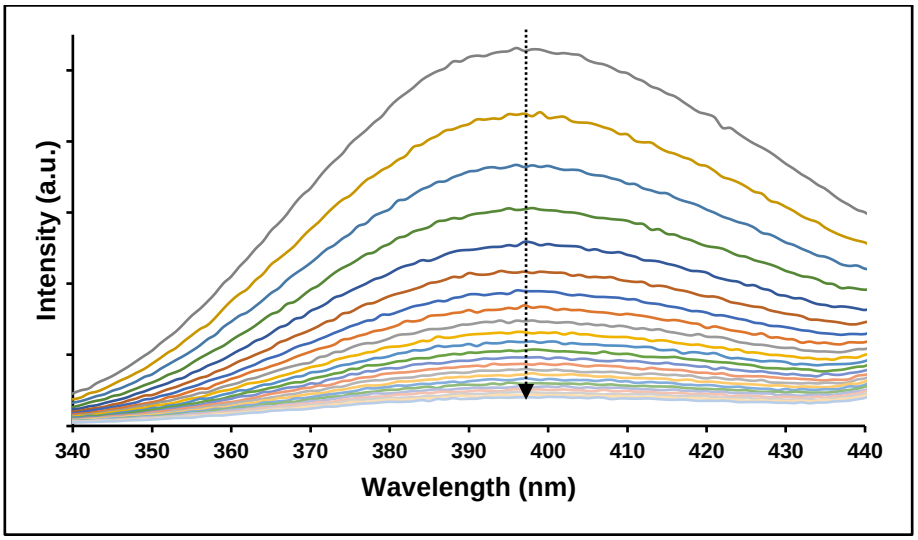

Figure 5.13 – Warfarin displacement luminescent titration of 0–1.16mM $[Ir(bpy)_2(qtpy)]^{3+}$ into a solution of 3.07 x 10^{-8}M BSA in 5mM tris buffer, 25mM NaCl, pH 7.4 at ambient temperature. [Warfarin] = 2.55 x 10^{-4}M. Excitation wavelength: 278nm; emission region: 340–440nm. Excitation slit width = 5nm. Emission slit width = 5nm.

5.6.3 Subdomain IIIA (Sudlow Site II) Competition – Displacement of Ibuprofen from BSA-Ibuprofen Adduct by $[Ir(bpy)_2(qtpy)]^{3+}$

Competition of $[Ir(bpy)_2(qtpy)]^{3+}$ and Ibuprofen for BSA site II was also undertaken in a similar fashion to that reported for Warfarin but using Ibuprofen as the site marker. Initial addition of Ibuprofen to unbound BSA leads to a decrease in both emission intensity and wavelength. The BSA-Ibuprofen adduct formed was then titrated against $[Ir(bpy)_2(qtpy)]^{3+}$, leading to further quenching of emission (Fig 5.14).

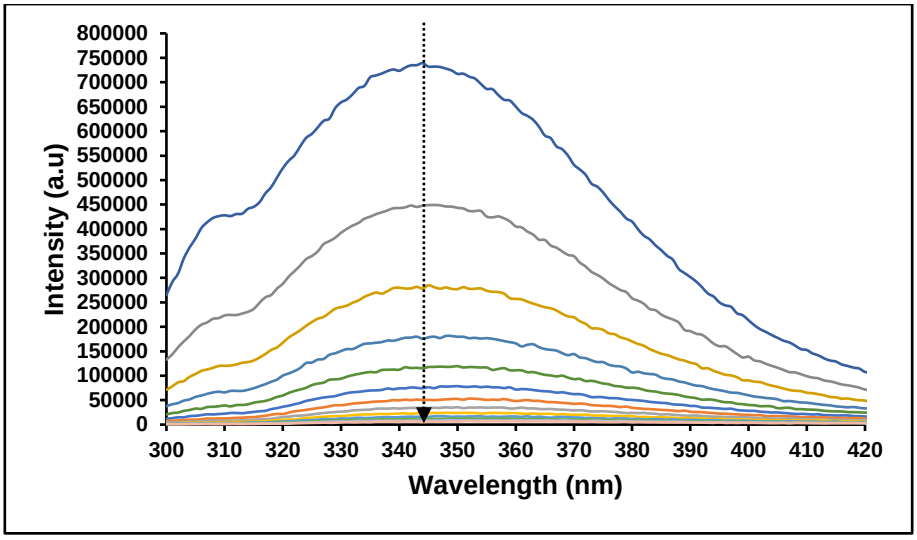

Figure 5.14 – Luminescence changes of BSA-bound Ibuprofen upon incremental additions of 0–1.16 x 10^{-4}M $[Ir(bpy)_2(qtpy)]^{3+}$. [BSA] = 2.45 x 10^{-7}M. [Ibuprofen] = 2.55 x 10^{-4}M.

5.6.4 BSA Binding with $[Ru(bpy)_2(qtpy)]^{2+}$

The UV-Vis and luminescence spectra of $[Ru(bpy)_2(qtpy)]^{2+}$ were first compared to those obtained previously (Figs. 5.15 and 5.16).

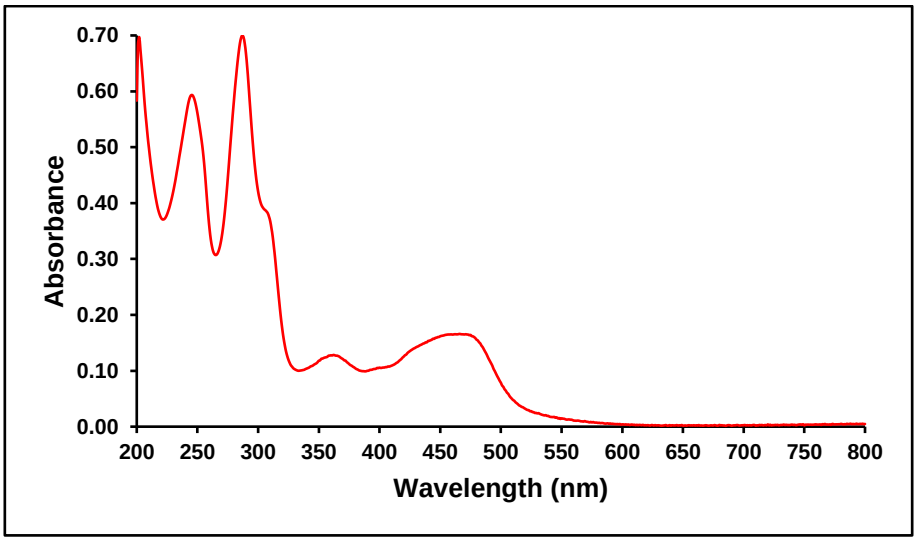

Figure 5.15 – Absorption spectrum of 11.50µM $[Ru(bpy)_2(qtpy)]Cl_2$ in 5mM tris, 25mM NaCl buffer at ambient temperature. Spectral shape and absorption wavelength analogous to those of $[Ru(bpy)_2(qtpy)]Cl_2$ by Dr Haslina Ahmad. [34]

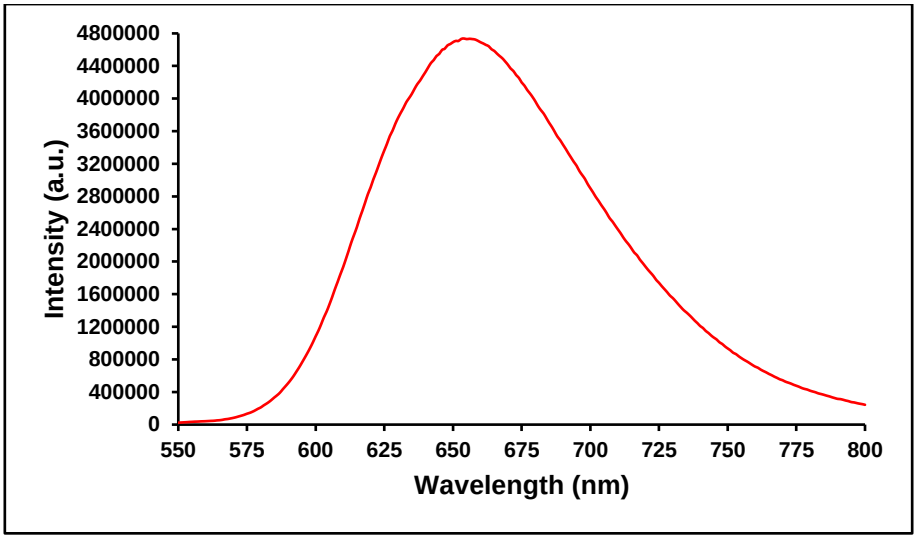

Figure 5.16 – Luminescence spectrum of 11.50µM $[Ru(bpy)_2(qtpy)]Cl_2$ in 5mM tris, 25mM NaCl buffer at ambient temperature. Excitation wavelength = 466nm. Excitation slit width = 5nm. Emission slit width = 5nm.

As complex $[Ru(bpy)_2(qtpy)]Cl_2$ shows appreciable absorption at wavelengths similar to that of BSA, its binding study with BSA could not be effectively progressed using absorption spectroscopy.

The BSA binding study of $[Ru(bpy)_2(qtpy)]^{2+}$ was then carried out in an analogous manner to that of $[Ir(bpy)_2(qtpy)]^{3+}$ (Fig. 5.17).

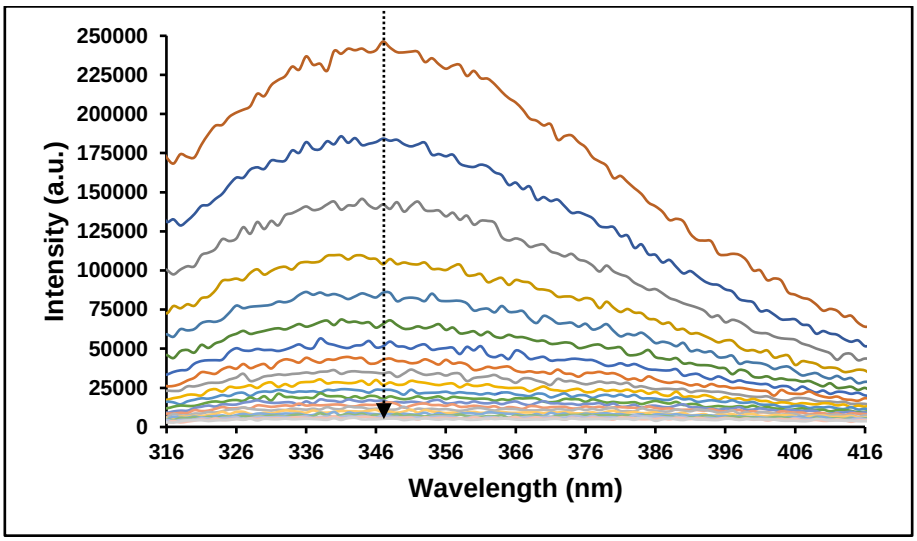

Figure 5.17 – Luminescent titration of 0–58.18µM $[Ru(bpy)_2(qtpy)]^{2+}$ into a solution of 3.07 x 10^{-8}M BSA in 5mM tris buffer, 25mM NaCl, pH 7.4 at ambient temperature. Excitation wavelength: 278nm; emission region: 316–416nm. Excitation slit width = 5nm. Emission slit width = 5nm.

5.6.4.1 Binding and Quenching Fits

Fig. 5.17 above was then fitted to the plot given in Fig. 5.18.

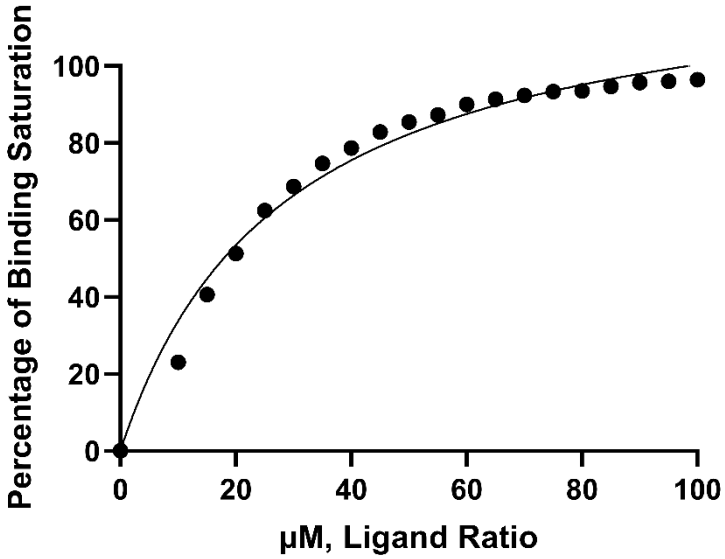

Figure 5.18 – Binding plot of BSA with $[Ru(bpy)_2(qtpy)]^{2+}$ derived from luminescent titration.

Using Equation 5.3, K_b and n values were obtained from the antilog of the intercept and slope of the plots of $Log_{10}[(F_0–F)/F]$ versus $Log_{10}[Q]$ at physiological pH 7.4, respectively, with K_b = 4.87 x $10^8 M^{-1}$ and N = ca. 1 (Fig. 5.19). The estimated values of the binding constant (K_b) and binding number (n) indicate a strong binding of the complex with BSA and are consistent with the non-linear SV-plot. The value of n being ca. 1 demonstrates the presence of a single type of binding between $[Ru(bpy)_2(qtpy)]^{2+}$ and BSA.

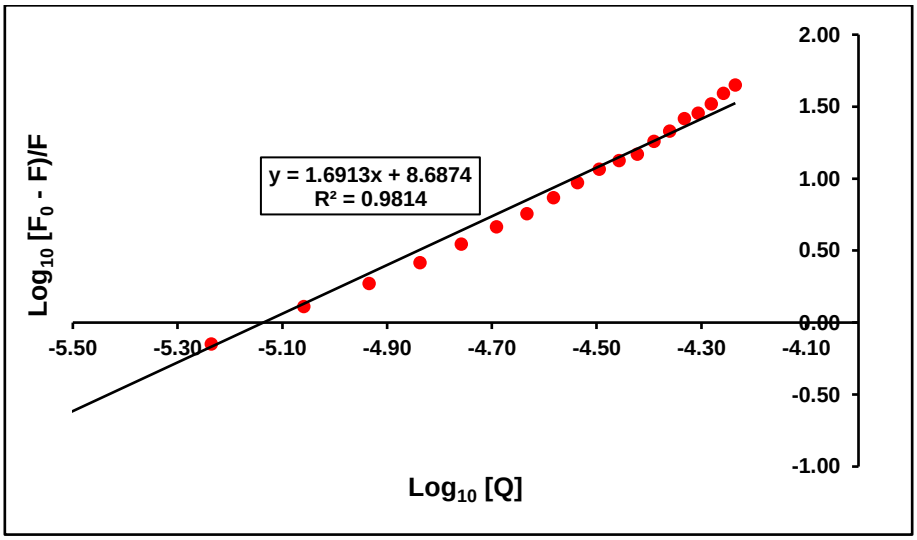

Figure 5.19 – Double–logarithmic plot for the interaction of 3.07 x 10^{-8}M BSA with 0–58.18µM $[Ru(bpy)_2(qtpy)]^{2+}$.

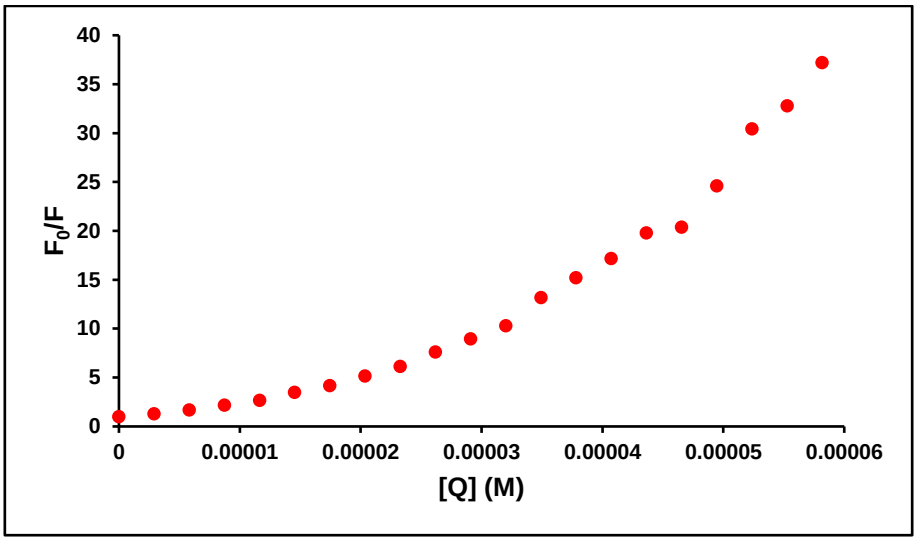

Figure 5.20 – Stern–Volmer plot for the quenching of 3.07 x 10^{-8}M BSA by 0–58.18µM $[Ru(bpy)_2(qtpy)]^{2+}$.

The quenching of emission by $[Ru(bpy)_2(qtpy)]^{2+}$ does not obey Stern-Volmer equation, suggesting a pure static quenching process. In fact, for these kinds of experiments, with excitation at wavelengths < 300nm and emission between 300–40nm, inner filter effects play a significant role, as the quencher's absorption is often expected in the same range where protein absorb.[35]

5.6.5 Subdomain IIA (Sudlow Site I) Competition – Displacement of Warfarin from BSA-Warfarin Adduct by $[Ru(bpy)_2(qtpy)]^{2+}$

Analogous experiments to those for $[Ir(bpy)_2(qtpy)]^{3+}$ were conducted with $[Ru(bpy)_2(qtpy)]^{2+}$. BSA-bound Warfarin emission decreases on addition of $[Ru(bpy)_2(qtpy)]^{2+}$, indicating the displacement of Warfarin from BSA-Warfarin adduct by $[Ru(bpy)_2(qtpy)]^{2+}$ (Fig. 5.21).

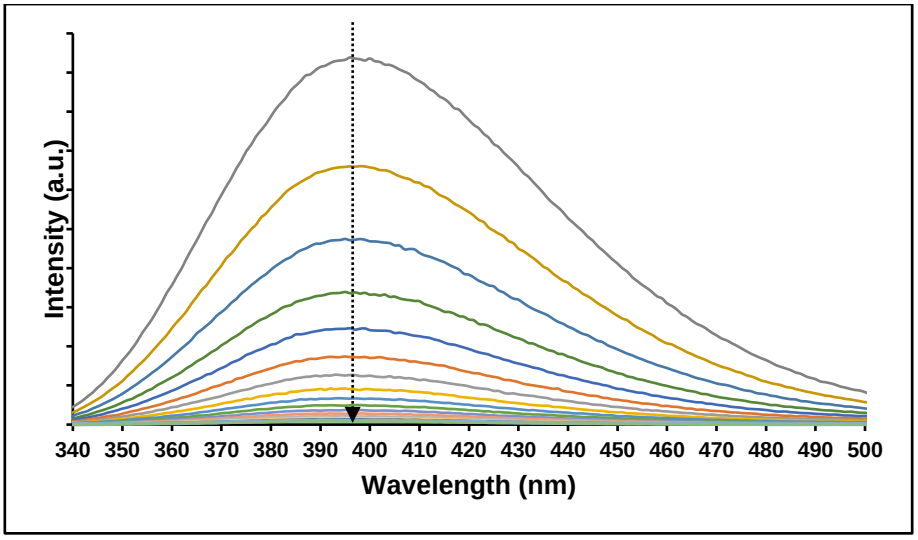

Figure 5.21 – Luminescence changes of BSA-bound Warfarin upon the incremental additions of 0–5.82 x 10^{-4}M $[Ru(bpy)_2(qtpy)]^{2+}$. [BSA] = 2.45 x 10^{-7}M. [Warfarin] = 2.55 x 10^{-4}M.

5.7.6 Subdomain IIIA (Sudlow Site II) Competition – Displacement of Ibuprofen from BSA-Ibuprofen Adduct by $[Ru(bpy)_2(qtpy)]^{2+}$

Ibuprofen displacement experiments for $[Ru(bpy)_2(qtpy)]^{2+}$ were conducted through the same method used for $[Ir(bpy)_2(qtpy)]^{3+}$ in which $[Ru(bpy)_2(qtpy)]^{2+}$ was added to the BSA-Ibuprofen adduct causing a gradual quenching of the BSA-Ibuprofen adduct emission (Fig. 5.22).

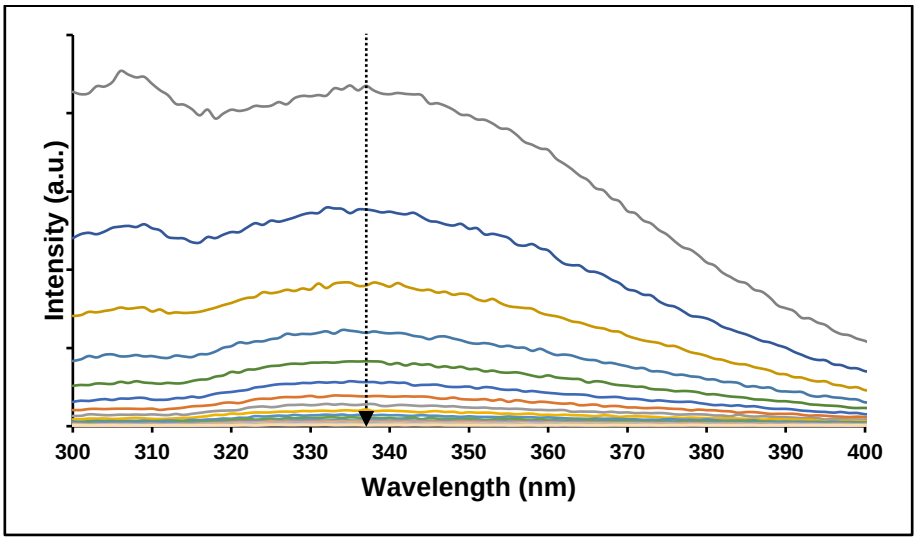

Figure 5.22 – Luminescence profile changes of BSA-bound Ibuprofen upon incremental additions of 0–1.16 x 10^{-4}M $[Ru(bpy)_2(qtpy)]^{2+}$. [BSA] = 2.45 x 10^{-7}M. [Ibuprofen] = 2.55 x 10^{-4}M.

5.6.7 BSA Binding with $[Ru(phen)_2(qtpy)]^{2+}$

The UV-Vis and luminescence spectra of $[Ru(phen)_2(qtpy)]^{2+}$ were first compared to those previously obtained (Figs. 5.23 and 5.24).

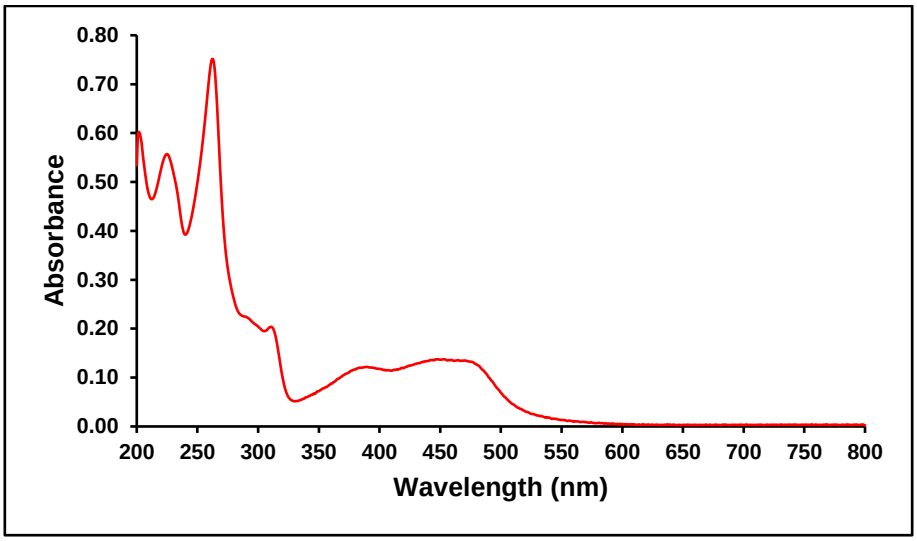

Figure 5.23 – Absorption spectrum of 12.70µM $[Ru(phen)_2(qtpy)]Cl_2$ in 5mM tris, 25mM NaCl buffer at ambient temperature. Spectral shape and absorption wavelength analogous to those of $[Ru(phen)_2(qtpy)]Cl_2$ by Dr Haslina Ahmad.[34]

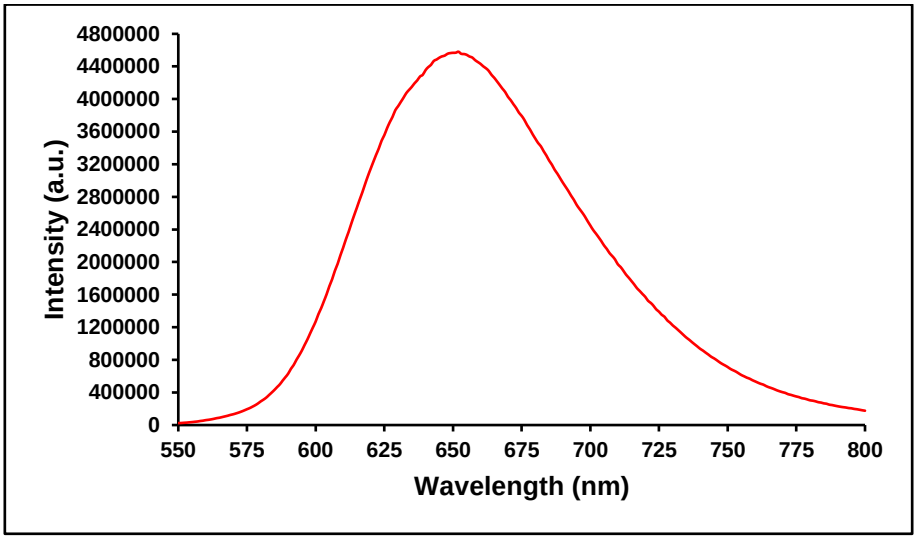

Figure 5.24 – Luminescence spectrum of 12.70µM $[Ru(phen)_2(qtpy)]Cl_2$ in 5mM tris, 25mM NaCl buffer at ambient temperature. Excitation wavelength = 475nm. Excitation slit width = 5nm. Emission slit width = 5nm.

Again, as complex $[Ru(phen)_2(qtpy)]Cl_2$ shows absorption at wavelengths similar to BSA, its binding study with BSA could not be effectively progressed using absorption spectroscopy.

The BSA binding study of $[Ru(phen)_2(qtpy)]^{2+}$ was carried out in an analogous manner to that of $[Ru(bpy)_2(qtpy)]^{2+}$. The gradual annihilation of BSA's emission intensity is given in Fig. 5.25.

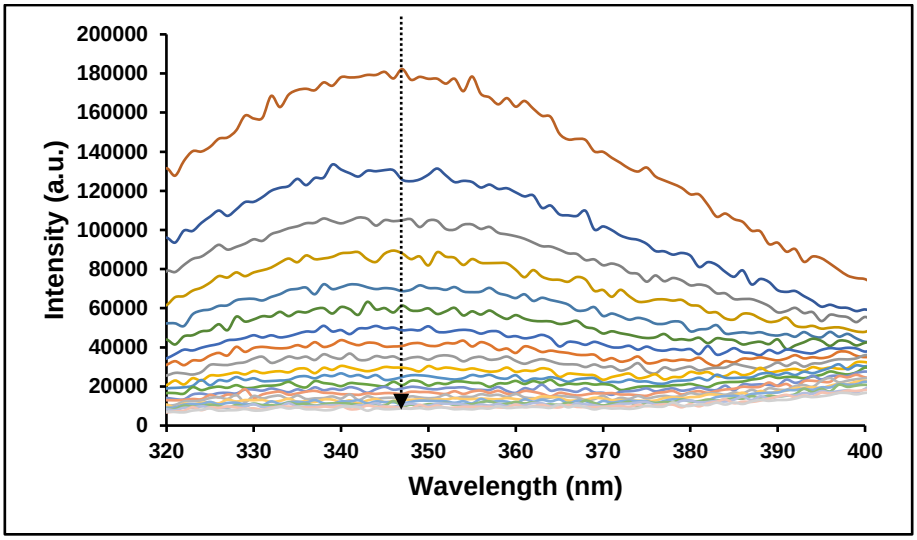

Figure 5.25 – Luminescent titration of 0–67.27µM $[Ru(phen)_2(qtpy)]^{2+}$ into a solution of 3.07 x 10^{-8}M BSA in 5mM tris buffer, 25mM NaCl, pH 7.4 at ambient temperature. Excitation wavelength: 278nm; emission region: 320–400nm. Excitation slit width = 5nm. Emission slit width = 5nm.

5.6.7.1 Binding and Quenching Fits

Fig. 5.25 above was then fitted to the plot given in Fig. 5.26.

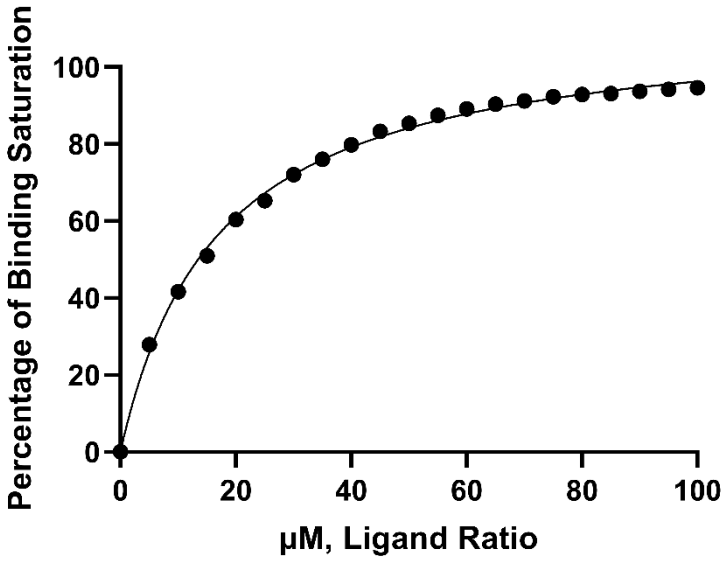

Figure 5.26 – Binding plot of BSA with $[Ru(phen)_2(qtpy)]^{2+}$ derived from luminescent titration.

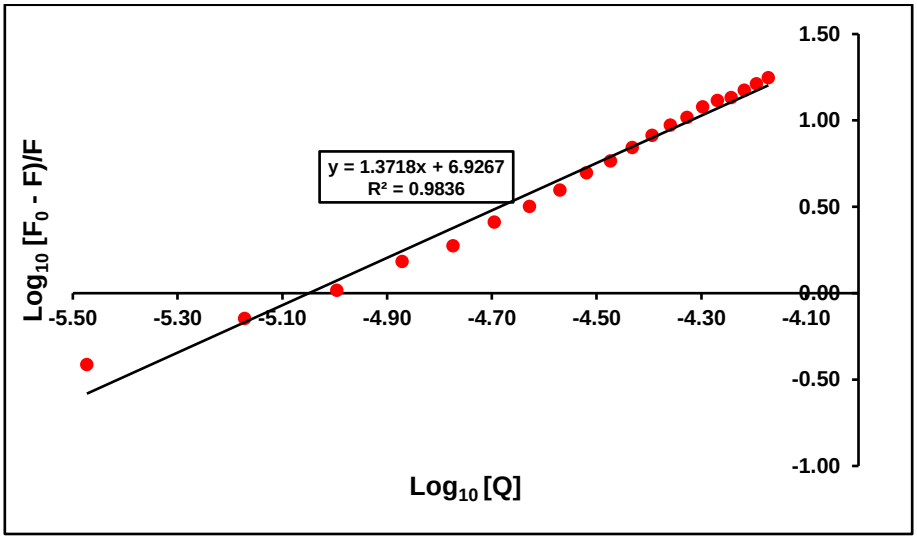

Figure 5.27 – Double–logarithmic plot for the interaction of 3.07 x 10^{-8}M BSA with 0–67.27µM $[Ru(phen)_2(qtpy)]^{2+}$.

Using Equation 3.3, K_b and n values were obtained from the antilog of the intercept and slope of the plots of $Log_{10}[(F_0–F)/F]$ versus $Log_{10}[Q]$ at physiological pH 7.4, respectively, with K_b = 8.45 x 10^6M^{-1} and N = ca. 1 (Fig. 5.27). The estimated values of binding constant (K_b) and binding number (n) indicates a strong binding of the complex with BSA. The value of n being ca. 1 demonstrates that a single type of binding occurs between $[Ru(phen)_2(qtpy)]^{2+}$ and BSA.

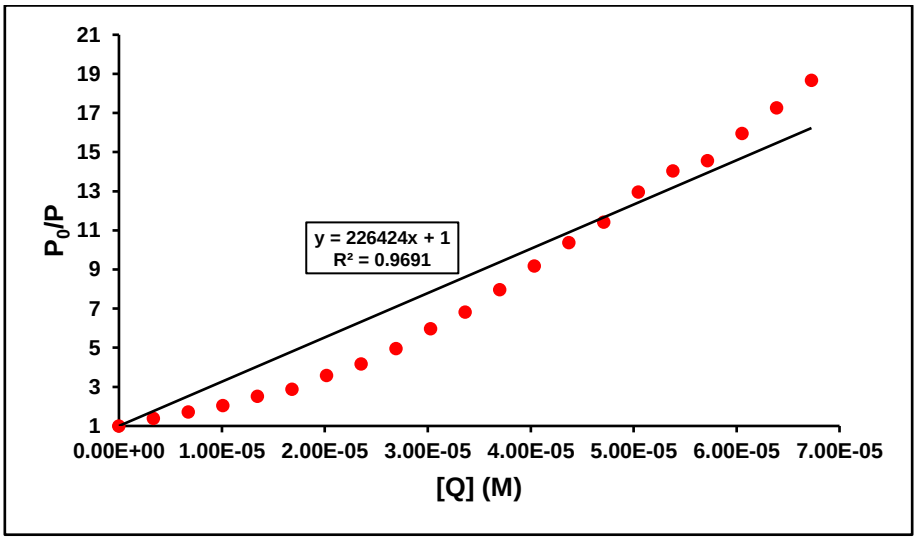

Figure 5.28 – Stern–Volmer plot for the quenching of 3.07 x 10^{-8}M BSA by 0–67.27µM $[Ru(phen)_2(qtpy)]^{2+}$.

The quenching of BSA's emission by $[Ru(phen)_2(qtpy)]^{2+}$ obeys Stern-Volmer equation. The data were fitted to a standard Stern-Volmer equation to obtain both the Stern-Volmer constant (K_{sv}) and quenching constant (K_q) for the quenching event (Fig. 5.28). The K_{sv} and K_q values thus obtained are 2.26 x $10^5 M^{-1}$ and 1.90 x $10^{13} M^{-1}$, respectively (τ_0 of BSA protein in tris buffer was measured to be 11.9225ns).

5.6.8 Subdomain IIA (Sudlow Site I) Competition – Displacement of Warfarin from BSA-Warfarin Adduct by $[Ru(phen)_2(qtpy)]^{2+}$

Analogous experiments as for $[Ru(bpy)_2(qtpy)]^{2+}$ were conducted for $[Ru(phen)_2(qtpy)]^{2+}$. Results show that $[Ru(phen)_2(qtpy)]^{2+}$ positively competed with Warfarin for BSA's site I, giving a decrease in BSA-bound Warfarin emission with increasing metal complex concentration (Fig. 5.29).

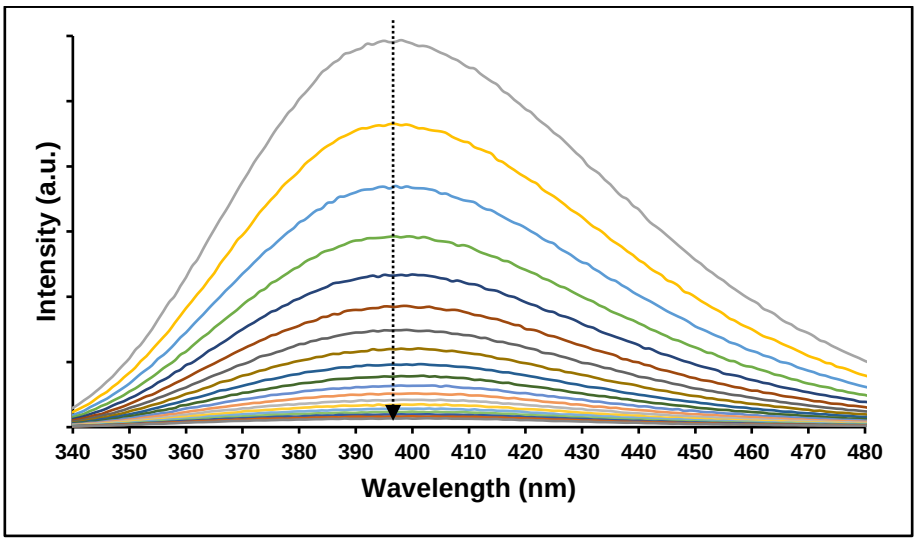

Figure 5.29 – Luminescence changes of BSA-bound Warfarin upon the incremental additions of 0–1.21 x 10^{-4}M $[Ru(phen)_2(qtpy)]^{2+}$. [BSA] = 2.45 x 10^{-7}M. [Warfarin] = 2.55 x 10^{-4}M.

5.6.9 Subdomain IIIA (Sudlow Site II) Competition – Displacement of Ibuprofen from BSA-Ibuprofen Adduct by $[Ru(phen)_2(qtpy)]^{2+}$

Analogous experiments as for $[Ru(bpy)_2(qtpy)]^{2+}$ were conducted for $[Ru(phen)_2(qtpy)]^{2+}$. BSA-Ibuprofen adduct was titrated against $[Ru(phen)_2(qtpy)]^{2+}$, leading to a distinct quenching of BSA-Ibuprofen adduct emission (Fig. 5.30).

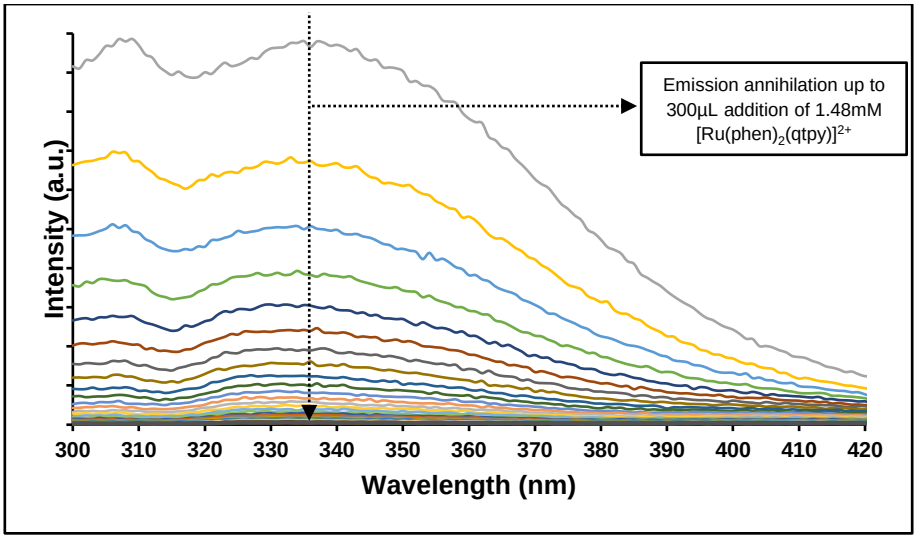

Figure 5.30 – Luminescence profile changes of BSA-bound Ibuprofen upon incremental additions of 0–2.02 x 10^{-4}M $[Ru(phen)_2(qtpy)]^{2+}$. [BSA] = 2.45 x 10^{-7}M. [Ibuprofen] = 2.55 x 10^{-4}M.

5.6.10 BSA Binding with $[Ru(dppz)_2(qtpy)]^{2+}$

The UV-Vis and luminescence spectra of $[Ru(dppz)_2(qtpy)]^{2+}$ were first compared to those obtained previously (Figs. 5.31 and 5.32).

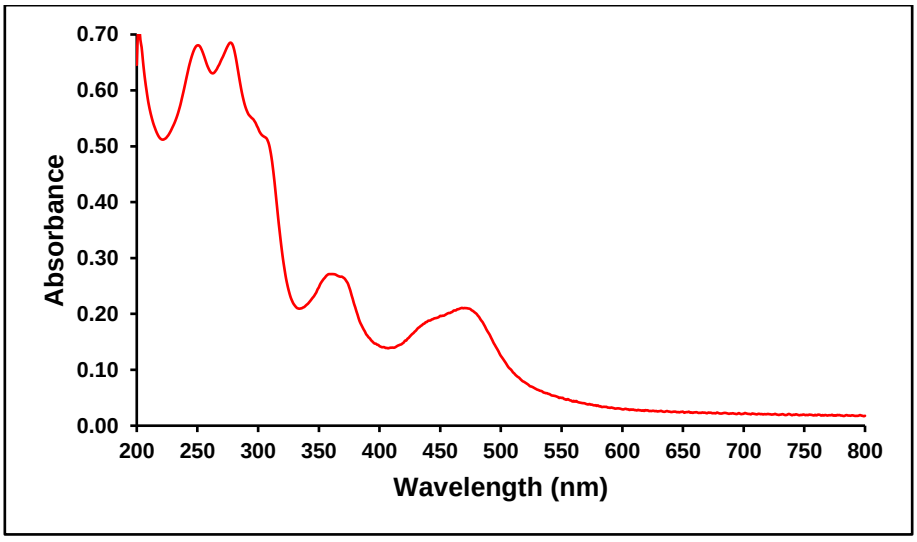

Figure 5.31 – Absorption spectrum of 21.50µM $[Ru(dppz)_2(qtpy)]Cl_2$ in 5mM tris, 25mM NaCl buffer at ambient temperature. Spectral shape and absorption wavelength analogous/comparable to those of $[Ru(dppz)_2(qtpy)]Cl_2$ by Dr Haslina Ahmad.[34]

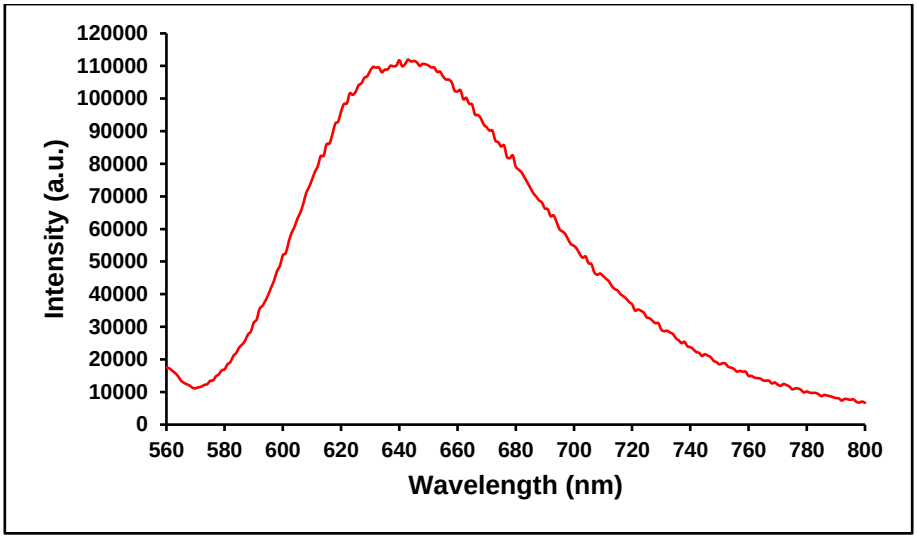

Figure 5.32 – Luminescence spectrum of 21.50µM $[Ru(dppz)_2(qtpy)]Cl_2$ in 5mM tris, 25mM NaCl buffer, pH 7.4 at ambient temperature. Excitation wavelength = 468nm. Excitation slit width = 5nm. Emission slit width = 5nm. Spectral shape and absorption wavelength analogous to those of $[Ru(phen)_2(qtpy)]Cl_2$ obtained in 5mM tris, 25mM NaCl buffer, pH 7.0 by Dr Haslina Ahmad.

The BSA binding study of $[Ru(dppz)_2(qtpy)]^{2+}$ was carried out in an analogous manner to that of $[Ru(bpy)_2(qtpy)]^{2+}$ (Fig. 5.33).

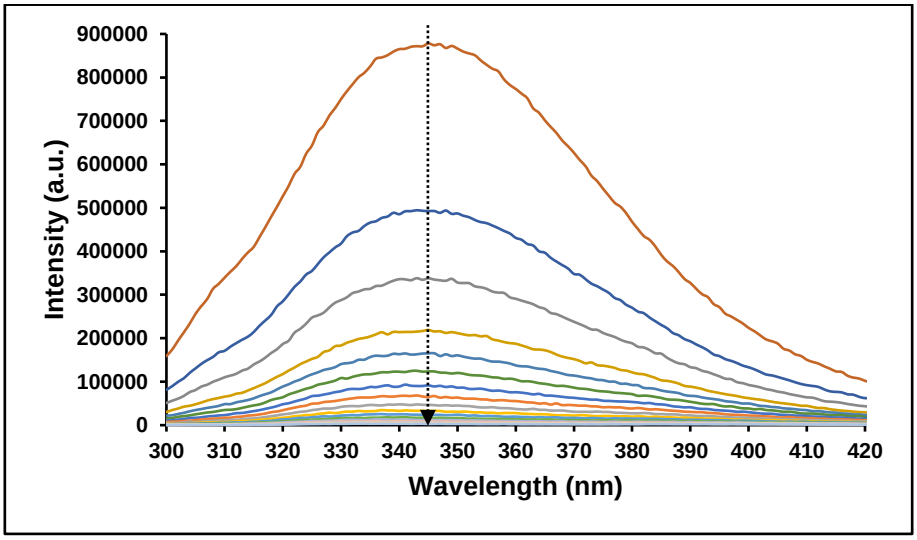

Figure 5.33 – Luminescent titration of 0–46.55µM $[Ru(dppz)_2(qtpy)]^{2+}$ into a solution of 8.37 x 10^{-8}M BSA in 5mM tris buffer, 25mM NaCl, pH 7.4 at ambient temperature. Excitation wavelength: 278nm; emission region: 300–420nm. Excitation slit width = 5nm. Emission slit width = 5nm.

5.6.10.1 Binding and Quenching Fits

Fig. 5.33 above was then fitted to the plot given in Fig. 5.34.

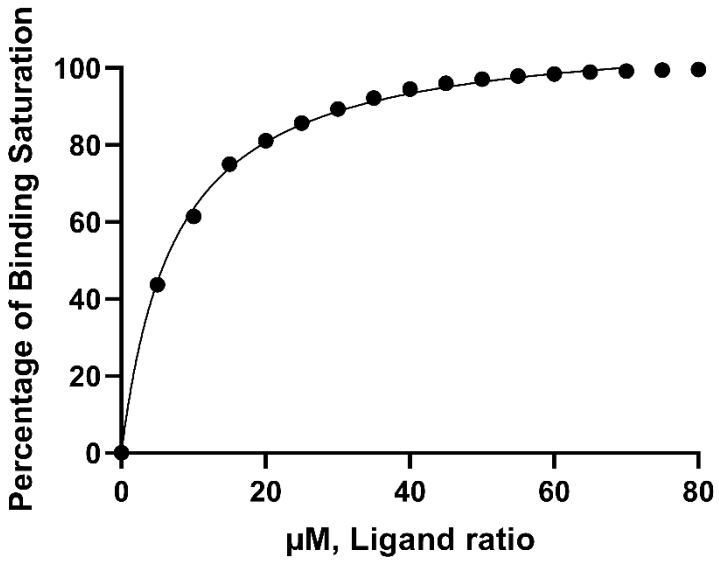

Figure 5.34 – Binding plot of BSA with $[Ru(dppz)_2(qtpy)]^{2+}$ derived from luminescent titration.

A fitting of the data to a double logarithmic plot furnished the values of the binding constant, K_b, and the number of the bound sites, n, which were obtained from the antilog of the intercept and slope, respectively of the plot of $Log_{10}[(F_0 - F)/F]$ versus $Log_{10}[Q]$ at physiological pH 7.4. K_b = 1.54 x $10^{11}M^{-1}$ and N = ca. 2 (Fig. 5.35). The estimated values of binding constant (K_b) and binding number (N) indicates a strong binding of the complex with BSA. The value of n being ca. 2 demonstrates that a complex type of binding occurs between $[Ru(dppz)_2(qtpy)]^{2+}$ and BSA.

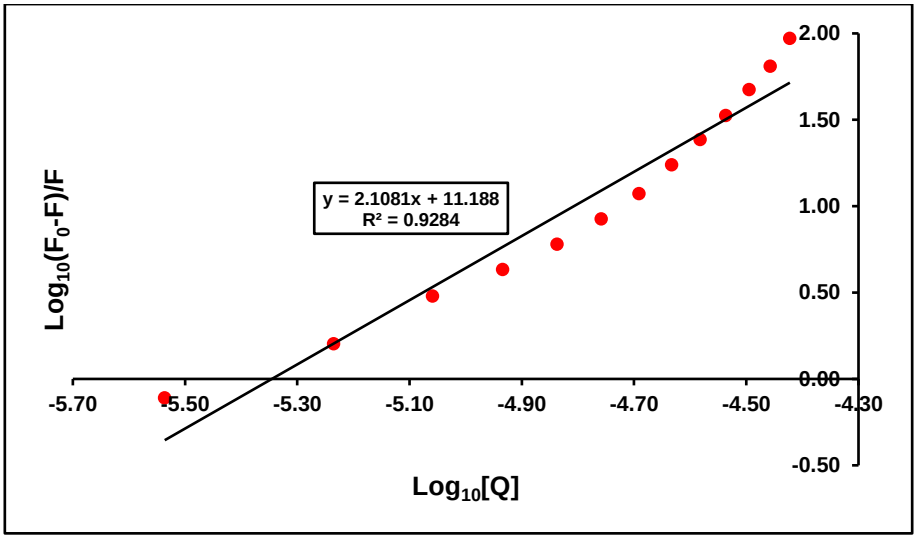

Figure 5.35 – Double–logarithmic plot for the interaction of 8.37 x 10^{-8}M BSA with 0–46.55μM $[Ru(dppz)_2(qtpy)]^{2+}$.

The quenching of BSA's emission by $[Ru(dppz)_2(qtpy)]^{2+}$ does not obey Stern-Volmer equation (Fig. 5.36). Instead, the quenching shows a positive deviation from Stern-Volmer Kinetics. As such, the data are consistent with a static process of interaction of the complex with BSA. Stern-Volmer constant (K_{sv}) and quenching constant (K_q) could not be estimated.

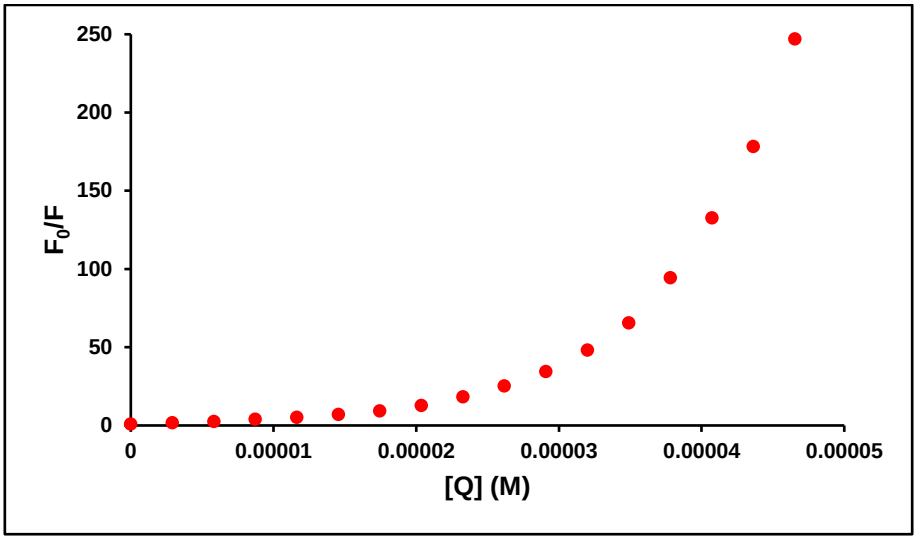

Figure 5.36 – Stern-Volmer plot for the quenching of 8.37 x 10^{-8}M BSA by 0–46.55µM $[Ru(dppz)_2(qtpy)]^{2+}$.

5.6.11 Subdomain IIA (Sudlow Site I) Competition – Displacement of Warfarin from BSA-Warfarin Adduct by $[Ru(dppz)_2(qtpy)]^{2+}$

Analogous experiments as for $[Ru(bpy)_2(qtpy)]^{2+}$ were conducted for $[Ru(dppz)_2(qtpy)]^{2+}$. Results show that $[Ru(phen)_2(qtpy)]^{2+}$ positively competed with Warfarin for BSA's site I, giving a decrease in BSA-bound Warfarin emission with increasing metal complex concentration (Fig. 5.37).

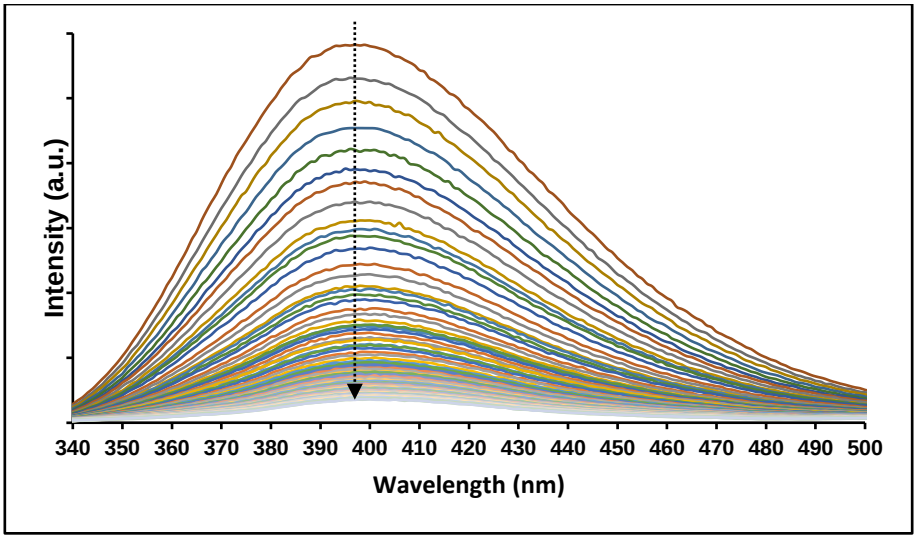

Figure 5.37 – Luminescence changes of BSA-bound Warfarin upon the incremental additions of 0–1.55 x 10^{-4}M $[Ru(dppz)_2(qtpy)]^{2+}$. [BSA] = 2.45 x 10^{-7}M. [Warfarin] = 2.55 x 10^{-4}M.

5.6.12 Subdomain IIIA (Sudlow Site II) Competition – Displacement of Ibuprofen from BSA-Ibuprofen Adduct by $[Ru(dppz)_2(qtpy)]^{2+}$

Analogous experiments as for $[Ru(dppz)_2(qtpy)]^{2+}$ were conducted for $[Ru(phen)_2(qtpy)]^{2+}$. Similar quenching behaviour of the complex's ^{3}MLCT was observed (Fig. 5.38).

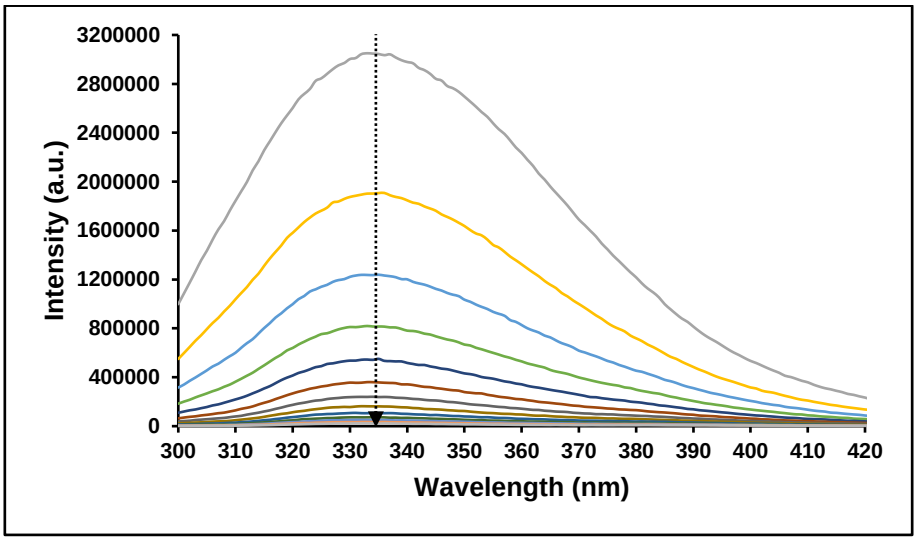

Figure 5.38 – First step of the luminescence profile changes of BSA-bound Ibuprofen upon incremental additions of 0–34.91µM $[Ru(dppz)_2(qtpy)]^{2+}$. [BSA] = 6.69 x 10^{-7}M. [Ibuprofen] = 2.55 x 10^{-4}M.

5.7 BSA-Binding Studies Summary

The binding studies of four complexes, i.e., $[Ir(bpy)_2(qtpy)]^{3+}$ and $[Ru(N–N)_2(qtpy)]^{2+}$ (where N–N = bpy, phen or dppz) with BSA were successfully undertaken. Experimental results show that all complexes investigated exhibit significant interactions with BSA, with $[Ru(dppz)_2(qtpy)]^{2+}$ having the highest K_b value and $[Ru(phen)_2(qtpy)]^{2+}$ having the lowest K_b value. In light of these results, it is possible that the complexes could be transported by BSA to reach their respective target(s), thus ensuring their biological activities. Contrariwise, the biological activity of these compounds may be inhibited to some extent as their high affinity for BSA will affect their overall bioavailability. Table 5.1 summarises the binding data for the compounds investigated. The relative emission decreases of BSA-bound Warfarin and/or BSA-bound Ibuprofen, as furnished by competition experiments, indicated that all the complexes investigated are binding to the Sudlow Site I and could be markers for this site. Temperature-switched experiments are underway to show the variation of the K_b values with increasing temperature and to see if there would be any resulting stabilisation of the complex-BSA adduct thereby formed. A thermodynamic profile of the interaction of these metal complexes with BSA could be created using isothermal titration calorimetry. ITC measures the heat that is either released or absorbed during biomolecular binding events, allowing precise measurements of binding constants, enthalpy (ΔH), and entropy (ΔS).

Table 5.1 – Summary of key BSA binding data for the compounds investigated.

Compound	K_{sv} (M^{-1})	K_q (M^{-1})	K_b (M^{-1})	N
$[Ir(bpy)_2(qtpy)]^{3+}$	1.52×10^5	1.27×10^{13}	5.94×10^4	1
$[Ru(bpy)_2(qtpy)]^{2+}$	Non-linear	Non-linear	4.87×10^8	1
$[Ru(phen)_2(qtpy)]^{2+}$	2.26×10^5	1.90×10^{13}	8.45×10^6	1
$[Ru(dppz)_2(qtpy)]^{2+}$	Non-linear	Non-linear	1.54×10^{11}	2

5.8 HSA Binding Investigations

HSA-drug interactions are an important factor in understanding the pharmacokinetics and pharmacological effects of drugs as drugs that bind to HSA can change the HSA binding behaviour and also potentially modulate the final therapeutic efficiency of the drugs.[36] It is often assumed that albumin binding typically reduces the amount of free drug available to exert therapeutic effects.[37–38] On the other hand, it has been demonstrated that albumin-binding can improve the pharmacokinetics of drugs, thus improving therapeutic use or reducing rapid clearance through other mechanisms.[39–40]

The experimental anticancer thiosemicarbazone, di-2-pyridylketone 4,4-dimethyl-3-thiosemicarbazone (Dp44mT), for instance, has been shown to be internalised by cancer cells via a putative carrier or receptor.[41–43] Interestingly, HSA enhances Dp44mT's uptake, toxicity, and apoptotic activity.[43] Considering Dp44mT targets lysosomes to induce apoptosis[44], and that HSA potentially undergoes lysosomal catabolism in tumors.[45–46] A possible explanation for the enhanced anticancer activity of Dp44mT is that HSA facilitates Dp44mT delivery to the lysosomes.[43, 47]

The study in this section explores the binding of three iridium(III) complexes and three ruthenium(II) complexes, $[Ir(N–N)_2(qtpy)]^{3+}$ and $[Ru(N–N)_2(qtpy)]^{2+}$ (where N–N = bpy, phen, or dppz) to HSA employing UV absorption spectroscopy and steady-state luminescence in an analogous manner to the interactions of the complexes with BSA. The probable binding site of the complexes to HSA was also investigated using molecular docking studies. In a later section, far-UV circular dichroism (CD) studies were employed to confirm the conformational changes of protein interaction with the metal complexes.

HSA shows a similar absorption spectrum to BSA with a maxima at ~ 278–280nm with no other major bands beyond 300 nm. By nature, protein do show any significant absorption beyond 300nm.

5.9 Luminescence Spectroscopic Studies

HSA luminescence spectroscopic studies follow the same procedure as for BSA luminescence spectroscopic studies.

5.9.1 $[Ir(bpy)_2(qtpy)]^{3+}$ Interaction with HSA

The result of $[Ir(bpy)_2(qtpy)]^{3+}$ binding to HSA is given in Fig. 5.39.

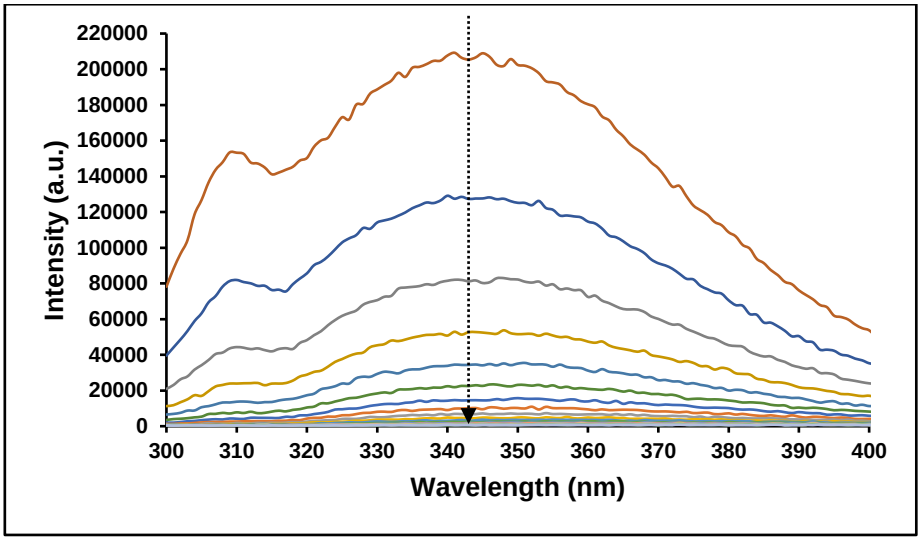

Figure 5.39 – Luminescent titration of 0–2.10 x 10^{-4}M $[Ir(bpy)_2(qtpy)]^{3+}$ into a solution of 0.25µM HSA in 5mM tris buffer, 25mM NaCl, pH 7.4 at ambient temperature. Excitation wavelength: 278nm; emission region: 300–400nm. Excitation slit width = 5nm. Emission slit width = 5nm.

5.9.1.1 Binding and Quenching Fits

Fig. 5.39 above was then fitted to the binding plot given in Fig. 5.40.

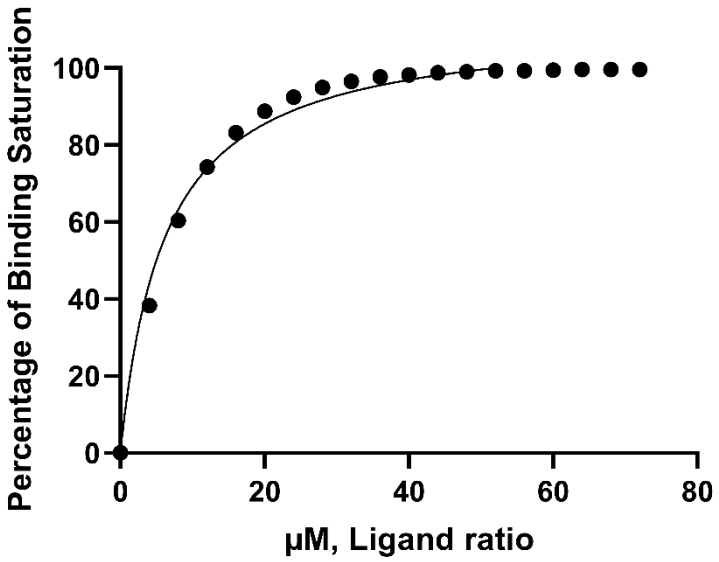

Figure 5.40 – Binding plot of HSA with $[Ir(bpy)_2(qtpy)]^{3+}$ derived from luminescent titration.

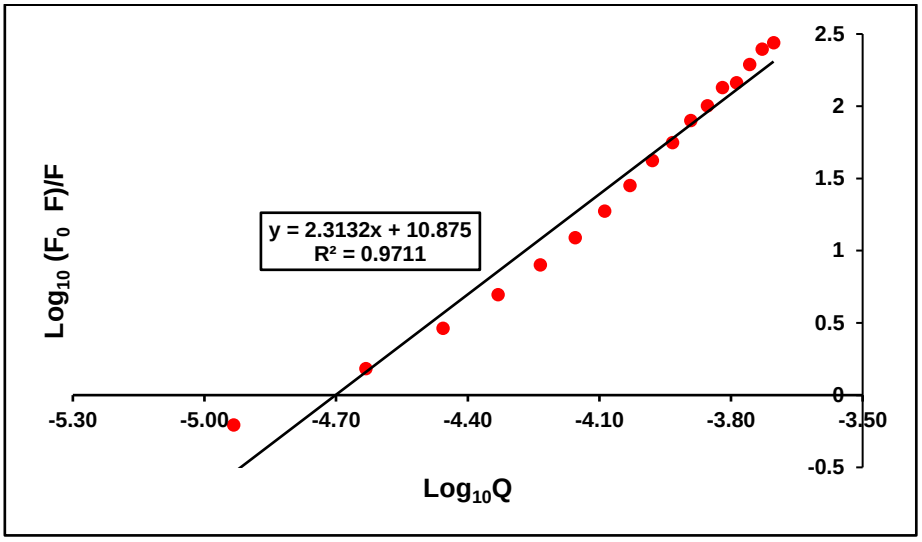

Figure 5.41 – Double–logarithmic plot for the interaction of 0.25µM HSA with 0–2.10 x 10^{-4}M $[Ir(bpy)_2(qtpy)]^{3+}$.

An evaluation of the double logarithmic plot in Fig. 5.41 gives the following binding parameters: K_b = 7.50 x 10^{10} and N = 2.

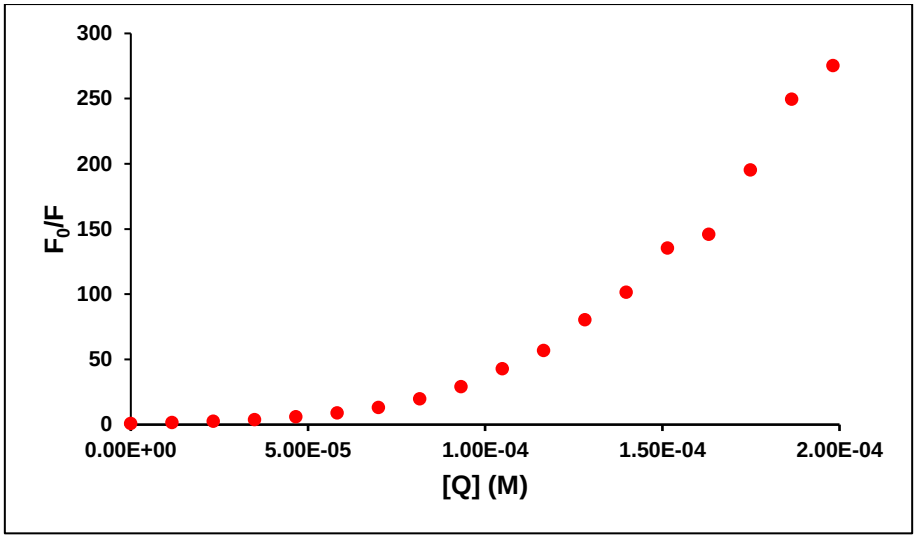

Figure 5.42 – Stern–Volmer plot for the quenching of 0.25µM HSA by 0–2.10 x 10^{-4}M $[Ir(bpy)_2(qtpy)]^{3+}$.

K_{SV} and K_q could not be computed as the Stern-Volmer plot is non-linear (Fig. 5.42).

5.9.2 $[Ir(phen)_2(qtpy)]^{3+}$ Interaction with HSA

The result of $[Ir(phen)_2(qtpy)]^{3+}$ binding to HSA is given in Fig. 5.43.

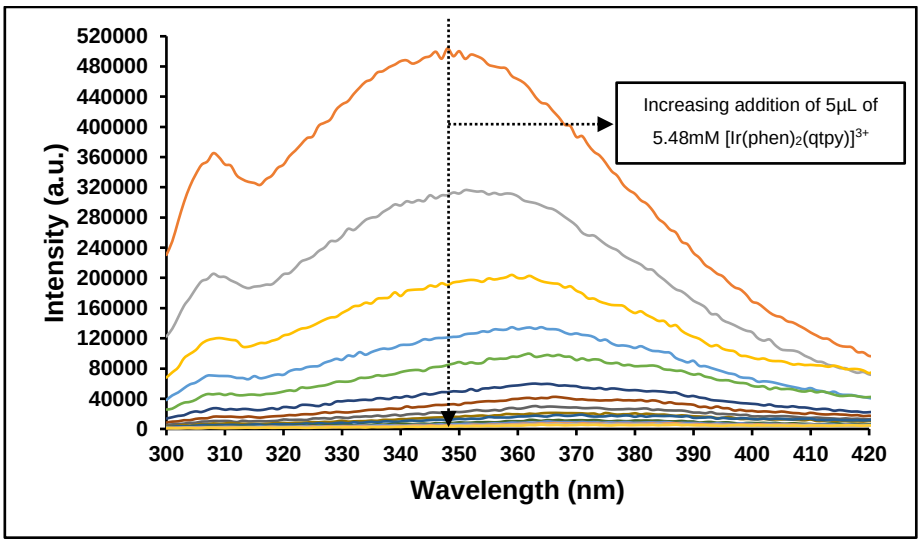

Figure 5.43 – Luminescent titration of 0–1.74 x 10^{-4}M $[Ir(phen)_2(qtpy)]^{3+}$ into a solution of 9.23 x 10^{-8}M HSA in 5mM tris buffer, 25mM NaCl, pH 7.4 at ambient temperature. HSA's intrinsic emission was gradually quenched with an associated red shift observed. Excitation wavelength: 278nm; emission region: 300–420nm. Excitation slit width = 5nm. Emission slit width = 5nm.

5.9.2.1 Binding and Quenching Fits

Fig. 5.43 above was then fitted to the binding plot given in Fig. 5.44.

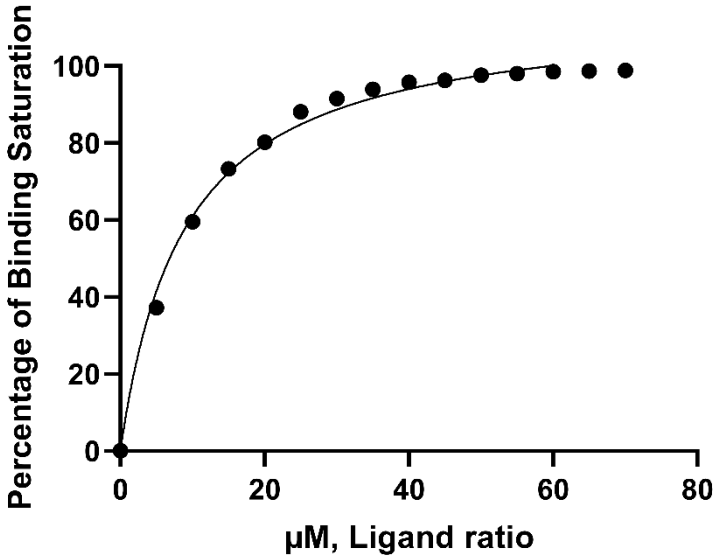

Figure 5.44 – Binding plot of HSA with $[Ir(phen)_2(qtpy)]^{3+}$ derived from luminescent titration.

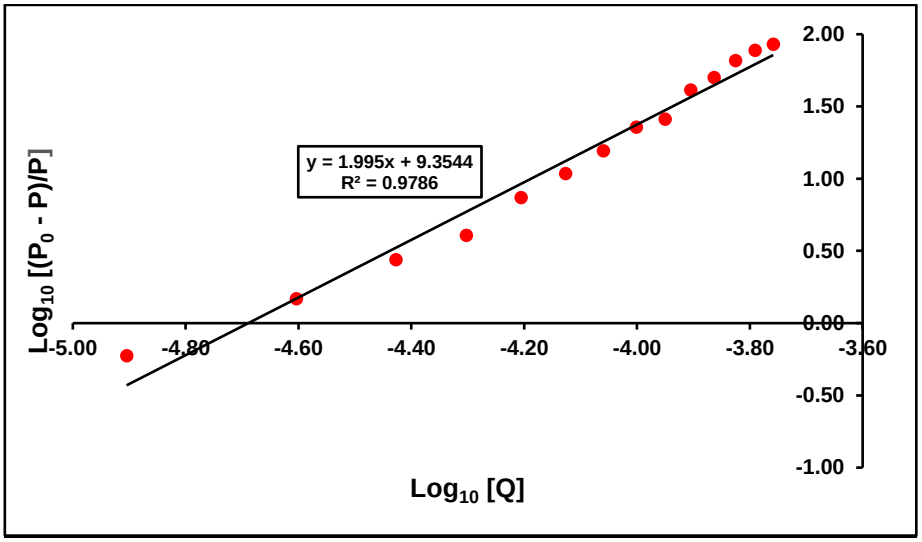

Figure 5.45 – Double-logarithmic plot for the interaction of 9.23 x 10^{-8}M HSA with 0–1.74 x 10^{-4}M $[Ir(phen)_2(qtpy)]^{3+}$.

An evaluation of the double logarithmic plot in Fig. 5.45 gives the following binding parameters: K_b = 2.26 x $10^9 M^{-1}$ and N = 2.

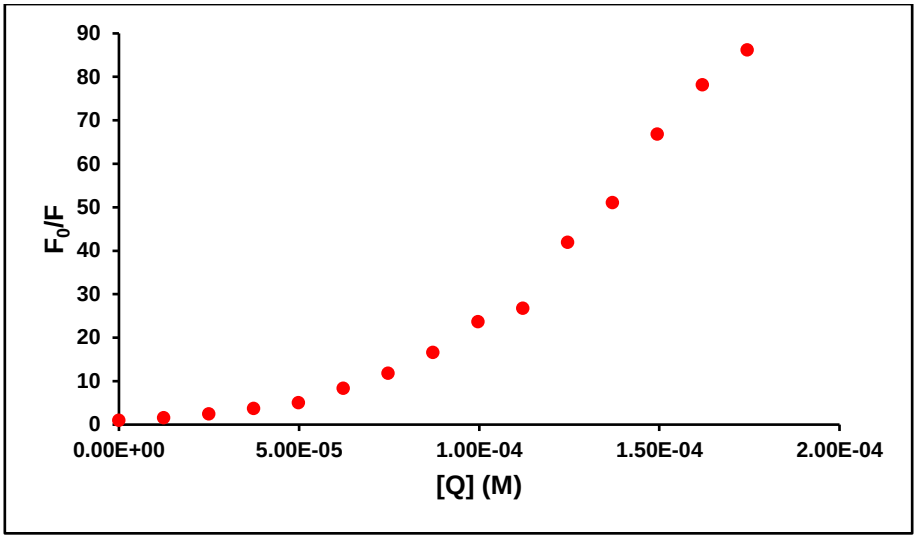

Figure 5.46 – Stern-Volmer plot for the quenching of 9.23 x 10^{-8}M HSA by 0–1.74 x 10^{-4}M $[Ir(phen)_2(qtpy)]^{3+}$.

K_{SV} and K_q could not be computed as the Stern-Volmer plot is non-linear (Fig. 5.46).

5.9.3 $[Ir(dppz)_2(qtpy)]^{3+}$ Interaction with HSA

The result of $[Ir(dppz)_2(qtpy)]^{3+}$ binding to HSA is given in Fig. 5.47.

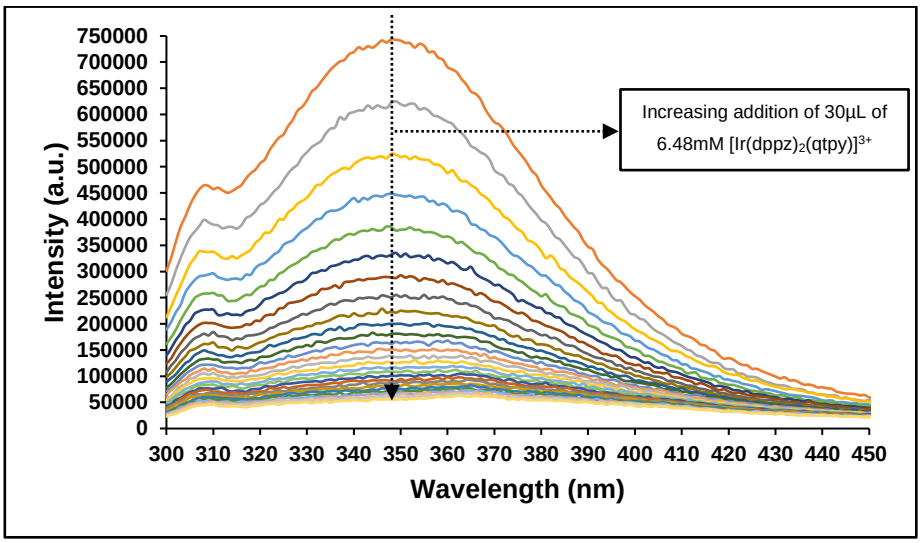

Figure 5.47 – Luminescent titration of 0–2.30mM $[Ir(dppz)_2(qtpy)]^{3+}$ into a solution of 2.80 x 10^{-7}M HSA in 5mM tris buffer, 25mM NaCl, pH 7.4 at ambient temperature. HSA's intrinsic emission was gradually quenched with an associated red shift observed. Excitation wavelength: 278nm; emission region: 300–450nm. Excitation slit width = 5nm. Emission slit width = 5nm.

5.9.3.1 Binding and Quenching Fits

Fig. 5.47 above was then fitted to the binding plot given in Fig. 5.48.

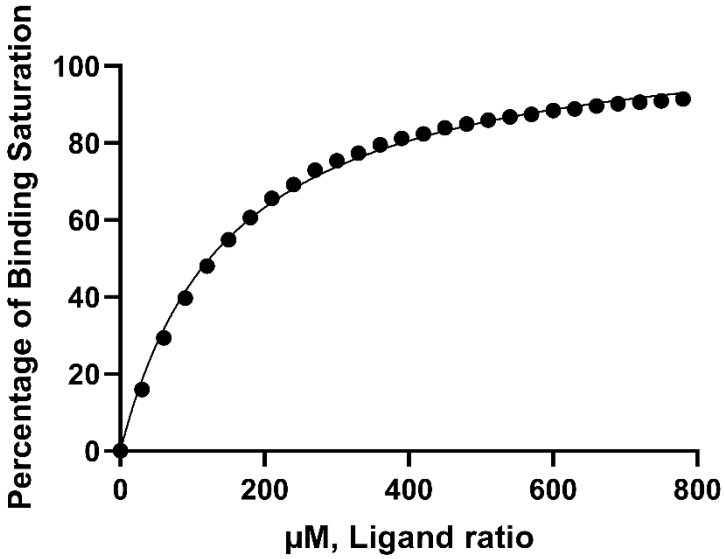

Figure 5.48 – Binding plot of HSA with $[Ir(dppz)_2(qtpy)]^{3+}$ derived from luminescent titration.

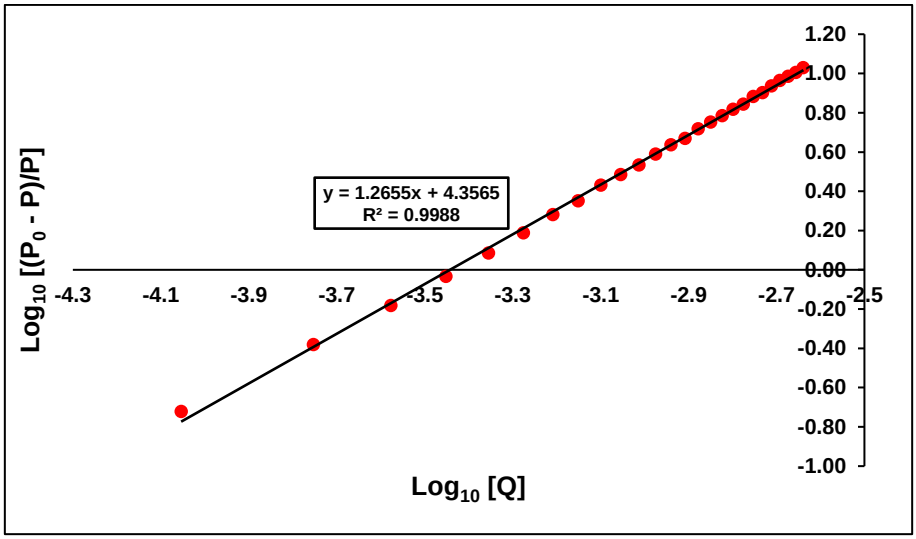

Figure 5.49 – Double-logarithmic plot for the interaction of 2.80 x 10^{-7}M HSA with 0–2.30mM $[Ir(dppz)_2(qtpy)]^{3+}$.

An evaluation of the double logarithmic plot in Fig. 5.49 gives the following binding parameters: K_b = 2.27 x 10^4M^{-1} and N = 1.

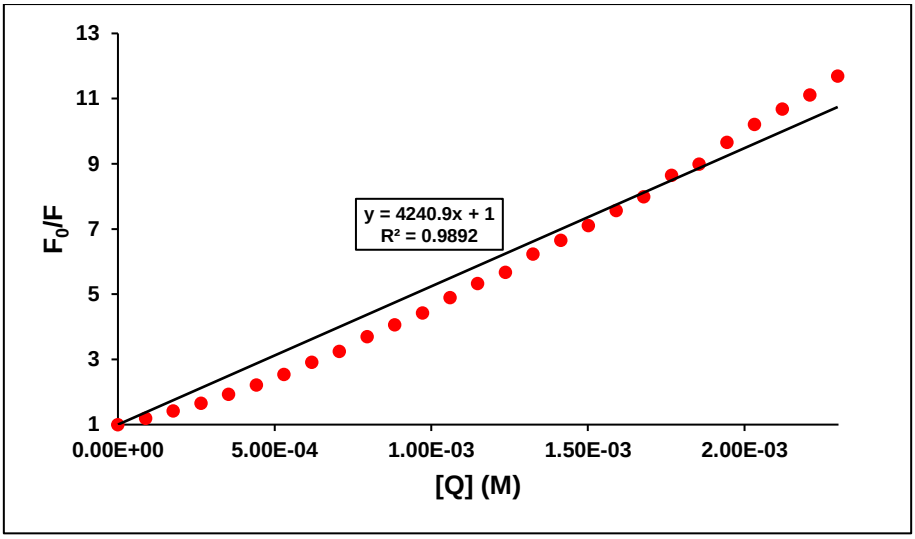

Figure 5.50 – Stern-Volmer plot for the quenching of 2.80 x 10^{-7}M HSA by 0–2.30mM $[Ir(dppz)_2(qtpy)]^{3+}$.

An evaluation of the Stern-Volmer plot in Fig. 5.50 gives the following quenching parameters: K_{sv} = 4.24 x $10^{3}M^{-1}$ and K_q = 3.56 x $10^{11}M^{-1}$ (τ_0 = 11.9225ns).

5.9.4 $[Ru(bpy)_2(qtpy)]^{2+}$ Interaction with HSA

The result of $[Ru(bpy)_2(qtpy)]^{3+}$ binding to HSA is given in Fig. 5.51.

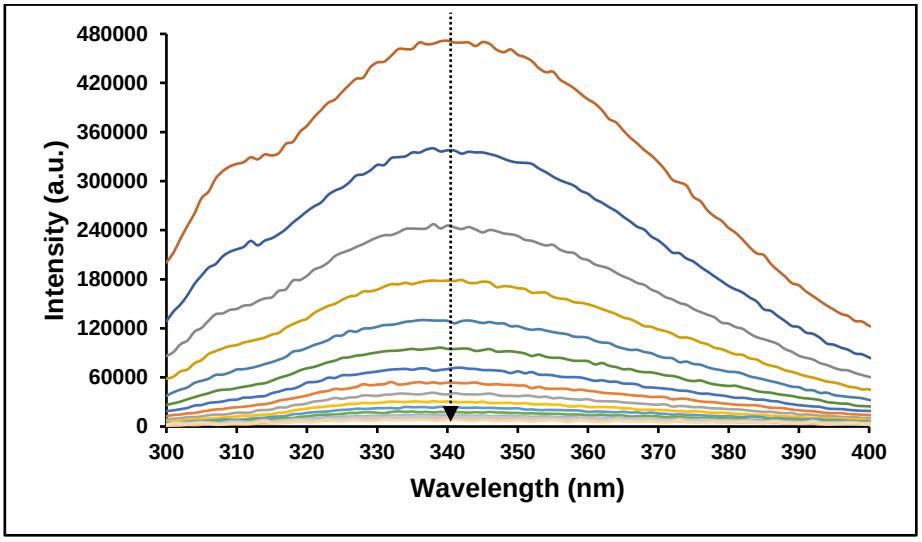

Figure 5.51 – Luminescent titration of 0–43.77µM $[Ru(bpy)_2(qtpy)]^{2+}$ into a solution of 5.59 x 10^{-7}M HSA in 5mM tris buffer, 25mM NaCl, pH 7.4 at ambient temperature. Excitation wavelength: 278nm; emission region: 300–400nm. Excitation slit width = 5nm. Emission slit width = 5nm. The emission at ~345nm was monitored.

5.9.4.1 Binding and Quenching Fits

Fig. 5.51 above was then fitted to the binding plot given in Fig. 5.52.

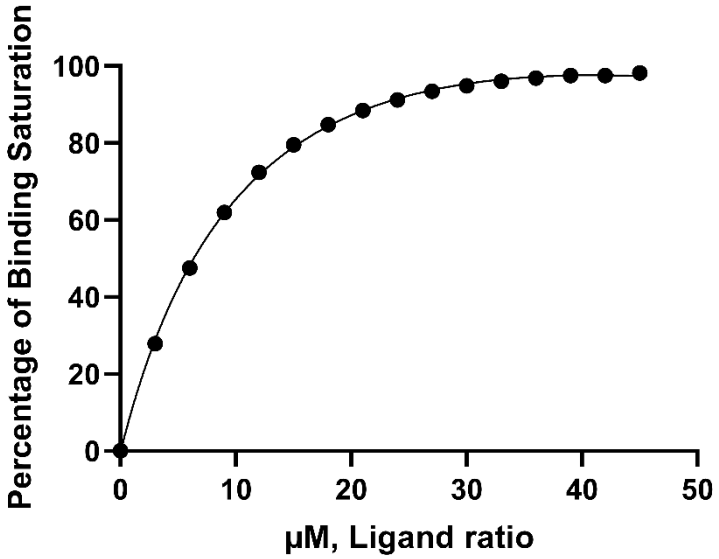

Figure 5.52 – Binding plot of HSA with $[Ru(bpy)_2(qtpy)]^{2+}$ derived from luminescent titration.

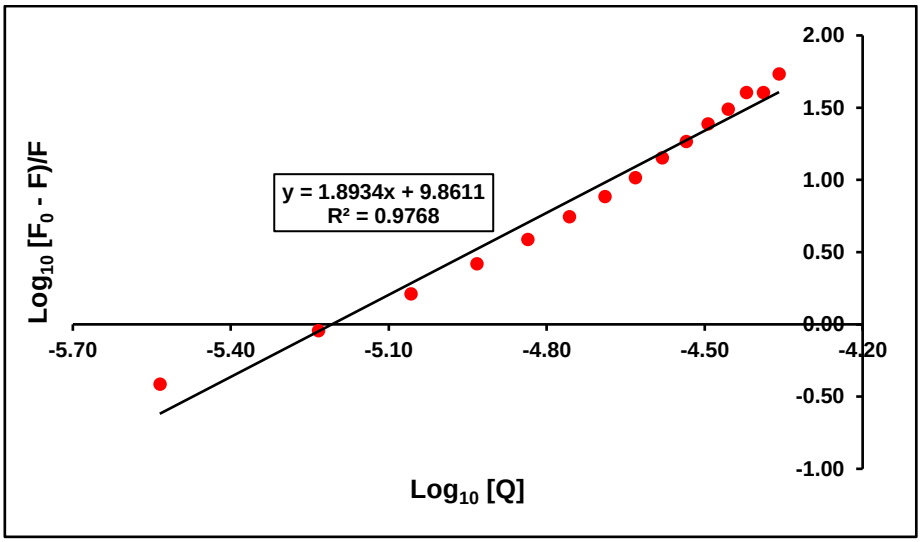

Figure 5.53 – Double–logarithmic plot for the interaction of 5.59 x 10^{-7}M HSA with 0–43.77µM $[Ru(bpy)_2(qtpy)]^{2+}$.

An evaluation of the plot in Fig. 5.53 gives the following binding parameters: K_b = 7.26 x $10^9 M^{-1}$ and N = 2.

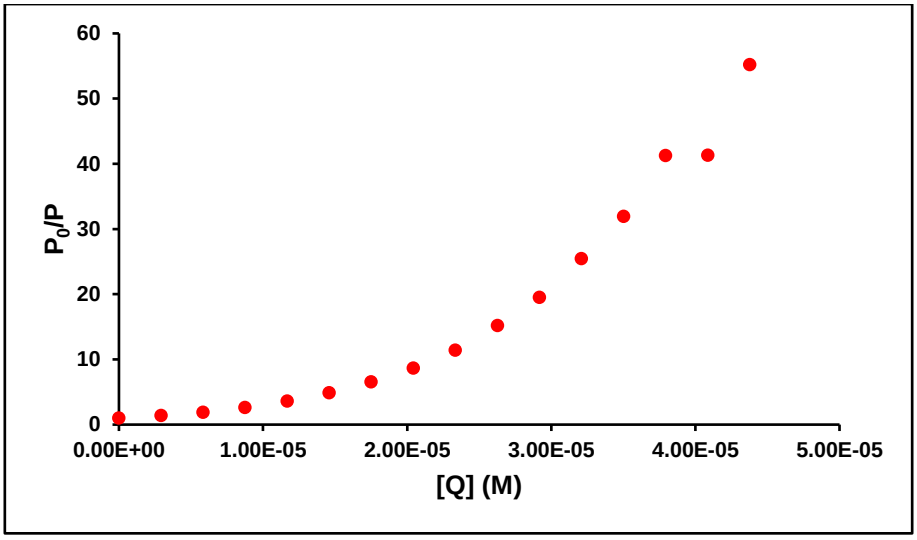

Figure 5.54 – Stern–Volmer plot for the quenching of 5.59 x 10^{-7}M HSA by 0–43.77µM $[Ru(bpy)_2(qtpy)]^{2+}$. The quenching of HSA's emission by $[Ru(bpy)_2(qtpy)]^{2+}$ shows a positive deviation form Stern-Volmer Kinetics.

The quenching of HSA's emission by $[Ru(bpy)_2(qtpy)]^{2+}$ does not obey Stern-Volmer equation well enough (Fig. 5.54). This perhaps suggests some static quenching taking place.

5.9.5 $[Ru(phen)_2(qtpy)]^{2+}$ Interaction with HSA

The result of $[Ru(phen)_2(qtpy)]^{3+}$ binding to HSA is given in Fig. 5.55.

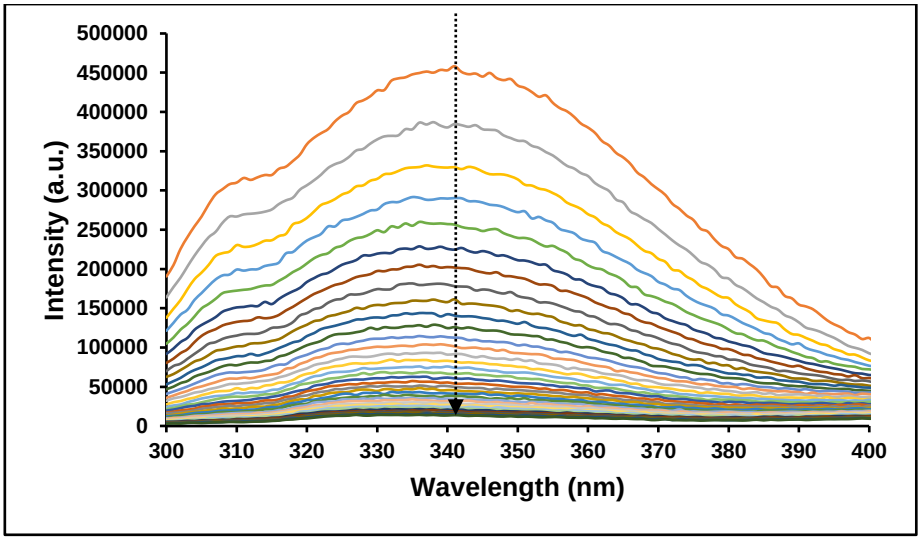

Figure 5.55 – Luminescent titration of 0–99.22µM $[Ru(phen)_2(qtpy)]^{2+}$ into a solution of 5.59 x 10^{-7}M HSA in 5mM tris buffer, 25mM NaCl, pH 7.4 at ambient temperature. Excitation wavelength: 278nm;

emission region: 300–400nm. Excitation slit width = 5nm. Emission slit width = 5nm. The emission at ~340nm was monitored.

5.9.5.1 Binding and Quenching Fits

Fig. 5.55 above was then fitted to the binding plot given in Fig. 5.56.

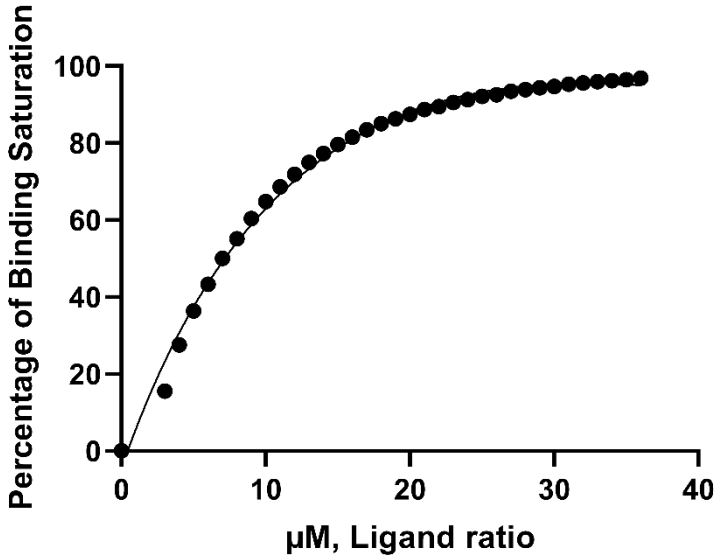

Figure 5.56 – Binding plot of HSA with $[Ru(phen)_2(qtpy)]^{2+}$ derived from luminescent titration.

An evaluation of the double logarithmic plot in Fig. 5.57 gives the following binding parameters: $K_b = 2.64 \times 10^7 M^{-1}$ and N = ca. 2.

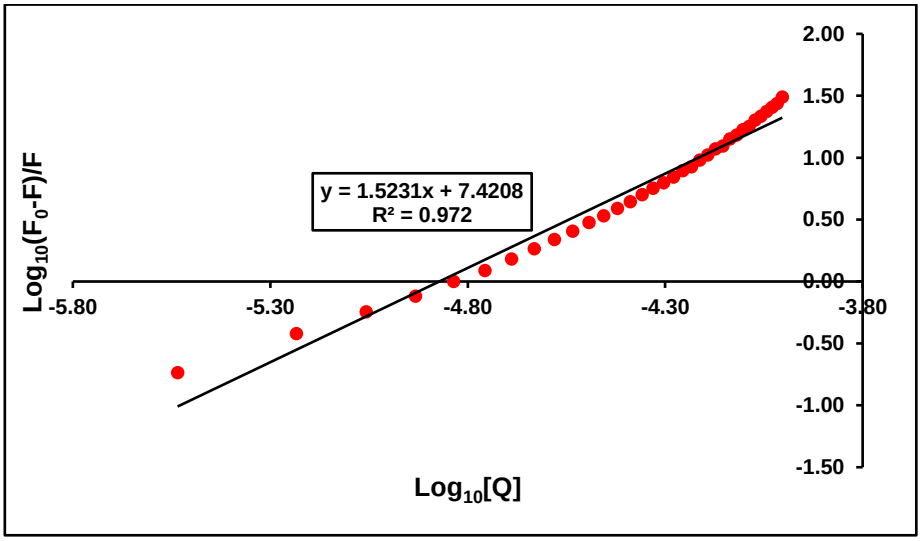

Figure 5.57 – Double–logarithmic plot for the interaction of 5.59×10^{-7}M HSA with 0–99.22µM $[Ru(phen)_2(qtpy)]^{2+}$.

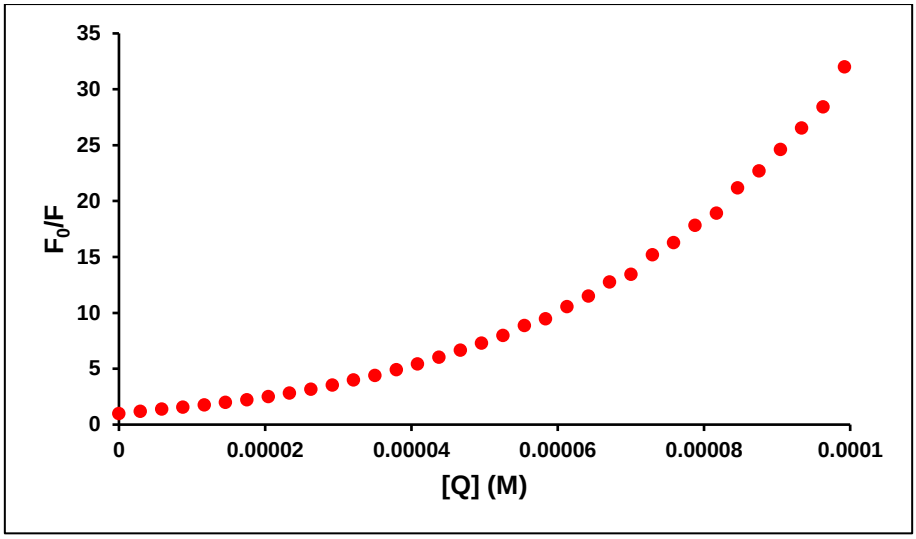

Figure 5.58 – Stern–Volmer plot for the quenching of 5.59 x 10^{-7}M HSA by 0–99.22µM $[Ru(phen)_2(qtpy)]^{2+}$. The quenching of HSA's emission by $[Ru(phen)_2(qtpy)]^{2+}$ shows a positive deviation form Stern-Volmer Kinetics.

The quenching of HSA's emission by $[Ru(phen)_2(qtpy)]^{2+}$ does not obey Stern-Volmer equation (Fig. 5.58). This perhaps suggests a more complex process of quenching than the mere simple quenching process observed in the case of $[Ir(bpy)_2(qtpy)]^{3+}$. This is seen in the obtainment of a curve instead of a straight line when the data were fitted to the classical Stern-Volmer equation/kinetics.

5.9.6 $[Ru(dppz)_2(qtpy)]^{2+}$ Interaction with HSA

The result of $[Ru(dppz)_2(qtpy)]^{3+}$ binding to HSA is given in Fig. 5.59.

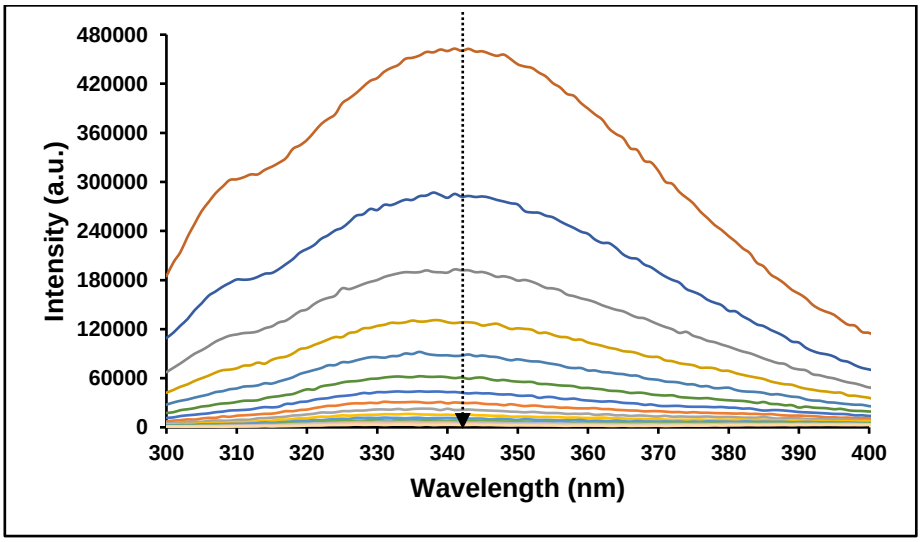

Figure 5.59 – Luminescent titration of 0–41.93µM $[Ru(dppz)_2(qtpy)]^{2+}$ into a solution of 5.59 x 10^{-7}M HSA in 5mM tris buffer, 25mM NaCl, pH 7.4 at ambient temperature. Excitation wavelength: 278nm; emission region: 300–400nm. Excitation slit width = 5nm. Emission slit width = 5nm. The emission at ~342nm was monitored.

5.9.6.1 Binding and Quenching Fits

Fig. 5.59 above was then fitted to the plots given in Fig. 5.60.

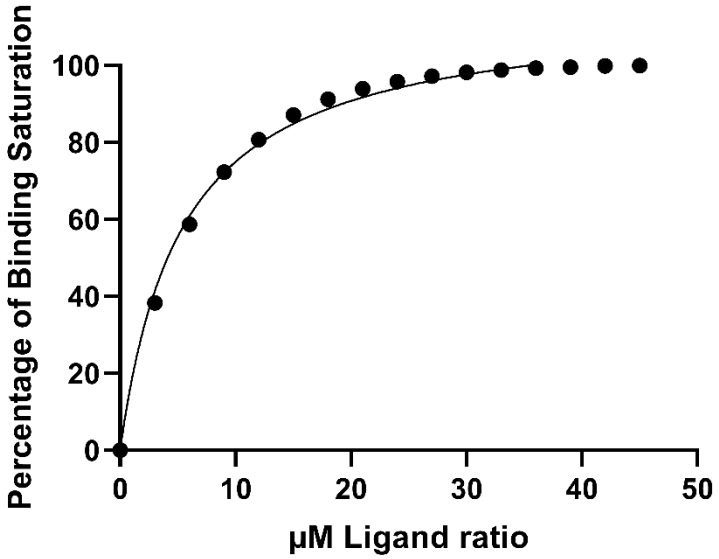

Figure 5.60 – Binding plot of HSA with $[Ru(dppz)_2(qtpy)]^{2+}$ derived from luminescent titration.

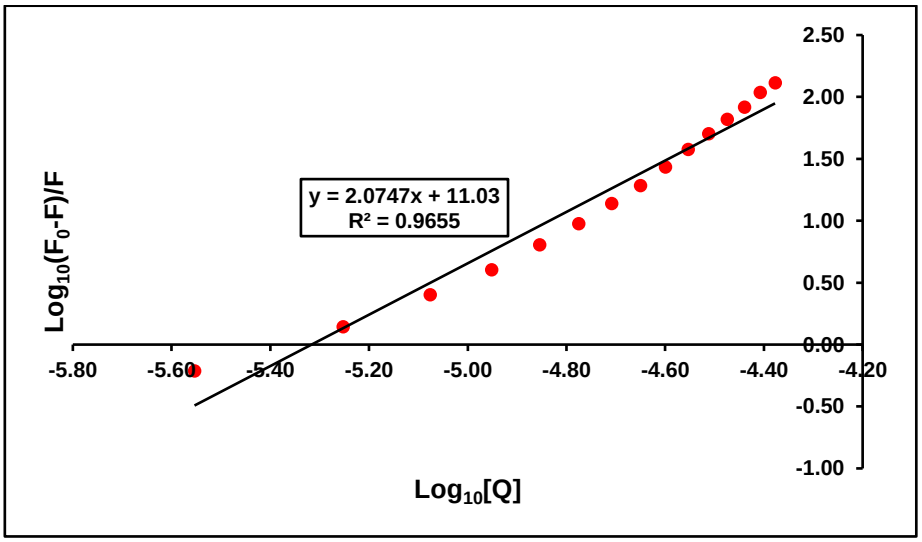

Figure 5.61 – Double–logarithmic plot for the interaction of 5.59 x 10^{-7}M HSA with 0–41.93µM $[Ru(dppz)_2(qtpy)]^{2+}$.

An evaluation of the double logarithmic plot in Fig. 5.61 gives the following binding parameters: K_b = 1.54 x $10^{11}M^{-1}$ and N = ca. 2.

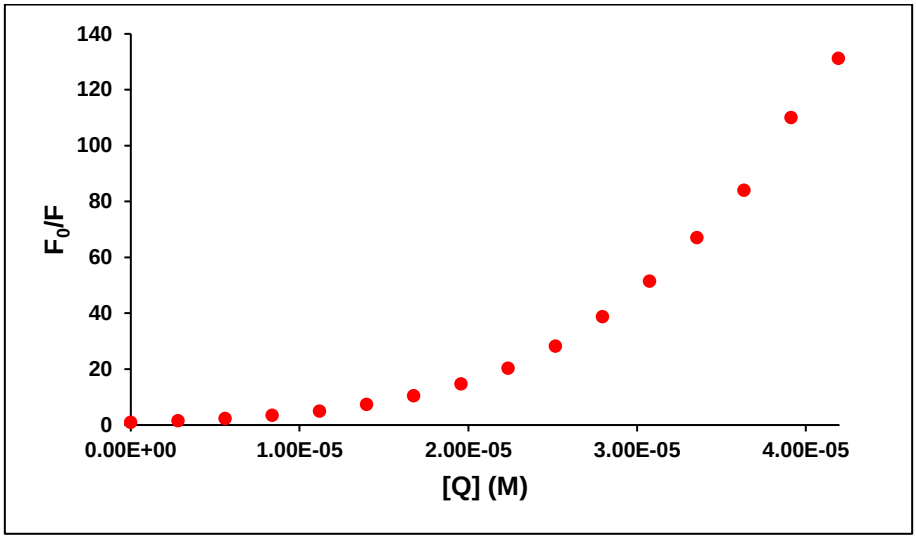

Figure 5.62 – Stern–Volmer plot for the quenching of 5.59 x 10^{-7}M HSA by 0–41.93µM $[Ru(dppz)_2(qtpy)]^{2+}$. The quenching of HSA's emission by $[Ru(dppz)_2(qtpy)]^{2+}$ shows a positive deviation from Stern-Volmer Kinetics.

The quenching of HSA's emission by $[Ru(dppz)_2(qtpy)]^{2+}$ does not obey Stern-Volmer kinetics (Fig. 5.62).

The values of K_b obtained in this work are comparable to those reported in previous works.[48]

5.9.7 Subdomain IIA (Sudlow Site I) Competition – Displacement of Warfarin from HSA-Warfarin Adduct by $[Ru(N–N)_2(qtpy)]^{2+}$ (where N–N = bpy, phen or dppz)

The experiments in this section were done analogously to those conducted for BSA. The complexes competed effectively for Warfarin. The next set of figures gives a summary of the results obtained.

5.9.7.1 $[Ru(bpy)_2(qtpy)]^{2+}$

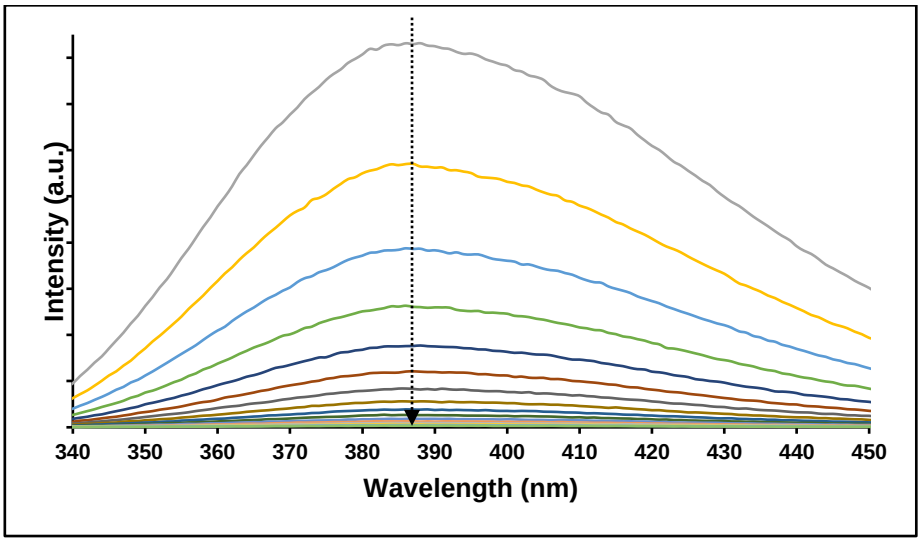

Figure 5.63 – Luminescence changes of HSA-bound Warfarin upon the incremental additions of 0–7.30 x 10^{-5}M $[Ru(bpy)_2(qtpy)]^{2+}$. [HSA] = 3.07 x 10^{-8}M. [Warfarin] = 2.55 x 10^{-4}M.

5.9.7.2 $[Ru(phen)_2(qtpy)]^{2+}$

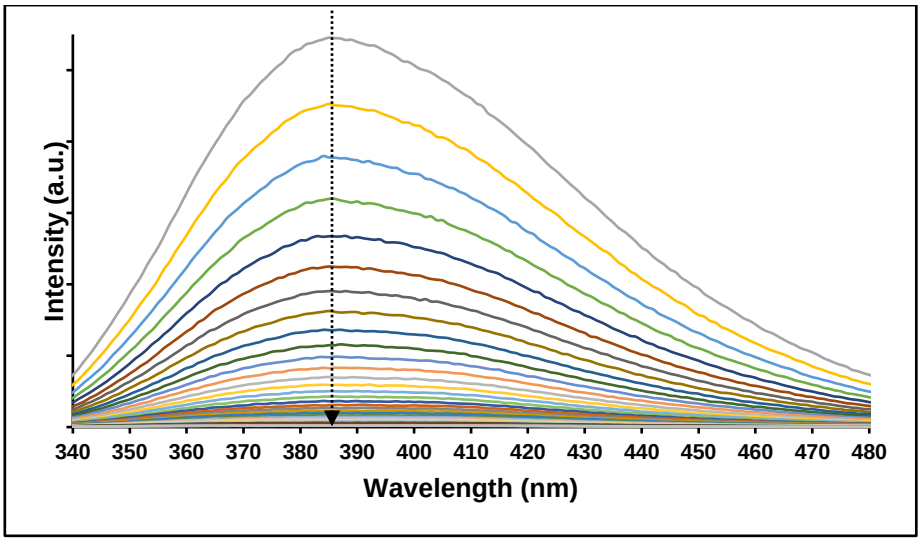

Figure 5.64 – Luminescence changes of HSA-bound Warfarin upon the incremental additions of 0–1.75 x 10^{-4}M $[Ru(phen)_2(qtpy)]^{2+}$. [HSA] = 2.24 x 10^{-6}M. [Warfarin] = 2.55 x 10^{-4}M.

5.9.7.3 $[Ru(dppz)_2(qtpy)]^{2+}$

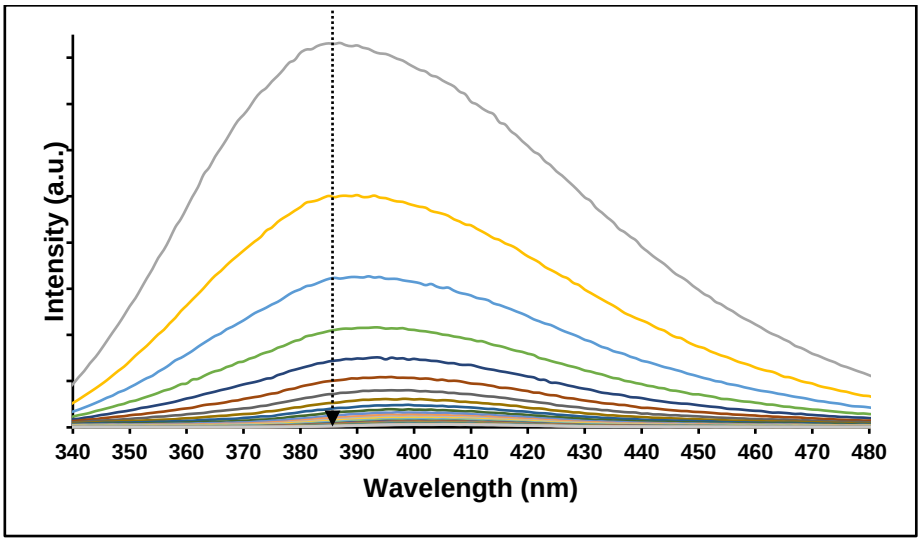

Figure 5.65 – Luminescence changes of HSA-bound Warfarin upon the incremental additions of 0–1.18 x 10^{-4}M $[Ru(dppz)_2(qtpy)]^{2+}$. [HSA] = 2.24 x 10^{-6}M. [Warfarin] = 2.55 x 10^{-4}M.

5.10 Subdomain IIIA (Sudlow Site II) Competition – Displacement of Ibuprofen from HSA-Ibuprofen Adduct by $[Ru(N–N)_2(qtpy)]^{2+}$ (where N–N = bpy, phen or dppz)

The experiments in this section were done analogously to those conducted for BSA. The complexes also show some degree of competition for Ibuprofen. The next set of figures gives a summary of the results obtained.

5.10.1 $[Ru(bpy)_2(qtpy)]^{2+}$

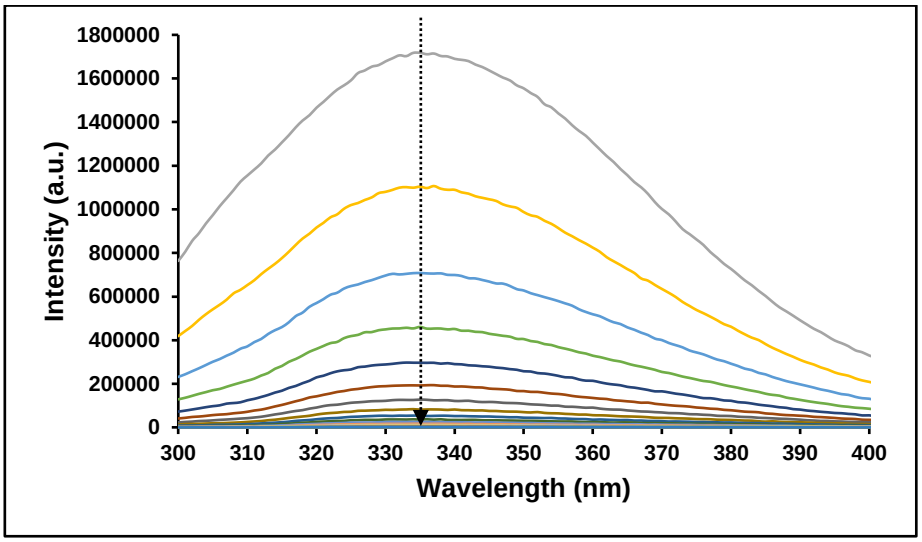

Figure 5.66 – Luminescence profile changes of HSA-bound Ibuprofen upon incremental additions of 0–9.73 x 10^{-5}M $[Ru(bpy)_2(qtpy)]^{2+}$. [HSA] = 2.24 x 10^{-6}M. [Ibuprofen] = 2.55 x 10^{-4}M.

5.10.2 $[Ru(phen)_2(qtpy)]^{2+}$

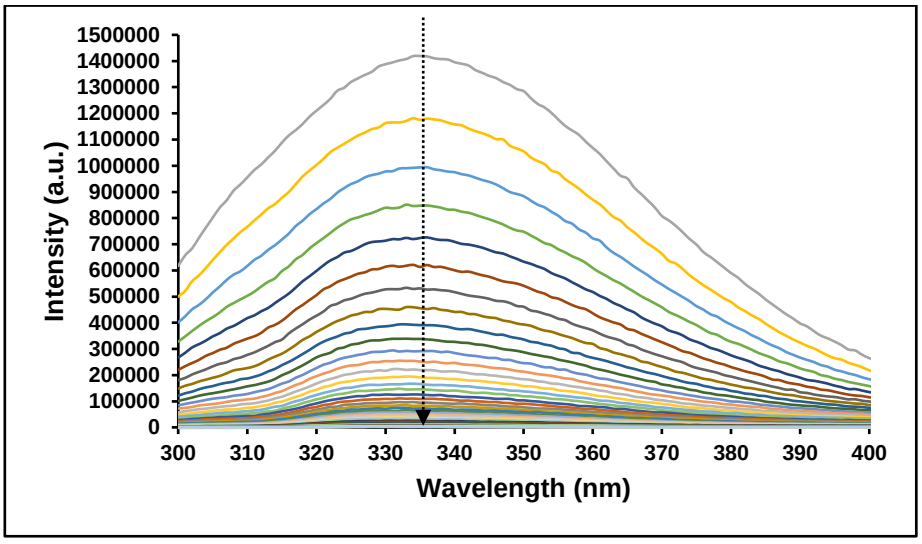

Figure 5.67 – Luminescence profile changes of HSA-bound Ibuprofen upon incremental additions of 0–2.43 x 10^{-4}M $[Ru(phen)_2(qtpy)]^{2+}$. [HSA] = 2.24 x 10^{-6}M. [Ibuprofen] = 2.55 x 10^{-4}M.

5.10.3 $[Ru(dppz)_2(qtpy)]^{2+}$

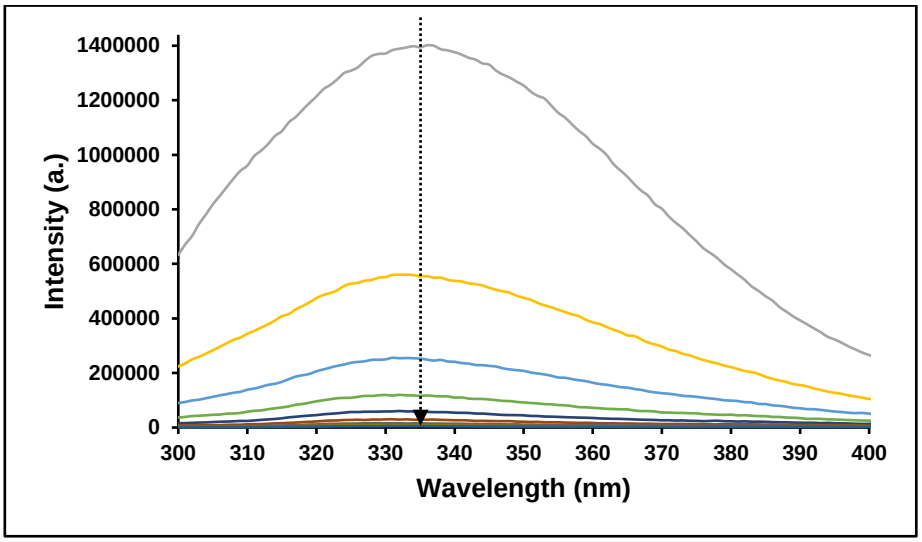

Figure 5.68 – Luminescence profile changes of HSA-bound Ibuprofen upon incremental additions of 0–3.73 x 10^{-5}M $[Ru(dppz)_2(qtpy)]^{2+}$. [HSA] = 2.24 x 10^{-6}M. [Ibuprofen] = 2.55 x 10^{-4}M.

5.11 Discussion

The three ruthenium(II) complexes investigated all positively competed better than warfarin for Sudlow Site I and to some extent, ibuprofen for Sudlow Site II. There is a decrease in the luminescence of Warfarin- or Ibuprofen-bound HSA with increasing concentration of the complexes. These results are indicative of competitive effects between the ruthenium(II) complexes and Warfarin/Ibuprofen for HSA Sudlow Site I and/or Sudlow Site II and confirm the affinity of the complexes for the sites.

Due to time constraint, the site competition studies of $[Ir(N–N)_2(qtpy)]^{3+}$ (where N–N = bpy, phen, or dppz) could not be progressed.

5.12 HSA-Binding Studies Summary

The binding studies of six complexes, i.e., $[Ir(bpy)_2(qtpy)]^{3+}$ and $[Ru(N–N)_2(qtpy)]^{2+}$ (where N–N = bpy, phen or dppz) with HSA were successfully undertaken. Experimental results show that all investigated complexes exhibit a strong interaction with HSA as indicated by their K_b values. $[Ru(dppz)_2(qtpy)]^{2+}$ has the highest K_b value whilst $[Ir(dppz)_2(qtpy)]^{3+}$ has the lowest

K_b value. Based on these results, it is possible that the complexes could be transported by HSA to reach their respective target(s) to effect their biological activities. This is particularly useful in targeted drug delivery. It is equally possible that the high affinity of these compounds for HSA can to some extent inhibit their therapeutic action when bound to DNA in cells. Table 5.2 summarises the binding data for the compounds investigated. Competition experiments showed that the compounds preferentially bind to Sudlow Site I more than Sudlow Site II. Temperature-switched experiments are underway to show the variation of the K_b values with increasing temperature and to see if there would be any resulting stabilisation of the complex-adduct thereby formed. A thermodynamic profile of the interaction of these metal complexes with I could be created using isothermal titration calorimetry. ITC measures the heat that is either released or absorbed during biomolecular binding events, allowing precise measurements of binding constants, enthalpy (ΔH), and entropy (ΔS).

Table 5.2 – Summary of key binding data for the compounds investigated.

Compound	K_{sv} (M^{-1})	K_q (M^{-1})	K_b (M^{-1})	N
$[Ir(bpy)_2(qtpy)]^{3+}$	Non-linear	Non-linear	7.50×10^{10}	2
$[Ir(phen)_2(qtpy)]^{3+}$	Non-linear	Non-linear	2.26×10^{9}	2
$[Ir(dppz)_2(qtpy)]^{3+}$	4.24×10^{3}	3.56×10^{11}	2.27×10^{4}	1
$[Ru(bpy)_2(qtpy)]^{2+}$	Non-linear	Non-linear	7.26×10^{9}	2
$[Ru(phen)_2(qtpy)]^{2+}$	Non-linear	Non-linear	2.64×10^{7}	2
$[Ru(dppz)_2(qtpy)]^{2+}$	Non-linear	Non-linear	1.54×10^{11}	2

5.13 Inductively Coupled Optical Emission Spectroscopy (ICP-OES)

To investigate the intracellular accumulation of $[Ru(N–N)_2(qtpy)]^{2+}$ (where N–N = bpy, phen, or dppz) within HSA, inductively coupled plasma-optical emission spectroscopy (ICP-OES) analysis of metal content was undertaken in accordance with a previously established procedure.[49] The protocol and instrumentation employed for ICP-OES are given in an appropriate section of the Experimental chapter. The results of the ICP-OES evaluation are summarised in Table 5.3.

Table 5.3 – Evaluation of metal binding by ICP-OES for samples with metallodrug: protein ratio incubated for 1h at 37°C temperature.

Protein	Concentration (μM)	Metallodrug	Metallodrug concentration (μM)	Detected Ru Content*	Approximate mole ratio of Ru: Protein
HSA	8.39	$[Ru(bpy)_2(qtpy)]^{2+}$	194.55	14.10	2:1
HSA	8.39	$[Ru(phen)_2(qtpy)]^{2+}$	194.55	5.94	1:1
HSA	8.39	$[Ru(dppz)_2(qtpy)]^{2+}$	194.55	9.32	1:1

*All results in mg/L as received.

The complex with the highest and lowest accumulations in HSA are $[Ru(bpy)_2(qtpy)]^{2+}$ and $[Ru(phen)_2(qtpy)]^{2+}$, respectively. $[Ru(dppz)_2(qtpy)]^{2+}$ exhibits an intermediate accumulation in HSA.

5.14 Molecular Docking Analysis

The binding of complexes $[Ru(bpy)_2(qtpy)]^{2+}$ **1**, $[Ru(phen)_2(qtpy)]^{2+}$ **2**, and $[Ru(dppz)_2(qtpy)]^{2+}$ **3** to both BSA and HSA was studied via molecular docking in a similar fashion to that of DNA-binding studies. And since competition experiments earlier conducted show the complexes displaces Warfarin and Ibuprofen to varying degrees, molecular docking to see which Sudlow Site (either I or II) is preferenced by the complexes was carried out.

5.14.1 BSA Docking with Reported Complexes

The docking of the investigated $[Ru(bpy)_2(qtpy)]^{2+}$ **1**, $[Ru(phen)_2(qtpy)]^{2+}$ **2**, and $[Ru(dppz)_2(qtpy)]^{2+}$ **3**, with BSA was carried out. The best docking results are given in the figures below.

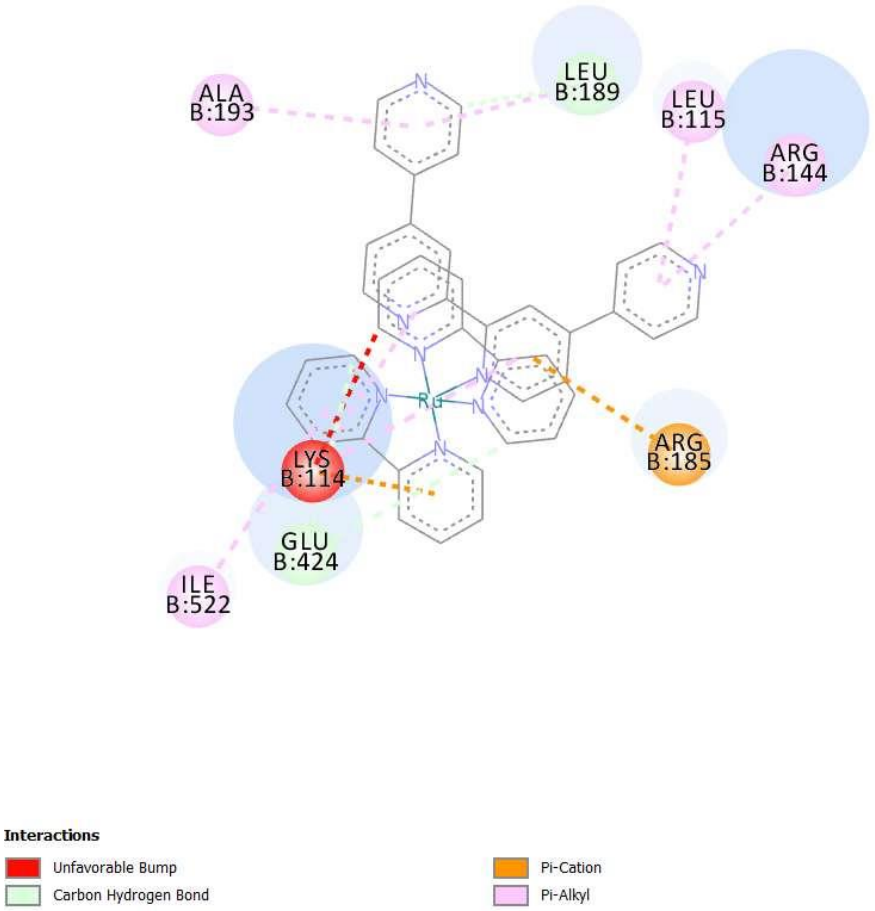

Figure 5.69 – Docking result of Complex **1** with BSA's Sudlow Site I (i.e., Warfarin site). Complex **1**'s docking score = -3.32.

Complex **1** shows preferential binding to Warfarin's amino acids LYS 114 and ARG 185, which tallies with a previous study.[50]

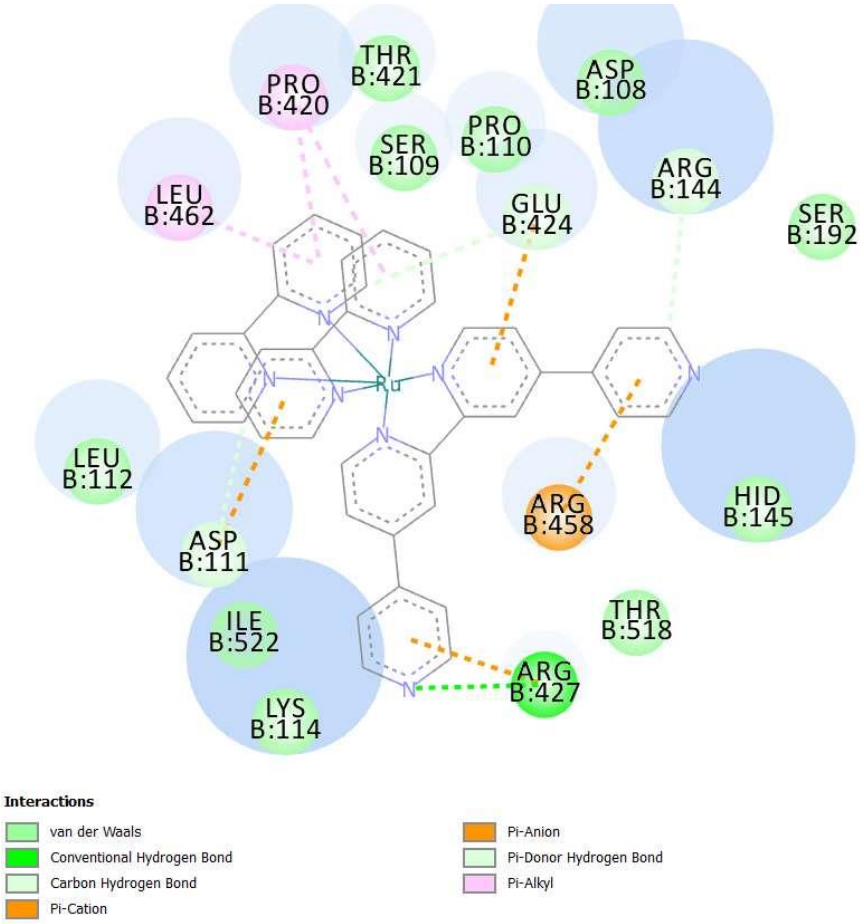

Figure 5.70 – Docking result of Complex **1** with BSA's Sudlow Site II (i.e., Ibuprofen site). Complex **1**'s docking score = - 4.42.

Complex **1** shows preferential binding to Ibuprofen's amino acids LEU 522, LEU 462, and ARG 144, which tallies with a previous study.[50]

The results above show that Complex **1** is a better Warfarin site binder than an Ibuprofen site binder as it has a lower negative score for its binding with Warfarin than for its binding to Ibuprofen.

The docking of Complex **3** did not yield any good docking scores and is, therefore, not reported.

5.14.2 HSA Docking with Reported Complexes

Similar to BSA docking studies, the docking investigations of the investigated complexes $[Ru(bpy)_2(qtpy)]^{2+}$ **1**, $[Ru(phen)_2(qtpy)]^{2+}$ **2**, and $[Ru(dppz)_2(qtpy)]^{2+}$ **3** with HSA were done. The best docking results are given in the figures below.

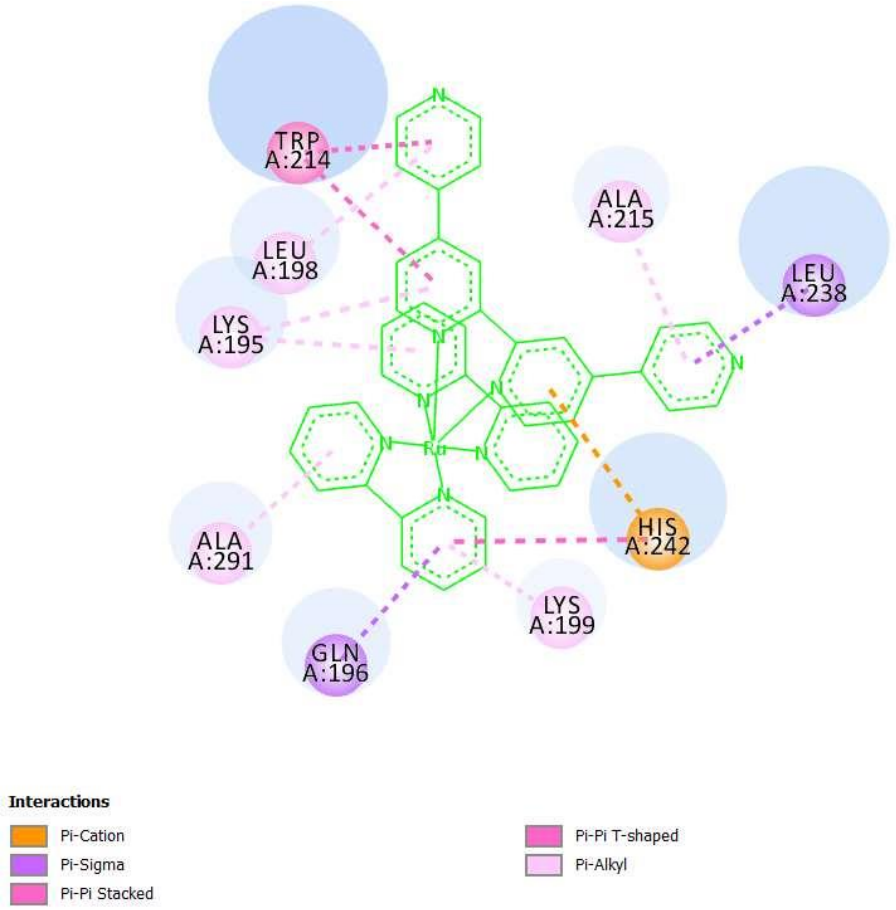

Figure 5.71 – Docking result of complex **1** with HSA's Sudlow Site I (i.e., Warfarin site). Complex **1**'s docking score = - 9.32.

Complex **1** shows preferential binding to Warfarin's amino acids LEU 238 and ALA 291, which tallies with a previous study.[50]

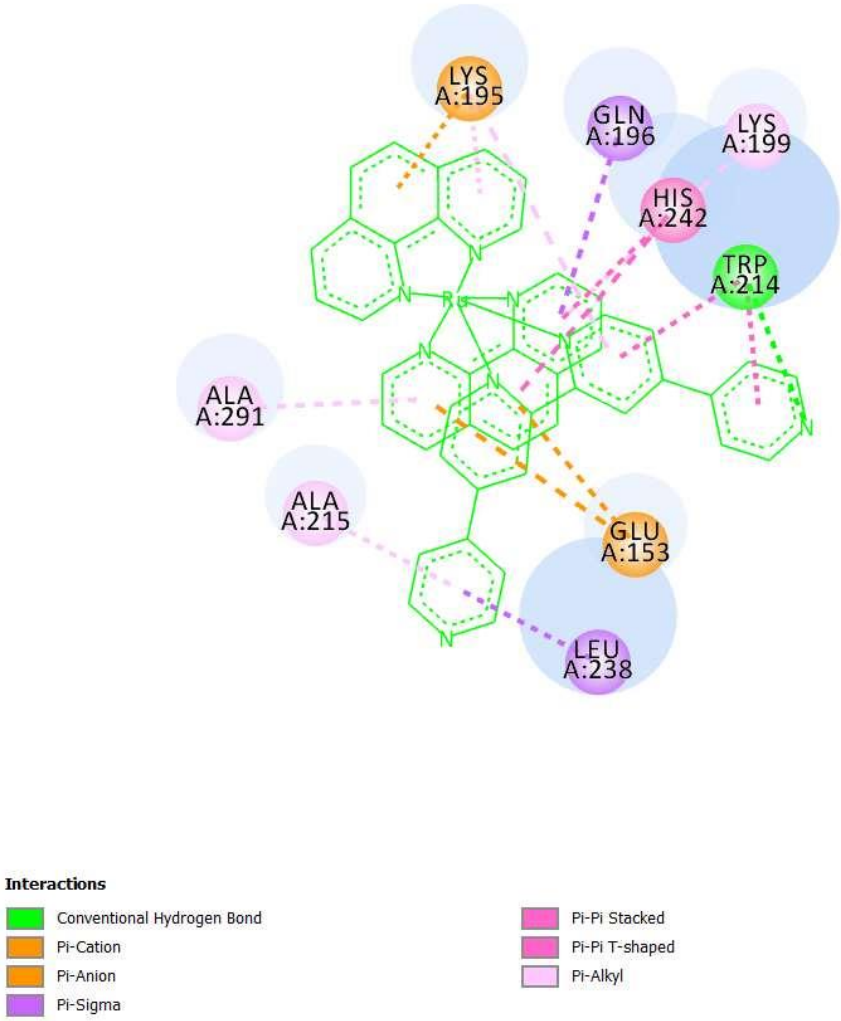

Figure 5.72 – Docking result of Complex **2** with HSA's Sudlow Site I (i.e., Warfarin site). Complex **2**'s docking score = - 8.51.

Complex **2** shows preferential binding to Warfarin's amino acids LEU 238 and ALA 291, which tallies with a previous study.[50]

The binding results above show that both Complexes **1** and **2** are true Warfarin site binders.

The docking of Complex **3** did not yield any good docking scores and is, therefore, not reported.

The docking studies of isostructural ruthenium(II) complexes to BSA and/or HSA could not be done due to time restraints.

5.15 Circular Dichroism Investigations of Protein Binding with $[Ir(N–N)_2(qtpy)]^{3+}$ and $[Ru(N–N)_2(qtpy)]^{2+}$ (N–N = bpy, phen, or dppz)

5.16 Introduction

Circular dichroism (CD) spectroscopy ranks high on the list of the valuable methods for the analysis of protein secondary structure and can provide an insight into the changes that occur in the structure of bovine serum albumin (BSA) and/or human serum albumin (HSA) during their binding with transition metal.[51]

The applications of transition metal complexes as therapeutics can be facilitated by a comprehensive understanding of their influence on biomolecules, and CD spectroscopy provides information regarding the secondary structure of proteins and nucleic acids, especially where X-ray crystallography is not feasible.[51, 52]

5.17 CD Spectroscopic Studies of $[Ir(N–N)_2(qtpy)]^{3+}$ and $[Ru(N–N)_2(qtpy)]^{2+}$ (N–N = bpy, phen, or dppz) Binding with BSA

CD spectroscopic investigations of the binding of BSA with $[Ir(bpy)_2(qtpy)]^{3+}$, $[Ru(bpy)_2(qtpy)]^{2+}$, $[Ru(phen)_2(qtpy)]^{2+}$, and $[Ru(dppz)_2(qtpy)]^{2+}$ were carried out. In these studies, approximately equimolar concentrations of the iridium(III) and ruthenium(II) complexes were used so as to make easy comparisons of their effects on the structure of BSA and HSA. As the complexes are racemic mixtures of enantiomers, they possess non-CD signal oof their own.

As a first step in all experiments, baselines were corrected using 2200µL of 5mM tris, 25mM NaCl buffer, pH 7.4. The specific protein under study was then scanned in a 3mL cuvette to which each of the iridium(III) or ruthenium(II) metal complexes were carefully titrated, and

the CD measurements then undertaken. The UV-Vis range studied in this work spans 190–250nm. A 5-minute equilibration time was employed for all CD titration experiments. CD instruments, also known as spectropolarimeters, evaluate the absorbance difference between the L and R circularly polarised components of plane polarised radiation ($\Delta A = A_L - A_R$) in terms of the ellipticity (θ) in degrees.[52] The instrument settings employed are given thus: sensitivity - standard (100mdeg); start - 250nm; end - 190nm; data pitch - 0.025nm; scanning mode - continuous; response - 1sec; band width - 1nm; slit width - 1000µm; accumulation - 3. Spectra are reported in molar ellipticity ([θ]) in mdeg = $cm^2dmol^{-1}deg$.

5.17.1 $[Ir(bpy)_2(qtpy)]^{3+}$ Binding with BSA

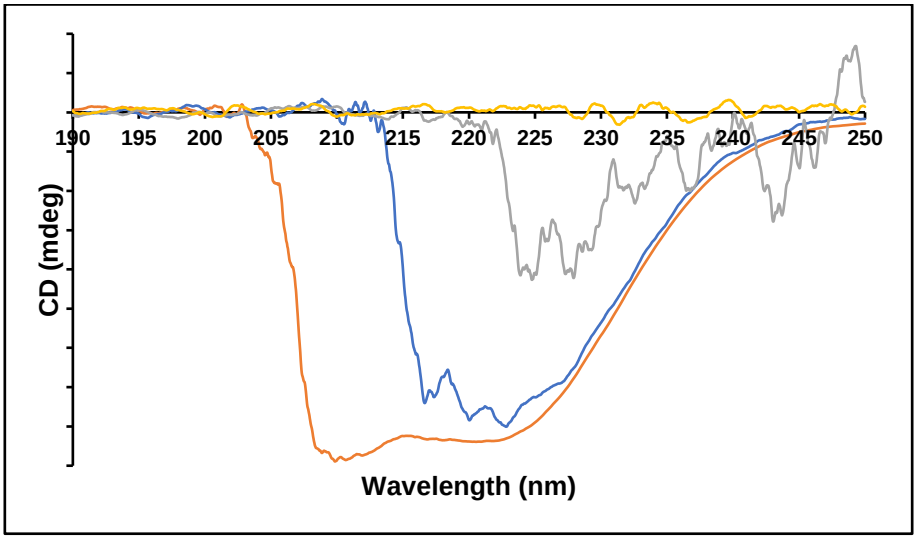

Figure 5.73 – Far-UV CD spectra of BSA (orange trace) and BSA in the presence of increasing 1.92mM $[Ir(bpy)_2(qtpy)]^{3+}$ (blue trace – 60µL; black trace – 120µL; and yellow trace – 180µL). There was a total disruption of CD's MRE signals at 208nm and 220nm. BSA's alpha helix increasing becomes randomly coiled such that fully bound BSA has a CD of ~ zero. Scan speed = 100nm/min.

5.17.2 $[Ru(bpy)_2(qtpy)]^{2+}$ Binding with BSA

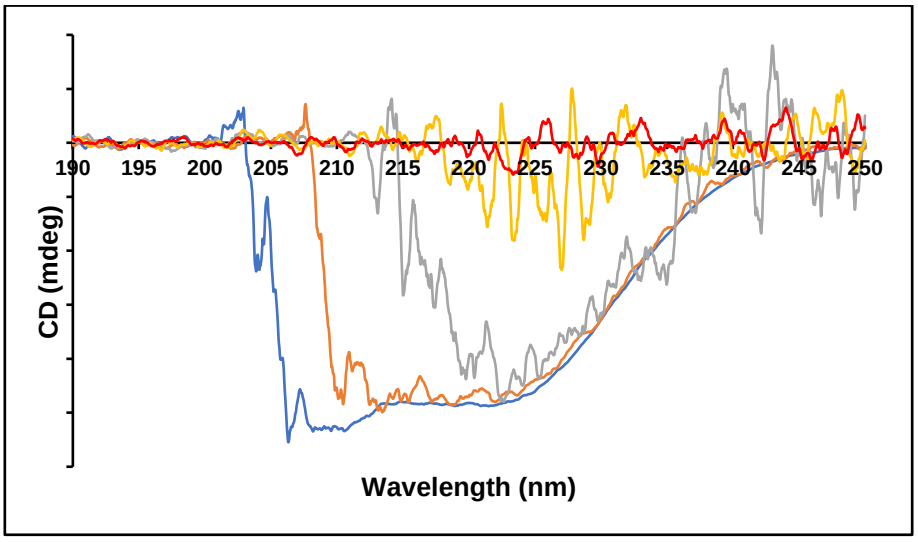

Figure 5.74 – Far-UV CD spectra of BSA (blue trace) and BSA in the presence of increasing 2.14mM $[Ru(bpy)_2(qtpy)]^{2+}$ (orange trace – 40µL; black trace – 80µL; yellow trace – 120µL; and red trace – 160µL). There was a total disruption of CD's MRE signals at 208nm and 220nm. BSA's alpha helix increasing becomes randomly coiled such that fully bound BSA has a CD of ~ zero.

5.17.3 $[Ru(phen)_2(qtpy)]^{2+}$ Binding with BSA

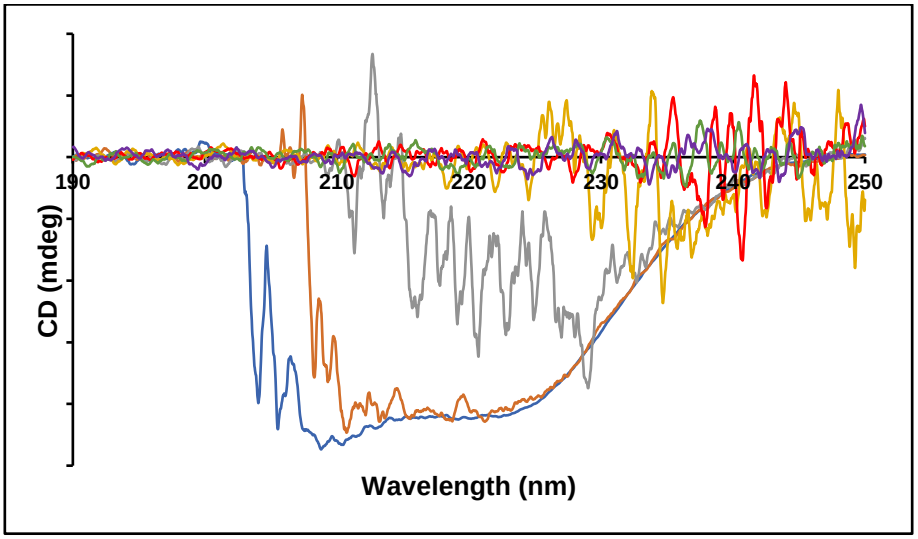

Figure 5.75 – Far-UV CD spectra of BSA (blue trace) and BSA in the presence of increasing 2.14mM $[Ru(phen)_2(qtpy)]^{2+}$ (orange trace – 40µL; black trace – 80µL; yellow trace – 120µL; red trace – 160µL; green trace – 200µL; and purple trace – 240µL). There is a total disruption of CD's MRE signals at 208nm and 220nm. BSA's alpha helix increasing becomes randomly coiled such that fully bound BSA has a CD of ~ zero.

5.17.4 $[Ru(dppz)_2(qtpy)]^{2+}$ Binding with BSA

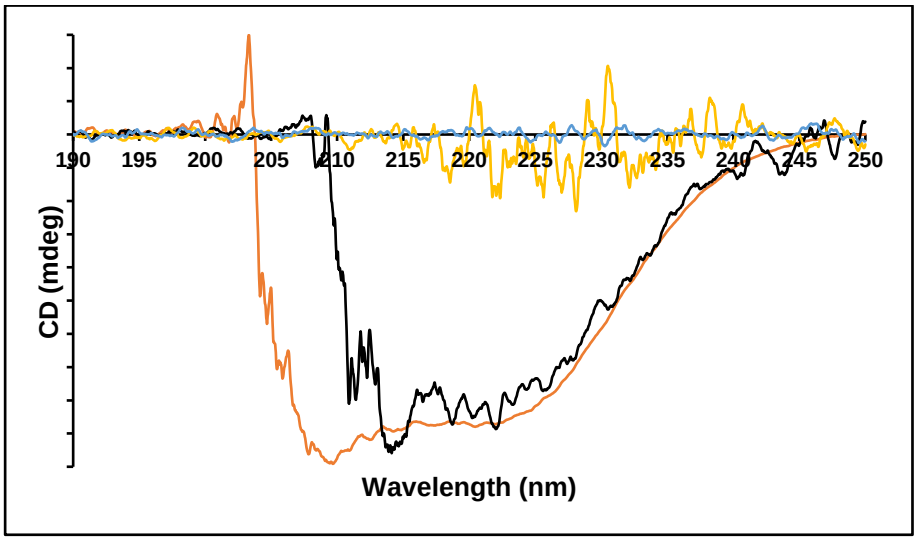

Figure 5.76 – Far-UV CD spectra of BSA (orange trace – 15µL and BSA in the presence of increasing 2.05mM $[Ru(dppz)_2(qtpy)]^{2+}$ (black trace – 40µL; yellow trace – 80µL; and blue trace – 120µL). There is a total disruption of CD's MRE signals at 208nm and 220nm. BSA's alpha helix increasing becomes randomly coiled such that fully bound BSA has a CD of ~ zero.

5.18 CD Spectroscopic Investigations of $[Ir(N–N)_2(qtpy)]^{3+}$ and $[Ru(N–N)_2(qtpy)]^{2+}$ (N–N = bpy, phen, or dppz) Binding with HSA

CD studies of HSA interactions with $[Ir(bpy)_2(qtpy)]^{3+}$, $[Ir(phen)_2(qtpy)]^{3+}$ $[Ir(dppz)_2(qtpy)]^{3+}$, $[Ru(bpy)_2(qtpy)]^{2+}$, $[Ru(phen)_2(qtpy)]^{2+}$, and $[Ru(dppz)_2(qtpy)]^{2+}$ were done analogously to those of BSA interactions. Interestingly and as expected, their binding interactions for HSA follow the same patterns as for BSA since both proteins are ~ 70% structurally similar.

5.18.1 $[Ir(bpy)_2(qtpy)]^{3+}$ Binding with HSA

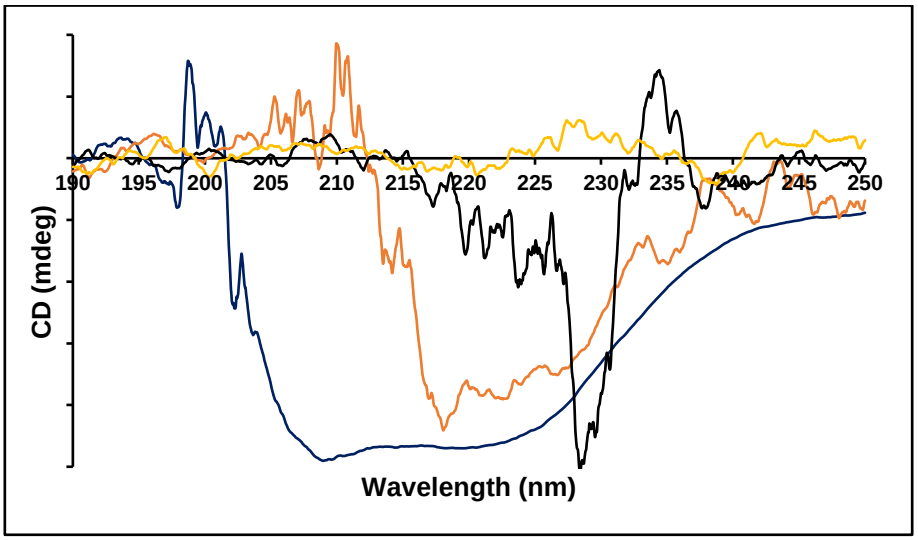

Figure 5.77 – Far-UV CD spectra of HSA (blue trace) and HSA in the presence of increasing 6.41mM $[Ir(bpy)_2(qtpy)]^{3+}$ (orange trace – 30µL; black trace – 60µL; and yellow trace – 90µL). There was a total disruption of CD's MRE signals at 208nm and 220nm. HSA's alpha helix became increasing randomly coiled such that fully bound HSA has a CD of ~ zero. Scan speed = 100nm/min.

5.18.2 $[Ir(phen)_2(qtpy)]^{3+}$ Binding with HSA

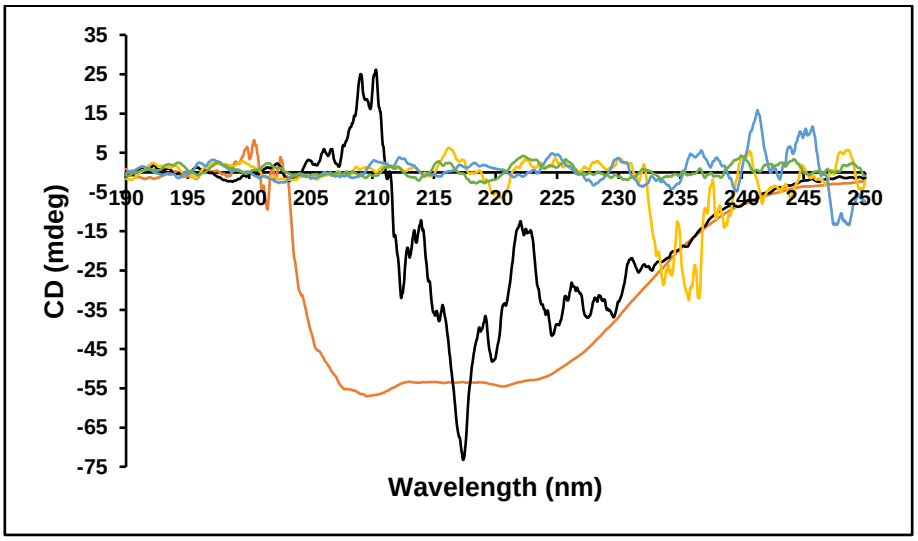

Figure 5.78 – Far-UV CD spectra of HSA (orange trace) and HSA in the presence of increasing 5.48mM $[Ir(phen)_2(qtpy)]^{2+}$ (black trace – 40µL; yellow trace – 80µL; blue trace – 120µL; and green trace – 160µL). There was a total disruption of CD's MRE signals at 208nm and 220nm. HSA's alpha helix became increasing randomly coiled such that fully bound HSA has a CD of ~ zero.

5.18.3 $[Ir(dppz)_2(qtpy)]^{3+}$ Binding with HSA

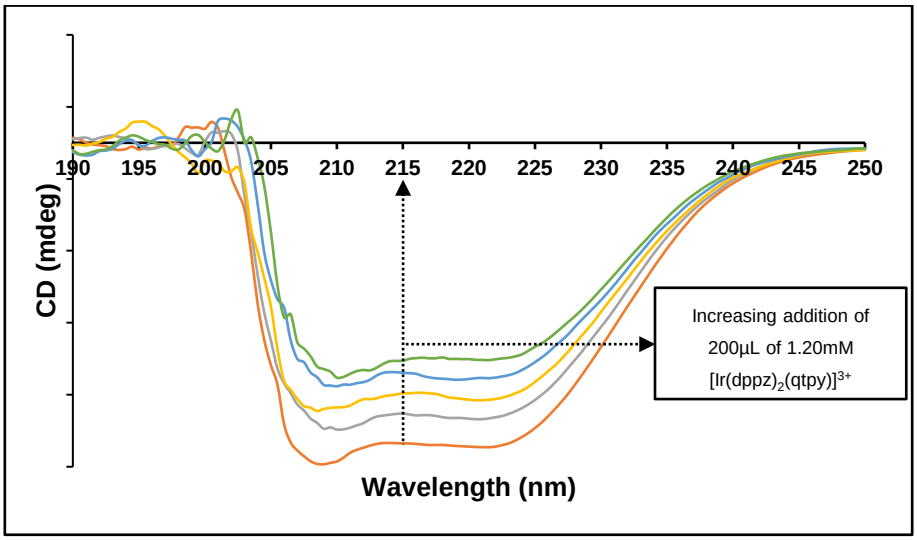

Figure 5.79 – Far-UV CD spectra of HSA (orange trace) and HSA in the presence of increasing 1.20mM $[Ir(dppz)_2(qtpy)]^{3+}$ (black trace – 200µL; yellow trace – 400µL; blue trace – 600µL; and green trace – 800 µL). There was a total disruption of CD's MRE signals at 208nm and 220nm. HSA's alpha helix became increasing randomly coiled with increasing addition of the metal complex. Scan speed = 200nm/min. NB: Experiment could not be completed due to an insufficient amount of the test compound, but the investigation supports the binding of the compound with HSA.

5.18.4 $[Ru(bpy)_2(qtpy)]^{2+}$ Binding with HSA

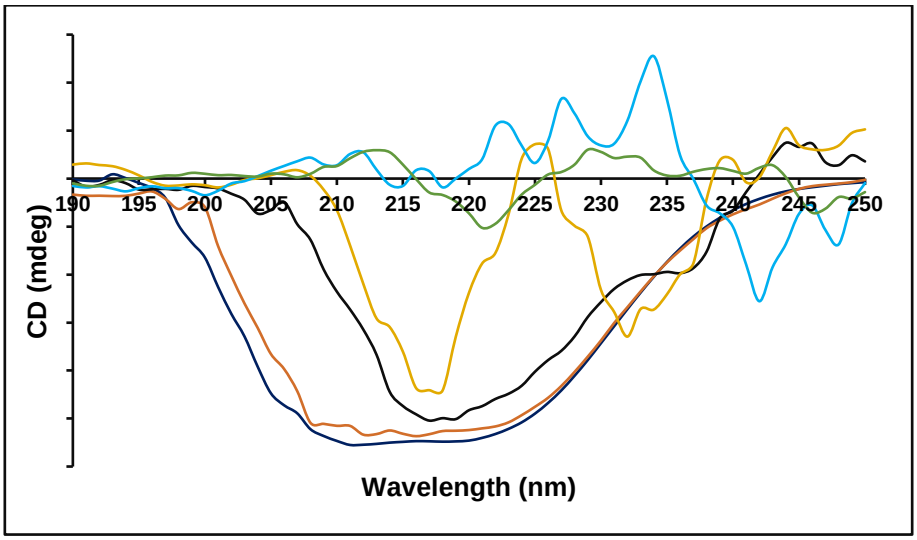

Figure 5.80 – Far-UV CD spectra of HSA (deep blue trace) and HSA in the presence of increasing 2.14mM $[Ru(bpy)_2(qtpy)]^{2+}$ (orange trace – 30µL; black trace – 60µL; yellow trace – 90µL; green trace – 120µL; and light blue – 150 µL). There was a total disruption of CD's MRE signals at 208nm and 220nm.

HSA's alpha helix became increasing randomly coiled such that fully bound HSA has a CD of ~ zero. Scan speed = 200nm/min.

5.18.5 $[Ru(phen)_2(qtpy)]^{2+}$ Binding with HSA

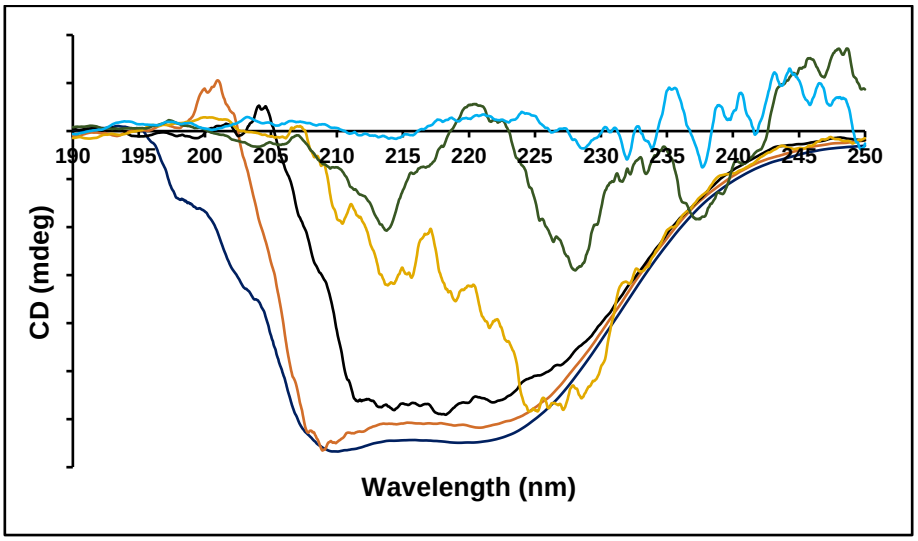

Figure 5.81 – Far-UV CD spectra of HSA (deep blue trace) and HSA in the presence of increasing 2.14mM $[Ru(phen)_2(qtpy)]^{2+}$ (orange trace – 30µL; black trace – 60µL; yellow trace – 90µL; green trace – 120µL; and light blue – 150µL). There was a total disruption of CD's MRE signals at 208nm and 220nm. HSA's alpha helix became increasing randomly coiled such that fully bound HSA has a CD of ~ zero. Scan speed = 200nm/min.

5.18.6 $[Ru(dppz)_2(qtpy)]^{2+}$ Binding with HSA

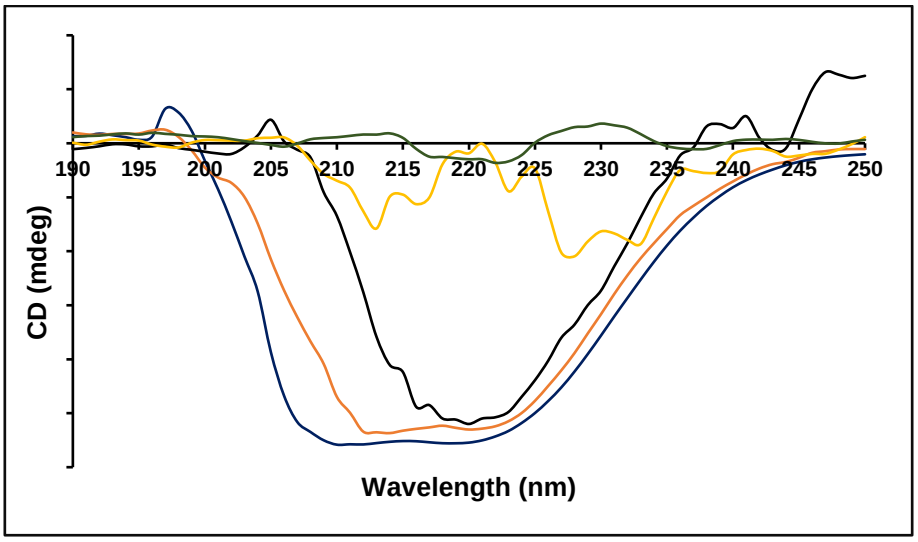

Figure 5.82 – Far-UV CD spectra of HSA (blue trace) and HSA in the presence of increasing 2.14mM $[Ru(dppz)_2(qtpy)]^{2+}$ (orange trace – 30µL; black trace – 60µL; yellow trace – 90µL; and green trace – 120µL). There was a total disruption of CD's MRE signals at 208nm and 220nm. HSA's alpha helix became increasing randomly coiled such that fully bound HSA has a CD of ~ zero. Scan speed = 200nm/min.

5.19 Discussion

Circular dichroism (CD) spectroscopy is a useful tool used in biochemistry, structural biology and pharmaceutical chemistry to extract information regarding the secondary structure of proteins and nucleic acids.[52–53] In this section, CD is used to probe BSA and/or HSA interactions with all the iridium(III) and ruthenium(II) complexes investigated. The CD spectra of BSA and/or HSA were recorded in absence and presence of iridium(III) and ruthenium(II) complexes, which exhibits two negative bands at ~ 208 and ~ 220nm, which are characteristic α-helix structure of protein. The negative band at ~ 208nm is due to the exciton splitting of the lowest peptide π-π* transition, while the negative band at ~ 220nm is due to the peptide n-π* transition.[51] Typical far-UV CD spectra of BSA and/or HSA in the absence and presence of the metal complexes explored in this work are presented in Figs. 5.73–5.82. The negative bands at ~ 208 and ~ 220nm were found to be collapsed by the addition of $[Ir(N–N)_2(qtpy)]^{3+}$ and $[Ru(N–N)_2(qtpy)]^{2+}$ (where N–N = bpy, phen, or dppz). This indicates that the secondary structure of the investigated proteins has been disrupted and unfolded.[54] The decrease in the negative ellipticity values of these bands shows the extent of conformational changes that occur upon the binding of iridium(III) and ruthenium(II) complexes with the proteins.[55–56]

These structural changes in BSA and/or HSA observed may affect the physiological functions of proteins. Interestingly, the denaturation characteristics of BSA and/or HSA follow the same general trend for all the complexes. These observations suggest that all the complexes investigated bind in a similar manner, which tally well with the luminescence quenching data presented in the preceding chapter on protein binding investigations. Similar unfolding patterns of the protein chains have also been reported in previous works[52, 57] and this may be an important in biological function. Although it is assumed that the biological effects of most transition metal-based drugs primarily proceed through a direct DNA damage, as in the case of most chemotherapeutic platinum complexes[58], it has been established the alteration or

inactivation of serum proteins may also represent a molecular basis for the therapeutic action of these antitumour agents.[59]

5.20 Chapter Summary

This chapter has successfully investigated the binding interactions of $[Ir(N–N)_2(qtpy)]^{3+}$ and $[Ru(N–N)_2(qtpy)]^{2+}$ (where N–N = bpy, phen, or dppz) with serum albumins, HSA and BSA, using UV-Vis absorption spectroscopy, steady-state luminescence, inductively coupled optical emission spectroscopy, molecular docking analysis, and circular dichroism.

5.21 References

1. A. Kumar Srivastav, S. K. Gupta, and U. Kumar, A molecular simulation approach towards the development of universal nanocarriers by studying the pH- and electrostatic-driven changes in the dynamic structure of albumin, *RSC Adv.*, 2020, 10, 13451–13459.
2. Y. Ni, Shaojing Su and S. Kokot, Spectrofluorimetric studies on the binding of salicylic acid to bovine serum albumin using warfarin and ibuprofen as site markers with the aid of parallel factor analysis, *Anal. Chim. Acta*, 2006, 580, 2006, 206–215.
3. S. Nehru, J. A. A. Priya, S. Hariharan, R. V. Solomon, and S. Veeralakshmi, Impacts of hydrophobicity and ionicity of phendione-based cobalt (II)/(III) complexes on binding with bovine serum albumin, *J. Biomol. Struct. Dyn.*, 2019, 1–11.
4. M. Denison, S. J. Steinke, A. Majeed, C. Turro, T. A. Kocarek, I. F. Sevrioukova, and J. J. Kodanko, Ir(III)-Based Agents for Monitoring the Cytochrome P450 3A4 Active Site Occupancy, *Inorg. Chem.,* 2022, 61, 35, 13673–13677.
5. G. Palermo, A. Magistrato, T. Riedel, T. von Erlach, C. A. Davey, P. J. Dyson, and U. Rothlisberger, Fighting Cancer with Transition Metal Complexes: From Naked DNA to Protein and Chromatin Targeting Strategies, *ChemMedChem*, *2*016, 11, 1199–1210.
6. M. Caterino, A. A. Petruk, A. Vergara, G. Ferraro, D. Marasco, F. Doctorovich, D. A. Estrin, and A. Merlino, Mapping the protein-binding sites for iridium(III)-based CO-releasing molecules, *Dalton Trans.*, 2016, 45, 12206–12214.
7. G. Sudlow, D. J. Birkett, D. N. Wade, The characterization of two specific drug binding sites on human serum albumin, *Mol. Pharmacol.*, 1975, 11, 824–832.
8. G. Sudlow, D. J. Birkett, D. N. Wade, Further characterization of specific drug binding sites on human serum albumin, *Mol. Pharmacol.,* 1976, 12, 1052–1061.
9. O. J. Bos, J. P. Remijn, M. J. Fischer, J. Wilting, L. H. Janssen, Location and characterization of the warfarin binding site of human serum albumin—A comparative study of two large fragments, *Biochem. Pharmacol.*, 1988, 37, 3905–3909.
10. O. J. Bos, M. J. Fischer, J. Wilting, L. H. Janssen, Drug-binding and other physicochemical properties of a large tryptic and a large peptic fragment of human serum albumin, *Biochim. Biophys. Acta*, 1988, 953, 37–47.
11. J. Ghuman, P. A. Zunszain, I. Petitpas, A. A. Bhattacharya, M. Otagiri, S. Curry, Structural basis of the drug-binding specificity of human serum albumin, *J. Mol. Biol.*, 2005, 353, 38–52.

12. F. Yang, J. Yue, L. Ma, Z. Ma, M. Li, X. Wu, H. Liang, Interactive associations of drug–drug and drug–drug–drug with IIA subdomain of human serum albumin, *Mol. Pharm.*, 2012, 9, 3259–3265.

13. S. Curry, Lessons from the crystallographic analysis of small molecule binding to human serum albumin, *Drug Metab. Pharmacokinet.*, 2009, 24, 342–357.

14. S. Curry, X-ray Crystallography of Albumin. In Human Serum Albumin—New Insights on Its Structural Dynamics, Functional Impacts and Pharmaceutical Applications; M. Otagiri, Ed.; Sojo University Publishing Center: Kumamoto, Japan, 2011; pp. 1–29.

15. S. Curry, H. Mandelkow, P. Brick, N. Franks, Crystal structure of human serum albumin complexed with fatty acid reveals an asymmetric distribution of binding sites, *Nat. Struct. Biol.*, 1998, 5, 827–835.

16. S. Lejon, I. M. Frick, L. Björck, M. Wikström, S. Svensson, Crystal structure and biological implications of a bacterial albumin binding module in complex with human serum albumin, *J. Biol. Chem.*, 2004, 279, 42924–42928.

17. A. A. Bhattacharya, S. Curry, N. P. Franks, Binding of the general anesthetics propofol and halothane to human serum albumin. High resolution crystal structures, *J. Biol. Chem.*, 2000, 275, 38731–38738.

18. S. Yamaguchi, G. Aldini, S. Ito, N. Morishita, T. Shibata, G. Vistoli, M. Carini, K. Uchida, Δ12-prostaglandin J2 as a product and ligand of human serum albumin: Formation of an unusual covalent adduct at His146, *J. Am. Chem. Soc.*, 2010, 132, 824–832.

19. H. Mao, P. J. Hajduk, R. Craig, R. Bell, T. Borre, S. W. Fesik, Rational design of diflunisal analogues with reduced affinity for human serum albumin, *J. Am. Chem. Soc.*, 2001, 123, 10429–10435.

20. F. Yang, Y. Zhang, and H. Liang, Interactive Association of Drugs Binding to Human Serum Albumin, *Int. J. Mol. Sci.*, 2014, 15, 3580–3595.

21. F. Yang, Y. Zhang, H. Liang, (2014) Interactive association of drugs binding to human serum albumin, 2014, *Int. J. MolSci.*, 15, 3580–3595.

22. J. R. Simard, P. A. Zunszain, J. A. Hamilton, S. Curry S, Location of high and low affinity fatty acid binding sites on human serum albumin revealed by NMR drug-competition analysis, *J. MolBiol.*, 2006, 361, 336-351.

23. F. Yang, Y. Zhang, H. Liang, Interactive association of drugs binding to human serum albumin, *Int J. MolSci.*, 2014, 15, 3580–3595.

24. H. Ahmad, A. Wragg, W Cullen, C. Wombwell, A. J. H. M. Meijer, and J. A. Thomas, From Intercalation to Groove Binding: Switching the DNA-Binding Mode of Isostructural Transition-Metal Complexes, *Chem. Eur. J.*, 2014, 20, 3089–3096.

25. S. Nehru, J. A. A. Priya, S. Hariharan, R. V. Solomon, and S. Veeralakshmi, Impacts of hydrophobicity and ionicity of phendione-based cobalt(II)/(III) complexes on binding with bovine serum albumin, *J. Biomol. Struct. Dyn.*, 2020, 38(7), 2057–2067.

26. J. W. Brauner, C. R. Flach and R. Mendelsohn, A Quantitative Reconstruction of the Amide I Contour in the IR Spectra of Globular Proteins: From Structure to Spectrum, *J. Am. Chem. Soc.*, 2005, 127, 109–115.

27. Q. Zeng and Y. Z. Wang, Extraction of proteins with ionic liquid aqueous two-phase system based on guanidine ionic liquid, *Talanta*, 2013, 116, 409–416.

28. J. Chen, Y. Wang, Q. Zeng, X. Ding and Y. Huang, Partition of proteins with extraction in aqueous two-phase system by hydroxyl ammonium-based ionic liquid, *Anal. Methods*, 2014, 6, 4067–4076.

29. T. Chatterjee, A. Pal, S. Dey, B. K. Chatterjee, and P. Chakrabarti, Interaction of Virstatin with Human Serum Albumin: Spectroscopic Analysis and Molecular Modeling, 2012, PLoS ONE 7(5): e37468.

30. Y. Ni, S. Su, S. Kokot, Spectrofluorimetric studies on the binding of salicylic acid to bovine serum albumin using warfarin and ibuprofen as site markers with the aid of parallel factor analysis, *Anal. Chim. Acta*, 2006, 580, 206–215.

31. F. Samari, B. Hemmateenejad, M. Shamsipur, M. Rashidi, H. & Samouei, Affinity of two novel five-coordinated anticancer Pt(II) complexes to human and bovine serum albumins: A spectroscopic approach, *Inorg. Chem.*, 2012, 51 (6), 3454–3464.

32. J. R. Lakowicz, Principles of fluorescence spectroscopy. New York: Springer Science & Business Media, 2007.

33. F. Li, Marshall Feterl, J. M. Warner, A. I. Day, F. R. Keene, and J. G. Collins, Protein binding by dinuclear polypyridyl ruthenium(II) complexes and the effect of cucurbit[10]uril encapsulation, *Dalton Trans.*, 2013, 42, 8868–8877.

34. H. Ahmad, Kinetically locked Metallomacrocycles as Self-Assembled Hosts for Biomolecules, PhD Thesis, University of Sheffield, 2010.

35. D. Genovese, M. Cingolani, E. Rampazzo, L. Prodi, N. Zaccheroni, Static quenching upon adduct formation: a treatment without shortcuts and approximations, *Chem. Soc. Rev.*, 2021, 50, 8414–8427.

36. F. Yang, Zhang, H. Liang, Interactive association of drugs binding to human serum albumin, *Int J MolSci*, 2014, 15, 3580–3595.

37. A. Lancon, D. Delmas, H. Osman, J. P. Thenot, B. Jannin, N. and Latruffe, Human hepatic cell uptake of resveratrol: involvement of both passive diffusion and carrier-mediated process, 2004, *Biochem. Biophys. Res. Comm.*, 316, 1132–1137.

38. K. Vuignier, J. Schappler, J. L. Veuthey, P. A. Carrupt, S. and Martel, Drug-protein binding: a critical review of analytical tools, *Anal. Bioanal. Chem.*, 2010, 398, 53–66.

39. M. S. Dennis, M. Zhang, Y. G. Meng, M. Kadkhodayan, D. Kirchhofer, D. Combs, and L. A. Damico, Albumin binding as a general strategy for improving the pharmacokinetics of proteins, *J. Biol. Chem.*, 2002, 277, 35035–35043.

40. A. M. Merlot, D. R. and Richardson, Receptor recognition and lysosomal targeting to enhance cytotoxicity of novel anti-cancer agents that bind iron and copper, *Vitam. Miner.*, 2014, 3:e125.

41. A. M. Merlot, D. S. Kalinowski, D. R. and Richardson, Novel chelators for cancer treatment: where are we now? *Antioxid. Redox Signal*, 2013a, 18, 973–1006.

42. A. M. Merlot, N. Pantarat, S. V. Menezes, S. Sahni, D. R. Richardson, and D. S. Kalinowski, Cellular uptake of the antitumor agent Dp44mT occurs via a carrier/receptor-mediated mechanism, *Mol. Pharmacol.*, 2013b, 84, 911–924.

43. A. M. Merlot, D. R. and Richardson, Receptor recognition and lysosomal targeting to enhance cytotoxicity of novel anti-cancer agents that bind iron and copper, *Vitam. Miner.*, 2014, 3:e125.

44. D. B. Lovejoy, P. J. Jansson, U. T. Brunk, J. Wong, P. Ponka, D. R. and Richardson, Antitumor activity of metal-chelating compound Dp44mT is mediated by formation of a redox-active copper complex that accumulates in lysosomes, 2011, *Cancer Res.*, 71, 5871–5880.

45. C. Andersson, B. M. Iresjo, K. and Lundholm, Identification of tissue sites for increased albumin degradation in sarcoma-bearing mice, *J. Surg. Res.*, 1991, 50, 156–162.

46. G. Stehle, H. Sinn, A. Wunder, H. H. Schrenk, J. C. Stewart, G. Hartung, W. Maier-Borst, D. L. Heenea, Plasma protein (albumin) catabolism by the tumor itself–implications for tumor metabolism and the genesis of cachexia, *Crit. Rev. Oncol. Hematol.*, 1997, 26, 77–100.

47. A. M. Merlot, D. S. Kalinowski, and D. R. Richardson, Unraveling the mysteries of serum albumin—more than just a serum protein, *Front. Physiol.*, 2014, 5, 299, 1–7.

48. F. Li, M. Feterl, J. M. Warner, A. I. Day, F. R. Keene, and J. G. Collins, Protein binding by dinuclear polypyridyl ruthenium(II) complexes and the effect of cucurbit[10]uril encapsulation, *Dalton Trans.*, 2013, 42, 8868–8877.

49. M. Groessl, M. Terenghi, A. Casini, L. Elviri, R. Lobinskic, and P. J. Dyson, Reactivity of anticancer metallodrugs with serum proteins: new insights from size exclusion chromatography-ICP-MS and ESI-MS, *J. Anal. At. Spectrom.*, 2010, 25, 305–313.

50. K. S. Neethu, J. Eswaran, Theetharappan M., S. P. Bhuvanesh Nattamai, M. A. Neelakantan, K. M. Velusamy, Organoruthenium (II) complexes featuring pyrazole-linked Schiff base ligands: Crystal structure, DNA/BSA interactions, cytotoxicity and molecular docking, *Appl. Organometal. Chem.*, 2019, 33, e4751.

51. G. Vignesh, S. Sugumar, S. Arunachalam, S. Vignesh, and R. A. James, A comparative study on the binding of single and double chain surfactant–cobalt(III) complexes with bovine serum albumin, *Spectrochimica Acta Part A: Molecular and Biomolecular Spectroscopy*, 2013, 113, 415–422.

52. S. M. Kelly, T. J. Jess, N. C. Price, How to study proteins by circular dichroism, *Biochimica et Biophysica Acta*, 2005, 1751,119–139.

53. A. J. Miles, Robert W. Janes and B. A. Wallace, Tools and methods for circular dichroism spectroscopy of proteins: a tutorial review, *Chem. Soc. Rev.*, 2021, 50, 8400.

54. M. Sogami, S. Era, S. Nagaoka, H. Inouye, Circular dichroic and fluoropolarimetric studies on tryptophyl residues in acid-induced isomerization of bovine plasma albumin, 1982, *Int. J. Pept. Protein Res.*, 19, 263–269.

55. W. C. Johnson Jr, Secondary structure of proteins through circular dichroism spectroscopy, *Annual review of biophysics and biophysical Chemistry*, 1988, 17(1), 145–166.

56. M. A. Andrade, P. Chacon, J. J. Merelo, and F. Moran, Evaluation of secondary structure of proteins from UV circular dichroism spectra using an unsupervised learning neural network, *Protein Engineering, Design and Selection*, 1993, 6 (4), 383–390.

57. N. Greenfield, G.D. Fasman, Computed Circular Dichroism Spectra for the Evaluation of Protein Conformation, *Biochem.*, 1969, 8, 4108–4116.

58. M. A. Jakupec, M. S. Galanski , V. B. Arion , C. G. Hartinger, and B. K. Keppler, Antitumour metal compounds: more than theme and variations, *Dalton Trans.*, 2008, 183-194.

59. B. K. Keppler, Metal Complexes in Cancer Chemotherapy, VCH Publishers, 1993.

6.0 Conclusions and Future Directions

6.1 Conclusions

The work reported in this thesis provides synthetic access to novel iridium(III) complexes, $[Ir(bpy)_2(qtpy)]^{3+}$ (**1**), $[Ir(phen)_2(qtpy)]^{3+}$ (**2**), and $[Ir(dppz)_2(qtpy)]^{3+}$ (**3**). All the complexes employ qtpy as the bridging ligand and bpy, phen, and dppz as the auxiliary ligands for Complexes **1**, **2**, and **3**, respectively. As the conventional reflux technique proved abortive for the generation of the complexes due to their incorporation of a kinetically stable iridium metal centre, optimised synthesis via microwave irradiation successfully led to the generation of the compounds. RP-HPLC-purified complexes were subjected to MS and ^{1}H NMR characterisation, thus confirming their identities. Structural identity elucidations of the precursors used for the synthesis of the title complexes were given by single crystal X-crystallography. Singlet oxygen measurements demonstrated that, of the three investigated complexes, Complex **3** incorporating a dppz ligand is particularly potentially useful, as it gives a singlet oxygen Φ_Δ of 0.71. Absorption spectroscopy demonstrated that the three complexes could be photoexcited at 310–324nm, 310nm, and 282nm, for $[Ir(bpy)_2(qtpy)]^{3+}$, $[Ir(phen)_2(qtpy)]^{3+}$, and $[Ir(dppz)_2(qtpy)]^{3+}$, respectively. Moreover, luminescence experiments demonstrating the photophysical characteristics of the complexes furnished that the complexes exhibit dual emission signatures, displaying consequent emissions up to 500nm. All three complexes display relatively short lifetimes in oxygenated conditions. DFT analyses of the optimised geometries of the complexes show that they are all six-coordinate, as expected, as they form pseudo-octahedral complexes with the iridium metal core in their structures. Complex **2** has the most compact structure and positive charge density of the three complexes. Moreover, the orbital distribution for the HOMO and LUMO maps is found in the polypyridyl rings. However, in the latter, the 5d-orbital on the iridium metal centre contributes to the LUMO map beside the polypyridyl rings.

The results of the research investigation in this thesis demonstrate that the three complexes studied are average duplex DNA binders but excellent G4 HTS DNA binders, even though their binding affinities to DNA biomolecule in cells, may be somewhat impeded by their ability to also bind to serum albumins. The work in this thesis has equally shown that the 3+ charge on the iridium(III) complexes does not improve their binding constants compared to

isostructural 2+ Ru(II) analogues.

It has been previously observed that complexes with a higher cationic charge tend to display larger DNA-binding affinities than their counterparts with a lower charge, as there is often a sizeable electrostatic contribution to the DNA-binding abilities of metal complexes. Even though this holds as a matter of principle in many DNA-binding events, it is equally not always true. The +3-charge iridium(III) complexes in this work display lower duplex DNA-binding affinities (K_b in the order of ~$10^4 M^{-1}$) than their +2-charge ruthenium(II) complexes (K_b in the order of $10^5 M^{-1}$). However, the complexes, particularly **1** and **3**, are excellent G-quadruplex HTS DNA binders as furnished from their estimated DNA-binding affinities (K_b in the order of $>10^{11} M^{-1}$), making them promising sequence-selective DNA binders. Their G-quadruplex DNA binding abilities were further substantiated by circular dichroism spectral experiments, whereby they could disrupt the structure of the G4 HTS sequence.

The decrease in the steady-state luminescence of the three complexes upon adding DNA is consistent with redox quenching. Oxidative damage of DNA is most common at guanine residues due to the high oxidative potential of this base relative to cytosine, thymine and adenine. After successive additions of guanosine-5'-monophosphate to aqueous solutions of Complexes **1**–**3**, the luminescence of each complex decreased. Stern-Volmer kinetics showed that the excited states of all three complexes are quenched by guanosine-5'-monophospate at rates comparable to photooxidising agents (K_q in the order of $10^{10} dm^3 mol^{-1} s^{-1}$). The complexes could also photoxidise adenine base within DNA, yielding K_q in the order of $10^9 – 10^{10} dm^3 mol^{-1} s^{-1}$, though not as strong as they oxidise guanine base. As these complexes selectively degrade GMP and AMP, they may have considerable potential as future photodynamic therapeutics, especially Complex **3**. The photonuclease activity of Complex **1** was investigated using supercoiled plasmid DNA. Electrophoretic studies using agarose gel show increased cleavage of plasmid DNA with increasing concentration of the test compound.

Further investigations using ICP-OES and protein-binding luminescence studies revealed that the complexes have a protein target in serum media, with their protein-binding affinities in the order of $10^4 – 10^{10} M^{-1}$. Circular dichroism experimental investigations further showed that the compounds could unfold the structures of serum albumins, both BSA and HSA, thus, likely

impinging on the physiological functions of the investigated proteins. The ICP-OES and protein-binding luminescence studies of isostructural ruthenium(II) analogues, $[Ru(bpy)_2(qtpy)]^{2+}$, $[Ru(phen)_2(qtpy)]^{2+}$, and $[Ru(dppz)_2(qtpy)]^{2+}$, of the iridium(III) complexes also showed that the ruthenium(II) set of complexes equally has a protein target in serum media, with their protein-binding affinities in the order of $10^6 – 10^{11} M^{-1}$.

The preliminary cellular uptake investigations of the complexes were carried out. Interestingly, all three complexes explored in this thesis were taken up within human oral squamous carcinoma cancer cells (H357). PrestoBlue™ assays on the complexes revealed that they display dark cytotoxicity, with their IC_{50} values being 242.9µM, 112.4µM, and 0.2182µM.

6.2 Future Directions

Perhaps the single biggest advantage of the iridium(III) systems studied in this work is the phototunability of their excited states, which gave rise to different emission properties of the three complexes. This interesting aspect of these systems can be taken advantage of in future studies to construct more highly tuned iridium(III)-based metal complexes, especially ones that can be employed as organelle-specific binding agents. Structural modification of the iridium(III) polypyridyl complexes to fine-tune their emission properties, cellular uptake level, and intercellular localisation abilities will pave the way for revolutionising the research field of the development of iridium(III)-based therapeutics.

The non-absorption of these compounds in the phototherapeutic window (650–850 nm) limits their practical application. However, this drawback could be overcome in future developments by two-photon activation and conjugation of the compounds to suitable near-infrared (NIR) emitting organic chromophores through the N–N/N^N' ligand amide group.[1] With this suggestion heeded, the author hopes that iridium(III)-based therapeutics will find further future application in the field of Bioinorganic Chemistry and Medical Chemistry.

Preliminary cytotoxic activities of the reported compounds against H357 (human oral squamous cell carcinoma) cancer cell line were undertaken through a collaboration with Galleh Raphael, a colleague based at the University of Sheffield's School of Dentistry. The

cytotoxicity assessment tests herein based on the PrestoBlue™ Assay and the protocol employed for cell culture are both described in the Experimental section of this thesis. The PrestoBlue™ Assay has the advantage of not being toxic and of being able to be performed on the same samples over a series of experiments, which eliminates sample-to-sample variability.[2] Results from preliminary cytotoxicity assays conducted are summarised in Figs. 6.1–6.3. The figures are curated by a fit to a nonlinear regression (variable slopes) analysis on GraphPad Prism software.

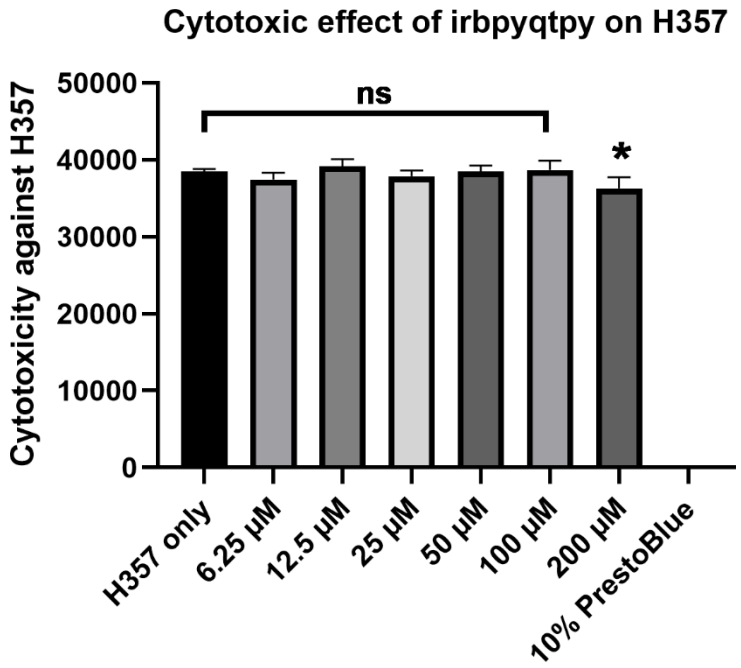

Figure 6.1 – PrestoBlue assay to determine cytotoxic effect of Complex **1** on H357 cancer cells.

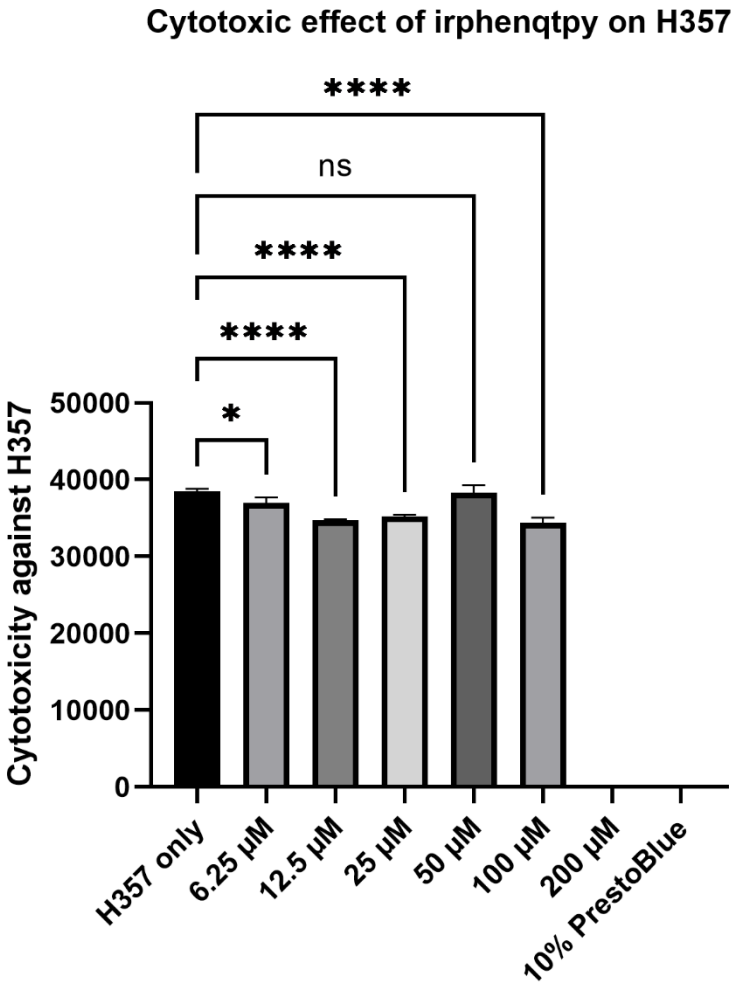

Figure 6.2 – PrestoBlue assay to determine cytotoxic effect of Complex **2** on H357 cancer cells.

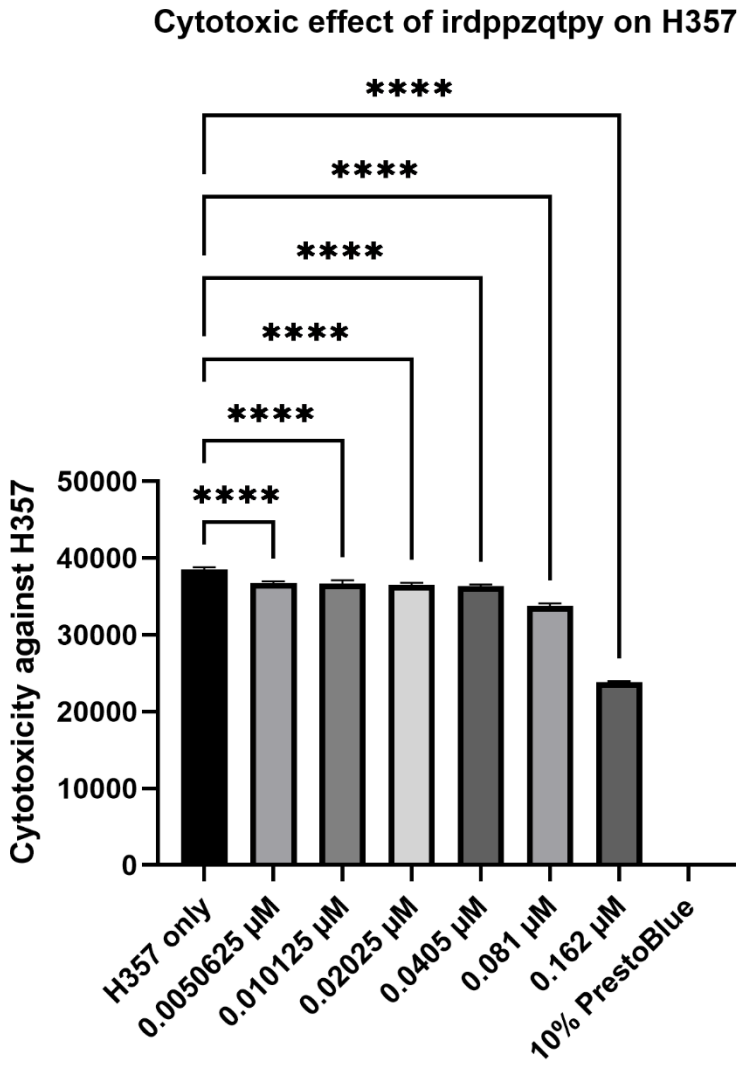

Figure 6.3 – PrestoBlue assay to determine cytotoxic effect of Complex **3** on H357 cancer cells.

Future work on the cellular investigations of these compounds will be to see whether or not their cytotoxic activities will increase or not upon photoirradiation as this could provide insights into their photodynamic therapeutic (PDT) properties. Moreover, imaging experiments to investigate the cellular internalisation and sub-cellular colocalisation of the test compounds will be necessary. Conventional luminescence microscopy and/or super-resolution microscopy (SRM) technologies will be highly relevant in this regards.

6.3 References

1. E. Zafon, I. Echevarría, S. Barrabés, B. R. Manzano, F. A. Jalón, A. M. Rodríguez, A. Massaguer, and G. Espino, Photodynamic Therapy with Mitochondria-targeted Biscyclometallated Ir(III) Complexes. Multi-action Mechanism and Strong influence of the Cyclometallating Ligand, *Dalton Trans.*, 2022, 51(1), 111–128.

2. R. Rahimi, M. Ochoa, A. Tamayol, S. Khalili, A. Khademhosseini, and B. Ziaie, Highly Stretchable Potentiometric pH Sensor Fabricated via Laser Carbonization and Machining of Carbon−Polyaniline Composite, *ACS Appl. Mater. Interfaces*, 2017, 9, 9015−9023.

7.0 Experimental

The various syntheses described in this section give only the isolated ligands or complexes. Detailed reports of their synthetic schemes have been given in Chapter Two of this thesis.

7.1 Materials and Equipment

Unless stated otherwise, all chemicals and solvents were purchased from commercial sources and were used as received. Ruthenium(II) and iridium(III) complexes were treated as toxic.

7.2 Reaction Conditions

Unless otherwise stated, all reactions proceeded under an inert atmosphere using either nitrogen (N_2) or argon (Ar) gas. Typically, iridium(III) polypyridyl complexes were prepared using Ar instead of N_2 as they are highly air sensitive.

7.3 Chromatography

Purifications of the ruthenium(II) polypyridyl complexes were done via cation exchange chromatography using SP Sephadex C-25 cation exchanger. Sephadex column sizes were approximately 500 x 10 mm. Purifications of the iridium(III) polypyridyl complexes were carried out using high-performance liquid chromatography (HPLC).

7.4 X-ray Crystallography

Structures were solved by Dr Craig Robertson in the University of Sheffield Department of Chemistry's X-ray structure determination service. A crystal with dimensions 0.1 x 0.3 x 0.3mm was selected under the polarizing microscope (MEIJI EMZ-13TR). Intensity data was collected on a Bruker Kappa APEX-II CCD diffractometer operating with a MoKα sealed-tube X-ray source of the crystal mounted in fomblin oil on a MicroMount (MiTeGen, USA) and cooled to 100 K in a stream of cold N_2 gas using an Oxford Cryosystems 700 Cryostream. Data were corrected for absorption using empirical methods (SADABS)[1] based upon symmetry equivalent reflections combined with measurements at different azimuthal angles.[2] The crystal

structures were solved and refined against F^2 values using ShelXT[3] for solution and ShelXL[4] for refinement accessed via the Olex2 programme.[5] Non-hydrogen atoms were refined anisotropically. Hydrogen atoms were placed in calculated positions with idealised geometries and then refined by employing a riding model and isotropic displacement parameters.

All crystal images are curated using either Mercury, OLEX2, and/or CrystalExplorer.

7.4.1 Crystal Growth Techniques

Crystals obtained in this report have been obtained majorly by three techniques succinctly discussed below:

1. Vapour Diffusion

This method works perfectly for milligram (mg) quantities of material. Typically, a solution of the compound of interest is prepared by dissolving in the first solvent, **S1**, and placed in a mass spectrometry tube, **MST** with the lid/cap slightly punctured. A second solvent (or antisolvent), **S2**, is placed in a large sample tube, **LST**. **S2** is selected so that the solute is less soluble when mixed with **S1**. The mass spectrometry tube containing **S1** is then gently placed in the **LST** containing **S2** and then sealed. Crystals will form as **S2** slowly diffuses into **MST** and **S1** slowly diffuses out of **MST**. Microcrystalline crusts will not form on the sides of **MST** if **S2** is more volatile than **S1**.

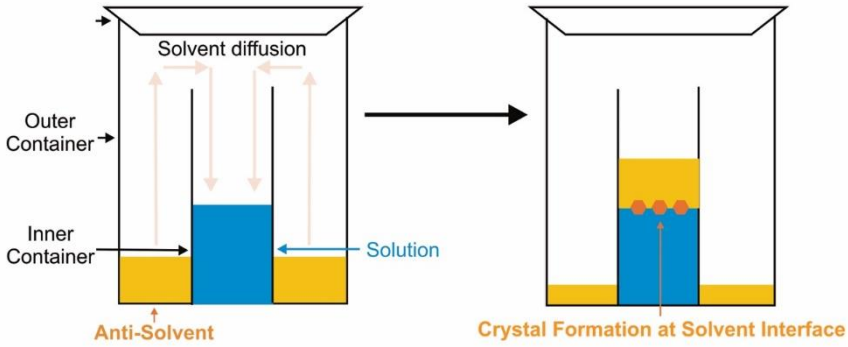

Figure 8.1 – Vapour diffusion technique (image adapted from Elsegood, Mark R.J., and C.L. Carpenter-Warren. 2019. "These Crystals Will Make Your Crystallographer Happy". figshare.[6]

2. Solvent Diffusion (Layering Technique)

This method is also suitable for mg amounts of materials that are sensitive to ambient laboratory conditions such as air and moisture. As a matter of fact, most crystals reported in this work have been grown using this technique. Typically, the compound is dissolved in the first solvent, **S1** and placed in a 5-mm NMR test tube. With the use of a syringe, the second solvent (or antisolvent), **S2** is then slowly dribbled into the tube, forming discreet layers of **S1** and **S2**. The CH_3NO_2/THF solvent combination works fine almost all the time for the growth of most crystals. It has been realised that this technique will only be successful if the density of **S2** < **S1** and care is exercised in creating the solvent layer.

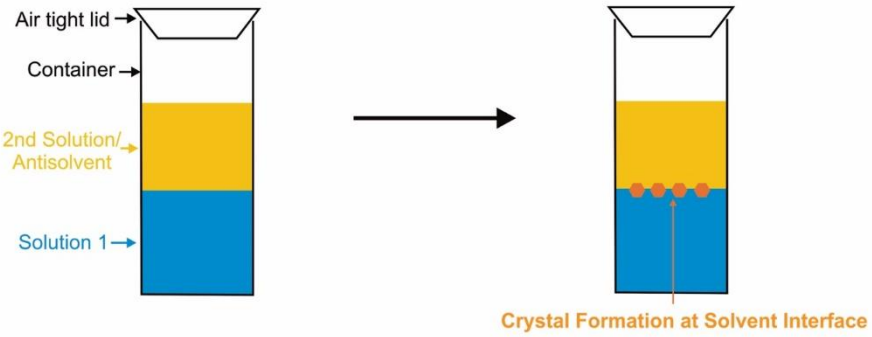

Figure 8.2 – Solvent diffusion technique (image adapted from Elsegood, Mark R.J., and C.L. Carpenter-Warren. 2019. "These Crystals Will Make Your Crystallographer Happy". figshare.[6]

3. Recrystallisation

The third method of crystal growth follows the same old procedure of recrystallisation used for the routine purification of many compounds. Basically, a solvent in which the compound of interest is insoluble at room temperature (but soluble at elevated temperature) is chosen. As the solution cools down after heating the mixture of the compound and choice solvent at the solvent's boiling point, crystals suitable for X-ray crystallography are typically formed after a few hours or even days.[7–8] Qtpy crystals, for instance, were obtained by this method.

7.5 Nuclear Magnetic Resonance (NMR) Spectroscopy

All ^{1}H NMR spectra were recorded using a Bruker AM250 machine working in a Fourier transform mode. The following abbreviations are used in the annotation of ^{1}H spectra: s = singlet, d = doublet, dd = doublet of doublet, t = triplet, and m = multiplet.

7.6 Mass Spectrometry (MS)

Fast-atom bombardment (FAB) mass spectra (MS) were recorded on a Kratos MS80 mass spectrometer working in positive ion mode with an m-nitrobenzyl alcohol matrix.

7.7 Microwave Irradiation

Reactions were performed in a modified Discover Microwave instrument on low-medium-high power. Reactions were carried out under a closed condition in either a 10mL vial or a 50mL round-bottom flask.

7.8 UV-Visible Absorption Spectroscopy

All UV-Visible spectra were recorded on a thermos regulated Varian-Carey Bio-300 UV-Visible spectrometer, using quartz cells of 10mm path length at 25^{o}C. Spectra were baseline corrected using Cary Win UV software and were diluted accordingly to give readings between 0 and 1.0 absorbance units.

7.9 Luminescence Spectroscopy

Luminescence spectra were recorded on a thermos regulated Jobin-Yvon FluoroMax-3 or FluoroMax-4 spectrophotometer operating in luminescence wavelength scan mode at 25^{o}C unless otherwise stated, with excitation and emission slit widths adjusted accordingly depending on the particular experiment.

7.10 High-performance Liquid Chromatography

For preparative HPLC employed for the purification of the complexes, the following system was adopted: 2 x Varian ProStar 210 solvent delivery modules with Varian ProStar 320 UV-Vis detector equipped with a Water XBridge Prep C18 5µm OBD 19 x 250 mm Column and a Varian ProStar 701 Fraction Collector and a Varian ProStar 410 Autosampler. HPLC grade-solvents employed were deionised/millipore water (with some 0.1% trifluoroacetic acid/formic acid, solvent A) and MeCN (solvent B). The flow rate was 17mLmin^{-1} and the chromatogram was detected at 241nm, 228nm, and 281nm for $[Ir(bpy)_2(qtpy)](CF_3SO_3)_3$, $[Ir(phen)_2(qtpy)](CF_3SO_3)_3$, and $[Ir(dppz_2(qtpy)](CF_3SO_3)_3$, respectively in MeCN.

7.11 DNA Binding Studies

7.11.1 Buffer Preparation

Tris buffer (pH 7.4) was prepared using Trizma HCl (Tris(hydroxymethyl)aminomethane base at 5mM concentrations in 5mM NaCl or 25mM NaCl or 50mM NaCl depending on the specific experiment. Trizma HCl and NaCl were measured into a volumetric flask and dissolved in deionised water (Millipore HPLC grade). The pH was adjusted using dilute HCl and additional water to achieve the correct volume. Buffer solutions were passed through a 0.2-micron Millipore filter and stored in a sterile glass bottle in the fridge at 4°C.

7.11.2 Duplex DNA Preparation

Calf-Thymus DNA (CT-DNA) was purchased from Sigma-Chemicals as the lyophilised solid sodium salt and used without any further purification. An average length of 200–300 base pairs was achieved by using a modified preparation by Chaires, *et al.*[9] Stock solutions of CT-DNA were prepared by dissolving the solid material in tris buffer (5mM tris, 5mM/25mM/50mM NaCl). A 30-minute sonication in an ice bath was performed on the stock solution using a Soniprep 150 ultrasonic disintegrator, fitted with a 19mm diameter probe. Five-minute periods of sonication were used, followed by 5minutess of cooling. The purity of the DNA samples was quantified using conventional absorbance measurements by measuring the ratio of contaminants to DNA with $A_{260}/A_{280} > 1.80$, indicating a protein-free sample. The concentration of the resulting solutions was also determined per base pair (bp) by UV spectroscopy using $\varepsilon_{260} = 13,200 M^{-1}cm^{-1}$ for CT-DNA.

7.11.3 G-quadruplex DNA Preparation

HPLC-purified human telomere sequence (HTS) quadruplex ($d[AG_3(T_2AG_3)_3]$) was purchased from Eurofins Genomics and used without any further purification. Stock solutions of G-quadruplex DNA were prepared by dissolving the solid material in tris buffer (5mM tris, 25mM NaCl). A simple chemical manipulation of the weight (4334µg) and molecular weight ($6967 gmol^{-1}$) gave the final concentration of 62.20µM of the DNA sample.

7.12 Agarose Gel Electrophoresis

The steps employed in setting up the electrophoretic experiment used in this thesis are highlighted below:

i. Set up the gel electrophoresis apparatus ensuring the corners at the bottom part of the gel chamber are well taped to be able to hold the gel after it solidifies. The tape should go up to at least 1cm to contain the volume/mass of the gel.

ii. Agarose powder (0.80g) was dissolved in 1X TAE (40mM tris-acetate, 1mM EDTA) (100 mL) and heated in autoclaved sterile glass bottle in the microwave for 2minutes at 30seconds on/off interval with swirling/shaking until all the solid dissolved and the solution was bubbling through (**caution:** do not overheat – it will bump; wear thermal gloves).

iii. The solution was left to cool down to 55°C by placing it in a water bath set to this temperature. This lasted for ca. 20minutes.

iv. This solution was then poured into a casting tray gel (ensuring no bubbles were present as much as possible) with a comb in place and was left to solidify for ca. 20–30minutes. It should go from a pale solution to a cloudy solid.

v. 1X TAE (1L) was poured into the gel chamber by the well by the black region until the gel chamber (both sides) is well covered.

vi. Once solidified, the comb was carefully removed for sample loading.

vii. 5µL of 500ng/µL of supercoiled pBR322 DNA was employed as DNA stock solution. The sample solutions used for the experiment were prepared thus:

Composition	**1**	**2**	**3**	**4**
Stock solution	6.70µL	6.70µL	6.70µL	6.70µL
Milli-Q H_2O	3.30µL	2.20µL	1.10µL	0
90µM of drug compound	0µL (control, i.e., untreated plasmid pBR322/ pUC19)	1.10µL (1X of the compound)	2.20µL (2X of the compound)	3.30µL (3X of the compound)

viii. 2µL 6X DNA Gel Loading Dye (blue in colour) was added to each sample solutions before loading onto the wells. This made the total volume of the sample solutions 12µL.

ix. The first well was loaded with 6µL of 1X DNA Gel Loading Dye (prepared from 6X solution by adding 30µL of milli-Q water to 6µL of the 6X solution of the MassRuler).

x. The samples were then loaded onto the wells. A total of 8 samples/wells (wells **5–8**, as given in a relevant section of Chapter 4, were simply a repetition of wells **1–4**) were made. Additional 5 wells were loaded with the gel loading dye.

xi. SYBR® Safe DNA Gel Stain (20µL) (red in colour) was mixed with 200mL of 1X TAE buffer and poured into a tray to stand.

xii. Gels were typically run at 100mV for ca. 20minutes. However, to achieve greater sample separation, it was run at 70mV for ca. 50minutes.

xiii. After the gel was successfully run, it was removed, and then inserted into the tray containing the solution prepared in step **xi** above and allowed to gently shake on a mini orbital shaker for ca. 25minutes.

xiv. DNA was visualised using Bio-Rad Chemidoc imaging system.

7.13 Singlet Oxygen Yield Measurement

Singlet oxygen measurements were obtained by Dr Alexander Auty. Singlet oxygen was detected directly in an organic solution by measurement of singlet oxygen luminescence (λ_{max} ~1275nm) following photoexcitation of the reported complexes at 25°C in air saturated MeCN. The yield of the formation of $^1O_2$, $\phi(^1O_2)$, was determined by measuring its phosphorescence intensity using an optically matched solution of 1-phenalenone as a reverence sensitiser.[10]

7.14 Circular Dichroism (CD)

Circular dichroism measurements were recorded on a Jasco J-810 spectropolarimeter at 25°C, scanning at 100nm/minute or 200nm/minute from 250–190nm for HSA and/or BSA and 310–240nm for G-quadruplex HTS DNA. The final CD spectra were the average of three scans. All CD experiments with either serum albumins or G4 HTS oligonucleotide sequence AGGGTTAGGGTTAGGGTTAGGG (22mer) or (d[$AG_3(T_2AG_3)_3$]) were carried out in 5mM tris, 25mM NaCl buffer solutions at pH 7.4 followed by the addition of the appropriate volume of either protein or G-quadruplex and then the test compounds.

7.15 Density Functional Theory and Molecular Docking

Gaussian 09 programme[11] was employed for all Density Functional Theory (DFT) calculations. The Becke-three-parameters Lee-Yang and Parr (B3LYP) method was used whilst the 6-31g(d) basis set was applied to all atoms except for iridium in which the LANL2DZ (Los Alamos National Laboratory 2 Double-Zeta) was beneficial. This method of mixing two different basis set is worthwhile to reduce the computational cost especially when a transition metal is involved in the calculation.[12–13] Applying effective core potential (ECP) basis set (LANL2DZ for transition metals is a common practice because ECPs are parameterised to implicitly account for scalar relativistic effects which are significant for transition metals.[14–15] The stability of the optimised geometries of the studied complexes was confirmed via frequency calculations which showed the absence of imaginary frequencies. TDDFT (Time Dependent-Density Functional Theory) calculations[16] was utilised to calculate optical transitions (UV-Vis) using the same level of theory on 100 states set in acetonitrile as the solvent via the Self-Consistent Reaction Field (SCRF).

The molecular docking studies of the reported complexes with duplex DNA were done using AutoDock 4.2[17] The protein databank[18] provided the structure (PDB ID:1N37)[19] of the duplex DNA. The binding site area had the grid parameters showed to be 16.993, 12.818, and 16.882 as the X, Y, and Z axes. The Discovery studio programme[20] was used to clean the duplex DNA by removing the complex bound to it. The docking and grid parameters were modified to include details such as the Van der Waals radii and atomic solvation volume for iridium as this was not present in the default. All other parameters used the default setting Lamarckian genetic algorithm[21] and performing a total of 10 runs for each complex. The docking pose with the highest binding energy was selected for result analysis.

7.16 Protocol Employed for the Preparation and Quantification of BSA and HSA

Samples of serum albumin was purified through a common protocol A few grammes of SA were placed inside a falcon tube well positioned in a beaker containing some iced water. A sufficient amount of tris buffer was then added to the protein to dissolve the SA. Afterwards, the entire setup was placed in a freezer and kept at 4°C. The SA was left for about 15 minutes

until it dissolved completely. The concentrations of BSA and HSA were determined spectrophotometrically from the respective molar extinction coefficient values of 43,800 and 36,500$M^{-1}cm^{-1}$ at 278nm.

7.17 Inductively Coupled Optical Emission Spectroscopy

For the evaluation of maximum metal binding, HSA protein concentration was fixed at 8.39µM, whilst each metal complex was added in 23-fold excesses. Metal complex solutions were added freshly prepared in tris buffer. Samples were then incubated for 1h at 37°C temperature. Samples were diluted by a factor of 20 using 1% nitric acid before injection and then accounted for this dilution in calculations. The instrument used was a spectro ciros vision ICP-OES with the following settings: plasma power: 1400W, coolant flow: 12L/min, auxiliary flow: 1L/min, nebuliser flow: 0.85L/min.

Quantification of the metal content in each chromatographic fraction was calculated directly from the integrated signal from the ICP-OES chromatograms using the formula $c_b = M_b \times c_{inj} \times D$, where c_b represents the initial concentration of metal in the original sample, M_b is the fraction of metal bound to protein in the chromatogram (calculated as a percentage of bound metal signal with respect to the total sum of signals), c_{inj} is the concentration of metal injected for analysis and D is the dilution factor applied to the samples prior to injection.[22]

7.18 Cellular Studies

7.18.1 PrestoBlue™ Assay

PrestoBlue™ is a ready-to-use cell viability reagent that is used for rapid evaluation of cell viability and proliferation of diverse range of cell types as well as cytotoxicity. PrestoBlue™ reagent is quickly reduced by metabolically active cells, providing a quantitative measure of viability and cytotoxicity in as little as 10 minutes.[23] PrestoBlue (PB) and Alamar Blue (AB) reagents are resazurin-based, which is a water-soluble dye formerly used in the detection of bacterial or fungal contamination of biological fluids.[24] The assay depends on the ability of

viable and metabolically active cells to reduce resazurin to a red fluorescent compound, resorufin, which can then be quantified either fluorometrically or colorimetrically.[24]

7.18.2 Protocol Employed for Cell Culture

In a 24-well tissue culture plate, H357 cells were seeded at 2 $x10^5$ /mL and incubated at 37ºC, 5% CO_2 for 24hours. Culture supernatants were discarded, and wells washed with PBS, varying concentrations of Complex **1, 2**, or **3** were added and incubated for 24hours. The wells were washed and 1mL of 10% PrestoBlue™ reagent prepared in non-supplemented DMEM was added to the wells and incubated at 37ºC, 5% CO_2 for 1hr after which, 100µL from each well were transferred to flat bottom transparent 96-well plate in triplicate and the reaction fluorescence was read at excitation 560nm and emission at 590nm using TECAN M200 plate reader. Data represent single experiment with each condition repeated in triplicate. Ordinary one-way ANOVA with Dunnett's Multiple Comparison tests were conducted using Prism GrapPad (version 9.2.0). P value = <0.0001.

7.19 Anion Metathesis

All complexes were synthesised as their triflate salts and characterised as such unless otherwise stated. Anion metathesis to their chloride salts was achieved by refluxing the compounds dissolved in a minimal amount of acetone and copious amount of milli-Q water in Dowex® ion exchange resin over the course of 1–2 days. The anion exchanger was then filtered off and the desired chloride compounds in solution were afforded by subjecting to rotary evaporation to remove off water and acetone and by drying *in vacuo.*

7.20 Synthesis

7.20.1 2,2’:4,4”:4’:4”’-quaterpyridine[25]

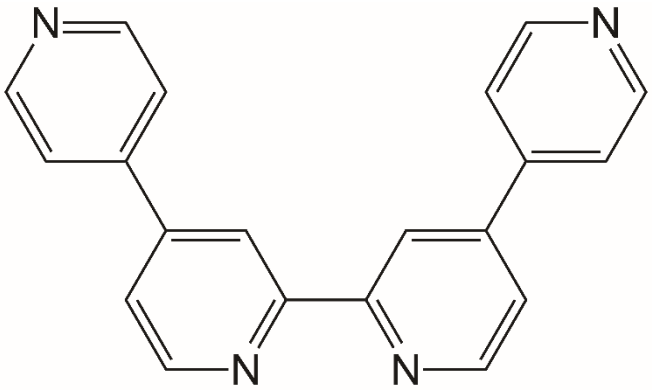

Figure 8.3 – Qtpy.

4,4’-bpy (20.42 g, 70.19mmol) was weighed into a 500mL two-neck round-bottom flask to which fresh Pd/C (2.20g) was added. DMF (300mL) that has been deaerated for ca. 15minutes was then transferred into the flask. The reaction was left to progress under an N_2 atmosphere while being refluxed at 153°C for ca. 120hours. Once the reaction was complete, and the mixture had cooled down to room temperature, DMF was removed on a rotavap to afford a mass of black residue. Chloroform (100mL) was added to the black residue, and the mixture was allowed to reflux under stirring for a further ca. 30minutes. Once cooled, the Pd/C catalyst was filtered off through celite to yield a clear yellow solution. Afterwards, chloroform was removed *in vacuo* and the crude mass acquired was left to stir in acetone (60mL) for ca. 30minutes to remove any unreacted 4,4’-bpy. The mixture was filtered under vacuum, and the residue was collected. The filtrate was concentrated by rotary evaporation to yield more portions of the desired product. There were several repetitions of this process, and the various portions of the product were reunited. The compound obtained was then recrystallised from EtOH to yield crystals of qtpy ligand, which is often a creamy solid but sometimes an off-white solid. The yield was calculated against 4,4’-bpy with the characterisation data given below:

Yield: 6.84 g (33.71 %).

ESI-MS, m/z: 311 $[M + 1]^+$.

^{1}H NMR (400 MHz, d^3-$CDCl_3$): δ_H = 8.85 (dd, *J* = 5.1, 2H), 8.81– 8.79 (m, 6H), 7.71 (dd, *J* = 4.5, 1.6 Hz, 4H), 7.63 (dd, *J* = 5.1, 1.8 Hz, 2H).

7.20.2 1,10-phenanthroline-5,6-dione (dpq)[26]

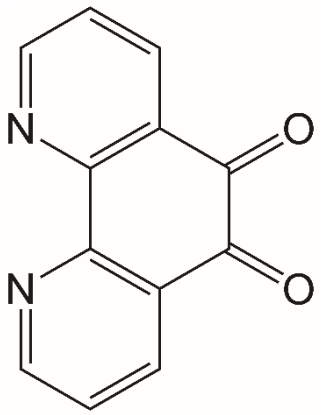

Figure 8.4 – 1,10-phenanthroline-5,6-dione (dpq).

1,10-phenanthroline (5.00g) was dissolved into 60% H_2SO_4 (35mL). $KBrO_3$ (18.30g) was slowly added to the mixture formed. The reaction mixture was set aside to cool to room temperature and then placed in an ice-bath. Crushed ice (30.00g) was added to the solution to afford further cooling. The solution was neutralised to pH 5–6 by adding aqueous NaOH (20M) dropwise. A yellow precipitate was obtained and filtered and washed with H_2O (157.50mL). This suspension was extracted with chloroform, collected by vacuum evaporation, dried, and recrystallised from EtOH to yield pure dpq crystals as canary yellow solids. The yield was calculated against phen with the characterisation data given below:

Yield (isolated): 2.18g (37.39%).

ESI-MS, m/z: 211 $[M + H]^+$.

^{1}H NMR (400 MHz, d^3-$CDCl_3$): δ_H = 9.15 (dd, *J* = 4.6, 1.7 Hz, 2H), 8.54 (dd, *J* = 7.9, 1.7 Hz, 2H), 7.62 (dd, *J* = 7.9, 4.7 Hz, 2H).

7.20.3 Dipyrido[3,2-a:2',3'-c]phenazine (dppz)[26]

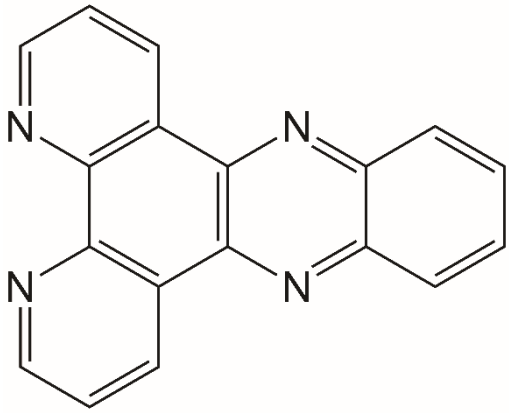

Figure 8.5 – Dppz.

Dpq (3.00g) in EtOH (30mL) and *o*-phenylenediamine (3.00g) in EtOH (30 mL) were mixed and the solution was boiled for ca. 30minutes. Brown crystals were obtained upon cooling, which were filtered, washed with H_2O (50mL) and recrystallised from EtOH (20mL) to afford the desired dppz as brown-orange needles. The yield was calculated against dpq with the characterisation data given below:

Yield: 2.75 g (68.24%).

ESI-MS, m/z: 283 $[M + H]^+$.

^{1}H NMR (400 MHz, d^3-$(CH_3)_2CO$): δ_H = 9.67 (dd, *J* = 1.8 Hz, 2H), 9.24 (dd, *J* = 4.3, 1.7 Hz, 2H), 8.43 (dd, *J* = 7.9, 4.7 Hz, 2H), 8.08 (dd, *J* = 6.3, 3.2Hz, 2H), 7.95 (dd, *J* = 8.1, 4.4Hz, 2H).

7.20.4 $Ru(bpy)_2Cl_2$[27]

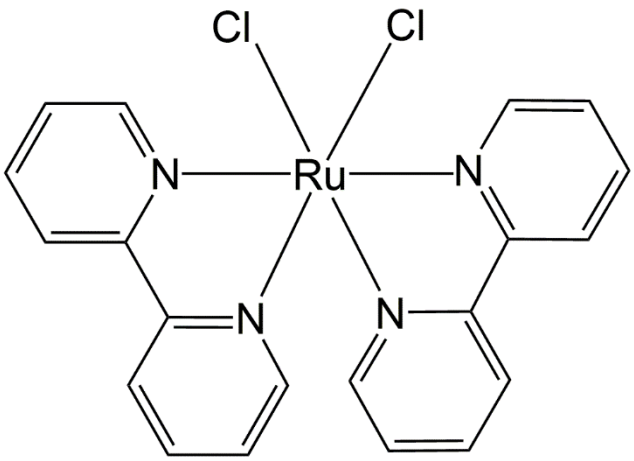

Figure 8.6 – $Ru(bpy)_2Cl_2$.

$RuCl_3.3H_2O$ (5.00g, 19.10mmol), bpy (6.00g, 38.45mmol), and LiCl (5.50g) were dissolved in fresh DMF (30mL) and heated to reflux for ca. ≥ 8 hours. The solution obtained was allowed to cool to room temperature, poured into stirred acetone (100mL) and cooled to 4°C for ca. 24 hours. The crude solid product obtained was recovered by vacuum filtration and then washed with copious amounts of H_2O and Et_2O. The clean product was then dried *in vacuo* and obtained as the desired compound. The yield was calculated against $RuCl_3.3H_2O$ with the characterisation data given below:

Yield: 5.56g (60.11%).

ESI-MS, m/z: 449 [$M^+ – Cl^-$].

7.20.5 $Ru(phen)_2Cl_2$[27]

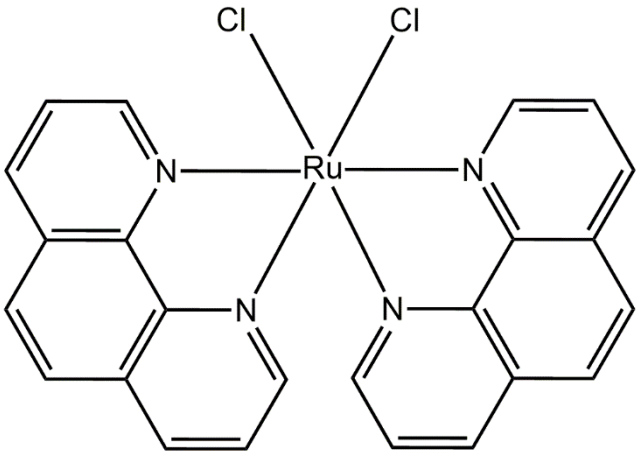

Figure 8.7 – $Ru(phen)_2Cl_2$.

This compound was prepared analogously to $Ru(bpy)_2Cl_2$ using $RuCl_3.3H_2O$ (5.00g, 16.10mmol), phen (6.90g, 38.30mmol), and LiCl (5.50g). The yield was calculated against $RuCl_3.3H_2O$ with the characterisation data given below:

Yield: 3.25g (31.96%).

ESI-MS, m/z: 497 [$M^+ – Cl^-$].

7.20.6 $Ru(dppz)_2Cl_2$[27]

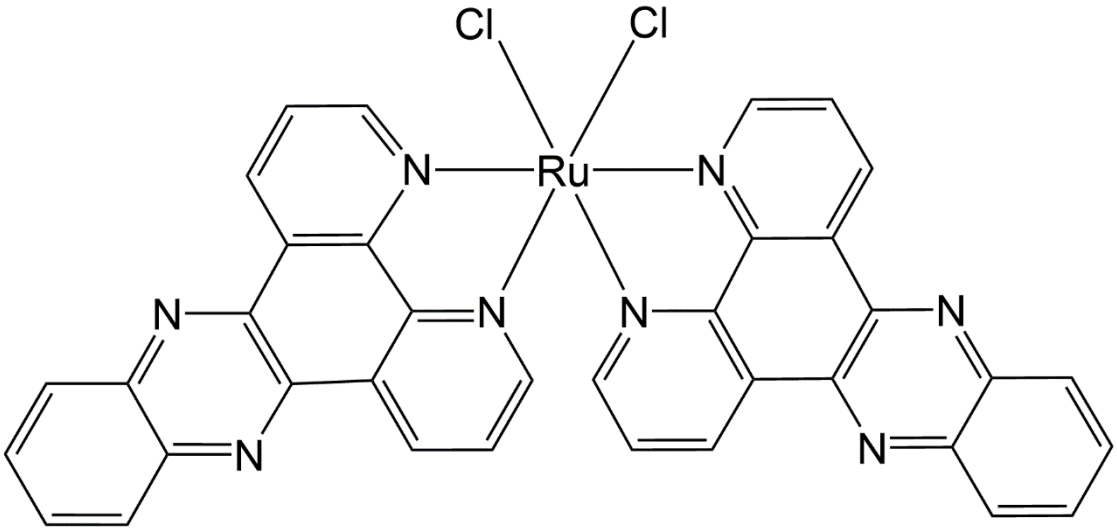

Figure 8.8 – $Ru(dppz)_2Cl_2$.

This compound was prepared analogously to $Ru(bpy)_2Cl_2$ using $RuCl_3.3H_2O$ (0.48g, 3.82mmol), dppz (1.04g, 7.64mmol), and LiCl (0.55g). The yield was calculated against $RuCl_3.3H_2O$ with the characterisation data given below:

Yield: 1.03g (76.30%).

ESI-MS, m/z: 701 [$M^+ – Cl^-$].

7.20.7 [Ru(bpy)$_2$(qtpy)](PF6)$_2$[28]

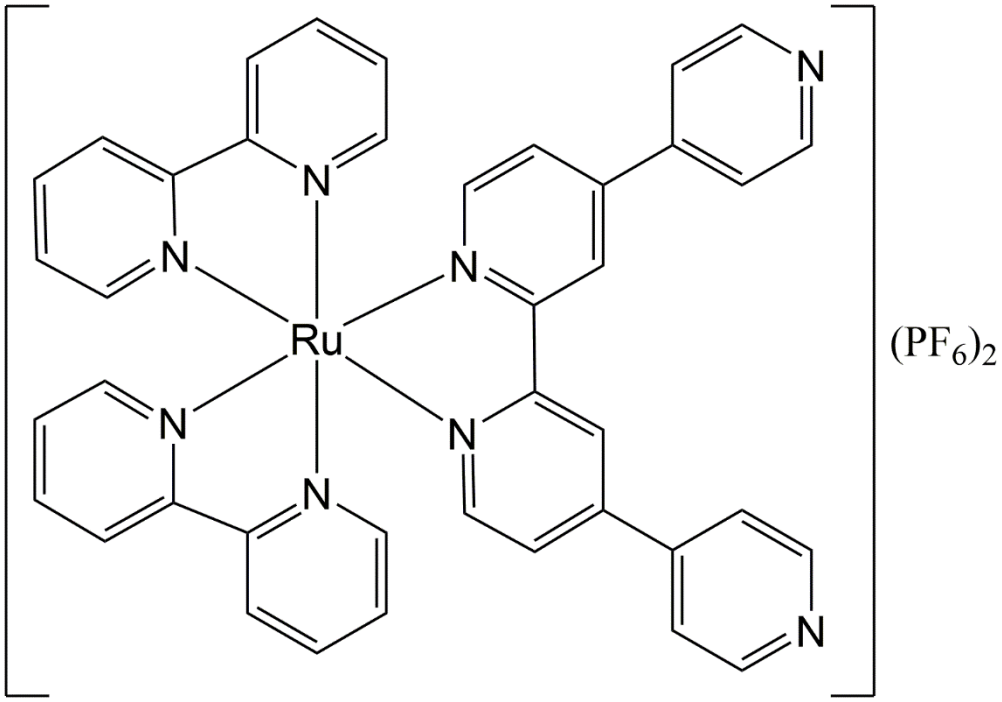

Figure 8.9 – [Ru(bpy)$_2$(qtpy)](PF$_6$)$_2$.

Ru(bpy)$_2$Cl$_2$ (0.20g, 3.85mmol) and qtpy (0.119g, 3.87mmol) were heated to reflux in freshly distilled, dry ethylene glycol at 198°C for ca. 2hours, 30minutes. Upon cooling, the unreacted starting materials were filtered out of the reaction mixture. The desired product was isolated by the addition of aqueous NH_4PF_6, filtered, washed with copious amounts of H_2O and Et_2O and then dried *in vacuo*. The yield was calculated against qtpy with the characterisation data given below:

Yield: 0.42g (66.67%).

ESI-MS, m/z (%): 362 [M^{2+} – $2PF_6^-$].

^{1}H NMR (400 MHz, *d*^{3}-CD$_3$CN): δ_H 8.98 (d, J = 1.8 Hz, 2H), 8.84 (dd, J = 4.5, 1.7 Hz, 4H), 8.55 (d, J = 8.1 Hz, 4H), 8.11 (m, J = 8.0, 3.6, 1.5 Hz, 4H), 7.89 (d, J = 6.0 Hz, 2H), 7.86 (dd, J = 4.5, 1.7 Hz, 4H), 7.83 (d, 2H), 7.79 (d, J = 5.0 Hz, 2H), 7.75 (dd, J = 6.0, 2.0 Hz, 2H), 7.48 – 7.43 (m, 4H).

7.20.8 $[Ru(phen)_2(qtpy)](PF_6)_2$[28]

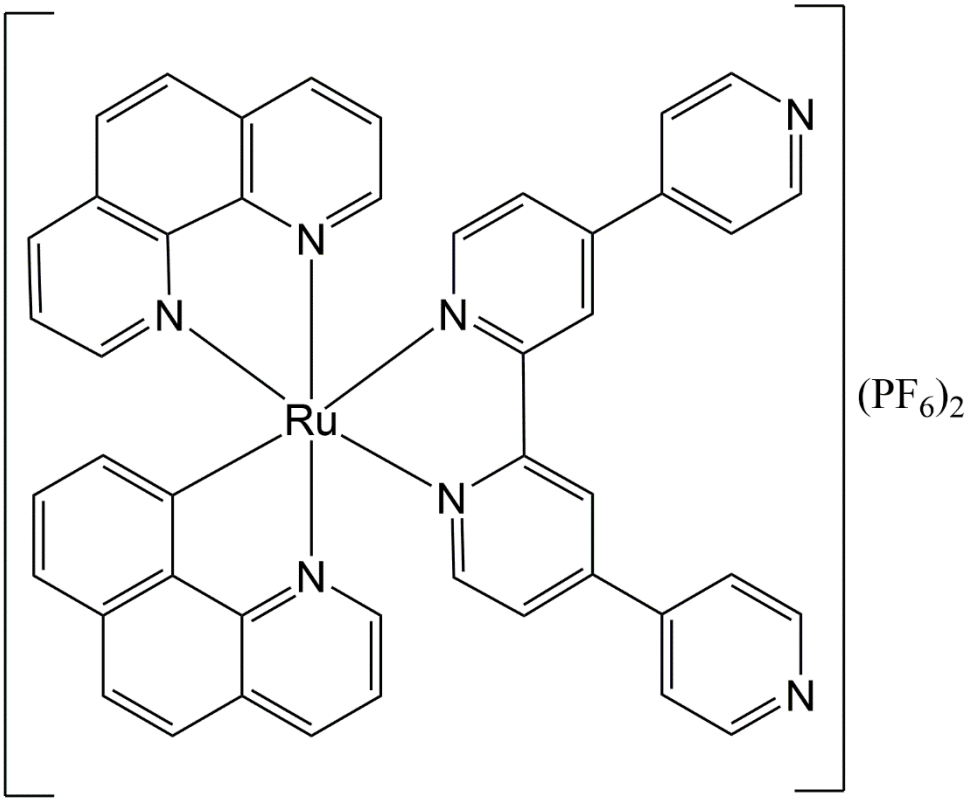

Figure 8.10 – $[Ru(phen)_2(qtpy)](PF_6)_2$.

This compound was prepared analogously to $[Ru(bpy)_2(qtpy)](PF_6)_2$ using $Ru(phen)_2Cl_2$ (0.74g, 1.288mmol) and qtpy (0.40g, 1.28mmol). The yield was calculated against qtpy with the characterisation data given below:

Yield: 0.42g (30.66%).

ES-MS, m/z: 917 $[M^+ – PF_6^-]$, 386 $[M^{2+} – 2PF_6^-]$.

^{1}H NMR (400 MHz, *d*^{3}-CD_3CN): δ_H 9.00 (s, 2H), 8.83 (dd, J = 9.4, 5.8 Hz, 4H), 8.76 (dd, J = 6.0 Hz, 2H), 8.71 (d, J = 8.2 Hz, 2H), 8.61 (d, J = 8.4 Hz, 2H), 8.32 (d, J = 4.2 Hz, 2H), 8.31 – 8.29 (m, 6H), 7.94 (dd, 2H), 7.84 (dd, J = 4.8 Hz, 2H), 7.78 (d, J = 4.9 Hz, 2H), 7.62 – 7.58 (m, J = 8.2, 4.7 Hz, 4H).

7.20.9 $[Ru(dppz)_2(qtpy)](PF_6)_2$[28]

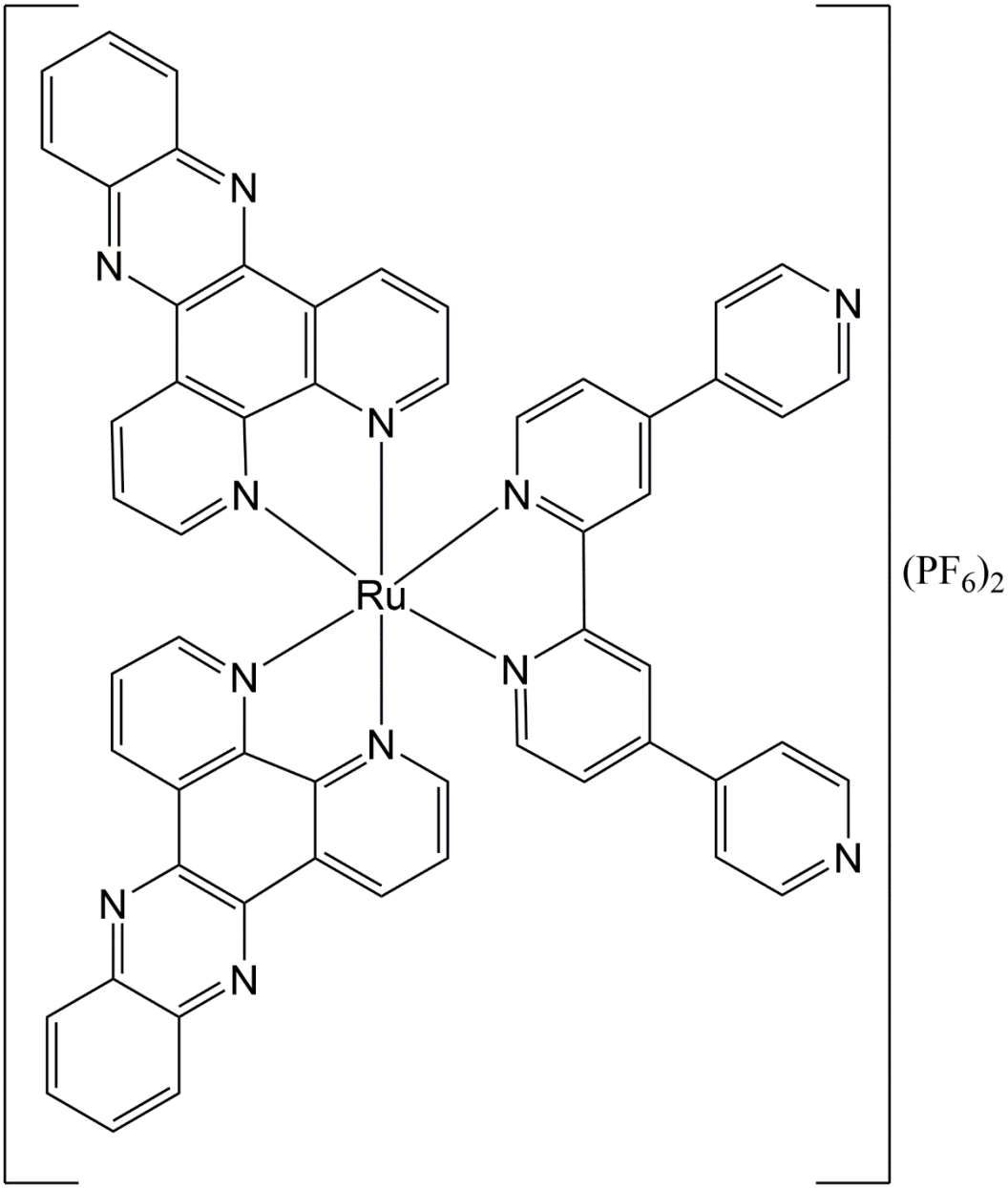

Figure 8.11 – $[Ru(dppz)_2(qtpy)](PF_6)_2$.

This compound was prepared analogously to $[Ru(bpy)_2(qtpy)](PF_6)_2$ using $Ru(dppz)_2Cl_2$ (0.25 g, 0.32 mmol) and qtpy (0.10 g, 0.32 mmol). The yield was calculated against qtpy with the characterisation data given below:

Yield: 0.40 g (93.04 %).

ESI-MS, m/z: 1121 $[M^+ – PF_6^-]$, 488 $[M^{2+} – 2PF_6^-]$.

^{1}H NMR (400 MHz, *d*^{3}-CD_3CN): δ_H = 9.79 (dd, 2H, J_{HH} = 8.3 Hz, 1.2 Hz), 9.68 (dd, 2H, J_{HH} = 8.2 Hz, 1.3 Hz), 9.10 (s, 2H), 8.85 (dd, 4H, J_{HH} = 4.6 Hz, 1.7 Hz), 8.54 (m, 4H), 8.44 (dd, 2H, J_{HH} = 5.4 Hz, 1.5 Hz), 8.23 (dd, 2H, J_{HH} = 5.4 Hz, 1.5 Hz), 8.19 (m, 4H), 8.07 (d, 2H, J_{HH} = 5.9 Hz), 8.03 (dd, 2H, J_{HH} = 8.1 Hz, 5.4 Hz), 7.91 (dd, 4H, J_{HH} = 4.6 Hz, 1.7 Hz), 7.83 (dd, 2H, J_{HH} = 8.1 Hz, 5.4 Hz), 7.71(dd, 2H, J_{HH} = 6.0 Hz, 1.9 Hz).

7.20.10 $[Ir(bpy)_2Cl_2]PF_6$[29]

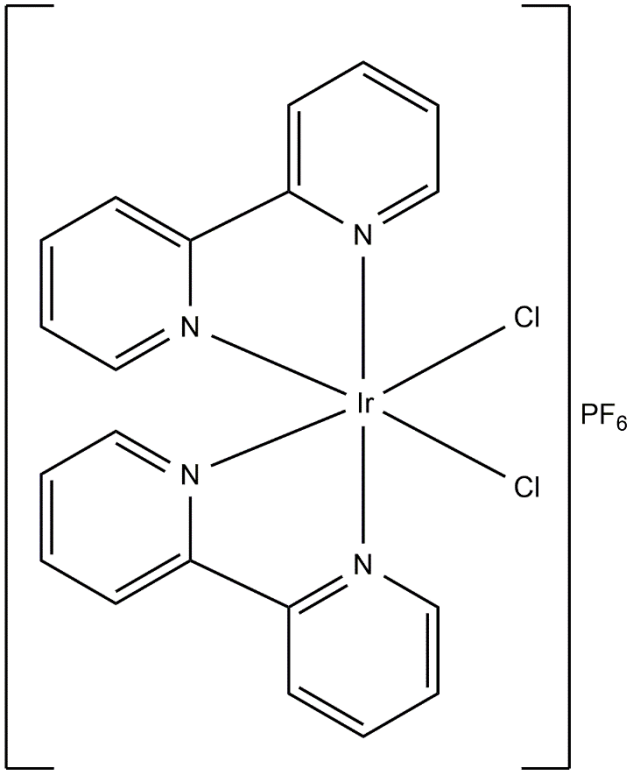

Figure 8.12 – $[Ir(bpy)_2Cl_2]PF_6$.

Under a N_2 atmosphere, $IrCl_3.3H_2O$/iridium trichloride(III) trihydrate (1.50g, 5.0mmol) and 2,2'-bipyridine (1.31g, 8.40mmol) were suspended in ethylene glycol (35mL) and heated at 198^{o}C under reflux for ca. 21 hours under an N_2 purging atmosphere. Upon cooling, the unreacted starting materials were filtered out of the reaction mixture. The addition of aqueous NH_4PF_6 precipitated out the desired complex as a bright orange solid which was collected by vacuum filtration, washed with Et_2O and dried *in vacuo*. The yield was calculated against $IrCl_3.3H_2O$ with the characterisation data given below:

Yield: 2.00g (60%).

ESI-MS, m/z: 575 [$M^+ – PF_6$].

7.20.11 $[Ir(bpy)_2Cl_2]Cl$[29]

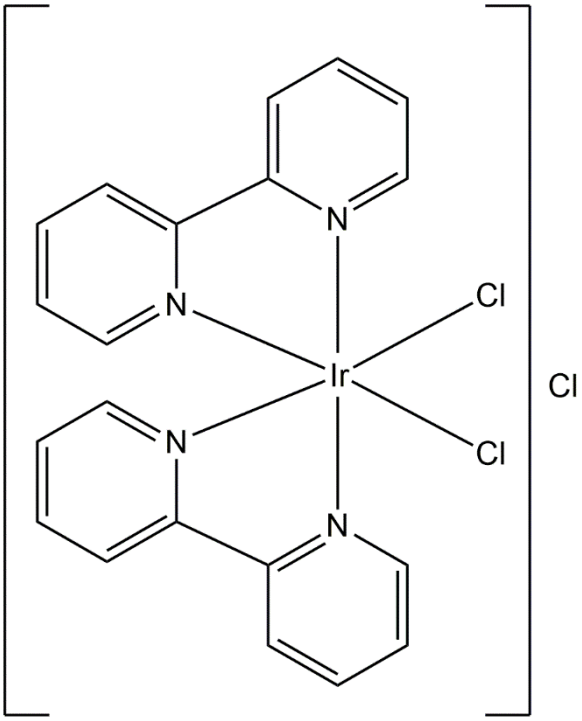

Figure 8.13 – $[Ir(bpy)_2Cl_2]Cl$.

This compound was obtained via the counter anion metathesis of $[Ir(bpy)_2Cl_2]PF_6$ thus: $[Ir(bpy)_2Cl_2]PF_6$ (1.00g, 1.39mmol) was dissolved in acetone (10mL), and TBAC (0.50g) was also suspended in acetone (10mL). The second solution was slowly poured into the first to give instant precipitation of an orange solid. This was left in the fridge for ca. 2hours to yield maximum precipitation and collected by vacuum filtration. The product was dried under vacuum. The yield was calculated against $[Ir(bpy)_2Cl_2]PF_6$ with the characterisation data given below:

Yield: 0.89g (89%).

ESI-MS; m/z: 575 [$M^+ – Cl^-$].

7.20.12 $[Ir(bpy)_2Cl_2]CF_3SO_3$[29]

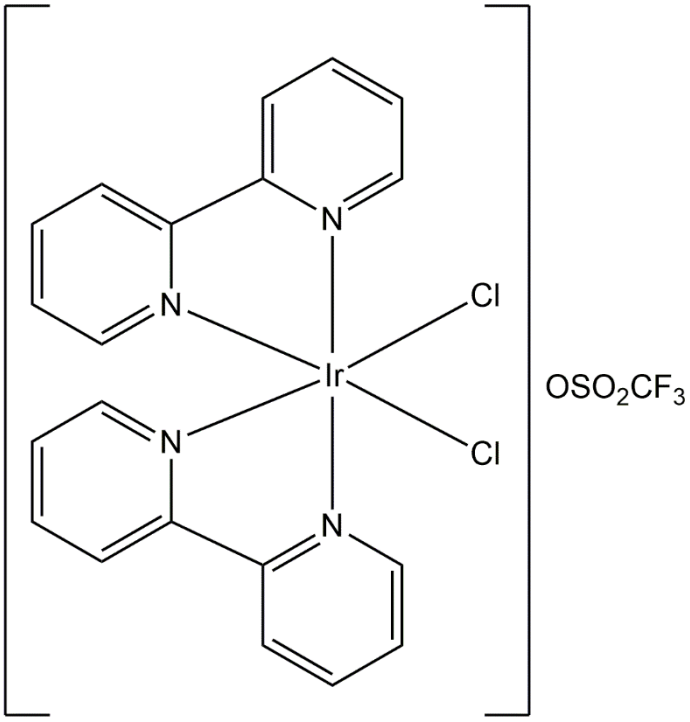

Figure 8.14 – $[Ir(bpy)_2Cl_2]CF_3SO_3$.

$[Ir(bpy)_2Cl_2]Cl$ (0.525g, 0.860mmol) was suspended in MeCN (100mL) with stirring. Triflic acid (TFMS) (0.35mL, 3.95mmol) was carefully added dropwise to the solution to give dissolution. The solution was stirred for ca. 1hour at room temperature while constantly monitoring with thin layer chromatography (TLC) (CH_3CN:H_2O:KOH: v/v, 8:1:1). The volume of solvent was reduced under vacuum by ca. 75% and the solution was placed in a freezer overnight to give a bright orange precipitate. This was collected by centrifugation to yield $[Ir(bpy)_2Cl_2]CF_3SO_3$. The yield was calculated against $[Ir(bpy)_2Cl_2]Cl$ with the characterisation data given below:

Yield: 0.37 g (59.68%).

ESI-MS; m/z: 575 [$M^+ – CF_3SO_3$].

^{1}H NMR (400 MHz, DMSO): δ_H 9.64 (d, *J* = 5.5 Hz, 2H), 8.93 (d, *J* = 8.1 Hz, 4H), 8.83 (d, *J* = 8.1 Hz, 2H), 8.52 (t, *J* = 7.9 Hz, 2H), 8.21 (t, *J* = 7.8 Hz, 2H), 8.12 (t, *J* = 6.7 Hz, 2H), 7.83 (d, *J* = 5.6 Hz, 2H), 7.51 (t, *J* = 6.7 Hz, 2H).

7.20.13 $[Ir(bpy)_2(CF_3SO_3)_2][CF_3SO_3]$[29]

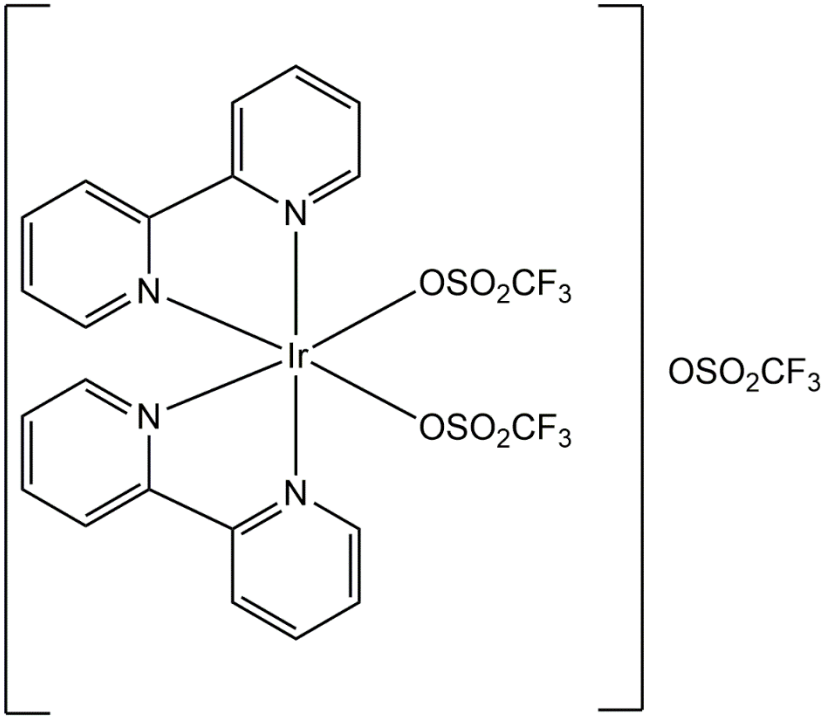

Figure 8.15 – $[Ir(bpy)_2(CF_3SO_3)_2]CF_3SO_3$.

Under an N_2 atmosphere, $[Ir(bpy)_2Cl_2]CF_3SO_3$ (0.63g, 0.87mmol) was suspended in *o*-dichlorobenzene (10mL) with stirring. TFMS (1.4mL, 15.87mmol) was carefully added dropwise to give white fumes and dissolution of the solid. The reaction solution was a heterogeneous two-phase green-yellow liquid which was refluxed for ca. 3hours. Cooling of the solution was performed until ambient temperature was reached. The solution was then decanted into ice-cold Et_2O (30mL) to give precipitation of a green solid. The reaction mixture obtained was cooled in the fridge overnight to give further precipitation. The desired product was collected using vacuum filtration as a finely divided pale greenish-yellow solid and then dried *in vacuo*. The yield was calculated against $[Ir(bpy)_2Cl_2]CF_3SO_3$ with the characterisation data given below:

Yield: 0.69g (83.13%).

ESI-MS, m/z: 803 $[M^+ – CF_3SO_3]$, 653 $[M^+ – 2CF_3SO_3]$, 327 $[M^{2+} – 3CF_3SO_3]$.

^{1}H NMR (400 MHz, DMSO): δ_H 9.07 – 9.01 (m, 4H), 8.86 (d, J = 8.1 Hz, 2H), 8.70 (t, J = 8.0 Hz, 2H), 8.37 (t, J = 6.8 Hz, 2H), 8.26 (t, J = 7.9 Hz, 2H), 7.73 (d, J = 6.0 Hz, 2H), 7.55 (t, J = 6.8 Hz, 2H).

7.20.14 $[Ir(bpy)_2(qtpy)](CF_3SO_3)_3$ (New Complex)

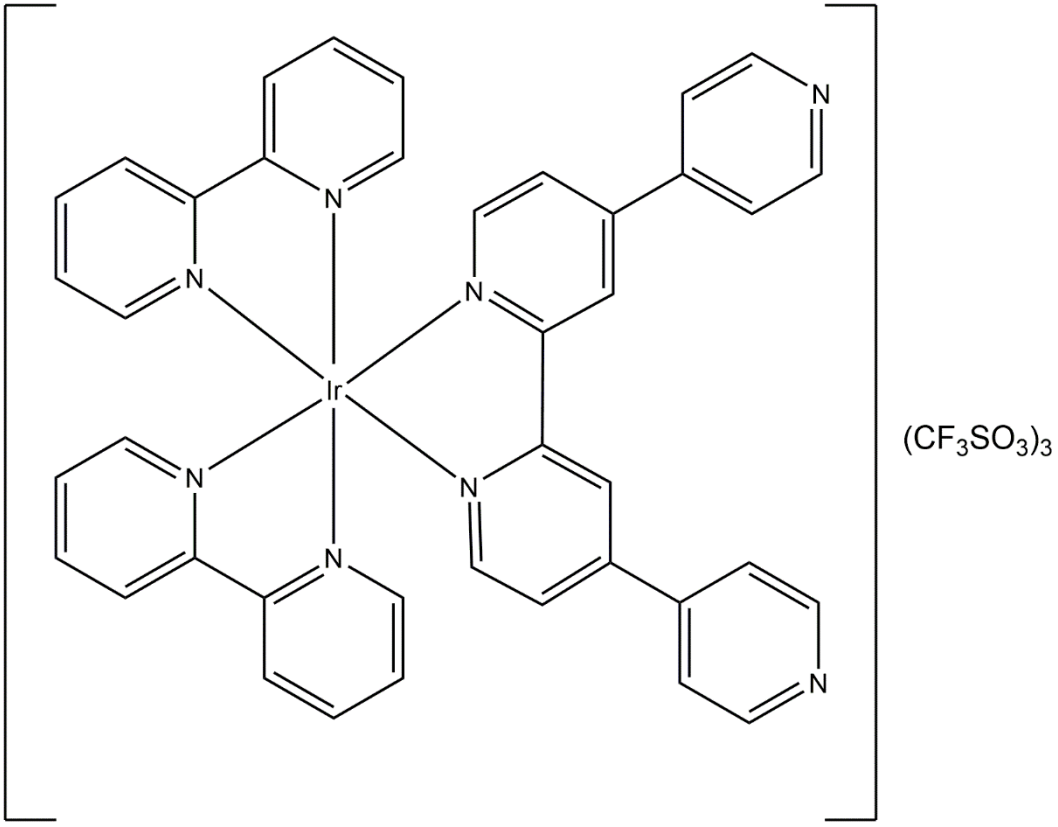

Figure 8.16 – $[Ir(bpy)_2(qtpy)](CF_3SO_3)_3$.

$[Ir(bpy)_2(CF_3SO_3)_2]CF_3SO_3$ (0.20g, 0.210mmol) and qtpy (0.24g, 0.774mmol) were suspended in ethanol (15mL) in a 50mL round-bottom flask and the mixture was well purged with Ar for ca. 30minutes and allowed to stir and reflux under this condition. The reaction mixture, which was initially a faint yellowish suspension, became increasingly deeply yellow with the passage of time. After the completion dissolution of the reacting materials at ca. 2 days, the mixture was then subjected to microwave irradiation for ca. 9 hours in a 50mL round-bottom flask under a closed reflux condition. The desired complex was isolated by precipitating the reaction mixture with chilled Et_2O. Further precipitation of the complex was afforded by keeping the mixture cool at 0°C in a fridge. All portions were then reunited and dried *in vacuo*. Purification of the product was afforded by HPLC at a detection wavelength of 241nm, thus: a sample of the product was dissolved in MeCN and eluted through a column initially using 5% MeCN in water (0.1% TFA), which was increased over 20minutes to 95% organic phase at the flow rate of 17ml/min. The desired peak, which was eluted at 6.90minutes as detected by UV-Vis

spectroscopy, was collected and analysed. The yield of the crude product was calculated against $[Ir(bpy)_2(CF_3SO_3)_2]CF_3SO_3$ with the characterisation data given below.

Yield: 0.24 g (88.89 %).

ESI-MS, m/z: 272 [M^{3+}].

^{1}H NMR (400 MHz, *d*^{3}-(MeOD): δ 9.87 (d, *J* = 5.8 Hz, 1H), 9.45 (d, *J* = 4.7 Hz, 1H), 8.73 (d, *J* = 8.5 Hz, 2H), 8.68 – 8.61 (m, 3H), 8.55 (d, *J* = 10.8 Hz, 5H), 8.32 (s, 2H), 8.15 (t, *J* = 7.1 Hz, 1H), 8.09 – 8.03 (m, 2H), 7.96 (d, *J* = 6.6 Hz, 1H), 7.86 (dd, *J* = 23.0, 16.9 Hz, 4H), 7.55 (s, 1H), 7.36 (d, *J* = 5.9 Hz, 1H).

7.20.15 $[Ir(phen)_2Cl_2]PF_6$[29]

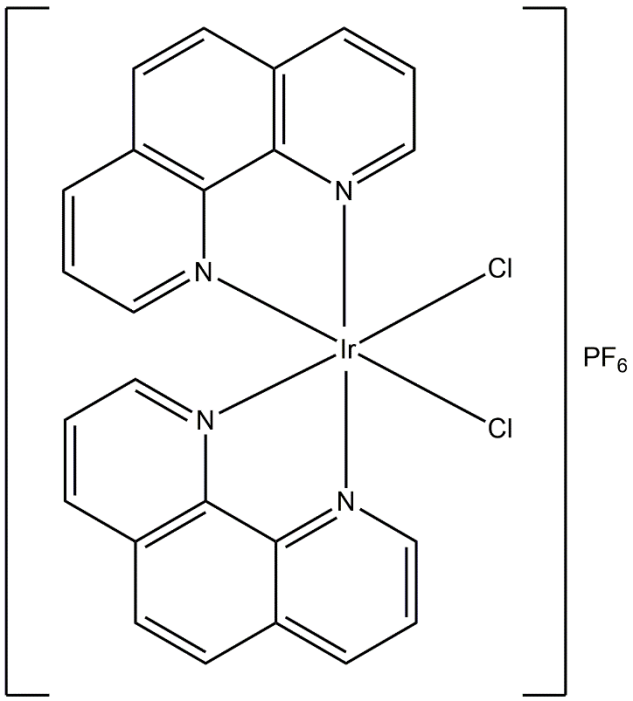

Figure 8.17 – $[Ir(phen)_2Cl_2]PF_6$.

This compound was prepared analogously to $[Ir(bpy)_2Cl_2]PF_6$ using $IrCl_3.3H_2O$/iridium trichloride(III) hydrate (1.50g, 5.00mmol) and phen (1.512g, 8.40mmol) suspended in ethylene glycol (35mL). The yield was calculated against $IrCl_3.xH_2O$ with the characterisation data given below:

Yield: 3.544 g (97.20 %).

ESI-MS, m/z: 623 [$M^+ - PF_6$].

7.20.16 $[Ir(phen)_2Cl_2]Cl$[29]

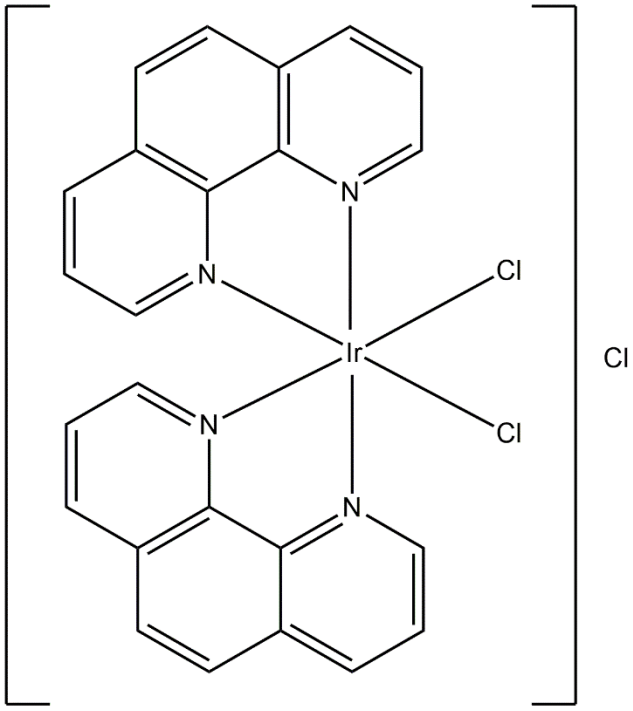

Figure 8.18 – $[Ir(phen)_2Cl_2]Cl$.

This compound was prepared analogously to $[Ir(bpy)_2Cl_2]Cl$ using $[Ir(phen)_2Cl_2]PF_6$ (2.00g, 2.66mmol) dissolved in acetone to which TBAC (0.50g) suspended in acetone (10 mL) was added. The yield was calculated against $[Ir(phen)_2Cl_2]PF_6$ with the characterisation data given below:

Yield: 1.55 g (90.64 %).

ESI-MS, m/z: 623 [$M^+ - 2Cl^-$].

7.20.17 $[Ir(phen)_2Cl_2]CF_3SO_3$[29]

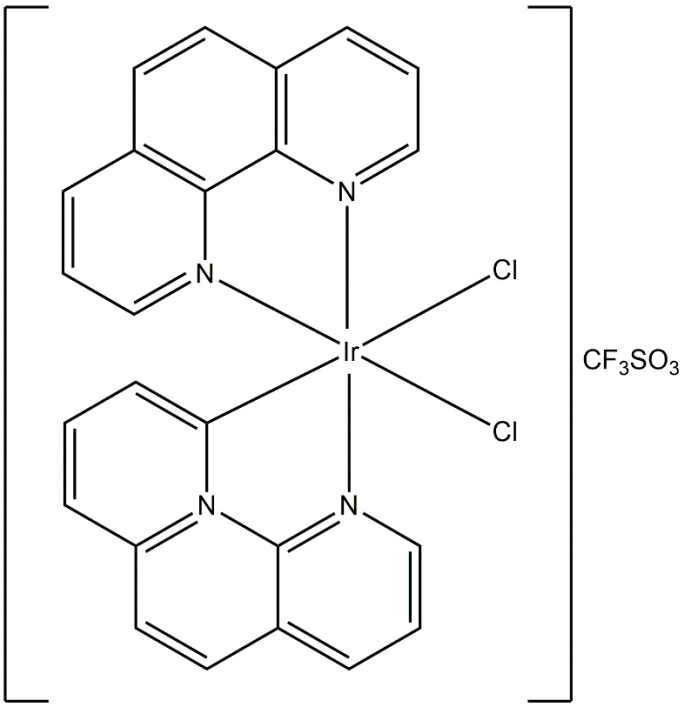

Figure 8.19 – $[Ir(phen)_2Cl_2]CF_3SO_3$.

This compound was prepared analogously to $[Ir(bpy)_2Cl_2]CF_3SO_3$ using $[Ir(phen)_2Cl_2]Cl$ (1.00g, 1.52mmol) stirred in MeCN (200mL) to which TFMS (0.54mL, 6.0mmol) was added. The yield was calculated against $[Ir(phen)_2Cl_2]Cl$ with the characterisation data given below:

Yield: 0.74g (63.25%).

ESI-MS, m/z: 623 $[M^+ – CF_3SO_3]$.

7.20.18 $[Ir(phen)_2(CF_3SO_3)_2]CF_3SO_3$[29]

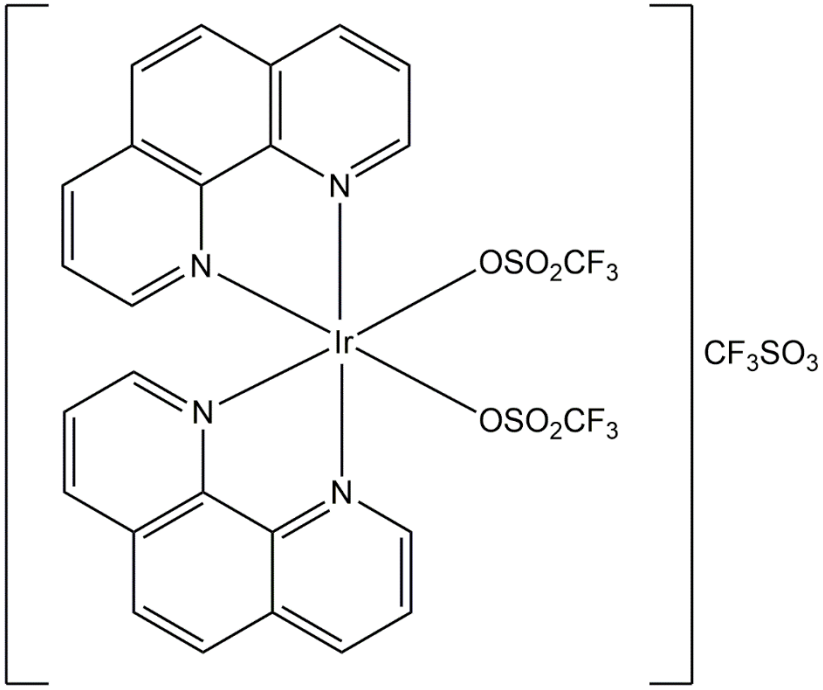

Figure 8.20 – $[Ir(phen)_2(CF_3SO_3)_2]CF_3SO_3$.

This compound was prepared analogously to $[Ir(bpy)_2(CF_3SO_3)_2]CF_3SO_3$ using $[Ir(phen)_2Cl_2]CF_3SO_3$ (0.65g, 0.66mmol) suspended in *o*-dichlorobenzene (10mL) to which TFMS (1.4mL, 15.80mmol) was added. Ice-cold Et_2O (20mL) was then added to precipitate the desired product. The yield was calculated against $[Ir(phen)_2Cl_2]CF_3SO_3$ with the characterisation data given below:

Yield: 0.84 g (99.88%).

ESI-MS, m/z: 851 $[M^+ – CF_3SO_3]$; 351 $[M^{2+} – 2CF_3SO_3]$.

^{1}H NMR (400 MHz, DMSO): δ_H 9.44 (d, *J* = 5.2 Hz, 2H), 9.34 (d, *J* = 8.3 Hz, 2H), 8.82 (d, *J* = 8.1 Hz, 2H), 8.72 (dd, *J* = 8.3, 5.4 Hz, 2H), 8.59 (d, *J* = 8.9 Hz, 2H), 8.43 (d, *J* = 8.9 Hz, 2H), 8.00 (d, *J* = 5.5 Hz, 2H), 7.74 (dd, *J* = 8.2, 5.7 Hz, 2H).

7.20.19 $[Ir(phen)_2(qtpy)](CF_3SO_3)_3$ (New Complex)

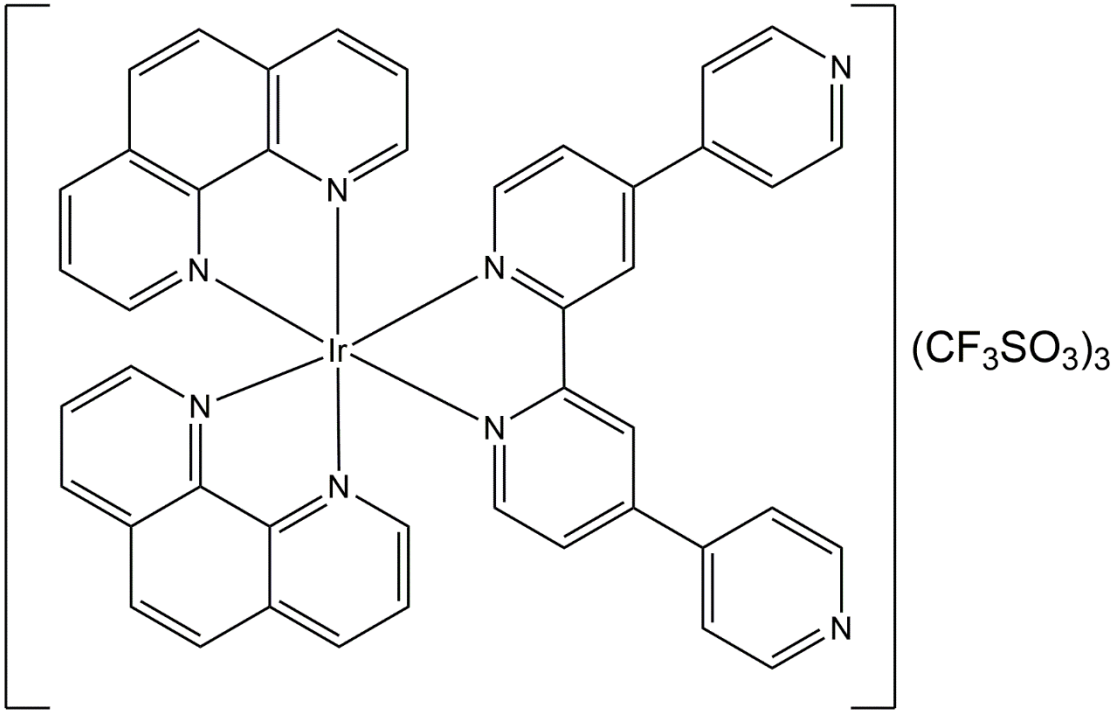

Figure 8.21 – $[Ir(phen)_2(qtpy)](CF_3SO_3)_3$.

The experimental procedure for the synthesis of this complex followed from that of $[Ir(bpy)_2(qtpy)](CF_3SO_3)_3$ thus: $[Ir(phen)_2(CF_3SO_3)_2]CF_3SO_3$ (0.2g, 0.196mmol) and qtpy (0.20g, 0.646mmol) were suspended in EtOH (35mL) in a 50mL round-bottom flask and the mixture was well purged with Ar for ca. 30minutes and allowed to stir and reflux under this condition. The reaction mixture, which was initially a faint yellowish suspension, became increasingly deeply yellow with the passage of time. Complete dissolution of the reacting materials was attained at ca. 1 hour whilst the mixture was allowed to further reflux for ca. 1–2days. The reaction mixture, which was initially a faint yellowish suspension, became increasingly intensely yellow with the passage of time. After the complete dissolution of the reacting materials at ca. 2 days, the mixture was then subjected to microwave irradiation for ca. 9 hours in a 50mL round-bottom flask under a closed reflux condition. The desired complex was isolated by precipitating the reaction mixture with chilled Et_2O. Further precipitation of the complex was afforded by keeping the mixture cool at 0°C in a fridge. All portions were then reunited and dried *in vacuo*. Purification of the product was afforded by HPLC at a detection wavelength of 228nm, thus: a sample of the product was dissolved in MeCN and eluted through a column initially using 5% MeCN in water (0.1% TFA), which was increased

over 20minutes to 95% organic phase at the flow rate of 17ml/min. The desired peak, which was eluted at 8.16minutes as detected by UV-Vis spectroscopy, was collected and analysed. The yield of the crude product was calculated against $[Ir(phen)_2(CF_3SO_3)_2]CF_3SO_3$ with the characterisation data given below:

Yield: 0.17g (50%).

ESI-MS, m/z: 506 [M^{2+}], 287 [M^{3+}].

^{1}H NMR (400 MHz, d^3-(acetone) δ_H: 10.30 (d, 2H), 10.18 (dt, *J* = 11.1, 6.3 Hz, 2H), 10.05 (dd, *J* = 9.8, 5.1 Hz, 2H), 9.74 (d, *J* = 5.4 Hz, 2H), 9.40 – 9.16 (m, 2H), 8.93 (t, *J* = 8.9 Hz, 2H), 8.86 – 8.73 (m, 2H), 8.71 – 8.37 (m, 4H), 8.27 – 8.20 (dd, 4H), 8.16 (d, *J* = 5.4 Hz, 2H), 8.03 (d, *J* = 5.5 Hz, 2H), 7.96 – 7.84 (m, 2H), 7.76 (m, *J* = 25.2, 8.4, 5.5 Hz, 4H).

7.20.20 $[Ir(dppz)_2Cl_2]PF_6$ (New Intermediate Complex)

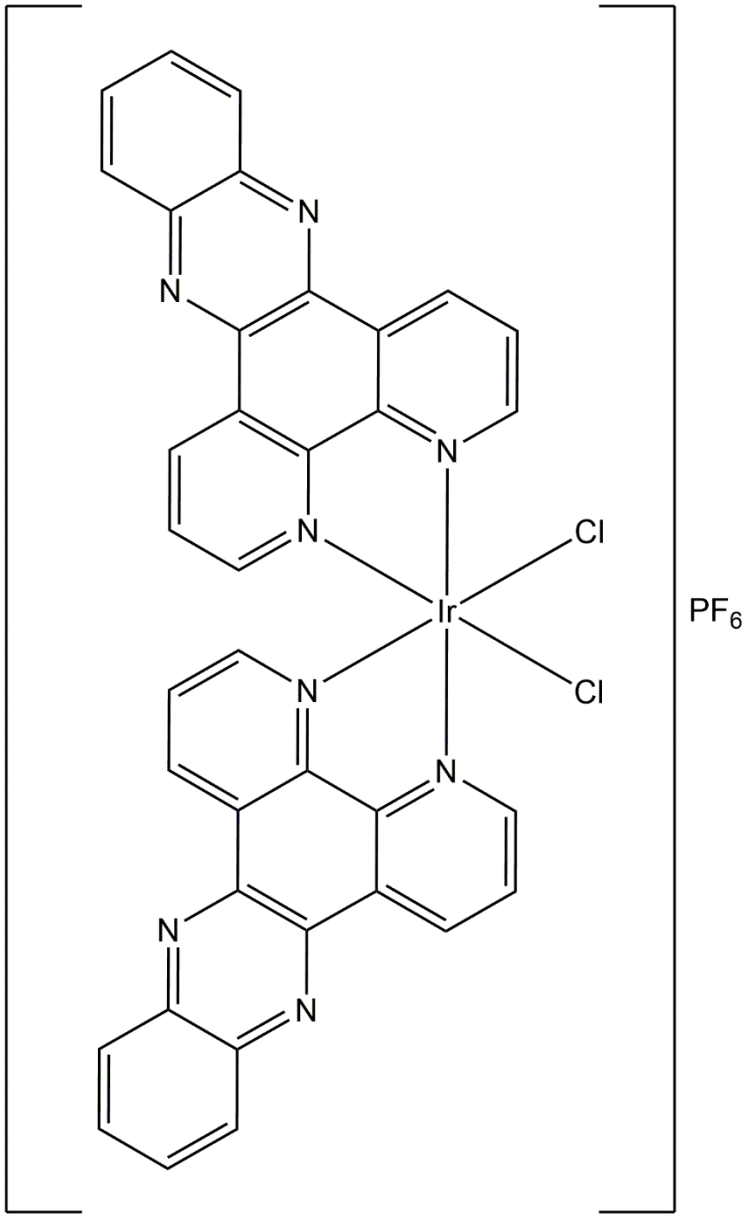

Figure 8.22 – $[Ir(dppz)_2Cl_2]PF_6$.

This compound was prepared analogously to $[Ir(bpy)_2Cl_2]PF_6$ using $IrCl_3.3H_2O$/iridium trichloride(III) hydrate (3.00g, 10.0mmol) and dppz (4.737g, 16.80mmol) suspended in ethylene glycol (35mL) and water (5mL). The yield was calculated against $IrCl_3.xH_2O$ with the characterisation data given below:

Yield: 3.96g (81.15%).

ESI-MS, m/z: 827 $[M^+ – PF_6]$.

^{1}H NMR (400 MHz, d^3-$(CH_3)_2CO$) δ_H: 10.34 (d, *J* = 4.5 Hz, 2H), 10.12 (d, *J* = 8.2 Hz, 2H), 9.71 (d, *J* = 8.2 Hz, 2H), 8.76 (dd, *J* = 8.3, 5.4 Hz, 2H), 8.60 (d, *J* = 8.0 Hz, 2H), 8.56 – 8.44 (m, 4H), 8.31 – 8.16 (m, 4H), 7.97 (dd, *J* = 8.1, 5.5 Hz, 2H).

7.20.21 $[Ir(dppz)_2Cl_2]Cl$ (New Intermediate Complex)

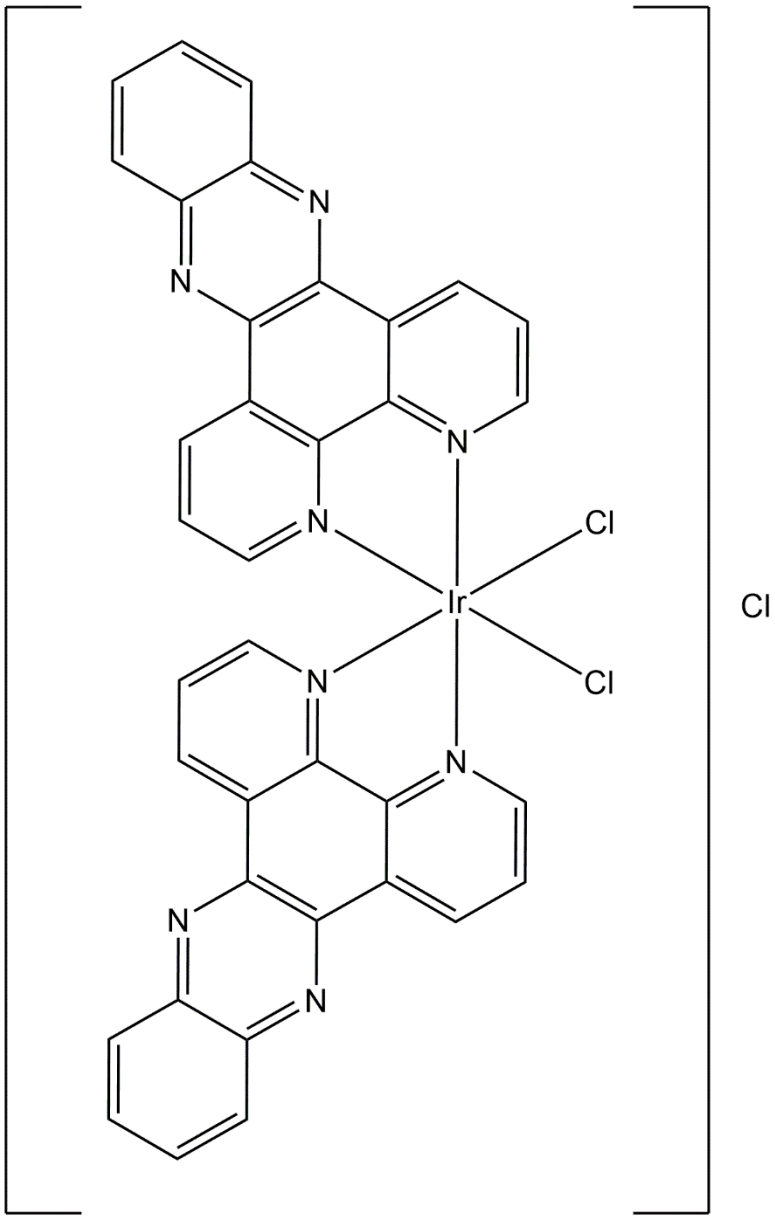

Figure 8.23 – $[Ir(dppz)_2Cl_2]Cl$.

This compound was prepared analogously to $[Ir(bpy)_2Cl_2]Cl$ using $[Ir(dppz)_2Cl_2]PF_6$ (2.50g, 3.475mmol) dissolved in acetone to which TBAC (0.80g) suspended in acetone (10mL) was

added. The yield was calculated against $[Ir(dppz)_2Cl_2]PF_6$ with the characterisation data given below:

Yield: 2.32 g (92.80 %).

ESI-MS, m/z: 827 $[M^+ - Cl]$.

7.20.22 $[Ir(dppz)_2Cl_2]CF_3SO_3$ (New Intermediate Complex)

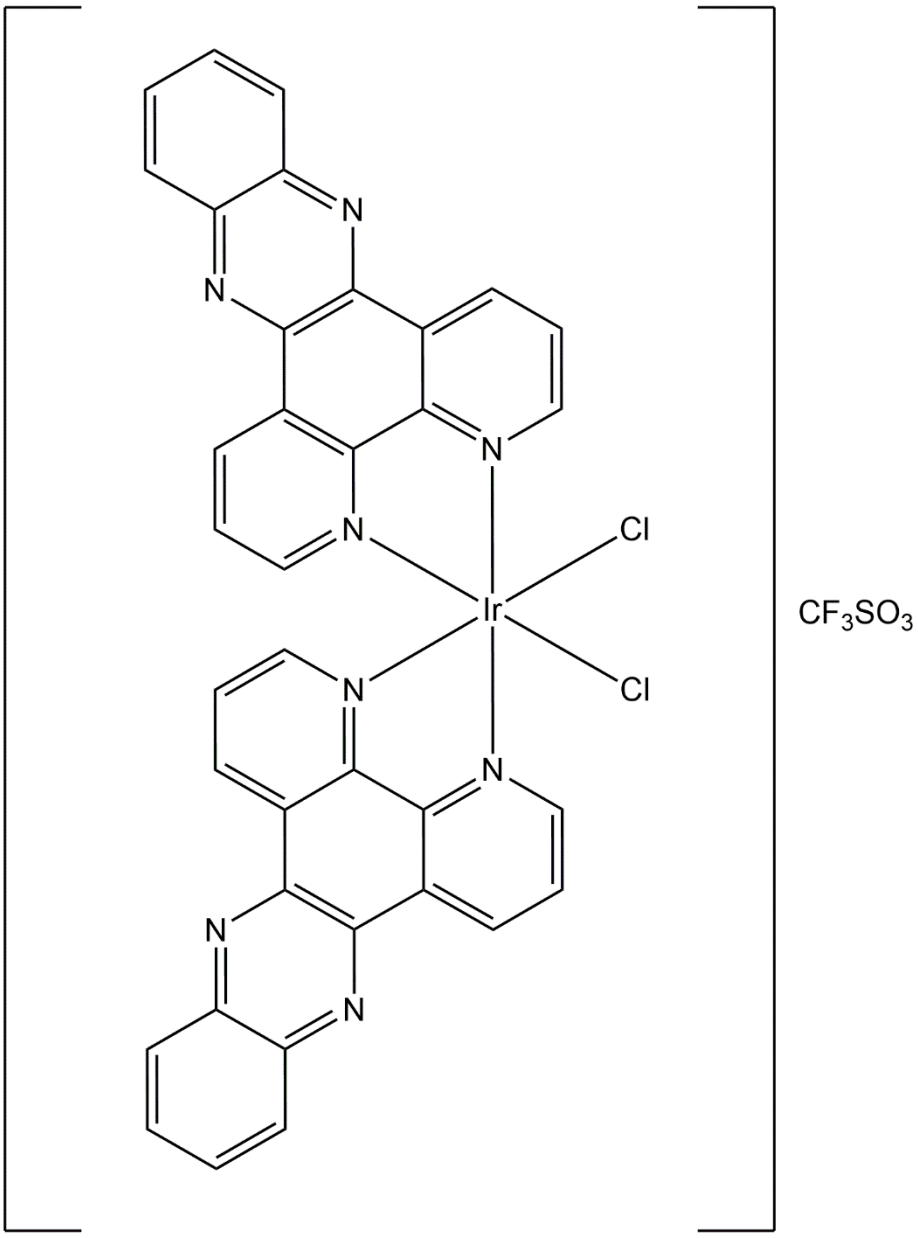

Figure 8.24 – $[Ir(dppz)_2Cl_2]CF_3SO_3$.

This compound was prepared analogously to $[Ir(bpy)_2Cl_2]CF_3SO_3$ using $[Ir(dppz)_2Cl_2]Cl$ (0.685g, 0.795mmol) suspended in MeCN (100 mL) to which TFMS (0.35 mL, 3.95mmol) was added. The compound, which is a brownish-black micro-powder, was isolated by concentrating the reaction product on a rotavap, precipitating with chilled Et_2O, filtering, washing with a copious amount of Et_2O and drying *in vacuo*. More precipitates were obtained by a repetition of this procedure, whereupon the desired complex was afforded by combining all the separate portions together. The yield was calculated against $[Ir(dppz)_2Cl_2]Cl$ with the characterisation data given below:

Yield: 0.71g (91.03%).

ESI-MS, m/z: 827 $[M^+ - CF_3SO_3]$.

^{1}H NMR (400 MHz, d^3-$(CH_3)_2CO$) δ_H: 10.34 (dd, *J* = 5.5, 1.2 Hz, 2H), 10.13 (dd, *J* = 8.3, 1.2 Hz, 2H), 9.77 – 9.68 (dd, 2H), 8.75 (dd, *J* = 8.3, 5.5 Hz, 2H), 8.63 – 8.60 (m, 2H), 8.56 – 8.50 (m, 4H), 8.31 – 8.19 (m, 4H), 7.97 (dd, *J* = 8.2, 5.6 Hz, 2H).

7.20.23 $[Ir(dppz)_2(CF_3SO_3)_2]CF_3SO_3$ (New Intermediate Complex)

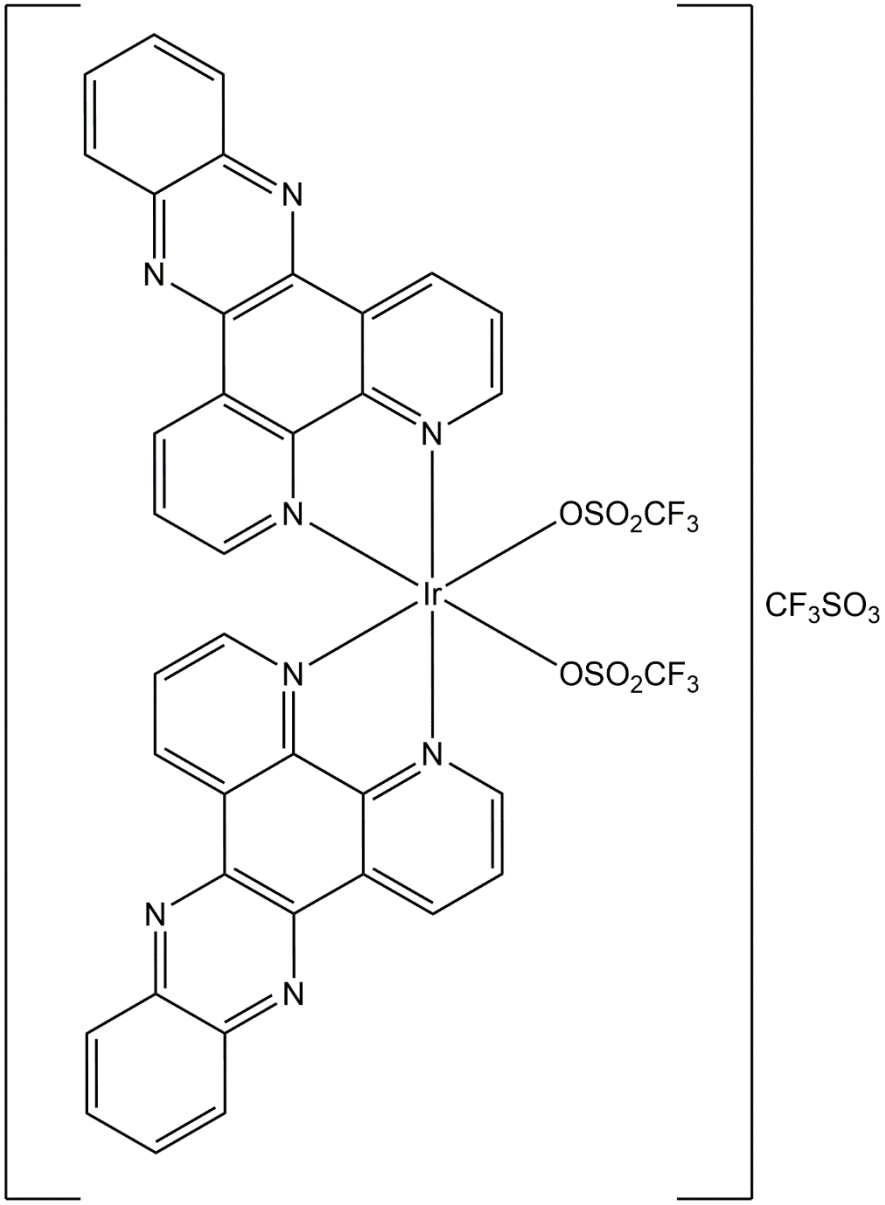

Figure 8.25 – $[Ir(dppz)_2(CF_3SO_3)_2]CF_3SO_3$.

This compound was prepared analogously to $[Ir(bpy)_2(CF_3SO_3)_2]CF_3SO_3$ using $[Ir(dppz)_2Cl_2]CF_3SO_3$ (0.213g, 0.22mmol) suspended in *o*-dichlorobenzene (10mL) to which TFMS (0.47mL, 5.26mmol) was added. The yield was calculated against $[Ir(dppz)_2Cl_2]CF_3SO_3$ with the characterisation data given below:

Yield: 0.17g (65.38%).

ESI-MS, m/z: 1055 $[M^+ – CF_3SO_3]$, 453 $[M^{2+} – 2CF_3SO_3]$.

^{1}H NMR (400 MHz, d^3-$(CH_3)_2CO$) δ_H: 10.30 (d, *J* = 8.3 Hz, 2H), 9.87 (d, *J* = 5.5 Hz, 2H), 9.78 (d, *J* = 8.1 Hz, 2H), 9.00 (m, 2H), 8.64 (d, *J* = 8.2 Hz, 2H), 8.56 – 8.49 (m, 2H), 8.29 (m, 2H), 8.00 (dd, *J* = 24.0, 18.2 Hz, 2H), 7.60 (dd, *J* = 6.0, 3.6 Hz, 2H), 7.47 – 7.30 (m, 2H).

7.20.24 $[Ir(dppz)_2(qtpy)](CF_3SO_3)_3$ (New Complex)

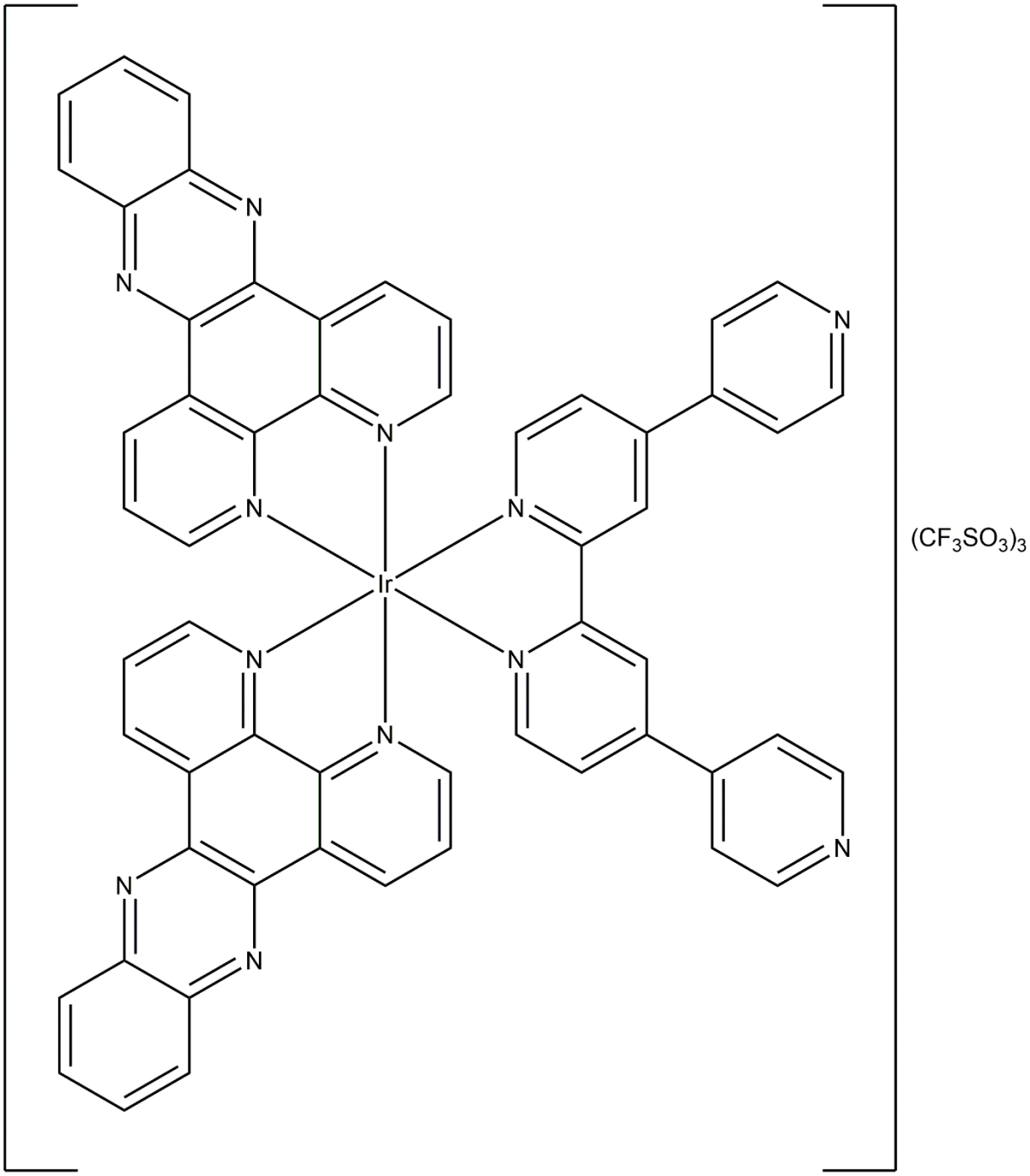

Figure 8.26 – $[Ir(dppz)_2(qtpy)](CF_3SO_3)_3$.

The experimental procedure for the synthesis of this complex followed from that of $[Ir(bpy)_2(qtpy)](CF_3SO_3)_3$ thus: $[Ir(dppz)_2(CF_3SO_3)_2]CF_3SO_3$ (0.150g, 0.125mmol) and qtpy (0.116 g, 0.374 mmol) were suspended in ethanol (25mL) in a 50 mL round-bottom flask and the mixture was well purged with Ar for ca. 30 minutes and allowed to stir and reflux under this condition. The reaction mixture, which was initially a faint yellowish suspension, became increasingly deeply yellow with time. After the complete dissolution of the reacting materials at ca. 2 days, the mixture was then subjected to microwave irradiation for ca. 9 hours in a 50mL round-bottom flask under a closed reflux condition. The desired complex was isolated by precipitating the reaction mixture with chilled Et_2O. Further precipitation of the complex was afforded by keeping the mixture cool at 0°C in a fridge. All portions were then reunited and dried *in vacuo*. Purification of the product was afforded by HPLC at a detection wavelength of 282nm, thus: a sample of the product was dissolved in MeCN and eluted through a column initially using 5% MeCN in water (0.1% TFA), which was increased over 20minutes to 95% organic phase at the flow rate of 17ml/min. The desired peak, which was eluted at 12.35minutes as detected by UV-Vis spectroscopy, was collected and analysed. The yield of the crude product was calculated against $[Ir(dppz)_2(CF_3SO_3)_2]CF_3SO_3$ with the characterisation data given below:

Yield: 14.50mg (7.63%).

ESI-MS, m/z: 356 $[M^{3+} - 3CF_3SO_3]$.

^{1}H NMR (400 MHz, *d*^{3}-(MeOD) δ_H: 10.37 (d, *J* = 5.4 Hz, 2H), 10.22 (dd, *J* = 13.0, 8.0 Hz, 2H), 9.85 (d, *J* = 8.0 Hz, 2H), 9.78 (d, *J* = 8.1 Hz, 2H), 9.70 (d, *J* = 5.2 Hz, 2H), 8.81 (m, 4H), 8.74 – 8.61 (m, 4H), 8.59 – 8.52 (m, 2H), 8.34 (d, *J* = 5.3 Hz, 2H), 8.29 – 8.17 (m, 4H), 7.89 (m, 2H), 7.77 (m, 4H).

7.21 References

1. Bruker (2016), SADABS. Bruker Axs Inc., Madison, Wisconsin, USA.

2. L. Krause, R. Herbst-Irmer, G. M. Sheldrick, and D. Stalke, Comparison of silver and molybdenum microfocus X-ray sources for single-crystal structure Determination, *J. Appl. Cryst.*, 2015, 48, 3–10.

3. G. M. Sheldrick, SHELXT - Integrated space-group and crystal-structure determination, *Acta Cryst.*, 2015, A71, 3-8.

4. G. M. Sheldrick, Crystal structure refinement with SHELXL, *Acta Cryst.*, 2015, C71, 3-8.

5. O. V. Dolomanov, L. J. Bourhis, R. J. Glides, J. A. K. Howard, and H. Puschmann, OLEX2: a complete structure solution, refinement and analysis program, *J. Appl. Cryst.*, 42, 339–341.

6. https://hdl.handle.net/2134/21243.

7. P. D. Boyle, Growing Crystals That Will Make Your Crystallographer Happy.

8. H. Hope, Apparatus for growth of crystals for X-ray diffraction study, Apparatus for growth of crystals for X-ray diffraction study, *J. Appl. Cryst.*, 1971, 4(4), 333–333.

9. J. B. Chaires, N. Dattagupta and D. M. Crothers, Studies on Interaction of Anthracycline Antibiotics and Deoxyribonucleic Acid: Equilibrium Binding Studies on Interaction of Daunomycin with Deoxyribonucleic Acid, *Biochemistry*, 1982, 21, 3933–3940.

10. N. M. Shavaleev, H. Adams, J. Best, R. Edge, S. Navaratnam and J. A. Weinstein, Deep-red luminescence and efficient singlet oxygen generation by cyclometalated platinum(II) complexes with 8-hydroxyquinolines and quinoline-8-thiol, *Inorg. Chem.*, 2006, 45, 9410–9415.

11. M. J. Frisch, G. W. Trucks, H. B. Schlegel, G. E. Scuseria, M. A. Robb, J. R. Cheeseman, G. Scalmani, V. Barone, G. A. Petersson, and H. Nakatsuji, Gaussian 09: 512, 2019.

12. Y. Yang, M. N. Weaver, K. M. Merz, Assessment of the "6-31+Gt; + LANL2DZ" Mixed Basis Set Coupled with Density Functional Theory Methods and the Effective Core Potential: Prediction of Heats of Formation and Ionization Potentials for First-Row-Transition-Metal Complexes, *J. Phys. Chem. A*, 2009, 113 (36), 9843–9851.

13. M. X. Song, G. Q. Xi, H. Y. Chi, K. C. He, L. U. Peng, Z. K. Qin, Y. L. Zhang, L. U. Shi-Quan, H. J. A. Zhang, Theoretical Study: Green Phosphorescent Iridium(III) Complexes with Low-Efficiency Roll-Off, *Appl. Organomet. Chem.*, 2020, 34(5), 1–9.

14. B. Liu, S. Monro, Z. Li, M. A. Jabed, D. Ramirez, C. G. Cameron, K. Colón, J. Roque, S. Kilina, J. Tian, New Class of Homoleptic and Heteroleptic Bis(Terpyridine) Iridium(III) Complexes with Strong Photodynamic Therapy Effects, *ACS Appl. Bio Mater.*, 2019, 2 (7), 2964–2977.

15. S. S. Bhat, N. Shivalingegowda, V. K. Revankar, N. K. Lokanath, M. S. Kugaji, V. Kumbar, K. Bhat, Synthesis, Structural Characterization and Biological Properties of Phosphorescent Iridium(III) Complexes, *New J. Chem.*, 2020, 177, 127–137.

16. M. E. Casida, C. Jamorski, K. C. Casida, D. R. Salahub, Molecular Excitation Energies to High-Lying Bound States from Time-Dependent Density-Functional Response Theory: Characterization and Correction of the Time-Dependent Local Density Approximation Ionization Threshold, *J. Chem. Phys.*, 1998, 108 (11), 4439–4449.

17. G. M. Morris, H. Ruth, W. Lindstrom, M. F. Sanner, R. K. Belew, D. S. Goodsell, A. J. Olson, AutoDock4 and AutoDockTools4: Automated Docking with Selective Receptor Flexibility, *J. Comput. Chem.*, 2009, 30(16), 2785–2791.

18. S. K. Burley, H. M. Berman, C. Christie, J. M. Duarte, Z. Feng, J. Westbrook, J. Young, C. Zardecki, RCSB Protein Data Bank: Sustaining a Living Digital Data Resource That Enables Breakthroughs in Scientific Research and Biomedical Education, *Protein Sci.*, 2018, 27 (1), 316–330.

19. M. S. Searle, A. J. Maynard, H. E. L. Williams, DNA Recognition by the Anthracycline Antibiotic Respinomycin D: NMR Structure of the Intercalation Complex with $d(AGACGTCT)_2$, *Org. Biomol. Chem.*, 2003, 1(1), 60–66.

20. D. S. BIOvlA, Discovery Studio Modeling Environment. Dassault Systèmes, San Diego 2015.

21. G. M. Morris, D. S. Goodsell, R. S. Halliday, R. Huey, W. E. Hart, R. K. Belew, A. J. Olson, Automated Docking Using a Lamarckian Genetic Algorithm and an Empirical Binding Free Energy Function, *J. Comput. Chem.*, 1998, 19(14), 1639–1662.

22. M. Groessl, M. Terenghi, A. Casini, L. Elviri, R. Lobinskic, and P. J. Dyson, Reactivity of anticancer metallodrugs with serum proteins: new insights from size exclusion chromatography-ICP-MS and ESI-MS, *J. Anal. At. Spectrom.*, 2010, 25, 305–313.

23. Johnson and M. Spence (eds.), Molecular Probes Handbook: A Guide to Fluorescent Probes and Labeling Technologies, 11^{th} Edition, Life Technologies Corporation, 2010, 1060.

24. M. Boncler, M. Różalski, U. Krajewska, A. Podsędek, C. Watala, Comparison of PrestoBlue and MTT assays of cellular viability in the assessment of anti-proliferative

effects of plant extracts on human endothelial cells, *J. Pharma. and Toxicol. Methods*, 2014, 69, 9–16.

25. R. J. Morgan, A. D. Baker, 2,2':4,4":4',4"'-Quaterpyridyl: A Building Block for the Preparation of Novel Redox Reagents. 1. Preparation and Quaternization, *J. Org. Chem.*, 55(7), 1990, 55(7), 1987–1993.

26. J.E. Dickeson and L.A. Summers, Derivatives of 1, 10-Phenanthroline-5, 6-quinone, *Austr. J. Chem.*, 1970, 23, 1023–1027.

27. B. P. Sullivan, D. J. Salmon, and T. J Meyer, Mixed Phosphine 2,2'-Bipyridine Complexes of Ruthenium, *Inorg. Chem.*, 1978, 17, 3334–3341.

28. M. A. Hayes, C. A. Meckal, E. Schatz, M. D. Ward, Derivatives of tris(2,2′-bipyridine)ruthenium(II) with pendant pyridyl or phenol ligands, *Journal of the Chemical Society, Dalton Transactions*, 1992, 703–708.

29. Biophysical studies on a novel family of iridium polypyridyl complexes, S.M. Stimpson, PhD Thesis, University of Sheffield, 2018.

9.0 Appendix

This chapter includes additional information and/or explanation on the synthesis, characterisation, or analysis of the precursors and/or title complexes produced in this thesis. Including these data is intended to assist with future continuations or replications of this work.

9.1 Computational Data

9.1.1 DFT Studies on Title Complexes

Table 9.1 – DFT-derived UV-Visible Spectra Data of Title Complexes.

$[Ir(bpy)_2(qtpy)]^{3+}$		$[Ir(phen)_2(qtpy)]^{3+}$		$[Ir(dppz)_2(qtpy)]^{3+}$	
X	**Y**	**X**	**Y**	**X**	**Y**
Wavenumber (nm)	**Absorbance**	**Wavenumber (nm)**	**Absorbance**	**Wavenumber (nm)**	**Absorbance**
230.0	18852.360	230.0	8070.492	230.0	81.398
230.5	19767.758	230.5	8744.849	230.5	94.300
231.1	20695.217	231.1	9461.581	231.1	108.968
231.6	21633.239	231.6	10222.127	231.6	125.603
232.2	22580.327	232.2	11027.875	232.2	144.419
232.7	23535.006	232.7	11880.148	232.7	165.650
233.2	24495.827	233.2	12780.192	233.2	189.544
233.8	25461.382	233.8	13729.167	233.8	216.372
234.3	26430.313	234.3	14728.134	234.3	246.419
234.9	27401.324	234.9	15778.045	234.9	279.993
235.4	28373.188	235.4	16879.731	235.4	317.419
235.9	29344.756	235.9	18033.891	235.9	359.042
236.5	30314.963	236.5	19241.080	236.5	405.228
237.0	31282.834	237.0	20501.700	237.0	456.362
237.6	32247.488	237.6	21815.989	237.6	512.847
238.1	33208.139	238.1	23184.012	238.1	575.109
238.6	34164.104	238.6	24605.650	238.6	643.590
239.2	35114.793	239.2	26080.594	239.2	718.752

239.7	36059.718	239.7	27608.336	239.7	801.074
240.3	36998.485	240.3	29188.163	240.3	891.054
240.8	37930.792	240.8	30819.153	240.8	989.206
241.3	38856.423	241.3	32500.168	241.3	1096.060
241.9	39775.246	241.9	34229.852	241.9	1212.158
242.4	40687.201	242.4	36006.630	242.4	1338.059
243.0	41592.298	243.0	37828.707	243.0	1474.334
243.5	42490.605	243.5	39694.067	243.5	1621.562
244.0	43382.240	244.0	41600.478	244.0	1780.335
244.6	44267.364	244.6	43545.494	244.6	1951.252
245.1	45146.168	245.1	45526.458	245.1	2134.919
245.7	46018.865	245.7	47540.512	245.7	2331.947
246.2	46885.682	246.2	49584.605	246.2	2542.950
246.7	47746.847	246.7	51655.496	246.7	2768.548
247.3	48602.580	247.3	53749.773	247.3	3009.357
247.8	49453.089	247.8	55863.856	247.8	3265.996
248.4	50298.553	248.4	57994.016	248.4	3539.080
248.9	51139.122	248.9	60136.387	248.9	3829.222
249.4	51974.904	249.4	62286.981	249.4	4137.028
250.0	52805.961	250.0	64441.702	250.0	4463.102
250.5	53632.302	250.5	66596.365	250.5	4808.036
251.1	54453.880	251.1	68746.713	251.1	5172.418
251.6	55270.585	251.6	70888.433	251.6	5556.824
252.1	56082.245	252.1	73017.176	252.1	5961.822
252.7	56888.621	252.7	75128.576	252.7	6387.967
253.2	57689.404	253.2	77218.267	253.2	6835.806
253.8	58484.221	253.8	79281.902	253.8	7305.870
254.3	59272.629	254.3	81315.176	254.3	7798.681
254.8	60054.124	254.8	83313.838	254.8	8314.746
255.4	60828.137	255.4	85273.714	255.4	8854.562
255.9	61594.039	255.9	87190.723	255.9	9418.610
256.5	62351.150	256.5	89060.896	256.5	10007.359
257.0	63098.737	257.0	90880.391	257.0	10621.266
257.5	63836.025	257.5	92645.507	257.5	11260.773
258.1	64562.199	258.1	94352.707	258.1	11926.312
258.6	65276.414	258.6	95998.621	258.6	12618.298

259.2	65977.799	259.2	97580.068	259.2	13337.138
259.7	66665.467	259.7	99094.063	259.7	14083.223
260.2	67338.518	260.2	100537.833	260.2	14856.933
260.8	67996.051	260.8	101908.820	260.8	15658.636
261.3	68637.169	261.3	103204.693	261.3	16488.685
261.9	69260.987	261.9	104423.358	261.9	17347.422
262.4	69866.639	262.4	105562.958	262.4	18235.177
262.9	70453.284	262.9	106621.882	262.9	19152.266
263.5	71020.117	263.5	107598.768	263.5	20098.989
264.0	71566.367	264.0	108492.503	264.0	21075.634
264.6	72091.313	264.6	109302.225	264.6	22082.473
265.1	72594.281	265.1	110027.323	265.1	23119.762
265.6	73074.654	265.6	110667.435	265.6	24187.738
266.2	73531.875	266.2	111222.444	266.2	25286.621
266.7	73965.449	266.7	111692.479	266.7	26416.610
267.3	74374.948	267.3	112077.902	267.3	27577.882
267.8	74760.017	267.8	112379.308	267.8	28770.589
268.3	75120.367	268.3	112597.519	268.3	29994.859
268.9	75455.787	268.9	112733.569	268.9	31250.788
269.4	75766.136	269.4	112788.705	269.4	32538.447
270.0	76051.349	270.0	112764.369	270.0	33857.868
270.5	76311.434	270.5	112662.195	270.5	35209.050
271.0	76546.471	271.0	112483.993	271.0	36591.953
271.6	76756.612	271.6	112231.740	271.6	38006.495
272.1	76942.078	272.1	111907.572	272.1	39452.549
272.7	77103.156	272.7	111513.764	272.7	40929.941
273.2	77240.198	273.2	111052.727	273.2	42438.447
273.7	77353.616	273.7	110526.989	273.7	43977.787
274.3	77443.879	274.3	109939.185	274.3	45547.626
274.8	77511.509	274.8	109292.045	274.8	47147.570
275.4	77557.077	275.4	108588.380	275.4	48777.161
275.9	77581.200	275.9	107831.070	275.9	50435.876
276.4	77584.533	276.4	107023.053	276.4	52123.125
277.0	77567.768	277.0	106167.310	277.0	53838.248
277.5	77531.627	277.5	105266.855	277.5	55580.511
278.1	77476.858	278.1	104324.724	278.1	57349.108

278.6	77404.229	278.6	103343.962	278.6	59143.155
279.1	77314.527	279.1	102327.611	279.1	60961.691
279.7	77208.547	279.7	101278.705	279.7	62803.676
280.2	77087.095	280.2	100200.252	280.2	64667.992
280.8	76950.975	280.8	99095.231	280.8	66553.439
281.3	76800.993	281.3	97966.578	281.3	68458.739
281.8	76637.946	281.8	96817.182	281.8	70382.533
282.4	76462.624	282.4	95649.872	282.4	72323.382
282.9	76275.801	282.9	94467.415	282.9	74279.772
283.5	76078.236	283.5	93272.505	283.5	76250.108
284.0	75870.664	284.0	92067.756	284.0	78232.723
284.5	75653.802	284.5	90855.700	284.5	80225.877
285.1	75428.336	285.1	89638.781	285.1	82227.759
285.6	75194.926	285.6	88419.346	285.6	84236.490
286.2	74954.203	286.2	87199.647	286.2	86250.131
286.7	74706.762	286.7	85981.833	286.7	88266.679
287.2	74453.167	287.2	84767.952	287.2	90284.076
287.8	74193.945	287.8	83559.940	287.8	92300.213
288.3	73929.589	288.3	82359.630	288.3	94312.935
288.9	73660.552	288.9	81168.743	288.9	96320.042
289.4	73387.252	289.4	79988.888	289.4	98319.302
289.9	73110.069	289.9	78821.567	289.9	100308.448
290.5	72829.343	290.5	77668.167	290.5	102285.189
291.0	72545.381	291.0	76529.967	291.0	104247.215
291.6	72258.447	291.6	75408.135	291.6	106192.203
292.1	71968.775	292.1	74303.734	292.1	108117.822
292.6	71676.558	292.6	73217.717	292.6	110021.742
293.2	71381.957	293.2	72150.934	293.2	111901.635
293.7	71085.099	293.7	71104.132	293.7	113755.190
294.3	70786.079	294.3	70077.960	294.3	115580.111
294.8	70484.960	294.8	69072.967	294.8	117374.128
295.3	70181.777	295.3	68089.610	295.3	119135.003
295.9	69876.537	295.9	67128.257	295.9	120860.535
296.4	69569.220	296.4	66189.185	296.4	122548.566
297.0	69259.783	297.0	65272.590	297.0	124196.989
297.5	68948.159	297.5	64378.588	297.5	125803.753

298.0	68634.261	298.0	63507.216	298.0	127366.866
298.6	68317.982	298.6	62658.443	298.6	128884.405
299.1	67999.202	299.1	61832.167	299.1	130354.517
299.7	67677.780	299.7	61028.222	299.7	131775.428
300.2	67353.566	300.2	60246.381	300.2	133145.443
300.7	67026.397	300.7	59486.363	300.7	134462.954
301.3	66696.102	301.3	58747.834	301.3	135726.442
301.8	66362.500	301.8	58030.411	301.8	136934.482
302.4	66025.405	302.4	57333.668	302.4	138085.745
302.9	65684.628	302.9	56657.137	302.9	139179.002
303.4	65339.974	303.4	56000.315	303.4	140213.126
304.0	64991.252	304.0	55362.668	304.0	141187.094
304.5	64638.266	304.5	54743.629	304.5	142099.991
305.1	64280.827	305.1	54142.610	305.1	142951.007
305.6	63918.746	305.6	53558.998	305.6	143739.443
306.1	63551.839	306.1	52992.163	306.1	144464.708
306.7	63179.929	306.7	52441.461	306.7	145126.323
307.2	62802.845	307.2	51906.232	307.2	145723.916
307.8	62420.426	307.8	51385.812	307.8	146257.227
308.3	62032.518	308.3	50879.527	308.3	146726.105
308.8	61638.977	308.8	50386.701	308.8	147130.504
309.4	61239.671	309.4	49906.657	309.4	147470.488
309.9	60834.479	309.9	49438.718	309.9	147746.223
310.5	60423.292	310.5	48982.212	310.5	147957.979
311.0	60006.013	311.0	48536.474	311.0	148106.127
311.5	59582.561	311.5	48100.845	311.5	148191.134
312.1	59152.865	312.1	47674.676	312.1	148213.566
312.6	58716.871	312.6	47257.330	312.6	148174.076
313.2	58274.537	313.2	46848.182	313.2	148073.412
313.7	57825.837	313.7	46446.622	313.7	147912.402
314.2	57370.758	314.2	46052.056	314.2	147691.959
314.8	56909.304	314.8	45663.905	314.8	147413.074
315.3	56441.492	315.3	45281.611	315.3	147076.812
315.9	55967.353	315.9	44904.631	315.9	146684.308
316.4	55486.934	316.4	44532.443	316.4	146236.764
316.9	55000.295	316.9	44164.547	316.9	145735.442

317.5	54507.512	317.5	43800.462	317.5	145181.663
318.0	54008.671	318.0	43439.726	318.0	144576.802
318.6	53503.876	318.6	43081.903	318.6	143922.282
319.1	52993.241	319.1	42726.576	319.1	143219.571
319.6	52476.895	319.6	42373.349	319.6	142470.175
320.2	51954.976	320.2	42021.851	320.2	141675.639
320.7	51427.639	320.7	41671.731	320.7	140837.538
321.3	50895.044	321.3	41322.660	321.3	139957.474
321.8	50357.368	321.8	40974.331	321.8	139037.072
322.3	49814.795	322.3	40626.458	322.3	138077.976
322.9	49267.519	322.9	40278.778	322.9	137081.845
323.4	48715.743	323.4	39931.047	323.4	136050.347
324.0	48159.681	324.0	39583.043	324.0	134985.159
324.5	47599.553	324.5	39234.563	324.5	133887.959
325.0	47035.587	325.0	38885.424	325.0	132760.427
325.6	46468.017	325.6	38535.463	325.6	131604.237
326.1	45897.086	326.1	38184.534	326.1	130421.056
326.7	45323.039	326.7	37832.512	326.7	129212.540
327.2	44746.129	327.2	37479.285	327.2	127980.332
327.7	44166.612	327.7	37124.763	327.7	126726.057
328.3	43584.749	328.3	36768.868	328.3	125451.322
328.8	43000.803	328.8	36411.540	328.8	124157.712
329.4	42415.040	329.4	36052.734	329.4	122846.785
329.9	41827.729	329.9	35692.417	329.9	121520.075
330.4	41239.141	330.4	35330.572	330.4	120179.086
331.0	40649.544	331.0	34967.194	331.0	118825.291
331.5	40059.212	331.5	34602.291	331.5	117460.129
332.1	39468.416	332.1	34235.882	332.1	116085.009
332.6	38877.426	332.6	33867.997	332.6	114701.298
333.1	38286.512	333.1	33498.676	333.1	113310.331
333.7	37695.942	333.7	33127.969	333.7	111913.401
334.2	37105.982	334.2	32755.935	334.2	110511.765
334.8	36516.896	334.8	32382.642	334.8	109106.637
335.3	35928.945	335.3	32008.165	335.3	107699.191
335.8	35342.387	335.8	31632.586	335.8	106290.560
336.4	34757.474	336.4	31255.993	336.4	104881.834

336.9	34174.458	336.9	30878.483	336.9	103474.062
337.5	33593.583	337.5	30500.154	337.5	102068.248
338.0	33015.090	338.0	30121.112	338.0	100665.356
338.5	32439.214	338.5	29741.467	338.5	99266.306
339.1	31866.187	339.1	29361.332	339.1	97871.976
339.6	31296.233	339.6	28980.824	339.6	96483.201
340.2	30729.571	340.2	28600.062	340.2	95100.774
340.7	30166.414	340.7	28219.169	340.7	93725.448
341.2	29606.969	341.2	27838.268	341.2	92357.934
341.8	29051.436	341.8	27457.485	341.8	90998.901
342.3	28500.009	342.3	27076.946	342.3	89648.980
342.9	27952.875	342.9	26696.781	342.9	88308.764
343.4	27410.215	343.4	26317.116	343.4	86978.804
343.9	26872.201	343.9	25938.079	343.9	85659.618
344.5	26339.000	344.5	25559.800	344.5	84351.682
345.0	25810.770	345.0	25182.405	345.0	83055.442
345.6	25287.664	345.6	24806.021	345.6	81771.305
346.1	24769.827	346.1	24430.773	346.1	80499.647
346.6	24257.395	346.6	24056.787	346.6	79240.810
347.2	23750.498	347.2	23684.184	347.2	77995.103
347.7	23249.260	347.7	23313.087	347.7	76762.808
348.3	22753.796	348.3	22943.613	348.3	75544.174
348.8	22264.214	348.8	22575.880	348.8	74339.423
349.3	21780.616	349.3	22210.003	349.3	73148.751
349.9	21303.095	349.9	21846.093	349.9	71972.325
350.4	20831.739	350.4	21484.260	350.4	70810.290
351.0	20366.627	351.0	21124.610	351.0	69662.766
351.5	19907.832	351.5	20767.248	351.5	68529.848
352.0	19455.420	352.0	20412.274	352.0	67411.612
352.6	19009.452	352.6	20059.787	352.6	66308.112
353.1	18569.980	353.1	19709.880	353.1	65219.384
353.7	18137.050	353.7	19362.644	353.7	64145.444
354.2	17710.703	354.2	19018.169	354.2	63086.290
354.7	17290.972	354.7	18676.539	354.7	62041.906
355.3	16877.885	355.3	18337.834	355.3	61012.258
355.8	16471.464	355.8	18002.133	355.8	59997.298

356.4	16071.726	356.4	17669.511	356.4	58996.967
356.9	15678.681	356.9	17340.037	356.9	58011.190
357.4	15292.333	357.4	17013.781	357.4	57039.881
358.0	14912.682	358.0	16690.805	358.0	56082.946
358.5	14539.724	358.5	16371.170	358.5	55140.278
359.1	14173.448	359.1	16054.934	359.1	54211.762
359.6	13813.838	359.6	15742.150	359.6	53297.274
360.1	13460.875	360.1	15432.867	360.1	52396.683
360.7	13114.534	360.7	15127.134	360.7	51509.851
361.2	12774.788	361.2	14824.994	361.2	50636.633
361.8	12441.602	361.8	14526.486	361.8	49776.880
362.3	12114.942	362.3	14231.647	362.3	48930.438
362.8	11794.765	362.8	13940.512	362.8	48097.145
363.4	11481.029	363.4	13653.110	363.4	47276.841
363.9	11173.686	363.9	13369.470	363.9	46469.358
364.5	10872.686	364.5	13089.614	364.5	45674.529
365.0	10577.974	365.0	12813.565	365.0	44892.181
365.5	10289.493	365.5	12541.341	365.5	44122.143
366.1	10007.186	366.1	12272.957	366.1	43364.240
366.6	9730.989	366.6	12008.426	366.6	42618.298
367.2	9460.838	367.2	11747.757	367.2	41884.140
367.7	9196.666	367.7	11490.958	367.7	41161.591
368.2	8938.404	368.2	11238.033	368.2	40450.476
368.8	8685.982	368.8	10988.985	368.8	39750.620
369.3	8439.327	369.3	10743.812	369.3	39061.847
369.9	8198.364	369.9	10502.512	369.9	38383.986
370.4	7963.018	370.4	10265.080	370.4	37716.863
370.9	7733.210	370.9	10031.508	370.9	37060.307
371.5	7508.863	371.5	9801.786	371.5	36414.150
372.0	7289.897	372.0	9575.903	372.0	35778.224
372.6	7076.231	372.6	9353.845	372.6	35152.364
373.1	6867.783	373.1	9135.596	373.1	34536.407
373.6	6664.470	373.6	8921.138	373.6	33930.191
374.2	6466.210	374.2	8710.453	374.2	33333.557
374.7	6272.919	374.7	8503.519	374.7	32746.350
375.3	6084.512	375.3	8300.313	375.3	32168.415

375.8	5900.905	375.8	8100.810	375.8	31599.602
376.3	5722.013	376.3	7904.985	376.3	31039.761
376.9	5547.751	376.9	7712.811	376.9	30488.746
377.4	5378.034	377.4	7524.259	377.4	29946.415
378.0	5212.778	378.0	7339.298	378.0	29412.627
378.5	5051.896	378.5	7157.897	378.5	28887.244
379.0	4895.305	379.0	6980.024	379.0	28370.131
379.6	4742.920	379.6	6805.646	379.6	27861.155
380.1	4594.657	380.1	6634.727	380.1	27360.187
380.7	4450.431	380.7	6467.232	380.7	26867.101
381.2	4310.161	381.2	6303.125	381.2	26381.771
381.7	4173.762	381.7	6142.368	381.7	25904.077
382.3	4041.153	382.3	5984.923	382.3	25433.899
382.8	3912.253	382.8	5830.751	382.8	24971.121
383.4	3786.979	383.4	5679.813	383.4	24515.630
383.9	3665.253	383.9	5532.068	383.9	24067.313
384.4	3546.994	384.4	5387.476	384.4	23626.063
385.0	3432.125	385.0	5245.995	385.0	23191.772
385.5	3320.567	385.5	5107.584	385.5	22764.337
386.1	3212.244	386.1	4972.201	386.1	22343.655
386.6	3107.080	386.6	4839.802	386.6	21929.627
387.1	3005.000	387.1	4710.345	387.1	21522.156
387.7	2905.930	387.7	4583.787	387.7	21121.146
388.2	2809.797	388.2	4460.085	388.2	20726.503
388.8	2716.530	388.8	4339.195	388.8	20338.137
389.3	2626.057	389.3	4221.073	389.3	19955.958
389.8	2538.309	389.8	4105.676	389.8	19579.877
390.4	2453.217	390.4	3992.959	390.4	19209.811
390.9	2370.714	390.9	3882.879	390.9	18845.673
391.5	2290.733	391.5	3775.392	391.5	18487.382
392.0	2213.210	392.0	3670.453	392.0	18134.858
392.5	2138.079	392.5	3568.020	392.5	17788.020
393.1	2065.278	393.1	3468.049	393.1	17446.791
393.6	1994.745	393.6	3370.495	393.6	17111.094
394.2	1926.419	394.2	3275.315	394.2	16780.855
394.7	1860.242	394.7	3182.467	394.7	16456.000

395.2	1796.153	395.2	3091.907	395.2	16136.456
395.8	1734.098	395.8	3003.593	395.8	15822.153
396.3	1674.018	396.3	2917.482	396.3	15513.020
396.9	1615.860	396.9	2833.531	396.9	15208.988
397.4	1559.569	397.4	2751.699	397.4	14909.990
397.9	1505.093	397.9	2671.944	397.9	14615.959
398.5	1452.381	398.5	2594.225	398.5	14326.830
399.0	1401.382	399.0	2518.502	399.0	14042.536
399.6	1352.046	399.6	2444.732	399.6	13763.015
400.1	1304.327	400.1	2372.878	400.1	13488.203
400.6	1258.176	400.6	2302.898	400.6	13218.039
401.2	1213.548	401.2	2234.753	401.2	12952.460
401.7	1170.398	401.7	2168.405	401.7	12691.406
402.3	1128.682	402.3	2103.815	402.3	12434.818
402.8	1088.357	402.8	2040.946	402.8	12182.635
403.3	1049.382	403.3	1979.759	403.3	11934.801
403.9	1011.716	403.9	1920.218	403.9	11691.256
404.4	975.319	404.4	1862.286	404.4	11451.944
405.0	940.153	405.0	1805.928	405.0	11216.808
405.5	906.180	405.5	1751.107	405.5	10985.791
406.0	873.363	406.0	1697.789	406.0	10758.840
406.6	841.666	406.6	1645.940	406.6	10535.898
407.1	811.054	407.1	1595.524	407.1	10316.912
407.7	781.494	407.7	1546.510	407.7	10101.828
408.2	752.953	408.2	1498.864	408.2	9890.592
408.7	725.398	408.7	1452.553	408.7	9683.151
409.3	698.798	409.3	1407.545	409.3	9479.454
409.8	673.123	409.8	1363.810	409.8	9279.448
410.4	648.343	410.4	1321.317	410.4	9083.082
410.9	624.429	410.9	1280.035	410.9	8890.305
411.4	601.354	411.4	1239.934	411.4	8701.066
412.0	579.090	412.0	1200.986	412.0	8515.316
412.5	557.610	412.5	1163.161	412.5	8333.005
413.1	536.890	413.1	1126.432	413.1	8154.083
413.6	516.904	413.6	1090.771	413.6	7978.502
414.1	497.628	414.1	1056.150	414.1	7806.214

414.7	479.038	414.7	1022.543	414.7	7637.169
415.2	461.113	415.2	989.925	415.2	7471.321
415.8	443.829	415.8	958.269	415.8	7308.623
416.3	427.165	416.3	927.551	416.3	7149.028
416.8	411.100	416.8	897.745	416.8	6992.489
417.4	395.614	417.4	868.829	417.4	6838.960
417.9	380.689	417.9	840.778	417.9	6688.396
418.5	366.303	418.5	813.569	418.5	6540.751
419.0	352.440	419.0	787.181	419.0	6395.981
419.5	339.081	419.5	761.590	419.5	6254.041
420.1	326.210	420.1	736.776	420.1	6114.887
420.6	313.808	420.6	712.716	420.6	5978.476
421.2	301.861	421.2	689.391	421.2	5844.764
421.7	290.352	421.7	666.781	421.7	5713.709
422.2	279.266	422.2	644.865	422.2	5585.268
422.8	268.589	422.8	623.625	422.8	5459.398
423.3	258.306	423.3	603.041	423.3	5336.059
423.9	248.403	423.9	583.096	423.9	5215.209
424.4	238.867	424.4	563.770	424.4	5096.807
424.9	229.685	424.9	545.048	424.9	4980.813
425.5	220.845	425.5	526.911	425.5	4867.187
426.0	212.334	426.0	509.343	426.0	4755.889
426.6	204.141	426.6	492.327	426.6	4646.880
427.1	196.255	427.1	475.849	427.1	4540.121
427.6	188.664	427.6	459.891	427.6	4435.574
428.2	181.358	428.2	444.440	428.2	4333.201
428.7	174.326	428.7	429.480	428.7	4232.964
429.3	167.560	429.3	414.997	429.3	4134.827
429.8	161.048	429.8	400.978	429.8	4038.751
430.3	154.783	430.3	387.407	430.3	3944.702
430.9	148.755	430.9	374.273	430.9	3852.644
431.4	142.956	431.4	361.562	431.4	3762.540
432.0	137.376	432.0	349.261	432.0	3674.356
432.5	132.009	432.5	337.358	432.5	3588.057
433.0	126.846	433.0	325.842	433.0	3503.609
433.6	121.880	433.6	314.701	433.6	3420.979

434.1	117.104	434.1	303.922	434.1	3340.133
434.7	112.511	434.7	293.496	434.7	3261.038
435.2	108.093	435.2	283.412	435.2	3183.662
435.7	103.845	435.7	273.659	435.7	3107.972
436.3	99.760	436.3	264.226	436.3	3033.937
436.8	95.832	436.8	255.105	436.8	2961.526
437.4	92.056	437.4	246.285	437.4	2890.708
437.9	88.425	437.9	237.757	437.9	2821.453
438.4	84.934	438.4	229.513	438.4	2753.731
439.0	81.578	439.0	221.542	439.0	2687.512
439.5	78.353	439.5	213.838	439.5	2622.767
440.1	75.252	440.1	206.390	440.1	2559.468
440.6	72.271	440.6	199.192	440.6	2497.586
441.1	69.407	441.1	192.235	441.1	2437.094
441.7	66.654	441.7	185.512	441.7	2377.964
442.2	64.008	442.2	179.016	442.2	2320.168
442.8	61.465	442.8	172.738	442.8	2263.682
443.3	59.021	443.3	166.673	443.3	2208.477
443.8	56.673	443.8	160.813	443.8	2154.529
444.4	54.417	444.4	155.152	444.4	2101.812
444.9	52.249	444.9	149.683	444.9	2050.302
445.5	50.166	445.5	144.400	445.5	1999.973
446.0	48.165	446.0	139.298	446.0	1950.801
446.5	46.242	446.5	134.369	446.5	1902.763
447.1	44.395	447.1	129.610	447.1	1855.835
447.6	42.621	447.6	125.013	447.6	1809.994
448.2	40.916	448.2	120.575	448.2	1765.218
448.7	39.279	448.7	116.289	448.7	1721.485
449.2	37.706	449.2	112.151	449.2	1678.771
449.8	36.196	449.8	108.155	449.8	1637.057
450.3	34.745	450.3	104.298	450.3	1596.321
450.9	33.351	450.9	100.574	450.9	1556.541
451.4	32.013	451.4	96.979	451.4	1517.699
451.9	30.728	451.9	93.509	451.9	1479.773
452.5	29.494	452.5	90.160	452.5	1442.744
453.0	28.308	453.0	86.928	453.0	1406.592

453.6	27.170	453.6	83.808	453.6	1371.299
454.1	26.077	454.1	80.797	454.1	1336.847
454.6	25.028	454.6	77.891	454.6	1303.216
455.2	24.020	455.2	75.088	455.2	1270.389
455.7	23.053	455.7	72.382	455.7	1238.348
456.3	22.124	456.3	69.772	456.3	1207.076
456.8	21.232	456.8	67.253	456.8	1176.555
457.3	20.376	457.3	64.823	457.3	1146.770
457.9	19.554	457.9	62.479	457.9	1117.704
458.4	18.765	458.4	60.218	458.4	1089.341
459.0	18.007	459.0	58.036	459.0	1061.665
459.5	17.280	459.5	55.932	459.5	1034.660
460.0	16.582	460.0	53.902	460.0	1008.313
460.6	15.911	460.6	51.945	460.6	982.607
461.1	15.268	461.1	50.056	461.1	957.528
461.7	14.651	461.7	48.236	461.7	933.063
462.2	14.058	462.2	46.479	462.2	909.196
462.7	13.489	462.7	44.786	462.7	885.915
463.3	12.943	463.3	43.153	463.3	863.206
463.8	12.419	463.8	41.578	463.8	841.056
464.4	11.916	464.4	40.060	464.4	819.452
464.9	11.433	464.9	38.596	464.9	798.382
465.4	10.970	465.4	37.185	465.4	777.832
466.0	10.526	466.0	35.824	466.0	757.792
466.5	10.099	466.5	34.512	466.5	738.249
467.1	9.689	467.1	33.247	467.1	719.191
467.6	9.296	467.6	32.028	467.6	700.608
468.1	8.919	468.1	30.853	468.1	682.487
468.7	8.557	468.7	29.720	468.7	664.819
469.2	8.210	469.2	28.628	469.2	647.593
469.8	7.877	469.8	27.576	469.8	630.798
470.3	7.557	470.3	26.561	470.3	614.423
470.8	7.250	470.8	25.584	470.8	598.460
471.4	6.956	471.4	24.641	471.4	582.898
471.9	6.674	471.9	23.733	471.9	567.728
472.5	6.403	472.5	22.858	472.5	552.940

473.0	6.142	473.0	22.015	473.0	538.525
473.5	5.893	473.5	21.202	473.5	524.475
474.1	5.654	474.1	20.419	474.1	510.780
474.6	5.424	474.6	19.665	474.6	497.432
475.2	5.203	475.2	18.938	475.2	484.423
475.7	4.992	475.7	18.237	475.7	471.744
476.2	4.789	476.2	17.562	476.2	459.387
476.8	4.594	476.8	16.912	476.8	447.345
477.3	4.408	477.3	16.286	477.3	435.610
477.9	4.229	477.9	15.682	477.9	424.174
478.4	4.057	478.4	15.101	478.4	413.031
478.9	3.892	478.9	14.540	478.9	402.172
479.5	3.734	479.5	14.001	479.5	391.592
480.0	3.582	480.0	13.481	480.0	381.283
480.6	3.436	480.6	12.980	480.6	371.238
481.1	3.296	481.1	12.498	481.1	361.452
481.6	3.162	481.6	12.034	481.6	351.917
482.2	3.034	482.2	11.586	482.2	342.628
482.7	2.911	482.7	11.155	482.7	333.578
483.3	2.792	483.3	10.740	483.3	324.761
483.8	2.679	483.8	10.340	483.8	316.173
484.3	2.570	484.3	9.955	484.3	307.806
484.9	2.465	484.9	9.584	484.9	299.656
485.4	2.365	485.4	9.227	485.4	291.716
486.0	2.269	486.0	8.883	486.0	283.983
486.5	2.177	486.5	8.552	486.5	276.450
487.0	2.088	487.0	8.233	487.0	269.113
487.6	2.004	487.6	7.926	487.6	261.967
488.1	1.922	488.1	7.630	488.1	255.006
488.7	1.844	488.7	7.345	488.7	248.227
489.2	1.769	489.2	7.071	489.2	241.625
489.7	1.697	489.7	6.807	489.7	235.195
490.3	1.628	490.3	6.553	490.3	228.932
490.8	1.562	490.8	6.308	490.8	222.834
491.4	1.499	491.4	6.072	491.4	216.895
491.9	1.438	491.9	5.845	491.9	211.111

492.4	1.380	492.4	5.627	492.4	205.479
493.0	1.324	493.0	5.416	493.0	199.994
493.5	1.270	493.5	5.214	493.5	194.654
494.1	1.218	494.1	5.018	494.1	189.453
494.6	1.169	494.6	4.831	494.6	184.389
495.1	1.122	495.1	4.650	495.1	179.459
495.7	1.076	495.7	4.476	495.7	174.658
496.2	1.032	496.2	4.308	496.2	169.984
496.8	0.991	496.8	4.147	496.8	165.432
497.3	0.950	497.3	3.992	497.3	161.001
497.8	0.912	497.8	3.842	497.8	156.687
498.4	0.875	498.4	3.698	498.4	152.486
498.9	0.840	498.9	3.560	498.9	148.397
499.5	0.806	499.5	3.426	499.5	144.416

Table 9.2 – XYZ coordinates of optimized structure of precursor compound **1**, $[Ir(bpy)_2(CF_3SO_3)_2]CF_3SO_3$.

Ir	-0.21574400	-0.50631700	0.11059200
N	1.01150300	-2.01230300	-0.45191300
N	-1.61400600	-1.83304500	0.75205300
N	1.08533500	-0.59853000	1.78134800
N	-1.50482000	-0.54140400	-1.54740000
C	0.84833000	-2.75578200	-1.56892000
C	1.78966400	-3.69308200	-1.96742100
C	2.94901400	-3.87103600	-1.19378800
C	3.11646400	-3.11757500	-0.03799800
C	2.13977400	-2.18903000	0.33609700
C	2.18215500	-1.39026800	1.55557700
C	3.23555000	-1.42728700	2.47953700
C	3.16634300	-0.65706300	3.64349900
C	2.03371100	0.12016500	3.86512600
C	1.00859400	0.12955000	2.90561000
C	-2.66059200	-2.07083800	-0.11392600
C	-3.69087000	-2.93745700	0.25703800
C	-3.66459300	-3.55443300	1.50530600

C	-2.59676100	-3.29406400	2.37525400
C	-1.59115900	-2.43186400	1.96540300
C	-1.39437200	0.22743600	-2.64483200
C	-2.36417000	0.20982900	-3.65414300
C	-3.47924700	-0.61222900	-3.51367100
C	-3.60186300	-1.38992200	-2.35960700
C	-2.60788300	-1.33664200	-1.37738600
S	-1.17742400	2.39971400	1.31032100
O	-1.45498900	0.98993500	0.57779400
O	-1.37616600	2.24490000	2.74670700
O	0.10386600	2.89995600	0.79159100
C	-2.62680700	3.38606200	0.55599800
F	-2.39457100	3.48499900	-0.74219700
F	-3.73042000	2.70205800	0.79157800
F	-2.63636300	4.55615500	1.14275200
S	2.13893700	1.00930800	-1.71458200
O	1.18982400	0.82385400	-0.41653100
O	2.81640300	-0.29144100	-1.84983700
O	1.40748500	1.57757800	-2.83569800
C	3.33949100	2.30159000	-0.99724100
F	4.24802600	2.51921700	-1.91797700
F	2.64641800	3.38114000	-0.71525500
F	3.87139700	1.76943900	0.09531200
H	-0.04414100	-2.56980900	-2.15108800
H	1.62498100	-4.26602100	-2.87430100
H	3.70525300	-4.59114100	-1.49262200
H	4.00167800	-3.25559700	0.57077400
H	4.10627200	-2.04606000	2.29700800
H	3.98106100	-0.67521600	4.36128600
H	1.91987800	0.72162300	4.76163100
H	0.11954300	0.73052200	3.05845500
H	-4.51471400	-3.12894300	-0.41993800
H	-4.46558100	-4.22630100	1.79980800
H	-2.54568600	-3.74804700	3.35950200
H	-0.75242200	-2.19720800	2.60694000
H	-0.52105700	0.86247100	-2.72581000

H	-2.22968300	0.84558900	-4.52349200
H	-4.24850400	-0.64535000	-4.27945300
H	-4.47132300	-2.02318900	-2.22795300

Table 9.3 – XYZ coordinates of optimized structure of precursor compound **2**, $[Ir(phen)_2(CF_3SO_3)_2]CF_3SO_3$.

Ir	0.03717800	-0.15711800	0.14111200
N	-1.24114200	-0.01554500	1.78583400
N	1.35680000	-0.43324300	-1.49992600
C	-2.33084900	-0.81980600	1.65529300
C	-1.16381800	0.84561200	2.81070700
C	-2.17671200	0.91234600	3.78617500
C	-3.28510400	0.08905200	3.68842400
C	-3.39247500	-0.81394600	2.59476000
C	-4.49508300	-1.69076100	2.37350600
C	-4.53637800	-2.52213900	1.26533300
C	-3.48092500	-2.52483200	0.30378000
C	-2.37523500	-1.66818600	0.50967400
C	-3.47610700	-3.32558500	-0.86883900
C	-2.41497000	-3.22743800	-1.76123600
C	-1.36775600	-2.34190900	-1.49744700
N	-1.33231800	-1.58855300	-0.37186100
C	2.28418300	-1.40522700	-1.25225300
C	3.29113300	-1.76686800	-2.18609100
C	3.31654800	-1.06514900	-3.42350800
C	2.40274300	-0.05486900	-3.63802500
C	1.44475300	0.25553500	-2.65163500
C	2.25582100	-2.00610600	0.03357300
C	3.22074700	-2.97326600	0.39808500
C	4.20137000	-3.36041900	-0.56954700
C	4.23123200	-2.77324800	-1.82212700
N	1.31057700	-1.54565900	0.90714200
C	1.30238300	-2.02334000	2.17710300
C	2.22034200	-2.97542900	2.60988900
C	3.18205600	-3.46488500	1.72194000

S	2.55971800	1.84086900	0.39705000
O	1.10243900	1.33552300	0.91189500
O	3.49242900	0.73995800	0.65528000
O	2.43911700	2.40937800	-0.93905700
C	2.79647200	3.22066700	1.67672400
S	-1.79847400	1.42458000	-2.05187000
O	-1.31591500	1.17022000	-0.54334800
O	-0.92690400	2.38907800	-2.70817100
O	-2.01713700	0.10767900	-2.66981400
C	-3.46458600	2.22722600	-1.66005700
F	1.88324500	4.14316200	1.44648600
F	2.62887700	2.67950800	2.87835000
F	4.01464200	3.68531500	1.52553800
F	-4.05491400	2.48516900	-2.80407900
F	-4.16686700	1.34534300	-0.94759500
F	-3.24426400	3.32088900	-0.95994700
H	-0.28665300	1.48296400	2.84374100
H	-2.07326300	1.62005400	4.60212500
H	-4.07514500	0.13412500	4.43326900
H	-5.31668600	-1.69719800	3.08409100
H	-5.38900600	-3.17794000	1.11404700
H	-4.30395900	-4.00100200	-1.06912300
H	-2.39430800	-3.81423700	-2.67337300
H	-0.54420500	-2.22259300	-2.18787400
H	4.06536300	-1.31034200	-4.17173700
H	2.41042200	0.53156300	-4.55087400
H	0.75838900	1.08042400	-2.80022000
H	4.94266500	-4.10740100	-0.30083400
H	4.99582300	-3.06276700	-2.53724000
H	0.54831200	-1.62290400	2.84208900
H	2.18070900	-3.32393300	3.63659100
H	3.90412400	-4.20825900	2.05022900

Table 9.4 – XYZ coordinates of optimized structure of precursor compound **3**, $[Ir(dppz)_2(CF_3SO_3)_2]CF_3SO_3$.

Ir	-0.04360800	0.26976500	0.12822600
C	-3.20880000	-2.81283100	2.15190700
C	-1.94258800	-2.71243100	2.70667700
C	-0.99129800	-1.86413700	2.12111100
N	-1.25678500	-1.14634900	1.02496000
C	-2.50183800	-1.23445300	0.46220000
C	-3.51142200	-2.05980200	1.00277500
C	-2.74426400	-0.42639600	-0.69784000
N	-1.70328800	0.34599600	-1.13244300
C	-1.89067600	1.17119800	-2.16853100
C	-3.11900100	1.22294200	-2.85300500
C	-4.17679200	0.43089800	-2.44421400
C	-4.00320100	-0.41683600	-1.33181200
N	1.14557400	-1.11043900	-0.85040800
C	2.39588200	-1.24208200	-0.30226900
C	3.39651200	-2.03494800	-0.89432400
C	3.07772900	-2.73302000	-2.07015300
C	1.80199000	-2.60610300	-2.60227100
C	0.86154100	-1.77703600	-1.97581700
C	2.64731900	-0.50952200	0.90403400
N	1.60696200	0.21320000	1.40094700
C	1.78466500	0.95713900	2.50051400
C	3.02397900	0.99668900	3.16926000
C	4.09150800	0.26282400	2.68793300
C	3.91662000	-0.51887600	1.52254200
C	-5.06144200	-1.26333000	-0.79674400
C	-4.81844800	-2.07855700	0.35618500
C	4.97444000	-1.30249600	0.91703900
C	4.72225200	-2.05880500	-0.27743100
N	-6.25373300	-1.24991100	-1.39924000
C	-7.21894900	-2.02844800	-0.88315400
C	-6.97364500	-2.84903100	0.27203500
N	-5.77105400	-2.86000600	0.87154400
C	-8.51160800	-2.04322500	-1.48801800
C	-9.52340200	-2.84790200	-0.95734700
C	-9.28315700	-3.65126900	0.17297800

C	-8.02829800	-3.66000700	0.78800700
N	6.18477000	-1.29236500	1.49680100
C	7.15433100	-2.00464500	0.91203700
C	6.90376600	-2.76056300	-0.28631600
N	5.68045500	-2.77425400	-0.85721600
C	8.46925100	-2.01127900	1.48839100
C	9.49007300	-2.74275200	0.88777700
C	9.23998700	-3.47999000	-0.28406500
C	7.96299800	-3.49678400	-0.87144500
S	1.78584400	1.76073700	-2.06175600
O	0.97641700	1.85457100	-0.71490800
O	3.12046200	1.19949300	-1.82283600
O	0.96159400	1.15764200	-3.12081900
C	1.93509800	3.59975400	-2.40803500
S	-0.97003600	3.15283000	1.23824000
O	-1.13567300	1.57398200	1.28607200
O	0.31818000	3.54640300	1.81317100
O	-1.39502200	3.67373700	-0.05910100
C	-2.30158300	3.54430100	2.49821100
F	2.54546700	4.18227100	-1.38946100
F	2.63644000	3.73967300	-3.52120000
F	0.70875200	4.08610100	-2.56248200
F	-1.98079200	2.95926100	3.65096100
F	-2.36310700	4.85444400	2.64355900
F	-3.46502300	3.06780000	2.05808600
H	-3.97009000	-3.45182500	2.58590600
H	-1.67305400	-3.27398100	3.59465600
H	-0.00113500	-1.75491700	2.54711900
H	-1.05601300	1.79227500	-2.45873500
H	-3.21838900	1.90506700	-3.69040200
H	-5.13636200	0.45838100	-2.94866500
H	3.83279100	-3.34564000	-2.55043600
H	1.52551800	-3.11703300	-3.51810100
H	-0.12216200	-1.62122300	-2.39894900
H	0.93932300	1.54346200	2.83539800
H	3.11910700	1.61519200	4.05517400

H	5.05941600	0.27868300	3.17667200
H	-8.68229000	-1.41885200	-2.35962600
H	-10.50444600	-2.85181400	-1.42201600
H	-10.08051500	-4.26984100	0.57287000
H	-7.83052900	-4.27284600	1.66201100
H	8.63780600	-1.43066800	2.39023800
H	10.48387400	-2.74361600	1.32395400
H	10.04387000	-4.04589100	-0.74506500
H	7.76741100	-4.06674100	-1.77446600

Table 9.5 – XYZ coordinates of optimized structure of Complex **1**, $[Ir(bpy)(qtpy)](CF_3SO_3)_3$.

Ir	1.27085800	-0.00363000	0.01104000
N	1.39231000	0.54069400	-2.00206600
N	-0.33405000	1.30693700	0.17744100
N	-0.34241600	-1.30673700	-0.18502200
N	1.35176400	-0.54791800	2.02638200
N	2.78706300	1.43711100	0.06675100
C	2.25890700	-1.52342400	2.33056500
C	2.38438100	-1.98840400	3.64155700
C	1.57997700	-1.45434300	4.64765900
C	0.66004300	-0.45803300	4.32122500
C	0.57350400	-0.03310200	2.99982200
C	3.45478100	1.82273800	1.17311000
C	4.46832900	2.77422400	1.13562600
C	4.80726400	3.34590800	-0.09074800
C	4.11848000	2.94801900	-1.23603200
C	3.10719300	1.98911400	-1.14122700
C	2.31774700	1.50401900	-2.28942700
C	2.47370400	1.96698700	-3.59784400
C	1.67963500	1.44482900	-4.61833500
C	0.73883500	0.46282800	-4.30858800
C	0.62316100	0.03839100	-2.98921300
C	-0.26070900	-2.64192100	-0.37511100
C	-1.37817000	-3.44939500	-0.49630500
C	-2.66942400	-2.89063700	-0.41706700

C	-2.73301000	-1.49771100	-0.21366000
C	-1.57933600	-0.72887800	-0.10157600
C	-1.57426600	0.73552000	0.09390100
C	-2.72361800	1.51285800	0.18775700
C	-2.65374800	2.90820600	0.37097100
C	-1.35957200	3.46037800	0.44839500
C	-0.24672800	2.64447700	0.34741700
C	-3.88569100	-3.71125700	-0.54493400
C	-3.86553400	3.73845200	0.47616500
C	-3.86932200	5.07321600	0.03647500
C	-5.04561200	5.81547300	0.15428900
N	-6.17455100	5.32805100	0.67963500
C	-6.16981100	4.06102700	1.10685300
C	-5.05490800	3.22603300	1.02252200
C	-3.89706700	-4.86861900	-1.34198500
C	-5.07842800	-5.60604900	-1.43780600
N	-6.20515300	-5.27821900	-0.79670900
C	-6.19279900	-4.18284400	-0.02990800
C	-5.07237700	-3.36534600	0.12410700
H	3.10185400	-2.76324100	3.88317200
H	1.67310200	-1.81212100	5.66835600
H	0.01606100	-0.01293900	5.07206400
H	-0.12503800	0.73786400	2.70017900
H	3.15766900	1.35438200	2.10294900
H	4.97638500	3.05482300	2.05203400
H	5.59474900	4.09011500	-0.15814600
H	4.37390100	3.38463000	-2.19405500
H	3.20636500	2.73157500	-3.82620700
H	1.79611700	1.80130100	-5.63709300
H	0.10036600	0.02879400	-5.07053400
H	-0.09258100	-0.72137700	-2.70204300
H	0.73645700	-3.06071700	-0.42754600
H	-1.24149200	-4.51693800	-0.62651100
H	-3.70245600	-1.01757200	-0.17246500
H	-3.69518300	1.04463300	0.09382000
H	-1.21715900	4.52219900	0.61370300

H	0.75259500	3.05571100	0.41852100
H	-2.99672300	5.52446600	-0.42571600
H	-5.08103100	6.84599200	-0.19089300
H	-7.09820400	3.69592100	1.53974900
H	-5.11271100	2.21672500	1.41905700
H	-3.02649900	-5.17755500	-1.91246000
H	-5.12000300	-6.49745500	-2.05917300
H	-7.11959700	-3.94813500	0.48830900
H	-5.12404800	-2.50826200	0.78896000
N	2.77764500	-1.45810400	-0.01533000
C	4.77201100	-3.39041600	0.18045100
C	3.06515900	-2.01706000	1.19767300
C	3.46577300	-1.84746100	-1.10780300
C	4.46760800	-2.81039900	-1.05108300
C	4.06275400	-2.98819800	1.31163300
H	3.19411900	-1.37288500	-2.04228500
H	4.99323200	-3.09341000	-1.95677800
H	4.29174800	-3.43077700	2.27359000
H	5.54898400	-4.14412200	0.26270000

Table 9.6 – XYZ coordinates of optimized structure of Complex **2**, $[Ir(phen)_2(qtpy)](CF_3SO_3)_3$.

Ir	0.68869805	-0.09918001	3.45141526
N	-1.38669211	-0.11305201	3.78683629
N	0.63209005	-1.08533108	1.61052812
N	2.74529821	0.10844301	3.20880624
N	0.81585406	1.82320014	2.66663621
N	0.60385904	0.75658406	5.36337340
N	0.69778205	-2.09970316	4.09268631
C	-2.35324018	-0.56636404	2.98108723
C	-3.70942028	-0.52307804	3.34414526
C	-4.07444231	0.00137000	4.57169935
C	-3.07437624	0.48671904	5.44709940
C	-1.73235013	0.40447903	5.00776238
C	-0.67477705	0.87506907	5.84223642
C	-0.96372808	1.43207811	7.10989354
C	0.13104401	1.88108314	7.88588562

C	1.41580111	1.76012013	7.38601855
C	1.61921312	1.19261809	6.11731646
C	0.72321406	-2.57097320	5.34413738
C	0.70646105	-3.94739230	5.62420444
C	0.66178905	-4.85885937	4.58383535
C	0.63384805	-4.39089234	3.24873025
C	0.64993005	-2.99030823	3.05237823
C	0.62429705	-2.45058119	1.73205413
C	0.59014405	-3.31371025	0.61214204
C	0.57102105	-2.71368521	-0.66913905
C	0.58558405	-1.33411810	-0.77555506
C	0.61667805	-0.54630004	0.38643903
C	-0.22822502	2.64592120	2.42701418
C	-0.06969201	3.92905530	1.93272215
C	1.21895609	4.43161034	1.66485613
C	2.29402617	3.55747927	1.91928715
C	2.08170616	2.27395617	2.41144019
C	3.15983324	1.30162810	2.68459721
C	4.50902735	1.54465112	2.44936219
C	5.48980242	0.57618404	2.74093321
C	5.02444338	-0.63791205	3.28354825
C	3.67063028	-0.83283106	3.49578327
C	1.43405011	5.79312645	1.14483009
C	6.92080554	0.82283706	2.49206619
C	7.34512854	1.64575612	1.43488811
C	8.71384068	1.83674814	1.24045910
N	9.65193473	1.28798510	2.01948615
C	9.24935573	0.50902504	3.02904223
C	7.90775461	0.23856402	3.30383825
C	0.48777904	6.40485651	0.30537802
C	0.74310106	7.69356758	-0.16638701
N	1.83974314	8.39007962	0.15031801
C	2.73602121	7.81273861	0.95742707
C	2.58877220	6.52404448	1.47249311
C	-3.34565526	1.05310808	6.73903850
C	-2.33361518	1.50799111	7.53575560

C	0.59387805	-5.24968140	2.09792616
C	0.57493604	-4.73296436	0.83354306
H	-2.04337316	-0.96797207	2.02375415
H	-4.45367234	-0.90229707	2.65220320
H	-5.11904639	0.04352300	4.86694737
H	-0.04260100	2.31634718	8.86595168
H	2.27429218	2.09548916	7.95785060
H	2.61524320	1.08357808	5.70521545
H	0.76284306	-1.83910614	6.14192045
H	0.73006906	-4.27610832	6.65760850
H	0.64940105	-5.92663543	4.78342537
H	0.54531704	-3.33729825	-1.55830112
H	0.57204505	-0.84569606	-1.74388513
H	0.62503405	0.53565104	0.32936103
H	-1.21205609	2.25117417	2.64808320
H	-0.94846007	4.54626135	1.78417313
H	3.30199325	3.88911430	1.70448613
H	4.81956837	2.50342219	2.05370416
H	5.71220445	-1.44365811	3.51368727
H	3.29882325	-1.76547713	3.90156430
H	6.63918853	2.09591516	0.74330105
H	9.07097267	2.45527919	0.42039603
H	10.03344078	0.08195201	3.64973828
H	7.65111857	-0.38165303	4.15717832
H	-0.41127903	5.88667943	-0.01406300
H	0.03539600	8.18530564	-0.82955806
H	3.61149027	8.40742965	1.20754109
H	3.34141326	6.12935646	2.14863216
H	-4.37688034	1.11475708	7.07310752
H	-2.55198120	1.93547315	8.50961965
H	0.58093904	-6.32440448	2.25165617
H	0.54743004	-5.39262140	-0.02841000

Table 9.7 – XYZ coordinates of optimized structure of Complex **3**, $[Ir(dppz)_2(CF_3SO_3)_2]CF_3SO_3$.

Ir	1.29434231	0.23502681	4.18100294

N	-0.74834295	0.52205787	4.54759773
N	1.05359819	-1.26085572	2.74503524
N	3.34617694	0.16081861	3.83293064
N	1.53833235	1.80084674	2.83178371
N	1.37877734	1.63486148	5.73545041
N	1.17780334	-1.45547710	5.41252344
C	-1.78053515	-0.07043652	3.92851464
C	-3.10734766	0.20235756	4.28167980
C	-3.37538667	1.10631314	5.29909477
C	-2.30483423	1.73638189	5.96232367
C	-0.99803434	1.41147261	5.55511390
C	0.14697063	2.01658733	6.18943279
C	-0.01379349	2.94988021	7.22993708
C	1.14821091	3.50101364	7.80324179
C	2.39153951	3.10929053	7.32914448
C	2.47470296	2.17328226	6.29161051
C	1.23957064	-1.49897108	6.75198297
C	1.13082591	-2.70402199	7.45615284
C	0.95169912	-3.89168768	6.76228489
C	0.88250906	-3.86577604	5.35604048
C	0.99838696	-2.61807612	4.71670040
C	0.93874036	-2.51378159	3.27992043
C	0.76657234	-3.65839300	2.48028020
C	0.71926355	-3.48321439	1.08406559
C	0.84260557	-2.20719540	0.55439640
C	1.00936483	-1.11406988	1.41210717
C	0.55554809	2.60766127	2.37864274
C	0.79005893	3.64308026	1.48975832
C	2.09467056	3.89319326	1.02289513
C	3.10625544	3.04442919	1.51116221
C	2.81854322	2.01751744	2.40464425
C	3.83049927	1.09720149	2.96302395
C	5.18501510	1.14262087	2.64858474
C	6.09651667	0.22724704	3.20841004
C	5.55905262	-0.72784793	4.09252121
C	4.20333478	-0.73052328	4.37400243

C	2.38999292	4.98397105	0.07592140
C	7.53401339	0.26905424	2.88322904
C	8.18118923	1.48229882	2.59512942
C	9.54572002	1.46277503	2.30280170
N	10.27582867	0.34313544	2.26707801
C	9.65926034	-0.81254948	2.53587827
C	8.30349373	-0.90566693	2.85449815
C	3.42290137	4.86862001	-0.86931316
C	3.65283184	5.92997433	-1.74587561
N	2.94878693	7.06659615	-1.72764502
C	1.96872783	7.17897811	-0.82490890
C	1.64416497	6.17415941	0.08793257
C	-2.49737061	2.70180786	7.04184156
C	-1.36119102	3.30385006	7.67033305
C	0.69942714	-5.06849357	4.54719024
C	0.64285636	-4.96563330	3.12084528
N	-3.73861576	2.99624274	7.41213429
C	-3.89670075	3.88827169	8.41023386
C	-2.74315176	4.49832710	9.04939912
N	-1.49267228	4.18494345	8.65568389
C	-5.20230247	4.23939879	8.84639763
C	-5.35351134	5.14930049	9.86572006
C	-4.22059242	5.74800816	10.49381816
C	-2.94157769	5.43426849	10.09953777
N	0.59084907	-6.23755776	5.16850364
C	0.42288239	-7.33601966	4.40557299
C	0.36520615	-7.23157303	2.95739458
N	0.47851549	-6.03415398	2.34896219
C	0.30014011	-8.61194893	5.01798264
C	0.12873734	-9.72646405	4.23167049
C	0.07219375	-9.62390352	2.80943511
C	0.18721719	-8.40721559	2.17997897
H	-1.53820538	-0.76818634	3.13645002
H	-3.91003963	-0.29896882	3.75163741
H	-4.38980573	1.34456946	5.60124408
H	1.04284395	4.22223345	8.60689761

H	3.30501799	3.51548731	7.75006185
H	3.43052165	1.84466260	5.90241668
H	1.38219463	-0.55552831	7.26447865
H	1.18848746	-2.69116814	8.53925934
H	0.86313619	-4.84519461	7.27230047
H	0.58664501	-4.35535762	0.45247565
H	0.81042635	-2.03952161	-0.51676413
H	1.10413364	-0.10500211	1.02982134
H	-0.44358793	2.39516421	2.73799545
H	-0.04788503	4.23686661	1.14271224
H	4.12949169	3.21479892	1.20112631
H	5.54694541	1.87749186	1.94075799
H	6.19806002	-1.45364682	4.58260568
H	3.77646749	-1.45014071	5.06137789
H	7.65690554	2.43247164	2.63765508
H	10.07502094	2.38904804	2.09163276
H	10.27512280	-1.70777362	2.49285949
H	7.86129396	-1.88055516	3.03564162
H	4.01306017	3.96157098	-0.96150231
H	4.43552347	5.86109085	-2.49780272
H	1.41690090	8.11600972	-0.82806737
H	0.85255553	6.34319159	0.81153680
H	-6.05273657	3.77495772	8.35871539
H	-6.34822798	5.42200380	10.20435567
H	-4.37975270	6.46225996	11.29569786
H	-2.06976438	5.88023124	10.56626263
H	0.34507710	-8.67259449	6.10015022
H	0.03388300	-10.70460258	4.69292072
H	-0.06416923	-10.52638997	2.22171744
H	0.14634823	-8.31178208	1.10015792

9.1.2 Optimised Geometries of Selected Precursors

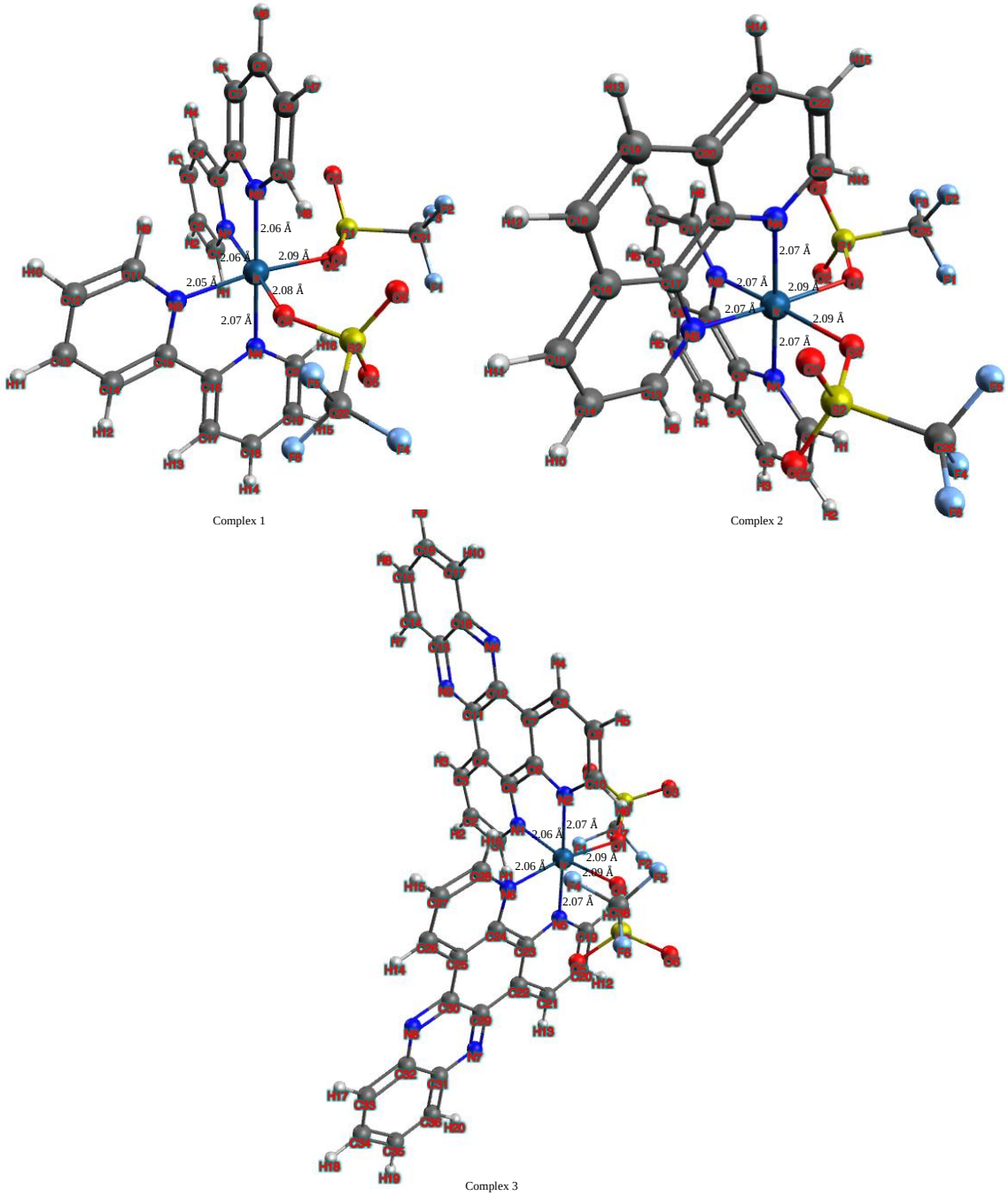

Figure 9.1 – Optimised Geometries of $[Ir(bpy)_2(CF_3SO_3)_2]CF_3SO_3$ (Complex **1**), $[Ir(phen)_2(CF_3SO_3)_2]CF_3SO_3$ (Complex **2**), and $[Ir(dppz)_2(CF_3SO_3)_2]CF_3SO_3$ (Complex **3**).

9.1.3 UV-Vis Spectral Studies Selected Precursors

9.1.3.1 Complex 1, $[Ir(bpy)_2(CF_3SO_3)_2]CF_3SO_3$

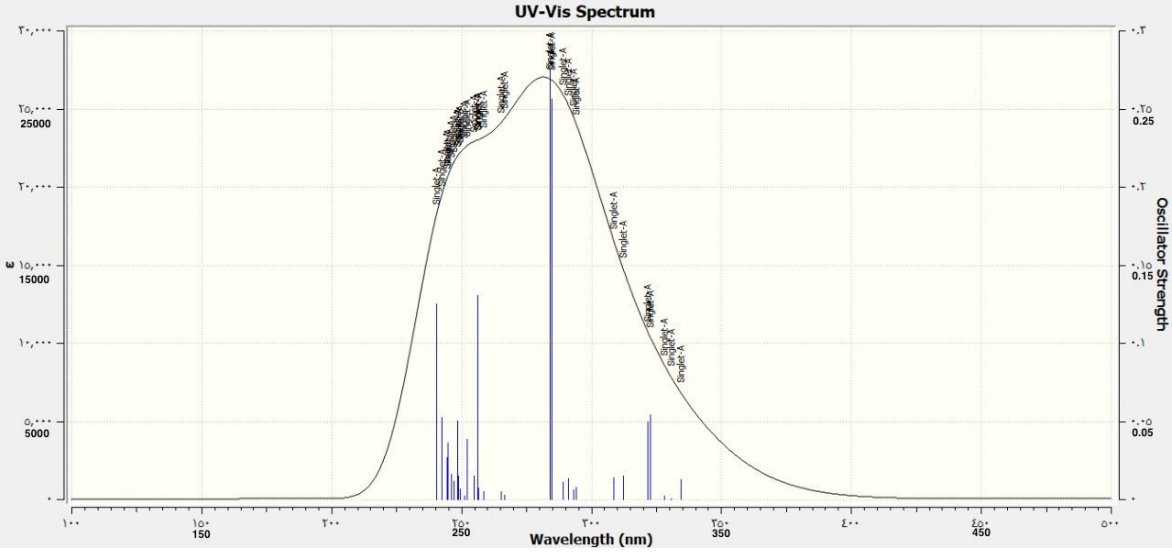

Figure 9.2 – UV-Vis spectrum of $[Ir(bpy)_2(CF_3SO_3)_2]CF_3SO_3$.

9.1.3.2 Complex 2, $[Ir(phen)_2(CF_3SO_3)_2]CF_3SO_3$

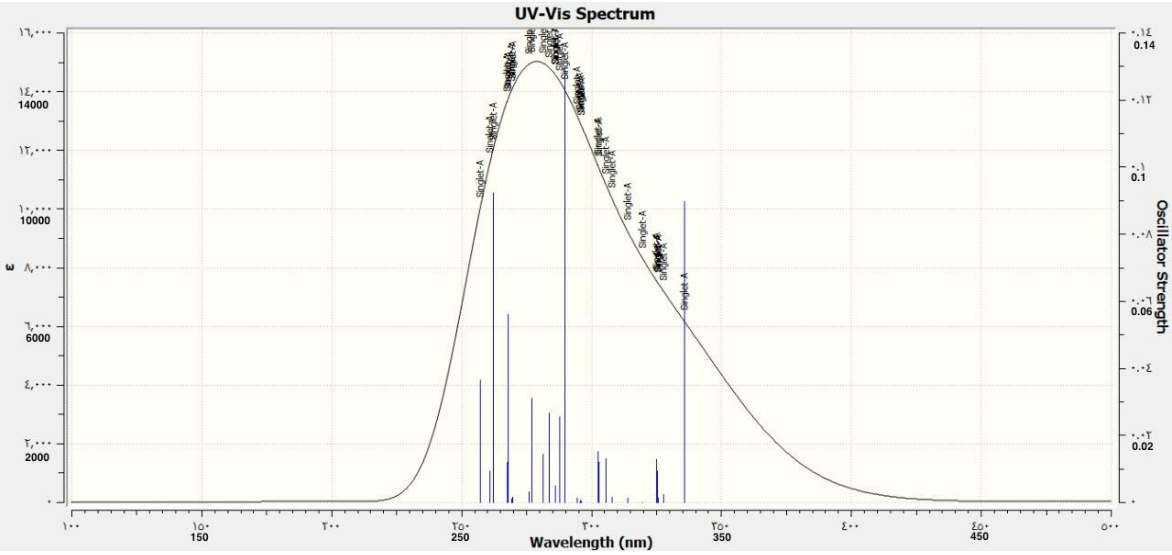

Figure 9.3 – UV-Vis spectrum of $[Ir(phen)_2(CF_3SO_3)_2]CF_3SO_3$.

9.1.3.3 Complex 3, $[Ir(dppz)_2(CF_3SO_3)_2]CF_3SO_3$

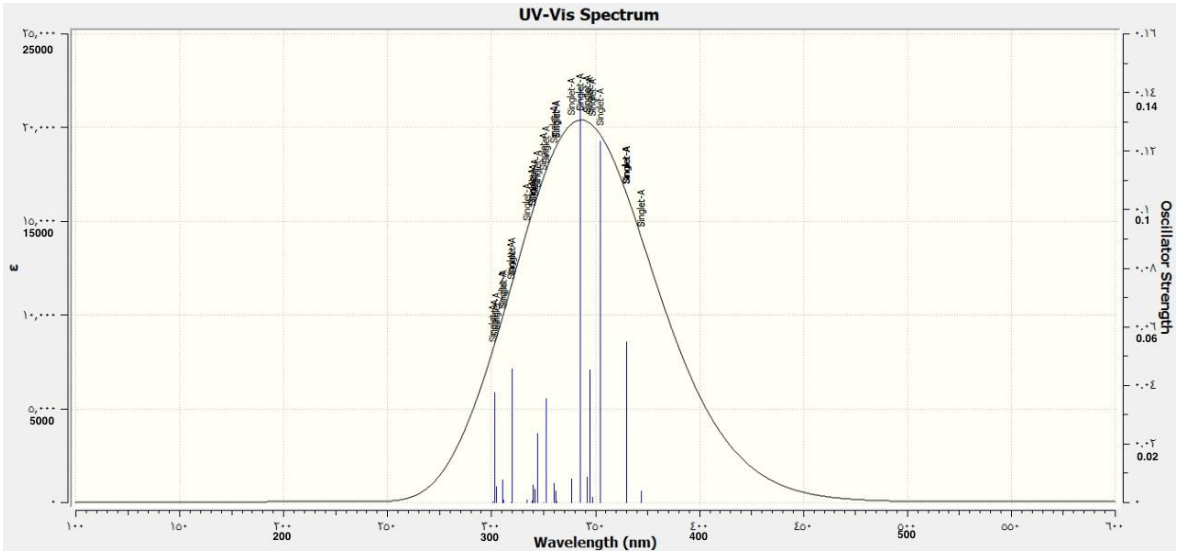

Figure 9.4 – UV-Vis spectrum of $[Ir(dppz)_2(CF_3SO_3)_2]CF_3SO_3$.

9.1.3.4 Ligand 1 (bpy)

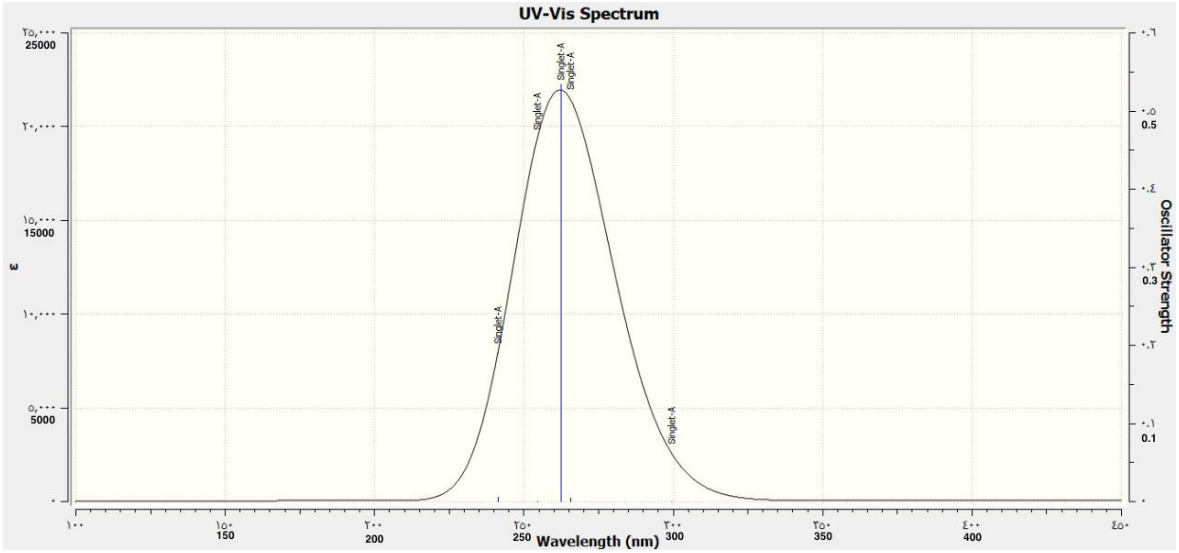

Figure 9.5 – UV-Vis spectrum of bpy.

9.1.3.5 Ligand 2 (phen)

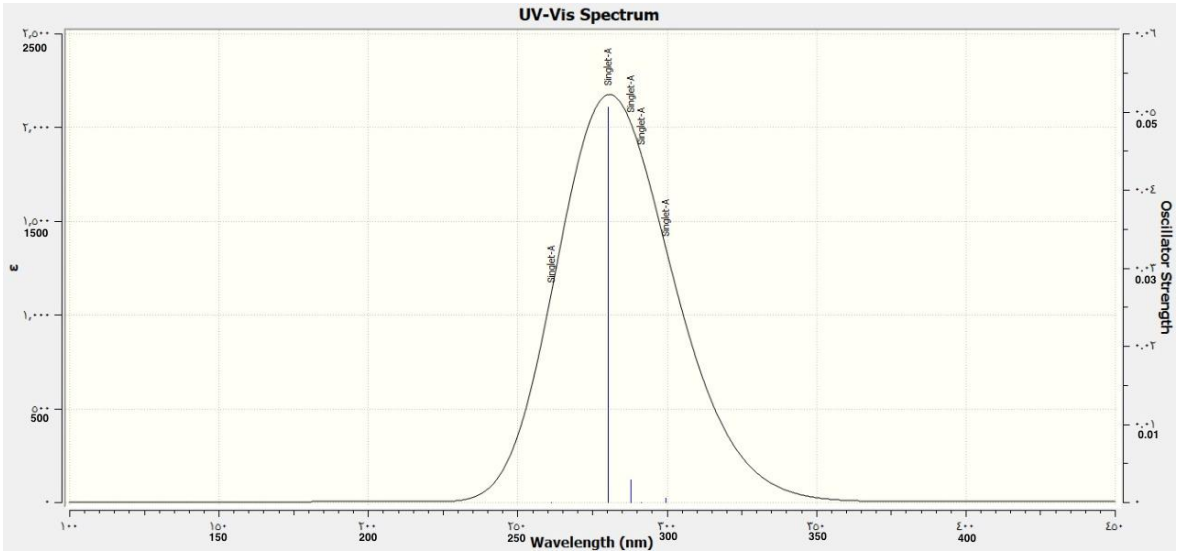

Figure 9.6 – UV-Vis spectrum of phen.

9.1.3.6 Ligand 3 (dppz)

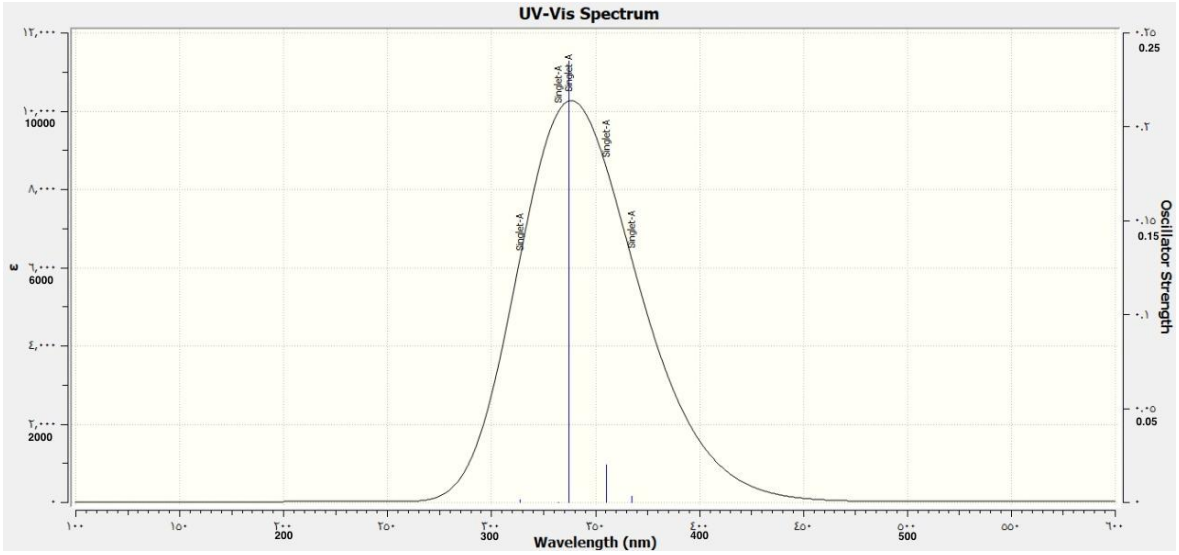

Figure 9.7 – UV-Vis spectrum of dppz.

9.1.3.7 Ligand 4 (qtpy)

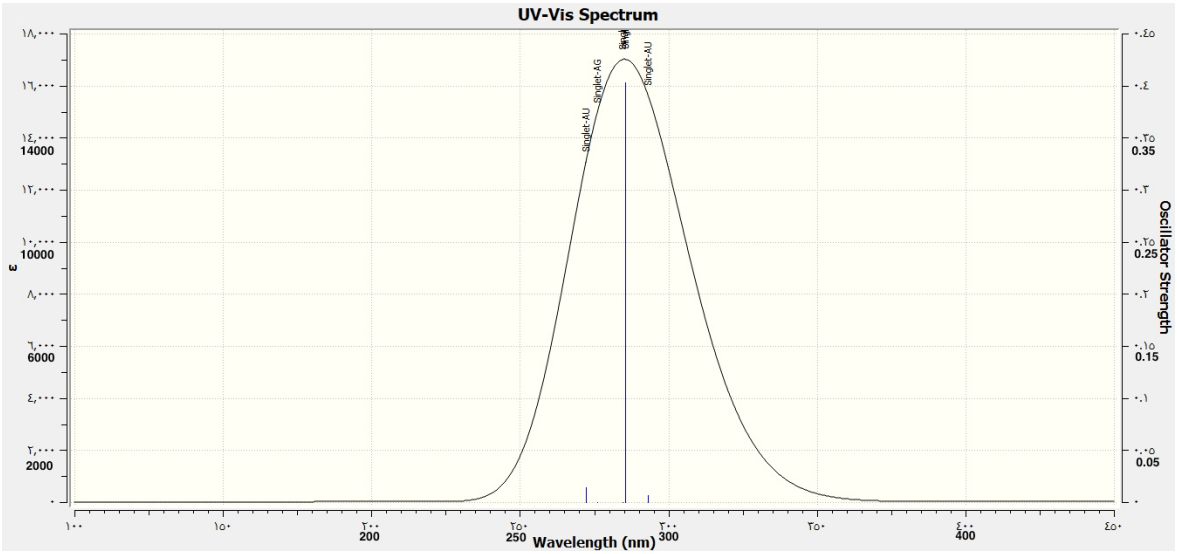

Figure 9.8 – UV-Vis spectrum of qtpy.

Table 9.8 – Summary of DFT Simulated UV-Vis Spectroscopic analyses.

	Wavelength (nm)
Complex **1**	283.96
Complex **2**	277.15
Complex **3**	342.61
Ligand **1**	262.3
Ligand **2**	280.34
Ligand **3**	337.2
Ligand **4**	285.45

9.2 X-ray Crystallographic Summary

9.2.1 $[Ir(bpy)_2Cl_2]PF_6$

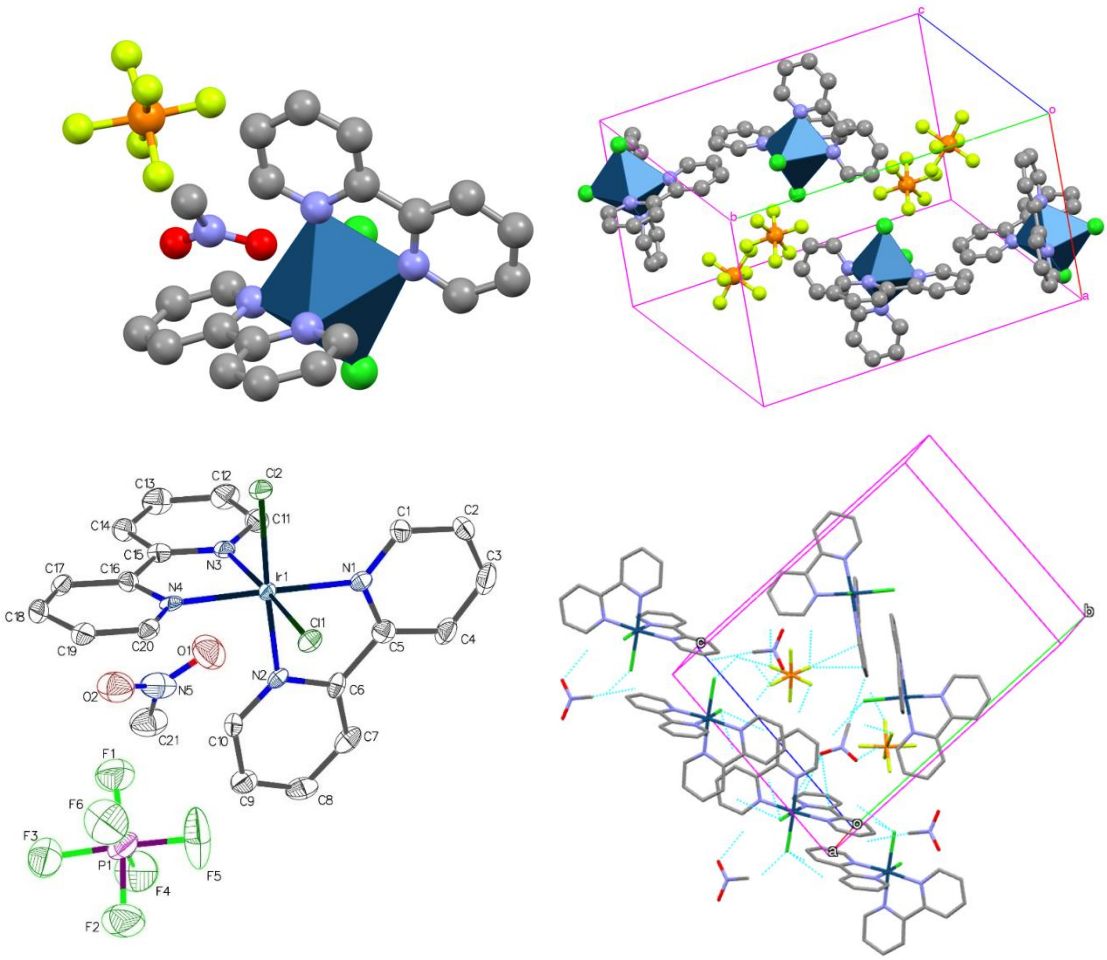

Figure 9.9 – Crystal structure of $[Ir(bpy)_2Cl_2]PF_6$ (**top left**), its packing diagram showing layers of the compound with PF_6 counterion in channels between them (**top right**) (**NB:** Solvent molecules are removed for clarity), its ORTEP diagram and atom labelling scheme showing 50% thermal ellipsoids (**bottom left**), and its packing structure showing nearest contacts in the compound (**bottom right**). Atom labelling – blue: Ir; grey: C; purple: N; deep green: Cl; light green: F; orange: P.

9.2.2 HSA for $[Ir(bpy)_2Cl_2]PF_6$

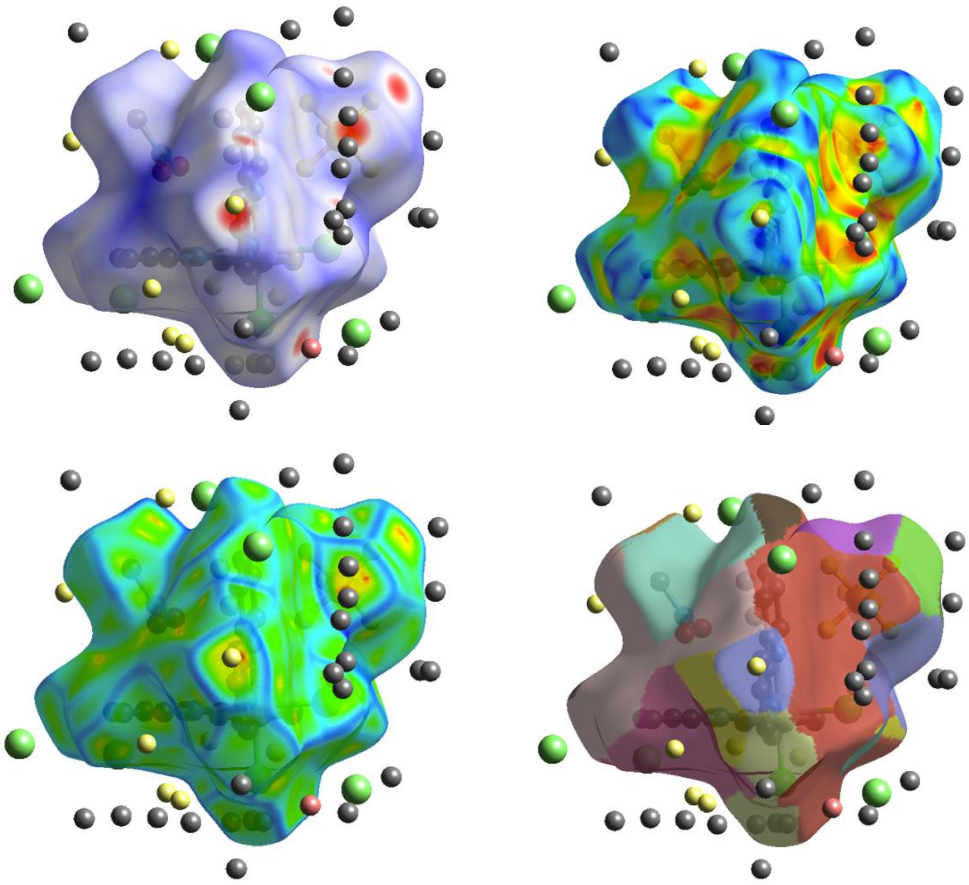

Figure 9.10 – Hirshfeld surfaces of $[Ir(bpy)_2Cl_2]PF_6$ mapped with d_{norm} (**top left**), shape index (**top right**), curvedness (**down left**) and Fragment Patch **(bottom right**) for all bond types showing neighbouring contact atoms.

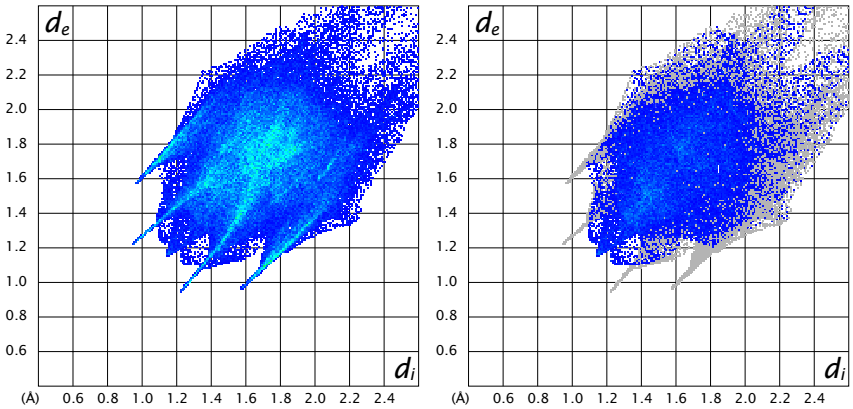

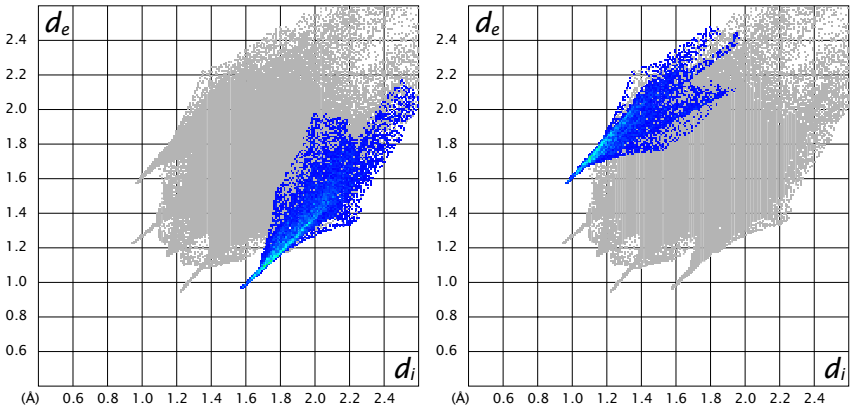

Figure 9.11 – 2D fingerprint plots of $[Ir(bpy)_2Cl_2]PF_6$ for all interactions (surface area covered = 100.0%) (**top left**), H•••H interactions (surface area covered = 26.2%) (**top right**), H•••Cl/Cl•••H interactions (surface covered = 6.5% and 9.7%) (**bottom left** and **bottom right**) present in the compound.

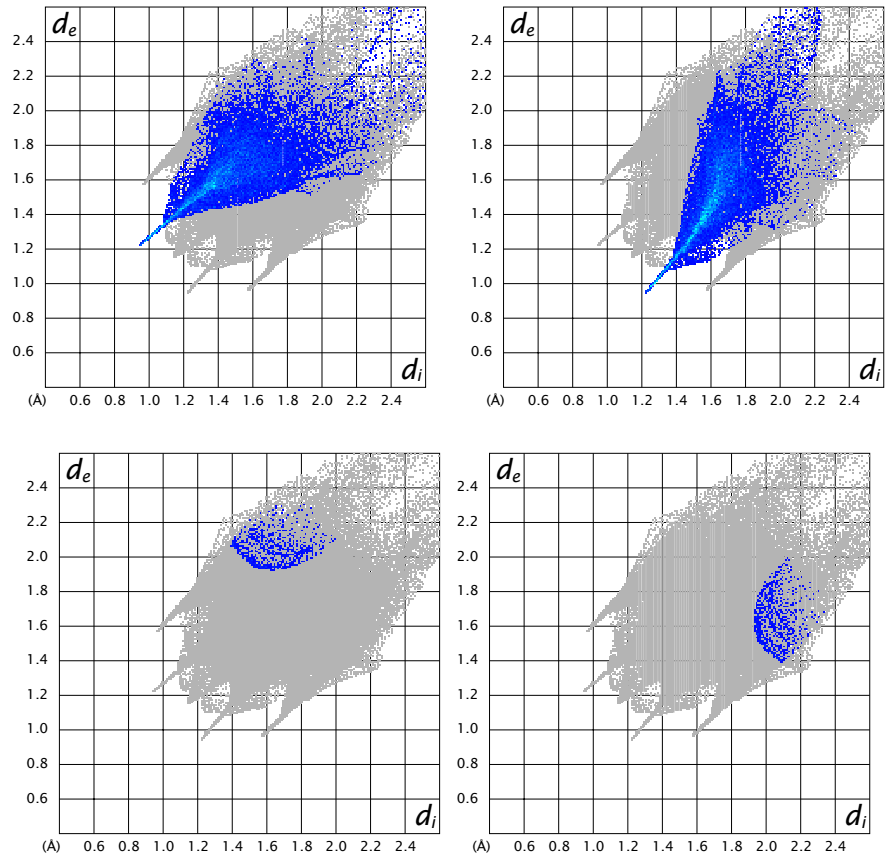

Figure 9.12 – 2D fingerprint plots of $[Ir(bpy)_2Cl_2]PF_6$ for H•••F/F•••H interactions (surface covered = 15.8% and 16.6% (**top left and top right**) and H•••N/N•••H interactions (surface covered = 0.7% and 0.7%) (**bottom left** and **bottom right**) present in the compound.

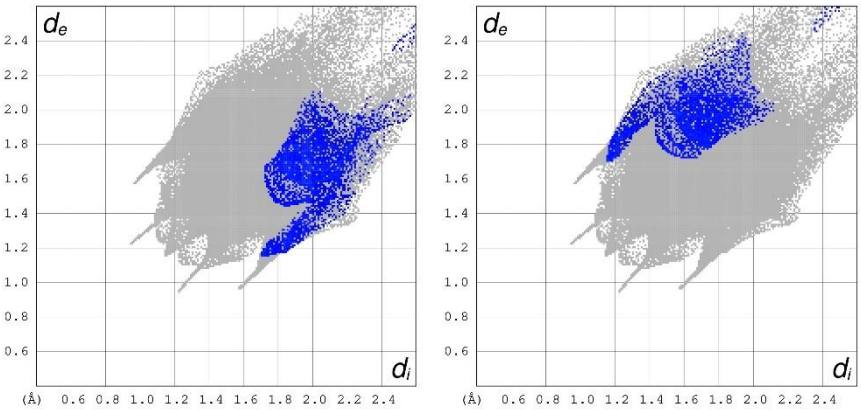

Figure 9.13 – 2D fingerprint plots of $[Ir(bpy)_2Cl_2]PF_6$ for C•••H/H•••C interactions (surface covered = 4.2% and 3.6%) present in the compound.

All other crystallographic data obtained for $[Ir(bpy)_2Cl_2]PF_6$ can be found in an appropriate section of this Appendix.

9.2.3 HSA for $[Ir(bpy)_2Cl_2]Cl$

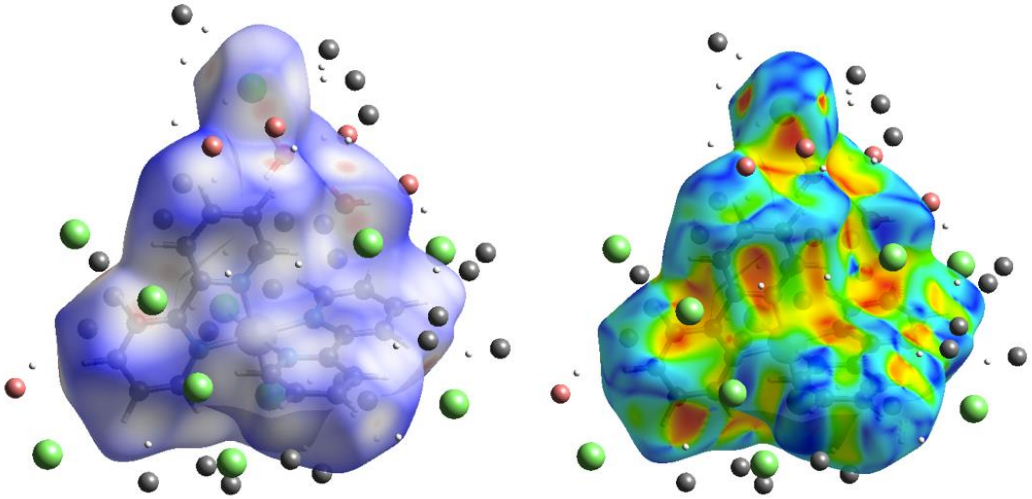

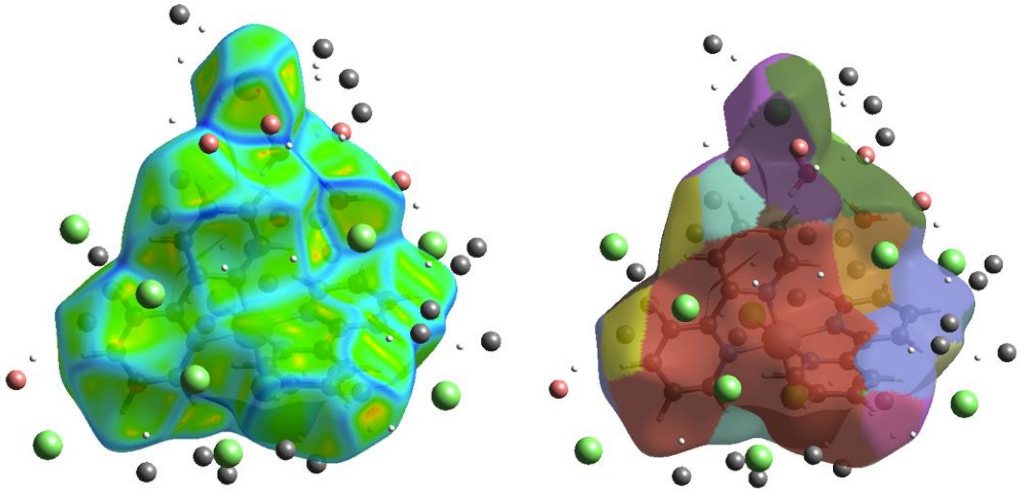

Figure 9.14 – Hirshfeld surfaces of $[Ir(bpy)_2Cl_2]Cl.2H_2O$ mapped with d_{norm} (**top left**), shape index (**top right**), curvedness (**bottom left**) and Fragment Patch (**bottom right**) for all intermolecular contacts present in the compound showing neighbouring contact atoms. Atom labelling is omitted for clarity.

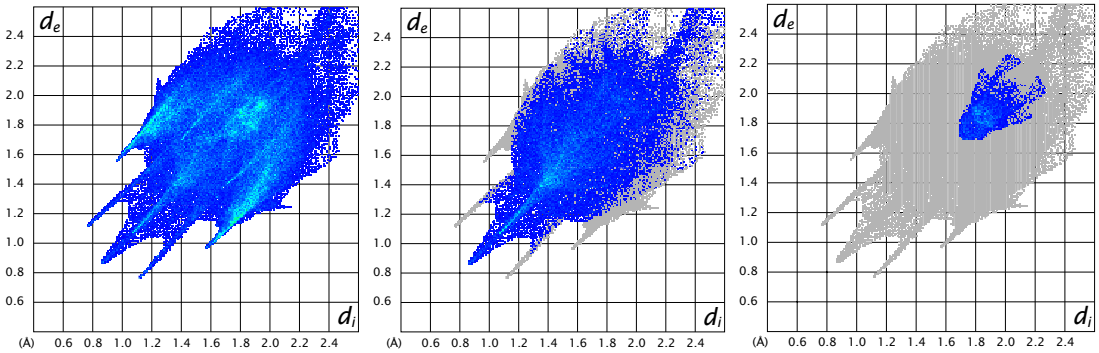

Figure 9.15 – 2D fingerprint plots of $[Ir(bpy)_2Cl_2]Cl.2H_2O$ for all interactions present in the compound (**left**) (surface covered = 100%), H•••H interactions (**middle**) (surface covered = 37.7%) and C•••C interactions (**right**) (surface covered = 4.4%) present in the compound.

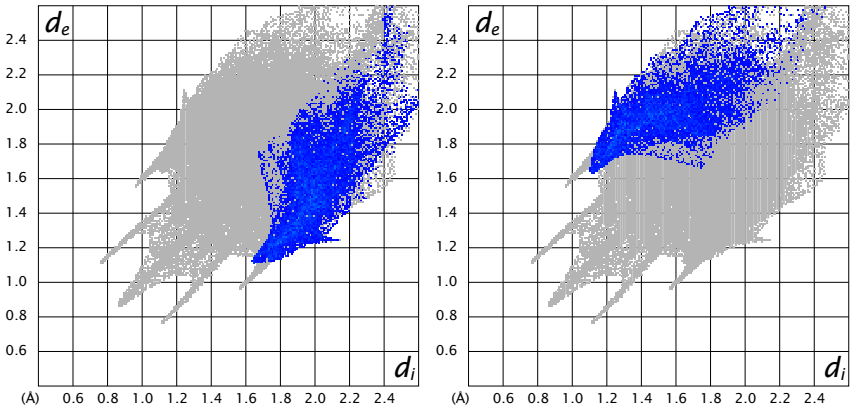

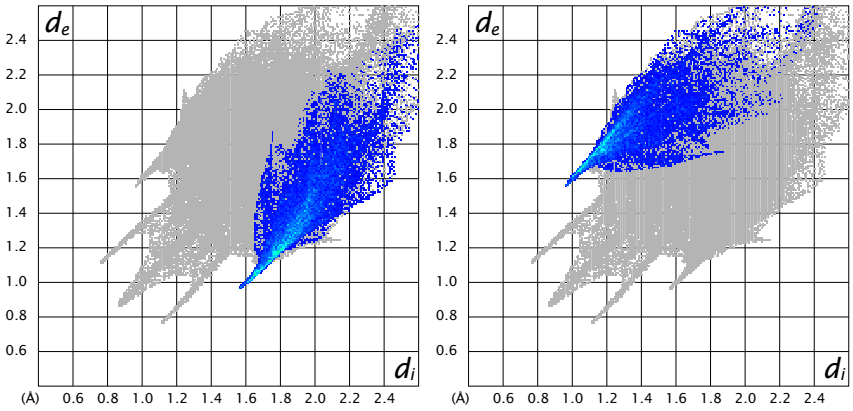

Figure 9.16 – 2D fingerprint plots of $[Ir(bpy)_2Cl_2]Cl.2H_2O$ for C•••H/H•••C interactions (surface covered = 10.3% and 8.7%) (**top left and top right**) and Cl•••H/H•••Cl interactions (surface covered = 15.8% and 11.7%) (**bottom left** and **bottom right**) present in the compound.

9.2.4 $[Ir(bpy)_2Cl_2]CF_3SO_3$

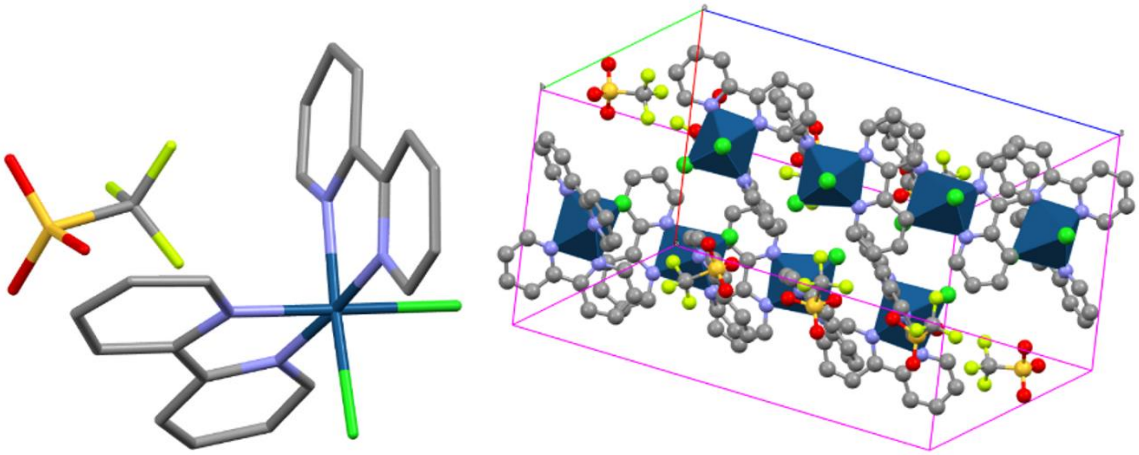

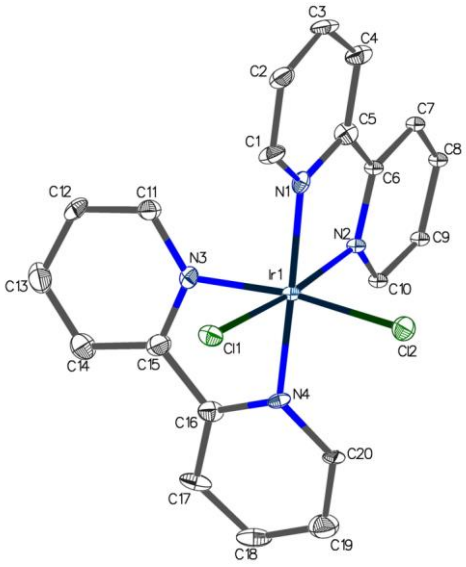

Figure 9.17 – Crystal structure of monoclinic $[Ir(bpy)_2Cl_2]CF_3SO_3$ (**top left**), its packing diagram with CF_3SO_3 counterions arrayed in the channels (**top right**), its ORTEP diagram showing atom labelling scheme drawn at 50% thermal probability (**bottom**). Atom labelling – blue: Ir; grey: C; purple: N; deep green: Cl; light green: F; red: O; yellow: S.

All other crystallographic data obtained for $[Ir(bpy)_2Cl_2]CF_3SO_3$ can be found in an appropriate section of this Appendix.

9.2.5 HSA for $[Ir(bpy)_2Cl_2]CF_3SO_3$

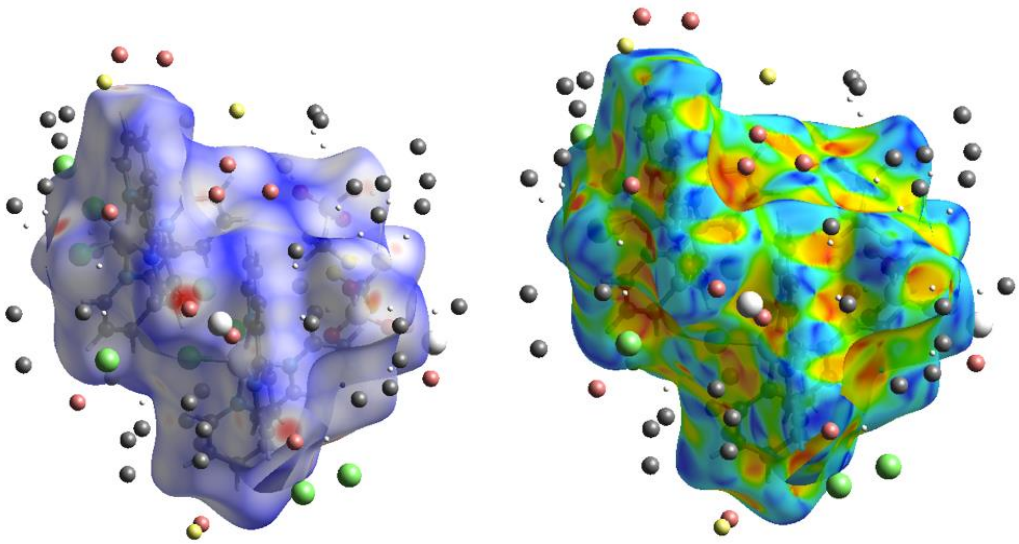

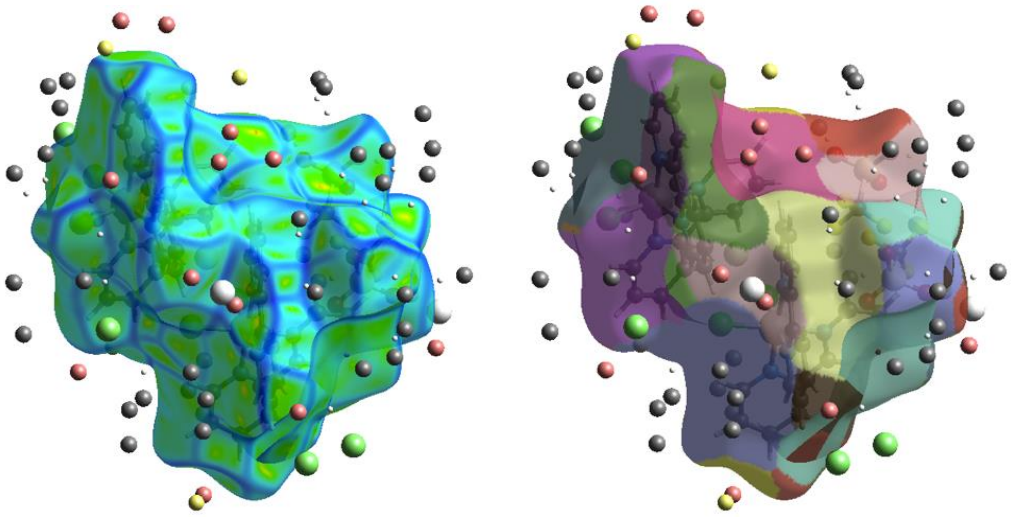

Figure 9.18 – Hirshfeld surfaces of $[Ir(bpy)_2Cl_2]CF_3SO_3$ mapped with d_{norm} (**top left**), shape index (**top right**), curvedness (**bottom left**) and Fragment Patch (**bottom right**) for all the bond types present in the compound.

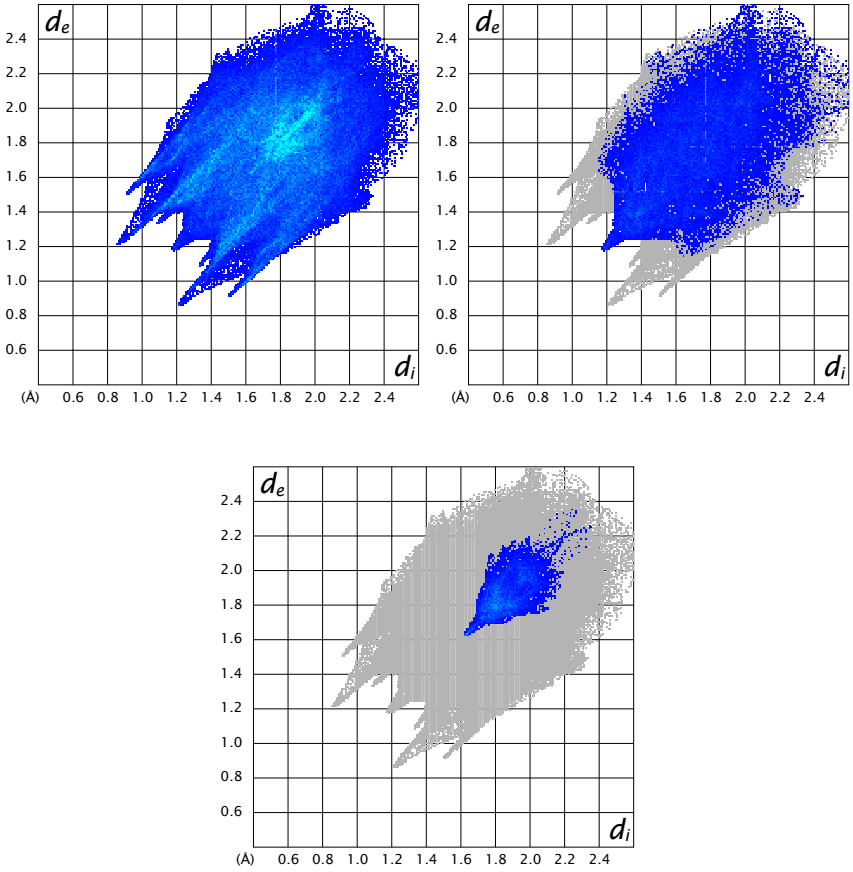

Figure 9.19 – 2D fingerprint plots of $[Ir(bpy)_2Cl_2]CF_3SO_3$ for all the interactions (surface covered = 100.0%) (**top left**), H•••H interactions (surface covered = 21.5%) (**top right**) and C•••C interactions (surface covered = 5.5%) (**bottom**) present in the compound.

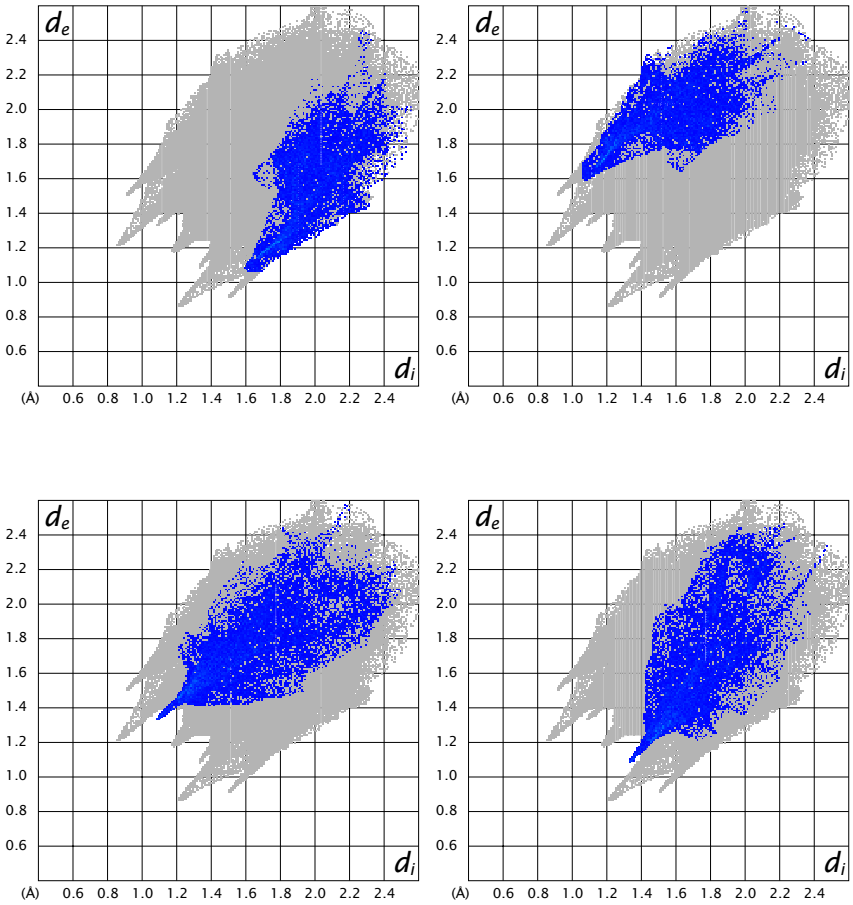

Figure 9.20 – 2D fingerprint plots of $[Ir(bpy)_2Cl_2]CF_3SO_3$ ligand for C•••H/H•••C interactions (surface covered = 6.1% and 5.7%) (**top left and top right**) and H•••F/F•••H interactions (surface covered = 7.3% and 7.3%) (**bottom left** and **bottom right**) present in the compound.

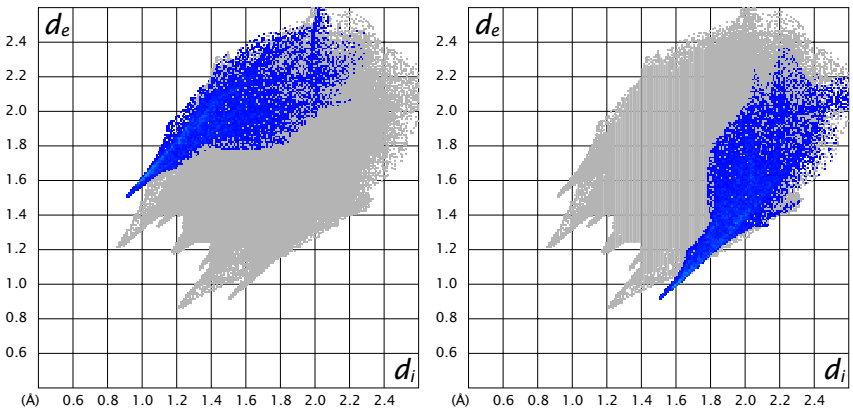

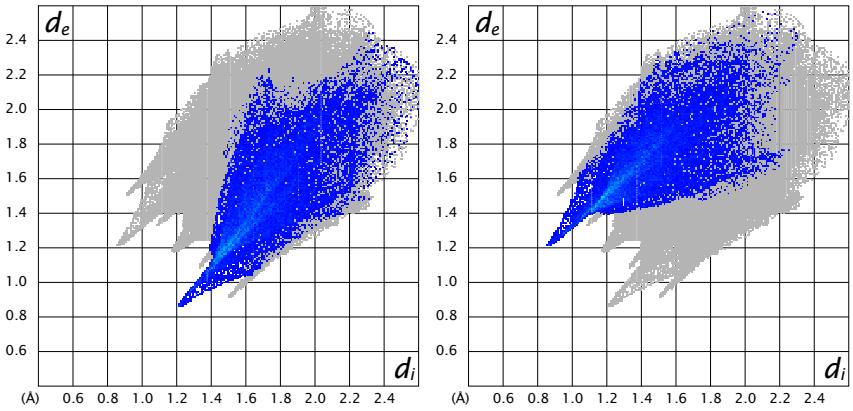

Figure 9.21 – 2D fingerprint plots of $[Ir(bpy)_2Cl_2]CF_3SO_3$ ligand for H•••Cl/Cl•••H interactions (surface covered = 6.4% and 7.6%) (**top left** and **top right**) and O•••H/H•••O interactions (surface covered = 13.2% and 11.8%) (**bottom left** and **bottom right**) present in the compound.

9.2.6 HSA for $[Ir(bpy)_2(CF_3SO_3)_2]CF_3SO_3$

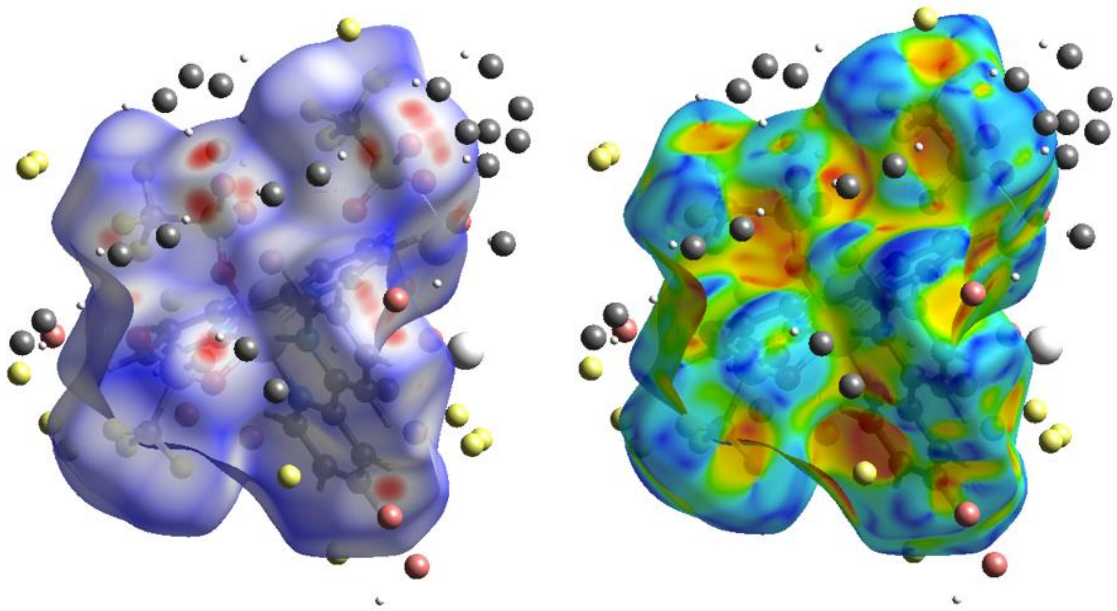

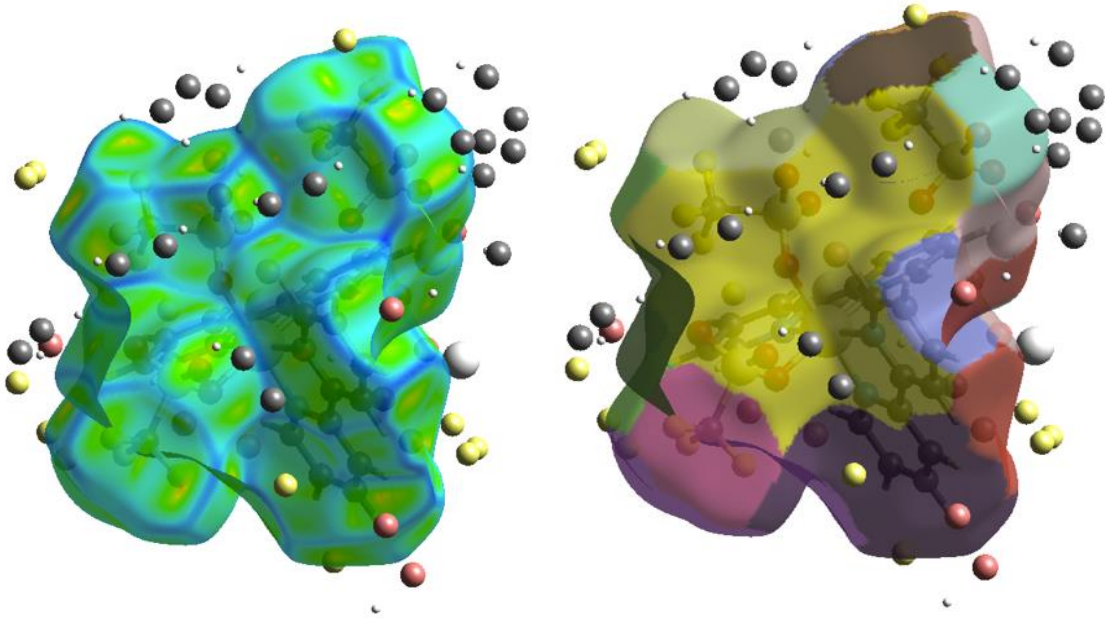

Figure 9.22 – Hirshfeld surfaces of $[Ir(bpy)_2(CF_3SO_3)_2]CF_3SO_3$ mapped with (**top left**), shape index (**top right**), curvedness (**bottom left**) and Fragment Patch (**bottom right**). Atom labelling is omitted for clarity.

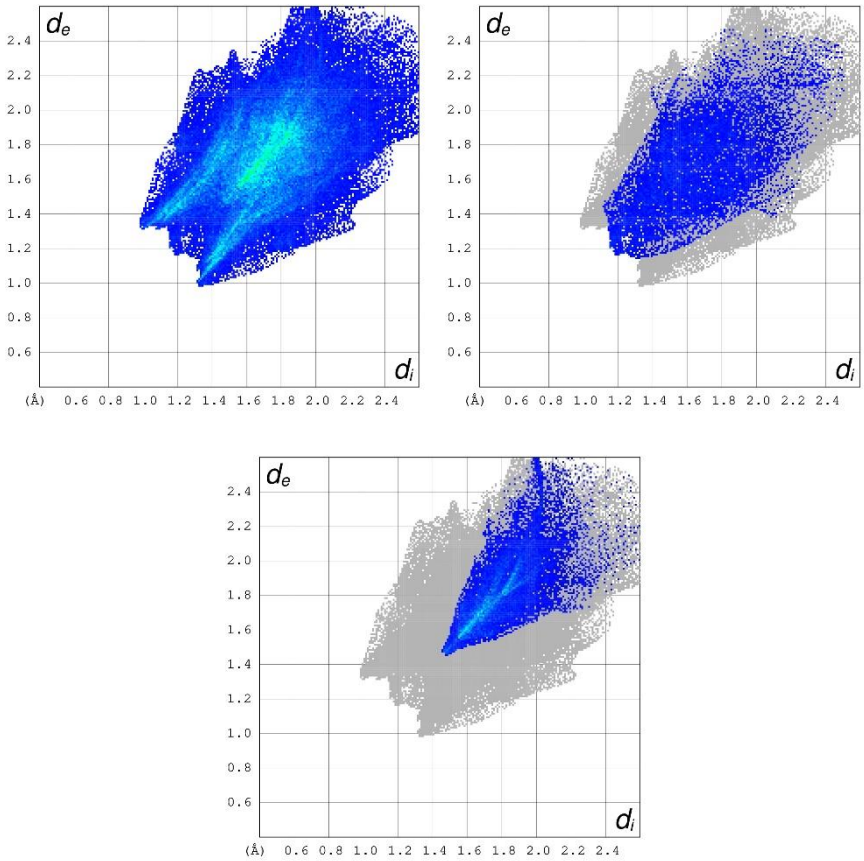

Figure 9.23 – 2D fingerprint plots of $[Ir(bpy)_2(CF_3SO_3)_2]CF_3SO_3$ for all interactions (surface covered = 100.0%) (**top left**), H•••H interactions (surface covered = 11.5%) (**top left**) and F•••F interactions (surface covered = 13.5%) (**bottom**) present in the compound.

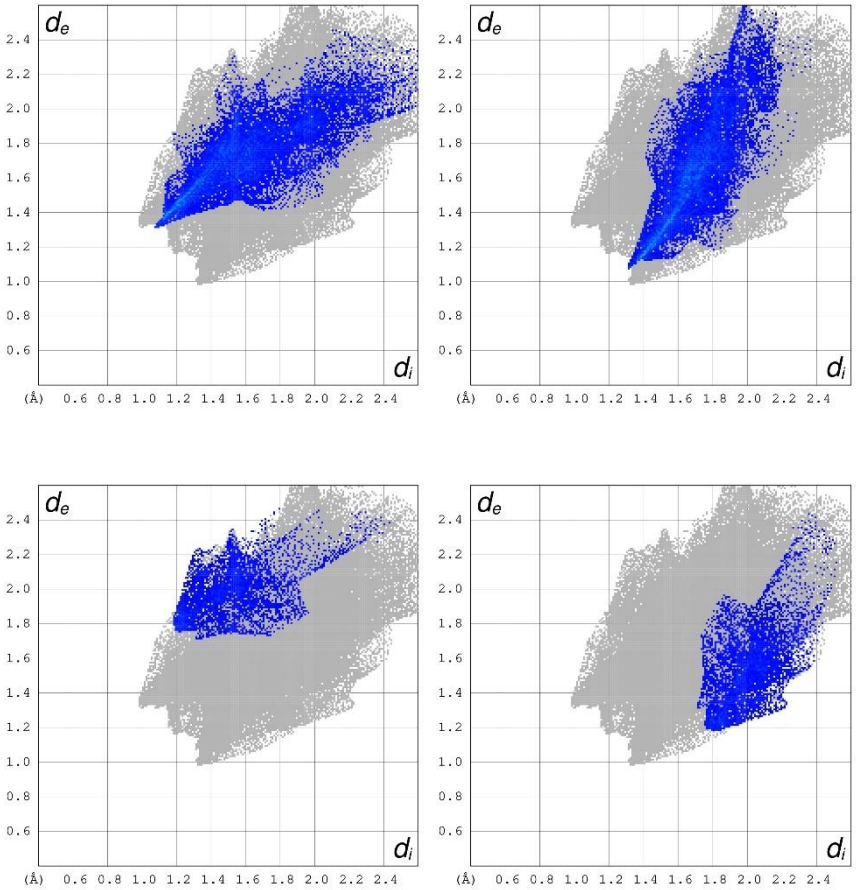

Figure 9.24 – 2D fingerprint plots of $[Ir(bpy)_2(CF_3SO_3)_2]CF_3SO_3$ for H•••F/F•••H interactions (surface covered = 12.8% and 13.3%) (**top left** and **top right**) and H•••C/C•••H interactions (surface covered = 3.4% and 4.2%) (**bottom left** and **bottom right**) present in the compound.

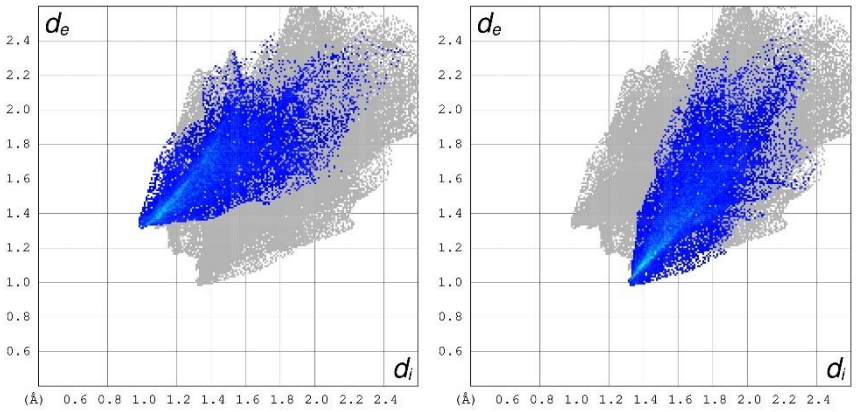

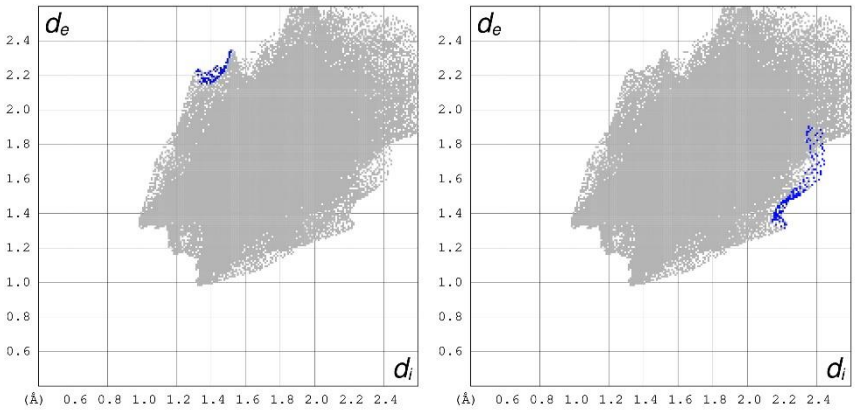

Figure 9.25 – 2D fingerprint plots of $[Ir(bpy)_2(CF_3SO_3)_2]CF_3SO_3$ for H•••O/O•••H interactions (surface covered = 13.4% and 14.4%) (**top left** and **top right**) and H•••N/N•••H interactions (surface covered = 0.1% and 0.1%) (**bottom left** and **bottom right**) present in the compound.

9.2.7 $[Ir(phen)_2Cl_2]PF_6$

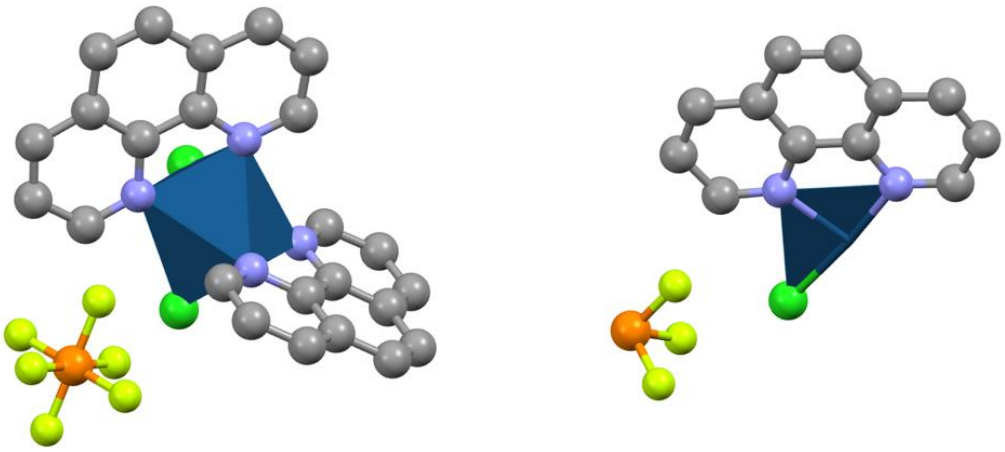

Figure 9.26 – left: crystal structure of $[Ir(phen)_2Cl_2]PF_6$; **right:** asymmetric unit of $[Ir(phen)_2Cl_2]PF_6$ showing PF_3 (i.e., the "half" of PF_6) arrayed in an "index finger-middle finger-ring finger" pattern. Atom labelling – blue: Ir; grey: C; purple: N; deep green: Cl; light green: F; orange: P. MeCN solvent molecules and hydrogen atoms have been removed for clarity.

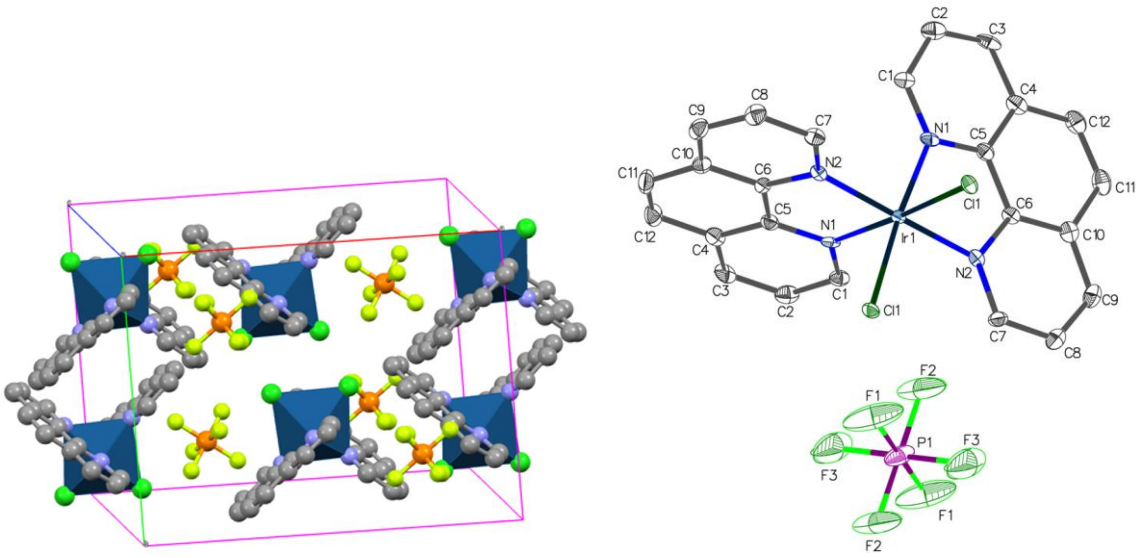

Figure 9.27 – Packing diagram of $[Ir(phen)_2Cl_2]PF_6$ showing layers of the compound with PF_6 counterion in channels between them (**left**) and the compound's ORTEP diagram with atom labelling showing 50% thermal ellipsoids (**right**). Atom labelling – blue: Ir; grey: C; purple: N; deep green: Cl; light green: F; orange: P.

All other crystallographic data obtained for $[Ir(phen)_2Cl_2]PF_6$ can be found in an appropriate section of this Appendix.

9.2.8 HSA for $[Ir(phen)_2Cl_2]PF_6$

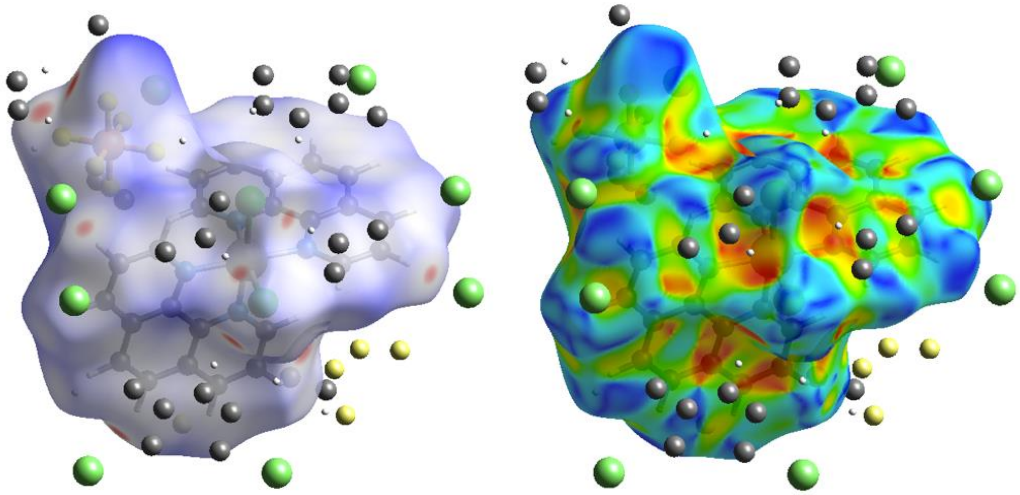

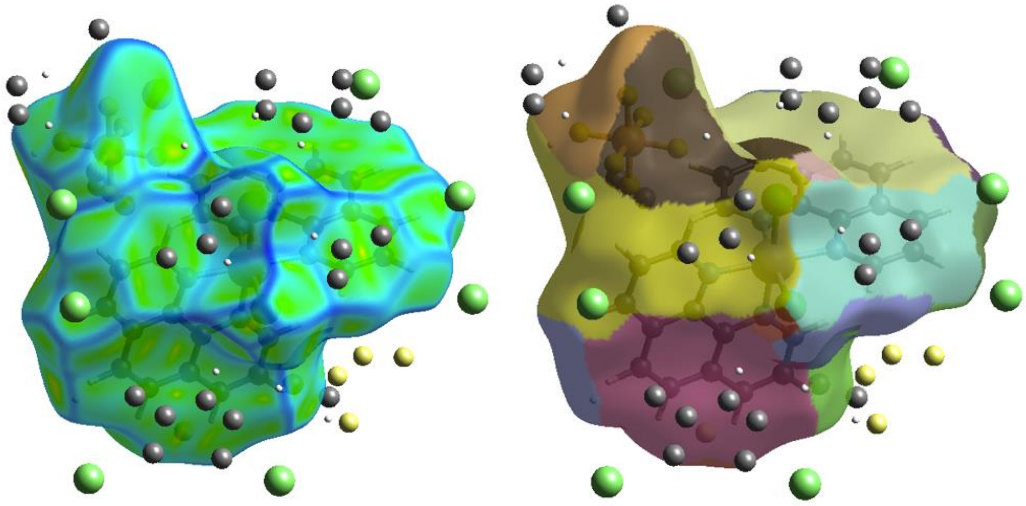

Figure 9.28 – Hirshfeld surfaces of $[Ir(phen)_2Cl_2]PF_6$ mapped with d_{norm} (**top left**), shape index (**top right**), curvedness (**bottom left**) and Fragment Patch (**bottom right**) for all the bond types present in the compound showing neighbouring contacts atoms.

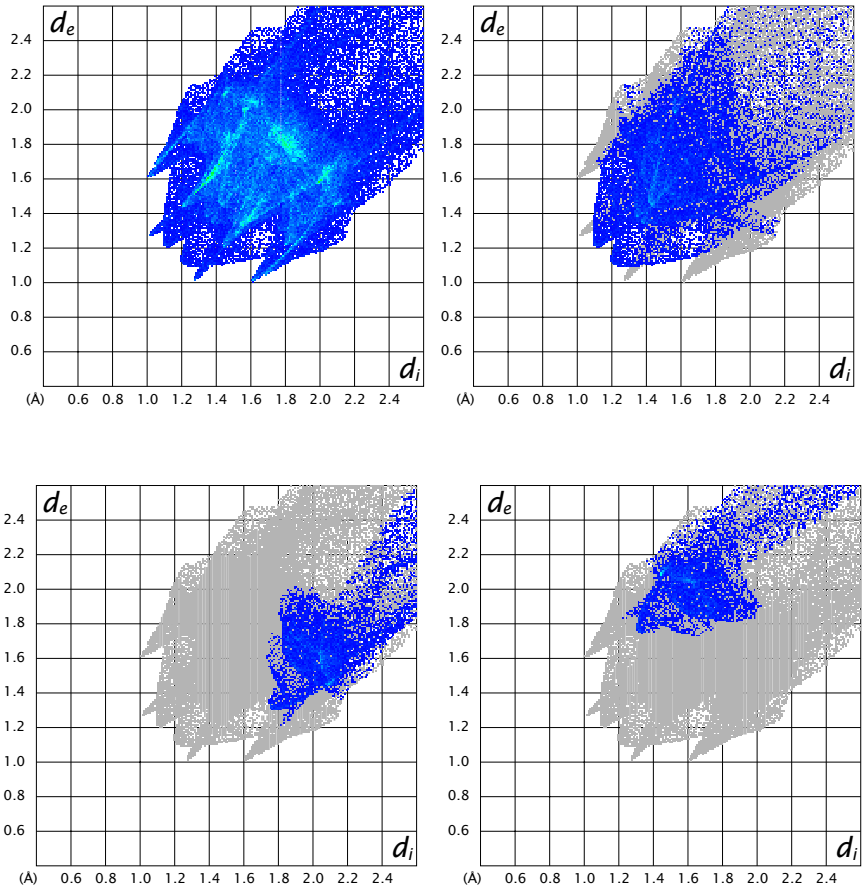

Figure 9.29 – 2D fingerprint plots of $[Ir(phen)_2Cl_2]PF_6$ for all the interactions (surface covered = 100.0%) (**top left**), H•••H interactions (surface covered = 20.9%) (**top right**) and C•••H/H•••C interactions (surface covered = 10.2% and 8.1%) (**bottom left** and **bottom right**) present in the compound.

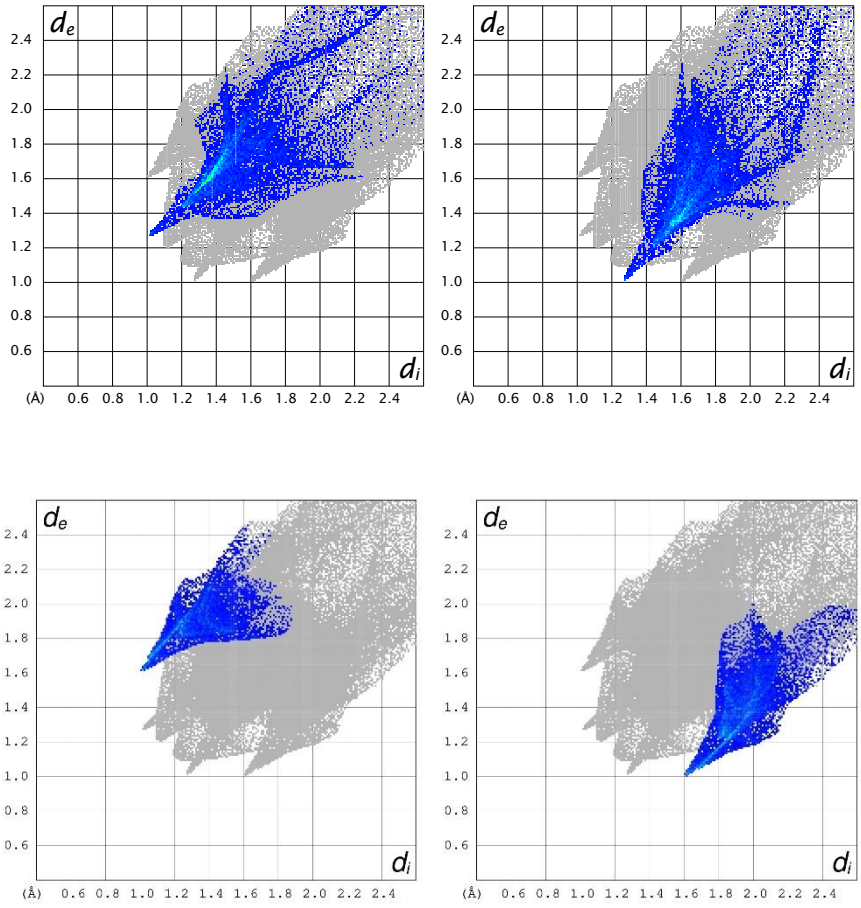

Figure 9.30 – 2D fingerprint plots of $[Ir(phen)_2Cl_2]PF_6$ ligand for H•••F/F•••H interactions (surface covered = 14.9% and 15.5%) (**top left** and **top right**) and H•••Cl/Cl•••H interactions (surface covered = 6.7% and 9.8%) (**bottom left** and **bottom right**) present in the compound.

9.2.9 $[Ir(phen)_2Cl_2]CF_3SO_3$

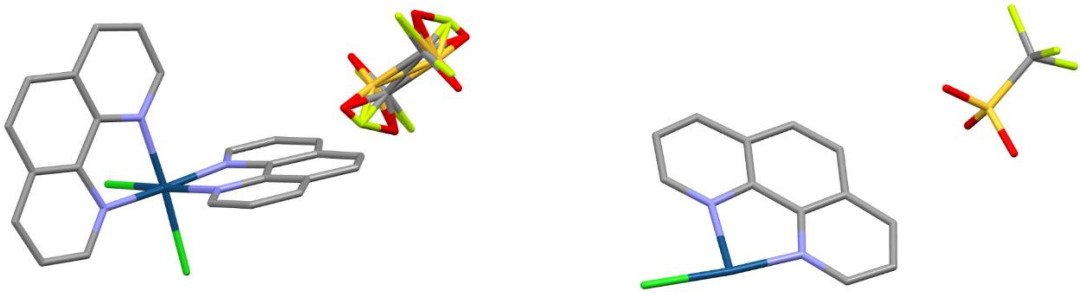

Figure 9.31 – Crystal structure of $[Ir(phen)_2Cl_2]CF_3SO_3$ indicating some disorder in the triflate counterion (**left**) and the asymmetric unit of the compound (**right**). Hydrogen atoms are omitted for clarity. Atom labelling – blue: Ir; grey: C; purple: N; red: O; light green: F; deep green: Cl; yellow: S.

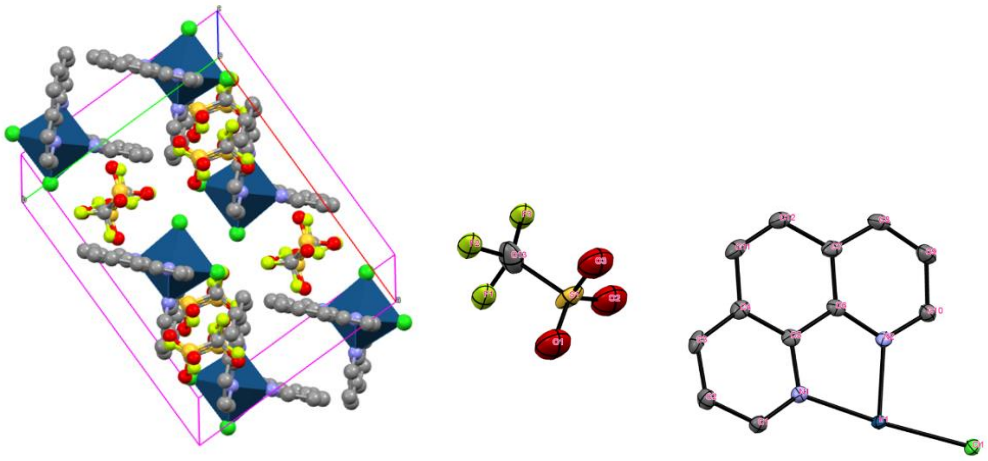

Figure 9.32 – Unit cell packing diagram of $[Ir(phen)_2Cl_2]CF_3SO_3$ and the ORTEP diagram (**left**) of the compound with atom labelling scheme for its asymmetric unit drawn at 50% thermal ellipsoids (**right**). Hydrogen atoms are omitted for clarity.

The HSA could not be obtained for the compound since it has fractional occupancies, meaning it is disordered. All other crystallographic data obtained for the $[Ir(phen)_2Cl_2]CF_3SO_3\ CH_3NO_2$ can be found in an appropriate section of this Appendix.

9.2.10 HSA for $[Ir(dppz)_2Cl_2]PF_6$

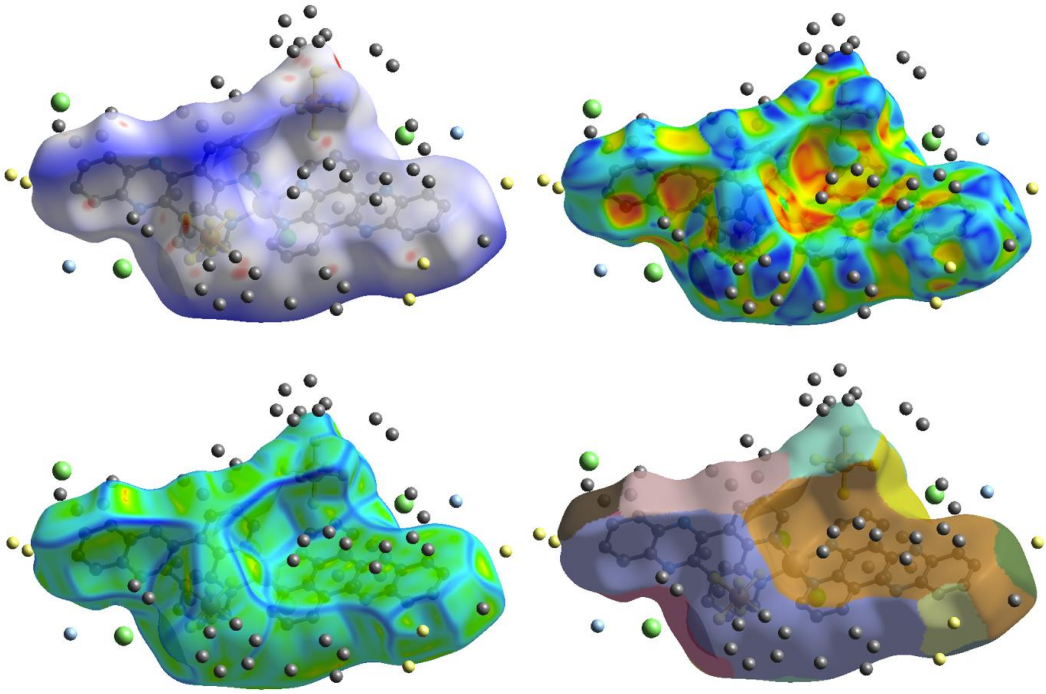

Figure 9.33 – Hirshfeld surfaces of $[Ir(dppz)_2Cl_2]PF_6$ mapped with d_{norm} (**top left**), shape index (**top right**), curvedness (**bottom left**) and Fragment Patch (**bottom right**) for all intermolecular contacts present in the compound. Atom labelling is omitted for clarity.

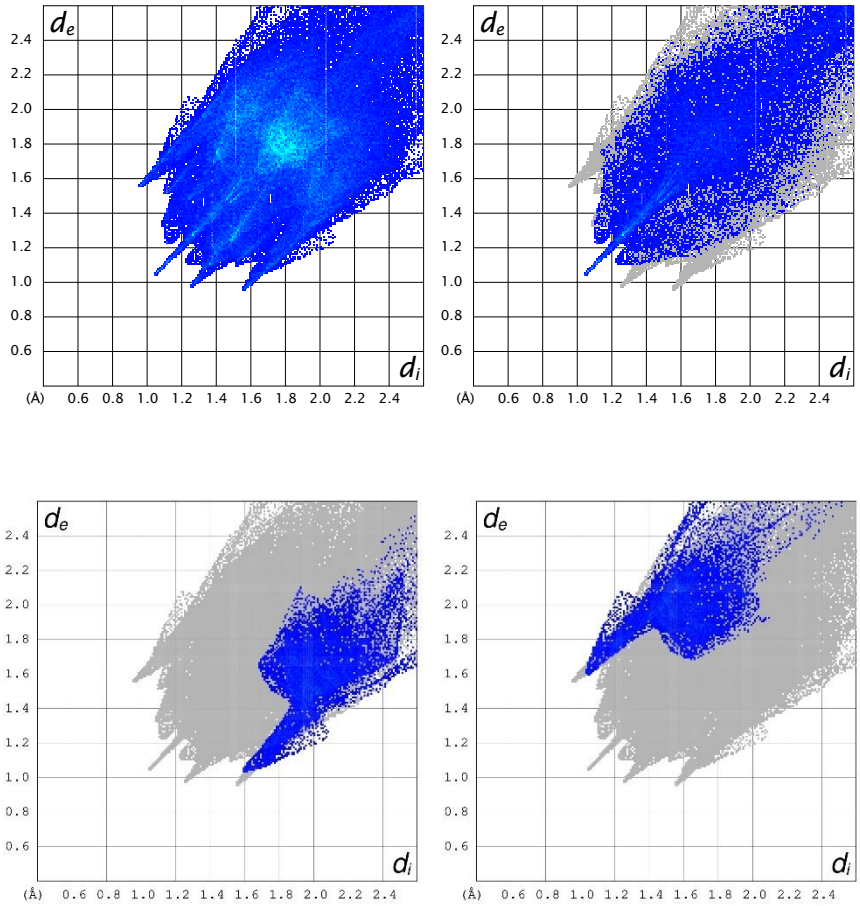

Figure 9.34 – 2D fingerprint plots of $[Ir(dppz)_2Cl_2]PF_6$ for all interactions (surface covered = 100.0%) (**top left**), H•••H interactions (surface covered = 27.8%) (**top right**) and H•••N/N•••H interactions (surface covered = 3.2% and 3.7%) (**bottom left** and **bottom right**) present in the compound.

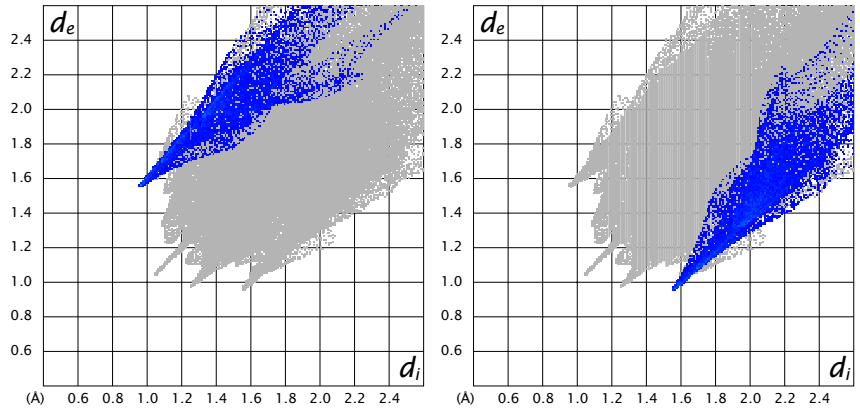

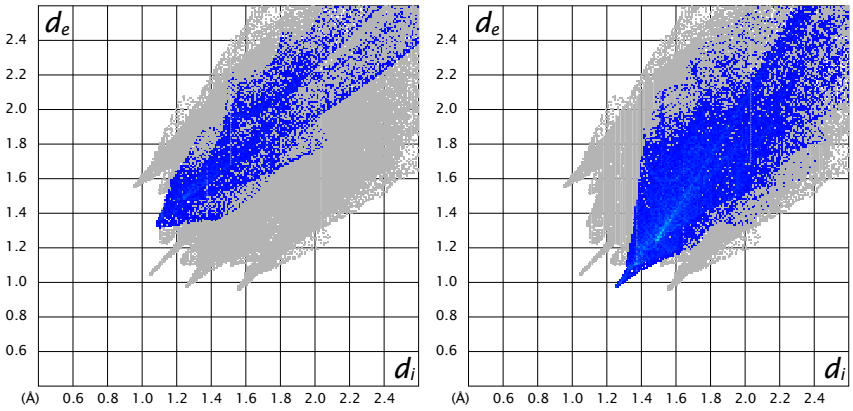

Figure 9.35 – 2D fingerprint plots of $[Ir(dppz)_2Cl_2]PF_6$ for C•••H/H•••C interactions (surface covered = 10.0% and 7.1%) (**top left** and **top right**) and H•••F/F•••H interactions (surface covered = 5.0% and 17%) (**bottom left** and **bottom right**) present in the compound.

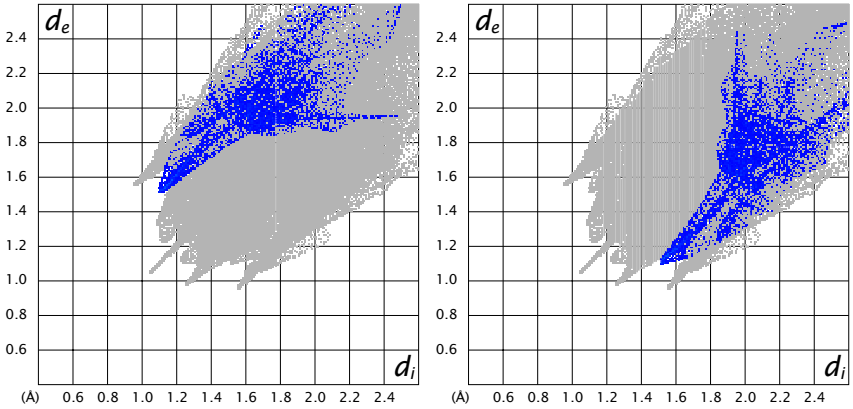

Figure 9.36 – 2D fingerprint plots of $[Ir(dppz)_2Cl_2]PF_6$ for H•••N/N•••H interactions (surface covered = 3.2% and 3.7%) present in the compound.

9.2.11 HSA for $[Ir(dppz)_2(CF_3SO_3)_2]CF_3SO_3$

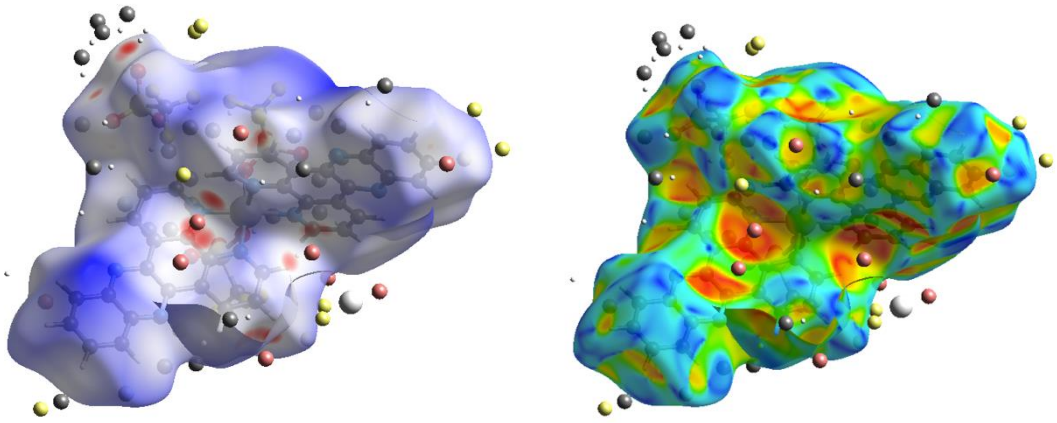

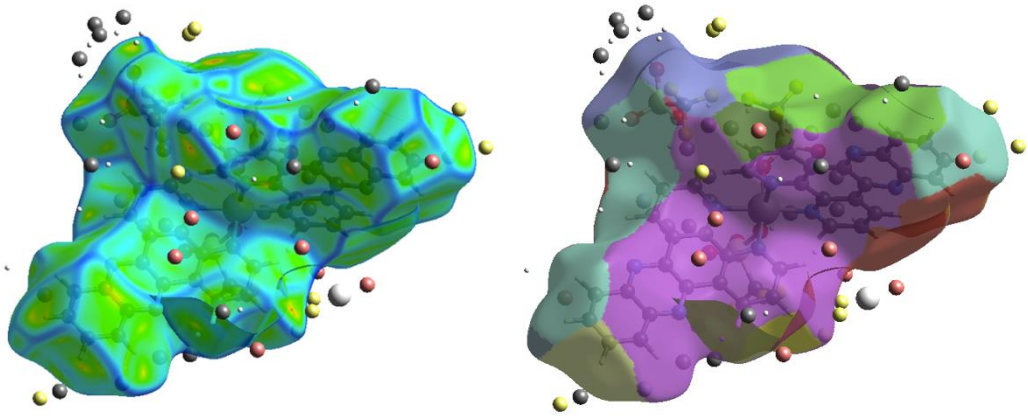

Figure 9.37 – Hirshfeld surfaces of $[Ir(dppz)_2(CF_3SO_3)_2]CF_3SO_3$ mapped with d_{norm} (**top left**), shape index (**top right**), curvedness (**bottom left**) and Fragment Patch (**bottom right**) for all the interactions showing neighbouring contact atoms.

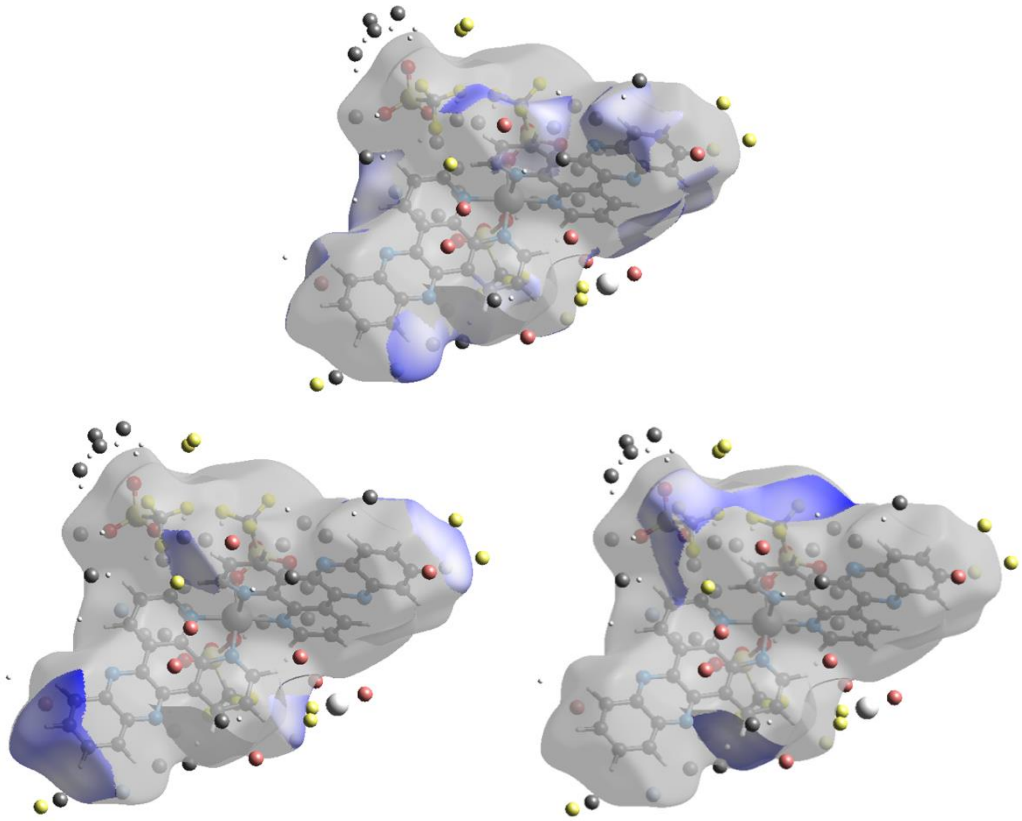

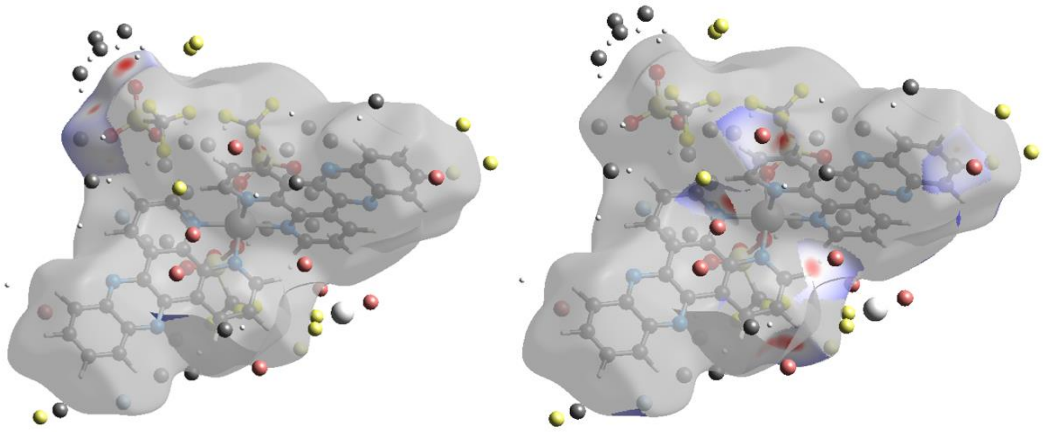

Figure 9.38 – Hirshfeld surfaces of $[Ir(dppz)_2(CF_3SO_3)_2]CF_3SO_3$ mapped with d_{norm} for H•••H interactions (**top**), H•••F/F•••H interactions (**middle**), and O•••H/H•••O interactions (**bottom**) showing neighbouring contact atoms.

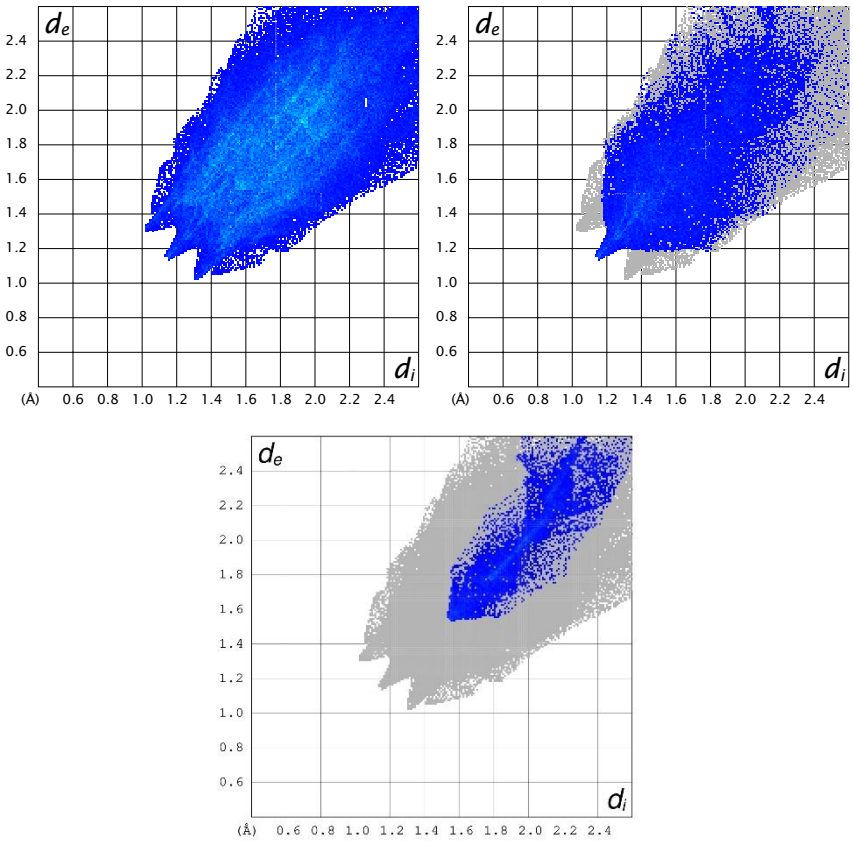

Figure 9.39 – 2D fingerprint plots of $[Ir(dppz)_2(CF_3SO_3)_2]CF_3SO_3$ for all the interactions (surface covered = 100.0%) (**top left**), H•••H interactions (surface covered = 18.9.0%) (**top right**) and F•••F interactions (surface covered = 5.3%) (**bottom**) present in the compound.

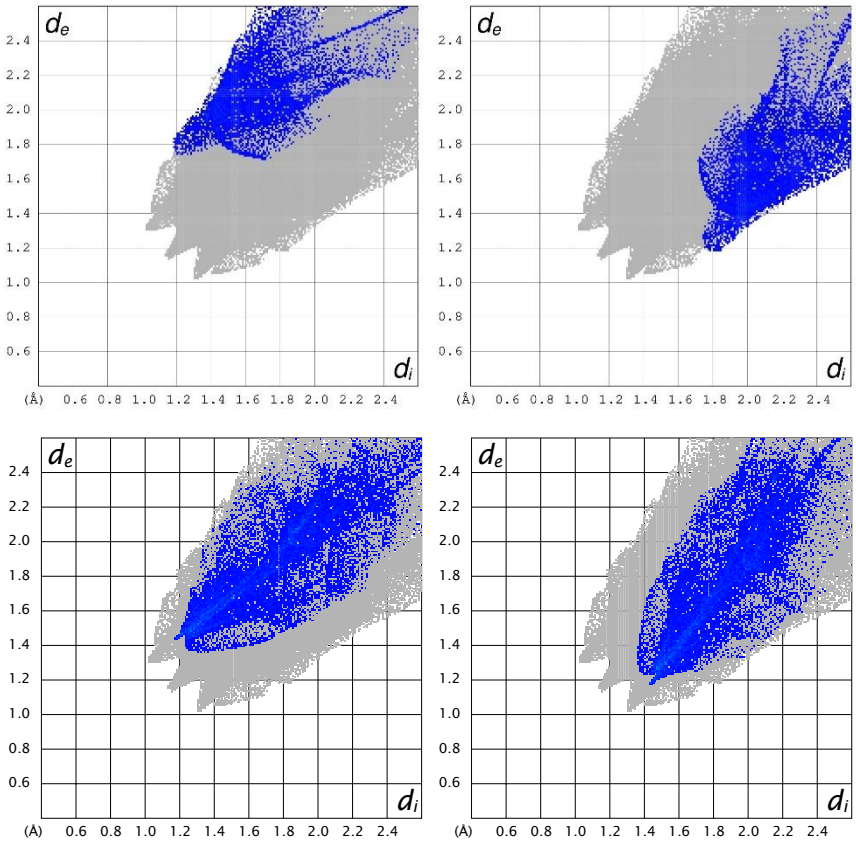

Figure 9.40 – 2D fingerprint plots of $[Ir(dppz)_2(CF_3SO_3)_2]CF_3SO_3$ for H•••C/C•••H interactions (surface covered = 4.0% and 5.4%) (**top**) and H•••F/F•••H interactions (surface covered = 10.1% and 10.2) (**bottom left** and **bottom right**) present in the compound.

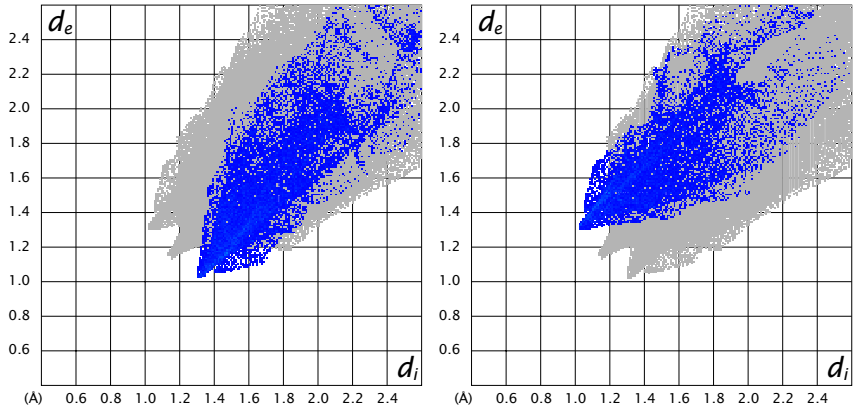

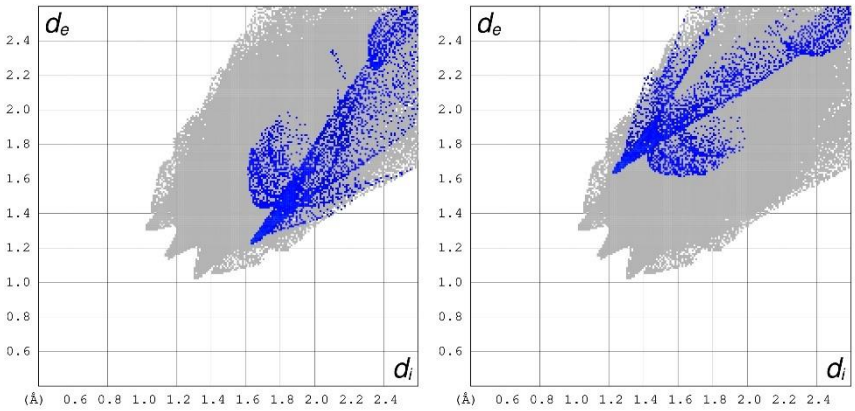

Figure 9.41 – 2D fingerprint plots of $[Ir(dppz)_2(CF_3SO_3)_2]CF_3SO_3$ for O•••H/H•••O interactions (surface covered = 8.2% and 7.0%) (**top**) and N•••H/H•••N interactions (surface covered = 2.7% and 2.2%) (**bottom**) present in the compound.

9.2.12 Crystal Structure Summary of $[Ir(phen)_2Cl(CH_3CN)](CF_3SO_3)_2CH_3NO_2$, - The first Adventitious Discovery

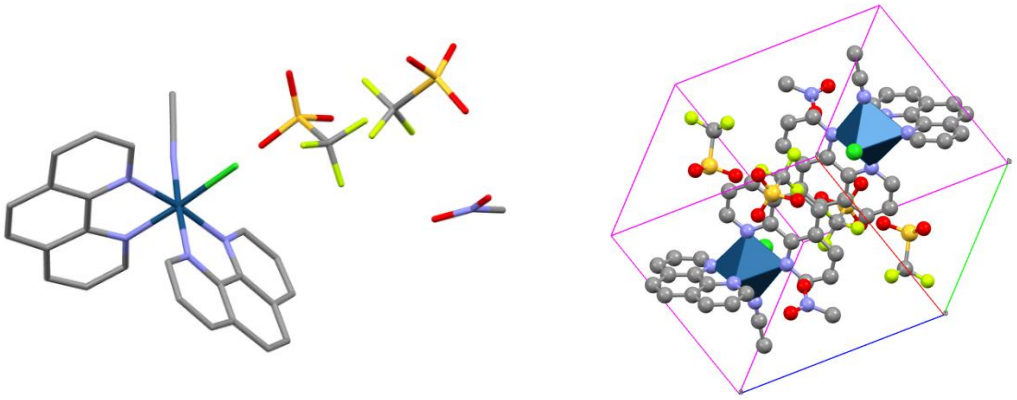

Figure 9.42 – Crystal structure of triclinic $[Ir(phen)_2Cl(CH_3CN)](CF_3SO_3)_2CH_3NO_2$ (**left**) and its packing diagram with CF_3SO_3 counterions arrayed both in the channels and along the diagonals (**right**). Z = 2. Unit cell parameters: α/° = 88.414(2); β/° = 76.882(2); γ/° = 72.523(2). Space group = P-1. Final R indexes [I>=2σ (I)] value = 0.0597. Atom labelling – blue: Ir; grey: C; purple: N; deep green: Cl; light green: F; yellow: S; red: O.

All other crystallographic data obtained for the $[Ir(phen)_2Cl(CH_3CN)](CF_3SO_3)_2CH_3NO_2$ can be found in an appropriate section of this Appendix.

9.2.13 HSA for $[Ir(phen)_2Cl(CH_3CN)](CF_3SO_3)_2CH_3NO_2$

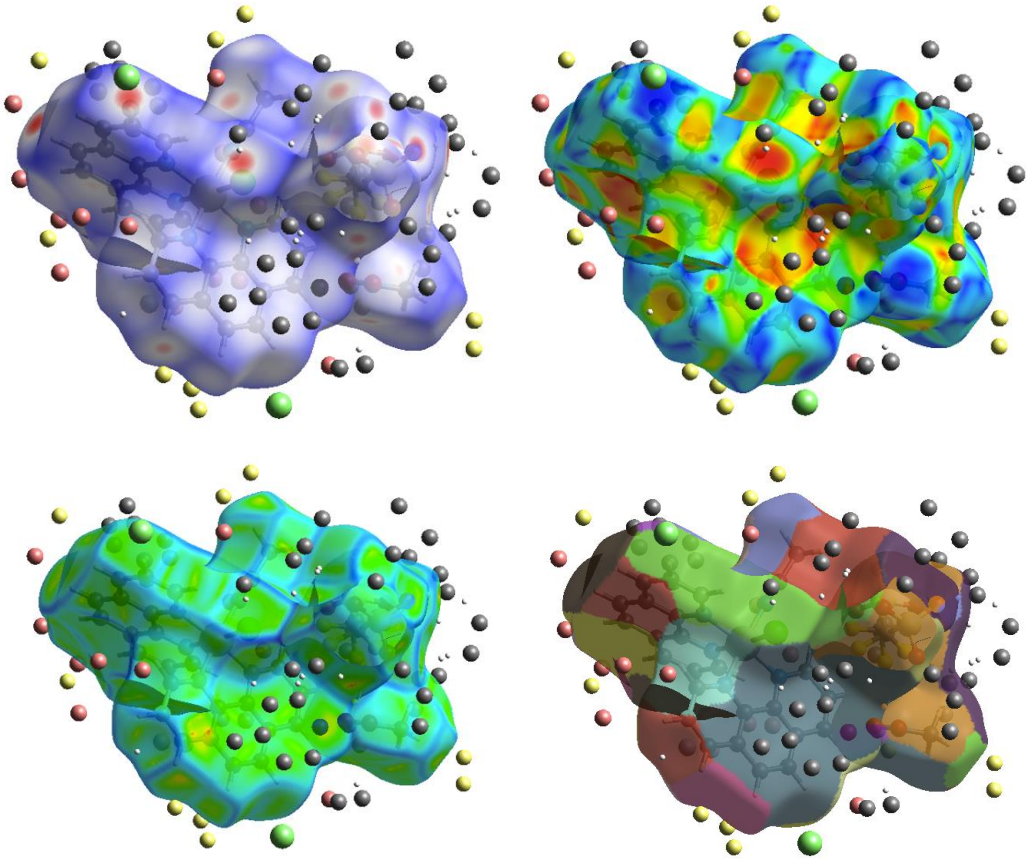

Figure 9.43 – Hirshfeld surfaces of $[Ir(phen)_2Cl(CH_3CN)](CF_3SO_3)_2CH_3NO_2$ mapped with d_{norm} (**top left**), shape index (**top right**), curvedness (**bottom left**) and Fragment Patch (**bottom right**) for all intermolecular contacts present in the compound showing neighbouring contacts atoms. Atom labelling is omitted for clarity.

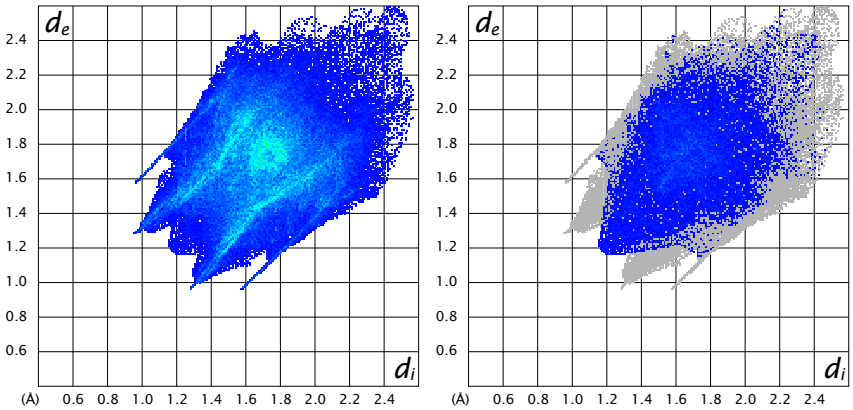

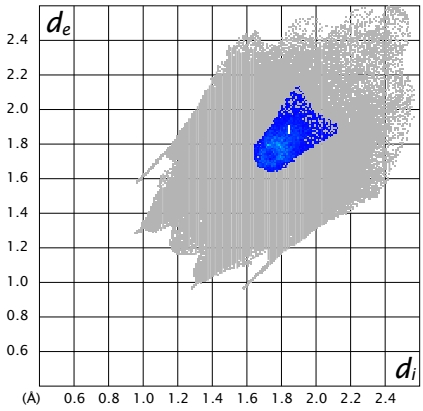

Figure 9.44 – 2D fingerprint plots of $[Ir(phen)_2Cl(CH_3CN)](CF_3SO_3)_2CH_3NO_2$ for all interactions (surface covered = 100.0%) (**top left**), H•••H interactions (surface covered = 15.8%) (**top right**) present in the compound, and C•••C interactions (surface covered = 3.7%) (**bottom**) present in the compound.

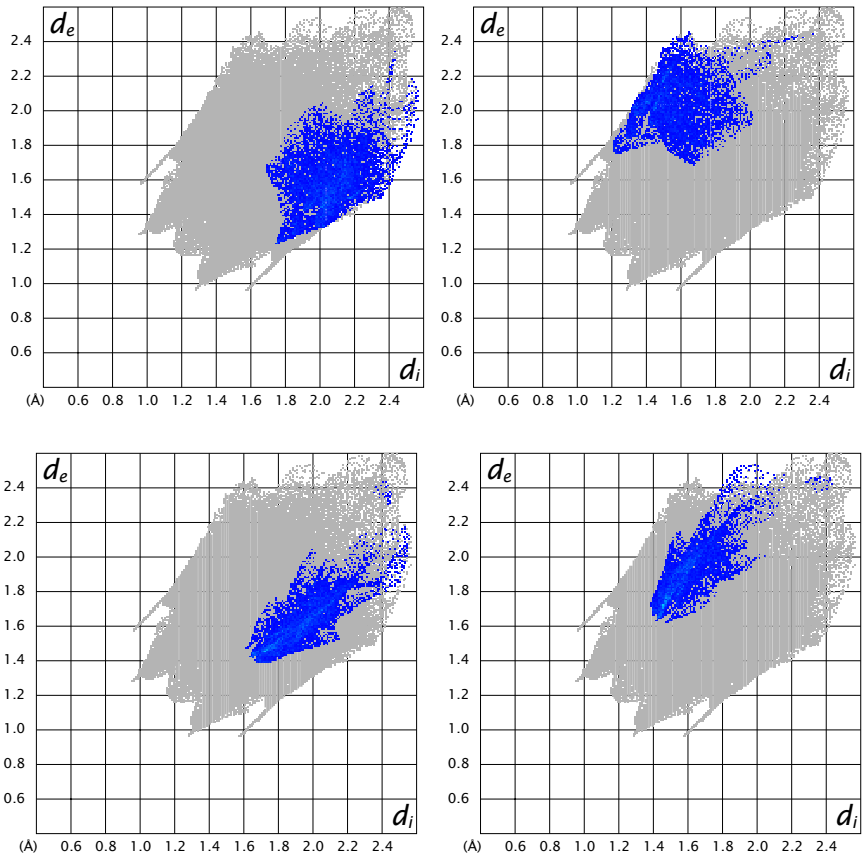

Figure 9.45 – 2D fingerprint plots of $[Ir(phen)_2Cl(CH_3CN)](CF_3SO_3)_2CH_3NO_2$ for C•••H/H•••C interactions (surface covered = 6.1% and 4.6%) (**top**) and C•••O/O•••C interactions (surface covered = 4.6% and 4.0%) (**bottom**) present in the compound.

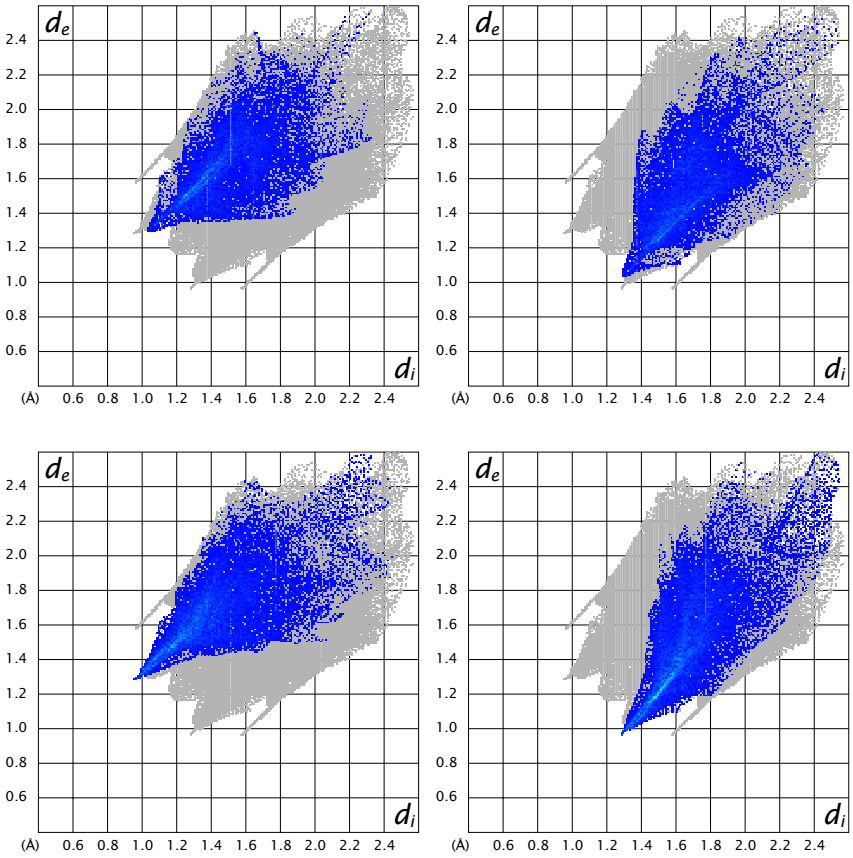

Figure 9.46 – 2D fingerprint plots of $[Ir(phen)_2Cl(CH_3CN)](CF_3SO_3)_2CH_3NO_2$ for H•••F/F•••H (surface covered = 10.5% and 11.0%) (**top**) and H•••O/O•••H (surface covered = 13.4% and 15.1%) (**bottom**) interactions present in the compound.

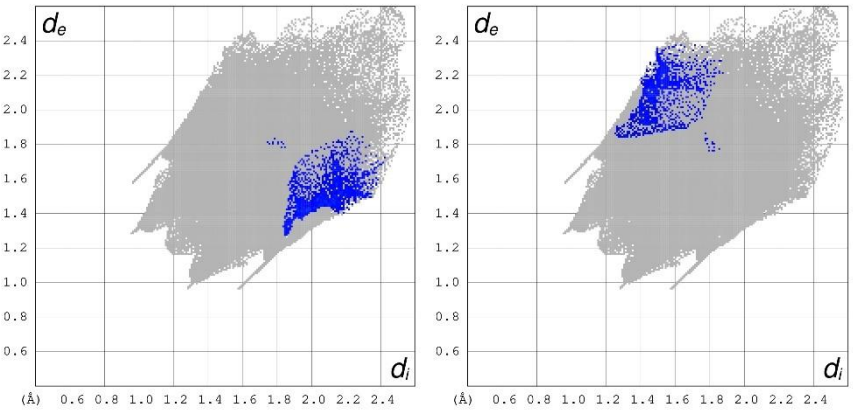

Figure 9.47 – 2D fingerprint plots of $[Ir(phen)_2Cl(CH_3CN)](CF_3SO_3)_2CH_3NO_2$ for N•••H/H•••N interactions (surface covered = 2.7% and 2.2%) present in the compound.

9.2.14 Crystal Structure Summary of $[Ir(bpy)_2Cl_2]CH_3OH$ - The Second Adventitious Discovery

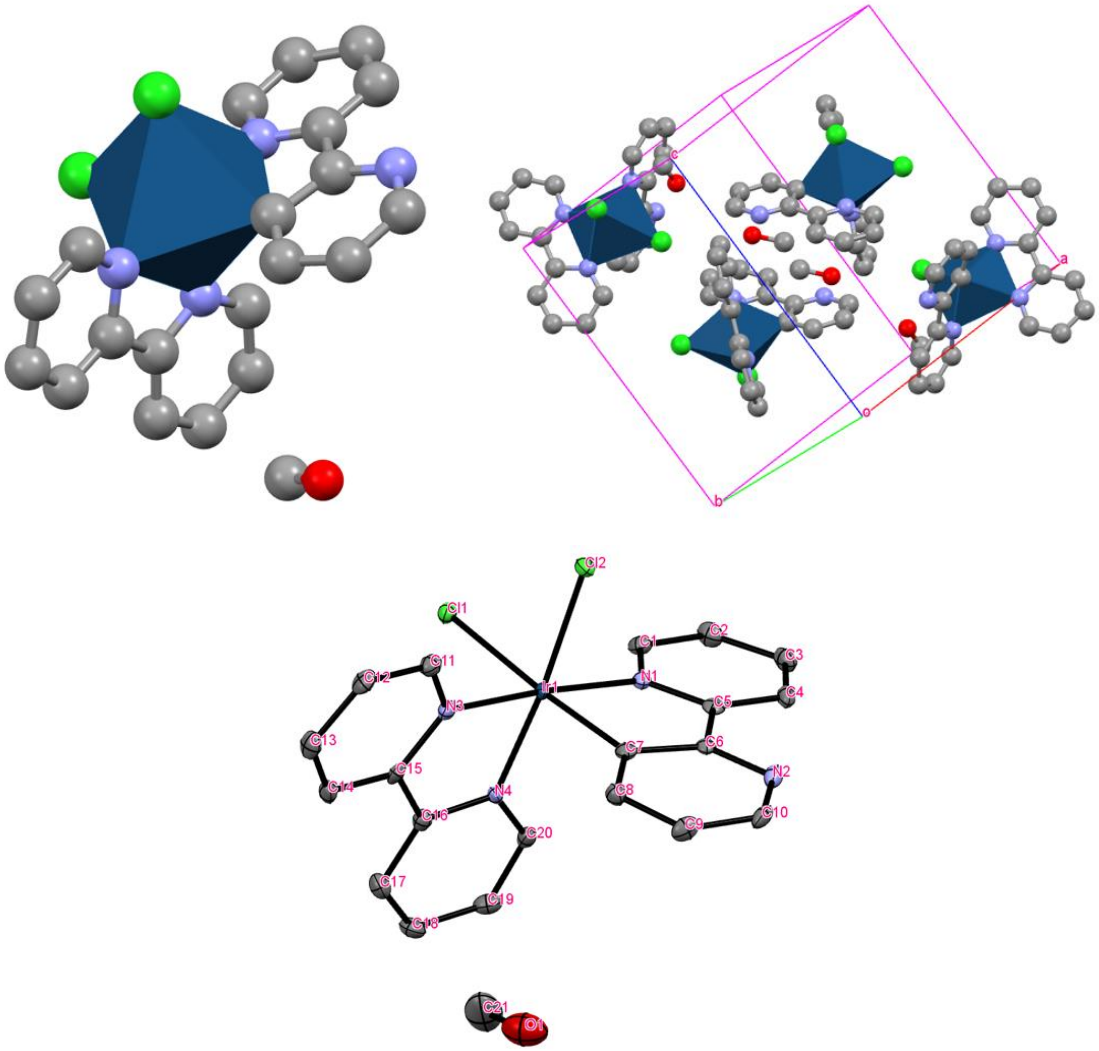

Figure 9.48 – Crystal structure of monoclinic $[Ir(bpy)_2Cl_2]CH_3OH$ co-crystallised with a molecule of CH_3OH (**top left**), its unit cell packing structure (**top right**), and its ORTEP diagram with atom labelling scheme showing 50% thermal ellipsoids (**bottom**). Colour scheme – blue: Ir; grey: C; purple: N; light green: Cl: red: O. Space group = $P2_1/c$. Final R indexes [I>=2σ (I)] value = 0.0402. Unit cell parameters: α/° = 90; β/° = 92.707(2); γ/° = 90. Z = 4.

An unanticipated compound crystallised as $[Ir(bpy)_2Cl_2]CH_3OH$ from crude, impure $[Ir(bpy)_2(qtpy)]Cl_3$ in methanolic solution. The full crystal structure shows that the title complex comprises one Ir(III) atom, two bpy ligands, two chloride ligands, and one methanol molecule. It is believed that the bpy ligands are coordinating through the methanol molecule

through an activated C–H bond. Since the compound's Z value equals 4, it has four molecules of itself in the unit cell, and besides, the asymmetric unit is for the full complex.

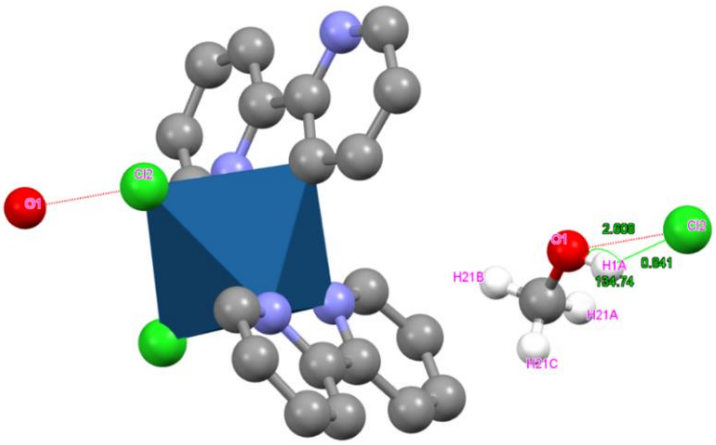

Figure 9.49 – Structure of $[Ir(bpy)_2Cl_2]CH_3OH$ showing hydrogen bonding O1–H1A•••$Cl2^1$ interaction in the compound and the length of such interaction. The bond angle of H_2O in the CH_3OH molecule in the compound is also presented. **NB:** $[Ir(bpy)_2Cl_2]CH_3OH$ is a hydrate, and a hydrate by definition is a crystal that contains at least one hydrogen bond donor group like OH, NH, or SH.

Hydrogen bonding O1–H1A•••$Cl2^1$ and π- π stacking interactions in the compound are responsible for the formation and strengthening of the compound's molecular assembly. The bond angle of H_2O molecule (109.43°) present in $[Ir(bpy)_2Cl_2]CH_3OH$ is slightly higher than the ideal bond angle of H_2O (104.5°).

Table 9.9 – Hydrogen Bonds for $[Ir(bpy)_2Cl_2]CH_3OH$.

D	H	A	d(D-H)/Å	d(H-A)/Å	d(D-A)/Å	D-H-A/°
O1	H1A	$Cl2^1$	0.84	2.61	3.255(4)	134.8

All other crystallographic data obtained for the $[Ir(bpy)_2Cl_2]CH_3OH$ can be found in an appropriate section of this Appendix.

9.2.15 HSA for $[Ir(bpy)_2Cl_2]CH_3OH$

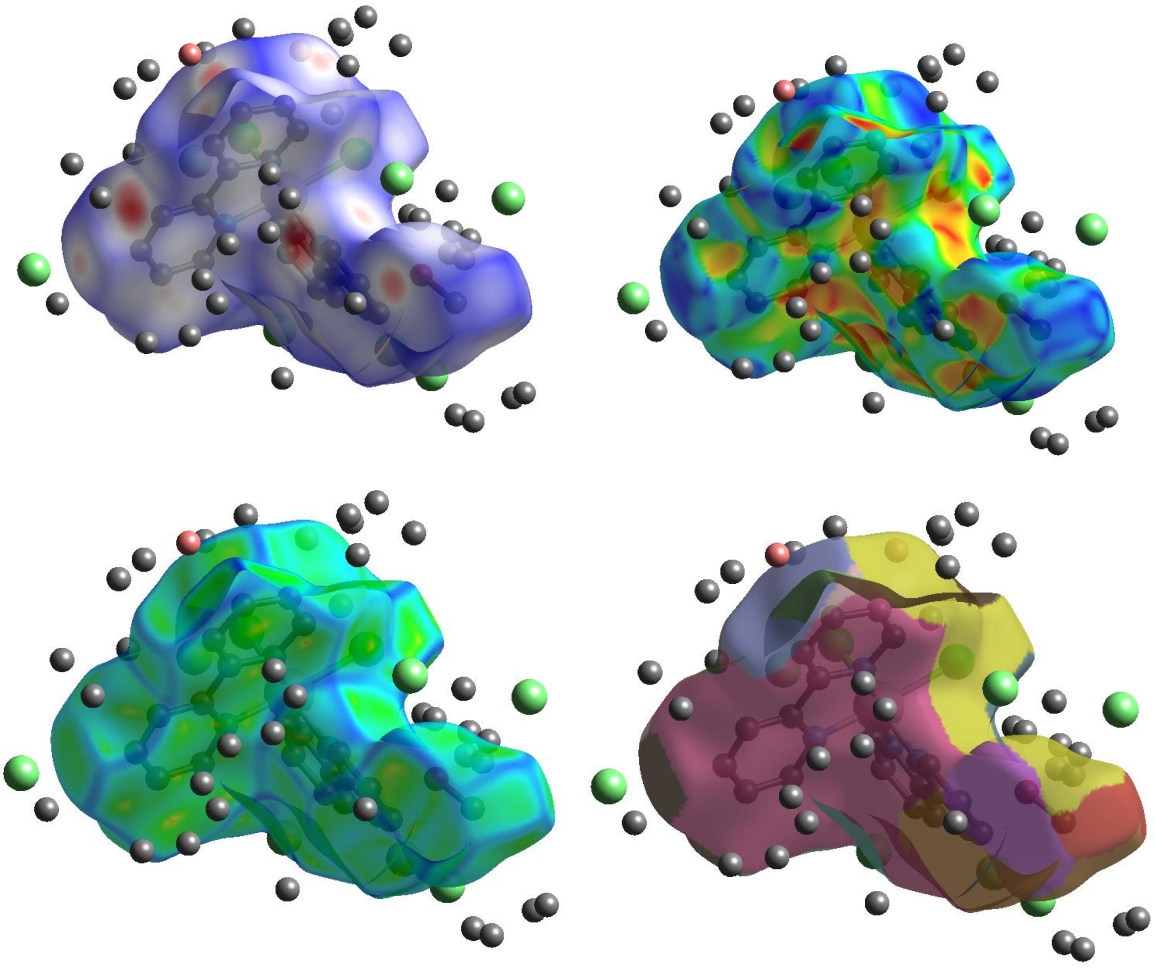

Figure 9.50 – Hirshfeld surfaces of $[Ir(bpy)_2Cl_2]CH_3OH$ mapped with d_{norm} (**top left**), shape index (**top right**), curvedness (**bottom left**) and Fragment Patch (**bottom right**) for all intermolecular contacts present in the compound showing neighbouring contacts atoms. Atom labelling is omitted for clarity.

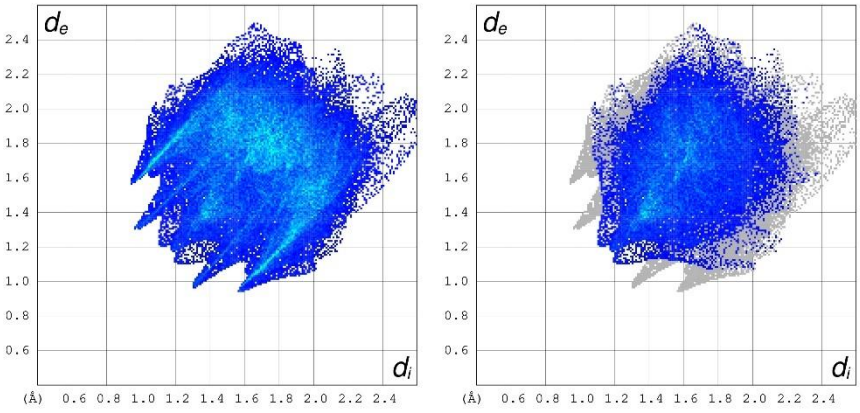

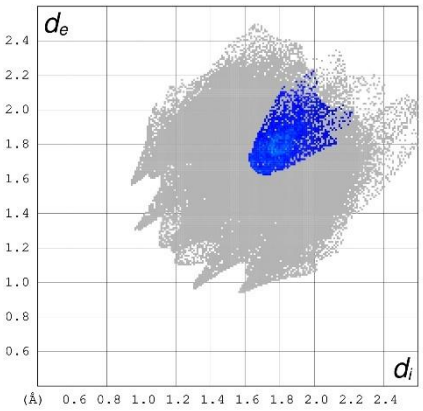

Figure 9.51 – 2D fingerprint plots of $[Ir(bpy)_2Cl_2]CH_3OH$ for all interactions (surface covered = 100.0%) (**top left**), H•••H interactions (surface covered = 41.8%) (**top right**) and C•••C interactions (surface covered = 4.0%) (**bottom**) present in the compound.

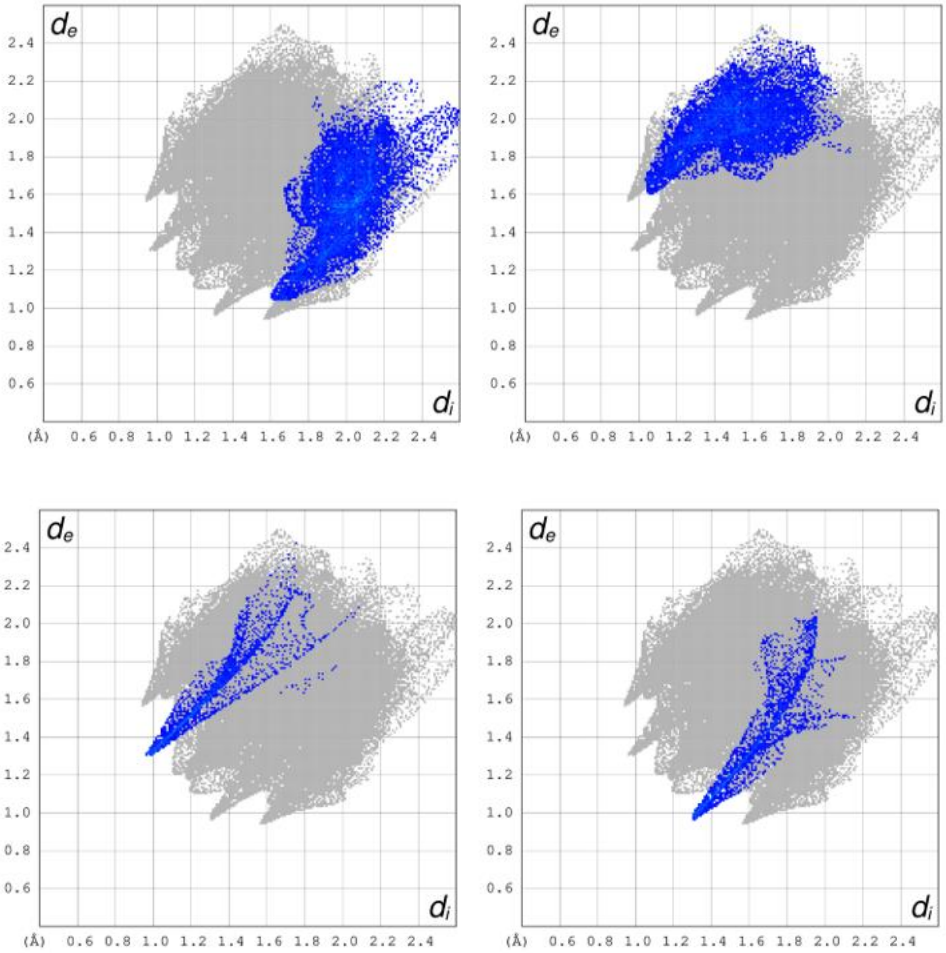

Figure 9.52 – 2D fingerprint plots of $[Ir(bpy)_2Cl_2]CH_3OH$ for C•••H/H•••C (surface covered = 11.5% and 9.6%) (**top**) and H•••O/O•••H (surface covered = 2.6% and 2.8%) interactions (**bottom**) present in the compound.

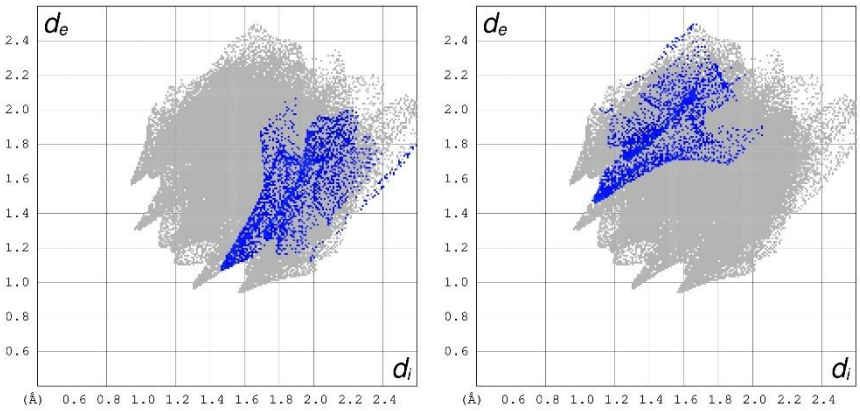

Figure 9.53 – 2D fingerprint plots of [[Ir(bpy)$_2$Cl$_2$]CH$_3$OH for N•••H/H•••N interactions (surface covered = 2.7% and 2.3%) present in the compound.

9.2.16 [Ir(dppz)$_2$Cl$_2$(CF$_3$SO$_3$)$_2$] - The Third Adventitious Discovery

Another crystal, [Ir(dppz)$_2$Cl$_2$(CF$_3$SO$_3$)$_2$], was serendipitously discovered, albeit some disorder in the triflate ligands/ions exist in the molecule.

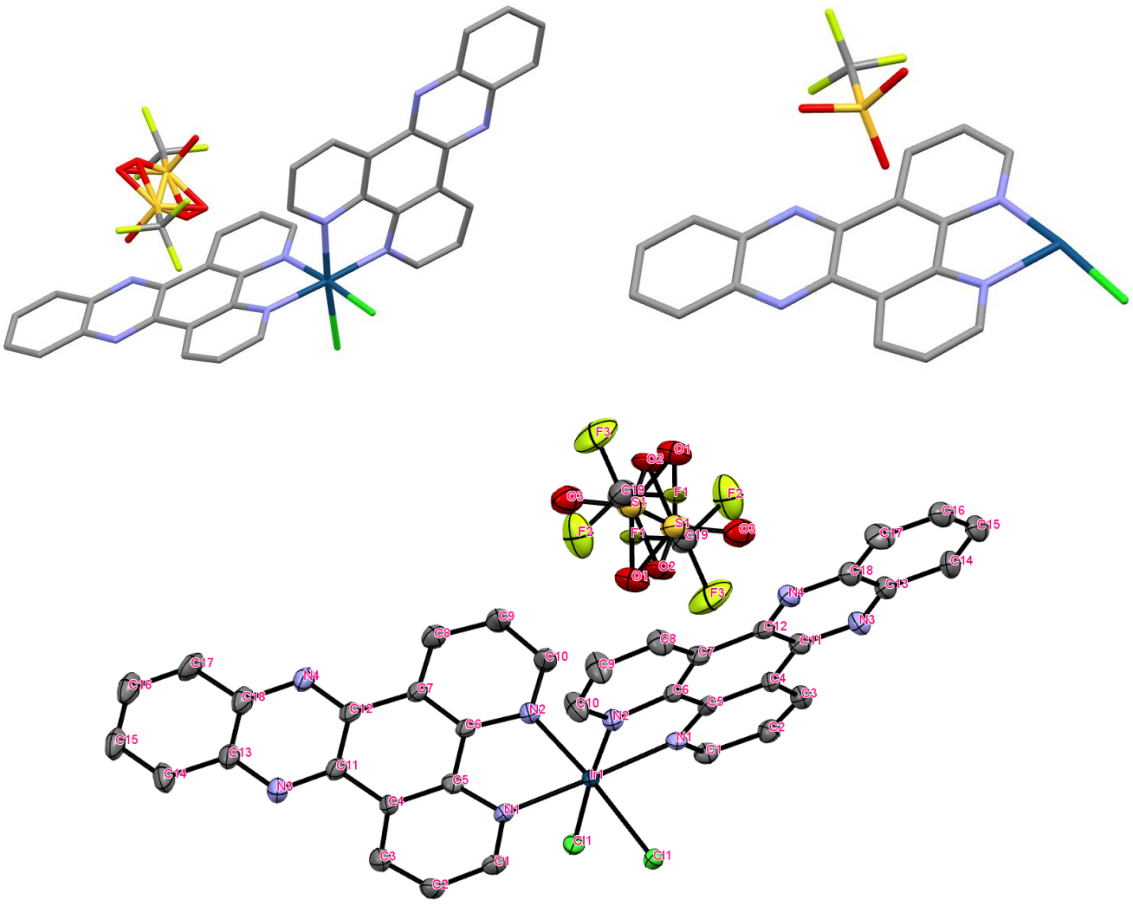

Figure 9.54 – Crystal structure of monoclinic [Ir(dppz)$_2$Cl$_2$(CF$_3$SO$_3$)$_2$] (**top left**), its asymmetric unit (**top right**), and its ORTEP diagram with atom labelling showing 50% thermal ellipsoids (**bottom**). Atom

labelling – grey: Ir; black: C; blue: N; green: Cl; dark yellow: F; pastel yellow: S; red: O. Space group = C2/c. Final R indexes [I>=2σ (I)] value = 0.0478. Unit cell parameters: α/° = 90; β/° = 103.831(3); γ/° = 90.

The HSA for this crystal could not be computed as there are fractional disorders in the crystal lattice of the compound. All other crystallographic data obtained for the $[Ir(dppz)_2Cl_2(CF_3SO_3)_2]\,CH_3NO_2$ can be found in an appropriate section of this Appendix.

9.3 Supplementary Crystallographic Data

Below gives the crystal data summary for the ligand and/or complexes discovered in this work in no particular order.

9.3.1 IAJ676s (Qtpy)

The data below is for the ligand, 2,2':4,4'':4',4'''-quaterpyridine, abbreviated to qtpy.

Table 9.10 – Fractional Atomic Coordinates ($\times 10^4$) and Equivalent Isotropic Displacement Parameters ($Å^2 \times 10^3$) for qtpy. U_{eq} is defined as 1/3 of the trace of the orthogonalised U_{IJ} tensor.

Atom	*x*	*y*	*z*	U(eq)
N1	725(4)	3451.3(15)	3653.4(13)	19.9(3)
N10	5896(4)	9805.1(16)	1593.9(14)	25.5(4)
C2	647(4)	4898.2(18)	4379.7(14)	17.2(4)
C3	1688(4)	6157.3(18)	4004.3(15)	18.1(4)
C4	2805(4)	5946.6(18)	2829.8(15)	17.7(4)
C5	2848(4)	4450.7(18)	2073.9(15)	19.0(4)
C6	1820(4)	3259.6(18)	2526.3(15)	20.6(4)
C7	3904(4)	7278.6(18)	2400.4(15)	18.1(4)
C8	5635(4)	8611.5(18)	3246.9(16)	21.3(4)
C9	6585(5)	9824.1(19)	2805.3(16)	23.8(4)
C11	4220(5)	8521.0(19)	788.5(17)	24.0(4)
C12	3199(4)	7249.8(19)	1144.1(16)	21.3(4)

Table 9.11 – Anisotropic Displacement Parameters ($Å^2×10^3$) for qtpy. The Anisotropic displacement factor exponent takes the form: $-2\pi^2[h^2a^{*2}U_{11}+2hka^*b^*U_{12}+\ldots]$.

Atom	U_{11}	U_{22}	U_{33}	U_{23}	U_{13}	U_{12}
N1	21.6(8)	17.7(7)	21.2(8)	6.8(6)	3.6(6)	0.7(6)
N10	31.4(9)	20.5(8)	27.9(9)	10.2(7)	9.4(7)	2.5(6)
C2	15.9(8)	17.4(8)	18.7(9)	7.3(7)	-0.5(6)	1.3(6)
C3	17.9(9)	16.1(8)	20.5(9)	6.8(7)	1.0(7)	-0.1(6)
C4	15.0(8)	17.4(8)	21.2(9)	7.3(7)	0.3(6)	-0.3(6)
C5	19.0(9)	21.0(9)	17.8(9)	7.1(7)	2.8(7)	0.1(7)
C6	23.5(9)	16.3(8)	21.5(9)	4.2(7)	3.7(7)	1.6(7)
C7	17.5(9)	17.4(8)	21.8(9)	8.2(7)	5.8(7)	3.2(6)
C8	23.4(9)	20.7(9)	21.0(9)	7.6(7)	4.1(7)	1.8(7)
C9	26.6(10)	18.8(9)	25.3(9)	5.1(7)	4.9(7)	-0.3(7)
C11	29.3(10)	22.7(9)	22.0(9)	8.5(7)	6.5(7)	3.1(7)
C12	24.6(9)	18.6(9)	21.2(9)	6.7(7)	4.1(7)	-0.3(7)

Table 9.12 – Bond Lengths for qtpy.

Atom	Atom	Length/Å	Atom	Atom	Length/Å
N1	C2	1.343(2)	C4	C5	1.388(2)
N1	C6	1.333(2)	C4	C7	1.486(2)
N10	C9	1.336(2)	C5	C6	1.379(2)
N10	C11	1.333(2)	C7	C8	1.387(2)
C2	C2[1]	1.482(3)	C7	C12	1.383(2)
C2	C3	1.385(2)	C8	C9	1.381(2)
C3	C4	1.384(2)	C11	C12	1.381(2)

[1]-X,1-Y,1-Z

Table 9.13 – Bond Angles for qtpy.

Atom	Atom	Atom	Angle/°	Atom	Atom	Atom	Angle/°
C6	N1	C2	117.10(13)	C6	C5	C4	119.02(15)
C11	N10	C9	116.52(14)	N1	C6	C5	123.91(15)
N1	C2	C2[1]	116.76(17)	C8	C7	C4	121.35(15)
N1	C2	C3	122.60(15)	C12	C7	C4	121.41(15)

C3	C2	C2[1]	120.64(18)	C12	C7	C8	117.23(14)
C4	C3	C2	119.86(15)	C9	C8	C7	119.30(15)
C3	C4	C5	117.50(14)	N10	C9	C8	123.72(16)
C3	C4	C7	120.90(15)	N10	C11	C12	123.68(16)
C5	C4	C7	121.60(14)	C11	C12	C7	119.54(16)

[1]-X,1-Y,1-Z

Table 9.14 – Hydrogen Atom Coordinates (Å×10^4) and Isotropic Displacement Parameters (Å^2×10^3) for qtpy.

Atom	*x*	*y*	*z*	U(eq)
H3	1635.19	7163.37	4552.1	22
H5	3573.8	4250.03	1257.03	23
H6	1897.93	2242.02	2003.26	25
H8	6161.25	8689.56	4120.99	26
H9	7796.73	10722.68	3396.63	29
H11	3700.05	8478.37	-78.6	29
H12	2019.79	6361.46	529.93	26

Crystal Structure Determination of Qtpy

Crystal Data for $C_{20}H_{14}N_4$ (M = 310.35 g/mol): triclinic, space group P-1 (no. 2), a = 3.7794(9) Å, b = 9.132(2) Å, c = 11.115(3) Å, α = 106.477(2)°, β = 96.768(2)°, γ = 92.720(2)°, V = 363.98(15) Å^3, Z = 1, T = 109.99(1) K, μ(MoKα) = 0.087 mm^{-1}, *Dcalc* = 1.416 g/cm^3, 6826 reflections measured (3.858° ≤ 2Θ ≤ 54.506°), 1617 unique (R_{int} = 0.0357, R_{sigma} = 0.0452) which were used in all calculations. The final R_1 was 0.0473 (I > 2σ(I)) and wR_2 was 0.1254 (all data).

9.3.2 IAJ693v_0m ([Ir(phen)$_2$Cl$_2$]PF$_6$)

Table 9.15 – Crystal data and structure refinement for IAJ693v_0m.

Identification code	IAJ693v_0m
Empirical formula	$C_{24}H_{16}Cl_2F_6IrN_4P$
Formula weight	768.48
Temperature/K	100.03

Crystal system	monoclinic
Space group	C2/c
a/Å	16.2872(7)
b/Å	12.6546(6)
c/Å	13.0156(6)
α/°	90
β/°	102.739(2)
γ/°	90
Volume/Å^3	2616.6(2)
Z	4
ρ_{calc}g/cm^3	1.951
μ/mm^{-1}	12.934
F(000)	1472.0
Crystal size/mm^3	0.145 × 0.099 × 0.049
Radiation	CuKα (λ = 1.54178)
2Θ range for data collection/°	8.934 to 133.464
Index ranges	-19 ≤ h ≤ 19, -15 ≤ k ≤ 15, -15 ≤ l ≤ 14
Reflections collected	13964
Independent reflections	2298 [R_{int} = 0.0478, R_{sigma} = 0.0324]
Data/restraints/parameters	2298/0/174
Goodness-of-fit on F^2	1.053
Final R indexes [I>=2σ (I)]	R_1 = 0.0340, wR_2 = 0.0923
Final R indexes [all data]	R_1 = 0.0349, wR_2 = 0.0931
Largest diff. peak/hole / e Å^{-3}	2.49/-1.91

Table 9.16 – Fractional Atomic Coordinates (×10^4) and Equivalent Isotropic Displacement Parameters (Å^2×10^3) for IAJ693v_0m. U_{eq} is defined as 1/3 of the trace of the orthogonalised U_{IJ} tensor.

Atom	***x***	***y***	***z***	**U(eq)**
Ir1	5000	3178.7(2)	7500	8.20(14)
Cl1	6046.2(7)	4487.4(10)	7690.0(10)	13.1(3)
N1	4068(3)	2065(4)	7200(4)	12.0(9)
N2	4790(3)	3126(3)	5892(4)	10.5(9)
C1	3723(4)	1564(5)	7895(5)	14.1(11)
C2	3054(4)	857(5)	7566(5)	20.1(13)
C3	2743(4)	655(5)	6517(5)	18.4(12)

C4	3094(4)	1207(4)	5768(5)	16.1(12)
C5	3760(4)	1901(4)	6155(5)	13.5(12)
C6	4139(3)	2479(4)	5444(4)	10.7(10)
C7	5181(4)	3657(5)	5256(4)	14.9(11)
C8	4919(4)	3609(5)	4162(5)	19.3(12)
C9	4244(4)	2994(5)	3702(5)	18.9(12)
C10	3841(4)	2386(4)	4355(4)	15.2(11)
C11	3142(4)	1688(5)	3978(5)	21.5(14)
C12	2801(4)	1117(5)	4659(5)	20.0(12)
P1	7500	2500	5000	29.8(6)
F1	7265(5)	3018(4)	6001(6)	80(2)
F2	6713(4)	1744(5)	4912(5)	69.1(19)
F3	8054(5)	1651(7)	5706(7)	108(3)

Table 9.17 – Anisotropic Displacement Parameters ($Å^2 \times 10^3$) for IAJ693v_0m. The Anisotropic displacement factor exponent takes the form: $-2\pi^2[h^2a^{*2}U_{11}+2hka^*b^*U_{12}+\ldots]$.

Atom	**U_{11}**	**U_{22}**	**U_{33}**	**U_{23}**	**U_{13}**	**U_{12}**
Ir1	7.67(19)	6.86(19)	10.3(2)	0	2.43(12)	0
Cl1	10.1(6)	12.6(6)	16.0(6)	0.9(5)	1.5(5)	-3.3(5)
N1	9(2)	12(2)	17(2)	-0.9(18)	7.0(18)	2.6(18)
N2	10(2)	3(2)	18(3)	-0.3(16)	0.5(18)	1.6(16)
C1	13(3)	12(3)	18(3)	-1(2)	7(2)	-1(2)
C2	20(3)	18(3)	25(3)	-1(2)	11(2)	0(2)
C3	12(3)	13(3)	31(3)	-4(2)	7(2)	-6(2)
C4	14(3)	11(3)	24(3)	-2(2)	4(2)	0(2)
C5	11(3)	13(3)	16(3)	-1(2)	3(2)	2(2)
C6	12(3)	4(2)	16(3)	-3(2)	3(2)	0(2)
C7	14(3)	15(3)	17(3)	3(2)	7(2)	-1(2)
C8	23(3)	20(3)	16(3)	3(2)	5(2)	1(3)
C9	24(3)	20(3)	12(3)	0(2)	3(2)	4(2)
C10	16(3)	12(3)	17(3)	-2(2)	3(2)	3(2)
C11	22(3)	22(3)	17(3)	-6(2)	-3(2)	-2(2)
C12	18(3)	16(3)	24(3)	-6(2)	0(2)	-3(2)
P1	37.5(14)	24.6(13)	36.0(14)	11.0(10)	27.0(11)	11.8(11)
F1	132(6)	49(3)	89(5)	-21(3)	91(5)	-26(4)
F2	83(4)	82(4)	59(4)	-16(3)	50(3)	-44(3)

F3	68(4)	136(7)	140(7)	108(6)	65(5)	61(4)

Table 9.18 – Bond Lengths for IAJ693v_0m.

Atom	Atom	Length/Å	Atom	Atom	Length/Å
Ir1	Cl1[1]	2.3498(12)	C4	C12	1.421(9)
Ir1	Cl1	2.3498(12)	C5	C6	1.423(8)
Ir1	N1[1]	2.045(5)	C6	C10	1.398(8)
Ir1	N1	2.045(5)	C7	C8	1.395(8)
Ir1	N2[1]	2.046(5)	C8	C9	1.371(9)
Ir1	N2	2.046(5)	C9	C10	1.412(9)
N1	C1	1.327(8)	C10	C11	1.438(9)
N1	C5	1.358(8)	C11	C12	1.354(9)
N2	C6	1.364(7)	P1	F1	1.580(5)
N2	C7	1.332(7)	P1	F1[2]	1.579(5)
C1	C2	1.402(9)	P1	F2	1.584(6)
C2	C3	1.372(9)	P1	F2[2]	1.584(6)
C3	C4	1.418(8)	P1	F3	1.565(6)
C4	C5	1.401(8)	P1	F3[2]	1.565(6)

[1]1-X,+Y,3/2-Z; [2]3/2-X,1/2-Y,1-Z

Table 9.19 – Bond Angles for IAJ693v_0m.

Atom	Atom	Atom	Angle/°	Atom	Atom	Atom	Angle/°
Cl1	Ir1	Cl1[1]	90.38(6)	N1	C5	C6	117.1(5)
N1	Ir1	Cl1	175.13(14)	C4	C5	C6	120.1(5)
N1	Ir1	Cl1[1]	88.58(13)	N2	C6	C5	116.0(5)
N1[1]	Ir1	Cl1[1]	175.13(14)	N2	C6	C10	123.2(5)
N1[1]	Ir1	Cl1	88.58(14)	C10	C6	C5	120.8(5)
N1	Ir1	N1[1]	92.9(3)	N2	C7	C8	122.1(5)
N1	Ir1	N2	80.36(18)	C9	C8	C7	120.4(6)
N1[1]	Ir1	N2[1]	80.36(18)	C8	C9	C10	118.8(6)
N1[1]	Ir1	N2	97.03(18)	C6	C10	C9	117.4(5)
N1	Ir1	N2[1]	97.03(18)	C6	C10	C11	118.0(5)
N2[1]	Ir1	Cl1[1]	94.84(13)	C9	C10	C11	124.6(6)
N2	Ir1	Cl1[1]	87.80(13)	C12	C11	C10	120.8(6)
N2	Ir1	Cl1	94.84(13)	C11	C12	C4	121.9(6)

N2[1]	Ir1	Cl1	87.80(13)	F1[2]	P1	F1	180.0(6)
N2[1]	Ir1	N2	176.3(2)	F1	P1	F2	88.3(3)
C1	N1	Ir1	127.4(4)	F1[2]	P1	F2	91.7(3)
C1	N1	C5	119.4(5)	F1[2]	P1	F2[2]	88.3(3)
C5	N1	Ir1	113.0(4)	F1	P1	F2[2]	91.7(3)
C6	N2	Ir1	113.3(4)	F2	P1	F2[2]	180.0
C7	N2	Ir1	128.6(4)	F3	P1	F1[2]	89.2(4)
C7	N2	C6	118.1(5)	F3[2]	P1	F1[2]	90.8(4)
N1	C1	C2	121.0(5)	F3	P1	F1	90.8(4)
C3	C2	C1	120.9(6)	F3[2]	P1	F1	89.2(4)
C2	C3	C4	118.5(5)	F3	P1	F2	88.9(4)
C3	C4	C12	124.3(5)	F3[2]	P1	F2	91.1(4)
C5	C4	C3	117.3(5)	F3[2]	P1	F2[2]	88.9(4)
C5	C4	C12	118.4(5)	F3	P1	F2[2]	91.1(4)
N1	C5	C4	122.8(5)	F3	P1	F3[2]	180.0(6)

[1]1-X,+Y,3/2-Z; [2]3/2-X,1/2-Y,1-Z

Table 9.20 – Torsion Angles for IAJ693v_0m.

A	**B**	**C**	**D**	**Angle/°**	**A**	**B**	**C**	**D**	**Angle/°**
Ir1	N1	C1	C2	176.5(4)	C3	C4	C12	C11	177.9(6)
Ir1	N1	C5	C4	-177.1(4)	C4	C5	C6	N2	-179.2(5)
Ir1	N1	C5	C6	2.2(6)	C4	C5	C6	C10	1.7(8)
Ir1	N2	C6	C5	-4.3(6)	C5	N1	C1	C2	0.9(8)
Ir1	N2	C6	C10	174.8(4)	C5	C4	C12	C11	-0.6(9)
Ir1	N2	C7	C8	-174.2(4)	C5	C6	C10	C9	179.3(5)
N1	C1	C2	C3	0.7(9)	C5	C6	C10	C11	-0.1(8)
N1	C5	C6	N2	1.4(7)	C6	N2	C7	C8	3.3(8)
N1	C5	C6	C10	-177.7(5)	C6	C10	C11	C12	-1.8(9)
N2	C6	C10	C9	0.3(8)	C7	N2	C6	C5	177.9(5)
N2	C6	C10	C11	-179.1(5)	C7	N2	C6	C10	-3.1(8)
N2	C7	C8	C9	-0.8(9)	C7	C8	C9	C10	-2.0(9)
C1	N1	C5	C4	-1.0(8)	C8	C9	C10	C6	2.2(8)
C1	N1	C5	C6	178.4(5)	C8	C9	C10	C11	-178.4(6)
C1	C2	C3	C4	-2.3(9)	C9	C10	C11	C12	178.7(6)

C2	C3	C4	C5	2.2(8)	C10	C11	C12	C4	2.3(10)
C2	C3	C4	C12	-176.4(6)	C12	C4	C5	N1	178.0(5)
C3	C4	C5	N1	-0.6(8)	C12	C4	C5	C6	-1.3(8)
C3	C4	C5	C6	-180.0(5)					

Table 9.21 – Hydrogen Atom Coordinates (Å×10^4) and Isotropic Displacement Parameters (Å^2×10^3) for IAJ693v_0m.

Atom	*x*	*y*	*z*	U(eq)
H1	3932.36	1686.46	8626.14	17
H2	2812.14	513.05	8077.47	24
H3	2303.54	156.13	6297.42	22
H7	5653.64	4081.35	5557.4	18
H8	5208.52	4005.44	3733.2	23
H9	4052.66	2977.14	2958.3	23
H11	2917.79	1627.5	3242.49	26
H12	2353.49	643.31	4387.47	24

Table 9.22 – Solvent masks information for IAJ693v_0m.

Number	X	Y	Z	Volume	Electron count	Content
1	0.000	0.500	-0.766	177.8	51.5	MeCN
2	0.500	0.000	-0.549	177.8	51.5	MeCN

Crystal Structure Determination of IAJ693v_0m

Crystal Data for $C_{24}H_{16}Cl_2F_6IrN_4P$ (*M* =768.48 g/mol): monoclinic, space group C2/c (no. 15), *a* = 16.2872(7) Å, *b* = 12.6546(6) Å, *c* = 13.0156(6) Å, *β* = 102.739(2)°, *V* = 2616.6(2) Å^3, *Z* = 4, *T* = 100.03 K, μ(CuKα) = 12.934 mm^{-1}, *Dcalc* = 1.951 g/cm^3, 13964 reflections measured (8.934° ≤ 2Θ ≤ 133.464°), 2298 unique (R_{int} = 0.0478, R_{sigma} = 0.0324) which were used in all calculations. The final R_1 was 0.0340 (I > 2σ(I)) and wR_2 was 0.0931 (all data).

9.3.3 Iaj687k_0m [Ir(bpy)$_2$(CF$_3$SO$_3$)$_2$]CF$_3$SO$_3$

Table 9.23 – Crystal data and structure refinement for iaj687k_0m.

Identification code	iaj687k_0m
Empirical formula	$C_{23}H_{16}F_9IrN_4O_9S_3$

Formula weight	951.78
Temperature/K	100
Crystal system	triclinic
Space group	P-1
a/Å	8.3337(6)
b/Å	9.9623(8)
c/Å	18.5605(14)
α/°	104.574(3)
β/°	92.555(3)
γ/°	97.512(3)
Volume/Å^3	1473.7(2)
Z	2
ρ_{calc}g/cm^3	2.145
μ/mm^{-1}	4.859
F(000)	920.0
Crystal size/mm^3	0.54 × 0.12 × 0.104
Radiation	MoKα (λ = 0.71073)
2Θ range for data collection/°	2.274 to 54.968
Index ranges	-10 ≤ h ≤ 10, -12 ≤ k ≤ 12, -24 ≤ l ≤ 24
Reflections collected	44185
Independent reflections	6753 [R_{int} = 0.0580, R_{sigma} = 0.0411]
Data/restraints/parameters	6753/0/442
Goodness-of-fit on F^2	1.027
Final R indexes [I>=2σ (I)]	R_1 = 0.0390, wR_2 = 0.0965
Final R indexes [all data]	R_1 = 0.0459, wR_2 = 0.1005
Largest diff. peak/hole / e Å^{-3}	5.57/-1.16

Table 9.24 – Fractional Atomic Coordinates (×10^4) and Equivalent Isotropic Displacement Parameters (Å^2×10^3) for iaj687k_0m. U_{eq} is defined as 1/3 of the trace of the orthogonalised U_{IJ} tensor.

Atom	***x***	***y***	***z***	**U(eq)**
Ir1	5083.6(2)	6591.5(2)	7730.1(2)	7.22(7)
S1	6866.1(16)	9647.8(14)	7545.2(8)	11.2(3)
S2	7887.2(17)	6733.1(15)	9047.2(8)	13.8(3)
F1	8365(5)	11123(4)	8837(2)	24.0(8)
F2	5756(5)	10873(4)	8817(2)	25.0(8)

F3	7009(5)	12277(4)	8244(2)	24.1(8)
F4	9107(6)	6342(5)	10277(2)	41.4(11)
F5	6540(6)	6424(5)	10256(2)	37.8(11)
F6	7414(6)	4570(4)	9630(3)	40.5(11)
O1	6854(5)	8364(4)	7819(2)	13.0(8)
O2	8362(5)	9969(4)	7230(2)	16.8(9)
O3	5368(5)	9741(4)	7162(2)	15.4(8)
O4	6216(5)	6207(4)	8678(2)	15.5(8)
O5	9119(5)	6120(5)	8625(3)	26.5(11)
O6	8166(6)	8220(5)	9374(2)	23.4(10)
N1	3722(5)	6922(5)	6883(3)	10.8(9)
N2	3619(5)	7861(5)	8325(3)	10.0(9)
N3	3625(5)	4779(5)	7641(2)	9.6(9)
N4	6443(5)	5222(5)	7115(2)	9.2(9)
C1	3946(7)	6445(6)	6162(3)	11.8(11)
C2	2912(7)	6655(6)	5601(3)	14.9(11)
C3	1629(7)	7392(6)	5803(3)	13.7(11)
C4	1413(7)	7913(6)	6559(3)	11.9(11)
C5	2494(6)	7679(5)	7094(3)	9.9(10)
C6	2453(6)	8235(6)	7906(3)	10.0(10)
C7	1374(7)	9097(6)	8253(3)	14.8(11)
C8	1513(7)	9605(6)	9022(3)	16.6(12)
C9	2700(8)	9210(6)	9441(3)	18.6(12)
C10	3738(7)	8334(6)	9077(3)	13.3(11)
C11	2135(7)	4680(6)	7904(3)	13.7(11)
C12	1165(7)	3384(6)	7793(3)	17.0(12)
C13	1737(7)	2191(6)	7411(4)	19.5(13)
C14	3281(7)	2283(6)	7156(3)	16.2(12)
C15	4199(7)	3606(6)	7269(3)	12.2(11)
C16	5821(7)	3848(6)	6997(3)	11.4(11)
C17	6657(7)	2798(6)	6641(3)	13.9(11)
C18	8153(7)	3160(6)	6383(3)	14.7(11)
C19	8754(7)	4559(6)	6484(3)	13.3(11)
C20	7877(7)	5580(6)	6852(3)	12.2(11)
C21	7001(8)	11059(6)	8416(3)	16.6(12)
C22	7718(8)	5955(7)	9847(4)	23.4(14)

S3	7349.3(17)	7216.6(14)	4898.5(8)	12.8(3)
F7	8793(5)	9777(4)	5535(2)	33.8(10)
F8	7264(6)	9598(4)	4532(2)	35.0(10)
F9	6180(5)	9503(4)	5560(2)	32.5(10)
O7	7602(5)	6928(5)	5617(2)	22.5(10)
O8	8670(5)	7009(5)	4425(2)	21.7(9)
O9	5753(5)	6696(5)	4521(2)	21.0(9)
C23	7390(8)	9120(7)	5141(3)	21.8(13)

Table 9.25 – Anisotropic Displacement Parameters ($Å^2×10^3$) for iaj687k_0m. The Anisotropic displacement factor exponent takes the form: $-2\pi^2[h^2a^{*2}U_{11}+2hka^*b^*U_{12}+\ldots]$.

Atom	**U_{11}**	**U_{22}**	**U_{33}**	**U_{23}**	**U_{13}**	**U_{12}**
Ir1	5.63(11)	7.50(11)	8.50(11)	1.77(7)	0.30(7)	1.58(7)
S1	10.6(6)	9.6(6)	13.2(6)	3.3(5)	0.0(5)	0.8(5)
S2	11.2(7)	17.7(7)	11.1(6)	0.3(5)	-0.5(5)	4.3(5)
F1	23(2)	24.0(19)	20.9(19)	0.4(15)	-9.2(15)	2.2(15)
F2	27(2)	25.3(19)	20.1(19)	1.1(15)	11.6(16)	1.9(16)
F3	39(2)	9.5(16)	23.0(19)	2.5(14)	-0.5(17)	3.6(15)
F4	41(3)	54(3)	27(2)	14(2)	-22(2)	3(2)
F5	41(3)	58(3)	20(2)	17(2)	10.6(18)	10(2)
F6	60(3)	25(2)	38(3)	15.6(19)	-12(2)	2(2)
O1	10.9(19)	9.6(18)	18(2)	4.3(15)	-2.2(16)	-0.1(15)
O2	14(2)	16(2)	21(2)	8.1(17)	0.5(17)	-0.9(16)
O3	14(2)	13.8(19)	17(2)	4.0(16)	-1.9(16)	-0.3(16)
O4	17(2)	20(2)	9.9(19)	5.5(16)	-2.5(16)	3.6(17)
O5	16(2)	37(3)	23(2)	-4(2)	3.9(19)	12(2)
O6	25(2)	20(2)	21(2)	-0.8(18)	-0.2(19)	-0.4(19)
N1	7(2)	12(2)	13(2)	2.8(18)	-1.2(17)	-0.4(17)
N2	6(2)	12(2)	13(2)	4.0(17)	2.8(17)	2.0(17)
N3	9(2)	10(2)	10(2)	4.7(17)	0.3(17)	0.2(17)
N4	7(2)	12(2)	10(2)	3.9(17)	-0.3(17)	2.7(17)
C1	11(3)	12(3)	12(3)	2(2)	1(2)	2(2)
C2	14(3)	18(3)	11(3)	2(2)	1(2)	0(2)
C3	11(3)	14(3)	16(3)	5(2)	-3(2)	0(2)
C4	10(3)	11(2)	15(3)	5(2)	0(2)	1(2)
C5	9(3)	8(2)	13(3)	2(2)	1(2)	2(2)

C6	5(2)	12(2)	12(3)	3(2)	1(2)	0(2)
C7	10(3)	17(3)	19(3)	6(2)	1(2)	6(2)
C8	14(3)	16(3)	18(3)	0(2)	7(2)	4(2)
C9	24(3)	17(3)	13(3)	0(2)	5(2)	4(2)
C10	15(3)	16(3)	10(3)	3(2)	1(2)	5(2)
C11	13(3)	14(3)	16(3)	5(2)	2(2)	3(2)
C12	8(3)	23(3)	22(3)	11(2)	-1(2)	1(2)
C13	14(3)	11(3)	33(4)	11(2)	-2(3)	-5(2)
C14	14(3)	12(3)	24(3)	7(2)	-2(2)	2(2)
C15	9(3)	13(3)	14(3)	4(2)	-1(2)	2(2)
C16	15(3)	13(3)	5(2)	3(2)	-4(2)	0(2)
C17	14(3)	11(3)	15(3)	4(2)	-2(2)	0(2)
C18	15(3)	19(3)	13(3)	5(2)	2(2)	8(2)
C19	10(3)	17(3)	13(3)	4(2)	1(2)	5(2)
C20	11(3)	11(2)	14(3)	5(2)	1(2)	-1(2)
C21	21(3)	14(3)	13(3)	0(2)	-1(2)	1(2)
C22	26(4)	27(3)	17(3)	8(3)	-10(3)	3(3)
S3	12.3(7)	13.8(6)	13.2(6)	4.0(5)	1.5(5)	3.5(5)
F7	39(2)	24(2)	30(2)	-0.6(17)	0.1(19)	-8.9(18)
F8	59(3)	23(2)	30(2)	16.3(17)	8(2)	14(2)
F9	38(2)	25(2)	33(2)	-2.0(17)	13.0(19)	16.4(18)
O7	22(2)	30(2)	17(2)	10.4(19)	-1.4(18)	2.3(19)
O8	18(2)	29(2)	19(2)	4.2(18)	5.6(18)	8.9(19)
O9	15(2)	24(2)	21(2)	1.6(18)	-1.7(17)	2.1(18)
C23	32(4)	18(3)	16(3)	4(2)	6(3)	7(3)

Table 9.26 – Bond Lengths for iaj687k_0m.

Atom	Atom	Length/Å	Atom	Atom	Length/Å
Ir1	O1	2.114(4)	N4	C20	1.350(7)
Ir1	O4	2.102(4)	C1	C2	1.396(8)
Ir1	N1	2.016(5)	C2	C3	1.388(8)
Ir1	N2	2.032(5)	C3	C4	1.397(8)
Ir1	N3	2.006(4)	C4	C5	1.395(8)
Ir1	N4	2.045(5)	C5	C6	1.471(7)
S1	O1	1.490(4)	C6	C7	1.392(8)

S1	O2	1.433(4)	C7	C8	1.383(8)
S1	O3	1.435(4)	C8	C9	1.388(9)
S1	C21	1.844(6)	C9	C10	1.386(8)
S2	O4	1.492(4)	C11	C12	1.394(8)
S2	O5	1.427(4)	C12	C13	1.377(9)
S2	O6	1.435(5)	C13	C14	1.390(8)
S2	C22	1.842(7)	C14	C15	1.396(8)
F1	C21	1.335(7)	C15	C16	1.475(8)
F2	C21	1.324(7)	C16	C17	1.379(8)
F3	C21	1.331(7)	C17	C18	1.392(8)
F4	C22	1.331(8)	C18	C19	1.381(8)
F5	C22	1.329(8)	C19	C20	1.387(8)
F6	C22	1.322(8)	S3	O7	1.446(4)
N1	C1	1.333(7)	S3	O8	1.442(4)
N1	C5	1.364(7)	S3	O9	1.443(4)
N2	C6	1.365(7)	S3	C23	1.831(6)
N2	C10	1.350(7)	F7	C23	1.347(8)
N3	C11	1.355(7)	F8	C23	1.339(7)
N3	C15	1.357(7)	F9	C23	1.336(8)
N4	C16	1.358(7)			

Table 9.27 – Bond Angles for iaj687k_0m.

Atom	**Atom**	**Atom**	**Angle/°**	**Atom**	**Atom**	**Atom**	**Angle/°**
O4	Ir1	O1	90.32(16)	C4	C5	C6	124.5(5)
N1	Ir1	O1	94.82(17)	N2	C6	C5	114.4(5)
N1	Ir1	O4	172.48(17)	N2	C6	C7	120.0(5)
N1	Ir1	N2	80.39(19)	C7	C6	C5	125.6(5)
N1	Ir1	N4	98.57(18)	C8	C7	C6	119.9(5)
N2	Ir1	O1	89.40(17)	C7	C8	C9	119.4(5)
N2	Ir1	O4	94.20(17)	C10	C9	C8	119.0(5)
N2	Ir1	N4	176.63(18)	N2	C10	C9	121.4(5)
N3	Ir1	O1	173.19(16)	N3	C11	C12	120.9(5)
N3	Ir1	O4	85.91(17)	C13	C12	C11	119.2(5)
N3	Ir1	N1	89.50(18)	C12	C13	C14	120.1(5)

N3	Ir1	N2	96.52(18)	C13	C14	C15	118.7(5)
N3	Ir1	N4	80.24(18)	N3	C15	C14	121.0(5)
N4	Ir1	O1	93.89(17)	N3	C15	C16	115.1(5)
N4	Ir1	O4	86.53(17)	C14	C15	C16	123.9(5)
O1	S1	C21	103.0(3)	N4	C16	C15	114.2(5)
O2	S1	O1	111.1(2)	N4	C16	C17	121.4(5)
O2	S1	O3	119.0(3)	C17	C16	C15	124.4(5)
O2	S1	C21	103.1(3)	C16	C17	C18	119.0(5)
O3	S1	O1	114.6(2)	C19	C18	C17	119.2(5)
O3	S1	C21	103.7(3)	C18	C19	C20	119.7(5)
O4	S2	C22	98.7(3)	N4	C20	C19	120.8(5)
O5	S2	O4	113.3(3)	F1	C21	S1	111.0(4)
O5	S2	O6	117.8(3)	F2	C21	S1	111.7(4)
O5	S2	C22	106.3(3)	F2	C21	F1	108.2(5)
O6	S2	O4	113.4(3)	F2	C21	F3	108.6(5)
O6	S2	C22	104.8(3)	F3	C21	S1	108.8(4)
S1	O1	Ir1	132.9(2)	F3	C21	F1	108.5(5)
S2	O4	Ir1	130.1(2)	F4	C22	S2	108.7(5)
C1	N1	Ir1	124.6(4)	F5	C22	S2	110.4(4)
C1	N1	C5	120.4(5)	F5	C22	F4	107.9(5)
C5	N1	Ir1	115.1(4)	F6	C22	S2	111.9(4)
C6	N2	Ir1	114.9(4)	F6	C22	F4	109.2(5)
C10	N2	Ir1	124.9(4)	F6	C22	F5	108.6(6)
C10	N2	C6	120.2(5)	O7	S3	C23	103.0(3)
C11	N3	Ir1	124.3(4)	O8	S3	O7	115.2(3)
C11	N3	C15	120.1(5)	O8	S3	O9	114.8(3)
C15	N3	Ir1	115.5(4)	O8	S3	C23	103.1(3)
C16	N4	Ir1	114.6(4)	O9	S3	O7	115.3(3)
C20	N4	Ir1	125.6(4)	O9	S3	C23	102.9(3)
C20	N4	C16	119.8(5)	F7	C23	S3	110.7(4)
N1	C1	C2	121.8(5)	F8	C23	S3	111.6(4)
C3	C2	C1	118.8(5)	F8	C23	F7	107.4(5)
C2	C3	C4	119.4(5)	F9	C23	S3	111.4(4)
C5	C4	C3	119.2(5)	F9	C23	F7	107.5(5)
N1	C5	C4	120.5(5)	F9	C23	F8	108.1(5)
N1	C5	C6	115.0(5)				

Table 9.28 – Torsion Angles for iaj687k_0m.

A	B	C	D	Angle/°	A	B	C	D	Angle/°
Ir1	N1	C1	C2	176.9(4)	C1	N1	C5	C6	-175.5(5)
Ir1	N1	C5	C4	-176.5(4)	C1	C2	C3	C4	0.6(8)
Ir1	N1	C5	C6	5.2(6)	C2	C3	C4	C5	-0.1(8)
Ir1	N2	C6	C5	-1.4(6)	C3	C4	C5	N1	-1.6(8)
Ir1	N2	C6	C7	179.7(4)	C3	C4	C5	C6	176.6(5)
Ir1	N2	C10	C9	179.3(4)	C4	C5	C6	N2	179.3(5)
Ir1	N3	C11	C12	177.3(4)	C4	C5	C6	C7	-1.9(9)
Ir1	N3	C15	C14	-178.6(4)	C5	N1	C1	C2	-2.3(8)
Ir1	N3	C15	C16	0.8(6)	C5	C6	C7	C8	-176.9(5)
Ir1	N4	C16	C15	5.9(6)	C6	N2	C10	C9	-0.3(8)
Ir1	N4	C16	C17	-175.0(4)	C6	C7	C8	C9	-2.1(9)
Ir1	N4	C20	C19	175.5(4)	C7	C8	C9	C10	1.2(9)
O1	S1	C21	F1	61.2(4)	C8	C9	C10	N2	0.0(9)
O1	S1	C21	F2	-59.6(5)	C10	N2	C6	C5	178.2(5)
O1	S1	C21	F3	-179.5(4)	C10	N2	C6	C7	-0.7(8)
O2	S1	O1	Ir1	-136.0(3)	C11	N3	C15	C14	-0.5(8)
O2	S1	C21	F1	-54.4(5)	C11	N3	C15	C16	178.9(5)
O2	S1	C21	F2	-175.3(4)	C11	C12	C13	C14	1.4(9)
O2	S1	C21	F3	64.8(5)	C12	C13	C14	C15	-2.5(9)
O3	S1	O1	Ir1	2.3(4)	C13	C14	C15	N3	2.0(9)
O3	S1	C21	F1	-179.1(4)	C13	C14	C15	C16	-177.3(5)
O3	S1	C21	F2	60.1(5)	C14	C15	C16	N4	174.9(5)
O3	S1	C21	F3	-59.8(5)	C14	C15	C16	C17	-4.1(9)
O4	S2	C22	F4	-178.0(5)	C15	N3	C11	C12	-0.6(8)
O4	S2	C22	F5	-59.9(5)	C15	C16	C17	C18	177.4(5)
O4	S2	C22	F6	61.3(5)	C16	N4	C20	C19	-2.3(8)
O5	S2	O4	Ir1	-71.7(4)	C16	C17	C18	C19	-0.5(8)
O5	S2	C22	F4	64.6(5)	C17	C18	C19	C20	1.1(8)
O5	S2	C22	F5	-177.3(4)	C18	C19	C20	N4	0.3(8)
O5	S2	C22	F6	-56.1(6)	C20	N4	C16	C15	-176.1(5)
O6	S2	O4	Ir1	66.0(4)	C20	N4	C16	C17	3.0(8)
O6	S2	C22	F4	-60.9(5)	C21	S1	O1	Ir1	114.1(3)
O6	S2	C22	F5	57.2(5)	C22	S2	O4	Ir1	176.3(3)
O6	S2	C22	F6	178.4(5)	O7	S3	C23	F7	56.9(5)

N1	C1	C2	C3	0.6(8)	O7	S3	C23	F8	176.5(5)
N1	C5	C6	N2	-2.4(7)	O7	S3	C23	F9	-62.6(5)
N1	C5	C6	C7	176.4(5)	O8	S3	C23	F7	-63.3(5)
N2	C6	C7	C8	1.8(8)	O8	S3	C23	F8	56.3(5)
N3	C11	C12	C13	0.2(9)	O8	S3	C23	F9	177.2(4)
N3	C15	C16	N4	-4.5(7)	O9	S3	C23	F7	177.1(4)
N3	C15	C16	C17	176.5(5)	O9	S3	C23	F8	-63.3(5)
N4	C16	C17	C18	-1.5(8)	O9	S3	C23	F9	57.6(5)
C1	N1	C5	C4	2.8(8)					

Table 9.29 – Hydrogen Atom Coordinates (Å×10^4) and Isotropic Displacement Parameters (Å^2×10^3) for iaj687k_0m.

Atom	*x*	*y*	*z*	U(eq)
H1	4832.82	5949.96	6027.1	14
H2	3083.67	6299.17	5089.54	18
H3	903.37	7539.87	5430.06	16
H4	541.46	8421.14	6706.3	14
H7	542.38	9335.97	7961.98	18
H8	801.97	10217.92	9260.44	20
H9	2798.52	9536.04	9970.56	22
H10	4552.25	8061.78	9361.98	16
H11	1747.09	5505.68	8168.39	16
H12	120.71	3323.68	7978.08	20
H13	1076.42	1304.46	7322.05	23
H14	3701.71	1462.49	6908.77	19
H17	6218.41	1841.14	6573.53	17
H18	8752.74	2452.52	6139.64	18
H19	9764.03	4821.62	6302.55	16
H20	8290.59	6542.13	6918.81	15

Crystal Structure Determination of Iaj687k_0m

Crystal Data for $C_{23}H_{16}F_9IrN_4O_9S_3$ (*M* =951.78 g/mol): triclinic, space group P-1 (no. 2), *a* = 8.3337(6) Å, *b* = 9.9623(8) Å, *c* = 18.5605(14) Å, *α* = 104.574(3)°, *β* = 92.555(3)°, *γ* = 97.512(3)°, *V* = 1473.7(2) Å^3, *Z* = 2, *T* = 100 K, μ(MoKα) = 4.859 mm^{-1}, *Dcalc* = 2.145 g/cm^3, 44185 reflections measured (2.274° ≤ 2Θ ≤ 54.968°), 6753 unique (R_{int} = 0.0580, R_{sigma} = 0.0411) which were used in all calculations. The final R_1 was 0.0390 (I > 2σ(I)) and wR_2 was 0.1005 (all data).

9.3.4 2021NCS0465_LJM1a $[Ir(phen)_2Cl_2]CF_3SO_3$

Table 9.30 – Crystal data and structure refinement for 2021NCS0465_LJM1a.

Identification code	2021NCS0465_LJM1a
Empirical formula	$C_{25}H_{16}Cl_2F_3IrN_4O_3S$
Formula weight	772.58
Temperature/K	100.00(10)
Crystal system	monoclinic
Space group	C2/c
a/Å	16.0688(3)
b/Å	13.0219(3)
c/Å	13.0165(3)
α/°	90
β/°	101.766(2)
γ/°	90
Volume/Å^3	2666.43(10)
Z	4
ρ_{calc}g/cm^3	1.925
μ/mm^{-1}	12.782
F(000)	1488.0
Crystal size/mm^3	0.111 × 0.033 × 0.028
Radiation	Cu Kα (λ = 1.54184)
2Θ range for data collection/°	8.816 to 140.594
Index ranges	-19 ≤ h ≤ 19, -15 ≤ k ≤ 15, -15 ≤ l ≤ 15
Reflections collected	24863
Independent reflections	2530 [R_{int} = 0.0242, R_{sigma} = 0.0127]
Data/restraints/parameters	2530/123/189
Goodness-of-fit on F^2	1.074
Final R indexes [I>=2σ (I)]	R_1 = 0.0380, wR_2 = 0.1019
Final R indexes [all data]	R_1 = 0.0382, wR_2 = 0.1021
Largest diff. peak/hole / e Å^{-3}	4.31/-2.32

Table 9.31 – Fractional Atomic Coordinates (×10^4) and Equivalent Isotropic Displacement Parameters (Å^2×10^3) for 2021NCS0465_LJM1a. U_{eq} is defined as 1/3 of the trace of the orthogonalised U_{IJ} tensor.

Atom	*x*	*y*	*z*	U(eq)
Ir1	5000	3198.9(2)	7500	12.22(14)
Cl1	6057.5(8)	4475.7(10)	7682.1(10)	17.9(3)
N1	4072(3)	2107(4)	7227(4)	14.5(9)
N2	4793(3)	3142(3)	5898(4)	15.1(10)
C1	3733(4)	1603(4)	7930(5)	18.0(11)
C2	3070(4)	901(5)	7630(5)	22.1(12)
C3	2753(4)	715(4)	6586(5)	21.9(12)
C4	3104(3)	1249(4)	5827(5)	18.8(11)
C5	3762(4)	1937(4)	6186(5)	16.7(11)
C6	4143(3)	2495(4)	5469(4)	16.4(11)
C7	3842(4)	2398(5)	4385(4)	20.3(12)
C8	4242(4)	2996(5)	3726(5)	23.7(12)
C9	4909(4)	3624(5)	4160(5)	24.5(13)
C10	5176(4)	3683(4)	5252(4)	18.8(11)
C11	2803(4)	1151(5)	4711(5)	23.9(12)
C12	3148(4)	1707(5)	4025(5)	23.7(13)
S1	2773(3)	-2007(4)	5499(3)	35.0(10)
F1	2949(7)	-3844(8)	5306(7)	45.4(17)
F3	2666(8)	-3175(8)	3829(8)	45.4(17)
F2	1681(8)	-3484(10)	4781(11)	45.4(17)
O1	2645(12)	-2096(14)	6499(9)	73(3)
O3	2141(10)	-1196(11)	5103(11)	73(3)
O2	3540(9)	-1698(15)	5293(18)	73(3)
C13	2436(9)	-3098(12)	4755(10)	49(4)

Table 9.32 – Anisotropic Displacement Parameters (Å2×103) for 2021NCS0465_LJM1a. The Anisotropic displacement factor exponent takes the form: -2π2[h2a*2U11+2hka*b*U12+…].

Atom	U_{11}	U_{22}	U_{33}	U_{23}	U_{13}	U_{12}
Ir1	10.57(19)	13.5(2)	12.04(19)	0	1.06(12)	0
Cl1	14.3(6)	18.5(6)	19.2(6)	2.5(5)	-0.9(5)	-3.7(5)
N1	13(2)	15(2)	15(2)	-1.6(18)	3.5(17)	1.4(18)
N2	13(2)	14(2)	17(2)	1.2(16)	-0.2(18)	1.7(16)
C1	19(3)	19(3)	16(3)	-3(2)	6(2)	-1(2)
C2	22(3)	24(3)	23(3)	0(2)	9(2)	-4(2)

C3	15(3)	18(3)	32(3)	-5(2)	4(2)	-4(2)
C4	14(3)	20(3)	22(3)	-3(2)	3(2)	3(2)
C5	14(3)	16(3)	19(3)	0(2)	2(2)	5(2)
C6	16(3)	17(3)	16(3)	1(2)	4(2)	5(2)
C7	20(3)	20(3)	19(3)	-1(2)	-1(2)	5(2)
C8	30(3)	26(3)	14(3)	2(2)	2(2)	6(3)
C9	32(3)	23(3)	19(3)	3(2)	8(2)	2(3)
C10	21(3)	18(3)	18(3)	1(2)	5(2)	0(2)
C11	18(3)	26(3)	25(3)	-8(2)	-2(2)	0(2)
C12	24(3)	26(3)	18(3)	-5(2)	-2(2)	2(2)
S1	27.7(18)	57(2)	24.5(18)	-20.7(17)	14.5(15)	-15.4(16)
F1	68(4)	48(3)	25(3)	-11(2)	21(3)	-25(3)
F3	68(4)	48(3)	25(3)	-11(2)	21(3)	-25(3)
F2	68(4)	48(3)	25(3)	-11(2)	21(3)	-25(3)
O1	93(7)	82(7)	46(5)	-19(5)	14(5)	-18(5)
O3	93(7)	82(7)	46(5)	-19(5)	14(5)	-18(5)
O2	93(7)	82(7)	46(5)	-19(5)	14(5)	-18(5)
C13	73(8)	39(8)	45(8)	2(6)	34(8)	-5(6)

Table 9.33 – Bond Lengths for 2021NCS0465_LJM1a.

Atom	Atom	Length/Å		Atom	Atom	Length/Å
Ir1	$Cl1^1$	2.3545(12)		C5	C6	1.416(8)
Ir1	Cl1	2.3545(12)		C6	C7	1.401(8)
Ir1	N1	2.038(5)		C7	C8	1.407(9)
Ir1	$N1^1$	2.038(5)		C7	C12	1.436(9)
Ir1	N2	2.045(5)		C8	C9	1.373(9)
Ir1	$N2^1$	2.045(5)		C9	C10	1.402(8)
N1	C1	1.330(8)		C11	C12	1.353(9)
N1	C5	1.363(8)		S1	O1	1.364(11)
N2	C6	1.370(7)		S1	O3	1.482(12)
N2	C10	1.338(7)		S1	O2	1.375(12)
C1	C2	1.398(8)		S1	C13	1.741(13)
C2	C3	1.373(9)		F1	C13	1.378(12)
C3	C4	1.417(8)		F3	C13	1.335(11)
C4	C5	1.392(8)		F2	C13	1.320(11)

C4	C11	1.440(8)				

[1]1-X,+Y,3/2-Z

Table 9.34 – Bond Angles for 2021NCS0465_LJM1a.

Atom	Atom	Atom	Angle/°		Atom	Atom	Atom	Angle/°
Cl1	Ir1	Cl1[1]	90.15(6)		N1	C5	C4	122.5(5)
N1[1]	Ir1	Cl1	89.31(14)		N1	C5	C6	116.9(5)
N1[1]	Ir1	Cl1[1]	175.82(13)		C4	C5	C6	120.6(5)
N1	Ir1	Cl1[1]	89.31(13)		N2	C6	C5	116.3(5)
N1	Ir1	Cl1	175.82(13)		N2	C6	C7	122.9(5)
N1[1]	Ir1	N1	91.5(3)		C7	C6	C5	120.7(5)
N1[1]	Ir1	N2	96.53(18)		C6	C7	C8	117.2(5)
N1	Ir1	N2[1]	96.53(18)		C6	C7	C12	118.1(6)
N1	Ir1	N2	80.56(18)		C8	C7	C12	124.7(6)
N1[1]	Ir1	N2[1]	80.57(18)		C9	C8	C7	119.6(6)
N2[1]	Ir1	Cl1[1]	95.27(13)		C8	C9	C10	120.1(6)
N2[1]	Ir1	Cl1	87.65(13)		N2	C10	C9	121.5(5)
N2	Ir1	Cl1	95.27(13)		C12	C11	C4	121.4(6)
N2	Ir1	Cl1[1]	87.65(13)		C11	C12	C7	121.0(6)
N2	Ir1	N2[1]	175.9(2)		O1	S1	O3	99.6(9)
C1	N1	Ir1	127.7(4)		O1	S1	O2	121.8(12)
C1	N1	C5	119.1(5)		O1	S1	C13	111.8(8)
C5	N1	Ir1	113.1(4)		O3	S1	C13	105.9(7)
C6	N2	Ir1	112.9(4)		O2	S1	O3	107.6(11)
C10	N2	Ir1	128.4(4)		O2	S1	C13	108.7(9)
C10	N2	C6	118.6(5)		F1	C13	S1	101.6(9)
N1	C1	C2	121.7(5)		F3	C13	S1	116.9(9)
C3	C2	C1	120.0(5)		F3	C13	F1	99.8(10)
C2	C3	C4	118.9(5)		F2	C13	S1	118.6(10)
C3	C4	C11	124.1(5)		F2	C13	F1	100.0(11)
C5	C4	C3	117.7(5)		F2	C13	F3	114.8(12)
C5	C4	C11	118.1(5)					

[1]1-X,+Y,3/2-Z

Table 9.35 – Torsion Angles for 2021NCS0465_LJM1a.

A	B	C	D	Angle/°		A	B	C	D	Angle/°
Ir1	N1	C1	C2	177.1(4)		C5	C4	C11	C12	0.2(9)
Ir1	N1	C5	C4	-177.6(4)		C5	C6	C7	C8	178.6(5)
Ir1	N1	C5	C6	2.5(6)		C5	C6	C7	C12	-0.9(8)
Ir1	N2	C6	C5	-3.6(6)		C6	N2	C10	C9	2.0(8)
Ir1	N2	C6	C7	174.6(4)		C6	C7	C8	C9	1.3(9)
Ir1	N2	C10	C9	-174.1(4)		C6	C7	C12	C11	-1.2(9)
N1	C1	C2	C3	0.2(9)		C7	C8	C9	C10	-1.3(9)
N1	C5	C6	N2	0.8(7)		C8	C7	C12	C11	179.4(6)
N1	C5	C6	C7	-177.5(5)		C8	C9	C10	N2	-0.4(9)
N2	C6	C7	C8	0.4(8)		C10	N2	C6	C5	179.7(5)
N2	C6	C7	C12	-179.1(5)		C10	N2	C6	C7	-2.1(8)
C1	N1	C5	C4	-0.3(8)		C11	C4	C5	N1	177.9(5)
C1	N1	C5	C6	179.8(5)		C11	C4	C5	C6	-2.2(8)
C1	C2	C3	C4	-0.5(9)		C12	C7	C8	C9	-179.3(6)
C2	C3	C4	C5	0.4(8)		O1	S1	C13	F1	-61.0(12)
C2	C3	C4	C11	-177.3(6)		O1	S1	C13	F3	-168.4(12)
C3	C4	C5	N1	0.1(8)		O1	S1	C13	F2	47.3(14)
C3	C4	C5	C6	180.0(5)		O3	S1	C13	F1	-168.5(10)
C3	C4	C11	C12	177.9(6)		O3	S1	C13	F3	84.1(13)
C4	C5	C6	N2	-179.1(5)		O3	S1	C13	F2	-60.2(13)
C4	C5	C6	C7	2.6(8)		O2	S1	C13	F1	76.2(13)
C4	C11	C12	C7	1.5(9)		O2	S1	C13	F3	-31.2(16)
C5	N1	C1	C2	0.2(8)		O2	S1	C13	F2	-175.5(15)

Table 9.36 – Hydrogen Atom Coordinates (Åx10^4) and Isotropic Displacement Parameters (Å2x10^3) for 2021NCS0465_LJM1a.

Atom	*x*	*y*	*z*	U(eq)
H1	3947.84	1722.94	8656.01	22
H2	2838.3	553.83	8149.5	27
H3	2304.91	235.05	6375.84	26
H8	4052.67	2966.41	2986.4	28
H9	5188.72	4018.66	3718.1	29

H10	5640.29	4117.43	5541.73	23
H11	2353.58	687.03	4451.57	29
H12	2927.32	1639.21	3293.14	28

Table 9.37 – Atomic Occupancy for 2021NCS0465_LJM1a.

Atom	Occupancy		Atom	Occupancy		Atom	Occupancy
S1	0.5		F1	0.5		F3	0.5
F2	0.5		O1	0.5		O3	0.5
O2	0.5		C13	0.5			

Table 9.38 – Solvent masks information for 2021NCS0465_LJM1a.

Number	X	Y	Z	Volume	Electron count	Content
1	0.000	0.500	-0.437	167.4	41.5	?
2	0.500	0.000	0.705	167.4	41.5	?

Crystal structure determination of 2021NCS0465_LJM1a

Crystal Data for $C_{25}H_{16}Cl_2F_3IrN_4O_3S$ (M =772.58 g/mol): monoclinic, space group C2/c (no. 15), a = 16.0688(3) Å, b = 13.0219(3) Å, c = 13.0165(3) Å, β = 101.766(2)°, V = 2666.43(10) Å^3, Z = 4, T = 100.00(10) K, μ(Cu Kα) = 12.782 mm^{-1}, *Dcalc* = 1.925 g/cm^3, 24863 reflections measured (8.816° ≤ 2Θ ≤ 140.594°), 2530 unique (R_{int} = 0.0242, R_{sigma} = 0.0127) which were used in all calculations. The final R_1 was 0.0380 (I > 2σ(I)) and wR_2 was 0.1021 (all data).

9.3.5 IAJ688k_0m $[Ir(phen)_2(CF_3SO_3)_2]CF_3SO_3$

Table 9.39 – Crystal data and structure refinement for IAJ688k_0m.

Identification code	IAJ688k_0m
Empirical formula	$C_{27}H_{16}F_9IrN_4O_9S_3$
Formula weight	999.82
Temperature/K	100
Crystal system	triclinic
Space group	P-1
a/Å	13.5471(11)

b/Å	16.7910(13)
c/Å	17.6060(13)
α/°	103.907(4)
β/°	95.410(4)
γ/°	90.424(4)
Volume/Å^3	3868.2(5)
Z	4
ρ_{calc}g/cm^3	1.717
μ/mm^{-1}	3.707
F(000)	1936.0
Crystal size/mm^3	0.4 × 0.15 × 0.15
Radiation	MoKα (λ = 0.71073)
2Θ range for data collection/°	3.014 to 57.626
Index ranges	-18 ≤ h ≤ 18, -22 ≤ k ≤ 22, -23 ≤ l ≤ 23
Reflections collected	123461
Independent reflections	20111 [R_{int} = 0.0835, R_{sigma} = 0.0640]
Data/restraints/parameters	20111/990/971
Goodness-of-fit (S) on F^2	1.032
Final R indexes [I>=2σ (I)]	R_1 = 0.0483, wR_2 = 0.1062
Final R indexes [all data]	R_1 = 0.0801, wR_2 = 0.1226
Largest diff. peak/hole / e Å^{-3}	3.21/-2.27

Table 9.40 – Fractional Atomic Coordinates (×10^4) and Equivalent Isotropic Displacement Parameters (Å^2×10^3) for IAJ688k_0m. U_{eq} is defined as 1/3 of the trace of the orthogonalised U_{IJ} tensor.

Atom	*x*	*y*	*z*	U(eq)
Ir1B	9382.2(2)	1863.2(2)	3001.8(2)	19.24(6)
S1B	10742.2(11)	273.4(10)	2890.4(9)	22.7(3)
F1B	12095(4)	-726(3)	2345(3)	57.3(13)
F2B	11000(3)	-523(3)	1455(2)	42.2(10)
F3B	12108(3)	418(3)	1986(3)	46.7(11)
O1B	10221(3)	867(3)	2503(2)	26.2(9)
O2B	11403(3)	644(3)	3563(3)	33.6(11)
O3B	10106(4)	-386(3)	2958(3)	36.7(11)
O4B	9177(3)	2145(3)	1906(2)	27.0(10)
O6B	10801(4)	2064(3)	1403(3)	40.5(12)

N1B	10563(4)	2691(3)	3302(3)	22.1(10)
N2B	8640(4)	2886(3)	3405(3)	21.9(10)
N3B	9417(3)	1536(3)	4030(3)	21.0(10)
N4B	8181(3)	1063(3)	2744(3)	20.1(10)
C1B	11529(5)	2560(4)	3237(4)	26.2(13)
C2B	12235(5)	3204(5)	3432(4)	32.7(14)
C3B	11960(6)	3993(5)	3692(4)	39.8(17)
C4B	10932(5)	4146(5)	3768(4)	37.5(16)
C5B	10270(5)	3472(4)	3567(4)	26.2(13)
C6B	10533(7)	4948(5)	4027(6)	58(2)
C7B	9557(7)	5051(6)	4085(6)	64(3)
C8B	8864(6)	4359(5)	3879(5)	40.8(17)
C9B	7821(6)	4419(5)	3930(5)	44.8(18)
C10B	7241(5)	3717(5)	3705(4)	37.7(17)
C11B	7662(5)	2960(4)	3443(4)	28.5(14)
C12B	9245(5)	3577(4)	3621(4)	28.2(13)
C13B	10051(5)	1790(5)	4675(4)	32.1(15)
C14B	10017(5)	1477(5)	5325(4)	38.6(16)
C15B	9325(6)	871(5)	5321(4)	39.6(17)
C16B	8638(5)	576(4)	4659(4)	30.0(14)
C17B	8721(5)	941(4)	4028(4)	23.8(12)
C18B	7895(5)	-52(5)	4577(4)	37.6(16)
C19B	7269(5)	-302(5)	3915(5)	36.4(15)
C20B	7320(4)	73(4)	3272(4)	27.4(13)
C21B	6696(5)	-136(4)	2567(4)	32.0(14)
C22B	6820(5)	255(4)	1979(4)	31.4(14)
C23B	7577(4)	852(4)	2074(4)	26.3(13)
C24B	8047(4)	685(4)	3333(3)	21.7(11)
C25B	11531(5)	-161(4)	2125(4)	30.4(14)
C26B	9279(6)	2417(6)	577(5)	56.8(18)
S1BA	9712(8)	2493(8)	1474(6)	36(3)
F4BA	9210(30)	1560(11)	346(18)	65.9(12)
F5BA	9940(20)	2570(30)	91(19)	65.9(12)
F6BA	8304(15)	2540(40)	460(50)	65.9(12)
O5BA	9500(30)	3370(20)	1460(30)	49(7)
S1BB	9771.3(13)	1828.4(12)	1226.3(10)	22.7(5)

F4BB	9526(5)	3241(4)	878(4)	65.9(12)
F5BB	8301(5)	2363(6)	430(9)	65.9(12)
F6BB	9650(5)	2222(5)	-109(4)	65.9(12)
O5BB	9477(4)	1019(3)	806(3)	36.6(14)
Ir1A	4059.8(2)	2586.9(2)	795.9(2)	19.38(6)
S1A	4859.2(12)	2206.9(10)	2446.1(9)	26.0(3)
S2A	5419.2(12)	1547.0(11)	-431.0(9)	29.9(4)
F1A	4462(3)	653(3)	2338(3)	44.6(11)
F2A	3591(3)	1486(3)	3115(2)	39.3(10)
F3A	5129(3)	1319(3)	3466(3)	51.7(12)
F4A	6925(4)	1025(4)	330(3)	63.2(15)
F5A	5887(4)	79(3)	-292(4)	75.8(18)
F6A	6856(4)	630(4)	-918(3)	62.8(14)
O1A	4089(3)	2090(3)	1780(2)	23.0(9)
O2A	5837(3)	2017(3)	2218(3)	35.3(11)
O3A	4749(4)	2949(3)	3038(3)	38.6(12)
O4A	5009(3)	1657(3)	343(2)	24.8(9)
O5A	4742(4)	1174(4)	-1087(3)	46.3(14)
O6A	6008(4)	2240(3)	-491(3)	42.1(13)
N1A	5184(4)	3422(3)	1335(3)	23.7(10)
N2A	3228(4)	3496(3)	1336(3)	23.1(10)
N3A	3869(4)	2966(3)	-215(3)	23.6(10)
N4A	2905(4)	1807(3)	241(3)	20.7(10)
C1A	6156(5)	3349(4)	1309(4)	28.7(14)
C2A	6822(6)	3970(4)	1745(4)	35.8(16)
C3A	6482(5)	4663(4)	2211(4)	33.6(15)
C4A	5455(5)	4746(4)	2254(4)	28.0(13)
C5A	4826(5)	4107(4)	1799(3)	22.9(12)
C6A	5000(6)	5446(4)	2719(4)	37.0(16)
C7A	4002(6)	5497(4)	2704(5)	41.6(17)
C8A	3349(6)	4849(4)	2238(4)	33.5(14)
C9A	2315(6)	4863(5)	2194(5)	45.4(19)
C10A	1761(6)	4200(5)	1720(5)	42.5(18)
C11A	2253(5)	3524(4)	1303(4)	33.0(15)
C12A	3787(5)	4157(4)	1796(4)	25.5(12)
C13A	4375(6)	3546(5)	-415(4)	39.5(17)

C14A	4176(7)	3706(5)	-1156(5)	51(2)
C15A	3447(7)	3263(5)	-1693(5)	47.7(19)
C16A	2915(6)	2653(5)	-1493(4)	36.6(15)
C17A	3129(5)	2520(4)	-738(4)	27.6(13)
C18A	2145(6)	2146(5)	-1999(4)	39.9(16)
C19A	1645(6)	1558(5)	-1766(4)	39.3(16)
C20A	1868(5)	1416(4)	-1002(4)	29.7(13)
C21A	1417(5)	796(4)	-718(4)	32.3(14)
C22A	1709(5)	709(4)	18(4)	28.7(14)
C23A	2466(4)	1221(4)	491(4)	22.9(12)
C24A	2620(4)	1906(4)	-495(4)	23.9(12)
C25A	4483(5)	1374(4)	2869(4)	29.7(13)
C26A	6318(5)	776(5)	-323(4)	38.1(15)
S1AA	2390.5(16)	3047.7(12)	5855.6(11)	40.6(5)
F0AA	3959(5)	2170(5)	5740(4)	97(2)
F9	3756(4)	2912(5)	4904(4)	99(2)
F11	2851(5)	1835(4)	4748(4)	88(2)
O1AA	1697(4)	3271(3)	5273(3)	42.3(13)
O13	2011(5)	2444(5)	6224(4)	69.0(19)
O15	2932(6)	3709(4)	6391(4)	86(3)
C16	3285(7)	2462(6)	5273(6)	57(2)
S2AA	7635(2)	3262(2)	5711.4(19)	80.0(9)
F1AA	5905(7)	2633(6)	5770(6)	142(3)
F17	6346(11)	2466(12)	4634(7)	270(8)
F18	6984(12)	1788(7)	5442(11)	248(7)
O2AA	7871(8)	3249(8)	6535(5)	140(4)
O3AA	7134(8)	4032(6)	5616(7)	130(4)
O4AA	8395(6)	2993(5)	5200(4)	82(2)
C0AA	6675(12)	2504(9)	5338(8)	102(4)

Table 9.41 – Anisotropic Displacement Parameters ($Å^2 \times 10^3$) for IAJ688k_0m. The Anisotropic displacement factor exponent takes the form: $-2\pi^2[h^2a^{*2}U_{11}+2hka^*b^*U_{12}+\ldots]$.

Atom	U_{11}	U_{22}	U_{33}	U_{23}	U_{13}	U_{12}
Ir1B	16.51(11)	24.50(13)	15.50(11)	3.29(9)	-0.72(8)	2.45(9)
S1B	20.4(7)	27.7(8)	19.6(7)	5.0(6)	1.1(6)	4.2(6)

F1B	59(3)	66(3)	48(3)	13(2)	11(2)	41(3)
F2B	39(2)	52(3)	26(2)	-6.8(18)	2.3(17)	7(2)
F3B	37(2)	60(3)	43(3)	7(2)	18(2)	-3(2)
O1B	25(2)	34(2)	20(2)	5.7(18)	4.5(17)	12.0(18)
O2B	30(2)	46(3)	22(2)	5(2)	-2.3(19)	5(2)
O3B	41(3)	43(3)	27(3)	13(2)	-1(2)	-5(2)
O4B	26(2)	36(3)	20(2)	8.6(18)	2.0(17)	6.3(19)
O6B	29(3)	58(3)	36(3)	14(2)	3(2)	-5(2)
N1B	17(2)	26(2)	22(3)	5(2)	-5.2(19)	-0.9(19)
N2B	20(2)	26(3)	16(2)	-1(2)	-4.2(18)	4.4(19)
N3B	16(2)	29(3)	16(2)	3(2)	0.7(17)	2.9(19)
N4B	13(2)	21(2)	25(2)	3.8(19)	-0.6(18)	1.2(18)
C1B	23(3)	31(3)	25(3)	9(3)	1(2)	3(2)
C2B	23(3)	45(4)	32(4)	14(3)	-5(3)	-3(3)
C3B	39(3)	37(4)	37(4)	4(3)	-16(3)	-8(3)
C4B	35(3)	36(3)	38(4)	7(3)	-8(3)	-3(3)
C5B	28(3)	24(3)	24(3)	4(2)	-2(2)	1(2)
C6B	53(4)	32(4)	79(7)	-1(4)	-11(4)	-6(3)
C7B	56(4)	34(4)	93(8)	-1(5)	-3(5)	2(3)
C8B	41(3)	31(3)	42(4)	-4(3)	-1(3)	5(3)
C9B	39(4)	42(4)	47(5)	0(4)	3(3)	15(3)
C10B	26(3)	36(4)	46(4)	1(3)	0(3)	12(3)
C11B	21(3)	38(3)	25(3)	4(3)	1(2)	10(3)
C12B	31(3)	30(3)	19(3)	-1(2)	0(2)	4(2)
C13B	27(3)	46(4)	18(3)	0(3)	-2(2)	-1(3)
C14B	34(4)	59(5)	21(3)	8(3)	-2(3)	4(3)
C15B	40(4)	58(5)	24(3)	18(3)	2(3)	8(3)
C16B	29(3)	39(4)	25(3)	13(3)	8(2)	8(3)
C17B	24(3)	28(3)	19(3)	4(2)	5(2)	3(2)
C18B	40(4)	42(4)	39(4)	24(3)	12(3)	4(3)
C19B	30(3)	37(4)	48(4)	20(3)	11(3)	3(3)
C20B	17(3)	26(3)	40(3)	8(3)	6(2)	5(2)
C21B	20(3)	31(4)	42(4)	1(3)	5(3)	2(3)
C22B	23(3)	34(4)	32(3)	-2(3)	-1(3)	1(3)
C23B	22(3)	32(3)	21(3)	2(3)	-2(2)	5(2)
C24B	18(3)	25(3)	21(3)	3(2)	4(2)	5(2)

C25B	25(3)	33(3)	30(3)	0(3)	3(2)	11(2)
C26B	63(4)	74(4)	42(4)	31(4)	0(3)	10(4)
S1BA	31(5)	44(8)	38(5)	19(5)	3(4)	1(5)
F4BA	68(2)	85(3)	54(2)	40(2)	-4.6(17)	4(2)
F5BA	68(2)	85(3)	54(2)	40(2)	-4.6(17)	4(2)
F6BA	68(2)	85(3)	54(2)	40(2)	-4.6(17)	4(2)
O5BA	37(17)	40(12)	82(19)	25(8)	33(17)	-4(10)
S1BB	21.4(9)	28.9(12)	18.3(9)	6.2(7)	3.1(7)	0.8(7)
F4BB	68(2)	85(3)	54(2)	40(2)	-4.6(17)	4(2)
F5BB	68(2)	85(3)	54(2)	40(2)	-4.6(17)	4(2)
F6BB	68(2)	85(3)	54(2)	40(2)	-4.6(17)	4(2)
O5BB	36(3)	31(3)	36(3)	-8(2)	7(3)	-2(2)
Ir1A	23.01(12)	19.29(12)	14.37(11)	1.15(9)	2.20(9)	-1.63(9)
S1A	23.2(7)	30.4(9)	24.1(8)	6.9(6)	-0.7(6)	-0.7(6)
S2A	29.6(8)	35.1(9)	22.5(8)	2.6(7)	1.8(6)	1.2(7)
F1A	48(3)	31(2)	54(3)	8.7(19)	3(2)	1.8(19)
F2A	36(2)	49(3)	37(2)	15(2)	12.0(18)	0.3(19)
F3A	51(3)	64(3)	44(3)	31(2)	-20(2)	-6(2)
F4A	52(3)	87(4)	45(3)	11(3)	-12(2)	22(3)
F5A	58(3)	42(3)	135(6)	29(3)	31(3)	10(2)
F6A	56(3)	83(4)	54(3)	15(3)	31(2)	28(3)
O1A	20(2)	30(2)	19(2)	5.4(17)	3.5(16)	-1.4(17)
O2A	18(2)	43(3)	48(3)	16(2)	2(2)	-3(2)
O3A	47(3)	33(3)	30(3)	-2(2)	-1(2)	-2(2)
O4A	34(2)	18(2)	23(2)	3.2(17)	7.4(18)	2.0(18)
O5A	39(3)	57(4)	31(3)	-7(2)	-7(2)	6(3)
O6A	47(3)	43(3)	39(3)	14(2)	11(2)	-9(2)
N1A	29(2)	23(3)	17(2)	1.7(19)	5(2)	-2(2)
N2A	29(2)	24(3)	15(2)	-0.1(19)	6.7(19)	-2(2)
N3A	32(3)	20(3)	18(2)	2.6(19)	3(2)	2(2)
N4A	19(2)	21(2)	18(2)	-2.3(19)	0.7(18)	2.7(19)
C1A	28(3)	28(3)	26(3)	-2(3)	6(2)	-4(2)
C2A	35(4)	36(4)	31(4)	-1(3)	-1(3)	-10(3)
C3A	41(3)	31(3)	24(3)	0(3)	2(3)	-18(3)
C4A	45(3)	22(3)	17(3)	5(2)	7(2)	-7(2)
C5A	35(3)	20(3)	16(3)	6(2)	8(2)	-1(2)

C6A	55(4)	23(3)	30(4)	-2(3)	8(3)	-13(3)
C7A	58(4)	24(3)	39(4)	-5(3)	17(3)	-1(3)
C8A	48(3)	22(3)	31(4)	2(3)	15(3)	0(3)
C9A	49(4)	32(4)	52(5)	-1(3)	21(4)	7(3)
C10A	39(4)	35(4)	54(5)	6(3)	14(3)	8(3)
C11A	31(3)	32(4)	34(4)	2(3)	10(3)	3(3)
C12A	36(3)	21(3)	20(3)	4(2)	8(2)	2(2)
C13A	52(4)	38(4)	32(4)	15(3)	7(3)	-9(3)
C14A	74(6)	48(5)	38(4)	23(4)	9(4)	-4(4)
C15A	68(5)	50(5)	31(4)	21(3)	6(3)	10(4)
C16A	50(4)	37(4)	24(3)	11(3)	0(3)	11(3)
C17A	31(3)	26(3)	24(3)	3(2)	2(2)	8(2)
C18A	51(4)	42(4)	24(3)	7(3)	-9(3)	17(3)
C19A	39(4)	48(4)	24(3)	0(3)	-10(3)	8(3)
C20A	23(3)	36(4)	24(3)	-3(2)	-2(2)	7(2)
C21A	19(3)	36(4)	33(3)	-6(3)	-4(2)	1(3)
C22A	24(3)	24(3)	33(3)	-2(3)	1(2)	0(2)
C23A	23(3)	24(3)	22(3)	4(2)	6(2)	-1(2)
C24A	22(3)	28(3)	21(3)	4(2)	1(2)	5(2)
C25A	28(3)	32(3)	31(3)	14(3)	-2(2)	4(3)
C26A	30(3)	46(4)	37(4)	5(3)	8(3)	6(3)
S1AA	54.9(12)	32.9(10)	25.9(9)	-2.0(7)	-12.6(8)	-1.1(8)
F0AA	71(4)	126(6)	108(5)	60(5)	-6(4)	36(4)
F9	46(3)	175(7)	106(5)	90(5)	13(3)	9(4)
F11	116(5)	67(4)	65(4)	-15(3)	7(3)	28(3)
O1AA	46(3)	38(3)	38(3)	2(2)	-5(2)	2(2)
O13	78(5)	90(5)	44(4)	32(4)	-5(3)	-14(4)
O15	136(7)	39(4)	61(4)	-9(3)	-53(4)	-9(4)
C16	48(5)	62(5)	64(5)	25(4)	-1(4)	11(4)
S2AA	75.5(19)	91(2)	68.9(19)	8.2(16)	14.9(15)	-0.4(17)
F1AA	113(6)	149(8)	163(8)	22(7)	56(6)	-27(5)
F17	240(14)	430(20)	100(7)	10(10)	-11(7)	-221(14)
F18	276(15)	82(6)	402(19)	26(9)	207(14)	8(7)
O2AA	140(9)	214(13)	62(6)	26(7)	8(5)	3(8)
O3AA	153(9)	73(6)	180(10)	41(6)	73(8)	39(6)
O4AA	77(5)	92(6)	74(5)	7(4)	32(4)	22(4)

C0AA	124(9)	92(7)	78(7)	-16(7)	45(6)	-35(7)

Table 9.42 – Bond Lengths for IAJ688k_0m.

Atom	Atom	Length/Å	Atom	Atom	Length/Å
Ir1B	O1B	2.091(4)	Ir1A	N3A	2.025(5)
Ir1B	O4B	2.089(4)	Ir1A	N4A	2.046(5)
Ir1B	N1B	2.056(5)	S1A	O1A	1.470(4)
Ir1B	N2B	2.009(5)	S1A	O2A	1.436(5)
Ir1B	N3B	2.011(5)	S1A	O3A	1.438(5)
Ir1B	N4B	2.048(5)	S1A	C25A	1.825(7)
S1B	O1B	1.484(4)	S2A	O4A	1.491(4)
S1B	O2B	1.424(5)	S2A	O5A	1.418(5)
S1B	O3B	1.432(5)	S2A	O6A	1.436(5)
S1B	C25B	1.817(7)	S2A	C26A	1.814(8)
F1B	C25B	1.329(8)	F1A	C25A	1.338(8)
F2B	C25B	1.328(7)	F2A	C25A	1.322(8)
F3B	C25B	1.325(8)	F3A	C25A	1.325(7)
O4B	S1BA	1.325(12)	F4A	C26A	1.326(9)
O4B	S1BB	1.498(5)	F5A	C26A	1.319(9)
O6B	S1BA	1.649(13)	F6A	C26A	1.308(8)
O6B	S1BB	1.432(5)	N1A	C1A	1.328(8)
N1B	C1B	1.339(8)	N1A	C5A	1.363(8)
N1B	C5B	1.357(8)	N2A	C11A	1.318(8)
N2B	C11B	1.337(8)	N2A	C12A	1.379(8)
N2B	C12B	1.371(8)	N3A	C13A	1.321(9)
N3B	C13B	1.337(7)	N3A	C17A	1.377(8)
N3B	C17B	1.368(8)	N4A	C23A	1.328(8)
N4B	C23B	1.343(7)	N4A	C24A	1.366(8)
N4B	C24B	1.364(8)	C1A	C2A	1.401(9)
C1B	C2B	1.395(9)	C2A	C3A	1.364(10)
C2B	C3B	1.360(10)	C3A	C4A	1.406(10)
C3B	C4B	1.430(11)	C4A	C5A	1.401(9)
C4B	C5B	1.394(9)	C4A	C6A	1.441(10)
C4B	C6B	1.442(11)	C5A	C12A	1.410(9)
C5B	C12B	1.410(9)	C6A	C7A	1.354(11)

C6B	C7B	1.345(13)	C7A	C8A	1.435(10)
C7B	C8B	1.443(11)	C8A	C9A	1.397(11)
C8B	C9B	1.427(11)	C8A	C12A	1.404(9)
C8B	C12B	1.402(10)	C9A	C10A	1.387(11)
C9B	C10B	1.366(11)	C10A	C11A	1.405(10)
C10B	C11B	1.390(9)	C13A	C14A	1.397(10)
C13B	C14B	1.374(10)	C14A	C15A	1.378(12)
C14B	C15B	1.376(11)	C15A	C16A	1.379(11)
C15B	C16B	1.407(10)	C16A	C17A	1.404(9)
C16B	C17B	1.404(9)	C16A	C18A	1.433(10)
C16B	C18B	1.425(10)	C17A	C24A	1.408(9)
C17B	C24B	1.431(8)	C18A	C19A	1.357(11)
C18B	C19B	1.352(10)	C19A	C20A	1.427(10)
C19B	C20B	1.429(10)	C20A	C21A	1.418(10)
C20B	C21B	1.403(9)	C20A	C24A	1.405(8)
C20B	C24B	1.396(9)	C21A	C22A	1.360(10)
C21B	C22B	1.373(10)	C22A	C23A	1.402(8)
C22B	C23B	1.399(9)	S1AA	O1AA	1.443(5)
C26B	S1BA	1.606(13)	S1AA	O13	1.444(7)
C26B	F4BA	1.397(16)	S1AA	O15	1.418(6)
C26B	F5BA	1.355(16)	S1AA	C16	1.804(10)
C26B	F6BA	1.341(16)	F0AA	C16	1.346(10)
C26B	S1BB	1.771(9)	F9	C16	1.308(11)
C26B	F4BB	1.384(9)	F11	C16	1.315(11)
C26B	F5BB	1.324(9)	S2AA	O2AA	1.460(10)
C26B	F6BB	1.322(9)	S2AA	O3AA	1.501(10)
S1BA	O5BA	1.51(4)	S2AA	O4AA	1.436(7)
S1BB	O5BB	1.417(6)	S2AA	C0AA	1.778(14)
Ir1A	O1A	2.093(4)	F1AA	C0AA	1.337(15)
Ir1A	O4A	2.086(4)	F17	C0AA	1.262(18)
Ir1A	N1A	2.059(5)	F18	C0AA	1.32(2)
Ir1A	N2A	2.008(5)			

Table 9.43 – Bond Angles for IAJ688k_0m.

Atom	**Atom**	**Atom**	**Angle/°**	**Atom**	**Atom**	**Atom**	**Angle/°**

O4B	Ir1B	O1B	88.84(17)	N2A	Ir1A	N3A	91.1(2)
N1B	Ir1B	O1B	95.10(19)	N2A	Ir1A	N4A	96.5(2)
N1B	Ir1B	O4B	88.93(19)	N3A	Ir1A	O1A	172.23(18)
N2B	Ir1B	O1B	173.9(2)	N3A	Ir1A	O4A	93.58(19)
N2B	Ir1B	O4B	86.19(19)	N3A	Ir1A	N1A	96.4(2)
N2B	Ir1B	N1B	81.2(2)	N3A	Ir1A	N4A	81.4(2)
N2B	Ir1B	N3B	92.8(2)	N4A	Ir1A	O1A	90.85(18)
N2B	Ir1B	N4B	97.0(2)	N4A	Ir1A	O4A	87.47(18)
N3B	Ir1B	O1B	92.58(18)	N4A	Ir1A	N1A	176.9(2)
N3B	Ir1B	O4B	173.31(18)	O1A	S1A	C25A	99.0(3)
N3B	Ir1B	N1B	97.5(2)	O2A	S1A	O1A	113.7(3)
N3B	Ir1B	N4B	81.1(2)	O2A	S1A	O3A	117.8(3)
N4B	Ir1B	O1B	86.83(18)	O2A	S1A	C25A	105.6(3)
N4B	Ir1B	O4B	92.49(19)	O3A	S1A	O1A	112.7(3)
N4B	Ir1B	N1B	177.6(2)	O3A	S1A	C25A	105.4(3)
O1B	S1B	C25B	98.3(3)	O4A	S2A	C26A	98.4(3)
O2B	S1B	O1B	114.3(3)	O5A	S2A	O4A	114.2(3)
O2B	S1B	O3B	116.9(3)	O5A	S2A	O6A	117.6(3)
O2B	S1B	C25B	105.5(3)	O5A	S2A	C26A	106.0(3)
O3B	S1B	O1B	113.1(3)	O6A	S2A	O4A	113.5(3)
O3B	S1B	C25B	106.2(3)	O6A	S2A	C26A	104.3(3)
S1B	O1B	Ir1B	128.6(3)	S1A	O1A	Ir1A	128.0(3)
S1BA	O4B	Ir1B	136.6(5)	S2A	O4A	Ir1A	124.4(3)
S1BB	O4B	Ir1B	125.9(3)	C1A	N1A	Ir1A	128.7(4)
C1B	N1B	Ir1B	129.1(4)	C1A	N1A	C5A	119.7(5)
C1B	N1B	C5B	118.8(5)	C5A	N1A	Ir1A	111.5(4)
C5B	N1B	Ir1B	112.1(4)	C11A	N2A	Ir1A	128.4(4)
C11B	N2B	Ir1B	128.1(4)	C11A	N2A	C12A	118.7(6)
C11B	N2B	C12B	119.1(6)	C12A	N2A	Ir1A	112.9(4)
C12B	N2B	Ir1B	112.7(4)	C13A	N3A	Ir1A	127.9(5)
C13B	N3B	Ir1B	128.6(5)	C13A	N3A	C17A	119.8(6)
C13B	N3B	C17B	117.9(6)	C17A	N3A	Ir1A	112.3(4)
C17B	N3B	Ir1B	113.4(4)	C23A	N4A	Ir1A	128.4(4)
C23B	N4B	Ir1B	128.0(4)	C23A	N4A	C24A	119.3(5)
C23B	N4B	C24B	119.0(5)	C24A	N4A	Ir1A	112.2(4)
C24B	N4B	Ir1B	112.9(4)	N1A	C1A	C2A	121.0(6)

N1B	C1B	C2B	121.7(6)	C3A	C2A	C1A	120.4(7)
C3B	C2B	C1B	120.7(7)	C2A	C3A	C4A	119.3(6)
C2B	C3B	C4B	118.5(7)	C3A	C4A	C6A	124.8(6)
C3B	C4B	C6B	124.6(7)	C5A	C4A	C3A	117.6(6)
C5B	C4B	C3B	117.6(7)	C5A	C4A	C6A	117.5(6)
C5B	C4B	C6B	117.8(7)	N1A	C5A	C4A	122.0(6)
N1B	C5B	C4B	122.7(6)	N1A	C5A	C12A	117.3(5)
N1B	C5B	C12B	116.6(6)	C4A	C5A	C12A	120.8(6)
C4B	C5B	C12B	120.7(6)	C7A	C6A	C4A	121.4(6)
C7B	C6B	C4B	121.7(8)	C6A	C7A	C8A	121.6(7)
C6B	C7B	C8B	121.0(8)	C9A	C8A	C7A	124.5(7)
C9B	C8B	C7B	124.2(7)	C9A	C8A	C12A	118.2(6)
C12B	C8B	C7B	117.6(7)	C12A	C8A	C7A	117.3(7)
C12B	C8B	C9B	118.2(7)	C10A	C9A	C8A	119.2(7)
C10B	C9B	C8B	118.5(7)	C9A	C10A	C11A	119.2(7)
C9B	C10B	C11B	120.6(7)	N2A	C11A	C10A	122.6(7)
N2B	C11B	C10B	122.0(7)	N2A	C12A	C5A	116.7(5)
N2B	C12B	C5B	117.3(6)	N2A	C12A	C8A	121.9(6)
N2B	C12B	C8B	121.6(6)	C8A	C12A	C5A	121.4(6)
C8B	C12B	C5B	121.1(6)	N3A	C13A	C14A	120.6(7)
N3B	C13B	C14B	122.2(7)	C15A	C14A	C13A	120.7(8)
C13B	C14B	C15B	120.0(6)	C14A	C15A	C16A	119.2(7)
C14B	C15B	C16B	120.6(7)	C15A	C16A	C17A	118.2(7)
C15B	C16B	C18B	126.1(7)	C15A	C16A	C18A	124.7(7)
C17B	C16B	C15B	115.3(6)	C17A	C16A	C18A	117.1(7)
C17B	C16B	C18B	118.6(6)	N3A	C17A	C16A	121.4(6)
N3B	C17B	C16B	124.0(6)	N3A	C17A	C24A	117.2(6)
N3B	C17B	C24B	116.7(5)	C16A	C17A	C24A	121.3(6)
C16B	C17B	C24B	119.2(6)	C19A	C18A	C16A	121.9(7)
C19B	C18B	C16B	122.1(7)	C18A	C19A	C20A	121.1(7)
C18B	C19B	C20B	120.5(7)	C21A	C20A	C19A	125.2(6)
C21B	C20B	C19B	124.6(6)	C24A	C20A	C19A	118.1(7)
C24B	C20B	C19B	118.6(6)	C24A	C20A	C21A	116.6(6)
C24B	C20B	C21B	116.7(6)	C22A	C21A	C20A	119.8(6)
C22B	C21B	C20B	119.9(6)	C21A	C22A	C23A	120.3(7)
C21B	C22B	C23B	120.5(6)	N4A	C23A	C22A	121.3(6)

N4B	C23B	C22B	120.6(6)	N4A	C24A	C17A	116.9(5)
N4B	C24B	C17B	115.7(5)	N4A	C24A	C20A	122.6(6)
N4B	C24B	C20B	123.3(5)	C20A	C24A	C17A	120.5(6)
C20B	C24B	C17B	120.9(6)	F1A	C25A	S1A	110.8(5)
F1B	C25B	S1B	109.8(5)	F2A	C25A	S1A	111.5(5)
F2B	C25B	S1B	111.6(4)	F2A	C25A	F1A	108.0(5)
F2B	C25B	F1B	107.5(6)	F2A	C25A	F3A	109.2(6)
F3B	C25B	S1B	110.6(5)	F3A	C25A	S1A	110.2(5)
F3B	C25B	F1B	109.1(6)	F3A	C25A	F1A	107.1(6)
F3B	C25B	F2B	108.1(6)	F4A	C26A	S2A	111.3(5)
F4BA	C26B	S1BA	97.2(15)	F5A	C26A	S2A	112.0(5)
F5BA	C26B	S1BA	116.0(17)	F5A	C26A	F4A	107.3(7)
F5BA	C26B	F4BA	100(2)	F6A	C26A	S2A	109.9(6)
F6BA	C26B	S1BA	116(4)	F6A	C26A	F4A	107.9(6)
F6BA	C26B	F4BA	96(3)	F6A	C26A	F5A	108.3(7)
F6BA	C26B	F5BA	123(4)	O1AA	S1AA	O13	114.6(4)
F4BB	C26B	S1BB	110.7(6)	O1AA	S1AA	C16	103.1(4)
F5BB	C26B	S1BB	114.7(7)	O13	S1AA	C16	101.2(5)
F5BB	C26B	F4BB	106.5(8)	O15	S1AA	O1AA	115.8(4)
F6BB	C26B	S1BB	112.4(6)	O15	S1AA	O13	113.8(4)
F6BB	C26B	F4BB	104.9(7)	O15	S1AA	C16	106.2(5)
F6BB	C26B	F5BB	107.0(9)	F0AA	C16	S1AA	109.9(7)
O4B	S1BA	O6B	109.8(8)	F9	C16	S1AA	111.5(7)
O4B	S1BA	C26B	117.1(8)	F9	C16	F0AA	108.0(8)
O4B	S1BA	O5BA	117.7(16)	F9	C16	F11	108.2(9)
C26B	S1BA	O6B	104.0(7)	F11	C16	S1AA	111.0(7)
O5BA	S1BA	O6B	125.6(14)	F11	C16	F0AA	108.2(8)
O5BA	S1BA	C26B	77.0(19)	O2AA	S2AA	O3AA	112.7(7)
O4B	S1BB	C26B	99.7(3)	O2AA	S2AA	C0AA	105.7(7)
O6B	S1BB	O4B	112.8(3)	O3AA	S2AA	C0AA	102.0(8)
O6B	S1BB	C26B	106.0(4)	O4AA	S2AA	O2AA	116.2(6)
O5BB	S1BB	O4B	112.7(3)	O4AA	S2AA	O3AA	115.4(6)
O5BB	S1BB	O6B	120.5(4)	O4AA	S2AA	C0AA	102.6(6)
O5BB	S1BB	C26B	102.0(4)	F1AA	C0AA	S2AA	111.4(9)
O4A	Ir1A	O1A	86.53(16)	F17	C0AA	S2AA	113.7(12)
N1A	Ir1A	O1A	91.36(18)	F17	C0AA	F1AA	107.4(16)

N1A	Ir1A	O4A	94.77(19)	F17	C0AA	F18	112.5(15)
N2A	Ir1A	O1A	89.24(19)	F18	C0AA	S2AA	109.2(14)
N2A	Ir1A	O4A	174.27(18)	F18	C0AA	F1AA	102.1(13)
N2A	Ir1A	N1A	81.5(2)				

Table 9.44 – Hydrogen Atom Coordinates (Å×10^4) and Isotropic Displacement Parameters (Å^2×10^3) for IAJ688k_0m.

Atom	***x***	***y***	***z***	**U(eq)**
H1B	11738.24	2014.84	3054.21	31
H2B	12914.61	3090.28	3381.67	39
H3B	12440.01	4431.76	3821.41	48
H6B	10970.16	5416.74	4158.65	70
H7B	9320.18	5588.47	4265.96	77
H9B	7535.67	4936.29	4116.58	54
H10B	6544.33	3746.85	3727.13	45
H11B	7243.17	2481.2	3287.23	34
H13B	10541.5	2200.7	4684.19	38
H14B	10471.01	1678.45	5777.79	46
H15B	9311.54	650.07	5768.53	48
H18B	7837.92	-303.03	5001.06	45
H19B	6791.09	-730.08	3877.16	44
H21B	6187.68	-548.08	2495.46	38
H22B	6389.71	118.26	1505.89	38
H23B	7663.54	1110.97	1659.27	32
H1A	6404.45	2867.59	989.83	34
H2A	7515.23	3908.53	1716.43	43
H3A	6933.46	5086.51	2502.96	40
H6A	5409.85	5882.3	3042.62	44
H7A	3726.5	5973.14	3009.43	50
H9A	1994.48	5321.3	2486.63	55
H10A	1056.54	4202.18	1677.94	51
H11A	1867.65	3069.67	983.83	40
H13A	4879.83	3857.67	-50.83	47
H14A	4546.26	4126.12	-1290.58	61
H15A	3313.09	3375.51	-2195.99	57

H18A	1980.01	2224.26	-2512.47	48
H19A	1138.31	1234.28	-2117.99	47
H21A	912.32	440.95	-1040.18	39
H22A	1397.59	300.56	212.84	34
H23A	2670.04	1147.23	999.86	27

Table 9.45 – Atomic Occupancy for IAJ688k_0m.

Atom	Occupancy	Atom	Occupancy	Atom	Occupancy
S1BA	0.156(5)	F4BA	0.156(5)	F5BA	0.156(5)
F6BA	0.156(5)	O5BA	0.156(5)	S1BB	0.844(5)
F4BB	0.844(5)	F5BB	0.844(5)	F6BB	0.844(5)
O5BB	0.844(5)				

Table 9.46 – Solvent masks information for IAJ688k_0m.

Number	X	Y	Z	Volume	Electron count	Content
1	-0.055	-0.555	-0.055	821.6	244.7	ether
2	0.500	0.500	0.500	94.5	22.3	

Crystal Structure Determination of IAJ688k_0m

Crystal Data for $C_{27}H_{16}F_9IrN_4O_9S_3$ (M =999.82 g/mol): triclinic, space group P-1 (no. 2), a = 13.5471(11) Å, b = 16.7910(13) Å, c = 17.6060(13) Å, α = 103.907(4)°, β = 95.410(4)°, γ = 90.424(4)°, V = 3868.2(5) Å^3, Z = 4, T = 100 K, μ(MoKα) = 3.707 mm^{-1}, *Dcalc* = 1.717 g/cm^3, 123461 reflections measured (3.014° ≤ 2Θ ≤ 57.626°), 20111 unique (R_{int} = 0.0835, R_{sigma} = 0.0640) which were used in all calculations. The final R_1 was 0.0483 (I > 2σ(I)) and wR_2 was 0.1226 (all data).

9.3.6 2021ncs0466z $[Ir(dppz)_2Cl_2]PF_6$

Table 9.47 – Crystal data and structure refinement for 2021ncs0466z.

Identification code	2021ncs0466z
Empirical formula	$C_{36}H_{20}Cl_2F_6IrN_8P$
Formula weight	972.67

Temperature/K	100.00(10)
Crystal system	triclinic
Space group	P-1
a/Å	10.7932(3)
b/Å	12.4240(4)
c/Å	16.5232(5)
α/°	102.166(3)
β/°	94.123(2)
γ/°	114.224(3)
Volume/Å^3	1943.78(11)
Z	2
ρ_{calc}g/cm^3	1.662
μ/mm^{-1}	8.888
F(000)	944.0
Crystal size/mm^3	0.133 × 0.092 × 0.026
Radiation	Cu Kα (λ = 1.54178)
2Θ range for data collection/°	8.09 to 140.664
Index ranges	-12 ≤ h ≤ 13, -15 ≤ k ≤ 14, -20 ≤ l ≤ 20
Reflections collected	34132
Independent reflections	7208 [R_{int} = 0.0491, R_{sigma} = 0.0310]
Data/restraints/parameters	7208/0/490
Goodness-of-fit on F^2	1.050
Final R indexes [I>=2σ (I)]	R_1 = 0.0427, wR_2 = 0.1091
Final R indexes [all data]	R_1 = 0.0450, wR_2 = 0.1114
Largest diff. peak/hole / e Å^{-3}	1.73/-2.07

Table 9.48 – Fractional Atomic Coordinates (×10^4) and Equivalent Isotropic Displacement Parameters (Å2×10^3) for 2021ncs0466z. Ueq is defined as 1/3 of the trace of the orthogonalised UIJ tensor.

Atom	***x***	***y***	***z***	**U(eq)**
Ir1	4732.6(2)	1078.5(2)	2608.4(2)	42.42(10)
Cl1	3637.9(17)	-1006.5(11)	2553.7(8)	54.4(3)
Cl2	6841.1(16)	1019.7(14)	2364.4(8)	56.5(3)
N1	5683(5)	2859(4)	2523(3)	43.0(9)
N2	4200(5)	785(4)	1345(3)	43.3(9)
N3	6722(4)	5110(4)	434(3)	41.8(9)

N4	5158(4)	2893(4)	-823(3)	42.3(9)
N5	3003(5)	1211(4)	2959(2)	43.0(10)
N6	5224(5)	1407(4)	3878(3)	45.4(10)
N7	881(5)	1549(4)	5427(3)	44.7(10)
N8	3193(5)	1552(4)	6364(3)	45.5(10)
C1	6421(6)	3859(5)	3143(3)	45.3(12)
C2	7089(6)	4971(5)	2981(3)	48.4(12)
C3	7015(6)	5086(5)	2166(3)	45.0(11)
C4	6238(5)	4041(4)	1511(3)	38.5(10)
C5	5580(5)	2935(5)	1712(3)	39.1(10)
C6	4780(5)	1814(4)	1068(3)	39.5(10)
C7	4613(5)	1791(5)	224(3)	39.5(10)
C8	3816(5)	673(5)	-366(3)	41.5(11)
C9	3240(5)	-363(5)	-84(3)	41.5(11)
C10	3441(5)	-290(5)	761(3)	42.1(11)
C11	6094(5)	4060(5)	623(3)	39.5(11)
C12	6587(5)	5078(5)	-394(3)	42.4(11)
C13	7235(6)	6176(5)	-636(4)	47.0(12)
C14	7099(6)	6141(6)	-1472(4)	50.3(13)
C15	6357(6)	5040(6)	-2103(4)	51.9(13)
C16	5709(6)	3960(6)	-1890(3)	48.4(12)
C17	5803(5)	3959(5)	-1028(3)	42.8(11)
C18	5292(5)	2924(5)	-18(3)	38.3(10)
C19	1927(6)	1168(4)	2481(3)	42.7(11)
C20	819(6)	1261(4)	2806(3)	44.5(12)
C21	773(5)	1375(4)	3651(3)	41.3(11)
C22	1887(6)	1402(4)	4169(3)	41.4(11)
C23	2972(5)	1331(4)	3804(3)	41.1(11)
C24	4191(5)	1416(4)	4299(3)	41.2(11)
C25	4277(6)	1523(4)	5159(3)	44.6(12)
C26	5501(7)	1637(5)	5603(3)	52.5(14)
C27	6527(7)	1629(6)	5179(4)	57.9(15)
C28	6385(6)	1508(5)	4312(3)	50.6(13)
C29	1935(6)	1489(4)	5073(3)	42.0(12)
C30	968(6)	1617(4)	6268(3)	46.3(12)
C31	-80(6)	1715(5)	6690(3)	50.3(13)

C32	4(7)	1771(5)	7536(3)	52.4(14)
C33	1136(7)	1722(5)	7982(3)	53.2(14)
C34	2159(6)	1624(5)	7597(3)	52.2(14)
C35	2132(6)	1592(4)	6729(3)	47.7(13)
C36	3110(6)	1511(4)	5550(3)	44.0(12)
P1A	0	0	0	39.7(4)
F1A	1510(3)	1011(3)	468.4(18)	47.0(7)
F2A	-596(3)	305(3)	831.5(17)	50.6(7)
F3A	287(3)	-1011(3)	333.5(19)	50.0(7)
P1B	5000	5000	5000	63.8(7)
F1B	6139(5)	5891(3)	4585(2)	76.8(12)
F2B	4219(5)	4116(3)	4082(2)	72.3(11)
F3B	4092(5)	5744(3)	4942(2)	74.2(11)

Table 9.49 – Anisotropic Displacement Parameters (Å2×103) for 2021ncs0466z. The Anisotropic displacement factor exponent takes the form: -2π2[h2a*2U11+2hka*b*U12+…].

Atom	**U_{11}**	**U_{22}**	**U_{33}**	**U_{23}**	**U_{13}**	**U_{12}**
Ir1	59.41(16)	38.13(14)	28.06(13)	6.09(9)	-6.57(9)	23.25(11)
Cl1	84.6(10)	35.6(6)	36.9(6)	7.5(5)	-13.1(6)	25.1(6)
Cl2	69.9(9)	62.8(8)	39.7(7)	1.0(6)	-6.2(6)	40.3(7)
N1	51(2)	51(2)	28(2)	7.7(18)	-0.8(18)	25(2)
N2	54(3)	40(2)	37(2)	5.8(18)	1.2(19)	25(2)
N3	41(2)	48(2)	39(2)	13.3(19)	3.4(18)	20.3(19)
N4	41(2)	53(2)	33(2)	9.2(19)	1.6(17)	23(2)
N5	65(3)	31(2)	23.3(19)	7.6(16)	-6.9(18)	13.8(19)
N6	63(3)	36(2)	38(2)	10.1(18)	-1(2)	23(2)
N7	62(3)	32(2)	27(2)	4.9(16)	-7.6(19)	12(2)
N8	63(3)	32(2)	31(2)	10.4(17)	-8(2)	12(2)
C1	58(3)	39(3)	32(2)	3(2)	-3(2)	19(2)
C2	60(3)	45(3)	33(3)	3(2)	-1(2)	21(3)
C3	52(3)	41(3)	38(3)	7(2)	1(2)	20(2)
C4	45(3)	42(3)	30(2)	8(2)	0(2)	23(2)
C5	45(3)	43(3)	29(2)	5(2)	-4(2)	22(2)
C6	45(3)	38(2)	35(2)	8(2)	-1(2)	20(2)
C7	44(3)	45(3)	29(2)	4(2)	-1(2)	23(2)

C8	45(3)	51(3)	29(2)	5(2)	-1(2)	25(2)
C9	42(3)	42(3)	35(3)	1(2)	-4(2)	19(2)
C10	46(3)	43(3)	33(2)	2(2)	-6(2)	22(2)
C11	39(2)	47(3)	33(2)	7(2)	2(2)	22(2)
C12	41(3)	54(3)	37(3)	13(2)	3(2)	25(2)
C13	51(3)	50(3)	45(3)	18(2)	6(2)	25(3)
C14	52(3)	59(3)	45(3)	22(3)	6(2)	26(3)
C15	59(3)	65(4)	42(3)	24(3)	8(3)	32(3)
C16	54(3)	60(3)	34(3)	12(2)	3(2)	29(3)
C17	45(3)	51(3)	37(3)	15(2)	6(2)	25(2)
C18	39(2)	44(3)	30(2)	4(2)	-0.8(19)	20(2)
C19	59(3)	36(2)	30(2)	7.8(19)	-6(2)	19(2)
C20	57(3)	36(2)	31(2)	7(2)	-11(2)	15(2)
C21	51(3)	35(2)	30(2)	7.8(19)	-5(2)	13(2)
C22	61(3)	32(2)	23(2)	6.8(18)	-5(2)	15(2)
C23	57(3)	29(2)	28(2)	7.9(18)	-10(2)	13(2)
C24	55(3)	29(2)	29(2)	6.0(18)	-12(2)	11(2)
C25	63(3)	32(2)	32(2)	7.4(19)	-10(2)	17(2)
C26	75(4)	47(3)	30(3)	14(2)	-9(3)	23(3)
C27	65(4)	60(4)	48(3)	16(3)	-9(3)	29(3)
C28	64(3)	49(3)	35(3)	10(2)	-9(2)	25(3)
C29	62(3)	28(2)	28(2)	9.7(18)	-7(2)	13(2)
C30	66(3)	32(2)	30(2)	8(2)	-4(2)	12(2)
C31	64(3)	38(3)	36(3)	10(2)	-6(2)	12(3)
C32	71(4)	40(3)	34(3)	10(2)	4(3)	14(3)
C33	74(4)	40(3)	29(2)	9(2)	-2(3)	11(3)
C34	68(4)	40(3)	33(3)	12(2)	-10(3)	11(3)
C35	69(4)	31(2)	30(2)	9(2)	-6(2)	11(2)
C36	64(3)	32(2)	28(2)	8.3(19)	-9(2)	15(2)
P1A	43.9(9)	50.2(10)	24.3(8)	10.9(7)	-0.2(7)	20.4(8)
F1A	45.2(16)	53.2(17)	35.2(15)	7.1(13)	-4.1(12)	18.6(14)
F2A	51.2(17)	72(2)	28.0(14)	11.0(14)	2.6(12)	28.3(16)
F3A	54.4(17)	59.7(18)	43.4(16)	24.1(14)	6.0(14)	27.4(15)
P1B	108.3(19)	32.2(9)	43.0(11)	10.2(8)	22.7(12)	21.3(11)
F1B	124(3)	39.4(17)	58(2)	15.3(16)	37(2)	23(2)
F2B	115(3)	43.8(18)	45.9(19)	6.8(15)	20(2)	24(2)

F3B	125(3)	48.4(19)	51(2)	12.4(16)	23(2)	39(2)

Table 9.50 – Bond Lengths for 2021ncs0466z.

Atom	Atom	Length/Å		Atom	Atom	Length/Å
Ir1	Cl1	2.3428(13)		C12	C17	1.427(8)
Ir1	Cl2	2.3669(15)		C13	C14	1.368(8)
Ir1	N1	2.063(5)		C14	C15	1.407(8)
Ir1	N2	2.039(4)		C15	C16	1.370(8)
Ir1	N5	2.053(5)		C16	C17	1.421(7)
Ir1	N6	2.037(4)		C19	C20	1.384(8)
N1	C1	1.327(7)		C20	C21	1.379(7)
N1	C5	1.362(6)		C21	C22	1.410(7)
N2	C6	1.366(6)		C22	C23	1.381(8)
N2	C10	1.352(6)		C22	C29	1.469(6)
N3	C11	1.318(7)		C23	C24	1.451(7)
N3	C12	1.355(6)		C24	C25	1.391(7)
N4	C17	1.350(7)		C25	C26	1.402(8)
N4	C18	1.317(6)		C25	C36	1.452(8)
N5	C19	1.332(7)		C26	C27	1.355(9)
N5	C23	1.376(6)		C27	C28	1.399(8)
N6	C24	1.359(7)		C29	C36	1.432(7)
N6	C28	1.343(7)		C30	C31	1.405(8)
N7	C29	1.337(7)		C30	C35	1.437(8)
N7	C30	1.367(6)		C31	C32	1.379(7)
N8	C35	1.345(8)		C32	C33	1.411(9)
N8	C36	1.331(6)		C33	C34	1.349(9)
C1	C2	1.365(8)		C34	C35	1.425(7)
C2	C3	1.384(7)		P1A	F1A^{1}	1.601(3)
C3	C4	1.395(7)		P1A	F1A	1.601(3)
C4	C5	1.389(7)		P1A	F2A^{1}	1.598(3)
C4	C11	1.470(7)		P1A	F2A	1.598(3)
C5	C6	1.440(7)		P1A	F3A^{1}	1.602(3)
C6	C7	1.387(7)		P1A	F3A	1.602(3)
C7	C8	1.395(7)		P1B	F1B^{2}	1.591(3)

C7	C18	1.453(7)		P1B	F1B	1.591(3)
C8	C9	1.377(7)		P1B	F2B	1.604(4)
C9	C10	1.377(7)		P1B	F2B[2]	1.604(4)
C11	C18	1.449(7)		P1B	F3B	1.609(4)
C12	C13	1.413(7)		P1B	F3B[2]	1.609(4)

[1]-X,-Y,-Z; [2]1-X,1-Y,1-Z

Table 9.51 – Bond Angles for 2021ncs0466z.

Atom	**Atom**	**Atom**	**Angle/°**		**Atom**	**Atom**	**Atom**	**Angle/°**
Cl1	Ir1	Cl2	93.32(6)		N5	C19	C20	122.4(5)
N1	Ir1	Cl1	174.04(11)		C21	C20	C19	120.5(5)
N1	Ir1	Cl2	84.90(13)		C20	C21	C22	118.2(5)
N2	Ir1	Cl1	93.63(13)		C21	C22	C29	123.0(5)
N2	Ir1	Cl2	88.28(13)		C23	C22	C21	118.0(4)
N2	Ir1	N1	80.64(16)		C23	C22	C29	119.0(5)
N2	Ir1	N5	97.92(16)		N5	C23	C22	123.3(5)
N5	Ir1	Cl1	87.86(12)		N5	C23	C24	115.1(5)
N5	Ir1	Cl2	173.61(11)		C22	C23	C24	121.6(4)
N5	Ir1	N1	94.54(16)		N6	C24	C23	116.2(4)
N6	Ir1	Cl1	87.31(12)		N6	C24	C25	123.2(5)
N6	Ir1	Cl2	93.50(14)		C25	C24	C23	120.6(5)
N6	Ir1	N1	98.46(16)		C24	C25	C26	117.6(5)
N6	Ir1	N2	177.94(16)		C24	C25	C36	119.0(5)
N6	Ir1	N5	80.28(17)		C26	C25	C36	123.4(5)
C1	N1	Ir1	127.5(4)		C27	C26	C25	118.9(5)
C1	N1	C5	120.0(5)		C26	C27	C28	121.2(6)
C5	N1	Ir1	112.4(3)		N6	C28	C27	120.6(6)
C6	N2	Ir1	113.8(3)		N7	C29	C22	119.1(5)
C10	N2	Ir1	128.3(4)		N7	C29	C36	121.8(4)
C10	N2	C6	117.7(4)		C36	C29	C22	119.0(5)
C11	N3	C12	116.7(5)		N7	C30	C31	120.3(5)
C18	N4	C17	117.5(5)		N7	C30	C35	120.5(5)
C19	N5	Ir1	128.8(3)		C31	C30	C35	119.3(5)
C19	N5	C23	117.5(5)		C32	C31	C30	120.2(6)
C23	N5	Ir1	113.7(3)		C31	C32	C33	120.3(6)
C24	N6	Ir1	114.2(3)		C34	C33	C32	121.1(5)

C28	N6	Ir1	127.1(4)		C33	C34	C35	120.5(6)
C28	N6	C24	118.4(5)		N8	C35	C30	121.8(5)
C29	N7	C30	116.9(5)		N8	C35	C34	119.7(5)
C36	N8	C35	117.2(5)		C34	C35	C30	118.6(6)
N1	C1	C2	120.9(5)		N8	C36	C25	117.6(5)
C1	C2	C3	120.9(5)		N8	C36	C29	121.8(5)
C2	C3	C4	118.5(5)		C29	C36	C25	120.5(4)
C3	C4	C11	123.0(5)		F1A	P1A	F1A^{1}	180.0
C5	C4	C3	118.0(4)		F1A	P1A	F3A^{1}	90.23(16)
C5	C4	C11	118.9(4)		F1A	P1A	F3A	89.77(16)
N1	C5	C4	121.6(4)		F1A^{1}	P1A	F3A	90.23(16)
N1	C5	C6	117.2(4)		F1A^{1}	P1A	F3A^{1}	89.77(16)
C4	C5	C6	121.2(4)		F2A	P1A	F1A	89.58(15)
N2	C6	C5	115.7(4)		F2A	P1A	F1A^{1}	90.42(15)
N2	C6	C7	122.6(5)		F2A^{1}	P1A	F1A^{1}	89.58(15)
C7	C6	C5	121.7(5)		F2A^{1}	P1A	F1A	90.42(15)
C6	C7	C8	118.6(5)		F2A	P1A	F2A^{1}	180.0
C6	C7	C18	119.1(4)		F2A	P1A	F3A^{1}	90.34(16)
C8	C7	C18	122.3(4)		F2A^{1}	P1A	F3A^{1}	89.66(16)
C9	C8	C7	118.6(5)		F2A^{1}	P1A	F3A	90.35(16)
C10	C9	C8	120.4(5)		F2A	P1A	F3A	89.65(16)
N2	C10	C9	122.0(5)		F3A	P1A	F3A^{1}	180.0
N3	C11	C4	118.8(5)		F1B	P1B	F1B^{2}	180.0
N3	C11	C18	121.9(5)		F1B^{2}	P1B	F2B^{2}	89.70(19)
C18	C11	C4	119.3(5)		F1B	P1B	F2B	89.70(19)
N3	C12	C13	119.3(5)		F1B	P1B	F2B^{2}	90.30(19)
N3	C12	C17	121.5(5)		F1B^{2}	P1B	F2B	90.3(2)
C13	C12	C17	119.2(5)		F1B	P1B	F3B	90.5(2)
C14	C13	C12	119.2(5)		F1B^{2}	P1B	F3B	89.5(2)
C13	C14	C15	122.1(5)		F1B	P1B	F3B^{2}	89.5(2)
C16	C15	C14	120.2(5)		F1B^{2}	P1B	F3B^{2}	90.5(2)
C15	C16	C17	119.5(5)		F2B	P1B	F2B^{2}	180.0(3)
N4	C17	C12	121.1(5)		F2B^{2}	P1B	F3B^{2}	90.2(2)
N4	C17	C16	119.2(5)		F2B^{2}	P1B	F3B	89.8(2)
C16	C17	C12	119.8(5)		F2B	P1B	F3B^{2}	89.8(2)
N4	C18	C7	118.9(4)		F2B	P1B	F3B	90.2(2)

N4	C18	C11	121.4(5)		F3B	P1B	F3B[2]	180.0
C11	C18	C7	119.8(4)					

[1]-X,-Y,-Z; [2]1-X,1-Y,1-Z

Table 9.52 – Torsion Angles for 2021ncs0466z.

A	B	C	D	Angle/°		A	B	C	D	Angle/°
Ir1	N1	C1	C2	174.4(4)		C11	C4	C5	C6	0.9(7)
Ir1	N1	C5	C4	-175.1(4)		C12	N3	C11	C4	178.4(4)
Ir1	N1	C5	C6	3.7(6)		C12	N3	C11	C18	-0.2(7)
Ir1	N2	C6	C5	-4.2(6)		C12	C13	C14	C15	-1.4(8)
Ir1	N2	C6	C7	176.0(4)		C13	C12	C17	N4	-179.4(5)
Ir1	N2	C10	C9	-175.4(4)		C13	C12	C17	C16	1.3(7)
Ir1	N5	C19	C20	179.5(4)		C13	C14	C15	C16	1.9(9)
Ir1	N5	C23	C22	-178.2(4)		C14	C15	C16	C17	-0.7(8)
Ir1	N5	C23	C24	3.5(5)		C15	C16	C17	N4	179.8(5)
Ir1	N6	C24	C23	-6.6(5)		C15	C16	C17	C12	-0.9(8)
Ir1	N6	C24	C25	174.6(4)		C17	N4	C18	C7	-179.9(4)
Ir1	N6	C28	C27	-174.3(4)		C17	N4	C18	C11	0.4(7)
N1	C1	C2	C3	0.1(9)		C17	C12	C13	C14	-0.2(8)
N1	C5	C6	N2	0.3(7)		C18	N4	C17	C12	-0.7(7)
N1	C5	C6	C7	-179.9(4)		C18	N4	C17	C16	178.6(5)
N2	C6	C7	C8	0.2(7)		C18	C7	C8	C9	178.2(5)
N2	C6	C7	C18	-178.6(5)		C19	N5	C23	C22	0.3(7)
N3	C11	C18	N4	0.0(7)		C19	N5	C23	C24	-177.9(4)
N3	C11	C18	C7	-179.6(4)		C19	C20	C21	C22	0.4(7)
N3	C12	C13	C14	179.9(5)		C20	C21	C22	C23	1.0(7)
N3	C12	C17	N4	0.5(8)		C20	C21	C22	C29	-178.4(4)
N3	C12	C17	C16	-178.8(5)		C21	C22	C23	N5	-1.4(7)
N5	C19	C20	C21	-1.5(8)		C21	C22	C23	C24	176.7(4)
N5	C23	C24	N6	2.0(6)		C21	C22	C29	N7	-0.1(7)
N5	C23	C24	C25	-179.1(4)		C21	C22	C29	C36	-179.9(4)
N6	C24	C25	C26	0.6(7)		C22	C23	C24	N6	-176.2(4)
N6	C24	C25	C36	-179.4(4)		C22	C23	C24	C25	2.6(7)
N7	C29	C36	N8	2.3(7)		C22	C29	C36	N8	-178.0(4)

N7	C29	C36	C25	-176.1(4)		C22	C29	C36	C25	3.7(7)
N7	C30	C31	C32	179.3(5)		C23	N5	C19	C20	1.2(7)
N7	C30	C35	N8	2.8(7)		C23	C22	C29	N7	-179.5(4)
N7	C30	C35	C34	-177.9(4)		C23	C22	C29	C36	0.7(7)
C1	N1	C5	C4	0.4(7)		C23	C24	C25	C26	-178.2(4)
C1	N1	C5	C6	179.2(5)		C23	C24	C25	C36	1.9(7)
C1	C2	C3	C4	0.2(8)		C24	N6	C28	C27	-0.4(8)
C2	C3	C4	C5	-0.1(7)		C24	C25	C26	C27	-0.4(8)
C2	C3	C4	C11	-179.8(5)		C24	C25	C36	N8	176.6(4)
C3	C4	C5	N1	-0.2(7)		C24	C25	C36	C29	-5.0(7)
C3	C4	C5	C6	-178.9(5)		C25	C26	C27	C28	-0.1(9)
C3	C4	C11	N3	-0.2(7)		C26	C25	C36	N8	-3.3(7)
C3	C4	C11	C18	178.5(5)		C26	C25	C36	C29	175.1(5)
C4	C5	C6	N2	179.1(4)		C26	C27	C28	N6	0.5(9)
C4	C5	C6	C7	-1.1(8)		C28	N6	C24	C23	178.7(4)
C4	C11	C18	N4	-178.6(4)		C28	N6	C24	C25	-0.1(7)
C4	C11	C18	C7	1.7(7)		C29	N7	C30	C31	178.3(4)
C5	N1	C1	C2	-0.4(8)		C29	N7	C30	C35	-1.6(7)
C5	C4	C11	N3	-179.9(5)		C29	C22	C23	N5	178.0(4)
C5	C4	C11	C18	-1.2(7)		C29	C22	C23	C24	-3.8(7)
C5	C6	C7	C8	-179.5(5)		C30	N7	C29	C22	179.4(4)
C5	C6	C7	C18	1.6(7)		C30	N7	C29	C36	-0.8(7)
C6	N2	C10	C9	-0.5(7)		C30	C31	C32	C33	-0.4(8)
C6	C7	C8	C9	-0.6(7)		C31	C30	C35	N8	-177.1(5)
C6	C7	C18	N4	178.4(4)		C31	C30	C35	C34	2.2(7)
C6	C7	C18	C11	-1.9(7)		C31	C32	C33	C34	0.3(8)
C7	C8	C9	C10	0.4(8)		C32	C33	C34	C35	1.2(8)
C8	C7	C18	N4	-0.4(7)		C33	C34	C35	N8	176.9(5)
C8	C7	C18	C11	179.3(5)		C33	C34	C35	C30	-2.4(8)
C8	C9	C10	N2	0.1(8)		C35	N8	C36	C25	177.4(4)
C10	N2	C6	C5	-179.9(4)		C35	N8	C36	C29	-1.0(7)
C10	N2	C6	C7	0.3(7)		C35	C30	C31	C32	-0.8(8)
C11	N3	C12	C13	179.9(5)		C36	N8	C35	C30	-1.4(7)
C11	N3	C12	C17	0.0(7)		C36	N8	C35	C34	179.4(5)
C11	C4	C5	N1	179.6(4)		C36	C25	C26	C27	179.5(5)

Table 9.53 – Hydrogen Atom Coordinates (Å×10^4) and Isotropic Displacement Parameters (Å^2×10^3) for 2021ncs0466z.

Atom	*x*	*y*	*z*	U(eq)
H1	6484.51	3801.2	3707.12	54
H2	7611.74	5674.42	3434.62	58
H3	7483.61	5860.58	2055.95	54
H8	3673.73	627.59	-948.26	50
H9	2699.03	-1133.32	-476.75	50
H10	3035.61	-1016.99	940.75	50
H13	7758.88	6929.53	-223.33	56
H14	7518.13	6883.54	-1631.56	60
H15	6305.58	5044.73	-2678.67	62
H16	5199.49	3217.64	-2315.52	58
H19	1921.21	1069.56	1894.1	51
H20	82.56	1246.31	2445.18	53
H21	12.26	1434.78	3876.99	50
H26	5608.31	1718.31	6191.93	63
H27	7359.49	1706.31	5476.1	69
H28	7116.27	1498.64	4027.97	61
H31	-847.64	1743.48	6392.98	60
H32	-704.96	1843.03	7819.81	63
H33	1177.36	1757.55	8564.33	64
H34	2903.31	1577.02	7906.69	63

Table 9.54 – Solvent masks information for 2021ncs0466z.

Number	X	Y	Z	Volume	Electron count	Content
1	0.000	0.500	-0.134	444.2	108.9	2 THF

Crystal structure determination of 2021ncs0466z

Crystal Data for $C_{36}H_{20}Cl_2F_6IrN_8P$ (*M* =972.67 g/mol): triclinic, space group P-1 (no. 2), *a* = 10.7932(3) Å, *b* = 12.4240(4) Å, *c* = 16.5232(5) Å, *α* = 102.166(3)°, *β* = 94.123(2)°, *γ* = 114.224(3)°, *V* = 1943.78(11) Å^3, *Z* = 2, *T* = 100.00(10) K, μ(Cu Kα) = 8.888 mm^{-1}, *Dcalc* = 1.662 g/cm^3, 34132 reflections

measured (8.09° ≤ 2Θ ≤ 140.664°), 7208 unique (R_{int} = 0.0491, R_{sigma} = 0.0310) which were used in all calculations. The final R_1 was 0.0427 (I > 2σ(I)) and wR_2 was 0.1114 (all data).

9.3.7 IAJ686s_10-9A $[Ir(dppz)_2(CF_3SO_3)_2]CF_3SO_3$

Table 9.55 – Crystal data and structure refinement for IAJ686s_10-9A.

Identification code	IAJ686s_10-9A
Empirical formula	$C_{39}H_{20}F_9IrN_8O_9S_3$
Formula weight	1204.01
Temperature/K	100.02
Crystal system	monoclinic
Space group	$P2_1/n$
a/Å	13.799(9)
b/Å	25.457(17)
c/Å	14.074(10)
α/°	90
β/°	117.137(6)
γ/°	90
Volume/Å^3	4400(5)
Z	4
ρ_{calc}g/cm^3	1.818
μ/mm^{-1}	3.279
F(000)	2352.0
Crystal size/mm^3	0.441 × 0.2 × 0.154
Radiation	MoKα (λ = 0.71073)
2Θ range for data collection/°	3.2 to 46.504
Index ranges	-15 ≤ h ≤ 15, -28 ≤ k ≤ 28, -15 ≤ l ≤ 15
Reflections collected	27501
Independent reflections	6143 [R_{int} = 0.1730, R_{sigma} = 0.2289]
Data/restraints/parameters	6143/620/616
Goodness-of-fit on F^2	1.105
Final R indexes [I>=2σ (I)]	R_1 = 0.1177, wR_2 = 0.2317
Final R indexes [all data]	R_1 = 0.2542, wR_2 = 0.2935
Largest diff. peak/hole / e Å^{-3}	2.71/-2.69

Table 9.56 – Fractional Atomic Coordinates ($\times 10^4$) and Equivalent Isotropic Displacement Parameters ($Å^2 \times 10^3$) for IAJ686s_10-9A. U_{eq} is defined as 1/3 of the trace of the orthogonalised U_{IJ} tensor.

Atom	*x*	*y*	*z*	U(eq)
Ir1	6178.8(10)	7478.6(6)	3441.6(9)	40.1(4)
S1	5545(8)	6703(4)	1342(7)	59(3)
S2	4019(8)	8233(4)	2571(7)	58(3)
F1	7615(18)	6798(10)	1846(17)	97(7)
F2	6568(19)	6994(9)	250(17)	86(6)
F3	6751(19)	6215(9)	672(17)	97(7)
F4	4404(17)	8372(9)	4556(16)	88(7)
F5	2896(18)	8000(10)	3602(18)	98(7)
F6	3040(20)	8811(9)	3371(19)	101(7)
O1	5734(13)	7210(7)	1948(14)	29(4)
O2	5730(20)	6273(9)	2053(19)	80(8)
O3	4596(18)	6704(9)	350(17)	67(7)
O4	4571(18)	7730(8)	2887(15)	51(5)
O5	4730(20)	8678(10)	2687(19)	73(7)
O6	3047(19)	8197(9)	1608(17)	64(6)
N1	7590(20)	7141(9)	3923(17)	39(5)
N2	5830(20)	6760(9)	3898(17)	37(5)
N3	9600(20)	5556(10)	5680(20)	47(6)
N4	7690(20)	5186(11)	5720(20)	56(7)
N5	6720(20)	8188(9)	3152(18)	43(6)
N6	6620(30)	7832(12)	4990(20)	70(7)
N7	8510(20)	9731(11)	5067(19)	51(7)
N8	8140(20)	9393(10)	6782(18)	39(6)
C1	8500(20)	7337(11)	3940(20)	38(6)
C2	9470(30)	7045(14)	4290(20)	52(8)
C3	9580(30)	6561(14)	4720(30)	60(9)
C4	8640(30)	6347(12)	4740(20)	38(6)
C5	7700(30)	6637(12)	4370(20)	38(6)
C6	6760(20)	6448(12)	4360(20)	35(6)
C7	6670(20)	5937(12)	4740(20)	33(6)
C8	5690(20)	5774(12)	4640(20)	35(6)
C9	4800(30)	6095(12)	4220(20)	47(8)
C10	4870(30)	6585(12)	3870(30)	48(8)

C11	8670(30)	5830(13)	5250(30)	49(8)
C12	7740(20)	5660(12)	5270(20)	35(6)
C13	9620(30)	5117(13)	6190(30)	52(8)
C14	10560(30)	4821(12)	6680(20)	48(7)
C15	10560(30)	4342(14)	7170(30)	64(10)
C16	9670(30)	4195(15)	7220(30)	75(12)
C17	8670(30)	4438(13)	6710(30)	62(10)
C18	8640(30)	4928(12)	6191(19)	35(6)
C19	6760(20)	8328(13)	2280(20)	42(7)
C20	7180(20)	8815(12)	2250(20)	43(8)
C21	7620(20)	9151(13)	3130(20)	45(7)
C22	7580(20)	8991(12)	4060(20)	36(6)
C23	7130(20)	8490(12)	4030(20)	37(7)
C24	7030(20)	8302(12)	4970(20)	38(7)
C25	7350(20)	8601(12)	5890(20)	35(6)
C26	7140(30)	8368(13)	6680(30)	51(8)
C27	6690(20)	7881(14)	6590(20)	51(6)
C28	6380(20)	7601(14)	5590(20)	51(6)
C29	7980(20)	9280(12)	5040(20)	38(7)
C30	7820(30)	9114(13)	5910(20)	44(7)
C31	8930(30)	9998(12)	6020(20)	44(8)
C32	8600(30)	9847(13)	6810(20)	45(7)
C33	8980(30)	10190(12)	7730(20)	49(8)
C34	9550(30)	10615(14)	7830(30)	61(10)
C35	9780(30)	10751(15)	7060(30)	66(11)
C36	9550(30)	10460(13)	6150(30)	57(9)
C37	6660(30)	6695(17)	1000(30)	64(6)
C38	3570(30)	8364(15)	3580(30)	58(6)
S3	2856(8)	6678(4)	5107(7)	55(3)
F7	3855(14)	7559(8)	5840(14)	67(5)
F8	4912(17)	6907(8)	6239(16)	76(6)
F9	3960(16)	7031(8)	7036(14)	68(5)
O7	3187(17)	6150(9)	5469(16)	54(5)
O8	2848(17)	6813(9)	4132(15)	56(6)
O9	1884(18)	6858(9)	5166(16)	60(6)
C39	3920(30)	7071(15)	6070(30)	55(6)

Table 9.57 – Anisotropic Displacement Parameters ($Å^2×10^3$) for IAJ686s_10-9A. The Anisotropic displacement factor exponent takes the form: $-2\pi^2[h^2a^{*2}U_{11}+2hka^*b^*U_{12}+\ldots]$.

Atom	U_{11}	U_{22}	U_{33}	U_{23}	U_{13}	U_{12}
Ir1	33.6(7)	52.9(8)	30.6(6)	0.2(8)	11.8(5)	-0.3(9)
S1	68(7)	60(7)	38(5)	-6(5)	14(5)	-9(5)
S2	57(7)	69(7)	40(5)	3(5)	14(5)	6(5)
F1	73(11)	140(20)	66(12)	-28(12)	22(10)	-3(13)
F2	100(17)	100(15)	67(12)	-1(11)	45(11)	-13(13)
F3	120(19)	89(13)	88(16)	-24(11)	54(14)	8(13)
F4	73(13)	130(20)	52(9)	-11(12)	20(9)	9(12)
F5	80(15)	111(16)	94(17)	30(14)	33(12)	-10(12)
F6	116(19)	85(14)	108(17)	13(13)	56(14)	43(13)
O1	8(10)	45(10)	37(9)	10(7)	13(7)	-3(8)
O2	100(20)	56(12)	72(15)	23(13)	31(13)	-16(13)
O3	62(12)	76(18)	39(11)	-3(10)	3(11)	-20(12)
O4	61(11)	61(12)	35(11)	1(9)	25(9)	4(9)
O5	84(16)	71(13)	67(17)	4(13)	36(13)	-7(13)
O6	62(13)	79(18)	41(11)	13(11)	15(11)	1(11)
N1	42(10)	39(11)	21(11)	-8(9)	3(9)	-20(8)
N2	40(10)	41(10)	21(12)	-11(8)	6(11)	-1(7)
N3	38(12)	43(14)	59(17)	-1(11)	22(13)	1(9)
N4	45(12)	48(14)	56(18)	13(11)	7(13)	0(10)
N5	72(16)	31(10)	35(10)	-1(7)	32(11)	-19(10)
N6	120(20)	54(12)	35(10)	-20(9)	30(11)	-38(13)
N7	43(17)	65(14)	35(11)	-6(9)	9(12)	-12(11)
N8	46(16)	34(12)	30(10)	-2(9)	11(11)	4(10)
C1	51(13)	37(16)	32(16)	-19(11)	22(13)	-13(9)
C2	60(15)	66(17)	50(20)	7(15)	41(16)	3(13)
C3	44(14)	66(18)	70(20)	15(16)	28(18)	2(12)
C4	43(12)	52(13)	25(15)	-3(11)	22(13)	5(9)
C5	49(11)	44(12)	33(16)	-1(11)	28(13)	6(9)
C6	43(11)	38(12)	24(15)	-2(10)	16(12)	2(8)
C7	37(10)	46(12)	18(14)	1(10)	15(11)	5(8)
C8	41(11)	31(14)	40(17)	-10(12)	23(13)	2(9)
C9	47(13)	41(14)	60(20)	-3(14)	29(15)	10(11)
C10	47(12)	31(14)	60(20)	-10(13)	23(15)	4(11)

C11	47(12)	50(14)	60(20)	6(13)	32(14)	11(10)
C12	36(10)	34(13)	30(16)	-5(10)	10(12)	3(9)
C13	53(13)	41(16)	60(20)	0(12)	26(15)	7(11)
C14	47(14)	41(16)	46(19)	-9(12)	14(15)	2(12)
C15	69(19)	47(18)	80(30)	10(15)	40(20)	17(15)
C16	67(19)	70(20)	90(30)	40(20)	40(20)	26(15)
C17	62(18)	53(17)	70(20)	22(15)	32(18)	15(13)
C18	43(12)	46(14)	5(14)	-2(10)	0(12)	2(10)
C19	39(19)	62(16)	29(11)	6(11)	20(13)	0(13)
C20	40(20)	57(16)	34(12)	11(11)	22(14)	3(13)
C21	40(20)	58(17)	41(11)	5(10)	22(13)	5(14)
C22	20(16)	51(12)	30(10)	-2(8)	6(11)	0(11)
C23	38(18)	43(12)	36(10)	-8(8)	21(12)	3(11)
C24	41(18)	38(12)	30(10)	-11(8)	13(12)	-4(11)
C25	33(17)	43(12)	29(11)	-12(8)	15(12)	1(11)
C26	70(20)	52(15)	51(14)	-8(11)	43(17)	-2(13)
C27	32(13)	76(14)	21(10)	-1(9)	-9(10)	-23(11)
C28	32(13)	76(14)	21(10)	-1(9)	-9(10)	-23(11)
C29	27(18)	49(14)	32(10)	-4(9)	7(11)	2(11)
C30	47(19)	47(12)	38(11)	-13(9)	20(13)	-6(12)
C31	50(20)	41(15)	29(12)	4(10)	3(12)	-1(12)
C32	49(19)	38(13)	41(13)	-2(10)	15(14)	1(12)
C33	60(20)	40(16)	37(14)	-1(11)	10(14)	4(13)
C34	80(20)	51(18)	47(17)	-14(14)	21(18)	-12(15)
C35	70(30)	70(20)	45(16)	-15(13)	13(17)	-30(18)
C36	70(20)	52(17)	37(15)	1(12)	13(16)	-15(14)
C37	71(13)	81(16)	44(14)	-15(11)	29(10)	-1(14)
C38	62(16)	63(16)	48(10)	1(13)	24(10)	9(11)
S3	54(6)	72(7)	49(5)	0(5)	33(5)	-1(5)
F7	70(13)	67(11)	70(12)	11(9)	35(10)	6(9)
F8	65(11)	86(15)	76(14)	8(11)	29(10)	12(10)
F9	89(15)	72(14)	42(8)	2(9)	28(9)	1(11)
O7	45(14)	68(13)	51(14)	-4(10)	23(11)	-6(10)
O8	47(14)	103(18)	36(11)	1(10)	34(10)	3(12)
O9	57(13)	94(18)	48(14)	21(13)	42(11)	9(11)
C39	63(12)	63(12)	44(10)	3(11)	27(11)	1(11)

Table 9.58 – Bond Lengths for IAJ686s_10-9A.

Atom	Atom	Length/Å	Atom	Atom	Length/Å
Ir1	O1	2.022(18)	C4	C11	1.49(4)
Ir1	O4	2.09(2)	C5	C6	1.38(4)
Ir1	N1	1.95(3)	C6	C7	1.43(4)
Ir1	N2	2.07(2)	C7	C8	1.36(4)
Ir1	N5	2.06(2)	C7	C12	1.50(4)
Ir1	N6	2.17(3)	C8	C9	1.37(4)
S1	O1	1.50(2)	C9	C10	1.36(4)
S1	O2	1.43(2)	C11	C12	1.37(4)
S1	O3	1.41(2)	C13	C14	1.38(4)
S1	C37	1.80(4)	C13	C18	1.44(4)
S2	O4	1.45(2)	C14	C15	1.40(4)
S2	O5	1.46(3)	C15	C16	1.31(5)
S2	O6	1.41(2)	C16	C17	1.38(4)
S2	C38	1.82(4)	C17	C18	1.44(4)
F1	C37	1.34(4)	C19	C20	1.38(4)
F2	C37	1.26(4)	C20	C21	1.40(4)
F3	C37	1.33(4)	C21	C22	1.40(4)
F4	C38	1.33(4)	C22	C23	1.41(4)
F5	C38	1.32(4)	C22	C29	1.43(4)
F6	C38	1.31(4)	C23	C24	1.47(4)
N1	C1	1.34(3)	C24	C25	1.39(4)
N1	C5	1.41(4)	C25	C26	1.40(4)
N2	C6	1.39(3)	C25	C30	1.46(4)
N2	C10	1.38(4)	C26	C27	1.37(4)
N3	C11	1.34(4)	C27	C28	1.47(4)
N3	C13	1.32(4)	C29	C30	1.40(4)
N4	C12	1.38(4)	C31	C32	1.43(4)
N4	C18	1.34(4)	C31	C36	1.42(4)
N5	C19	1.30(3)	C32	C33	1.45(4)
N5	C23	1.35(3)	C33	C34	1.31(4)
N6	C24	1.33(4)	C34	C35	1.31(4)
N6	C28	1.19(4)	C35	C36	1.39(4)
N7	C29	1.35(4)	S3	O7	1.44(2)
N7	C31	1.37(4)	S3	O8	1.409(19)

N8	C30	1.31(3)	S3	O9	1.46(2)
N8	C32	1.31(4)	S3	C39	1.78(4)
C1	C2	1.41(4)	F7	C39	1.28(4)
C2	C3	1.35(4)	F8	C39	1.34(4)
C3	C4	1.41(4)	F9	C39	1.34(3)
C4	C5	1.37(4)			

Table 9.59 – Bond Angles for IAJ686s_10-9A.

Atom	**Atom**	**Atom**	**Angle/°**	**Atom**	**Atom**	**Atom**	**Angle/°**
O1	Ir1	O4	87.0(7)	N3	C13	C14	121(3)
O1	Ir1	N2	91.2(8)	N3	C13	C18	120(3)
O1	Ir1	N5	93.2(8)	C14	C13	C18	119(3)
O1	Ir1	N6	175.2(10)	C13	C14	C15	121(3)
O4	Ir1	N6	90.6(10)	C16	C15	C14	119(4)
N1	Ir1	O1	89.7(8)	C15	C16	C17	126(4)
N1	Ir1	O4	171.6(9)	C16	C17	C18	116(3)
N1	Ir1	N2	80.7(10)	N4	C18	C13	123(3)
N1	Ir1	N5	93.5(10)	N4	C18	C17	118(3)
N1	Ir1	N6	93.3(11)	C13	C18	C17	119(3)
N2	Ir1	O4	91.7(9)	N5	C19	C20	119(3)
N2	Ir1	N6	93.0(10)	C19	C20	C21	123(3)
N5	Ir1	O4	94.3(9)	C22	C21	C20	117(3)
N5	Ir1	N2	172.7(10)	C21	C22	C23	117(3)
N5	Ir1	N6	82.9(10)	C21	C22	C29	126(3)
O1	S1	C37	102.3(15)	C23	C22	C29	118(3)
O2	S1	O1	109.4(13)	N5	C23	C22	122(3)
O2	S1	C37	106.0(18)	N5	C23	C24	118(3)
O3	S1	O1	113.7(14)	C22	C23	C24	119(3)
O3	S1	O2	119.0(16)	N6	C24	C23	122(3)
O3	S1	C37	104.7(16)	N6	C24	C25	116(3)
O4	S2	O5	114.7(15)	C25	C24	C23	123(3)
O4	S2	C38	104.0(15)	C24	C25	C26	115(3)
O5	S2	C38	102.8(17)	C24	C25	C30	117(3)
O6	S2	O4	111.9(15)	C26	C25	C30	128(3)
O6	S2	O5	117.1(15)	C27	C26	C25	124(3)

O6	S2	C38	104.4(17)	C26	C27	C28	117(3)
S1	O1	Ir1	140.6(11)	N6	C28	C27	113(3)
S2	O4	Ir1	134.8(14)	N7	C29	C22	116(3)
C1	N1	Ir1	129(2)	N7	C29	C30	122(3)
C1	N1	C5	115(3)	C30	C29	C22	122(3)
C5	N1	Ir1	117(2)	N8	C30	C25	117(3)
C6	N2	Ir1	110.9(19)	N8	C30	C29	123(3)
C10	N2	Ir1	129(2)	C29	C30	C25	120(3)
C10	N2	C6	120(3)	N7	C31	C32	119(3)
C13	N3	C11	118(3)	N7	C31	C36	120(3)
C18	N4	C12	114(3)	C36	C31	C32	121(3)
C19	N5	Ir1	127(2)	N8	C32	C31	123(3)
C19	N5	C23	122(3)	N8	C32	C33	122(3)
C23	N5	Ir1	110.8(19)	C31	C32	C33	115(3)
C24	N6	Ir1	106(2)	C34	C33	C32	123(3)
C28	N6	Ir1	118(2)	C33	C34	C35	120(4)
C28	N6	C24	136(3)	C34	C35	C36	126(4)
C29	N7	C31	115(3)	C35	C36	C31	116(3)
C30	N8	C32	117(3)	F1	C37	S1	112(2)
N1	C1	C2	123(3)	F2	C37	S1	117(3)
C3	C2	C1	122(3)	F2	C37	F1	108(3)
C2	C3	C4	117(3)	F2	C37	F3	104(3)
C3	C4	C11	122(3)	F3	C37	S1	109(3)
C5	C4	C3	120(3)	F3	C37	F1	106(3)
C5	C4	C11	118(3)	F4	C38	S2	111(3)
C4	C5	N1	124(3)	F5	C38	S2	113(3)
C4	C5	C6	123(3)	F5	C38	F4	106(3)
C6	C5	N1	114(3)	F6	C38	S2	110(3)
N2	C6	C7	118(3)	F6	C38	F4	110(3)
C5	C6	N2	118(3)	F6	C38	F5	107(3)
C5	C6	C7	124(3)	O7	S3	O9	115.2(13)
C6	C7	C12	112(3)	O7	S3	C39	103.7(16)
C8	C7	C6	120(3)	O8	S3	O7	115.7(14)
C8	C7	C12	128(3)	O8	S3	O9	112.4(13)
C7	C8	C9	121(3)	O8	S3	C39	103.9(16)
C10	C9	C8	120(3)	O9	S3	C39	104.1(16)

C9	C10	N2	121(3)	F7	C39	S3	114(3)
N3	C11	C4	119(3)	F7	C39	F8	108(3)
N3	C11	C12	123(3)	F7	C39	F9	107(3)
C12	C11	C4	118(3)	F8	C39	S3	112(3)
N4	C12	C7	114(3)	F8	C39	F9	103(3)
C11	C12	N4	122(3)	F9	C39	S3	111(2)
C11	C12	C7	125(3)				

Table 9.60 – Hydrogen Atom Coordinates (Å×10^4) and Isotropic Displacement Parameters (Å^2×10^3) for IAJ686s_10-9A.

Atom	*x*	*y*	*z*	U(eq)
H1	8493.85	7687.67	3707.43	46
H2	10070.62	7192.33	4220.72	62
H3	10245.45	6373.83	4999.3	71
H8	5620.93	5432.35	4876.91	43
H9	4118.69	5975.19	4158.71	56
H10	4257.85	6810.98	3615.92	57
H14	11209.11	4943.15	6677.8	58
H15	11193.96	4128.46	7467.46	77
H16	9720.96	3893.78	7633.31	90
H17	8033.01	4290.99	6710.32	74
H19	6500.79	8100.51	1683.13	50
H20	7168.68	8926.1	1602.01	51
H21	7946.01	9476.73	3104.95	54
H26	7333.72	8560.23	7321.44	61
H27	6580.1	7732.18	7155.62	61
H28	6026.22	7268.65	5427.8	61
H33	8800.21	10103.18	8287.51	58
H34	9793.8	10822.98	8456.46	74
H35	10144.93	11077.67	7133.56	79
H36	9786.62	10564.55	5641.48	69

Crystal Structure Determination of IAJ686s_10-9A

Crystal Data for $C_{39}H_{20}F_9IrN_8O_9S_3$ (*M* =1204.01 g/mol): monoclinic, space group $P2_1/n$ (no. 14), *a* = 13.799(9) Å, *b* = 25.457(17) Å, *c* = 14.074(10) Å, *β* = 117.137(6)°, *V* = 4400(5) Å^3, *Z* = 4, *T* = 100.02 K, μ(MoKα) = 3.279 mm^{-1}, *Dcalc* = 1.818 g/cm^3, 27501 reflections measured (3.2° ≤ 2Θ ≤ 46.504°),

6143 unique (R_{int} = 0.1730, R_{sigma} = 0.2289) which were used in all calculations. The final R_1 was 0.1177 (I > 2σ(I)) and wR_2 was 0.2935 (all data).

9.3.8 IAJ695v_0m ($[Ir(dppz)_2Cl_2](CF_3SO_3)_2$ – An Adventitious Discovery

Table 9.61 – Crystal data and structure refinement for IAJ695v_0m.

Identification code	IAJ695v_0m
Empirical formula	$C_{37}H_{20}Cl_2F_3IrN_8O_3S$
Formula weight	976.77
Temperature/K	99.99
Crystal system	monoclinic
Space group	C2/c
a/Å	22.2065(17)
b/Å	13.8983(10)
c/Å	13.0161(10)
α/°	90
β/°	103.831(3)
γ/°	90
Volume/Å^3	3900.7(5)
Z	4
ρ_{calc}g/cm^3	1.663
μ/mm^{-1}	8.919
F(000)	1904.0
Crystal size/mm^3	0.154 × 0.106 × 0.056
Radiation	CuKα (λ = 1.54178)
2Θ range for data collection/°	7.568 to 133.424
Index ranges	-26 ≤ h ≤ 26, -16 ≤ k ≤ 16, -13 ≤ l ≤ 15
Reflections collected	17672
Independent reflections	3435 [R_{int} = 0.0287, R_{sigma} = 0.0206]
Data/restraints/parameters	3435/123/285
Goodness-of-fit on F^2	1.184
Final R indexes [I>=2σ (I)]	R_1 = 0.0478, wR_2 = 0.1285
Final R indexes [all data]	R_1 = 0.0483, wR_2 = 0.1287

Largest diff. peak/hole / e $Å^{-3}$	3.79/-1.52

Table 9.62 – Fractional Atomic Coordinates ($\times 10^4$) and Equivalent Isotropic Displacement Parameters ($Å^2 \times 10^3$) for IAJ695v_0m. U_{eq} is defined as 1/3 of the trace of the orthogonalised U_{IJ} tensor.

C2	5045(4)	1219(5)	4221(6)	25.2(16)
N3	6621(3)	2886(5)	4137(5)	29.2(15)
C3	5561(4)	1725(6)	4155(6)	28.0(17)
N4	7179(3)	4006(5)	5928(5)	26.9(14)
C4	5866(3)	2294(5)	4999(6)	21.5(15)
C5	5643(3)	2274(5)	5925(6)	21.4(15)
C6	5941(3)	2822(5)	6839(6)	19.9(14)
C7	6438(3)	3422(5)	6851(6)	22.6(15)
C8	6677(4)	3972(6)	7751(6)	29.4(17)
C9	6404(4)	3902(7)	8595(7)	38(2)
C10	5910(4)	3263(6)	8546(6)	32.5(19)
C11	6411(3)	2893(5)	4999(6)	23.9(16)
C12	6690(4)	3464(5)	5906(6)	24.0(16)
C13	7124(4)	3448(6)	4146(7)	30.2(18)
C14	7378(4)	3464(7)	3232(8)	37(2)
C15	7878(4)	4029(7)	3230(8)	38(2)
C16	8145(4)	4590(6)	4109(8)	38(2)
C17	7920(4)	4589(6)	5006(8)	37(2)
C18	7403(4)	4012(6)	5041(7)	30.2(18)
F1	6215(4)	5727(6)	6100(7)	31(2)
S1	4980(2)	5283(3)	5292(4)	34.9(9)
O1	5013(9)	5759(11)	4309(11)	42(4)
F2	5637(5)	5537(10)	7231(7)	58(3)
O2	5124(8)	4261(8)	5349(13)	37(4)
F3	5560(7)	6789(7)	6284(11)	68(4)
O3	4437(5)	5540(9)	5663(10)	43(3)
C19	5637(5)	5834(8)	6256(9)	39(3)

Table 9.63 – Anisotropic Displacement Parameters ($Å^2 \times 10^3$) for IAJ695v_0m. The Anisotropic displacement factor exponent takes the form: $-2\pi^2[h^2a^{*2}U_{11}+2hka^*b^*U_{12}+\ldots]$.

Atom	U_{11}	U_{22}	U_{33}	U_{23}	U_{13}	U_{12}
Ir1	16.9(2)	12.9(2)	17.3(2)	0	7.00(16)	0
Cl1	20.8(8)	18.5(8)	26.4(9)	-1.9(6)	8.6(7)	-3.3(6)
N1	25(3)	14(3)	24(3)	0(2)	10(3)	-3(2)
C1	22(4)	19(4)	26(4)	-2(3)	3(3)	-3(3)
N2	29(3)	20(3)	27(3)	-1(3)	14(3)	-1(3)
C2	31(4)	21(4)	23(4)	-5(3)	6(3)	-2(3)
N3	34(4)	27(3)	31(4)	2(3)	18(3)	-2(3)
C3	36(4)	25(4)	27(4)	1(3)	15(3)	1(3)
N4	25(3)	23(3)	35(4)	4(3)	13(3)	-1(3)
C4	25(4)	17(3)	27(4)	0(3)	15(3)	0(3)
C5	23(4)	17(3)	26(4)	2(3)	10(3)	6(3)
C6	19(3)	14(3)	28(4)	1(3)	10(3)	1(3)
C7	23(4)	17(4)	30(4)	0(3)	10(3)	-3(3)
C8	27(4)	29(4)	32(4)	-3(3)	7(3)	-8(3)
C9	45(5)	37(5)	37(5)	-15(4)	18(4)	-21(4)
C10	42(5)	36(5)	23(4)	-10(3)	12(4)	-18(4)
C11	21(4)	20(4)	33(4)	2(3)	11(3)	-1(3)
C12	26(4)	14(3)	35(4)	3(3)	14(3)	2(3)
C13	32(4)	24(4)	41(5)	5(3)	21(4)	2(3)
C14	40(5)	36(5)	46(5)	6(4)	29(4)	7(4)
C15	32(4)	36(5)	56(6)	12(4)	29(4)	4(4)
C16	26(4)	34(5)	60(6)	14(4)	23(4)	5(4)
C17	25(4)	30(4)	57(6)	3(4)	15(4)	-10(3)
C18	22(4)	28(4)	46(5)	7(4)	17(3)	3(3)
F1	46(5)	25(4)	24(4)	19(4)	16(4)	21(4)
S1	40(2)	27(2)	37(2)	3.9(17)	8.4(18)	3.1(18)
O1	51(10)	34(7)	39(9)	11(6)	7(6)	-4(6)
F2	46(6)	98(9)	29(5)	-8(5)	4(4)	-4(6)
O2	51(10)	27(6)	32(9)	16(6)	8(7)	7(5)
F3	87(9)	34(5)	75(9)	-23(5)	1(7)	8(5)
O3	36(6)	38(7)	55(8)	6(6)	10(6)	4(5)
C19	45(6)	36(6)	36(6)	0(6)	8(6)	12(6)

Table 9.64 – Bond Lengths for IAJ695v_0m.

Atom	Atom	Length/Å		Atom	Atom	Length/Å
Ir1	Cl1	2.3545(16)		C6	C7	1.382(10)
Ir1	Cl1[1]	2.3545(16)		C7	C8	1.393(11)
Ir1	N1[1]	2.050(6)		C7	C12	1.469(11)
Ir1	N1	2.050(6)		C8	C9	1.380(12)
Ir1	N2	2.031(6)		C9	C10	1.401(11)
Ir1	N2[1]	2.031(6)		C11	C12	1.435(11)
N1	C1	1.340(9)		C13	C14	1.433(11)
N1	C5	1.350(9)		C13	C18	1.419(13)
C1	C2	1.400(11)		C14	C15	1.361(13)
N2	C6	1.372(9)		C15	C16	1.395(14)
N2	C10	1.329(10)		C16	C17	1.375(13)
C2	C3	1.367(11)		C17	C18	1.411(11)
N3	C11	1.313(10)		F1	C19	1.355(11)
N3	C13	1.361(11)		S1	O1	1.457(10)
C3	C4	1.391(11)		S1	O2	1.454(11)
N4	C12	1.316(10)		S1	O3	1.447(10)
N4	C18	1.361(10)		S1	C19	1.848(13)
C4	C5	1.408(10)		F2	C19	1.335(11)
C4	C11	1.469(10)		F3	C19	1.340(11)
C5	C6	1.434(10)				

[1]1-X,+Y,3/2-Z

Table 9.65 – Bond Angles for IAJ695v_0m.

Atom	Atom	Atom	Angle/°		Atom	Atom	Atom	Angle/°
Cl1[1]	Ir1	Cl1	91.10(8)		C6	C7	C8	118.9(7)
N1	Ir1	Cl1[1]	86.02(17)		C6	C7	C12	118.5(7)
N1	Ir1	Cl1	95.26(17)		C8	C7	C12	122.5(7)
N1[1]	Ir1	Cl1	86.02(17)		C9	C8	C7	118.6(7)
N1[1]	Ir1	Cl1[1]	95.26(17)		C8	C9	C10	119.8(8)
N1	Ir1	N1[1]	178.2(3)		N2	C10	C9	121.8(7)
N2	Ir1	Cl1[1]	87.95(18)		N3	C11	C4	117.2(7)
N2[1]	Ir1	Cl1	87.95(18)		N3	C11	C12	122.4(7)
N2[1]	Ir1	Cl1[1]	175.17(18)		C12	C11	C4	120.5(7)

N2	Ir1	Cl1	175.17(18)		N4	C12	C7	118.8(7)
N2	Ir1	N1[1]	98.8(2)		N4	C12	C11	121.7(7)
N2	Ir1	N1	80.0(2)		C11	C12	C7	119.4(7)
N2[1]	Ir1	N1[1]	80.0(2)		N3	C13	C14	119.2(8)
N2[1]	Ir1	N1	98.8(2)		N3	C13	C18	121.3(7)
N2[1]	Ir1	N2	93.4(4)		C18	C13	C14	119.4(8)
C1	N1	Ir1	127.3(5)		C15	C14	C13	119.7(9)
C1	N1	C5	118.9(6)		C14	C15	C16	120.5(8)
C5	N1	Ir1	113.3(5)		C17	C16	C15	121.8(8)
N1	C1	C2	121.6(7)		C16	C17	C18	119.5(9)
C6	N2	Ir1	114.0(5)		N4	C18	C13	121.1(7)
C10	N2	Ir1	127.5(5)		N4	C18	C17	119.7(8)
C10	N2	C6	118.5(7)		C17	C18	C13	119.1(8)
C3	C2	C1	119.5(7)		O1	S1	C19	102.2(8)
C11	N3	C13	116.6(7)		O2	S1	O1	115.5(9)
C2	C3	C4	120.0(7)		O2	S1	C19	104.0(8)
C12	N4	C18	116.9(7)		O3	S1	O1	113.7(9)
C3	C4	C5	117.5(7)		O3	S1	O2	114.5(8)
C3	C4	C11	124.5(7)		O3	S1	C19	104.9(6)
C5	C4	C11	118.0(7)		F1	C19	S1	118.4(9)
N1	C5	C4	122.5(7)		F2	C19	F1	109.0(10)
N1	C5	C6	116.6(6)		F2	C19	S1	109.7(9)
C4	C5	C6	120.9(7)		F2	C19	F3	104.5(12)
N2	C6	C5	115.1(6)		F3	C19	F1	104.2(11)
N2	C6	C7	122.3(7)		F3	C19	S1	110.1(9)
C7	C6	C5	122.6(7)					

Table 9.66 – Torsion Angles for IAJ695v_0m.

A	**B**	**C**	**D**	**Angle/°**		**A**	**B**	**C**	**D**	**Angle/°**
Ir1	N1	C1	C2	-171.3(5)		C6	C7	C12	N4	-177.4(7)
Ir1	N1	C5	C4	172.6(5)		C6	C7	C12	C11	0.7(11)
Ir1	N1	C5	C6	-7.8(8)		C7	C8	C9	C10	2.1(14)
Ir1	N2	C6	C5	6.1(8)		C8	C7	C12	N4	3.3(11)
Ir1	N2	C6	C7	-175.7(6)		C8	C7	C12	C11	-178.6(7)
Ir1	N2	C10	C9	177.1(7)		C8	C9	C10	N2	-1.5(15)

N1	C1	C2	C3	1.8(12)		C10	N2	C6	C5	-175.7(7)
N1	C5	C6	N2	1.2(9)		C10	N2	C6	C7	2.4(11)
N1	C5	C6	C7	-176.9(7)		C11	N3	C13	C14	179.5(7)
C1	N1	C5	C4	-0.1(10)		C11	N3	C13	C18	-0.2(12)
C1	N1	C5	C6	179.5(6)		C11	C4	C5	N1	179.7(6)
C1	C2	C3	C4	-3.8(12)		C11	C4	C5	C6	0.1(10)
N2	C6	C7	C8	-1.7(11)		C12	N4	C18	C13	-0.8(11)
N2	C6	C7	C12	179.0(7)		C12	N4	C18	C17	179.0(7)
C2	C3	C4	C5	3.9(11)		C12	C7	C8	C9	178.7(8)
C2	C3	C4	C11	-177.9(7)		C13	N3	C11	C4	179.6(7)
N3	C11	C12	N4	-0.8(12)		C13	N3	C11	C12	0.3(11)
N3	C11	C12	C7	-178.8(7)		C13	C14	C15	C16	0.0(13)
N3	C13	C14	C15	179.6(8)		C14	C13	C18	N4	-179.2(7)
N3	C13	C18	N4	0.4(12)		C14	C13	C18	C17	0.9(12)
N3	C13	C18	C17	-179.5(8)		C14	C15	C16	C17	0.6(14)
C3	C4	C5	N1	-1.9(11)		C15	C16	C17	C18	-0.5(13)
C3	C4	C5	C6	178.4(7)		C16	C17	C18	N4	179.8(8)
C3	C4	C11	N3	0.2(11)		C16	C17	C18	C13	-0.3(13)
C3	C4	C11	C12	179.4(7)		C18	N4	C12	C7	179.0(7)
C4	C5	C6	N2	-179.2(6)		C18	N4	C12	C11	1.0(11)
C4	C5	C6	C7	2.7(11)		C18	C13	C14	C15	-0.8(13)
C4	C11	C12	N4	180.0(7)		O1	S1	C19	F1	-60.0(11)
C4	C11	C12	C7	2.0(11)		O1	S1	C19	F2	174.1(11)
C5	N1	C1	C2	0.2(11)		O1	S1	C19	F3	59.6(12)
C5	C4	C11	N3	178.4(7)		O2	S1	C19	F1	60.6(11)
C5	C4	C11	C12	-2.3(11)		O2	S1	C19	F2	-65.3(11)
C5	C6	C7	C8	176.3(7)		O2	S1	C19	F3	-179.8(11)
C5	C6	C7	C12	-3.0(11)		O3	S1	C19	F1	-178.8(9)
C6	N2	C10	C9	-0.8(13)		O3	S1	C19	F2	55.3(10)
C6	C7	C8	C9	-0.6(12)		O3	S1	C19	F3	-59.3(11)

Table 9.67 – Hydrogen Atom Coordinates (Å×10^4) and Isotropic Displacement Parameters (Å^2×10^3) for IAJ695v_0m.

Atom	***x***	***y***	***z***	**U(eq)**
H1	4494.65	863.65	5214.36	28

H2	4821.1	860.2	3631.09	30
H3	5712.91	1688.76	3532.56	34
H8	7021.51	4385.92	7783.17	35
H9	6549.87	4286.1	9207.4	46
H10	5731.05	3210.11	9137.9	39
H14	7198.02	3083.22	2631.16	45
H15	8047.32	4041.17	2624.53	46
H16	8491.69	4984.04	4088.36	45
H17	8111.65	4974.08	5597.48	44

Table 9.68 – Atomic Occupancy for IAJ695v_0m.

Atom	Occupancy		Atom	Occupancy		Atom	Occupancy
F1	0.5		S1	0.5		O1	0.5
F2	0.5		O2	0.5		F3	0.5
O3	0.5		C19	0.5			

Table 9.69 – Solvent masks information for IAJ695v_0m.

Number	X	Y	Z	Volume	Electron count	Content
1	0.250	0.250	0.500	146.3	12.0	?
2	0.250	0.750	0.000	146.3	12.0	?
3	0.750	0.250	0.000	146.3	12.0	?
4	0.750	0.750	0.500	146.3	12.0	?

Crystal Structure Determination of IAJ695v_0m

Crystal Data for $C_{37}H_{20}Cl_2F_3IrN_8O_3S$ (M = 976.77 g/mol): monoclinic, space group C2/c (no. 15), a = 22.2065(17) Å, b = 13.8983(10) Å, c = 13.0161(10) Å, β = 103.831(3)°, V = 3900.7(5) Å^3, Z = 4, T = 99.99 K, μ(CuKα) = 8.919 mm^{-1}, *Dcalc* = 1.663 g/cm^3, 17672 reflections measured (7.568° ≤ 2Θ ≤ 133.424°), 3435 unique (R_{int} = 0.0287, R_{sigma} = 0.0206) which were used in all calculations. The final R_1 was 0.0478 (I > 2σ(I)) and wR_2 was 0.1287 (all data).

9.3.9 IAJ697v_0m ($[Ir(phen)_2Cl(CH_3CN)](CF_3SO_3)_2CH_3NO_2$ – An Adventitious Discovery

Table 9.70 – Crystal data and structure refinement for iaj697v_0m.

Identification code	iaj697v_0m
Empirical formula	$C_{29}H_{22}ClF_6IrN_6O_8S_2$
Formula weight	988.29
Temperature/K	99.99
Crystal system	triclinic
Space group	P-1
a/Å	10.4846(4)
b/Å	12.0754(4)
c/Å	13.9975(5)
α/°	88.414(2)
β/°	76.882(2)
γ/°	72.523(2)
Volume/Å^3	1644.68(10)
Z	2
ρ_{calc}g/cm^3	1.996
μ/mm^{-1}	10.660
F(000)	964.0
Crystal size/mm^3	0.26 × 0.195 × 0.036
Radiation	CuKα (λ = 1.54178)
2Θ range for data collection/°	6.49 to 133.58
Index ranges	$-11 \leq h \leq 12$, $-14 \leq k \leq 14$, $-16 \leq l \leq 16$
Reflections collected	18034
Independent reflections	5705 [R_{int} = 0.0703, R_{sigma} = 0.0666]
Data/restraints/parameters	5705/0/480
Goodness-of-fit on F^2	1.112
Final R indexes [I>=2σ (I)]	R_1 = 0.0597, wR_2 = 0.1610
Final R indexes [all data]	R_1 = 0.0670, wR_2 = 0.1666
Largest diff. peak/hole / e Å^{-3}	3.57/-1.80

Table 9.71 – Fractional Atomic Coordinates ($\times 10^4$) and Equivalent Isotropic Displacement Parameters ($Å^2 \times 10^3$) for iaj697v_0m. U_{eq} is defined as 1/3 of the trace of the orthogonalised U_{IJ} tensor.

Atom	*x*	*y*	*z*	U(eq)
Ir1	4102.3(4)	2981.6(3)	7849.8(3)	18.57(16)
Cl1	3535(2)	5001.9(19)	8104.0(17)	26.4(5)
N1	5090(9)	2581(7)	8989(6)	24.1(17)
N2	4684(8)	1222(7)	7719(6)	20.0(15)
N3	5853(9)	2992(7)	6870(6)	25.5(17)
N4	3353(8)	3277(7)	6612(6)	20.4(15)
N5	2272(9)	3039(7)	8758(6)	27.9(18)
C1	5189(12)	3303(10)	9649(8)	32(2)
C2	5995(14)	2872(10)	10321(8)	40(3)
C3	6649(11)	1714(10)	10354(8)	32(2)
C4	6483(10)	937(9)	9701(7)	27(2)
C5	5690(10)	1412(8)	9026(7)	21.7(18)
C6	5459(9)	672(8)	8348(7)	21.1(18)
C7	4359(10)	557(8)	7103(7)	24.3(19)
C8	4856(11)	-659(9)	7084(7)	27(2)
C9	5644(10)	-1208(8)	7716(8)	27(2)
C10	5963(10)	-542(9)	8376(7)	25(2)
C11	6758(10)	-1014(9)	9083(8)	30(2)
C12	7026(11)	-294(9)	9716(7)	29(2)
C13	7104(11)	2844(9)	7037(8)	30(2)
C14	8195(10)	2882(9)	6265(8)	28(2)
C15	7999(10)	3136(9)	5341(8)	30(2)
C16	6711(11)	3305(8)	5152(7)	26(2)
C17	5649(9)	3224(8)	5944(7)	19.6(18)
C18	4302(10)	3383(8)	5809(7)	21.9(19)
C19	2061(10)	3418(8)	6524(7)	23.2(19)
C20	1728(11)	3653(9)	5605(8)	29(2)
C21	2670(11)	3773(8)	4798(7)	24.2(19)
C22	4027(11)	3623(8)	4869(7)	23.4(19)
C23	5098(10)	3723(8)	4080(7)	23.7(19)
C24	6395(11)	3583(9)	4209(7)	27(2)
C25	1229(10)	3142(9)	9247(7)	25(2)
C26	-116(11)	3245(10)	9872(8)	35(2)

S1	-1809(3)	5464(2)	8043.6(18)	26.9(5)
F1	518(7)	5991(7)	7618(5)	46.8(17)
F2	-338(7)	5918(6)	6373(5)	40.0(15)
F3	-1237(7)	7364(6)	7398(6)	47.1(17)
O1	-2052(9)	5940(7)	9031(6)	40.1(18)
O2	-1031(8)	4274(7)	7868(6)	35.6(17)
O3	-2984(8)	5822(7)	7605(6)	35.0(17)
C27	-639(11)	6222(10)	7323(8)	32(2)
S2	520(3)	10744(3)	7797(2)	40.2(6)
F4	286(9)	8715(8)	8369(7)	66(2)
F5	2138(11)	8607(8)	7326(8)	74(3)
F6	290(20)	8996(14)	6856(11)	146(8)
O4	1341(12)	10711(9)	8501(7)	56(2)
O5	-919(12)	11209(14)	8153(13)	117(7)
O6	1074(9)	11110(8)	6861(7)	47(2)
C28	854(16)	9167(13)	7565(12)	55(4)
O7	3415(14)	9206(9)	5090(10)	73(3)
O8	3375(12)	10997(9)	5030(7)	57(3)
N6	2911(12)	10194(10)	4905(8)	48(3)
C29	1750(20)	10503(17)	4491(14)	71(5)

Table 9.72 – Anisotropic Displacement Parameters ($Å^2 \times 10^3$) for iaj697v_0m. The Anisotropic displacement factor exponent takes the form: $-2\pi^2[h^2a^{*2}U_{11}+2hka^*b^*U_{12}+\ldots]$.

Atom	**U_{11}**	**U_{22}**	**U_{33}**	**U_{23}**	**U_{13}**	**U_{12}**
Ir1	19.6(2)	20.5(2)	16.3(2)	-0.50(14)	-5.92(15)	-5.58(15)
Cl1	32.5(12)	21.7(10)	24.9(11)	-0.8(8)	-7.7(9)	-7.2(9)
N1	27(4)	24(4)	25(4)	-4(3)	-8(3)	-12(3)
N2	15(4)	27(4)	17(4)	2(3)	-3(3)	-4(3)
N3	26(4)	20(4)	27(4)	-1(3)	0(3)	-5(3)
N4	16(4)	23(4)	24(4)	-5(3)	-5(3)	-6(3)
N5	27(5)	25(4)	26(4)	1(3)	-2(4)	-2(3)
C1	42(6)	37(6)	23(5)	0(4)	-17(5)	-14(5)
C2	60(8)	43(6)	24(5)	-8(5)	-18(5)	-18(6)
C3	33(5)	45(6)	28(5)	3(4)	-22(5)	-15(5)

C4	22(5)	39(6)	21(5)	3(4)	-7(4)	-11(4)
C5	20(4)	30(5)	19(4)	3(4)	-8(4)	-11(4)
C6	18(4)	20(4)	20(4)	4(3)	1(4)	-3(3)
C7	22(5)	26(5)	25(5)	0(4)	-5(4)	-8(4)
C8	29(5)	32(5)	20(5)	-3(4)	-3(4)	-10(4)
C9	24(5)	21(4)	31(5)	1(4)	1(4)	-2(4)
C10	22(5)	30(5)	21(5)	-2(4)	-2(4)	-5(4)
C11	24(5)	34(5)	32(5)	5(4)	-9(4)	-8(4)
C12	28(5)	32(5)	22(5)	2(4)	-7(4)	-3(4)
C13	31(5)	37(5)	29(5)	4(4)	-22(5)	-10(4)
C14	16(4)	34(5)	39(6)	6(4)	-8(4)	-13(4)
C15	21(5)	31(5)	39(6)	2(4)	-3(4)	-11(4)
C16	32(5)	20(4)	23(5)	-2(4)	-4(4)	-7(4)
C17	19(4)	20(4)	20(4)	4(3)	-6(4)	-6(3)
C18	23(5)	17(4)	23(5)	-3(3)	-3(4)	-4(4)
C19	24(5)	29(5)	24(5)	3(4)	-16(4)	-11(4)
C20	32(5)	28(5)	29(5)	-3(4)	-11(4)	-10(4)
C21	33(5)	24(5)	18(4)	-4(3)	-11(4)	-7(4)
C22	34(5)	19(4)	23(5)	-2(3)	-15(4)	-8(4)
C23	29(5)	27(5)	19(4)	1(4)	-6(4)	-13(4)
C24	29(5)	31(5)	18(5)	-1(4)	-2(4)	-9(4)
C25	23(5)	33(5)	25(5)	1(4)	-17(5)	-10(4)
C26	29(5)	45(6)	28(5)	3(5)	-1(5)	-10(5)
S1	26.7(12)	29.4(12)	23.1(11)	-0.8(9)	-7.1(10)	-5.2(9)
F1	28(3)	68(5)	50(4)	1(3)	-15(3)	-16(3)
F2	35(3)	57(4)	27(3)	1(3)	-5(3)	-13(3)
F3	41(4)	34(3)	62(5)	0(3)	-4(3)	-10(3)
O1	40(4)	47(5)	28(4)	-5(3)	-4(3)	-9(4)
O2	29(4)	36(4)	39(4)	-4(3)	-6(3)	-6(3)
O3	27(4)	47(4)	35(4)	2(3)	-9(3)	-14(3)
C27	26(5)	39(6)	30(5)	-2(4)	-7(4)	-7(4)
S2	30.0(14)	41.3(15)	43.5(16)	8.5(12)	-5.4(12)	-5.1(11)
F4	60(5)	65(5)	82(6)	37(5)	-21(5)	-29(4)
F5	78(7)	46(5)	82(7)	-17(4)	10(5)	-15(4)
F6	280(20)	153(12)	129(11)	87(10)	-149(14)	-171(15)
O4	75(7)	53(6)	42(5)	-5(4)	-20(5)	-16(5)

O5	39(6)	111(11)	148(14)	94(11)	19(7)	16(6)
O6	43(5)	46(5)	54(5)	14(4)	-16(4)	-16(4)
C28	64(9)	62(8)	73(10)	18(7)	-49(8)	-46(8)
O7	85(8)	42(6)	92(9)	0(5)	-25(7)	-14(5)
O8	81(7)	54(6)	41(5)	-15(4)	0(5)	-34(5)
N6	55(7)	45(6)	43(6)	-1(5)	-7(5)	-15(5)
C29	79(12)	77(11)	65(10)	3(9)	-27(9)	-26(10)

Table 9.73 – Bond Lengths for iaj697v_0m.

Atom	Atom	Length/Å		Atom	Atom	Length/Å
Ir1	Cl1	2.348(2)		C15	C16	1.388(15)
Ir1	N1	2.063(8)		C16	C17	1.407(14)
Ir1	N2	2.028(8)		C16	C24	1.439(14)
Ir1	N3	2.029(8)		C17	C18	1.422(13)
Ir1	N4	2.039(8)		C18	C22	1.413(13)
Ir1	N5	2.030(9)		C19	C20	1.408(14)
N1	C1	1.330(13)		C20	C21	1.357(15)
N1	C5	1.366(13)		C21	C22	1.406(14)
N2	C6	1.358(12)		C22	C23	1.416(14)
N2	C7	1.357(13)		C23	C24	1.372(15)
N3	C13	1.343(13)		C25	C26	1.453(15)
N3	C17	1.369(13)		S1	O1	1.450(8)
N4	C18	1.354(13)		S1	O2	1.420(8)
N4	C19	1.348(12)		S1	O3	1.446(8)
N5	C25	1.123(14)		S1	C27	1.849(11)
C1	C2	1.392(16)		F1	C27	1.319(13)
C2	C3	1.365(17)		F2	C27	1.330(13)
C3	C4	1.402(15)		F3	C27	1.328(13)
C4	C5	1.398(14)		S2	O4	1.442(10)
C4	C12	1.424(15)		S2	O5	1.416(11)
C5	C6	1.428(14)		S2	O6	1.423(9)
C6	C10	1.404(14)		S2	C28	1.854(15)
C7	C8	1.402(14)		F4	C28	1.333(17)
C8	C9	1.369(15)		F5	C28	1.281(19)

C9	C10	1.399(15)		F6	C28	1.314(17)
C10	C11	1.434(15)		O7	N6	1.199(15)
C11	C12	1.386(16)		O8	N6	1.240(15)
C13	C14	1.395(15)		N6	C29	1.41(2)
C14	C15	1.368(16)				

Table 9.74 – Bond Angles for iaj697v_0m.

Atom	**Atom**	**Atom**	**Angle/°**		**Atom**	**Atom**	**Atom**	**Angle/°**
N1	Ir1	Cl1	94.9(2)		N3	C13	C14	120.1(9)
N2	Ir1	Cl1	175.1(2)		C15	C14	C13	121.0(9)
N2	Ir1	N1	80.3(3)		C14	C15	C16	119.8(9)
N2	Ir1	N3	90.1(3)		C15	C16	C17	117.3(9)
N2	Ir1	N4	96.4(3)		C15	C16	C24	124.2(10)
N2	Ir1	N5	91.8(3)		C17	C16	C24	118.5(9)
N3	Ir1	Cl1	89.6(2)		N3	C17	C16	122.3(9)
N3	Ir1	N1	92.7(3)		N3	C17	C18	117.1(8)
N3	Ir1	N4	81.1(3)		C16	C17	C18	120.6(9)
N3	Ir1	N5	175.7(3)		N4	C18	C17	116.3(8)
N4	Ir1	Cl1	88.4(2)		N4	C18	C22	124.0(9)
N4	Ir1	N1	173.0(3)		C22	C18	C17	119.7(9)
N5	Ir1	Cl1	88.8(2)		N4	C19	C20	119.9(9)
N5	Ir1	N1	91.4(3)		C21	C20	C19	121.8(10)
N5	Ir1	N4	94.9(3)		C20	C21	C22	119.5(9)
C1	N1	Ir1	128.2(7)		C18	C22	C23	119.2(9)
C1	N1	C5	119.7(9)		C21	C22	C18	116.2(9)
C5	N1	Ir1	112.2(6)		C21	C22	C23	124.7(9)
C6	N2	Ir1	114.6(6)		C24	C23	C22	121.3(9)
C7	N2	Ir1	127.5(6)		C23	C24	C16	120.6(9)
C7	N2	C6	117.9(8)		N5	C25	C26	178.5(11)
C13	N3	Ir1	128.2(7)		O1	S1	C27	102.4(5)
C13	N3	C17	119.3(9)		O2	S1	O1	116.3(5)
C17	N3	Ir1	112.4(6)		O2	S1	O3	114.8(5)
C18	N4	Ir1	113.1(6)		O2	S1	C27	103.0(5)
C19	N4	Ir1	128.2(7)		O3	S1	O1	114.8(5)
C19	N4	C18	118.7(8)		O3	S1	C27	102.8(5)

C25	N5	Ir1	175.6(8)		F1	C27	S1	111.7(8)
N1	C1	C2	119.6(10)		F1	C27	F2	108.4(9)
C3	C2	C1	122.1(10)		F1	C27	F3	108.7(9)
C2	C3	C4	118.7(9)		F2	C27	S1	110.9(8)
C3	C4	C12	123.8(9)		F3	C27	S1	110.5(7)
C5	C4	C3	117.2(10)		F3	C27	F2	106.4(9)
C5	C4	C12	118.9(9)		O4	S2	C28	100.3(6)
N1	C5	C4	122.6(9)		O5	S2	O4	115.9(10)
N1	C5	C6	117.2(8)		O5	S2	O6	116.0(7)
C4	C5	C6	120.2(9)		O5	S2	C28	105.9(9)
N2	C6	C5	115.5(8)		O6	S2	O4	113.4(6)
N2	C6	C10	123.4(9)		O6	S2	C28	102.7(7)
C10	C6	C5	121.0(9)		F4	C28	S2	109.6(12)
N2	C7	C8	121.2(9)		F5	C28	S2	112.9(9)
C9	C8	C7	120.6(9)		F5	C28	F4	108.3(12)
C8	C9	C10	119.2(9)		F5	C28	F6	108.2(17)
C6	C10	C11	117.9(9)		F6	C28	S2	110.3(11)
C9	C10	C6	117.6(9)		F6	C28	F4	107.5(11)
C9	C10	C11	124.5(9)		O7	N6	O8	123.7(13)
C12	C11	C10	121.1(10)		O7	N6	C29	120.6(13)
C11	C12	C4	120.8(9)		O8	N6	C29	115.7(13)

Table 9.75 – Torsion Angles for iaj697v_0m.

A	B	C	D	Angle/°		A	B	C	D	Angle/°
Ir1	N1	C1	C2	-175.0(8)		C10	C11	C12	C4	1.9(16)
Ir1	N1	C5	C4	176.4(7)		C12	C4	C5	N1	177.5(9)
Ir1	N1	C5	C6	-4.7(10)		C12	C4	C5	C6	-1.4(14)
Ir1	N2	C6	C5	2.5(10)		C13	N3	C17	C16	0.5(13)
Ir1	N2	C6	C10	179.9(7)		C13	N3	C17	C18	-179.5(9)
Ir1	N2	C7	C8	179.1(7)		C13	C14	C15	C16	-3.2(16)
Ir1	N3	C13	C14	-179.9(7)		C14	C15	C16	C17	1.1(14)
Ir1	N3	C17	C16	178.3(7)		C14	C15	C16	C24	179.6(10)
Ir1	N3	C17	C18	-1.8(10)		C15	C16	C17	N3	0.2(14)
Ir1	N4	C18	C17	2.6(10)		C15	C16	C17	C18	-179.8(9)
Ir1	N4	C18	C22	-178.1(7)		C15	C16	C24	C23	179.2(9)

Ir1	N4	C19	C20	177.9(7)		C16	C17	C18	N4	179.4(8)
N1	C1	C2	C3	-2.8(19)		C16	C17	C18	C22	0.1(13)
N1	C5	C6	N2	1.6(12)		C17	N3	C13	C14	-2.5(14)
N1	C5	C6	C10	-175.9(8)		C17	C16	C24	C23	-2.3(14)
N2	C6	C10	C9	0.1(14)		C17	C18	C22	C21	-179.7(8)
N2	C6	C10	C11	-179.4(9)		C17	C18	C22	C23	-1.1(13)
N2	C7	C8	C9	2.5(15)		C18	N4	C19	C20	1.0(13)
N3	C13	C14	C15	3.9(16)		C18	C22	C23	C24	0.4(14)
N3	C17	C18	N4	-0.6(12)		C19	N4	C18	C17	-179.9(8)
N3	C17	C18	C22	-179.9(8)		C19	N4	C18	C22	-0.7(13)
N4	C18	C22	C21	1.0(13)		C19	C20	C21	C22	2.1(14)
N4	C18	C22	C23	179.6(8)		C20	C21	C22	C18	-1.7(13)
N4	C19	C20	C21	-1.7(15)		C20	C21	C22	C23	179.8(9)
C1	N1	C5	C4	-3.7(14)		C21	C22	C23	C24	178.9(9)
C1	N1	C5	C6	175.2(9)		C22	C23	C24	C16	1.3(15)
C1	C2	C3	C4	-1.1(18)		C24	C16	C17	N3	-178.4(9)
C2	C3	C4	C5	2.4(16)		C24	C16	C17	C18	1.6(13)
C2	C3	C4	C12	-175.0(10)		O1	S1	C27	F1	61.1(9)
C3	C4	C5	N1	-0.1(14)		O1	S1	C27	F2	-177.8(7)
C3	C4	C5	C6	-179.0(9)		O1	S1	C27	F3	-60.1(9)
C3	C4	C12	C11	176.4(10)		O2	S1	C27	F1	-60.0(9)
C4	C5	C6	N2	-179.5(8)		O2	S1	C27	F2	61.1(8)
C4	C5	C6	C10	3.0(14)		O2	S1	C27	F3	178.9(8)
C5	N1	C1	C2	5.1(16)		O3	S1	C27	F1	-179.6(8)
C5	C4	C12	C11	-1.0(15)		O3	S1	C27	F2	-58.5(8)
C5	C6	C10	C9	177.3(9)		O3	S1	C27	F3	59.3(9)
C5	C6	C10	C11	-2.2(14)		O4	S2	C28	F4	67.9(10)
C6	N2	C7	C8	-2.8(13)		O4	S2	C28	F5	-52.8(12)
C6	C10	C11	C12	-0.3(15)		O4	S2	C28	F6	-174.0(13)
C7	N2	C6	C5	-175.8(8)		O5	S2	C28	F4	-53.0(12)
C7	N2	C6	C10	1.6(13)		O5	S2	C28	F5	-173.7(12)
C7	C8	C9	C10	-0.7(15)		O5	S2	C28	F6	65.2(16)
C8	C9	C10	C6	-0.5(14)		O6	S2	C28	F4	-175.1(8)
C8	C9	C10	C11	179.0(10)		O6	S2	C28	F5	64.2(12)
C9	C10	C11	C12	-179.8(10)		O6	S2	C28	F6	-57.0(14)

Table 9.76 – Hydrogen Atom Coordinates (Å×10^4) and Isotropic Displacement Parameters (Å^2×10^3) for iaj697v_0m.

Atom	*x*	*y*	*z*	U(eq)
H1	4713.38	4109.8	9661.43	38
H2	6092.15	3400.11	10769.72	48
H3	7206.72	1439.65	10811.73	38
H7	3784.46	922.57	6676.83	29
H8	4644.32	-1105.45	6628.65	33
H9	5970.13	-2032.78	7705.35	33
H11	7107.26	-1833.08	9117.57	36
H12	7578.94	-625.98	10164.81	34
H13	7245.87	2713.57	7682.81	36
H14	9087.96	2727.95	6382.73	34
H15	8741.51	3196.95	4829.64	36
H19	1375.72	3358.67	7081.28	28
H20	820.53	3729.51	5547.46	34
H21	2413.72	3957.38	4190.76	29
H23	4915.21	3889.79	3448.67	28
H24	7090.76	3670.37	3671.65	32
H26A	-484.48	2666.15	9652.56	53
H26B	-736.7	4025.81	9832.74	53
H26C	-33.54	3112.62	10552.24	53
H29A	920.97	10554.24	5007.41	107
H29B	1852.9	9911.17	3989.6	107
H29C	1657.18	11256.9	4190.97	107

Crystal Structure Determination of Iaj697v_0m

Crystal Data for $C_{29}H_{22}ClF_6IrN_6O_8S_2$ (*M* = 988.29 g/mol): triclinic, space group P-1 (no. 2), *a* = 10.4846(4) Å, *b* = 12.0754(4) Å, *c* = 13.9975(5) Å, *α* = 88.414(2)°, *β* = 76.882(2)°, *γ* = 72.523(2)°, *V* = 1644.68(10) Å^3, *Z* = 2, *T* = 99.99 K, μ(CuKα) = 10.660 mm^{-1}, *Dcalc* = 1.996 g/cm^3, 18034 reflections measured (6.49° ≤ 2Θ ≤ 133.58°), 5705 unique (R_{int} = 0.0703, R_{sigma} = 0.0666) which were used in all calculations. The final R_1 was 0.0597 (I > 2σ(I)) and wR_2 was 0.1666 (all data).

9.3.10 IAJ696v ([Ir(phen)$_2$Cl$_2$]Cl, crystallised as [Ir(phen)$_2$Cl$_2$]Cl H_2O MeCN

Table 9.77 – Crystal data and structure refinement for IAJ696v.

Identification code	IAJ696v
Empirical formula	$C_{25}H_{19.5}Cl_3IrN_{4.5}O$
Formula weight	697.50
Temperature/K	100.01
Crystal system	orthorhombic
Space group	Pbcn
a/Å	12.8589(9)
b/Å	23.1485(16)
c/Å	16.4518(12)
α/°	90
β/°	90
γ/°	90
Volume/Å^3	4897.1(6)
Z	8
ρ_{calc}g/cm^3	1.892
μ/mm^{-1}	13.798
F(000)	2696.0
Crystal size/mm^3	0.4 × 0.05 × 0.024
Radiation	CuKα (λ = 1.54178)
2Θ range for data collection/°	7.638 to 133.642
Index ranges	-15 ≤ h ≤ 15, -27 ≤ k ≤ 27, -19 ≤ l ≤ 18
Reflections collected	73957
Independent reflections	4344 [R_{int} = 0.0603, R_{sigma} = 0.0230]
Data/restraints/parameters	4344/320/307
Goodness-of-fit on F^2	1.055
Final R indexes [I>=2σ (I)]	R_1 = 0.0470, wR_2 = 0.1198
Final R indexes [all data]	R_1 = 0.0498, wR_2 = 0.1227
Largest diff. peak/hole / e Å^{-3}	4.07/-2.60

Table 9.78 – Fractional Atomic Coordinates ($\times 10^4$) and Equivalent Isotropic Displacement Parameters ($Å^2 \times 10^3$) for IAJ696v. U_{eq} is defined as 1/3 of the trace of the orthogonalised U_{IJ} tensor.

Atom	*x*	*y*	*z*	U(eq)
Ir1	6483.0(2)	6834.4(2)	4823.3(2)	17.76(13)
Cl1	5263.6(13)	6741.7(7)	5883.0(10)	26.7(4)
Cl2	7833.7(14)	7063.9(8)	5727.4(11)	33.1(4)
Cl3	8110.4(18)	5177.5(9)	2899(3)	83.3(12)
O1	10339(9)	5496(4)	3541(6)	112(4)
N1	6706(5)	5959(3)	4865(3)	22.3(11)
N2	5340(4)	6587(2)	4045(3)	17.6(10)
N3	6269(5)	7703(3)	4684(4)	26.1(12)
N4	7472(4)	6976(2)	3878(3)	18.6(10)
C1	7402(6)	5662(3)	5292(5)	28.1(15)
C2	7435(7)	5059(3)	5267(5)	36.7(17)
C3	6748(7)	4761(3)	4791(5)	37.4(18)
C4	6004(6)	5063(3)	4334(4)	26.1(14)
C5	6009(5)	5663(3)	4396(4)	20.5(12)
C6	5276(5)	5998(3)	3961(4)	19.1(12)
C7	4658(5)	6916(3)	3660(4)	23.5(14)
C8	3877(6)	6682(3)	3167(5)	29.0(15)
C9	3801(5)	6096(3)	3077(4)	26.9(14)
C10	4511(5)	5734(3)	3469(4)	23.4(13)
C11	4526(6)	5115(3)	3408(5)	31.3(15)
C12	5231(6)	4798(3)	3818(5)	30.5(15)
C13	5659(7)	8056(3)	5118(5)	34.5(18)
C14	5646(9)	8646(4)	4971(6)	50(2)
C15	6248(9)	8880(3)	4363(6)	49(2)
C16	6892(7)	8523(3)	3889(5)	33.7(16)
C17	6874(6)	7930(3)	4087(4)	24.8(13)
C18	7504(5)	7544(3)	3642(4)	20.3(12)
C19	8039(5)	6594(3)	3473(4)	21.8(13)
C20	8645(5)	6752(3)	2799(5)	24.8(14)
C21	8676(5)	7322(3)	2553(5)	24.7(13)
C22	8111(5)	7735(3)	2984(4)	23.2(13)
C23	8109(6)	8343(3)	2806(5)	31.3(15)
C24	7534(7)	8713(3)	3239(5)	36.8(17)

N5	5000	8062(6)	2500	84(2)
C25	5000	8559(7)	2500	84(2)
C26	5000	9174(7)	2500	84(2)

Table 9.79 – Anisotropic Displacement Parameters ($Å^2×10^3$) for IAJ696v. The Anisotropic displacement factor exponent takes the form: $-2\pi^2[h^2a^{*2}U_{11}+2hka^*b^*U_{12}+\ldots]$.

Atom	**U_{11}**	**U_{22}**	**U_{33}**	**U_{23}**	**U_{13}**	**U_{12}**
Ir1	20.63(19)	7.19(18)	25.5(2)	0.49(10)	-2.09(10)	-3.06(9)
Cl1	34.9(9)	15.1(7)	29.9(8)	-1.4(6)	5.8(7)	-4.5(6)
Cl2	36.0(9)	28.3(9)	35.1(9)	0.8(7)	-11.5(7)	-11.8(7)
Cl3	35.6(12)	14.4(9)	200(4)	18.8(14)	6.6(17)	5.0(8)
O1	167(11)	101(7)	69(6)	-51(5)	-51(7)	29(7)
N1	22(3)	17(3)	28(3)	4(2)	1(2)	-1(2)
N2	19(2)	10(2)	23(3)	-2(2)	2(2)	-1.8(19)
N3	35(3)	15(3)	28(3)	-2(2)	-1(2)	-5(2)
N4	18(2)	11(2)	27(3)	3(2)	-5(2)	-3.0(19)
C1	31(4)	21(3)	33(4)	8(3)	-4(3)	2(3)
C2	44(4)	23(3)	43(4)	13(3)	0(3)	8(3)
C3	51(4)	10(3)	52(5)	7(3)	3(3)	3(3)
C4	40(4)	8(3)	30(3)	4(2)	8(3)	-3(2)
C5	22(3)	13(3)	26(3)	1(2)	7(2)	-1(2)
C6	22(3)	9(2)	26(3)	-1(2)	4(2)	-3(2)
C7	19(3)	18(3)	33(4)	0(3)	0(3)	6(2)
C8	22(3)	29(3)	36(4)	1(3)	-4(3)	2(3)
C9	21(3)	36(3)	24(3)	-3(3)	-2(3)	-4(3)
C10	26(3)	16(3)	28(3)	-3(2)	3(3)	-7(2)
C11	36(4)	18(3)	40(4)	-7(3)	7(3)	-12(3)
C12	46(4)	12(3)	34(4)	-2(3)	9(3)	-9(3)
C13	56(5)	16(3)	32(4)	-6(3)	9(3)	-3(3)
C14	86(7)	15(3)	50(5)	-9(3)	19(5)	4(4)
C15	91(7)	7(3)	47(5)	0(3)	13(4)	3(4)
C16	56(5)	9(3)	37(4)	2(3)	0(3)	-3(3)
C17	35(4)	11(3)	28(3)	1(2)	-3(3)	-4(2)
C18	22(3)	10(2)	29(3)	1(2)	-8(2)	-5(2)
C19	17(3)	10(3)	39(4)	4(2)	-3(3)	-1(2)

C20	16(3)	19(3)	40(4)	3(3)	0(3)	0(2)
C21	20(3)	21(3)	33(4)	6(3)	-3(3)	-4(2)
C22	20(3)	15(3)	35(3)	3(2)	-8(2)	-7(2)
C23	45(4)	17(3)	32(4)	5(3)	-4(3)	-6(3)
C24	63(5)	12(3)	36(4)	3(3)	-1(3)	-6(3)
N5	101(5)	40(3)	110(5)	0	-56(5)	0
C25	101(5)	40(3)	110(5)	0	-56(5)	0
C26	101(5)	40(3)	110(5)	0	-56(5)	0

Table 9.80 – Bond Lengths for IAJ696v.

Atom	Atom	Length/Å		Atom	Atom	Length/Å
Ir1	Cl1	2.3546(17)		C6	C10	1.414(9)
Ir1	Cl2	2.3476(17)		C7	C8	1.400(10)
Ir1	N1	2.047(6)		C8	C9	1.368(11)
Ir1	N2	2.032(5)		C9	C10	1.397(10)
Ir1	N3	2.043(6)		C10	C11	1.437(9)
Ir1	N4	2.036(6)		C11	C12	1.347(11)
N1	C1	1.330(9)		C13	C14	1.387(11)
N1	C5	1.366(9)		C14	C15	1.377(13)
N2	C6	1.372(8)		C15	C16	1.406(12)
N2	C7	1.323(9)		C16	C17	1.411(9)
N3	C13	1.337(10)		C16	C24	1.421(12)
N3	C17	1.358(10)		C17	C18	1.411(10)
N4	C18	1.371(8)		C18	C22	1.406(10)
N4	C19	1.325(9)		C19	C20	1.405(10)
C1	C2	1.397(10)		C20	C21	1.380(10)
C2	C3	1.368(12)		C21	C22	1.394(10)
C3	C4	1.404(11)		C22	C23	1.437(9)
C4	C5	1.394(9)		C23	C24	1.337(12)
C4	C12	1.443(11)		N5	C25	1.15(2)
C5	C6	1.415(9)		C25	C26	1.42(2)

Table 9.81 – Bond Angles for IAJ696v.

Atom	Atom	Atom	Angle/°		Atom	Atom	Atom	Angle/°
Cl2	Ir1	Cl1	92.54(7)		N1	C5	C6	116.6(6)
N1	Ir1	Cl1	88.76(16)		C4	C5	C6	120.4(6)
N1	Ir1	Cl2	95.70(17)		N2	C6	C5	117.0(6)
N2	Ir1	Cl1	87.64(15)		N2	C6	C10	122.0(6)
N2	Ir1	Cl2	176.66(15)		C10	C6	C5	121.1(6)
N2	Ir1	N1	81.0(2)		N2	C7	C8	122.0(6)
N2	Ir1	N3	96.3(2)		C9	C8	C7	119.9(7)
N2	Ir1	N4	90.9(2)		C8	C9	C10	119.9(7)
N3	Ir1	Cl1	94.74(18)		C6	C10	C11	117.5(7)
N3	Ir1	Cl2	87.01(18)		C9	C10	C6	117.4(6)
N3	Ir1	N1	175.5(2)		C9	C10	C11	125.1(7)
N4	Ir1	Cl1	175.17(15)		C12	C11	C10	121.1(7)
N4	Ir1	Cl2	89.18(16)		C11	C12	C4	121.8(6)
N4	Ir1	N1	95.6(2)		N3	C13	C14	121.0(8)
N4	Ir1	N3	80.8(2)		C15	C14	C13	120.5(8)
C1	N1	Ir1	128.6(5)		C14	C15	C16	120.2(7)
C1	N1	C5	118.7(6)		C15	C16	C17	115.7(7)
C5	N1	Ir1	112.7(4)		C15	C16	C24	125.3(7)
C6	N2	Ir1	112.8(4)		C17	C16	C24	119.0(7)
C7	N2	Ir1	128.2(4)		N3	C17	C16	123.5(7)
C7	N2	C6	118.9(6)		N3	C17	C18	117.4(6)
C13	N3	Ir1	128.3(5)		C16	C17	C18	119.1(7)
C13	N3	C17	119.1(6)		N4	C18	C17	116.3(6)
C17	N3	Ir1	112.5(5)		N4	C18	C22	122.4(6)
C18	N4	Ir1	112.9(4)		C22	C18	C17	121.3(6)
C19	N4	Ir1	128.4(4)		N4	C19	C20	121.9(6)
C19	N4	C18	118.7(6)		C21	C20	C19	119.8(7)
N1	C1	C2	121.4(7)		C20	C21	C22	119.4(7)
C3	C2	C1	120.1(7)		C18	C22	C23	117.6(7)
C2	C3	C4	119.7(7)		C21	C22	C18	117.7(6)
C3	C4	C12	124.9(6)		C21	C22	C23	124.6(7)
C5	C4	C3	117.0(7)		C24	C23	C22	121.4(7)
C5	C4	C12	118.0(7)		C23	C24	C16	121.6(7)
N1	C5	C4	123.0(6)		N5	C25	C26	180.0

Table 9.82 – Hydrogen Bonds for IAJ696v.

D	H	A	d(D-H)/Å	d(H-A)/Å	d(D-A)/Å	D-H-A/°
O1	H1A	Cl3	0.98	2.40	3.142(11)	132.1
C14	H14	O1[1]	0.95	2.39	3.176(11)	139.9

[1]-1/2+X,3/2-Y,1-Z

Table 9.83 – Torsion Angles for IAJ696v.

A	B	C	D	Angle/°		A	B	C	D	Angle/°
Ir1	N1	C1	C2	178.4(6)		C5	C6	C10	C11	-1.9(10)
Ir1	N1	C5	C4	-179.5(5)		C6	N2	C7	C8	-0.2(10)
Ir1	N1	C5	C6	0.9(7)		C6	C10	C11	C12	1.3(10)
Ir1	N2	C6	C5	-1.5(7)		C7	N2	C6	C5	-178.8(6)
Ir1	N2	C6	C10	177.8(5)		C7	N2	C6	C10	0.6(9)
Ir1	N2	C7	C8	-177.0(5)		C7	C8	C9	C10	-0.7(11)
Ir1	N3	C13	C14	176.4(7)		C8	C9	C10	C6	1.1(10)
Ir1	N3	C17	C16	-178.1(6)		C8	C9	C10	C11	-178.6(7)
Ir1	N3	C17	C18	2.6(8)		C9	C10	C11	C12	-179.0(7)
Ir1	N4	C18	C17	0.7(7)		C10	C11	C12	C4	-0.2(11)
Ir1	N4	C18	C22	-178.0(5)		C12	C4	C5	N1	-179.8(6)
Ir1	N4	C19	C20	176.2(5)		C12	C4	C5	C6	-0.3(10)
N1	C1	C2	C3	0.5(12)		C13	N3	C17	C16	-0.5(11)
N1	C5	C6	N2	0.4(9)		C13	N3	C17	C18	-179.8(7)
N1	C5	C6	C10	-179.0(6)		C13	C14	C15	C16	-0.8(17)
N2	C6	C10	C9	-1.0(10)		C14	C15	C16	C17	-0.4(14)
N2	C6	C10	C11	178.7(6)		C14	C15	C16	C24	179.1(10)
N2	C7	C8	C9	0.3(11)		C15	C16	C17	N3	1.1(12)
N3	C13	C14	C15	1.5(16)		C15	C16	C17	C18	-179.6(8)
N3	C17	C18	N4	-2.3(9)		C15	C16	C24	C23	-178.6(9)
N3	C17	C18	C22	176.4(6)		C16	C17	C18	N4	178.4(6)
N4	C18	C22	C21	1.5(10)		C16	C17	C18	C22	-2.9(10)
N4	C18	C22	C23	-178.3(6)		C17	N3	C13	C14	-0.8(13)
N4	C19	C20	C21	1.4(10)		C17	C16	C24	C23	0.9(13)
C1	N1	C5	C4	-1.1(10)		C17	C18	C22	C21	-177.1(6)
C1	N1	C5	C6	179.3(6)		C17	C18	C22	C23	3.1(10)
C1	C2	C3	C4	-0.6(13)		C18	N4	C19	C20	-1.9(9)

C2	C3	C4	C5	-0.2(12)		C18	C22	C23	C24	-1.3(11)
C2	C3	C4	C12	-179.2(7)		C19	N4	C18	C17	179.1(6)
C3	C4	C5	N1	1.0(10)		C19	N4	C18	C22	0.5(9)
C3	C4	C5	C6	-179.4(7)		C19	C20	C21	C22	0.7(10)
C3	C4	C12	C11	178.7(8)		C20	C21	C22	C18	-2.0(10)
C4	C5	C6	N2	-179.2(6)		C20	C21	C22	C23	177.7(7)
C4	C5	C6	C10	1.4(10)		C21	C22	C23	C24	178.9(7)
C5	N1	C1	C2	0.3(11)		C22	C23	C24	C16	-0.7(13)
C5	C4	C12	C11	-0.3(11)		C24	C16	C17	N3	-178.4(7)
C5	C6	C10	C9	178.3(6)		C24	C16	C17	C18	0.8(11)

Table 9.84 – Hydrogen Atom Coordinates ($Å \times 10^4$) and Isotropic Displacement Parameters ($Å^2 \times 10^3$) for IAJ696v.

Atom	***x***	***y***	***z***	**U(eq)**
H1A	9621(13)	5404(4)	3694(6)	168
H1B	10204(9)	5450(4)	3042(9)	168
H1	7887.98	5864.15	5621.18	34
H2	7936.14	4855.86	5580.76	44
H3	6774.27	4350.68	4770.04	45
H7	4699.22	7323.39	3719.66	28
H8	3400.29	6929.36	2896.12	35
H9	3266.81	5935.54	2747.66	32
H11	4030.29	4925.19	3072.42	38
H12	5218.89	4389.59	3766.8	37
H13	5226.98	7899.6	5531.47	41
H14	5219.58	8890.1	5293.92	60
H15	6227.74	9284.06	4262.61	58
H19	8035.94	6202.21	3644.42	26
H20	9032.87	6468.12	2513.02	30
H21	9077.68	7431.94	2093.34	30
H23	8523.74	8484.16	2371.96	38
H24	7556.19	9112.46	3108.9	44
H26A	5700.6	9315.22	2624.7	125
H26B	4511.54	9315.22	2911.88	125
H26C	4787.87	9315.22	1963.42	125

Table 9.85 – Atomic Occupancy for IAJ696v.

Atom	Occupancy		Atom	Occupancy		Atom	Occupancy
H26A	0.5		H26B	0.5		H26C	0.5

Crystal Structure Determination of IAJ696v

Crystal Data for $C_{25}H_{19.5}Cl_3IrN_{4.5}O$ (M = 697.50 g/mol): orthorhombic, space group Pbcn (no. 60), a = 12.8589(9) Å, b = 23.1485(16) Å, c = 16.4518(12) Å, V = 4897.1(6) Å^3, Z = 8, T = 100.01 K, μ(CuKα) = 13.798 mm^{-1}, *Dcalc* = 1.892 g/cm^3, 73957 reflections measured (7.638° ≤ 2Θ ≤ 133.642°), 4344 unique (R_{int} = 0.0603, R_{sigma} = 0.0230) which were used in all calculations. The final R_1 was 0.0470 (I > 2σ(I)) and wR_2 was 0.1227 (all data).

9.3.11 IAJ694v_0m $[Ir(bpy)_2Cl_2]Cl$, crystallised as $[Ir(bpy)_2Cl_2]Cl\ 2H_2O$

Table 9.86 – Crystal data and structure refinement for IAJ694v_0m.

Identification code	IAJ694v_0m
Empirical formula	$C_{20}H_{20}Cl_3IrN_4O_2$
Formula weight	646.95
Temperature/K	100.03
Crystal system	triclinic
Space group	P-1
a/Å	6.9350(5)
b/Å	12.3511(8)
c/Å	12.8977(9)
α/°	90.264(4)
β/°	94.047(4)
γ/°	100.007(4)
Volume/Å^3	1085.07(13)
Z	2
ρ_{calc}g/cm^3	1.980
μ/mm^{-1}	15.525
F(000)	624.0
Crystal size/mm^3	0.197 × 0.13 × 0.025
Radiation	CuKα (λ = 1.54178)
2Θ range for data collection/°	6.872 to 133.592

Index ranges	$-8 \leq h \leq 8, -14 \leq k \leq 14, -15 \leq l \leq 15$
Reflections collected	27062
Independent reflections	3787 [R_{int} = 0.0923, R_{sigma} = 0.0468]
Data/restraints/parameters	3787/239/277
Goodness-of-fit on F^2	1.261
Final R indexes [I>=2σ (I)]	R_1 = 0.0889, wR_2 = 0.2079
Final R indexes [all data]	R_1 = 0.0940, wR_2 = 0.2105
Largest diff. peak/hole / e $Å^{-3}$	5.28/-4.21

Table 9.87 – Fractional Atomic Coordinates ($\times 10^4$) and Equivalent Isotropic Displacement Parameters ($Å^2 \times 10^3$) for IAJ694v_0m. U_{eq} is defined as 1/3 of the trace of the orthogonalised U_{IJ} tensor.

Atom	***x***	***y***	***z***	**U(eq)**
Ir1	4010.0(11)	7852.2(6)	6294.4(6)	22.1(3)
Cl1	1471(6)	6487(3)	5601(4)	28.4(9)
N1	5420(20)	7508(12)	5038(12)	24(3)
C1	5420(20)	8027(15)	4121(14)	25(3)
Cl2	2441(6)	9217(4)	5516(4)	27.9(9)
N2	5330(20)	6636(13)	6861(12)	27(3)
C2	6250(30)	7662(16)	3268(16)	34(4)
N3	2660(20)	8174(12)	7583(12)	25(3)
C3	7170(30)	6743(15)	3362(15)	28(3)
N4	6060(20)	9075(12)	6971(12)	24(3)
C4	7240(30)	6241(16)	4306(15)	29(4)
C5	6350(30)	6619(15)	5131(15)	27(3)
C6	6360(20)	6128(15)	6178(15)	26(3)
C7	7250(20)	5247(15)	6476(15)	27(3)
C8	7230(30)	4908(16)	7496(16)	31(4)
C9	6200(30)	5417(17)	8187(16)	35(4)
C10	5290(30)	6271(17)	7860(15)	32(4)
C11	950(30)	7607(15)	7886(14)	27(3)
C12	0(30)	7928(18)	8695(15)	35(4)
C13	910(30)	8871(18)	9266(15)	36(4)
C14	2670(30)	9473(18)	8968(16)	35(4)
C15	3490(30)	9080(15)	8153(15)	27(3)
C16	5430(30)	9593(15)	7770(14)	26(3)

C17	6620(30)	10527(16)	8227(15)	30(4)
C18	8440(30)	10908(16)	7879(15)	31(4)
C19	9060(30)	10340(16)	7087(15)	31(4)
C20	7850(30)	9417(15)	6633(15)	28(3)
O1	980(20)	3879(13)	8997(12)	44(4)
O2	2290(20)	6032(13)	9831(13)	45(4)
Cl3	3883(7)	2283(4)	9649(4)	39.1(11)

Table 9.88 – Anisotropic Displacement Parameters ($Å^2×10^3$) for IAJ694v_0m. The Anisotropic displacement factor exponent takes the form: $-2\pi^2[h^2a^{*2}U_{11}+2hka^*b^*U_{12}+\ldots]$.

Atom	**U_{11}**	**U_{22}**	**U_{33}**	**U_{23}**	**U_{13}**	**U_{12}**
Ir1	14.4(4)	19.0(4)	31.9(4)	0.8(3)	-2.3(3)	2.1(3)
Cl1	15.7(19)	25(2)	42(3)	-4.7(18)	-4.6(17)	-0.2(16)
N1	10(6)	25(7)	36(6)	0(5)	-4(5)	-1(5)
C1	17(8)	22(8)	35(7)	-1(5)	-2(6)	3(6)
Cl2	23(2)	25(2)	38(2)	7.0(18)	-0.3(17)	10.3(17)
N2	9(6)	35(7)	37(6)	0(5)	-12(5)	7(5)
C2	35(10)	31(9)	37(8)	1(7)	5(8)	9(7)
N3	21(6)	25(7)	29(7)	5(5)	-4(5)	2(4)
C3	20(8)	24(8)	36(7)	-8(6)	-5(6)	-2(6)
N4	19(5)	21(6)	30(7)	7(5)	-8(5)	6(5)
C4	20(9)	31(9)	38(7)	-5(6)	-5(6)	9(7)
C5	23(8)	24(8)	32(6)	-7(5)	-10(6)	1(6)
C6	13(7)	25(8)	36(7)	-3(5)	-9(6)	1(6)
C7	15(8)	28(8)	37(7)	0(6)	-2(6)	4(6)
C8	20(9)	31(10)	41(8)	5(6)	-1(7)	2(7)
C9	37(10)	36(10)	31(8)	3(7)	-4(7)	11(8)
C10	20(9)	40(10)	33(7)	-1(7)	-10(6)	5(7)
C11	26(7)	23(8)	31(8)	5(6)	-3(6)	1(5)
C12	25(8)	52(10)	30(9)	3(7)	-3(6)	10(7)
C13	35(8)	52(10)	26(9)	3(7)	4(7)	18(7)
C14	32(8)	43(10)	32(9)	-2(7)	-4(6)	10(7)
C15	24(7)	21(7)	35(8)	4(6)	-1(6)	1(5)
C16	27(7)	23(7)	27(8)	7(5)	-4(5)	2(5)
C17	25(7)	28(8)	36(9)	1(6)	-8(6)	4(6)

C18	27(7)	32(9)	31(8)	-3(6)	-8(6)	-1(6)
C19	25(8)	30(8)	37(9)	-4(7)	-9(7)	5(6)
C20	20(6)	30(8)	30(9)	-1(6)	-5(6)	0(6)
O1	45(9)	43(9)	46(9)	0(7)	17(7)	9(7)
O2	40(9)	51(10)	45(9)	8(7)	-2(7)	12(7)
Cl3	34(3)	42(3)	43(3)	-2(2)	4(2)	9(2)

Table 9.89 – Bond Lengths for IAJ694v_0m.

Atom	Atom	Length/Å		Atom	Atom	Length/Å
Ir1	Cl1	2.340(4)		N4	C20	1.34(2)
Ir1	N1	2.031(15)		C4	C5	1.39(3)
Ir1	Cl2	2.352(4)		C5	C6	1.48(3)
Ir1	N2	2.007(15)		C6	C7	1.38(2)
Ir1	N3	2.036(16)		C7	C8	1.38(3)
Ir1	N4	2.031(15)		C8	C9	1.39(3)
N1	C1	1.35(2)		C9	C10	1.37(3)
N1	C5	1.37(2)		C11	C12	1.37(3)
C1	C2	1.39(3)		C12	C13	1.40(3)
N2	C6	1.38(2)		C13	C14	1.40(3)
N2	C10	1.37(2)		C14	C15	1.35(3)
C2	C3	1.40(3)		C15	C16	1.50(3)
N3	C11	1.35(2)		C16	C17	1.40(3)
N3	C15	1.35(2)		C17	C18	1.38(3)
C3	C4	1.37(3)		C18	C19	1.37(3)
N4	C16	1.35(2)		C19	C20	1.39(3)

Table 9.90 – Bond Angles for IAJ694v_0m.

Atom	Atom	Atom	Angle/°		Atom	Atom	Atom	Angle/°
Cl1	Ir1	Cl2	90.29(15)		C20	N4	Ir1	124.8(13)
N1	Ir1	Cl1	84.6(4)		C20	N4	C16	120.9(16)
N1	Ir1	Cl2	96.8(4)		C3	C4	C5	120.1(18)
N1	Ir1	N3	178.2(6)		N1	C5	C4	121.5(18)
N2	Ir1	Cl1	87.3(4)		N1	C5	C6	114.7(16)
N2	Ir1	N1	79.8(6)		C4	C5	C6	123.7(17)
N2	Ir1	Cl2	176.0(5)		N2	C6	C5	112.8(15)

N2	Ir1	N3	98.4(6)		N2	C6	C7	121.4(17)
N2	Ir1	N4	94.6(6)		C7	C6	C5	125.7(17)
N3	Ir1	Cl1	96.0(4)		C8	C7	C6	119.7(18)
N3	Ir1	Cl2	84.9(4)		C7	C8	C9	118.9(18)
N4	Ir1	Cl1	175.4(4)		C10	C9	C8	119.8(19)
N4	Ir1	N1	99.8(6)		N2	C10	C9	122.1(19)
N4	Ir1	Cl2	88.0(4)		N3	C11	C12	123.6(18)
N4	Ir1	N3	79.6(6)		C11	C12	C13	117.5(19)
C1	N1	Ir1	126.2(12)		C14	C13	C12	119.9(19)
C1	N1	C5	118.3(16)		C15	C14	C13	117.5(19)
C5	N1	Ir1	115.4(12)		N3	C15	C14	124.3(18)
N1	C1	C2	122.2(17)		N3	C15	C16	111.5(16)
C6	N2	Ir1	116.8(12)		C14	C15	C16	124.3(18)
C10	N2	Ir1	125.3(13)		N4	C16	C15	116.6(16)
C10	N2	C6	117.9(16)		N4	C16	C17	119.8(17)
C1	C2	C3	119.3(19)		C17	C16	C15	123.5(17)
C11	N3	Ir1	126.0(13)		C18	C17	C16	120.3(19)
C11	N3	C15	117.1(16)		C19	C18	C17	118.3(18)
C15	N3	Ir1	116.8(12)		C18	C19	C20	120.6(19)
C4	C3	C2	118.5(18)		N4	C20	C19	120.0(18)
C16	N4	Ir1	114.2(12)					

Table 9.91 – Hydrogen Bonds for IAJ694v_0m.

D	H	A	d(D-H)/Å	d(H-A)/Å	d(D-A)/Å	D-H-A/°
O1	H1A	Cl3	0.87	2.56	3.132(17)	124.3
O2	H2A	O1[1]	0.87	1.97	2.83(2)	166.5
O2	H2B	O1	0.87	1.99	2.84(2)	163.1

[1]-X,1-Y,2-Z

Table 9.92 – Torsion Angles for IAJ694v_0m.

A	B	C	D	Angle/°		A	B	C	D	Angle/°
Ir1	N1	C1	C2	-173.0(14)		C4	C5	C6	N2	-178.9(16)
Ir1	N1	C5	C4	175.1(13)		C4	C5	C6	C7	0(3)
Ir1	N1	C5	C6	-6.6(19)		C5	N1	C1	C2	3(3)
Ir1	N2	C6	C5	2.3(18)		C5	C6	C7	C8	176.6(16)
Ir1	N2	C6	C7	-177.0(13)		C6	N2	C10	C9	-1(3)

Ir1	N2	C10	C9	178.4(15)		C6	C7	C8	C9	4(3)
Ir1	N3	C11	C12	-172.6(14)		C7	C8	C9	C10	-3(3)
Ir1	N3	C15	C14	173.0(15)		C8	C9	C10	N2	1(3)
Ir1	N3	C15	C16	-7.2(19)		C10	N2	C6	C5	-178.2(15)
Ir1	N4	C16	C15	10.1(19)		C10	N2	C6	C7	3(2)
Ir1	N4	C16	C17	-172.9(13)		C11	N3	C15	C14	-3(3)
Ir1	N4	C20	C19	173.0(13)		C11	N3	C15	C16	176.7(15)
N1	C1	C2	C3	-1(3)		C11	C12	C13	C14	3(3)
N1	C5	C6	N2	3(2)		C12	C13	C14	C15	-3(3)
N1	C5	C6	C7	-177.9(16)		C13	C14	C15	N3	3(3)
C1	N1	C5	C4	-1(2)		C13	C14	C15	C16	-176.6(17)
C1	N1	C5	C6	177.4(14)		C14	C15	C16	N4	177.9(17)
C1	C2	C3	C4	-1(3)		C14	C15	C16	C17	1(3)
N2	C6	C7	C8	-4(3)		C15	N3	C11	C12	3(3)
C2	C3	C4	C5	3(3)		C15	C16	C17	C18	175.5(17)
N3	C11	C12	C13	-3(3)		C16	N4	C20	C19	-2(3)
N3	C15	C16	N4	-2(2)		C16	C17	C18	C19	-1(3)
N3	C15	C16	C17	-178.9(16)		C17	C18	C19	C20	1(3)
C3	C4	C5	N1	-2(3)		C18	C19	C20	N4	0(3)
C3	C4	C5	C6	-179.9(16)		C20	N4	C16	C15	-174.3(15)
N4	C16	C17	C18	-1(3)		C20	N4	C16	C17	3(3)

Table 9.93 – Hydrogen Atom Coordinates (Å×10^4) and Isotropic Displacement Parameters (Å^2×10^3) for IAJ694v_0m.

Atom	***x***	***y***	***z***	**U(eq)**
H1	4825.29	8663.95	4056.36	30
H2	6199.54	8034.71	2626.56	40
H3	7723.96	6470.59	2783.89	33
H4	7903.79	5633.8	4395.98	35
H7	7864.47	4877.25	5982.51	32
H8	7910.33	4337.99	7721.93	37
H9	6119.38	5171.88	8882.41	41
H10	4615.85	6619.45	8343.21	38
H11	385.58	6948.1	7516.56	33
H12	-1231.37	7526.6	8864.72	43
H13	320.54	9100.23	9854.4	43

H14	3276.29	10134.05	9323.48	43
H17	6163.85	10901.81	8781.35	36
H18	9250.63	11547.58	8180.27	37
H19	10319.77	10578.86	6844.62	37
H20	8285.52	9028.48	6083.9	33
H1A	969.68	3174.34	8996.04	66
H1B	1613.69	4172.19	8480.67	66
H2A	1309.91	6172.52	10166.5	67
H2B	1998.79	5329.73	9692.68	67

Crystal Structure Determination of IAJ694v_0m

Crystal Data for $C_{20}H_{20}Cl_3IrN_4O_2$ (M =646.95 g/mol): triclinic, space group P-1 (no. 2), a = 6.9350(5) Å, b = 12.3511(8) Å, c = 12.8977(9) Å, α = 90.264(4)°, β = 94.047(4)°, γ = 100.007(4)°, V = 1085.07(13) Å^3, Z = 2, T = 100.03 K, μ(CuKα) = 15.525 mm^{-1}, $Dcalc$ = 1.980 g/cm^3, 27062 reflections measured (6.872° ≤ 2Θ ≤ 133.592°), 3787 unique (R_{int} = 0.0923, R_{sigma} = 0.0468) which were used in all calculations. The final R_1 was 0.0889 (I > 2σ(I)) and wR_2 was 0.2105 (all data).

9.3.12 IAJ698v_4 $[Ir(bpy)_2Cl_2]CF_3SO_3$

Table 9.94 – Crystal data and structure refinement for iaj698v_4.

Identification code	iaj698v_4
Empirical formula	$C_{21}H_{16}Cl_2F_3IrN_4O_3S$
Formula weight	724.54
Temperature/K	100.03
Crystal system	monoclinic
Space group	$P2_1/c$
a/Å	13.9986(6)
b/Å	11.9949(5)
c/Å	28.4445(15)
α/°	90
β/°	103.191(2)
γ/°	90
Volume/Å^3	4650.1(4)
Z	8
ρ_{calc}g/cm^3	2.070

μ/mm^{-1}	14.597
F(000)	2784.0
Crystal size/mm^3	? × ? × ?
Radiation	CuKα (λ = 1.54178)
2Θ range for data collection/°	6.382 to 138.696
Index ranges	? ≤ h ≤ ?, ? ≤ k ≤ ?, ? ≤ l ≤ ?
Reflections collected	8236
Independent reflections	8236 [R_{int} = ?, R_{sigma} = 0.0465]
Data/restraints/parameters	8236/584/595
Goodness-of-fit on F^2	1.091
Final R indexes [I>=2σ (I)]	R_1 = 0.0821, wR_2 = 0.2646
Final R indexes [all data]	R_1 = 0.0934, wR_2 = 0.2774
Largest diff. peak/hole / e $Å^{-3}$	3.56/-4.47

Table 9.95 – Fractional Atomic Coordinates ($\times 10^4$) and Equivalent Isotropic Displacement Parameters ($Å^2 \times 10^3$) for iaj698v_4. U_{eq} is defined as 1/3 of the trace of the orthogonalised U_{IJ} tensor.

Atom	***x***	***y***	***z***	**U(eq)**
Ir1	6239.5(4)	-2751.1(5)	5574.9(2)	10.4(2)
Cl1	5526(2)	-4414(3)	5755.2(12)	16.5(7)
Cl2	5408(3)	-1709(3)	6044.0(13)	18.0(7)
N1	5117(9)	-2436(11)	4979(4)	11(2)
N2	6770(8)	-1351(10)	5346(4)	10.4(2)
N3	7030(8)	-3780(10)	5246(4)	12(2)
N4	7440(8)	-3047(10)	6137(4)	11(2)
C1	4274(11)	-3026(14)	4816(5)	17(3)
C2	3553(12)	-2742(13)	4406(6)	19(3)
C3	3672(11)	-1804(14)	4152(5)	17(3)
C4	4526(11)	-1140(14)	4324(5)	18(3)
C5	5237(10)	-1474(13)	4741(5)	14(2)
C6	6172(10)	-901(12)	4933(5)	10.4(2)
C7	6457(10)	48(12)	4709(5)	10.4(2)
C8	7375(10)	536(12)	4903(5)	10.4(2)
C9	7974(10)	73(12)	5323(5)	10.4(2)
C10	7661(10)	-881(12)	5537(5)	10.4(2)
C11	6752(11)	-4062(13)	4777(5)	16(3)

C12	7241(11)	-4892(13)	4614(5)	17(3)
C13	8015(12)	-5476(14)	4925(6)	24(3)
C14	8308(11)	-5143(14)	5406(6)	21(3)
C15	7805(11)	-4274(13)	5561(5)	18(3)
C16	8073(10)	-3813(13)	6044(5)	16(3)
C17	8949(10)	-4073(14)	6396(5)	17(3)
C18	9184(11)	-3475(15)	6824(6)	22(3)
C19	8526(15)	-2695(14)	6919(7)	26(3)
C20	7687(12)	-2504(13)	6566(5)	16(3)
Ir2	6242.3(4)	-2235.5(5)	3113.1(2)	9.6(2)
Cl4	5728(2)	-597(3)	3429.0(12)	15.9(7)
Cl3	5499(2)	-3372(3)	3589.2(12)	16.7(7)
S1	10733(3)	-2758(3)	3171.1(15)	19.4(8)
S2	9463(3)	2500(3)	4282.8(15)	18.2(8)
F1	10080(8)	-725(10)	2994(4)	43(3)
F6	8109(9)	1133(10)	3806(5)	50(3)
F4	9392(13)	1222(13)	3539(5)	72(4)
F2	11488(8)	-824(9)	3516(4)	34(2)
F3	10166(10)	-1288(12)	3716(4)	54(3)
F5	9433(9)	337(9)	4200(5)	43(3)
O1	9732(9)	-3157(14)	3045(5)	42(3)
O6	9013(10)	3370(11)	3960(5)	37(3)
O4	9062(9)	2342(10)	4679(5)	30(3)
O2	11375(10)	-3241(11)	3605(5)	35(3)
O3	11173(9)	-2618(9)	2783(5)	25(3)
O5	10525(9)	2450(11)	4397(5)	30(3)
N5	5034(9)	-2100(10)	2545(4)	10(2)
N7	6780(9)	-3595(11)	2866(4)	16(2)
N6	6791(9)	-1202(10)	2682(4)	12(2)
N8	7504(9)	-2475(11)	3646(4)	11(2)
C21	4151(11)	-2628(14)	2497(5)	17(3)
C37	8827(10)	-3744(13)	3976(5)	16(3)
C33	7709(11)	-5423(14)	2556(6)	21(3)
C22	3383(12)	-2568(15)	2086(6)	21(3)
C42	9097(14)	1237(16)	3934(7)	34(3)
C23	3516(11)	-1947(15)	1687(6)	23(3)

C35	7634(10)	-4036(12)	3156(5)	11(2)
C24	4410(11)	-1398(14)	1735(6)	20(3)
C40	7815(10)	-1838(13)	4048(5)	13(3)
C25	5160(10)	-1470(12)	2177(5)	11(2)
C32	6831(12)	-5021(14)	2273(6)	21(3)
C26	6137(10)	-956(11)	2264(5)	9(2)
C34	8097(11)	-4969(13)	3008(6)	21(3)
C27	6378(10)	-197(12)	1940(5)	13(3)
C36	8018(10)	-3410(12)	3609(5)	13(2)
C28	7311(10)	323(13)	2068(6)	16(3)
C39	8610(13)	-2128(14)	4419(6)	23(3)
C29	7958(11)	46(14)	2515(6)	20(3)
C41	10598(12)	-1322(16)	3356(6)	26(3)
C30	7690(10)	-725(13)	2799(5)	14(3)
C31	6395(10)	-4100(13)	2439(5)	16(3)
C38	9127(10)	-3100(14)	4375(5)	18(3)

Table 9.96 – Anisotropic Displacement Parameters ($Å^2×10^3$) for iaj698v_4. The Anisotropic displacement factor exponent takes the form: $-2\pi^2[h^2a^{*2}U_{11}+2hka^*b^*U_{12}+\ldots]$.

Atom	U_{11}	U_{22}	U_{33}	U_{23}	U_{13}	U_{12}
Ir1	11.4(4)	11.3(4)	7.2(4)	0.8(2)	-0.4(2)	1.5(2)
Cl1	17.9(16)	16.3(17)	14.9(17)	3.1(13)	2.9(13)	0.6(13)
Cl2	19.4(17)	18.9(18)	17.0(17)	-0.1(14)	6.9(13)	2.9(14)
N1	10(5)	13(5)	13(5)	-3(4)	5(4)	0(4)
N2	11.4(4)	11.3(4)	7.2(4)	0.8(2)	-0.4(2)	1.5(2)
N3	12(5)	9(5)	14(4)	-2(4)	3(4)	-5(4)
N4	10(5)	16(5)	6(4)	1(4)	3(4)	-2(4)
C1	19(6)	20(7)	10(6)	-1(5)	0(5)	-6(5)
C2	23(7)	23(7)	11(6)	-3(5)	4(5)	2(5)
C3	17(6)	28(7)	6(6)	2(5)	0(5)	3(5)
C4	18(6)	26(7)	10(6)	0(5)	3(4)	1(5)
C5	8(5)	17(6)	16(6)	-1(5)	2(4)	-2(4)
C6	11.4(4)	11.3(4)	7.2(4)	0.8(2)	-0.4(2)	1.5(2)
C7	11.4(4)	11.3(4)	7.2(4)	0.8(2)	-0.4(2)	1.5(2)
C8	11.4(4)	11.3(4)	7.2(4)	0.8(2)	-0.4(2)	1.5(2)
C9	11.4(4)	11.3(4)	7.2(4)	0.8(2)	-0.4(2)	1.5(2)

C10	11.4(4)	11.3(4)	7.2(4)	0.8(2)	-0.4(2)	1.5(2)
C11	19(7)	15(6)	13(5)	1(5)	0(5)	-1(5)
C12	17(6)	18(6)	14(6)	-7(5)	-1(5)	-7(5)
C13	24(7)	17(7)	31(7)	-3(5)	3(6)	3(6)
C14	15(7)	23(7)	23(6)	0(5)	3(5)	5(5)
C15	19(6)	20(6)	13(5)	-1(4)	3(4)	0(5)
C16	12(5)	22(7)	13(5)	2(5)	4(4)	3(5)
C17	9(6)	27(7)	15(6)	10(5)	0(4)	0(5)
C18	18(7)	33(8)	13(6)	9(5)	2(5)	-4(5)
C19	30(7)	24(8)	20(7)	1(6)	-3(5)	-4(6)
C20	29(7)	13(6)	6(5)	4(4)	4(5)	0(6)
Ir2	9.5(4)	11.9(4)	5.8(4)	0.0(2)	-1.4(2)	0.6(2)
Cl4	15.7(16)	16.3(17)	14.9(16)	0.1(13)	1.6(13)	3.1(13)
Cl3	13.5(16)	22.0(18)	13.5(16)	4.8(13)	1.0(12)	-1.7(13)
S1	19(2)	17(2)	22(2)	-2.8(14)	3.5(16)	-4.3(14)
S2	13.0(18)	17.2(17)	25(2)	-3.2(16)	6.6(15)	-0.5(14)
F1	44(6)	46(6)	32(5)	-3(5)	-5(4)	30(5)
F6	43(5)	39(7)	54(7)	-2(6)	-17(5)	-15(5)
F4	118(11)	63(9)	44(7)	-21(6)	38(8)	-13(9)
F2	35(5)	30(5)	28(5)	-12(4)	-10(4)	-9(4)
F3	66(8)	66(8)	41(6)	-12(6)	33(6)	16(7)
F5	48(6)	19(5)	62(7)	0(5)	15(5)	6(4)
O1	23(6)	63(9)	40(8)	-5(7)	5(5)	-19(6)
O6	33(7)	24(6)	52(8)	1(6)	3(6)	1(5)
O4	25(6)	24(6)	40(7)	-15(5)	6(5)	-14(5)
O2	42(7)	35(7)	22(6)	2(5)	-7(5)	4(6)
O3	27(6)	13(5)	38(6)	2(5)	15(5)	-5(5)
O5	19(6)	32(6)	42(8)	10(6)	11(5)	-1(5)
N5	13(5)	13(5)	5(5)	-4(4)	5(4)	-4(4)
N7	15(5)	19(5)	10(5)	5(4)	-6(4)	-2(4)
N6	12(4)	9(5)	12(5)	0(4)	-1(4)	2(4)
N8	15(5)	13(5)	6(5)	2(4)	6(4)	-3(4)
C21	15(6)	25(8)	11(6)	-4(5)	6(4)	-8(5)
C37	14(6)	19(7)	15(5)	7(5)	5(4)	2(5)
C33	14(6)	20(7)	31(7)	0(5)	11(5)	-3(5)
C22	21(7)	27(8)	15(6)	1(6)	2(5)	-7(6)

C42	37(6)	30(7)	33(7)	-8(5)	5(6)	2(6)
C23	15(6)	35(8)	12(7)	6(6)	-9(5)	-8(6)
C35	11(5)	14(6)	9(5)	9(4)	3(4)	1(5)
C24	16(6)	27(8)	16(6)	4(6)	0(5)	-1(5)
C40	16(6)	20(7)	6(5)	-6(4)	6(4)	-5(5)
C25	11(5)	10(6)	13(5)	-4(4)	4(4)	-2(4)
C32	26(6)	22(7)	16(6)	-1(5)	7(5)	3(6)
C26	10(5)	6(6)	11(5)	2(4)	0(4)	2(4)
C34	13(6)	18(6)	33(7)	-1(5)	8(5)	0(5)
C27	9(5)	16(6)	11(6)	6(5)	-1(4)	1(5)
C36	11(5)	16(5)	14(5)	3(4)	4(4)	-2(4)
C28	11(5)	20(7)	20(6)	4(5)	7(5)	-1(5)
C39	21(7)	23(7)	20(7)	-6(5)	-2(5)	-8(5)
C29	8(6)	22(7)	28(7)	8(6)	-2(5)	1(5)
C41	16(6)	37(7)	22(6)	-6(5)	-3(4)	9(5)
C30	10(5)	20(6)	11(6)	-2(5)	1(4)	4(5)
C31	11(6)	19(6)	15(6)	0(5)	-1(4)	-3(5)
C38	9(6)	30(7)	13(6)	5(5)	0(5)	0(5)

Table 9.97 – Bond Lengths for iaj698v_4.

Atom	Atom	Length/Å		Atom	Atom	Length/Å
Ir1	Cl1	2.340(4)		S1	O2	1.470(13)
Ir1	Cl2	2.326(3)		S1	O3	1.392(13)
Ir1	N1	2.066(13)		S1	C41	1.824(19)
Ir1	N2	2.004(12)		S2	O6	1.437(14)
Ir1	N3	2.023(12)		S2	O4	1.382(15)
Ir1	N4	2.069(12)		S2	O5	1.450(12)
N1	C1	1.36(2)		S2	C42	1.819(19)
N1	C5	1.37(2)		F1	C41	1.33(2)
N2	C6	1.387(18)		F6	C42	1.35(2)
N2	C10	1.363(18)		F4	C42	1.28(2)
N3	C11	1.344(19)		F2	C41	1.36(2)
N3	C15	1.37(2)		F3	C41	1.30(2)
N4	C16	1.343(19)		F5	C42	1.34(2)

N4	C20	1.358(19)		N5	C21	1.368(19)
C1	C2	1.40(2)		N5	C25	1.335(19)
C2	C3	1.37(2)		N7	C35	1.393(18)
C3	C4	1.43(2)		N7	C31	1.35(2)
C4	C5	1.42(2)		N6	C26	1.358(18)
C5	C6	1.469(19)		N6	C30	1.353(19)
C6	C7	1.41(2)		N8	C40	1.360(19)
C7	C8	1.405(19)		N8	C36	1.35(2)
C8	C9	1.408(19)		C21	C22	1.40(2)
C9	C10	1.41(2)		C37	C36	1.41(2)
C11	C12	1.35(2)		C37	C38	1.36(2)
C12	C13	1.42(2)		C33	C32	1.39(2)
C13	C14	1.39(2)		C33	C34	1.39(2)
C14	C15	1.38(2)		C22	C23	1.41(2)
C15	C16	1.45(2)		C23	C24	1.39(2)
C16	C17	1.43(2)		C35	C34	1.41(2)
C17	C18	1.39(2)		C35	C36	1.48(2)
C18	C19	1.38(3)		C24	C25	1.44(2)
C19	C20	1.38(2)		C40	C39	1.39(2)
Ir2	Cl4	2.342(3)		C25	C26	1.469(19)
Ir2	Cl3	2.328(3)		C32	C31	1.40(2)
Ir2	N5	2.061(12)		C26	C27	1.391(19)
Ir2	N7	1.991(14)		C27	C28	1.42(2)
Ir2	N6	2.016(12)		C28	C29	1.42(2)
Ir2	N8	2.069(12)		C39	C38	1.39(2)
S1	O1	1.446(13)		C29	C30	1.34(2)

Table 9.98 – Bond Angles for iaj698v_4.

Atom	**Atom**	**Atom**	**Angle/°**		**Atom**	**Atom**	**Atom**	**Angle/°**
Cl2	Ir1	Cl1	92.15(13)		N6	Ir2	N8	98.7(5)
N1	Ir1	Cl1	93.0(4)		N8	Ir2	Cl4	97.0(4)
N1	Ir1	Cl2	89.2(3)		N8	Ir2	Cl3	85.0(3)
N1	Ir1	N4	175.5(4)		O1	S1	O2	116.7(9)
N2	Ir1	Cl1	173.8(3)		O1	S1	C41	103.0(9)
N2	Ir1	Cl2	90.4(3)		O2	S1	C41	102.3(8)

N2	Ir1	N1	81.3(5)		O3	S1	O1	115.0(8)
N2	Ir1	N3	94.5(5)		O3	S1	O2	114.6(8)
N2	Ir1	N4	95.7(5)		O3	S1	C41	102.1(8)
N3	Ir1	Cl1	83.5(3)		O6	S2	O5	116.8(8)
N3	Ir1	Cl2	172.4(4)		O6	S2	C42	103.2(9)
N3	Ir1	N1	97.2(5)		O4	S2	O6	115.0(9)
N3	Ir1	N4	79.6(5)		O4	S2	O5	113.5(8)
N4	Ir1	Cl1	89.8(3)		O4	S2	C42	102.4(8)
N4	Ir1	Cl2	94.3(3)		O5	S2	C42	103.5(9)
C1	N1	Ir1	128.4(11)		C21	N5	Ir2	127.2(10)
C1	N1	C5	117.7(13)		C25	N5	Ir2	115.3(9)
C5	N1	Ir1	113.8(9)		C25	N5	C21	117.4(13)
C6	N2	Ir1	113.9(9)		C35	N7	Ir2	116.4(10)
C10	N2	Ir1	126.2(9)		C31	N7	Ir2	125.3(10)
C10	N2	C6	119.8(12)		C31	N7	C35	118.3(13)
C11	N3	Ir1	123.2(10)		C26	N6	Ir2	113.1(9)
C11	N3	C15	123.0(13)		C30	N6	Ir2	124.9(10)
C15	N3	Ir1	113.3(10)		C30	N6	C26	121.9(12)
C16	N4	Ir1	115.0(10)		C40	N8	Ir2	126.4(10)
C16	N4	C20	117.4(13)		C36	N8	Ir2	116.0(10)
C20	N4	Ir1	127.4(10)		C36	N8	C40	117.4(13)
N1	C1	C2	124.1(15)		N5	C21	C22	124.5(14)
C3	C2	C1	119.2(15)		C38	C37	C36	120.0(14)
C2	C3	C4	118.1(14)		C34	C33	C32	120.4(15)
C5	C4	C3	120.1(14)		C21	C22	C23	118.9(15)
N1	C5	C4	120.6(13)		F6	C42	S2	111.5(13)
N1	C5	C6	114.2(12)		F4	C42	S2	112.5(15)
C4	C5	C6	125.0(14)		F4	C42	F6	106.0(17)
N2	C6	C5	116.6(12)		F4	C42	F5	110.0(17)
N2	C6	C7	121.4(12)		F5	C42	S2	110.2(13)
C7	C6	C5	122.0(12)		F5	C42	F6	106.4(16)
C8	C7	C6	119.1(12)		C24	C23	C22	116.9(14)
C7	C8	C9	119.0(13)		N7	C35	C34	121.2(14)
C8	C9	C10	120.1(13)		N7	C35	C36	114.5(13)
N2	C10	C9	120.7(12)		C34	C35	C36	124.3(13)
N3	C11	C12	118.3(14)		C23	C24	C25	121.1(14)

C11	C12	C13	121.6(14)		N8	C40	C39	122.9(15)
C14	C13	C12	118.9(15)		N5	C25	C24	121.1(13)
C15	C14	C13	118.0(15)		N5	C25	C26	113.0(12)
N3	C15	C14	120.1(14)		C24	C25	C26	125.7(13)
N3	C15	C16	116.6(13)		C33	C32	C31	118.4(15)
C14	C15	C16	123.3(14)		N6	C26	C25	118.1(12)
N4	C16	C15	114.0(13)		N6	C26	C27	120.3(12)
N4	C16	C17	120.8(14)		C27	C26	C25	121.5(12)
C17	C16	C15	125.1(14)		C33	C34	C35	118.7(15)
C18	C17	C16	119.6(15)		C26	C27	C28	117.7(13)
C19	C18	C17	119.0(15)		N8	C36	C37	121.9(14)
C20	C19	C18	117.9(16)		N8	C36	C35	113.3(12)
N4	C20	C19	125.0(16)		C37	C36	C35	124.8(13)
Cl3	Ir2	Cl4	92.92(12)		C27	C28	C29	119.3(13)
N5	Ir2	Cl4	88.0(3)		C40	C39	C38	118.9(15)
N5	Ir2	Cl3	96.1(3)		C30	C29	C28	119.5(14)
N5	Ir2	N8	174.8(5)		F1	C41	S1	111.1(12)
N7	Ir2	Cl4	175.8(4)		F1	C41	F2	108.6(16)
N7	Ir2	Cl3	88.9(4)		F2	C41	S1	111.3(11)
N7	Ir2	N5	95.5(5)		F3	C41	S1	110.7(14)
N7	Ir2	N6	93.5(5)		F3	C41	F1	108.9(14)
N7	Ir2	N8	79.4(5)		F3	C41	F2	106.1(14)
N6	Ir2	Cl4	84.9(3)		C29	C30	N6	121.1(13)
N6	Ir2	Cl3	175.9(3)		N7	C31	C32	122.8(14)
N6	Ir2	N5	80.4(5)		C37	C38	C39	118.9(14)

Table 9.99 – Torsion Angles for iaj698v_4.

A	**B**	**C**	**D**	**Angle/°**		**A**	**B**	**C**	**D**	**Angle/°**
Ir1	N1	C1	C2	180.0(11)		Ir2	N8	C40	C39	172.1(12)
Ir1	N1	C5	C4	-179.8(11)		Ir2	N8	C36	C37	-172.5(10)
Ir1	N1	C5	C6	4.4(15)		Ir2	N8	C36	C35	6.6(15)
Ir1	N2	C6	C5	2.7(16)		O1	S1	C41	F1	-62.3(14)
Ir1	N2	C6	C7	-176.6(10)		O1	S1	C41	F2	176.6(12)
Ir1	N2	C10	C9	176.1(10)		O1	S1	C41	F3	58.8(14)
Ir1	N3	C11	C12	-169.2(11)		O6	S2	C42	F6	-59.5(16)

Ir1	N3	C15	C14	168.6(12)		O6	S2	C42	F4	59.5(17)
Ir1	N3	C15	C16	-13.5(17)		O6	S2	C42	F5	-177.4(13)
Ir1	N4	C16	C15	1.3(16)		O4	S2	C42	F6	60.2(15)
Ir1	N4	C16	C17	178.1(11)		O4	S2	C42	F4	179.2(16)
Ir1	N4	C20	C19	-176.3(13)		O4	S2	C42	F5	-57.7(15)
N1	C1	C2	C3	-2(2)		O2	S1	C41	F1	176.1(12)
N1	C5	C6	N2	-4.8(18)		O2	S1	C41	F2	55.0(14)
N1	C5	C6	C7	174.6(13)		O2	S1	C41	F3	-62.8(13)
N2	C6	C7	C8	1(2)		O3	S1	C41	F1	57.2(14)
N3	C11	C12	C13	1(2)		O3	S1	C41	F2	-63.9(13)
N3	C15	C16	N4	8(2)		O3	S1	C41	F3	178.3(12)
N3	C15	C16	C17	-168.5(14)		O5	S2	C42	F6	178.4(13)
N4	C16	C17	C18	-4(2)		O5	S2	C42	F4	-62.6(17)
C1	N1	C5	C4	-3(2)		O5	S2	C42	F5	60.4(15)
C1	N1	C5	C6	-178.9(13)		N5	C21	C22	C23	1(3)
C1	C2	C3	C4	-1(2)		N5	C25	C26	N6	2.5(18)
C2	C3	C4	C5	2(2)		N5	C25	C26	C27	-174.6(13)
C3	C4	C5	N1	1(2)		N7	C35	C34	C33	3(2)
C3	C4	C5	C6	175.8(14)		N7	C35	C36	N8	-4.1(17)
C4	C5	C6	N2	179.7(14)		N7	C35	C36	C37	174.9(13)
C4	C5	C6	C7	-1(2)		N6	C26	C27	C28	-2(2)
C5	N1	C1	C2	4(2)		N8	C40	C39	C38	1(2)
C5	C6	C7	C8	-178.1(13)		C21	N5	C25	C24	-3(2)
C6	N2	C10	C9	1(2)		C21	N5	C25	C26	-179.1(12)
C6	C7	C8	C9	-1(2)		C21	C22	C23	C24	-2(3)
C7	C8	C9	C10	1(2)		C33	C32	C31	N7	-1(2)
C8	C9	C10	N2	-1(2)		C22	C23	C24	C25	0(3)
C10	N2	C6	C5	178.1(12)		C23	C24	C25	N5	3(2)
C10	N2	C6	C7	-1(2)		C23	C24	C25	C26	178.1(15)
C11	N3	C15	C14	-3(2)		C35	N7	C31	C32	-2(2)
C11	N3	C15	C16	174.5(13)		C24	C25	C26	N6	-173.1(14)
C11	C12	C13	C14	-3(2)		C24	C25	C26	C27	10(2)
C12	C13	C14	C15	2(2)		C40	N8	C36	C37	2(2)
C13	C14	C15	N3	1(2)		C40	N8	C36	C35	-178.9(12)
C13	C14	C15	C16	-176.6(15)		C40	C39	C38	C37	-1(2)
C14	C15	C16	N4	-174.1(15)		C25	N5	C21	C22	1(2)

C14	C15	C16	C17	9(3)		C25	C26	C27	C28	175.3(13)
C15	N3	C11	C12	2(2)		C32	C33	C34	C35	-6(2)
C15	C16	C17	C18	171.9(15)		C26	N6	C30	C29	3(2)
C16	N4	C20	C19	-1(2)		C26	C27	C28	C29	1(2)
C16	C17	C18	C19	5(2)		C34	C33	C32	C31	5(2)
C17	C18	C19	C20	-4(2)		C34	C35	C36	N8	173.1(13)
C18	C19	C20	N4	2(3)		C34	C35	C36	C37	-8(2)
C20	N4	C16	C15	-174.2(13)		C27	C28	C29	C30	2(2)
C20	N4	C16	C17	3(2)		C36	N8	C40	C39	-2(2)
Ir2	N5	C21	C22	-174.9(12)		C36	C37	C38	C39	1(2)
Ir2	N5	C25	C24	173.4(11)		C36	C35	C34	C33	-174.4(13)
Ir2	N5	C25	C26	-2.5(15)		C28	C29	C30	N6	-4(2)
Ir2	N7	C35	C34	-177.6(11)		C30	N6	C26	C25	-176.9(12)
Ir2	N7	C35	C36	-0.3(15)		C30	N6	C26	C27	0(2)
Ir2	N7	C31	C32	176.8(11)		C31	N7	C35	C34	1(2)
Ir2	N6	C26	C25	-1.2(15)		C31	N7	C35	C36	178.3(12)
Ir2	N6	C26	C27	175.9(11)		C38	C37	C36	N8	-2(2)
Ir2	N6	C30	C29	-172.6(12)		C38	C37	C36	C35	179.1(13)

Table 9.100 – Hydrogen Atom Coordinates ($Å \times 10^4$) and Isotropic Displacement Parameters ($Å^2 \times 10^3$) for iaj698v_4.

Atom	*x*	*y*	*z*	U(eq)
H1	4169.07	-3669.67	4992.08	20
H2	2987.37	-3196.59	4304.93	23
H3	3198.99	-1599.93	3869.14	21
H4	4618.83	-473.22	4159.63	22
H7	6034.31	355.94	4429.39	12
H8	7587.37	1167.92	4753.86	12
H9	8590.06	403.48	5463.36	12
H10	8075.63	-1199.2	5815.7	12
H11	6225.51	-3687.38	4566.83	19
H12	7062.96	-5089.2	4281.66	20
H13	8328.4	-6083.9	4808.28	29
H14	8837.94	-5501.46	5621.75	25
H17	9368.98	-4653.03	6336.22	21

H18	9789.1	-3599.58	7049.81	26
H19	8647.79	-2303.35	7216.55	31
H20	7247.03	-1948.99	6628.57	19
H21	4053.53	-3065.42	2760.27	20
H37	9161.7	-4418.42	3944.25	19
H33	8045.42	-6010.88	2438.53	25
H22	2780.12	-2941.99	2076.87	26
H23	3018.73	-1902.21	1397.63	27
H24	4529.23	-970.83	1473.31	24
H40	7473.67	-1165.44	4075.86	16
H32	6535.97	-5366.41	1974.9	25
H34	8664.06	-5283.86	3213.29	25
H27	5933.48	-33.1	1642	15
H28	7501.97	850.29	1858.13	20
H39	8797.28	-1670.16	4697.1	27
H29	8576.05	406.11	2611.15	24
H30	8137.85	-941.24	3088.51	16
H31	5802.13	-3814.53	2244.01	19
H38	9680.4	-3309.35	4620.27	22

Crystal Structure Determination of Iaj698v_4

Crystal Data for $C_{21}H_{16}Cl_2F_3IrN_4O_3S$ (M = 724.54 g/mol): monoclinic, space group $P2_1/c$ (no. 14), a = 13.9986(6) Å, b = 11.9949(5) Å, c = 28.4445(15) Å, β = 103.191(2)°, V = 4650.1(4) Å^3, Z = 8, T = 100.03 K, μ(CuKα) = 14.597 mm^{-1}, *Dcalc* = 2.070 g/cm^3, 8236 reflections measured (6.382° ≤ 2Θ ≤ 138.696°), 8236 unique (R_{int} = ?, R_{sigma} = 0.0465) which were used in all calculations. The final R_1 was 0.0821 (I > 2σ(I)) and wR_2 was 0.2774 (all data).

9.3.13 IAJ702v_0m $[Ir(bpy)_2Cl_2]PF_6$, crystallised as $[Ir(bpy)_2Cl_2]PF_6CH_3NO_2$

Table 9.101 – Crystal data and structure refinement for iaj702v_0m.

Identification code	iaj702v_0m
Empirical formula	$C_{21}H_{19}Cl_2F_6IrN_5O_2P$
Formula weight	781.48

Temperature/K	100.03
Crystal system	monoclinic
Space group	$P2_1/n$
a/Å	10.0704(4)
b/Å	18.3390(7)
c/Å	13.7594(5)
α/°	90
β/°	98.959(2)
γ/°	90
Volume/Å^3	2510.10(17)
Z	4
ρ_{calc}g/cm^3	2.068
μ/mm^{-1}	13.565
F(000)	1504.0
Crystal size/mm^3	0.256 × 0.106 × 0.018
Radiation	CuKα (λ = 1.54178)
2Θ range for data collection/°	8.096 to 133.122
Index ranges	$-11 \le h \le 11$, $-21 \le k \le 21$, $-16 \le l \le 16$
Reflections collected	28246
Independent reflections	4427 [R_{int} = 0.0679, R_{sigma} = 0.0397]
Data/restraints/parameters	4427/0/344
Goodness-of-fit on F^2	1.108
Final R indexes [I>=2σ (I)]	R_1 = 0.0430, wR_2 = 0.0999
Final R indexes [all data]	R_1 = 0.0480, wR_2 = 0.1026
Largest diff. peak/hole / e Å^{-3}	1.60/-1.19

Table 9.102 – Fractional Atomic Coordinates (×10^4) and Equivalent Isotropic Displacement Parameters (Å^2×10^3) for iaj702v_0m. U_{eq} is defined as 1/3 of the trace of the orthogonalised U_{IJ} tensor.

Atom	***x***	***y***	***z***	**U(eq)**
Ir1	7114.6(3)	4817.8(2)	2683.3(2)	14.19(11)
Cl1	4773.7(16)	4616.1(10)	2541.7(13)	21.7(4)
Cl2	7550.2(18)	3798.8(9)	3729.9(13)	24.6(4)
N1	7061(6)	4263(3)	1389(4)	19.0(13)
N2	6734(6)	5663(3)	1712(4)	17.7(12)
N3	9133(6)	5028(3)	2890(5)	20.1(13)

N4	7293(6)	5437(3)	3935(4)	18.9(13)
C1	7171(8)	3537(4)	1302(6)	26.3(17)
C2	7137(9)	3214(5)	385(6)	33(2)
C3	6962(9)	3639(6)	-443(7)	39(2)
C4	6819(8)	4383(5)	-357(6)	29.3(18)
C5	6881(7)	4686(4)	564(6)	23.5(16)
C6	6718(7)	5474(4)	750(5)	20.0(15)
C7	6554(8)	6003(5)	36(6)	28.3(18)
C8	6378(9)	6721(5)	272(6)	33.2(19)
C9	6352(8)	6902(5)	1242(6)	29.6(18)
C10	6544(7)	6352(4)	1952(5)	21.3(15)
C11	9987(8)	4764(4)	2327(6)	26.1(17)
C12	11316(8)	4958(5)	2481(7)	30.6(19)
C13	11793(8)	5436(5)	3240(7)	35(2)
C14	10899(8)	5694(4)	3835(6)	27.8(18)
C15	9566(8)	5469(4)	3647(6)	23.2(16)
C16	8555(8)	5691(4)	4259(5)	20.5(15)
C17	8818(8)	6099(4)	5116(6)	26.2(17)
C18	7782(9)	6249(4)	5645(6)	32.4(19)
C19	6511(9)	5994(4)	5287(5)	26.9(17)
C20	6287(8)	5589(4)	4443(5)	21.9(15)
P1	4018(2)	7613.9(15)	3428.9(17)	39.7(6)
F1	5368(7)	7176(4)	3732(5)	76(2)
F2	2784(8)	8161(4)	3140(5)	76(2)
F3	4636(7)	8254(4)	4201(5)	73(2)
F4	4736(7)	8016(4)	2610(5)	72(2)
F5	3450(9)	7049(5)	2639(6)	97(3)
F6	3358(9)	7258(4)	4251(5)	82(2)
O1	9675(8)	6398(4)	1724(6)	54.0(19)
O2	9333(8)	7138(4)	2905(5)	51.1(18)
N5	9710(8)	7020(4)	2102(7)	43(2)
C21	10239(10)	7606(6)	1594(8)	49(3)

Table 9.103 – Anisotropic Displacement Parameters ($Å^2 \times 10^3$) for iaj702v_0m. The Anisotropic displacement factor exponent takes the form: $-2\pi^2[h^2a^{*2}U_{11}+2hka^*b^*U_{12}+\ldots]$.

Atom	U_{11}	U_{22}	U_{33}	U_{23}	U_{13}	U_{12}
Ir1	12.79(16)	15.50(17)	13.78(16)	-0.37(11)	0.44(11)	0.22(11)
Cl1	13.7(8)	28.7(9)	22.3(9)	2.6(7)	1.5(6)	-0.9(7)
Cl2	27.4(9)	18.7(8)	25.2(9)	3.6(7)	-3.7(7)	1.4(7)
N1	13(3)	23(3)	20(3)	2(2)	0(2)	1(2)
N2	12(3)	23(3)	17(3)	2(2)	-2(2)	-1(2)
N3	23(3)	14(3)	22(3)	4(2)	-3(3)	0(2)
N4	23(3)	16(3)	16(3)	8(2)	0(2)	4(2)
C1	24(4)	20(4)	32(4)	-4(3)	-5(3)	-1(3)
C2	35(5)	26(4)	36(5)	-12(4)	-5(4)	9(4)
C3	29(4)	60(6)	26(5)	-20(4)	-5(4)	6(4)
C4	31(4)	41(5)	15(4)	-2(3)	0(3)	4(4)
C5	19(4)	26(4)	25(4)	0(3)	3(3)	0(3)
C6	21(4)	27(4)	12(3)	-1(3)	3(3)	-5(3)
C7	28(4)	43(5)	14(4)	9(3)	4(3)	-1(4)
C8	34(5)	31(5)	33(5)	17(4)	3(4)	2(4)
C9	28(4)	24(4)	34(5)	7(3)	-3(4)	-6(3)
C10	22(4)	21(4)	19(4)	-5(3)	-1(3)	-3(3)
C11	32(4)	24(4)	23(4)	1(3)	5(3)	3(3)
C12	15(4)	37(5)	40(5)	0(4)	5(3)	2(3)
C13	20(4)	33(5)	50(6)	5(4)	0(4)	-5(3)
C14	19(4)	21(4)	40(5)	-2(3)	-4(3)	-2(3)
C15	22(4)	21(4)	26(4)	2(3)	1(3)	5(3)
C16	27(4)	17(4)	18(4)	1(3)	3(3)	2(3)
C17	29(4)	22(4)	23(4)	1(3)	-10(3)	-1(3)
C18	52(5)	26(4)	17(4)	-3(3)	-3(4)	8(4)
C19	42(5)	29(4)	12(3)	6(3)	10(3)	9(4)
C20	26(4)	23(4)	16(4)	4(3)	2(3)	3(3)
P1	37.7(12)	55.5(15)	24.9(11)	4.7(10)	1.4(10)	12.3(11)
F1	75(5)	83(5)	64(4)	-8(4)	-4(4)	37(4)
F2	84(5)	86(5)	60(4)	3(4)	17(4)	43(4)
F3	72(5)	81(5)	61(4)	-17(4)	-5(4)	11(4)
F4	76(5)	82(5)	64(4)	8(4)	28(4)	8(4)
F5	97(6)	123(7)	75(5)	-65(5)	23(5)	-33(5)
F6	119(7)	81(5)	57(4)	13(4)	45(4)	4(5)
O1	71(5)	35(4)	56(5)	-1(3)	10(4)	-4(4)

O2	60(5)	49(4)	46(4)	9(3)	16(4)	13(4)
N5	34(4)	35(4)	60(6)	11(4)	3(4)	3(3)
C21	43(6)	43(6)	59(7)	16(5)	3(5)	-2(5)

Table 9.104 – Bond Lengths for iaj702v_0m.

Atom	Atom	Length/Å		Atom	Atom	Length/Å
Ir1	Cl1	2.3641(16)		C8	C9	1.380(12)
Ir1	Cl2	2.3582(17)		C9	C10	1.397(11)
Ir1	N1	2.044(6)		C11	C12	1.369(11)
Ir1	N2	2.044(6)		C12	C13	1.390(13)
Ir1	N3	2.044(6)		C13	C14	1.391(12)
Ir1	N4	2.047(6)		C14	C15	1.389(11)
N1	C1	1.343(10)		C15	C16	1.476(11)
N1	C5	1.364(10)		C16	C17	1.386(10)
N2	C6	1.366(9)		C17	C18	1.390(12)
N2	C10	1.327(9)		C18	C19	1.379(12)
N3	C11	1.336(10)		C19	C20	1.367(11)
N3	C15	1.338(10)		P1	F1	1.577(7)
N4	C16	1.362(10)		P1	F2	1.598(7)
N4	C20	1.347(10)		P1	F3	1.639(7)
C1	C2	1.389(11)		P1	F4	1.608(7)
C2	C3	1.369(13)		P1	F5	1.545(7)
C3	C4	1.379(13)		P1	F6	1.544(7)
C4	C5	1.375(11)		O1	N5	1.250(11)
C5	C6	1.481(11)		O2	N5	1.242(11)
C6	C7	1.372(11)		N5	C21	1.431(12)
C7	C8	1.374(12)				

Table 9.105 – Bond Angles for iaj702v_0m.

Atom	Atom	Atom	Angle/°		Atom	Atom	Atom	Angle/°
Cl2	Ir1	Cl1	90.84(6)		C6	C7	C8	120.9(8)
N1	Ir1	Cl1	87.69(17)		C7	C8	C9	118.8(7)
N1	Ir1	Cl2	96.60(17)		C8	C9	C10	118.8(8)

N1	Ir1	N3	96.1(2)		N2	C10	C9	121.5(7)
N1	Ir1	N4	174.7(2)		N3	C11	C12	121.2(8)
N2	Ir1	Cl1	88.96(16)		C11	C12	C13	119.7(8)
N2	Ir1	Cl2	176.85(17)		C12	C13	C14	118.5(7)
N2	Ir1	N1	80.2(2)		C15	C14	C13	119.0(8)
N2	Ir1	N3	91.7(2)		N3	C15	C14	120.9(7)
N2	Ir1	N4	96.5(2)		N3	C15	C16	116.1(7)
N3	Ir1	Cl1	176.23(18)		C14	C15	C16	123.0(7)
N3	Ir1	Cl2	88.73(17)		N4	C16	C15	114.2(6)
N3	Ir1	N4	79.8(2)		N4	C16	C17	120.5(7)
N4	Ir1	Cl1	96.43(18)		C17	C16	C15	125.2(7)
N4	Ir1	Cl2	86.70(16)		C16	C17	C18	119.5(7)
C1	N1	Ir1	125.4(5)		C19	C18	C17	118.5(7)
C1	N1	C5	119.4(7)		C20	C19	C18	120.6(8)
C5	N1	Ir1	115.1(5)		N4	C20	C19	121.0(7)
C6	N2	Ir1	114.5(5)		F1	P1	F2	171.7(5)
C10	N2	Ir1	125.3(5)		F1	P1	F3	88.2(4)
C10	N2	C6	120.2(6)		F1	P1	F4	87.5(4)
C11	N3	Ir1	124.5(5)		F2	P1	F3	85.1(4)
C11	N3	C15	120.7(7)		F2	P1	F4	87.4(4)
C15	N3	Ir1	114.8(5)		F4	P1	F3	87.7(4)
C16	N4	Ir1	114.9(5)		F5	P1	F1	93.1(5)
C20	N4	Ir1	125.2(5)		F5	P1	F2	93.3(5)
C20	N4	C16	119.9(6)		F5	P1	F3	175.8(5)
N1	C1	C2	120.8(8)		F5	P1	F4	88.4(5)
C3	C2	C1	119.6(8)		F6	P1	F1	92.5(5)
C2	C3	C4	119.6(8)		F6	P1	F2	92.3(4)
C5	C4	C3	119.2(8)		F6	P1	F3	89.5(4)
N1	C5	C4	121.2(7)		F6	P1	F4	177.2(5)
N1	C5	C6	114.5(6)		F6	P1	F5	94.4(5)
C4	C5	C6	124.2(7)		O1	N5	C21	118.1(9)
N2	C6	C5	115.5(6)		O2	N5	O1	122.4(8)
N2	C6	C7	119.7(7)		O2	N5	C21	119.5(9)
C7	C6	C5	124.8(7)					

Table 9.106 – Torsion Angles for iaj702v_0m.

A	B	C	D	Angle/°		A	B	C	D	Angle/°
Ir1	N1	C1	C2	-179.2(6)		C4	C5	C6	N2	176.3(7)
Ir1	N1	C5	C4	-179.7(6)		C4	C5	C6	C7	-3.5(12)
Ir1	N1	C5	C6	-1.6(8)		C5	N1	C1	C2	1.7(11)
Ir1	N2	C6	C5	4.1(8)		C5	C6	C7	C8	178.5(7)
Ir1	N2	C6	C7	-176.0(6)		C6	N2	C10	C9	-1.4(11)
Ir1	N2	C10	C9	176.9(5)		C6	C7	C8	C9	-0.7(12)
Ir1	N3	C11	C12	176.7(6)		C7	C8	C9	C10	1.7(12)
Ir1	N3	C15	C14	-176.1(6)		C8	C9	C10	N2	-0.7(12)
Ir1	N3	C15	C16	4.5(8)		C10	N2	C6	C5	-177.4(6)
Ir1	N4	C16	C15	-0.2(8)		C10	N2	C6	C7	2.4(10)
Ir1	N4	C16	C17	-178.1(5)		C11	N3	C15	C14	3.3(11)
Ir1	N4	C20	C19	178.3(5)		C11	N3	C15	C16	-176.2(6)
N1	C1	C2	C3	-1.4(12)		C11	C12	C13	C14	1.2(13)
N1	C5	C6	N2	-1.7(9)		C12	C13	C14	C15	-0.5(12)
N1	C5	C6	C7	178.5(7)		C13	C14	C15	N3	-1.7(12)
N2	C6	C7	C8	-1.4(12)		C13	C14	C15	C16	177.7(7)
N3	C11	C12	C13	0.3(12)		C14	C15	C16	N4	177.7(7)
N3	C15	C16	N4	-2.8(9)		C14	C15	C16	C17	-4.6(12)
N3	C15	C16	C17	174.9(7)		C15	N3	C11	C12	-2.6(11)
N4	C16	C17	C18	0.0(11)		C15	C16	C17	C18	-177.6(7)
C1	N1	C5	C4	-0.5(11)		C16	N4	C20	C19	-0.3(10)
C1	N1	C5	C6	177.6(6)		C16	C17	C18	C19	-1.1(12)
C1	C2	C3	C4	-0.1(13)		C17	C18	C19	C20	1.5(12)
C2	C3	C4	C5	1.3(13)		C18	C19	C20	N4	-0.8(11)
C3	C4	C5	N1	-1.0(12)		C20	N4	C16	C15	178.6(6)
C3	C4	C5	C6	-178.9(7)		C20	N4	C16	C17	0.7(10)

Table 9.107 – Hydrogen Atom Coordinates (Å×10^4) and Isotropic Displacement Parameters (Å^2×10^3) for iaj702v_0m.

Atom	*x*	*y*	*z*	U(eq)
H1	7272.06	3240.43	1875.17	32
H2	7235.9	2700.98	333.3	40

H3	6939.4	3423.2	-1072.75	47
H4	6678.25	4683.26	-926.28	35
H7	6562.46	5871.03	-630.96	34
H8	6275.01	7086.1	-224.37	40
H9	6207.18	7391.8	1424.28	36
H10	6537.62	6473.41	2622.7	26
H11	9667.08	4434.93	1809.29	31
H12	11909.49	4766.86	2071.52	37
H13	12708.58	5582.97	3349.47	42
H14	11194.96	6017.9	4363.08	33
H17	9699.99	6274.91	5339.09	31
H18	7945.38	6520.73	6239.12	39
H19	5785.65	6100.95	5630.44	32
H20	5407.47	5412.89	4211.48	26
H21A	9498.02	7908.44	1268.36	73
H21B	10744.25	7408.31	1099.49	73
H21C	10837.77	7904.06	2064.93	73

9.3.14 IAJ705v ([Ir(bpy)$_2$Cl$_2$]CH$_3$OH) – An Adventitious Discovery

Table 9.108 – Crystal data and structure refinement for IAJ705v.

Identification code	IAJ705v
Empirical formula	$C_{21}H_{19}Cl_2IrN_4O$
Formula weight	606.50
Temperature/K	100.01
Crystal system	monoclinic
Space group	$P2_1/c$
a/Å	14.4335(9)
b/Å	10.2762(6)
c/Å	13.3887(9)
α/°	90
β/°	92.707(2)
γ/°	90
Volume/Å^3	1983.6(2)

Z	4
ρ_{calc}g/cm^3	2.031
μ/mm^{-1}	15.684
F(000)	1168.0
Crystal size/mm^3	0.174 × 0.05 × 0.05
Radiation	CuKα (λ = 1.54178)
2Θ range for data collection/°	6.13 to 133.214
Index ranges	$-17 \leq h \leq 17$, $-12 \leq k \leq 12$, $-15 \leq l \leq 12$
Reflections collected	24670
Independent reflections	3471 [R_{int} = 0.0432, R_{sigma} = 0.0253]
Data/restraints/parameters	3471/0/264
Goodness-of-fit on F^2	1.106
Final R indexes [I>=2σ (I)]	R_1 = 0.0236, wR_2 = 0.0581
Final R indexes [all data]	R_1 = 0.0246, wR_2 = 0.0587
Largest diff. peak/hole / e Å^{-3}	1.11/-1.22

Table 9.109 – Fractional Atomic Coordinates (×10^4) and Equivalent Isotropic Displacement Parameters (Å^2×10^3) for IAJ705v. U_{eq} is defined as 1/3 of the trace of the orthogonalised U_{IJ} tensor.

Atom	***x***	***y***	***z***	**U(eq)**
Ir1	7575.5(2)	3666.4(2)	6000.2(2)	7.22(7)
Cl1	8688.1(6)	2120.2(8)	5259.0(6)	12.39(18)
Cl2	7357.2(6)	2170.3(8)	7301.4(6)	12.94(18)
N1	6417(2)	2855(3)	5286(2)	10.5(6)
N2	4912(2)	4957(3)	6623(2)	14.4(7)
N3	8673(2)	4599(3)	6697(2)	10.8(6)
N4	7884(2)	4960(3)	4930(2)	9.3(6)
C1	6434(3)	1885(4)	4615(3)	12.8(7)
C2	5631(3)	1321(4)	4227(3)	16.7(8)
C3	4779(3)	1760(4)	4542(3)	16.7(8)
C4	4769(3)	2772(4)	5221(3)	14.0(8)
C5	5598(3)	3311(4)	5589(3)	11.3(7)
C6	5685(3)	4405(4)	6288(3)	10.3(7)
C7	6594(3)	4812(4)	6543(3)	11.8(7)
C8	6694(3)	5913(4)	7142(3)	13.4(8)
C9	5895(3)	6526(4)	7464(3)	16.7(8)

C10	5029(3)	6003(4)	7213(3)	15.8(8)
C11	8983(3)	4402(4)	7654(3)	13.8(8)
C12	9740(3)	5063(4)	8060(3)	15.3(8)
C13	10208(3)	5941(4)	7480(3)	16.9(8)
C14	9881(3)	6154(4)	6503(3)	14.6(8)
C15	9109(3)	5476(4)	6128(3)	11.9(7)
C16	8682(3)	5653(4)	5117(3)	12.0(8)
C17	9016(3)	6484(4)	4403(3)	16.0(8)
C18	8527(3)	6618(4)	3492(3)	18.5(8)
C19	7703(3)	5948(4)	3327(3)	17.3(8)
C20	7408(2)	5121(4)	4060(3)	13.4(8)
O1	7317(3)	9505(4)	5986(3)	41.2(9)
C21	7747(4)	8885(5)	5253(6)	50.4(17)

Table 9.110 – Anisotropic Displacement Parameters ($Å^2×10^3$) for IAJ705v. The Anisotropic displacement factor exponent takes the form: $-2\pi^2[h^2a^{*2}U_{11}+2hka^*b^*U_{12}+\ldots]$.

Atom	U_{11}	U_{22}	U_{33}	U_{23}	U_{13}	U_{12}
Ir1	5.03(10)	7.54(10)	9.03(10)	0.18(5)	-0.40(6)	-0.49(5)
Cl1	9.1(4)	13.1(4)	15.0(4)	-0.5(3)	1.0(3)	1.2(3)
Cl2	11.3(4)	13.7(4)	13.9(4)	4.0(3)	0.9(3)	-1.7(3)
N1	9.0(15)	11.3(15)	11.3(16)	3.0(12)	-0.2(12)	-0.6(12)
N2	9.6(15)	21.7(18)	11.9(16)	4.4(13)	1.2(12)	2.5(13)
N3	8.0(14)	12.1(15)	12.4(16)	0.6(12)	1.0(12)	2.2(12)
N4	7.5(14)	6.9(14)	13.6(16)	-0.4(12)	2.9(12)	-1.0(11)
C1	14.6(18)	10.9(18)	12.5(19)	1.2(15)	-2.0(14)	1.4(15)
C2	19(2)	16(2)	15(2)	-1.6(15)	-1.8(16)	-3.0(15)
C3	15.2(19)	17(2)	18(2)	2.8(16)	-4.2(15)	-6.3(16)
C4	8.7(17)	19(2)	14.5(19)	5.5(15)	-1.3(14)	-1.8(15)
C5	14.3(18)	13.1(18)	6.6(18)	5.0(14)	0.8(14)	0.6(15)
C6	10.8(17)	11.6(18)	8.3(18)	4.8(14)	-0.3(13)	0.0(14)
C7	12.4(18)	11.9(18)	11.0(18)	4.5(14)	-0.6(14)	-0.1(14)
C8	11.6(18)	13.0(19)	15.5(19)	-0.4(15)	0.9(14)	-1.7(15)
C9	20(2)	17(2)	13(2)	-2.9(16)	1.9(16)	5.3(16)
C10	11.3(18)	21(2)	15(2)	2.8(16)	1.3(14)	7.3(16)
C11	13.5(18)	15.3(19)	12.5(19)	1.5(15)	0.5(14)	2.2(15)

C12	13.8(18)	18(2)	13(2)	-1.7(15)	-5.8(15)	2.4(16)
C13	12.1(18)	18(2)	20(2)	-5.5(17)	-2.7(15)	-2.2(16)
C14	8.8(18)	13.4(19)	22(2)	-1.3(15)	1.5(15)	-2.2(14)
C15	9.0(17)	12.3(18)	14.5(19)	-1.6(14)	1.1(14)	5.2(14)
C16	10.5(18)	11.7(18)	14.0(19)	-2.2(14)	0.0(14)	1.1(14)
C17	13.6(19)	17(2)	18(2)	0.7(16)	2.9(16)	-3.6(15)
C18	21(2)	14.7(19)	20(2)	6.8(16)	3.7(17)	-0.6(17)
C19	22(2)	13.6(19)	16(2)	2.5(16)	-1.8(16)	3.3(17)
C20	9.8(18)	11.0(19)	19(2)	-2.3(15)	-1.6(15)	1.5(14)
O1	58(2)	29(2)	36(2)	-0.8(16)	-6.9(17)	-5.3(18)
C21	42(3)	23(3)	87(5)	-13(3)	18(3)	-1(2)

Table 9.111 – Bond Lengths for IAJ705v.

Atom	Atom	Length/Å		Atom	Atom	Length/Å
Ir1	Cl1	2.4978(9)		C4	C5	1.388(5)
Ir1	Cl2	2.3558(9)		C5	C6	1.464(5)
Ir1	N1	2.062(3)		C6	C7	1.403(5)
Ir1	N3	2.039(3)		C7	C8	1.391(6)
Ir1	N4	2.020(3)		C8	C9	1.400(6)
Ir1	C7	2.005(4)		C9	C10	1.388(6)
N1	C1	1.343(5)		C11	C12	1.375(6)
N1	C5	1.352(5)		C12	C13	1.388(6)
N2	C6	1.348(5)		C13	C14	1.387(6)
N2	C10	1.340(6)		C14	C15	1.388(6)
N3	C11	1.353(5)		C15	C16	1.472(5)
N3	C15	1.354(5)		C16	C17	1.385(6)
N4	C16	1.366(5)		C17	C18	1.387(6)
N4	C20	1.335(5)		C18	C19	1.382(6)
C1	C2	1.376(6)		C19	C20	1.381(6)
C2	C3	1.393(6)		O1	C21	1.346(7)
C3	C4	1.381(6)				

Table 9.112 – Bond Angles for IAJ705v.

Atom	Atom	Atom	Angle/°		Atom	Atom	Atom	Angle/°
Cl2	Ir1	Cl1	89.40(3)		C3	C4	C5	119.9(4)

N1	Ir1	Cl1	94.65(9)		N1	C5	C4	120.5(4)
N1	Ir1	Cl2	86.86(9)		N1	C5	C6	114.1(3)
N3	Ir1	Cl1	88.88(9)		C4	C5	C6	125.5(4)
N3	Ir1	Cl2	95.56(9)		N2	C6	C5	119.2(3)
N3	Ir1	N1	175.75(12)		N2	C6	C7	125.0(4)
N4	Ir1	Cl1	88.26(9)		C7	C6	C5	115.8(3)
N4	Ir1	Cl2	174.79(9)		C6	C7	Ir1	113.9(3)
N4	Ir1	N1	97.97(12)		C8	C7	Ir1	129.1(3)
N4	Ir1	N3	79.75(12)		C8	C7	C6	117.0(3)
C7	Ir1	Cl1	175.03(11)		C7	C8	C9	118.7(4)
C7	Ir1	Cl2	89.64(11)		C10	C9	C8	119.8(4)
C7	Ir1	N1	80.42(14)		N2	C10	C9	122.7(4)
C7	Ir1	N3	96.06(14)		N3	C11	C12	121.4(4)
C7	Ir1	N4	93.09(13)		C11	C12	C13	119.9(4)
C1	N1	Ir1	124.8(3)		C14	C13	C12	118.5(4)
C1	N1	C5	120.1(3)		C13	C14	C15	119.6(4)
C5	N1	Ir1	115.0(3)		N3	C15	C14	121.1(4)
C10	N2	C6	116.8(3)		N3	C15	C16	114.4(3)
C11	N3	Ir1	125.3(3)		C14	C15	C16	124.4(4)
C11	N3	C15	119.4(3)		N4	C16	C15	114.6(3)
C15	N3	Ir1	115.3(2)		N4	C16	C17	120.9(4)
C16	N4	Ir1	115.2(2)		C17	C16	C15	124.5(4)
C20	N4	Ir1	125.4(3)		C16	C17	C18	119.2(4)
C20	N4	C16	119.3(3)		C19	C18	C17	119.3(4)
N1	C1	C2	121.6(4)		C20	C19	C18	118.9(4)
C1	C2	C3	119.2(4)		N4	C20	C19	122.3(4)
C4	C3	C2	118.7(4)					

Table 9.113 – Torsion Angles for IAJ705v.

A	**B**	**C**	**D**	**Angle/°**		**A**	**B**	**C**	**D**	**Angle/°**
Ir1	N1	C1	C2	174.7(3)		C4	C5	C6	C7	-178.5(4)
Ir1	N1	C5	C4	-175.1(3)		C5	N1	C1	C2	-0.7(6)
Ir1	N1	C5	C6	6.7(4)		C5	C6	C7	Ir1	-6.3(4)
Ir1	N3	C11	C12	179.0(3)		C5	C6	C7	C8	175.1(3)
Ir1	N3	C15	C14	-178.4(3)		C6	N2	C10	C9	1.1(6)

Ir1	N3	C15	C16	3.1(4)		C6	C7	C8	C9	1.1(5)
Ir1	N4	C16	C15	-8.3(4)		C7	C8	C9	C10	2.4(6)
Ir1	N4	C16	C17	174.0(3)		C8	C9	C10	N2	-3.6(6)
Ir1	N4	C20	C19	-174.4(3)		C10	N2	C6	C5	-176.1(3)
Ir1	C7	C8	C9	-177.3(3)		C10	N2	C6	C7	2.7(5)
N1	C1	C2	C3	-0.4(6)		C11	N3	C15	C14	1.4(5)
N1	C5	C6	N2	178.6(3)		C11	N3	C15	C16	-177.1(3)
N1	C5	C6	C7	-0.4(5)		C11	C12	C13	C14	1.7(6)
N2	C6	C7	Ir1	174.8(3)		C12	C13	C14	C15	-1.0(6)
N2	C6	C7	C8	-3.8(6)		C13	C14	C15	N3	-0.5(6)
N3	C11	C12	C13	-0.8(6)		C13	C14	C15	C16	177.8(4)
N3	C15	C16	N4	3.4(5)		C14	C15	C16	N4	-175.0(4)
N3	C15	C16	C17	-179.1(4)		C14	C15	C16	C17	2.5(6)
N4	C16	C17	C18	0.7(6)		C15	N3	C11	C12	-0.7(6)
C1	N1	C5	C4	0.8(5)		C15	C16	C17	C18	-176.8(4)
C1	N1	C5	C6	-177.4(3)		C16	N4	C20	C19	1.4(6)
C1	C2	C3	C4	1.4(6)		C16	C17	C18	C19	1.7(6)
C2	C3	C4	C5	-1.3(6)		C17	C18	C19	C20	-2.5(6)
C3	C4	C5	N1	0.2(6)		C18	C19	C20	N4	0.9(6)
C3	C4	C5	C6	178.3(4)		C20	N4	C16	C15	175.5(3)
C4	C5	C6	N2	0.4(6)		C20	N4	C16	C17	-2.2(5)

Table 9.114 – Hydrogen Atom Coordinates (Å×10^4) and Isotropic Displacement Parameters (Å^2×10^3) for IAJ705v.

Atom	***x***	***y***	***z***	**U(eq)**
H1	7013.95	1580.9	4403.17	15
H2	5656.31	639.51	3749.49	20
H3	4216.65	1370.92	4295.62	20
H4	4195.32	3098.08	5435.11	17
H8	7292.17	6241.49	7329.3	16
H9	5945.86	7298.43	7853.35	20
H10	4496.51	6403.02	7470.38	19
H11	8671.93	3794.72	8054.82	17
H12	9941.18	4917.3	8736.25	18

H13	10741.56	6386.43	7745.71	20
H14	10183.14	6761.42	6093.21	18
H17	9574.46	6955.3	4535.96	19
H18	8754.7	7165.62	2987.82	22
H19	7346.26	6054.11	2717.6	21
H20	6847.15	4651.06	3941.2	16
H1A	7493.94	10284.06	6013.06	62
H21A	7584.79	9302.35	4609.99	76
H21B	7550.29	7972.57	5229.21	76
H21C	8420.27	8928.72	5385.37	76

Crystal Structure Determination of IAJ705v

Crystal Data for $C_{21}H_{19}Cl_2IrN_4O$ (*M* =606.50 g/mol): monoclinic, space group $P2_1/c$ (no. 14), *a* = 14.4335(9) Å, *b* = 10.2762(6) Å, *c* = 13.3887(9) Å, *β* = 92.707(2)°, *V* = 1983.6(2) Å^3, *Z* = 4, *T* = 100.01 K, μ(CuKα) = 15.684 mm^{-1}, *Dcalc* = 2.031 g/cm^3, 24670 reflections measured (6.13° ≤ 2Θ ≤ 133.214°), 3471 unique (R_{int} = 0.0432, R_{sigma} = 0.0253) which were used in all calculations. The final R_1 was 0.0236 (I > 2σ(I)) and wR_2 was 0.0587 (all data).

9.3.15 IAJ701v_0m $[Ir(dppz)_2Cl_2]CF_3SO_3$, crystallised as $[Ir(dppz)_2Cl_2]CF_3SO_3CH_3NO_2$

Table 9.115 – Crystal data and structure refinement for IAJ701v_0m.

Identification code	IAJ701v_0m
Empirical formula	$C_{38}H_{23}Cl_2F_4IrN_9O_5S$
Formula weight	1056.81
Temperature/K	100.0
Crystal system	monoclinic
Space group	C2/c
a/Å	22.099(4)
b/Å	13.896(3)
c/Å	13.001(3)
α/°	90
β/°	104.058(7)

γ/°	90
Volume/Å^3	3872.8(13)
Z	4
ρ_{calc}g/cm^3	1.813
μ/mm^{-1}	9.125
F(000)	2068.0
Crystal size/mm^3	0.159 × 0.12 × 0.021
Radiation	CuKα (λ = 1.54178)
2Θ range for data collection/°	7.582 to 133.876
Index ranges	-26 ≤ h ≤ 25, -15 ≤ k ≤ 16, -15 ≤ l ≤ 15
Reflections collected	24261
Independent reflections	3434 [R_{int} = 0.0511, R_{sigma} = 0.0292]
Data/restraints/parameters	3434/264/304
Goodness-of-fit on F^2	1.224
Final R indexes [I>=2σ (I)]	R_1 = 0.0593, wR_2 = 0.1488
Final R indexes [all data]	R_1 = 0.0598, wR_2 = 0.1491
Largest diff. peak/hole / e Å^{-3}	3.90/-2.33

Table 9.116 – Fractional Atomic Coordinates (×10^4) and Equivalent Isotropic Displacement Parameters (Å^2×10^3) for IAJ701v_0m. U_{eq} is defined as 1/3 of the trace of the orthogonalised U_{IJ} tensor.

Atom	***x***	***y***	***z***	**U(eq)**
Ir1	5000	8280.9(4)	7500	16.84(18)
Cl1	5784.7(9)	9469.3(15)	7868.4(17)	22.9(5)
N1	5685(4)	7286(6)	7687(6)	24.0(16)
N2	5139(3)	8259(5)	6000(6)	22.6(15)
N3	7183(4)	6001(6)	5919(7)	27.5(16)
N4	6616(4)	7126(6)	4127(7)	29.0(17)
C1	5925(5)	6749(8)	8553(8)	33(2)
C2	6416(5)	6116(9)	8604(9)	41(3)
C3	6691(5)	6032(8)	7752(8)	30(2)
C4	6447(4)	6587(7)	6847(7)	23.8(18)
C5	5943(4)	7194(6)	6839(7)	20.9(16)
C6	5642(4)	7738(6)	5925(7)	20.9(16)
C7	5858(4)	7713(7)	4992(7)	23.9(18)
C8	5550(4)	8276(7)	4145(8)	27.6(19)

C9	5029(4)	8787(7)	4210(8)	26.6(19)
C10	4833(4)	8775(7)	5161(7)	23.4(18)
C11	6696(4)	6543(6)	5898(8)	23.0(17)
C12	6412(4)	7120(7)	4997(8)	25.0(18)
C13	7403(4)	5991(7)	5028(8)	29.1(19)
C14	7920(5)	5406(8)	4992(9)	34(2)
C15	8144(5)	5402(8)	4094(9)	34(2)
C16	7868(5)	5970(8)	3208(9)	35(2)
C17	7372(5)	6539(8)	3211(9)	34(2)
C18	7122(5)	6558(7)	4129(8)	30(2)
S1	4978(2)	4715(4)	5297(4)	34.9(11)
F1	5649(6)	4453(13)	7230(10)	56(4)
F2	6232(4)	4264(7)	6112(7)	78(3)
F3	5609(10)	3235(11)	6304(13)	75(5)
O1	4936(5)	4240(6)	4475(8)	69(3)
O2	4432(7)	4457(11)	5675(15)	49(4)
C19	5629(12)	4141(17)	6300(19)	43(4)
O3	7374(13)	8018(15)	9231(19)	185(9)
C20	8150(20)	7020(30)	9350(30)	93(10)
N5	7740(20)	7330(30)	9680(30)	99(9)

Table 9.117 – Anisotropic Displacement Parameters ($Å^2×10^3$) for IAJ701v_0m. The Anisotropic displacement factor exponent takes the form: $-2\pi^2[h^2a^{*2}U_{11}+2hka^*b^*U_{12}+\ldots]$.

Atom	**U_{11}**	**U_{22}**	**U_{33}**	**U_{23}**	**U_{13}**	**U_{12}**
Ir1	15.1(3)	15.8(3)	20.8(3)	0	6.41(19)	0
Cl1	19.7(10)	21.4(10)	28.6(11)	-1.0(8)	7.8(8)	-3.4(8)
N1	24(4)	24(4)	27(4)	2(3)	12(3)	6(3)
N2	25(4)	18(4)	26(4)	3(3)	7(3)	4(3)
N3	25(4)	24(4)	36(4)	-4(3)	12(3)	2(3)
N4	28(4)	29(4)	34(4)	0(3)	15(3)	2(3)
C1	40(5)	34(5)	28(5)	7(4)	12(4)	14(4)
C2	43(6)	44(6)	40(6)	16(5)	17(5)	22(5)
C3	24(5)	32(5)	34(5)	4(4)	6(4)	8(4)
C4	21(4)	22(5)	30(4)	1(3)	9(3)	3(3)
C5	17(4)	21(4)	26(4)	-1(3)	8(3)	-2(3)
C6	18(4)	20(4)	26(4)	-1(3)	7(3)	-4(3)

C7	25(4)	20(4)	30(4)	1(3)	12(3)	0(3)
C8	31(5)	27(5)	27(4)	-1(4)	12(4)	0(4)
C9	28(4)	25(5)	25(4)	4(4)	4(4)	3(4)
C10	21(4)	23(5)	26(4)	0(3)	4(3)	3(3)
C11	21(4)	16(4)	34(4)	-3(3)	10(3)	-2(3)
C12	24(4)	20(4)	34(4)	-1(3)	14(3)	1(3)
C13	23(4)	29(5)	39(5)	-4(4)	14(4)	0(3)
C14	22(5)	34(6)	48(5)	0(4)	13(4)	7(4)
C15	24(5)	30(5)	51(5)	-10(4)	17(4)	-1(4)
C16	31(5)	34(5)	45(5)	-9(4)	22(4)	-5(4)
C17	35(5)	31(5)	44(5)	-4(4)	24(4)	-5(4)
C18	28(5)	24(5)	41(5)	-2(4)	17(4)	0(3)
S1	33(3)	27(3)	44(3)	-4(2)	8(2)	-2(2)
F1	35(7)	96(10)	33(6)	7(6)	0(5)	8(7)
F2	70(5)	98(7)	71(6)	-27(5)	25(4)	-17(5)
F3	127(13)	35(6)	57(9)	26(6)	12(9)	12(7)
O1	76(7)	34(5)	76(6)	-9(5)	-20(5)	-1(5)
O2	35(7)	30(8)	74(11)	-1(8)	-2(7)	-8(6)
C19	48(7)	36(7)	40(7)	2(7)	1(7)	-9(8)
O3	270(30)	113(16)	180(20)	28(14)	59(19)	23(16)
C20	170(30)	59(19)	60(20)	-5(15)	45(18)	-48(16)
N5	160(30)	83(19)	62(18)	-8(14)	33(16)	-42(15)

Table 9.118 – Bond Lengths for IAJ701v_0m.

Atom	Atom	Length/Å		Atom	Atom	Length/Å
Ir1	Cl1	2.358(2)		C6	C7	1.407(13)
Ir1	Cl1[1]	2.358(2)		C7	C8	1.386(14)
Ir1	N1	2.021(7)		C7	C12	1.476(13)
Ir1	N1[1]	2.021(7)		C8	C9	1.373(14)
Ir1	N2	2.048(7)		C9	C10	1.405(13)
Ir1	N2[1]	2.047(7)		C11	C12	1.432(13)
N1	C1	1.348(12)		C13	C14	1.411(13)
N1	C5	1.364(11)		C13	C18	1.422(15)
N2	C6	1.349(12)		C14	C15	1.375(15)
N2	C10	1.343(12)		C15	C16	1.407(16)

N3	C11	1.309(12)		C16	C17	1.351(15)
N3	C13	1.362(13)		C17	C18	1.432(14)
N4	C12	1.315(12)		S1	O1	1.240(11)
N4	C18	1.369(12)		S1	O2	1.454(18)
C1	C2	1.385(14)		S1	C19	1.87(2)
C2	C3	1.391(15)		F1	C19	1.27(3)
C3	C4	1.400(13)		F2	C19	1.42(3)
C4	C5	1.395(12)		F3	C19	1.26(3)
C4	C11	1.469(13)		O3	N5	1.30(4)
C5	C6	1.429(13)		C20	N5	1.16(5)

Table 9.119 – Bond Angles for IAJ701v_0m.

Atom	**Atom**	**Atom**	**Angle/°**		**Atom**	**Atom**	**Atom**	**Angle/°**
$Cl1^{1}$	Ir1	Cl1	91.09(11)		C7	C6	C5	121.2(8)
N1	Ir1	Cl1	87.8(2)		C6	C7	C12	117.7(8)
$N1^{1}$	Ir1	$Cl1^{1}$	87.8(2)		C8	C7	C6	117.9(8)
N1	Ir1	$Cl1^{1}$	174.9(2)		C8	C7	C12	124.4(8)
$N1^{1}$	Ir1	Cl1	174.9(2)		C9	C8	C7	120.0(9)
$N1^{1}$	Ir1	N1	93.6(4)		C8	C9	C10	119.3(9)
$N1^{1}$	Ir1	N2	99.0(3)		N2	C10	C9	121.2(8)
$N1^{1}$	Ir1	$N2^{1}$	79.8(3)		N3	C11	C4	118.7(9)
N1	Ir1	$N2^{1}$	99.0(3)		N3	C11	C12	122.2(8)
N1	Ir1	N2	79.8(3)		C12	C11	C4	119.1(8)
N2	Ir1	Cl1	86.0(2)		N4	C12	C7	116.7(9)
$N2^{1}$	Ir1	$Cl1^{1}$	86.0(2)		N4	C12	C11	122.3(8)
N2	Ir1	$Cl1^{1}$	95.2(2)		C11	C12	C7	120.9(8)
$N2^{1}$	Ir1	Cl1	95.2(2)		N3	C13	C14	119.6(10)
$N2^{1}$	Ir1	N2	178.3(4)		N3	C13	C18	121.3(9)
C1	N1	Ir1	127.6(6)		C14	C13	C18	119.1(9)
C1	N1	C5	117.8(8)		C15	C14	C13	119.5(10)
C5	N1	Ir1	114.5(6)		C14	C15	C16	121.2(9)
C6	N2	Ir1	113.2(6)		C17	C16	C15	121.2(10)
C10	N2	Ir1	127.1(6)		C16	C17	C18	119.3(11)
C10	N2	C6	119.3(8)		N4	C18	C13	120.9(9)
C11	N3	C13	116.8(9)		N4	C18	C17	119.4(9)

C12	N4	C18	116.5(9)		C13	C18	C17	119.7(9)
N1	C1	C2	122.4(9)		O1	S1	O2	105.4(9)
C1	C2	C3	120.2(10)		O1	S1	C19	105.0(9)
C2	C3	C4	118.0(9)		O2	S1	C19	102.7(11)
C3	C4	C11	122.4(8)		F1	C19	S1	111.1(18)
C5	C4	C3	118.9(9)		F1	C19	F2	107.7(17)
C5	C4	C11	118.7(8)		F2	C19	S1	114.9(15)
N1	C5	C4	122.7(8)		F3	C19	S1	114.1(17)
N1	C5	C6	114.9(8)		F3	C19	F1	109(2)
C4	C5	C6	122.4(8)		F3	C19	F2	99(2)
N2	C6	C5	116.7(8)		C20	N5	O3	124(4)
N2	C6	C7	122.1(8)					

Table 9.120 – Torsion Angles for IAJ701v_0m.

A	**B**	**C**	**D**	**Angle/°**		**A**	**B**	**C**	**D**	**Angle/°**
Ir1	N1	C1	C2	-177.1(9)		C6	C7	C8	C9	-4.0(14)
Ir1	N1	C5	C4	176.0(7)		C6	C7	C12	N4	-178.4(8)
Ir1	N1	C5	C6	-6.4(10)		C6	C7	C12	C11	3.8(13)
Ir1	N2	C6	C5	7.8(10)		C7	C8	C9	C10	3.5(15)
Ir1	N2	C6	C7	-173.2(7)		C8	C7	C12	N4	-0.9(14)
Ir1	N2	C10	C9	171.5(7)		C8	C7	C12	C11	-178.7(9)
N1	C1	C2	C3	1.6(19)		C8	C9	C10	N2	-1.3(14)
N1	C5	C6	N2	-1.0(12)		C10	N2	C6	C5	-179.2(8)
N1	C5	C6	C7	179.9(8)		C10	N2	C6	C7	-0.2(13)
N2	C6	C7	C8	2.3(14)		C11	N3	C13	C14	-178.7(9)
N2	C6	C7	C12	180.0(8)		C11	N3	C13	C18	1.2(14)
N3	C11	C12	N4	1.4(15)		C11	C4	C5	N1	-179.5(8)
N3	C11	C12	C7	179.2(9)		C11	C4	C5	C6	3.1(13)
N3	C13	C14	C15	-179.6(9)		C12	N4	C18	C13	0.6(14)
N3	C13	C18	N4	-0.8(15)		C12	N4	C18	C17	-179.3(9)
N3	C13	C18	C17	179.2(9)		C12	C7	C8	C9	178.6(9)
C1	N1	C5	C4	-1.3(14)		C13	N3	C11	C4	-179.2(8)
C1	N1	C5	C6	176.3(9)		C13	N3	C11	C12	-1.5(13)
C1	C2	C3	C4	-1.4(17)		C13	C14	C15	C16	0.0(16)
C2	C3	C4	C5	0.0(15)		C14	C13	C18	N4	179.1(9)

C2	C3	C4	C11	-179.1(10)		C14	C13	C18	C17	-0.9(15)
C3	C4	C5	N1	1.4(14)		C14	C15	C16	C17	0.0(16)
C3	C4	C5	C6	-176.0(9)		C15	C16	C17	C18	-0.4(16)
C3	C4	C11	N3	-3.4(14)		C16	C17	C18	N4	-179.2(10)
C3	C4	C11	C12	178.8(9)		C16	C17	C18	C13	0.9(15)
C4	C5	C6	N2	176.6(8)		C18	N4	C12	C7	-178.7(8)
C4	C5	C6	C7	-2.4(14)		C18	N4	C12	C11	-0.9(14)
C4	C11	C12	N4	179.1(9)		C18	C13	C14	C15	0.5(15)
C4	C11	C12	C7	-3.1(13)		O1	S1	C19	F1	-168.6(16)
C5	N1	C1	C2	-0.2(16)		O1	S1	C19	F2	68.8(17)
C5	C4	C11	N3	177.5(8)		O1	S1	C19	F3	-45(2)
C5	C4	C11	C12	-0.3(13)		O2	S1	C19	F1	-58.5(18)
C5	C6	C7	C8	-178.7(8)		O2	S1	C19	F2	178.9(15)
C5	C6	C7	C12	-1.0(13)		O2	S1	C19	F3	66(2)
C6	N2	C10	C9	-0.4(13)						

Table 9.121 – Hydrogen Atom Coordinates (Å×10^4) and Isotropic Displacement Parameters (Å^2×10^3) for IAJ701v_0m.

Atom	*x*	*y*	*z*	U(eq)
H1	5751.83	6806.41	9151.18	40
H2	6565.79	5738.29	9222.16	49
H3	7033.91	5611.91	7783.11	36
H8	5699.49	8307.29	3520.12	33
H9	4802.9	9144.77	3618.26	32
H10	4477.52	9139.02	5210.77	28
H14	8110.82	5019.06	5584.05	41
H15	8491.82	5007.51	4070.61	41
H16	8032.34	5953.15	2598.27	42
H17	7191.53	6922.37	2609.45	41
H20A	7986.58	6497.02	8851.97	139
H20B	8477.64	6775.1	9932.94	139
H20C	8314.32	7531.7	8977.42	139

Table 9.122 – Atomic Occupancy for IAJ701v_0m.

Atom	Occupancy		Atom	Occupancy		Atom	Occupancy
S1	0.5		F1	0.5		F3	0.5
O2	0.5		C19	0.5		C20	0.5
H20A	0.5		H20B	0.5		H20C	0.5
N5	0.5						

Crystal Structure Determination of IAJ701v_0m

Crystal Data for $C_{38}H_{23}Cl_2F_4IrN_9O_5S$ (M =1056.81 g/mol): monoclinic, space group C2/c (no. 15), a = 22.099(4) Å, b = 13.896(3) Å, c = 13.001(3) Å, β = 104.058(7)°, V = 3872.8(13) Å^3, Z = 4, T = 100.0 K, μ(CuKα) = 9.125 mm^{-1}, *Dcalc* = 1.813 g/cm^3, 24261 reflections measured (7.582° ≤ 2Θ ≤ 133.876°), 3434 unique (R_{int} = 0.0511, R_{sigma} = 0.0292) which were used in all calculations. The final R_1 was 0.0593 (I > 2σ(I)) and wR_2 was 0.1491 (all data).